Vol. 65 ■ No. 6 ■ June 2024

JNM

The Journal of Nuclear Medicine

JNM Podcasts
jnm.snmjournals.org/podcasts

Coming soon:
a conversation on
^{212}Pb

FEATURED ARTICLE

Safety and Efficacy of Extended Therapy with [^{177}Lu]Lu-PSMA: A German Multicenter Study.
Robert Seifert et al. See page 909.

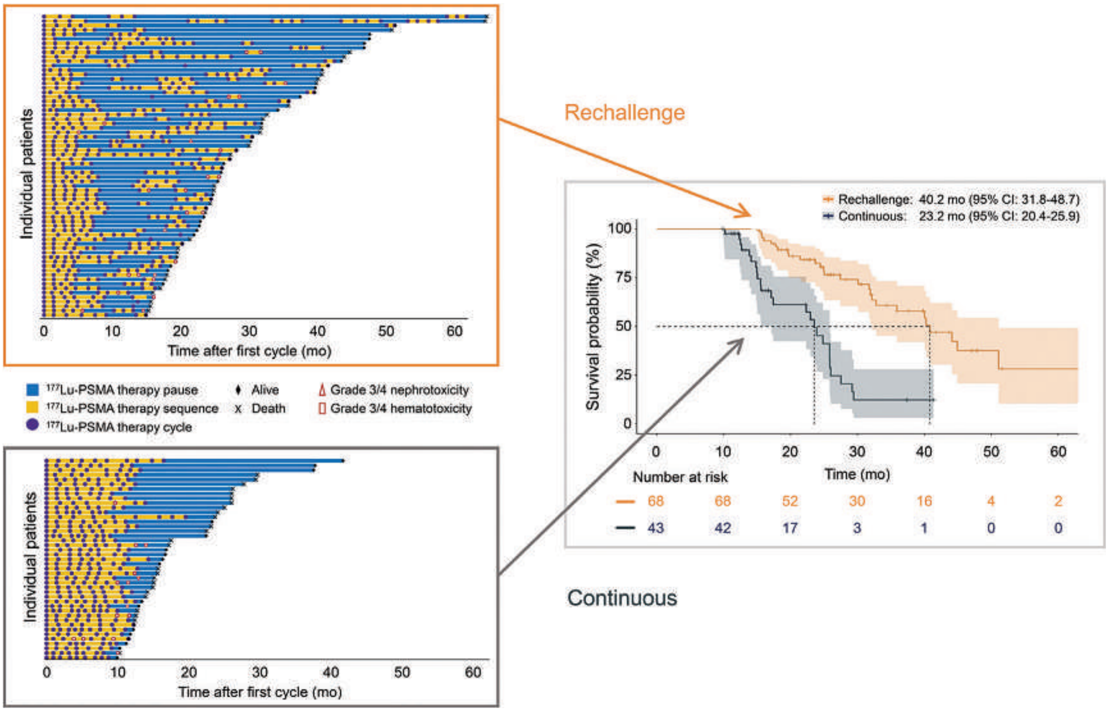

CLDN18.2 molecular imaging: ^{68}Ga PET targets expression of a transmembrane protein isoform as a promising biomarker in gastrointestinal cancer. Changsong Qi et al. See page 856.

SOCIETY OF
NUCLEAR MEDICINE &
MOLECULAR IMAGING

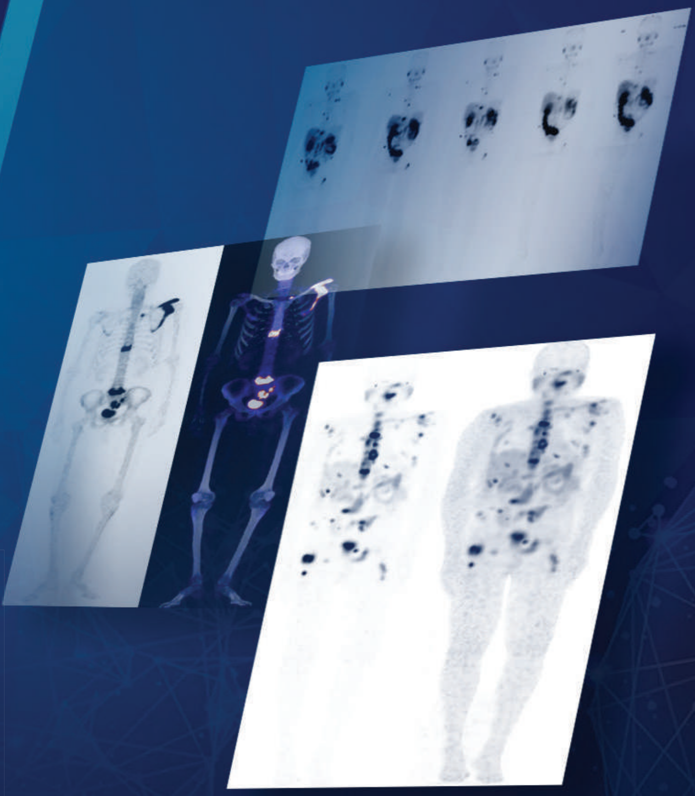

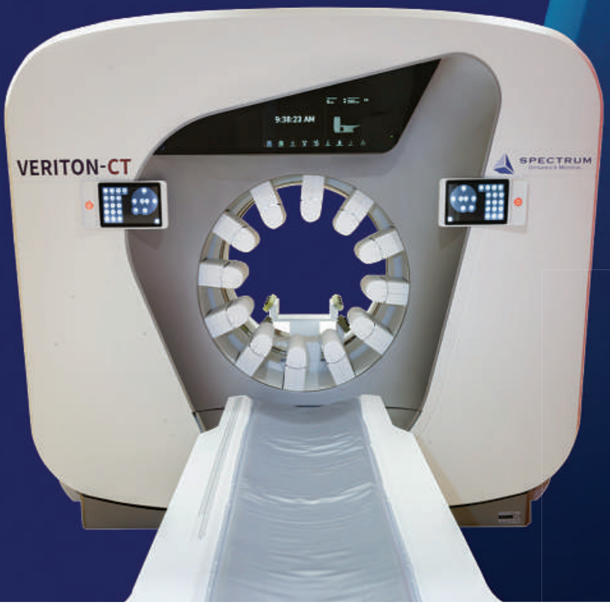
VERITON-CT
SPECTRUM

Now Available!

Radiopharmaceutical Therapy Accreditation

The new program offers facilities a mechanism for demonstrating their commitment to quality and patient safety in radiopharmaceutical therapy and **augments the existing IAC accreditation areas of Nuclear Cardiology, General Nuclear Medicine and PET**.

Radiopharmaceutical Therapy Accreditation Program

SNMMI SOCIETY OF NUCLEAR MEDICINE & MOLECULAR IMAGING | IAC INTERSOCIETAL ACCREDITATION COMMISSION

SNMMI and IAC are pleased to recognize the first three facilities to be awarded Radiopharmaceutical Therapy Accreditation:

BAMF Health | **Carilion Clinic Targeted Therapy Center** | **Stanford Health Care**

First to Earn Accreditation Discuss Value ...

"**The IAC application and review process was an in-depth and meaningful exercise that allowed us to identify opportunities for improvements. We are now better positioned to provide excellent care to our patients**. The IAC Radiopharmaceutical Therapy Accreditation is a testimony to the hard work of everyone involved in Theragnostics at Stanford and a guarantee of exceptional services for our patients, referring providers and payors."

Andrei Iagaru, MD and Tina Visser CNMT

Stanford Health Care | Stanford, CA

"**Preparation for accreditation made us stronger requiring >40 hours of technical support and allowed for improvement in several areas with new standards.** It is important for these standards to be embraced to solidify our utility in our patients' care pathways. We are very grateful for the recognition you have given our program and look forward to continuing to help define the path for excellence in these therapies in conjunction with the IAC."

Jackson W. Kiser, MD

Medical Director and Section Chief Molecular Imaging and Theranostics
Carilion Clinic Targeted Therapy Center

IAC

Improving health care through accreditation®

intersocietal.org | 800.838.2110

Visit IAC at SNMMI 2024 (Booth NPK7)!

Scan the QR code to complete an interest form or visit **intersocietal.org/nuclear**.

JNM

Volume 65 • Number 6 • June 2024

EDITOR'S PAGE

825 *JNM* Editors' Choice Awards for 2023
Johannes Czernin

DISCUSSIONS WITH LEADERS

826 Inventing His Own Career Path: Freek Beekman Talks with Johannes Czernin and Christine Mona About Success in Academia and Industry
Freek Beekman, Johannes Czernin, and Christine Mona

CONTINUING EDUCATION

829 Evaluation of Neurodegenerative Disorders with Amyloid-β, Tau, and Dopaminergic PET Imaging: Interpretation Pitfalls
Brian J. Burkett, Derek R. Johnson, and Val J. Lowe

ONCOLOGY

Clinical

838 MRI and ^{18}F-FET PET for Multimodal Treatment Monitoring in Patients with Brain Metastases: A Cost-Effectiveness Analysis
Jurij Rosen, Jan-Michael Werner, Garry S. Ceccon, Elena K. Rosen, Michael M. Wollring, Isabelle Stetter, Philipp Lohmann, Felix M. Mottaghy, Gereon R. Fink, Karl-Josef Langen, et al.

845 Detecting Metastatic Patterns of Oligometastatic Breast Cancer: A Comparative Analysis of ^{18}F-FDG PET/CT and Conventional CT Imaging
Rebecca Moser, Sophie Pfeiffer, Lisena Cala, Evelyn Klein, Marion Kiechle, Sophie T. Behzadi, Eva Fallenberg, Stephanie E. Combs, Wolfgang Weber, and Kai J. Borm

851 ■ BRIEF COMMUNICATION. Early Metabolic Response by PET Predicts Sensitivity to Next-Line Targeted Therapy in *EGFR*-Mutated Lung Cancer with Unknown Mechanism of Acquired Resistance
Martin Schuler, Jörg Hense, Kaid Darwiche, Sebastian Michels, Hubertus Hautzel, Carsten Kobe, Smiths Lueong, Martin Metzenmacher, Thomas Herold, Gregor Zaun, et al.

856 ■ FEATURED CLINICAL INVESTIGATION ARTICLE. ^{68}Ga-NC-BCH Whole-Body PET Imaging Rapidly Targets Claudin18.2 in Lesions in Gastrointestinal Cancer Patients
Changsong Qi, Rui Guo, Yan Chen, Chenzhen Li, Chang Liu, Miao Zhang, Cheng Zhang, Xiaotian Zhang, Xingguo Hou, Bo Chen, et al.

864 Detecting High-Dose Methotrexate–Induced Brain Changes in Pediatric and Young Adult Cancer Survivors Using [^{18}F]FDG PET/MRI: A Pilot Study
Lucia Baratto, Shashi B. Singh, Sharon E. Williams, Sheri L. Spunt, Jarrett Rosenberg, Lisa Adams, Vidyani Suryadevara, Michael Iv, and Heike Daldrup-Link

THERANOSTICS

Clinical

872 Diagnostic Potential of Supplemental Static and Dynamic ^{68}Ga-FAPI-46 PET for Primary ^{18}F-FDG–Negative Pulmonary Lesions
Manuel Röhrich, Johanna Daum, Ewgenija Gutjahr, Anna-Maria Spektor, Frederik M. Glatting, Yasemin Aylin Sahin, Hans Georg Buchholz, Jorge Hoppner, Cathrin Schroeter, Eleni Mavriopoulou, et al.

880 ^{68}Ga-Fibroblast Activation Protein Inhibitor PET/CT Improves Detection of Intermediate and Low-Grade Sarcomas and Identifies Candidates for Radiopharmaceutical Therapy
Helena Lanzafame, Ilektra A. Mavroeidi, Kim M. Pabst, Mélanie Desaulniers, Marc Ingenwerth, Nader Hirmas, Lukas Kessler, Michael Nader, Timo Bartel, Stephan Leyser, et al.

888 A Systematic Review on the Diagnostic Value of Fibroblast Activation Protein Inhibitor PET/CT in Genitourinary Cancers
Marinus J. Hagens, Pim J. van Leeuwen, Maurits Wondergem, Thierry N. Boellaard, Francesco Sanguedolce, Daniela E. Oprea-Lager, Axel Bex, André N. Vis, Henk G. van der Poel, and Laura S. Mertens; in collaboration with the EAU Section of Urological Imaging

897 Prospective Comparison of ^{68}Ga-NeoB and ^{68}Ga-PSMA-R2 PET/MRI in Patients with Biochemically Recurrent Prostate Cancer
Heying Duan, Hong Song, Guido A. Davidzon, Farshad Moradi, Tie Liang, Andreas Loening, Shreyas Vasanawala, and Andrei Iagaru

904 Development of a Visually Calculated SUV$_{mean}$ (HIT Score) on Screening PSMA PET/CT to Predict Treatment Response to ^{177}Lu-PSMA Therapy: Comparison with Quantitative SUV$_{mean}$ and Patient Outcomes
Mina Swiha, Nathan Papa, Zahra Sabahi, Narjess Ayati, Nikeith John, Sarennya Pathmanandavel, Megan Crumbaker, Sherrington Li, Shikha Agrawal, Maria Ayers, et al.

909 ■ FEATURED ARTICLE OF THE MONTH. Safety and Efficacy of Extended Therapy with [^{177}Lu]Lu-PSMA: A German Multicenter Study
Robert Seifert, Tugce Telli, Constantin Lapa, Mélanie Desaulniers, Turkay Hekimsoy, Wolfgang A. Weber, Christian Pfob, Boris Hadaschik, Martin Bögemann, Michael Schäfers, et al.

917 RECIP 1.0 Predicts Progression-Free Survival After [^{177}Lu]Lu-PSMA Radiopharmaceutical Therapy in Patients with Metastatic Castration-Resistant Prostate Cancer
Andrei Gafita, Loic Djaileb, Isabel Rauscher, Wolfgang P. Fendler, Boris Hadaschik, Steven P. Rowe, Ken Herrmann, Lilja B. Solnes, Jeremie Calais, Matthew B. Rettig, et al.

923 **Absorbed Dose–Response Relationship in Patients with Gastroenteropancreatic Neuroendocrine Tumors Treated with [^{177}Lu]Lu-DOTATATE: One Step Closer to Personalized Medicine**
Kévin Hebert, Lore Santoro, Maeva Monnier, Florence Castan, Ikrame Berkane, Eric Assénat, Cyril Fersing, Pauline Gélibert, Jean-Pierre Pouget, Manuel Bardiès, et al.

931 **Safety and Efficacy of *Para*-Aminohippurate Coinfusion for Renal Protection During Peptide Receptor Radiotherapy in Patients with Neuroendocrine Tumors**
Alexandros Moraitis, Walter Jentzen, Pedro Fragoso Costa, David Kersting, Stephan Himmen, Marta Coelho, Marian Meckel, Cees J.A. van Echteld, Wolfgang P. Fendler, Ken Herrmann, et al.

RADIOBIOLOGY/DOSIMETRY

Clinical

938 **^{68}Ga-FAP-2286 PET of Solid Tumors: Biodistribution, Dosimetry, and Comparison with ^{18}F-FDG**
Brad Kline, Surekha Yadav, Youngho Seo, Robin Cumming Ippisch, Jessa Castillo, Rahul R. Aggarwal, Robin Kate Kelley, Spencer C. Behr, Robert R. Flavell, Courtney Lawhn-Heath, et al.

CARDIOVASCULAR

Clinical

944 **Prognostic Value of [^{99m}Tc]Tc-DPD Quantitative SPECT/CT in Patients with Suspected and Confirmed Amyloid Transthyretin–Related Cardiomyopathy and Preserved Left Ventricular Function**
Federico Caobelli, Nasir Gözlügöl, Adam Bakula, Axel Rominger, Robin Schepers, Stefan Stortecky, Lukas Hunziker Munsch, Stephan Dobner, and Christoph Gräni

NEUROLOGY

Clinical

952 ■ **BRIEF COMMUNICATION. Improved Tau PET SUVR Quantification in 4-Repeat Tau Phenotypes with [^{18}F]PI-2620**
Gérard N. Bischof, Matthias Brendel, Henryk Barthel, Hendrik Theis, Michael Barbe, Peter Bartenstein, Joseph Claasen, Adrian Danek, Günter Höglinger, Johannes Levin, et al.

Translational/Basic

956 **PET Quantification of [^{18}F]VAT in Human Brain and Its Test–Retest Reproducibility and Age Dependence**
John L. O'Donnell, Anil Kumar Soda, Hao Jiang, Scott A. Norris, Baijayanta Maiti, Morvarid Karimi, Meghan C. Campbell, Stephen M. Moerlein, Zhude Tu, and Joel S. Perlmutter

AI/ADVANCED IMAGE ANALYSIS

Basic

962 **Is PET Radiomics Useful to Predict Pathologic Tumor Response and Prognosis in Locally Advanced Cervical Cancer?**
Angela Collarino, Vanessa Feudo, Tina Pasciuto, Anita Florit, Elisabeth Pfaehler, Marco de Summa, Nicolò Bizzarri, Salvatore Annunziata, Gian Franco Zannoni, Lioe-Fee de Geus-Oei, et al.

971 **Mapping ^{18}F-FDG Kinetics Together with Patient-Specific Bootstrap Assessment of Uncertainties: An Illustration with Data from a PET/CT Scanner with a Long Axial Field of View**
Qi Wu, Fengyun Gu, Liam D. O'Suilleabhain, Hasan Sari, Song Xue, Kuangyu Shi, Axel Rominger, and Finbarr O'Sullivan

980 **A Deep-Learning–Based Partial-Volume Correction Method for Quantitative ^{177}Lu SPECT/CT Imaging**
Julian Leube, Johan Gustafsson, Michael Lassmann, Maikol Salas-Ramirez, and Johannes Tran-Gia

THE ILLUSTRATED POST

988 **SSTR Antagonists as Theranostic Option in Merkel Cell Carcinoma**
Malte Kircher, Adriana Amerein, Mareike Augustin, Nic G. Reitsam, Johanna S. Enke, Marianne Patt, Georgine Wienand, Ralph A. Bundschuh, Christian H. Pfob, Constantin Lapa, et al.

THE ILLUSTRATED POST

990 **[^{18}F]Fluoroestradiol Uptake in Irradiated Lung Parenchyma and Draining Nodes**
Audrey A. Rich, Neil K. Taunk, David A. Mankoff, Austin R. Pantel, and Sophia R. O'Brien

LETTERS TO THE EDITOR

992 **Is Permeability Surface Area Product of [^{18}F]Florbetaben Comparable to That of H_2O?**
Masashi Kameyama

992 **Artificial Intelligence Algorithms Are Not Clairvoyant**
Bradley J. Beattie

993 ■ **REPLY. Artificial Intelligence Algorithms Are Not Clairvoyant**
Joyita Dutta, Vibha Balaji, and Tzu-An Song

DEPARTMENTS

8A **This Month in JNM**

11A **Message from the President**

JNM The Journal of
NUCLEAR MEDICINE

The Official Publication of **SNMMI**

MISSION STATEMENT: *The Journal of Nuclear Medicine* advances the knowledge and practice of molecular imaging and therapy and nuclear medicine to improve patient care through publication of original basic science and clinical research.

JNM (ISSN 0161-5505 [print]; ISSN 2159-662X [online]) is published monthly by SNMMI, 1850 Samuel Morse Drive, Reston, VA 20190-5316. Periodicals postage is paid at Herndon, VA, and additional mailing offices. Postmaster, send address changes to *The Journal of Nuclear Medicine,* 1850 Samuel Morse Drive, Reston, VA 20190-5316. The costs of publication of all nonsolicited articles in *JNM* were defrayed in part by the payment of page charges. Therefore, and solely to indicate this fact, these articles are hereby designated “advertisements” in accordance with 18 USC section 1734.

DISCLOSURE OF COMMERCIAL INTEREST: Johannes Czernin, MD, editor-in-chief of *The Journal of Nuclear Medicine,* has indicated that he is a founder of Sofie Biosciences and holds equity in the company and in intellectual property invented by him, patented by the University of California, and licensed to Sofie Biosciences. He is also a founder and board member of Trethera Therapeutics and holds equity in the company and in intellectual property invented by him, patented by the University of California, and licensed to Trethera Therapeutics. He also serves on the scientific advisory boards of RayzeBio and Aktis Oncology. No other potential conflicts of interest were reported. Manuscripts submitted to *JNM* with potential conflicts are handled by a guest editor.

EDITORIAL COMMUNICATIONS should be sent to: Editor-in-Chief, Johannes Czernin, MD, *JNM* Office, SNMMI, 1850 Samuel Morse Drive, Reston, VA 20190-5316. Phone: (703) 326-1185; Fax: (703) 708-9018. To submit a manuscript, go to https://submit-jnm.snmjournals.org.

BUSINESS COMMUNICATIONS concerning permission requests should be sent to the publisher, SNMMI, 1850 Samuel Morse Drive, Reston, VA 20190-5316; (703) 708-9000; home page address: jnm.snmjournals.org. Subscription requests and address changes should be sent to Membership Department, SNMMI at the address above. Notify the Society of change of address and telephone number at least 30 days before date of issue by sending both the old and new addresses. Claims for copies lost in the mail are allowed within 90 days of the date of issue. Claims are not allowed for issues lost as a result of insufficient notice of change of address. For information on advertising, contact Team SNMMI (Kevin Dunn, Rich Devanna, and Charlie Meitner; (201) 767-4170; fax: (201) 767-8065; TeamSNMMI@cunnasso.com). Advertisements are subject to editorial approval and are restricted to products or services pertinent to nuclear medicine. Closing date is the first of the month preceding the date of issue.

INDIVIDUAL SUBSCRIPTION RATES for the 2024 calendar year are $665 within the United States and Canada; $714 elsewhere. Make checks payable to the SNMMI. CPC IPM Sales Agreement No. 1415158. Sales of individual back copies from 1999 through the current issue are available for $60 at http://www.snmmi.org/subscribe (subscriptions@snmmi.org; fax: (703) 667-5134). Individual articles are available for sale online at http://jnm.snmjournals.org.

EDITOR-IN-CHIEF

Johannes Czernin, MD
University of California at Los Angeles
Los Angeles, California

IMMEDIATE PAST EDITOR

Dominique Delbeke, MD, PhD
Vanderbilt University Medical Center
Nashville, Tennessee

ASSOCIATE EDITORS, CONTINUING EDUCATION

Hossein Jadvar, MD, PhD, MPH, MBA, MSL, FACNM, FSNMMI
University of Southern California
Los Angeles, California
Lale Kostakoglu, MD, MPH
University of Virginia Health System
Charlottesville, Virginia

ASSOCIATE EDITORS

Ramsey Derek Badawi, PhD
UC Davis Medical Center
Sacramento, California
Henryk Barthel, MD, PhD
Leipzig University
Leipzig, Germany
Frank M. Bengel, MD
Hannover Medical School
Hannover, Germany
Lisa Bodei, MD, PhD
Memorial Sloan Kettering Cancer Center
New York, New York
Irene Buvat, PhD
Université Paris Sud
Orsay, France
Jérémie Calais, MD
University of California at Los Angeles
Los Angeles, California
Sharmila Dorbala, MBBS
Brigham and Women's Hospital
Lexington, Massachusetts
Alexander E. Drzezga, MD
University Hospital of Cologne
Cologne, Germany
Jan Grimm, MD, PhD
Memorial Sloan Kettering Cancer Center
New York, New York
Ken Herrmann, MD, MBA
Universitätsklinikum Essen
Essen, Germany
Thomas A. Hope, MD
University of California, San Francisco
San Francisco, California
Jason S. Lewis, PhD
Memorial Sloan Kettering Cancer Center
New York, New York
David A. Mankoff, MD, PhD
University of Pennsylvania
Philadelphia, Pennsylvania
Heiko Schöder, MD
Memorial Sloan Kettering Cancer Center
New York, New York
Wolfgang Weber, MD
Technical University of Munich
München, Germany

SERIES EDITOR, FOCUS ON MI

Carolyn J. Anderson, PhD
University of Missouri
Columbia, Missouri

SERIES EDITOR, HOT TOPICS

Heinrich R. Schelbert, MD, PhD
University of California at Los Angeles
Los Angeles, California

CONSULTING EDITORS

Nancy Knight, PhD
University of Maryland School of Medicine
Baltimore, Maryland
Barry A. Siegel, MD
Mallinckrodt Institute of Radiology
St. Louis, Missouri
Arnold M. Strashun, MD
SUNY Downstate Medical Center
Scarsdale, New York
H. William Strauss, MD
Memorial Sloan Kettering Cancer Center
New York, New York

ASSOCIATE EDITORS (INTERNATIONAL)

Gerald Antoch, MD
Dusseldorf, Germany
Richard P. Baum, MD, PhD
Bad Berka, Germany
Ambros J. Beer, MD
Ulm, Germany
François Bénard, MD, FRCPC
Vancouver, Canada
Thomas Beyer, PhD
Vienna, Austria
Andreas K. Buck, MD, PhD
Würzburg, Germany
Ignasi Carrió, MD
Barcelona, Spain
June-Key Chung, MD
Seoul, Korea
Matthias Eiber, MD
Munich, Germany
Louise M. Emmett, MBChB, FRACP, MD
Sydney, Australia
Stefano Fanti, MD
Bologna, Italy
Wolfgang Peter Fendler, MD
Munich, Germany
Markus Hacker, MD
Wien, Austria
Rodney J. Hicks, MD, FRACP
Melbourne, Australia
Michael S. Hofman, MBBS, FRACP
Melbourne, Australia
Ora Israel, MD
Haifa, Israel
Andreas Kjaer, MD, PhD, DMSc
Copenhagen, Denmark
Adriaan A. Lammertsma, PhD
Amsterdam, The Netherlands
Michael Lassman, PhD
Würzburg, Germany
Helmut R. Mäcke, PhD
Freiburg, Germany
Wim J.G. Oyen, MD, PhD
Milan, Italy
John O. Prior, MD, PhD
Lausanne, Switzerland
Osman Ratib, MD, PhD
Geneva, Switzerland
Mike Sathekge, MBChB, MMed, PhD
Pretoria, South Africa
Markus Schwaiger, MD
München, Germany
Andrew M. Scott, MD
Heidelberg, Australia
Nagara Tamaki, MD, PhD
Kyoto, Japan
Jia-He Tian, PhD
Beijing, China
Mei Tian, MD, PhD
Hangzhou, China

EDITORIAL CONSULTANTS

Martin S. Allen-Auerbach, MD
Los Angeles, California
Magnus Dahlbom, PhD
Los Angeles, California
Andrew Quon, MD
Los Angeles, California
Christiaan Schiepers, MD, PhD
Los Angeles, California
Daniel H. Silverman, MD, PhD
Los Angeles, California
Roger Slavik, PhD
Winterthur, Switzerland

EDITORIAL BOARD

Diane S. Abou, PhD
St. Louis, Missouri
Hojjat Ahmadzadehfar, MD
Dortmund, Germany
Valentina Ambrosini, MD, PhD
Bologna, Italy
Norbert Avril, MD
Cleveland, Ohio
Shadfar Bahri
Los Angeles, California
Jacques Barbet, PhD
Saint-Herbalin, France
Bradley Jay Beattie, PhD
New York, New York
Freek J. Beekman, PhD
Delft, The Netherlands
Matthias Richard Benz, MD
Los Angeles, California
Elie Besserer-Offroy, PhD, FACSc
Los Angeles, California
Pradeep Bhambhvani, MD
Birmingham, Alabama
Angelika Bischof-Delaloye, MD
Lausanne, Switzerland
Christina Bluemel, MD
Würzburg, Germany
Ronald Boellaard, PhD
Groningen, The Netherlands
Nicolaas Bohnen, MD
Ann Arbor, Michigan
Wesley E. Bolch, PhD
Gainesville, Florida
Elias H. Botvinick, MD
San Francisco, California
Winfried Brenner, MD, PhD
Berlin, Germany
Richard C. Brunken, MD
Cleveland, Ohio
Ralph Buchert, PhD
Hamburg, Germany
Alfred Buck, MD
Menzingen, Switzerland
Denis B. Buxton, PhD
Bethesda, Maryland
Weibo Cai, PhD
Madison, Wisconsin
Federico Caobelli, MD
Basel, Switzerland
Giuseppe Carlucci, PhD
Los Angeles, California
Richard E. Carson, PhD
New Haven, Connecticut
Paolo Castellucci, MD
Bologna, Italy
Franscesco Ceci, MD, PhD
Turin, Italy
Juliano J. Cerci
Curitiba, Brazil
Delphine Chen, MD
Seattle, Washington
Xiaoyuan Chen, PhD
Singapore
Simon R. Cherry
Davis, California
Arturo Chiti, MD
Rozzano, Italy
Peter M. Clark, PhD
Los Angeles, California
Christian Cohade, MD
Montreal, Canada
Ekaterina (Kate) Dadachova, PhD
Saskatoon, Canada
Issa J. Dahabreh, MD
Boston, Massachusetts
Heike Elisabeth Daldrup-Link, MD, PhD
Stanford, California
Farrokh Dehdashti, MD
St. Louis, Missouri
Robert C. Delgado-Bolton, MD, PhD
Logroño, Spain
Thorsten Derlin, MD
Hannover, Germany
Elisabeth G.E. de Vries, PhD
Groningen, The Netherlands
Marcelo F. Di Carli, MD
Boston, Massachusetts
David W. Dick, PhD
Iowa City, Iowa
Vasken Dilsizian, MD
Baltimore, Maryland
Jacob Dubroff, MD, PhD
Philadelphia, Pennsylvania
Janet F. Eary, MD
Bethesda, Maryland
W. Barry Edwards, PhD
Columbia, Missouri
David Eidelberg, MD
Manhasset, New York
Georges El Fakhri, PhD
Boston, Massachusetts
Peter J. Ell, MD
London, United Kingdom
Keigo Endo, MD
Nantan, Japan
Einat Even-Sapir, MD, PhD
Tel Aviv, Israel
Frederic H. Fahey, DSc
Boston, Massachusetts

EDITORIAL BOARD, continued

Melpomeni Fani, PhD, MSc
Basel, Switzerland
Andrea Farolfi, MD
Bologna, Italy
James W. Fletcher, MD
Indianapolis, Indiana
Amy M. Fowler, MD, PhD
Madison, Wisconsin
Kirk A. Frey, MD, PhD
Ann Arbor, Michigan
Andrei Gafita
Los Angeles, California
Victor H. Gerbaudo, PhD, MSHCA
Boston, Massachusetts
Frederik L. Giesel, MD, PhD, MBA
Düsseldorf, Germany
Karolien Goffin, MD, PhD
Leuven, Belgium
Serge Goldman, MD, PhD
Brussels, Belgium
Stanley J. Goldsmith, MD
New York, New York
Martin Gotthardt, MD, PhD
Nijmegen, The Netherlands
Michael Graham, MD, PhD
Iowa City, Iowa
David Groheux, MD, PhD
Paris, France
Uwe A. Haberkorn, MD
Heidelberg, Germany
Mathieu Hatt, PhD, HDR
Brest, France
Wolf-Dieter Heiss, MD
Cologne, Germany
Karl Herholz, MD
Manchester, United Kingdom
Thomas F. Heston, MD
Las Vegas, Nevada
John M. Hoffman, MD
Salt Lake City, Utah
Carl K. Hoh, MD
San Diego, California
Jason P. Holland, DPhil
Zurich, Switzerland
Roland Hustinx, MD, PhD
Liege, Belgium
Andrei H. Iagaru, MD
Stanford, California
Masanori Ichise, MD
Chiba, Japan
Amir Iravani, MD
Seattle, Washington
Heather A. Jacene, MD
Boston, Massachusetts
Francois Jamar, MD, PhD
Brussels, Belgium
Jae Min Jeong, PhD
Seoul, Korea
John A. Katzenellenbogen, PhD
Urbana, Illinois
Zohar Keidar, MD, PhD
Haifa, Israel
Kimberly A. Kelly, PhD
Charlottesville, Virginia
Laura M. Kenny, MD, PhD
London, United Kingdom
Fabian Kiessling, MD
Aachen, Germany
E. Edmund Kim, MD, MS
Orange, California
Francoise Kraeber-Bodéré, MD, PhD
Nantes, France
Clemens Kratochwil, MD
Heidelberg, Germany
Kenneth A. Krohn, PhD
Portland, Oregon
Brenda F. Kurland, PhD
Pittsburgh, Pennsylvania
Constantin Lapa, MD
Augsburg, Germany
Suzanne E. Lapi, PhD
Birmingham, Alabama
Steven M. Larson, MD
New York, New York
Dong Soo Lee, MD, PhD
Seoul, Korea
Jeffrey Leyton, PhD
Sherbrooke, Canada
Xiang-Guo Li, PhD
Turku, Finland
Hannah M. Linden, MD
Seattle, Washington
Martin A. Lodge, PhD
Baltimore, Maryland
Katharina Lückerath, PhD
Los Angeles, California
Susanne Lütje, MD, PhD
Bonn, Germany
Umar Mahmood, MD, PhD
Boston, Massachusetts
H. Charles Manning, PhD
Nashville, Tennessee
Giuliano Mariani, MD
Pisa, Italy
Chester A. Mathis, PhD
Pittsburgh, Pennsylvania
Alan H. Maurer, MD
Philadelphia, Pennsylvania
Jonathan McConathy, MD, PhD
Birmingham, Alabama
Alexander J.B. McEwan, MD
Edmonton, Canada
Yusuf Menda, MD
Iowa City, Iowa
Philipp T. Meyer, MD, PhD
Freiburg, Germany
Matthias Miederer, MD
Mainz, Germany
Jasna Mihailovic, MD, PhD
Sremska Kamenica, Serbia
Erik Mittra, MD, PhD
Portland, Oregon
Christine E. Mona, PhD
Los Angeles, California
Dae Hyuk Moon, MD
Seoul, Korea
Jennifer Murphy, PhD
Los Angeles, California
Helen Nadel, MD, FRCPC
Stanford, California
Matthias Nahrendorf, MD, PhD
Boston, Massachusetts
Yuji Nakamoto, MD, PhD
Kyoto, Japan
David A. Nathanson, PhD
Los Angeles, California
Nghi C. Nguyen, MD, PhD
Dallas, Texas
Sridhar Nimmagadda, PhD
Baltimore, Maryland
Egbert U. Nitzsche, MD
Aarau, Switzerland
Daniela E. Oprea-Lager, MD, PhD
Amsterdam, The Netherlands
Medhat M. Osman, MD, PhD
Saint Louis, Missouri
Christopher J. Palestro, MD
New Hyde Park, New York
Miguel Hernandez Pampaloni, MD, PhD
San Francisco, California
Neeta Pandit-Taskar, MD
New York, New York
Ashwin Singh Parihar, MBBS, MD
Saint Louis, Missouri
Michael E. Phelps, PhD
Los Angeles, California
Gerold Porenta, MD, PhD
Vienna, Austria
Sophie Poty, PhD
Montpellier, France
Edwin (Chuck) Pratt, PhD, MS Eng
New York, New York
Daniel A. Pryma, MD
Philadelphia, Pennsylvania
Valery Radchenko, PhD
Vancouver, Canada
Caius G. Radu, MD
Los Angeles, California
Isabel Rauscher, MD
Munich, Germany
Nick S. Reed, MBBS
Glasgow, United Kingdom
Mark Rijpkema, PhD
Nijmegen, The Netherlands
Steven P. Rowe, MD, PhD
Baltimore, Maryland
Mehran Sadeghi, MD
West Haven, Connecticut
Orazio Schillaci, MD
Rome, Italy
Charles Ross Schmidtlein, PhD
New York, New York
David M. Schuster, MD
Atlanta, Georgia
Travis Shaffer, PhD
Stanford, California
Sai Kiran Sharma, PhD
New York, New York
Anthony F. Shields, MD, PhD
Detroit, Michigan
Barry L. Shulkin, MD, MBA
Memphis, Tennessee
Yu Shyr, PhD
Nashville, Tennessee
Albert J. Sinusas, MD
New Haven, Connecticut
Riemer H.J.A. Slart, MD, PhD
Groningen, The Netherlands
Piotr Slomka, PhD, FACC
Los Angeles, California
Simon John Christoph Soerensen, MD
Stanford, California
Ida Sonni, MD
Los Angeles, California
Michael G. Stabin, PhD
Richland, Washington
Lisa J. States, MD
Philadelphia, Pennsylvania
Sven-Erik Strand, PhD
Lund, Sweden
Rathan M. Subramaniam, MD, PhD, MPH
Dunedin, New Zealand
John Sunderland, PhD
Iowa City, Iowa
Suleman Surti, PhD
Philadelphia, Pennsylvania
Julie Sutcliffe, PhD
Sacramento, California
David Taieb, MD, PhD
Marseille, France
Laura H. Tang, MD, PhD
New York, New York
Ukihide Tateishi, MD, PhD
Tokyo, Japan
James T. Thackeray, PhD
Hannover, Germany
Mathew L. Thakur, PhD
Philadelphia, Pennsylvania
Alexander Thiel, MD
Montreal, Canada
Daniel L.J. Thorek, PhD
St. Louis, Missouri
David W. Townsend, PhD
Singapore
Timothy Turkington, PhD
Durham, North Carolina
Gary A. Ulaner, MD, PhD
Irvine, California
David Ulmert, MD, PhD
Los Angeles, California
Lena M. Unterrainer, MD, MHBA
Munich, Germany
Christopher H. van Dyck, MD
New Haven, Connecticut
Douglas Van Nostrand, MD
Washington, District of Columbia
Patrick Veit-Haibach, MD
Toronto, Canada
Nerissa Viola-Villegas, PhD
Detroit, Michigan
John R. Votaw, PhD
Atlanta, Georgia
Richard L. Wahl, MD
St. Louis, Missouri
Anne Marie Wallace, MD
La Jolla, California
Martin A. Walter, MD
Geneva, Switzerland
Rudolf A. Werner, MD
Wuerzburg, Germany
Andreas G. Wibmer, MD
New York, New York
Anna M. Wu, PhD
Duarte, California
Randy Yeh, MD
New York, New York
Hyewon (Helen) Youn, PhD
Seoul, Korea
Pat B. Zanzonico, PhD
New York, New York
Brian M. Zeglis, PhD
New York, New York
Robert Zeiser, MD
Freiburg, Germany
Hong Zhang, MD, PhD
Hangzhou, China
Hongming Zhuang, MD, PhD
Philadelphia, Pennsylvania
Sibylle I. Ziegler, PhD
Munich, Germany

ASSISTANT TO THE EDITOR

Joshua N. Wachtel
Los Angeles, California

THIS MONTH IN
JNM

JNM* Editors' Choice Awards:** Johannes Czernin recognizes outstanding contributions to *JNM* in 2023, as selected for awards at the upcoming SNMMI Annual Meeting. . . . . ***Page 825

Discussions with leaders: Frederik (Freek) J. Beekman, PhD, distinguished inventor, entrepreneur, and professor of Applied Physics at the Technische Universiteit Delft, talks with Czernin and Mona about his career in academia and industry.. . . . . ***Page 826***

Amyloid-β, tau, and F-DOPA PET: Burkett and colleagues offer an educational overview of visual interpretation of amyloid, tau, and dopaminergic PET images; their roles in the clinical context; and potential pitfalls in interpretation. . . . . ***Page 829***

^{18}F-FET PET cost-effectiveness: Rosen and colleagues report on ^{18}F-FET PET for treatment monitoring of multimodal therapy, including checkpoint inhibitors, targeted therapies, radiotherapy, and associated combinations, in patients with brain metastases secondary to melanoma or non–small cell lung cancer.. . . . . ***Page 838***

PET/CT in oligometastatic breast cancer: Moser and colleagues assess the impact of ^{18}F-FDG PET/CT on the definition of oligometastatic disease and detection of metastatic patterns in breast cancer, emphasizing the importance of standardizing imaging definitions.. . . . . ***Page 845***

Predictive metabolic response in TKI therapy: Schuler and colleagues evaluate metabolic response on ^{18}F-FDG PET after short-course osimertinib to identify lung cancer patients with resistance to epidermal growth factor receptor tyrosine kinase inhibitors who will benefit from next-line osimertinib. . . . . ***Page 851***

CLDN18.2 molecular imaging in cancer: Qi and colleagues detail a first-in-human study of ^{68}Ga-NC-BCH PET and its biodistribution, metabolism, dosimetry, safety, and potential for quantifying claudin-18 isoform 2 expression in gastrointestinal cancer patients. ***Page 856***

PET/MRI and methotrexate neurotoxicity: Baratto and colleagues use [^{18}F]FDG PET/MRI to diagnose high-dose methotrexate–induced brain injury and correlate the results with cognitive impairment identified by neurocognitive testing in pediatric cancer survivors. . . . . ***Page 864***

^{68}Ga-FAPI-46 in ^{18}F-FDG–negative lung cancer: Röhrich and colleagues evaluate in lung cancer patients the diagnostic potential of static and dynamic ^{68}Ga-FAPI-46 PET imaging in ^{18}F-FDG–negative pulmonary lesions. . . . . ***Page 872***

^{68}Ga-FAPI PET and FAP-RPT in sarcoma: Lanzafame and colleagues describe the diagnostic performance and accuracy of ^{68}Ga-FAPI PET in patients with various bone and soft-tissue sarcomas, highlighting potential eligibility for FAP-targeted radiopharmaceutical therapy. . ***Page 880***

FAPI PET/CT in genitourinary cancers: Hagens and colleagues conduct a systematic analysis of current literature on the utility of FAPI PET/CT for staging patients with genitourinary malignancies.. . . . . ***Page 888***

Novel ^{68}Ga-labeled PET/MRI in prostate cancer: Duan and colleagues assess in a phase II study the feasibility, safety, and diagnostic performance of ^{68}Ga-NeoB and ^{68}Ga-PSMA-R2 PET/MRI for detection of biochemically recurrent prostate cancer. . . . . ***Page 897***

PSMA PET/CT heterogeneity intensity score: Swiha and colleagues develop a simple, clinically applicable PSMA PET/CT score, encompassing the elements of SUV$_{mean}$ without additional quantification, for use in predicting response to ^{177}Lu-PSMA therapy. ***Page 904***

Extended [^{177}Lu]Lu-PSMA therapy: Seifert and colleagues investigate the safety and efficacy of extended [^{177}Lu]Lu-PSMA radiopharmaceutical treatment in patients with metastatic castration-resistant prostate cancer who have received more than 6 cycles.. . . . . ***Page 909***

RECIP and progression-free survival prediction: Gafita and colleagues identify associations between interim PSMA PET/CT by Response Evaluation Criteria in Prostate-Specific Membrane Antigen Imaging 1.0 and short-term outcomes after radiopharmaceutical treatment for metastatic prostate cancer. ***Page 917***

[^{177}Lu]Lu-DOTATATE absorbed dose–response: Hebert and colleagues explore how postinfusion dosimetry can influence clinical management by predicting efficacy and toxicity in [^{177}Lu]Lu-DOTATATE treatment of gastroenteropancreatic neuroendocrine tumors. . ***Page 923***

PAH for renal protection in PRRT: Moraitis and colleagues document the safety and efficacy of *para*-aminohippurate coinfusion as an alternative to amino acid coinfusion during peptide receptor radiotherapy in patients with neuroendocrine tumors. . . . . ***Page 931***

^{68}Ga-FAP-2286 PET tumor dosimetry: Kline and colleagues detail the imaging characteristics of ^{68}Ga-FAP-2286, present dosimetry analysis, and compare the agent with ^{18}F-FDG and FAPI compounds. . . . . ***Page 938***

Quantitative SPECT prognosis in ATTR-CM: Caobelli and colleagues analyze the predictive and risk-stratifying value of quantitative [^{99m}Tc]Tc-DPD SPECT/CT in suspected and confirmed amyloid transthyretin–related cardiomyopathy at different disease stages. . . . . ***Page 944***

Tau PET in 4-repeat tauopathies: Bischof and colleagues report on the development and suitability of a technique for [^{18}F]PI-2620 PET for tracking of disease progression in patients clinically diagnosed with progressive supranuclear palsy or cortical basal syndrome. . . . . ***Page 952***

Human brain [^{18}F]VAT quantification: O'Donnell and colleagues characterize the distribution of this vesicular acetylcholine transporter–specific PET tracer in the brain and optimize methods for quantification in cholinergic pathways.. ***Page 956***

Radiomics in cervical cancer: Collarino and colleagues investigate whether radiomic features extracted from pretreatment [^{18}F]FDG PET can improve prediction of histopathologic tumor response and survival in patients with locally advanced cervical cancer treated with neoadjuvant chemoradiotherapy and surgery. . . . . . ***Page 962***

Bootstrapped kinetics of dynamic PET data: Wu and colleagues examine a nonparametric approach to mapping kinetic parameters and their uncertainties, using data from the emerging generation of dynamic whole-body PET/CT scanners. . . . . ***Page 971***

DL-based PVC: Leube and colleagues introduce, test, and validate a methodology for partial volume correction of ^{177}Lu SPECT/CT imaging using deep learning. . . . . ***Page 980***

SSTR antagonists in Merkel cell cancer: Kircher and colleagues describe ^{68}Ga-labeled somatostatin receptor antagonist PET/CT imaging in a patient with metastatic Merkel cell carcinoma and discuss the potential of SSTR antagonist imaging for peptide receptor radionuclide therapy candidate selection. . . . . ***Page 988***

[^{18}F]FES-avid irradiated lung: Rich and colleagues present a case study elucidating the nature of false-positive changes on [^{18}F]FES PET/CT after pulmonary radiation in a patient with breast cancer and demonstrate an associated finding of [^{18}F]FES-positive draining nodes. . . . ***Page 990***

LBCA®

Lobular
Breast
Cancer
Alliance

Awareness Education Advocacy Research

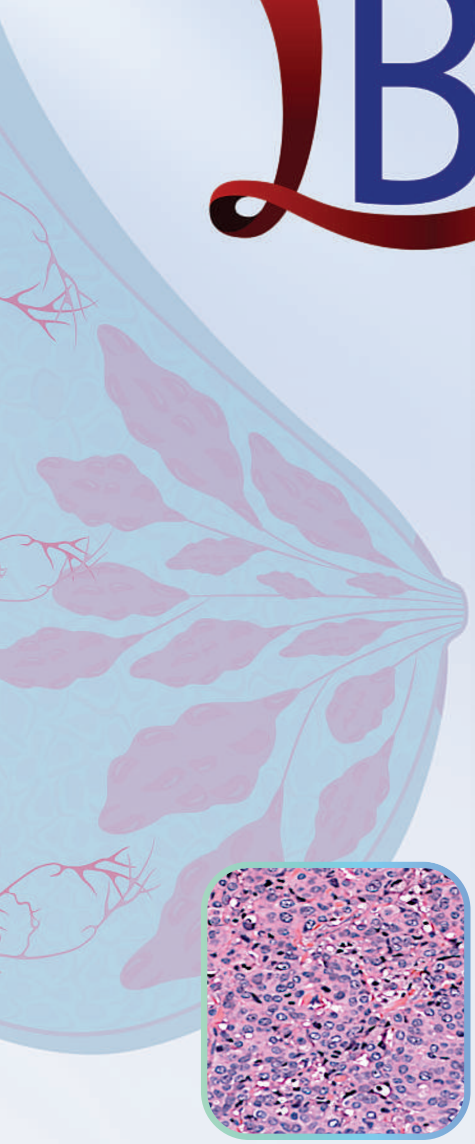

Did you know?

Invasive lobular carcinoma (ILC) tumors often elude detection with standard breast imaging because they do not form in lumps.

LOBULAR Breast Cancer

the 2nd most common Breast Cancer

- 15% of breast cancer diagnoses
- over 43,000 women diagnosed each year
- No targeted treatments

Learn about Lobular Breast Cancer and the ILC Patient Community

Check out our publications library

WWW.LOBULARBREASTCANCER.ORG

SNMMI would like to thank our Value Initiative Industry Alliance member companies for their support. Together we have made incredible progress advancing patient care and precision medicine.

Leadership Circle

BLUE EARTH DIAGNOSTICS
A Bracco Company

SIEMENS Healthineers

CardinalHealth
Essential to care™

CURIUM™
LIFE FORWARD

Eisai

GE HealthCare

itm
PASSION FOR PRECISION

LANTHEUS

Lilly

NOVARTIS

UNITED IMAGING

Visionary Member

mim SOFTWARE

Principal Member

BAYER

BRACCO
LIFE FROM INSIDE

CAPINTEC
A MIRION MEDICAL COMPANY

CELLECTAR BIOSCIENCES

cyclomedica

DAXOR
THE BLOOD VOLUME COMPANY™

EVERGREEN THERAGNOSTICS

Innervate Radiopharmaceuticals

isotopia
Nuclear Medicine

JUBILANT RADIOPHARMA

Life Molecular Imaging
HEALTH CARE

monrol

SHINE

SPECTRUM
DYNAMICS MEDICAL

Telix

Corporate Member

Debiopharm
WE DEVELOP FOR PATIENTS

HERMES MEDICAL SOLUTIONS

MEDTRACE

NorthStar
MEDICAL RADIOISOTOPES, LLC

RayzeBio

Voximetry

SNMMI | SOCIETY OF NUCLEAR MEDICINE & MOLECULAR IMAGING
VALUE INITIATIVE

Learn more about becoming a Value Initiative Member Company:
valueinitiative.snmmi.org

Innovation and Dedication Spur Excellence in Nuclear Medicine and Molecular Imaging

Helen R. Nadel, MD, FRCPC, FSNMMI, SNMMI President

Each June, nuclear medicine and molecular imaging professionals from around the world gather at the SNMMI Annual Meeting to hear first-hand about the latest research, celebrate successes in the field, and collaborate with peers to propel the field forward. This year's annual meeting will be held June 8–11 in Toronto, Ontario, where we look forward to seeing old friends and colleagues as well as making new connections. My term as SNMMI president will end at the annual meeting, and I am pleased to share with you the great progress that has been made by the society in the past year.

SNMMI strives to expand integration of best practices in all aspects of nuclear medicine to optimize patient care and access. With the tremendous growth of radiopharmaceutical therapies, much work has been completed in this area. The Radiopharmaceutical Therapy Center of Excellence now includes 79 approved centers, and the Radiopharmaceutical Therapy Registry is actively collecting data on patient safety and outcomes on Lutathera and Pluvicto (Novartis), with plans to add a radioactive iodine module. The SNMMI/Intersocietal Accreditation Commission therapy program, which launched at last year's annual meeting, has now accredited 3 sites. Pilot sites are being organized for SNMMI's new Therapy Clinical Trials Network, and a 1-day meeting is being planned for September 18, 2024, to address streamlining collaborations, focusing on study start-ups for radiopharmaceutical therapy trials. A Radiopharmaceutical Therapy Dosimetry Certificate program with 3 levels for technologists, physicians, and physicists is also being developed. Finally, a "Dose Optimization for Radiopharmaceutical Therapy Development Workshop" was held May 6–7, 2024, in Bethesda, Maryland, bringing together stakeholders from academia, industry, and federal agencies, including the U.S Food and Drug Administration (FDA), to discuss this important topic.

Additional SNMMI quality of practice initiatives include the development of procedure standards with peer nuclear medicine societies on a wide range of topics. The SNMMI Board of Directors recently approved the Joint EANM/EANO/RANO/SNMMI Practice Guideline/Procedure Standard for PET Imaging of Brain Metastases version 1.0 and the Joint SNMMI Procedure Standard/EANM Practice Guideline on ^{18}F-FDG Hybrid PET Use in Infection and Inflammation in Adults version 2.0. Other procedure standards approved over the past year cover consensus recommendations for PET/MRI in oncology, SPECT/CT in the quantitative assessment of the future liver remnant function, and estrogen-receptor imaging of patients with breast cancer.


Helen R. Nadel, MD, FRCPC, FSNMMI

The SNMMI Pediatric PET/MR Task Force, formed in 2022 under my leadership, continued its good work this past year. The task force developed and implemented a survey to identify current use and the perceived value of PET/MR for pediatrics. Also, an education exhibit titled "Pediatric PET/MRI: The How and Why" was presented at the RSNA 2023 Annual Meeting. The exhibit received a Certificate of Merit and was solicitated for *RadioGraphics* as a full-length manuscript!

The Mars Shot Research Fund continues to accelerate critical nuclear medicine and molecular imaging research. To date, the Mars Shot has raised $3.5 million to fund the translation of visionary research into tools or treatments that will improve patients' lives. Six exciting projects were funded in 2023 and are proceeding well. Soon, SNMMI will announce winners of 3 new $100,000 grants for innovative nuclear medicine research focused in 3 areas: diagnostic pathways in prostate cancer, community-based theranostics, and other topics addressed in the initial Mars Shot article published in *The Journal of Nuclear Medicine* (*JNM*). SNMMI also signed the 2024 Mars Shot cosponsorship agreement with the Lobular Breast Cancer Alliance, Inc., to advance invasive lobular carcinoma breast cancer imaging and treatments to improve patient outcomes. This new agreement will allow patient advocates to vote in the application review process.

The great research of nuclear medicine and molecular imaging professionals is also shared in *JNM.* A supplement titled *Advancing Global Nuclear Medicine: The Role and Future Contributions of China* was included with the May issue of the journal; it outlined the impressive basic research and clinical translation currently taking place in China. SNMMI also launched the *JNM* Podcast in January with its first episode, "The Future of FAPI Therapy," and second episode focused on "Advances in Dementia Imaging: Insights from Experts." Look for new episodes monthly!

This past year, SNMMI worked diligently to advocate for nuclear medicine and molecular imaging. The Beta Amyloid PET National Coverage Determination, which SNMMI has advocated to retire for many years, was officially retired by the Centers for Medicare and Medicaid Services (CMS) in October. In December,

---

DOI: 10.2967/jnumed.656PresMessage

SNMMI and the FIND Act Coalition met with staff at CMS to discuss unbundling radiopharmaceuticals and the 2024 proposed Outpatient Prospective Payment System (OPPS) rule. CMS, for the first time, opened the door to the possibility that it would consider unbundling radiopharmaceuticals by including a request for information in the OPPS proposed rule.

In November, SNMMI, the Medical Imaging & Technology Alliance, and the PET Coalition hosted a workshop with the FDA on PET manufacturing, with 232 in-person and 536 virtual attendees. SNMMI also hosted a Hill Day in April to address issues such as the FIND Act, the Nuclear Medicine Clarification Act, and research funding for nuclear medicine, drawing in 62 attendees. The FIND Act was included in a congressional hearing for the first time last year, and 4 members of Congress spoke in favor of the bill.

SNMMI outreach extended to patients, referring physicians, and the general public. Representatives from SNMMI presented at many medical meetings throughout the year, including the NANETS Medical Symposium, Society of Urologic Oncology Annual Meeting, and American Association of Geriatric Psychiatry Annual Meeting, among others. Two SNMMI Outreach Roadshow series targeting referring physicians were also held over the past year on breast imaging and PSMA imaging and therapy.

SNMMI's Patient Education Day in June 2023 drew 39 in-person attendees, and the live stream and recordings have received more than 7,600 total views to date. Two editions of a new quarterly SNMMI patient newsletter, *QuickScan*, have been emailed to 100+ patient groups; the most recent issue had a 55 percent open rate. SNMMI now offers a members-only online Outreach Toolkit at www.snmmi.org/OutreachToolkit so members can organize their own local outreach programs.

To educate the public about nuclear medicine and molecular imaging, SNMMI has executed a robust consumer awareness media outreach program. Since last June, SNMMI has placed stories about breast cancer, prostate cancer, dementia research, pediatric cancer, and obesity research on ABC, CBC, FOX, and NBC affiliates around the United States. In addition, SNMMI worked with Gray Media to package segments on prostate cancer and obesity which ran on as many as 192 different local TV stations nationwide.

SNMMI also reached members of the nuclear medicine community through meetings held throughout the year. The 2024 Mid-Winter and American College of Nuclear Medicine (ACNM) Annual Meeting was attended by more than 750 nuclear medicine professionals and industry partners from around the world. The meeting included 30 education sessions in 3 distinct tracks—an ACNM Annual Meeting track, a radiopharmaceutical therapy specialty track, and a general nuclear medicine track—and featured the largest tabletop exhibit hall in the meeting's history, with representatives from 49 companies. The meeting also included both a successful Future Leaders Academy, with 13 graduates, and SNMMI-TS Leadership Academy, with 17 graduates.

In September, SNMMI hosted its 2023 Therapeutics Conference in Baltimore, Maryland. The conference was a tremendous success, with nearly 350 nuclear medical professionals in attendance. The program included an outstanding lineup of speakers who discussed topics such as dosimetry, clinical trials, and disease-specific radiopharmaceutical therapies.

SNMMI hosted an Artificial Intelligence (AI) Summit—*AI in Action*—in February in Bethesda, Maryland. The summit drew a full house, involving more than 250 representatives—both in person and virtual—from major stakeholders in nuclear medicine and AI spaces to advance the implementation of practical, achievable AI.

This year's annual meeting will feature an expanded Knowledge Bowl with new technology, "Best of" sessions, and "Eye on U" sessions. An expanded Science Pavilion will offer increased POP and Meet the Author programming, and the exhibit hall will be the largest in SNMMI history! Popular social and networking events will also return, including the annual Hot Trot and the Drink & Think networking event.

In addition to serving as a scientific resource to nuclear medicine professionals, SNMMI also helps them advance their careers. SNMMI launched a Nuclear Medicine Careers website (nmcareers.snmmi.org) that includes information on career pathways for physicians, scientists, and technologists, job opportunities and career maps, a skills snapshot, and resources for individuals looking to serve as ambassadors in their community. SNMMI is also excited to release its *Jobs of Tomorrow* docuseries, a program that highlights different facets of nuclear medicine and therapy, examining how they have changed and will continue to change. The series of six 30-min videos will put eye-grabbing content in front of a massive new audience, positioning SNMMI as the leader in recruitment into the field.

This year I had the opportunity to travel around the world on behalf of SNMMI to collaborate with global leaders to advance the field of nuclear medicine. I attended the EANM Annual Meeting in Vienna, Austria; the Asia Oceania Congress of Nuclear Medicine and Biology in Amman, Jordan; the Canadian Association of Nuclear Medicine Annual Meeting in Ottawa, Ontario; the WARMTH International Congress of Radiopharmaceutical Therapy in Muscat, Oman; The Israeli Society of Nuclear Medicine Meeting in Tel Aviv, Israel; the Australia New Zealand Society of Nuclear Medicine Annual Scientific Meeting in Christchurch, New Zealand; the Therapeutic World Congress in Santiago, Chile; as well as many other meetings. I also traveled to the 20th Biennial Congress of the South African Society of Nuclear Medicine in Gqeberha and Pretoria, South Africa. In Pretoria, I was able to tour the under-construction NuMeRi facility, which will provide enabling support for health care research and development by South African researchers.

The Nuclear Medicine Global Initiative also continues its work. Current topics for the group include developing a global consensus on nomenclature for radiopharmaceutical therapies and creating a neuroblastoma registry for incidence and treatment.

To raise awareness and communicate with its various audiences, SNMMI has taken intentional steps to grow its social media presence. SNMMI has honed its social media strategy to optimize content for each platform, shifted the balance of content that SNMMI distributes, enhanced the brand aesthetic through elevated design, and created more video content to maximize both reach and engagement. This new strategy was piloted in early spring, and SNMMI is already seeing the benefits.

The accomplishments achieved by SNMMI over the past year could not have been made possible without the dedication of the society's more than 700 volunteers. I thank each of you for your service to SNMMI over the past year. I'm confident that as Cathy Sue Cutler, PhD, FSNMMI, takes the reigns as SNMMI president, the society will only continue its great work for our field.

JNM Editors' Choice Awards for 2023

Johannes Czernin

David Geffen School of Medicine, University of California Los Angeles, Los Angeles, California

Johanna Diekmann

Spencer D. Lindeman

Each year the associate editors and editorial board of *The Journal of Nuclear Medicine* (*JNM*) work with me to select outstanding contributions to the journal for recognition at the annual meeting of the Society of Nuclear Medicine and Molecular Imaging. The *JNM* Editors' Choice Awards for articles published in the journal in 2023 were chosen by anonymous vote from a group of diverse, high-quality, and cutting-edge submissions. This year, both awardees' articles focused on fibroblast activation protein−related research, an area of extraordinary promise and interest, with implications for theranostic innovation across a wide range of cancers and in promising cardiac and other applications.

In the category of best clinical article, the award went to Johanna Diekmann, from the Hannover Medical School (Germany), and coauthors Jonas Neuser, Manuel Röhrich, Thorsten Derlin, Carolin Zwadlo, Tobias Koenig, Desiree Weiberg, Felix Jäckle, Tibor Kempf, Tobias L. Ross, Jochen Tillmanns, James T. Thackeray, Julian Widder, Uwe Haberkorn, Johann Bauersachs, and Frank M. Bengel for "Molecular Imaging of Myocardial Fibroblast Activation in Patients with Advanced Aortic Stenosis Before Transcatheter Aortic Valve Replacement: A Pilot Study" (*J Nucl Med.* 2023;64:1279–1286). This contribution was also named the best overall article in the journal for 2023.

Spencer D. Lindeman, from Purdue University (West Lafayette, IN), and coauthors Ramesh Mukkamala, Autumn Horner, Pooja Tudi, Owen C. Booth, Roxanne Huff, Joshua Hinsey, Anders Hovstadius, Peter Martone, Fenghua Zhang, Madduri Srinivasarao, Abigail Cox, and Philip S. Low were the recipients of the award in the category of best basic science article for "Fibroblast Activation Protein–Targeted Radioligand Therapy for Treatment of Solid Tumors" (*J Nucl Med.* 2023;64:759–766).

With articles like these, *JNM* remains the international journal of choice for publishing clinical, basic, and translational research in nuclear medicine, molecular imaging, radiopharmaceutical therapy, and theranostics. This continued success is supported by our hard-working associate editors and editorial board, who collectively encourage our community to embrace the new techniques and agents that will benefit our patients today and enhance future understanding of the potential of molecular medicine.

DOI: 10.2967/jnumed.124.267935

Inventing His Own Career Path

Freek Beekman Talks with Johannes Czernin and Christine Mona About Success in Academia and Industry

Freek Beekman[1], Johannes Czernin[2,3], and Christine Mona[2,3]

[1]*Department of Radiation Science & Technology, Technische Universiteit Delft, Delft, The Netherlands;* [2]*David Geffen School of Medicine, UCLA, Los Angeles, California; and* [3]*Department of Molecular and Medical Pharmacology, UCLA, Los Angeles, California*

Johannes Czernin, MD, editor-in-chief of *The Journal of Nuclear Medicine* (*JNM*) and a professor at the David Geffen School of Medicine at UCLA, and Christine Mona, PhD, an assistant professor in Molecular and Medical Pharmacology at UCLA, spoke with Frederik (Freek) J. Beekman, PhD, a distinguished inventor, entrepreneur, and professor of Applied Physics at the Technische Universiteit Delft (TU Delft; The Netherlands), about his career in academia and industry. Dr. Beekman, who leads the Biomedical Imaging Division at TU Delft, is widely known for his innovations in advancing molecular imaging. He studied experimental physics at Radboud University Nijmegen (The Netherlands) and in 1995 received his doctorate from Utrecht University (The Netherlands), graduating in 1995 with a thesis entitled, "Fully 3D Reconstruction of SPECT Using Object Shape–Dependent Scatter Models." From 1995 to 2008, he was a faculty member at the Image Sciences Institute and Department of Nuclear Medicine at University Medical Centre Utrecht (UMC Utrecht). In 2007, he went to TU Delft to head the radiation detection and medical imaging section.

In 2006, Dr. Beekman founded MILabs BV, a molecular imaging spin-off from UMC Utrecht, focusing on his inventions in high-resolution PET and SPECT and the design of multimodal and stand-alone scanners for preclinical and clinical applications. MILabs was sold to the Rigaku Corp. in 2021. In 2023 Beekman launched the Molecular Imaging Foundation and Free Bee International BV, a company that currently focuses on novel γ-imaging devices for clinical use.

Dr. Beekman's work has advanced technologies in detectors, collimators, reconstruction algorithms, and artificial intelligence for various imaging modalities, including PET, SPECT, CT, and optical tomography. He has published more than 170 peer-reviewed articles and holds more than 20 patent families. Recognitions for his achievements have included the Physics Valorisation Prize from the Dutch Science Foundation, multiple SNMMI and IEEE awards, and two times the Innovation of the Year Award from the World Molecular Imaging Society. Many of the cutting-edge imaging systems pioneered by Dr. Beekman and his teams are deployed across biomedical research institutions worldwide, driving a broad range of discoveries and facilitating the development of novel tracers and pharmaceuticals.

Dr. Czernin: *You have the reputation of having been a difficult child and difficult student. How did you make it through high school? What was your career path when you converted to being a regular boring human being?*


Freek Beekman, PhD

Dr. Beekman: I hope I didn't become too boring! My parents divorced when I was young, and I had to move between my mother and father. That was difficult. And I was very short-sighted so couldn't read well at school. School was a mess. I also was not very good at sitting still and learning things; I was too active. Other things in my village were so much more interesting—like we had a big dirt-bike racing track. Every year there was a Motocross Grand Prix—that was something I liked. I got a moped, which I hid at a farm, when I was 13 y old. I bought it for $10 and repaired it. A year later I mounted the back part of a scooter to the back of a soapbox car to create a makeshift car, which I crashed during the first test drive. After that I got more serious motorbikes. I think that building, tuning, repairing, etc., improves problem-solving skills and brings unique perspectives.

Dr. Czernin: *How did you finish high school?*

Dr. Beekman: I didn't. I dropped out. Then I went to school to become an electrician but didn't do well there either, because I barely attended. However, I somehow finished that school. I still wanted to be a dirt-bike racer, but they wouldn't let me through because of my poor vision. Then I played in a rock band, where the members influenced me very positively. Some of them went to university, and I got interested in studying other things. I then went to a higher-level school to train to become a technician. After I was done with this school, I went into the chip industry. I joined Philips, where I invented something to improve etching of chips. I stayed there only a short time, because I then met Frans H.M. Corstens, MD, PhD, a nuclear medicine physician from Nijmegen. I was interested in medical technology, and I joined his group at Radboud University.

Dr. Czernin: *Where did this interest in medical technology come from?*

Dr. Beekman: My father was a vet. I always went with him to farms to treat animals. He performed surgery on all kinds of animals. When I was 7 y old, I assisted my father with a cesarean section on a cow, which probably ignited my fascination for technology to improve health care. Later, learning about the development of the CT scanner and its ability to replace invasive procedures further fueled that interest.

Dr. Mona: *Your path is quite diverse and somewhat nonlinear and chaotic. Do you think that a more conventional path would*

DOI: 10.2967/jnumed.124.267812

have led to this creativity and given you the resources to bounce from one idea to another?

Dr. Beekman: It's difficult to determine. Although some individuals with conventional paths are also creative, many don't necessarily innovate after completing higher education. On the other hand, some people who just quit the educational system become the greatest innovators in the world. Take Mark Zuckerberg or Steve Jobs.

Dr. Mona: *Could you expand on this?*

Dr. Beekman: Creative people are attracted by problems and then work to find the information they need to educate themselves to solve the problem. In school, students learn material and then forget it. I always want to learn things that I can use immediately. Maybe students should be challenged very often by problems that they want to solve at that moment. But that's, of course, difficult. You cannot have a curriculum in medical school, for example, composed solely of case studies. I think education is moving more toward problem solving. My 12-y-old son gets a much more interesting education than I had. Mathematics are immediately applied to real-world problems, and that is, of course, good. He's a little bit like me, so I don't know where this is going. And, he's likely to say, "Yeah, Daddy, I read your interview, and you didn't do so well at school either."

Dr. Mona: *Do you see a role for yourself in education in The Netherlands?*

Dr. Beekman: I try to get students to play with ideas. I want them to tell me that my idea is not the best one, that they can think of something better—because there's always something better. A mix of practical and theoretic education is important. You have to have a real feel for the process, for example, of building a machine. You need hands-on experience, and these kinds of skills aren't necessarily learned at university.

Dr. Czernin: *Dr. Mona referred to your "chaotic" educational path. How did that affect your ability to work in a company or structured environment? How did you manage to adapt to real-life challenges?*

Dr. Beekman: I think I never really adapted, which is perhaps both a problem and an advantage. I started MILabs, where I could do more or less what I wanted because I didn't have a supervisory board. Only at the end, when we had venture capital, we had a board, which made it more difficult, because there were too many nonproductive ideas that they thought I should follow up on. It's very important to listen but still go your own way. Sometimes this is a little bit like school—it can be a waste of time. That's maybe the same thing that has always been difficult for me.

Dr. Czernin: *Was the freedom to make decisions one motivation for you to leave academia and go into the business world, or did you have decision freedom in the hierarchy of your university as well?*

Dr. Beekman: I actually managed to have a reasonable amount of freedom within academia. So, founding MILabs in 2006 wasn't primarily about seeking more freedom. At the university we had built U-SPECT-I, which resulted in the 2004 SNM Annual Image of the Year and the 2005 *JNM* Best Basic Science Paper, demonstrating the potential for commercialization. People asked me then whether I wanted to start a business. What attracted me was the idea of transforming an idea into a product. And I thought, "Let's get the valorisation grants and create a device that all the researchers can use." But business developers then wanted a big stake in the start-up. That's when my lawyer said, "Drop them. Be CEO yourself, and get rid of them. You can always take on another CEO later if you'd like." So, the company started, and I was the CEO.

Dr. Mona: *When I listen to you, it's clear how much you value the freedom to operate. It's getting harder and harder to have this type of freedom. How much stability and how much freedom to operate should we have in research?*

Dr. Beekman: Freedom is good, but you should also persist. Both persistence and freedom are important. You can still write the grant proposals you want, can't you? Of course, they often have to fit into the needs and interests of the department in which you are working. But don't you join a department where there's synergy with your own plans?

Dr. Mona: *With innovation, one is always taking risks. I cannot see innovation without freedom, without risk. Following paths that are already explored rarely leads to innovation.*

Dr. Beekman: Freedom is essential. You have to have space for crazy good ideas. But writing a grant proposal on those ideas too quickly can be too crazy for the National Institutes of Health, for example. Getting grants can take a long time.

Dr. Mona: *So how do you navigate this balance between safety and innovation/freedom?*

Dr. Beekman: The mix of having a company and an academic appointment is ideal for me. At the university I can work on a new image reconstruction algorithm, which can take a long time because it involves deep and difficult research. But in the company I can have an idea for a new product that can be delivered in 3 months. It's very challenging at a university to organize and produce a fast adaptation to a machine or a new tool. In your own company, you can simply ask, "Can we make this happen by next week?"

> "The mix of having a company and an academic appointment is ideal for me . . . .It's very challenging at a university to organize and produce a fast adaptation to a machine or a new tool. In your own company, you can simply ask, 'Can we make this happen by next week?'"

Dr. Mona: *Would you be in favor of a hybrid system, where faculty have their research labs and also spin off companies where they can take risks?*

Dr. Beekman: Yes, that is nice. In a company you can do the really crazy things very quickly. That's why many of the big innovations come from companies.

Dr. Czernin: *Universities want to benefit from intellectual property. They structure technology transfer agreements that can be complex and convoluted and require special expertise. In addition, the universities may want ownership.*

Dr. Beekman: This is an intriguing area. Whether universities should have a stake in companies depends on the circumstances, but in many cases, it seems reasonable. In my experience, if you develop intellectual property using university funds, the university typically asserts ownership and seeks shares in your company or royalties. I encountered this with MILabs, where both the technology transfer offices of UMC Utrecht and TU Delft (where I later moved) obtained significant stakes. When we sold MILabs, they each made millions. This arrangement was fair, considering the universities' investments in patents developed during academic work. They also took a risk investing in a very small company with this very poor guy with not much money in the bank.

***Dr. Mona:** This brings us to the question of why you chose to sell MILabs. You had good university partners, good investors. Right now, there is a boom in nuclear medicine. Good imaging tools such as SPECT/CT and PET/CT are crucial to successful preclinical and clinical developments. So why did you sell?*

Dr. Beekman: The timing for the sale was opportune. Despite the challenges of the COVID-19 pandemic, MILabs experienced rapid growth, significantly boosting its value. Now I have newfound freedom, allowing me more time to spend with my children. Moreover, many innovators who sell their companies find themselves wanting to move on, as a result of corporate bureaucracy, for example. I remain active in the field and have already embarked on a new venture: Free Bee International, initially conceived as a lighthearted celebration of my newfound freedom and now focusing on molecular imaging.

***Dr. Mona:** How do you continue to create cutting-edge innovation? How do you stay creative?*

Dr. Beekman: One always sees only a part of the world. My patent lawyer has known me for 20 years. He says that I am more creative now than ever, since I am no longer a CEO. I also have hobbies—it's important to do other things with your brain to get distracted. Then you can be more creative.

***Dr. Mona:** You leave space for other interests to grow and to bring innovation to your primary field. It's a work/life balance in some ways.*

***Dr. Czernin:** When we say work/life balance, what does that trigger in your mind?*

Dr. Beekman: One of my role models and friends, Ronald Jaszczak, PhD, once shared with me over a significant number of beers the mantra "Work hard, play hard." I believe his message was about finding enjoyment outside of work, which in turn makes work more enjoyable. I truly believe in that.

***Dr. Czernin:** But your work/life balance means that you have a lot of fun at work, too?*

Dr. Beekman: Not many people work the way I do. I feel I have a great work/life balance, because the work can be a really fun part of life, so that I can do it for many hours. In the busy times at MILabs, I didn't often play guitar or paint. But it still felt great, because there were so many interesting things to do and I could create machines. That, for me, is like what going to art lessons may be for another person.

***Dr. Mona:** What is your advice for young people who are just starting in this booming field? How do we face future challenges?*

Dr. Beekman: If you have good ideas, go for it! Believe in yourself. Leave people behind who you think are smart but don't encourage you. Just go and listen closely to what is needed to take your next step. If you do all of this, success will come.

***Dr. Mona:** And what's next for you? You spoke a little bit about Free Bee—what is it?*

Dr. Beekman: Free Bee is dedicated to advancing γ-imaging technologies to address unmet needs in areas such as cancer research, diagnostics, and therapy. Although PET has seen rapid development, I believe there's untapped potential in SPECT, especially as radionuclide therapy grows. In addition, Free Bee is exploring breast-specific γ-imaging (BSGI) as a more accurate and painless alternative to x-rays for detecting breast cancer, particularly in women with dense breast tissue. In 20% of women, conventional x-ray imaging cannot visualize anything; an alternative is needed. The notion that BSGI can be dramatically improved is, for me, a no-brainer, and I believe it may even become the screening tool of choice: no pain, much more accuracy, and a dose similar to or lower than that from conventional x-ray imaging.

***Dr. Mona:** Do you have any interest in α-emitter imaging for theranostics? There is a very important unmet need as α-emitter–based therapies come to the market.*

Dr. Beekman: This is very important. For preclinical use we have already developed special SPECT methods (described in several articles, including in this journal) suitable for imaging high γ-energies or low abundances, needed to image distributions of α- and β-emitters. At Free Bee International and TU Delft we are working on novel technologies to meet these needs, as well as for clinical applications.

***Dr. Czernin:** Congratulations, Freek, for your great success, and thank you for spending this time with us and our readers.*

Evaluation of Neurodegenerative Disorders with Amyloid-β, Tau, and Dopaminergic PET Imaging: Interpretation Pitfalls

Brian J. Burkett, Derek R. Johnson, and Val J. Lowe

Department of Radiology, Mayo Clinic, Rochester, Minnesota

Learning Objectives: On successful completion of this activity, participants should be able to (1) understand the principles of visually interpreting amyloid, tau, and dopaminergic PET scans; (2) understand the role of amyloid, tau, and dopaminergic PET scans in clinical context; and (3) recognize potential pitfalls that could arise in correct visual interpretation and in imaging protocols for amyloid, tau, and dopaminergic PET scans.

Financial Disclosure: Dr. Burkett receives research support from GE Healthcare and the Radiological Society of North America. Dr. Johnson is a consultant for Telix and Novartis. Dr. Lowe serves as a consultant for Bayer Schering Pharma, Piramal Life Sciences, Life Molecular Imaging, Eisai Inc., AVID Radiopharmaceuticals, Eli Lilly and Co., and Merck Research and receives research support from Siemens Molecular Imaging, AVID Radiopharmaceuticals, and the National Institutes of Health (National Institute on Aging, National Cancer Institute). The authors of this article have indicated no other relevant relationships that could be perceived as a real or apparent conflict of interest.

CME Credit: SNMMI is accredited by the Accreditation Council for Continuing Medical Education (ACCME) to sponsor continuing education for physicians. SNMMI designates each *JNM* continuing education article for a maximum of 2.0 AMA PRA Category 1 Credits. Physicians should claim only credit commensurate with the extent of their participation in the activity. For CE credit, SAM, and other credit types, participants can access this activity through the SNMMI website (http://www.snmmilearningcenter.org) through June 2027.

Antiamyloid therapies for Alzheimer disease recently entered clinical practice, making imaging biomarkers for Alzheimer disease even more relevant to guiding patient management. Amyloid and tau PET are valuable tools that can provide objective evidence of Alzheimer pathophysiology in living patients and will increasingly be used to complement ^{18}F-FDG PET in the diagnostic evaluation of cognitive impairment and dementia. Parkinsonian syndromes, also common causes of dementia, can likewise be evaluated with a PET imaging biomarker, ^{18}F-DOPA, allowing in vivo assessment of the presynaptic dopaminergic neurons. Understanding the role of these PET biomarkers will help the nuclear medicine physician contribute to the appropriate diagnosis and management of patients with cognitive impairment and dementia. To successfully evaluate brain PET examinations for neurodegenerative diseases, knowledge of the necessary protocol details for obtaining a reliable imaging study, inherent limitations for each PET radiopharmaceutical, and pitfalls in image interpretation is critical. This review will focus on underlying concepts for interpreting PET examinations, important procedural details, and guidance for avoiding potential interpretive pitfalls for amyloid, tau, and dopaminergic PET examinations.

Key Words: dementia; neurodegenerative; amyloid; tau; brain PET

J Nucl Med 2024; 65:829–837
DOI: 10.2967/jnumed.123.266463

Over 55 million people worldwide live with dementia. The World Health Organization ranks dementia as the seventh leading cause of death (*1*). The most common type of dementia is Alzheimer disease (AD), characterized by neuropathologic hallmarks of extracellular amyloid-β plaques and intracellular hyperphosphorylated tau neurofibrillary tangles (*2*). Aside from AD, many other causes of dementia occur, with distinct neuropathologic features, presentations, and prognoses. Neurodegeneration is a feature of all types of dementia, whereas the underlying neuropathologic mechanism and distribution differ among types (*3,4*). For example, Parkinson disease and dementia with Lewy bodies are characterized by pathologic α-synuclein deposition, and pathologic tau deposition can underlie corticobasal degeneration and progressive supranuclear palsy (*5*).

Neuropathologic changes in dementia precede clinical onset during a latent period in which lab and imaging studies such as PET can detect abnormalities. Between different types of neurodegenerative entities, variations and overlap in clinical presentation and neuropathologic changes can lead to diagnostic ambiguity (*3*). For this reason, multiple imaging biomarkers for neuropathologic changes are useful for evaluating dementia in vivo. Furthermore, copathology is common, more so as patients age, which can further complicate and confound accurate diagnosis. With the clinical availability of targeted amyloid therapies for AD and other amyloid- and tau-targeted therapeutic agents under investigation, parsing out an accurate neurodegenerative diagnosis based on imaging biomarkers is more germane to clinical practice than ever before (*6,7*). The inaccurate characterization of a patient's underlying neurodegenerative disease may lead to inappropriate therapy, suboptimal supportive care, and provision of incorrect prognostic information. Nuclear medicine studies using multiple PET radiotracers assess an array of biomarkers that can be useful in the diagnosis and differentiation of neurodegenerative processes. This educational article will discuss the role of PET imaging of multiple imaging biomarkers in the evaluation of dementia, specifically amyloid, tau, and dopaminergic PET.

For AD, a conceptual framework, the ATN classification, has been introduced that incorporates categories of biomarkers for neuropathologic changes into a sequential model, reflecting the hypothesis that amyloid-β plaques ("A") develop initially, followed by pathologic tau deposition ("T"), neurodegeneration ("N"), and finally memory impairment and functional decline. Relevant biomarkers for measuring features of AD pathophysiology in living patients can be classified into one of these categories

---

Received Nov. 8, 2023; revision accepted Apr. 3, 2024.

For correspondence or reprints, contact Brian J. Burkett (burkett.brian@mayo.edu).

TABLE 1
ATN Biomarker Framework

ATN category	Pathophysiology	Biomarker(s)
A	Amyloid-β proteinopathy	Amyloid PET
		CSF hybrid ratios
		Amyloid-β42/40
		p-tau 181/amyloid-β42
		t-tau 231/amyloid-β42
T	Tau proteinopathy	Tau PET
		CSF hybrid ratios:
		Amyloid-β42/40
		p-tau 181/amyloid-β42
		t-tau 231/amyloid-β42
N	Neurodegeneration (injury of neuropil)	^{18}F-FDG PET
		MRI (volume assessment)
		CSF total tau
I	Inflammation (astrocyte activation)	CSF GFAP
V	Vascular brain injury	MRI (infarcts, white matter T2 hyperintensity, and abundant dilated prevascular spaces)
S	α-synuclein	CSF α-synuclein-SAA

CSF = cerebrospinal fluid; p-tau = hyperphosphorylated tau; t-tau = total tau; GFAP = glial fibrillary acidic protein; SAA = seed amplification assay.

(Tables 1 and 2) (*6,8*). Amyloid and tau PET are important imaging biomarkers for this framework. Neurodegeneration includes both decreased metabolic neuronal function as assessed by ^{18}F-FDG PET and structural changes such as volume loss, detected by MRI. The combined grouping of MRI and ^{18}F-FDG PET data into the neurodegeneration category is a limitation of the framework, as abnormalities on ^{18}F-FDG PET can precede structural changes on MRI, predict progression of cognitive decline, and categorize types of neurodegenerative conditions in the absence of specific changes on MRI (*9,10*). Although the ATN classification is a research framework and not intended as a clinical diagnostic staging mechanism for AD, it is useful to understand that PET examinations represent an array of biomarkers that underlie the biologic features of AD and illustrate that variable results in markers for tau and neurodegeneration can be seen in the Alzheimer continuum (Table 2) (*6*). This framework is actively being updated by the Alzheimer Association workgroup to incorporate additional biomarkers, including biomarkers for comorbid pathology such as vascular injury, neuroinflammation, and α-synucleinopathy. Further details of the revised criteria can be reviewed in a working draft currently available (Tables 1 and 2) (*6,11*). In clinical practice, ^{18}F-FDG PET and amyloid PET have complementary roles in that ^{18}F-FDG PET patterns can suggest alternative neurodegenerative diagnoses. Characteristic regions of AD pathology may be abnormal on ^{18}F-FDG PET in alternative non-AD causes of dementia and cognitive impairment, in which case amyloid PET may help clarify the diagnosis. The role of ^{18}F-FDG PET and MRI in dementia is discussed more extensively in other articles focused on those modalities (*4,12*). In addition to PET, serum and cerebrospinal fluid biomarkers for neuropathologic amyloid-β and tau can also be used but have the disadvantage of lacking information about spatial distribution. Corresponding to the spatial distribution of neurodegeneration, Alzheimer pathology can result in varied clinical presentations besides the more typical amnestic cognitive impairment, including

TABLE 2
NIA-AA Diagnostic Framework Classification

Research framework category	ATN classification
Normal	A− T− (N)−
AD pathologic change	
Alzheimer continuum	A+ T− (N)−
AD	A+ T+ (N)−
	A+ T+ (N)+
AD + suspected non-AD pathologic change	A+ T− (N)+
Non-AD pathologic change	A− T+ (N)-
	A− T− (N)+
	A− T+ (N)+

This framework is actively being updated, incorporating biomarkers of inflammation, vascular injury, and evidence of comorbid pathology. Furthermore, distinction will be made among tau PET staging categories of T_{MTL} (positive only in medial temporal lobes), T_{MOD} (moderate uptake in neocortical regions), and T_{HIGH} (high uptake in neocortical regions). For purposes of this article, only core biomarkers with regulatory approval are included. Proposed update can be accessed online (https://aaic.alz.org/diagnostic-criteria.asp#guidelines).

TABLE 3
AD Therapeutics

Drug	Phase 3 clinical trial	Trial finding summary	Current FDA status
Aducanumab	EMERGE, ENGAGE, NCT02477800, NCT02484547	Both halted at 50% enrollment on basis of futility analysis; EMERGE: Over 78 wk, average 22% slowing of cognitive decline in high-dose arm of study	Accelerated approval
Lecanemab	CLARITY-AD, NCT003887455	Over 18 mo, average 25% slowing of cognitive decline	Approved
Donanemab	TRAILBLAZER-ALZ2, NCT04437511	Over 18 mo, average 35% slowing of cognitive decline	Not approved; under consideration

posterior cortical atrophy, limbic predominant AD, behavioral variant/dysexecutive AD, and logopenic primary progressive aphasia. Interpreting multiple imaging biomarkers together and putting the spatial distribution of changes into context can help increase diagnostic certainty when an atypical AD presentation is suspected.

After AD, Parkinson disease is the second most common neurodegenerative condition. In Parkinson disease, intracellular Lewy bodies—aggregates of α-synuclein—drive degeneration of striatal dopaminergic neurons (*13,14*). L-6-^{18}F-fluoro-3,4-dihydroxyphenylalanine (^{18}F-DOPA) is a PET radiopharmaceutical that can detect uptake of dopamine precursor molecules in viable presynaptic dopaminergic neurons. Atypical parkinsonian disorders are also characterized by dopaminergic neurodegeneration but not necessarily Lewy body pathology. ^{18}F-DOPA can be useful for detecting striatal dopaminergic neuron loss in these conditions with high sensitivity and specificity above 90% (*15*).

AMYLOID PET

The guidelines of the Society for Nuclear Medicine and Molecular Imaging and the European Association of Nuclear Medicine define clinically appropriate use of amyloid PET, indicated in the setting of objective evidence of unexplained mild cognitive impairment assessed by a dementia expert. Amyloid PET is also appropriate for those who meet clinical criteria for possible AD but with uncertainty about the diagnosis, as well as patients who have progressive dementia at an atypically early age (<65 y) (*16,17*). Recently, disease-modifying amyloid antibody therapies have entered clinical practice. Confirmation of abnormal amyloid-β deposition as a therapeutic target may be obtained with amyloid PET (Table 3) (*18–21*). The clinical trials leading to accelerated U.S. Food and Drug Administration (FDA) approval of the amyloid-targeted therapies aducanumab and lecanemab used amyloid PET as a method to define amyloid-β positivity, a core inclusion criterion for the trials, as well as to evaluate therapeutic efficacy (*19–21*). Amyloid clearance measured on PET was a trial endpoint for both aducanumab and lecanemab (*19,20*). Follow-up amyloid PET scans after administration of antiamyloid therapies may be clinically useful for assessing response to treatment, in parallel to the use of amyloid PET as a biomarker in trials, although accessibility for this use is limited by reimbursement. For example, decreased amyloid-β deposition as evaluated by PET after lecanemab was correlated with the therapeutic benefit of delayed cognitive decline (*20*). Amyloid PET may provide clinically useful prognostic information when weighing the risks and benefits of continued therapy.

The amyloid radiotracer ^{11}C-Pittsburgh compound B was the first available amyloid tracer and has been used extensively in the research setting (*22*). At present, 3 amyloid radiotracers have FDA approval: ^{18}F-florbetaben, ^{18}F-florbetapir, and ^{18}F-flutemetamol (Table 4). Each of these has specific properties and differences in procedural standards and acceptable interpretation methods, as defined in the FDA package inserts (Table 4) (*23–25*). For each, the final goal in interpretation is a binary decision of positive

TABLE 4
Amyloid and Tau PET Radiotracer Properties

Radiotracer	Administered activity (MBq)	Uptake time (min)	PET scan duration (min)	Display parameters	Link to training modules
Amyloid-β					
^{18}F-florbetaben	300	45–130	20	Grayscale	https://www.neuraceqreadertraining.com/learn
^{18}F-florbetapir	370	30–50	10	Grayscale	https://amyvid.myregistrationp.com/amyvid/index.do
^{18}F-flutemetamol	185	90	20	Color scan (rainbow, vendor-specified)	https://www.readvizamyl.com/
Tau					
^{18}F-flortaucipir	370	80	20	Color scale (2 colors); transition at 1.65× cerebellar average	https://tauvidreadertraining.com/login/signup.php

or negative. As more experience with antiamyloid therapy accumulates, the ability to monitor changes and therapeutic response with amyloid PET may influence patient management decisions. If amyloid PET is used for monitoring treatment response, as has been done in the clinical trial setting, quantification techniques will also likely become germane to clinical interpretation.

For all FDA-approved amyloid tracers, image interpretation should be performed without consideration of collateral clinical information, mirroring the methods used in clinical studies assessing the radiotracers' performance (*4*). Although this approach may be counterintuitive, the aim is not to synthesize comprehensive information into a clinical diagnosis such as AD but rather to categorize the PET as a positive or negative biomarker for amyloid-β in an unbiased manner.

For all amyloid tracers, the underlying principle for image interpretation is that the tracer binds to normal white matter but spares gray matter. In a normal (negative) scan, this results in a clearly visible outline of the branching white matter structures (Fig. 1). Loss of gray–white differentiation, outward extension of radiotracer from the white matter to the cortical surface, or more intense gray matter radiotracer binding relative to white matter are features of abnormal scans.

For ^{18}F-fluorbetapir, a method for systematic image interpretation of grayscale axial images is defined, starting with inspection of the cerebellar gray–white differentiation and proceeding to the occipital lobe, the temporal lobe, the frontal lobe, and finally the parietal lobe. Each of these lobes in both hemispheres count as one region. A total of 2 regions must be abnormal for a scan to qualify as positive on the basis of loss of gray–white differentiation; however, one abnormal region may qualify a scan as positive on the basis of cortical uptake exceeding the adjacent white matter (*24*).

For ^{18}F-florbetaben, a similar method is defined scrolling from inferior to superior but with slightly different regions, starting with the cerebellum and proceeding to the temporal lobe, frontal lobe, precuneus and posterior cingulate, and finally the parietal lobe. These regions may contribute to a positive scan designation, with the precuneus and posterior cingulate considered separately from the parietal lobe. Positive scans require abnormal uptake in most slices within a brain region, and this uptake can be further subdivided into moderate amyloid-β deposition (small areas of abnormal uptake within ≥1 region) or pronounced amyloid-β deposition (large and confluent areas of abnormal uptake within ≥1 region) (*25*).

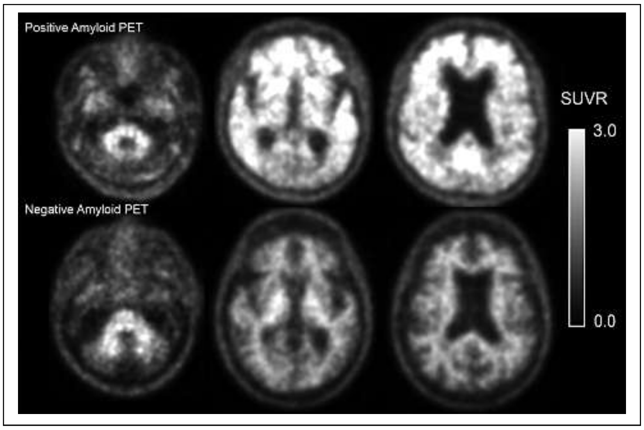

FIGURE 1. Amyloid PET. (Top row) Positive amyloid PET scan with loss of gray–white differentiation and areas of abnormally increased cortical uptake in multiple regions of cerebral hemispheres. This is compatible with presence of moderate to frequent amyloid-β neuritic plaques. (Bottom row) In contrast, negative amyloid PET scan has distinct gray–white contrast in all lobes, with distinctly visible branching white matter tracts. SUVR = SUV ratio.

For ^{18}F-flutemetamol, a manufacturer-specified color scale should be used with the pons set at 90% of the maximum intensity and a minimum intensity of 0. The following regions are reviewed separately in specified planes, each of which counts toward criteria for a positive scan: the frontal lobe (axial, optional sagittal), the precuneus/posterior cingulate (sagittal, optional coronal), the lateral temporal lobe (axial, optional coronal), the inferolateral parietal lobe (coronal, optional axial), and the striatum (axial, optional sagittal) (*23*). The striatum is assessed only for ^{18}F-flutemetamol, and the optional sagittal plane can be helpful for detecting a normal striatal gap between the frontal white matter and the thalamus.

Regionally positive amyloid PET scans can be more difficult to identify, and it is necessary to scrutinize each lobe of the cerebral

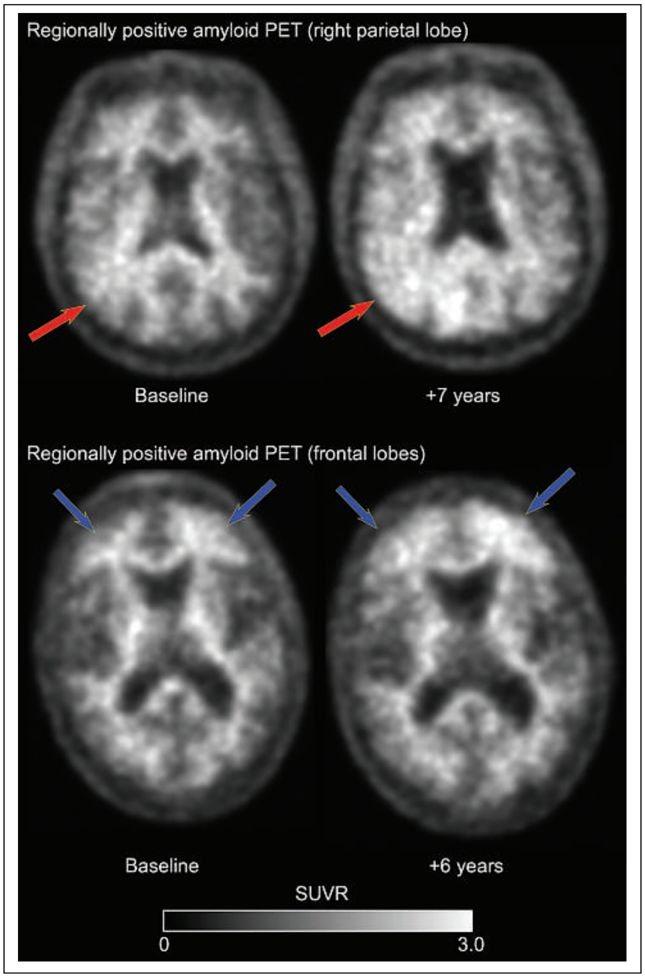

FIGURE 2. Regional positive amyloid PET: baseline and follow-up ^{11}C-PiB PET examinations. (Top row) Right parietal regionally positive examination with loss of gray–white contrast in right parietal lobe. Regional uptake progressed on follow-up in 7 y (arrows) and correlated to amyloid-β neuritic plaques at autopsy. Cerebrospinal fluid markers for amyloid were negative. (Bottom row) Bilateral frontal regionally positive examination with loss of gray–white contrast in left greater than right frontal lobes (arrows). Uptake progressed over 6 y and correlated with frontal amyloid-β neuritic plaques at autopsy. Cerebrospinal fluid markers for amyloid became positive in second case 7 y after baseline PET.

hemispheres for the integrity of the gray–white contrast (Fig. 2). Amyloid PET interpretation can also be challenging in the setting of brain parenchymal volume loss, a common scenario. Enlargement of the cerebrospinal fluid spaces due to volume loss may mimic a normal branching white matter pattern when the PET images are reviewed alone (Supplemental Fig. 1; supplemental materials are available at http://jnm.snmjournals.org). Use of multiplanar reconstructions and fusion with anatomic images can be most helpful for clarification of the outer borders of the cortex. Familiarity with the major white matter tracts can also be helpful, as the association tracts within a cerebral hemisphere should be clearly visible as distinct radiotracer-avid structures (Fig. 1). Other potential pitfalls that may result in an inaccurate interpretation can be technical in nature. A low-count study can reduce gray–white matter contrast, resulting in an inaccurate categorization of a normal scan as positive. When one is systematically reviewing the images, starting with the cerebellum may provide a reliable internal control for the degree of gray–white contrast to expect in the cerebral hemispheres. Increased image noise may be conspicuous in the extracranial soft tissue, an additional indicator of a low-count study. Increased uptake in an extracranial structure, such as the parotid glands, scalp, or even an osseous or intracranial mass, can impact automated windowing and leveling of the study, leading to an inaccurate interpretation. To correct the windowing and leveling of the examination, the abnormally radiotracer-avid structure can be omitted from a selected representative region of the brain that includes cerebral gray and white matter. Some intracranial masses such as meningiomas are known to bind to some amyloid radiotracers, and it is important to avoid mistaking such lesions for radiotracer-avid cortex (Supplemental Fig. 2) (*26*). Anatomic fusion images or comparison MRI examinations may be helpful for confirming the presence of a mass lesion and diagnosing such lesions more definitely.

A limitation of amyloid PET for characterizing AD pathology is that radiotracer binding correlated with both neuritic amyloid-β plaques and diffuse amyloid-β plaques. Diffuse plaques are noncompact deposits that lack neuritic components. Diffuse plaques are commonly found in aged brains and are not specific for AD. A positive amyloid PET study reflective of diffuse plaques may be present in pathologic aging or alternative neurodegenerative diagnoses (Fig. 3) (*27*). Tau PET may potentially provide additional diagnostic certainty. Cases of low amyloid-β plaque burden may be undetectable with amyloid PET, an additional limitation of the imaging modality (*27,28*). Follow-up scans may be useful for detecting progressive amyloid accumulation. Amyloid-β accumulation detected on amyloid PET has been observed with other neurodegenerative processes such as dementia with Lewy bodies, atypical AD, and frontotemporal lobar degeneration, and in isolation, a positive amyloid PET study should not be viewed as sufficient for a diagnosis of AD (*29,30*). Nevertheless, a negative amyloid PET study is able to reliably exclude AD—clinically valuable information in deciding whether to pursue antiamyloid therapy or whether to consider alternative diagnoses.

TAU PET

The spatial distribution of pathologic tau hyperphosphorylation and neurofibrillary tangle deposition corresponds to AD pathology, as characterized in Braak neurofibrillary tangle staging as a measure of abnormal tau at autopsy. Antemortem evaluation of pathologic tau distribution can be performed with PET. ^{18}F-flortaucipir (AV-1451) is the only FDA-approved radiopharmaceutical for tau PET and has been found to closely follow neurofibrillary tangle Braak staging for AD (Table 4) (*31,32*).

Per the FDA package insert, ^{18}F-flortaucipir is indicated to assess tau burden in cognitively impaired adults being evaluated for AD. The scan should be interpreted without consideration of collateral information such as clinical data or other biomarkers, which may bias the interpretation. At present, tau PET is not indicated for evaluating non-AD tauopathies or chronic traumatic encephalopathy (*32,33*).

^{18}F-flortaucipir binds with high affinity to paired helical filament tau, and abnormal radiotracer binding in the neocortex above background is the basis for identifying a positive tau PET scan (Fig. 4) (*34*). A threshold level of background uptake is set at 1.65-fold the average cerebellar uptake, and the manufacturer-specified display

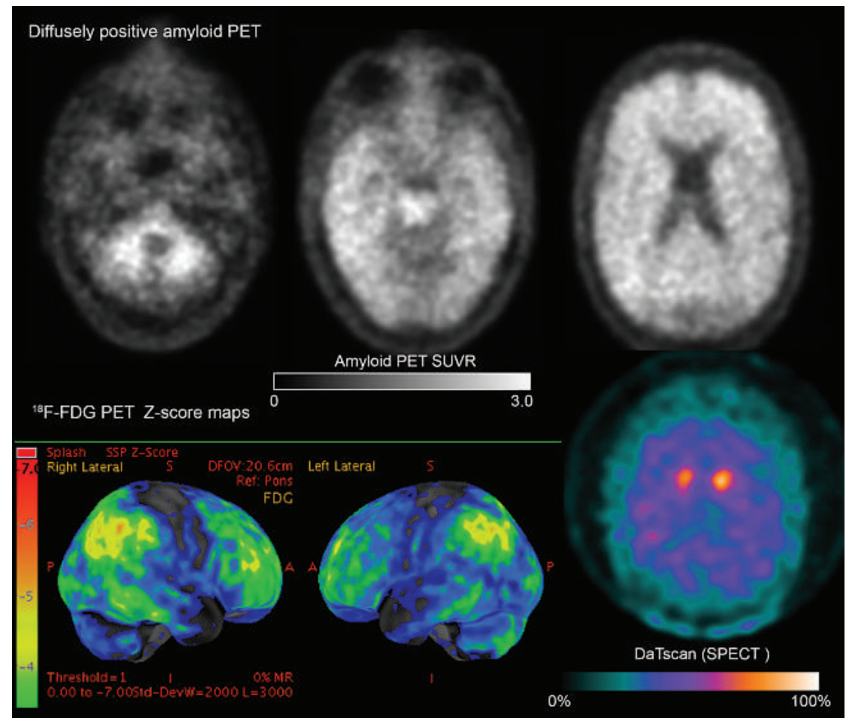

FIGURE 3. Pitfall of diffusely positive amyloid PET in dementia with Lewy bodies. (Top row) ^{11}C-PiB PET is positive and shows diffuse loss of gray–white contrast in both cerebral hemispheres. (Bottom row) ^{18}F-FDG PET *z* score map (left and center) in same person shows hypometabolism in occipital lobes, atypical region for AD, in pattern suggestive of dementia with Lewy bodies. ^{123}I-ioflupane SPECT (DaTscan; GE Healthcare) is abnormal (right), further supporting diagnosis of dementia with Lewy bodies, which was ultimately confirmed at autopsy. In non-Alzheimer neurodegenerative pathology, presence of diffuse plaques without neuritic components may still be associated with abnormal amyloid PET. SUVR = SUV ratio.

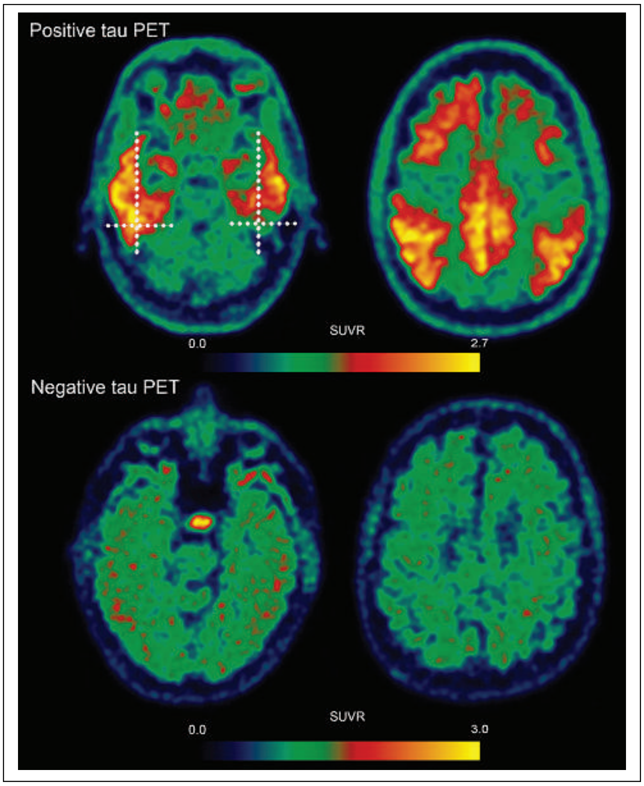

FIGURE 4. Tau PET with ^{18}F-flortaucipir. (Top row) Positive tau PET with areas of abnormally increased (red and orange color overlay) uptake in lateral temporal, frontal, and parietal lobes, including precuneus and posterior cingulate. Temporal lobes are divided into quadrants (dotted lines). Only uptake in posterolateral quadrant of temporal lobe should be used to consider ^{18}F-flortaucipir PET scan positive using visual interpretation. (Bottom row) Negative tau PET with no abnormally increased regions of uptake in cerebral hemispheres. SUVR = SUV ratio.

guidelines for ^{18}F-flortaucipir are devised to set the color scale to show a transition above background level uptake. Sequentially, neocortical uptake should be assessed in each lobe: temporal, occipital, parietal, and frontal. The temporal lobe should be subdivided into quadrants (Fig. 4) including anterolateral, anterior mesial, posterolateral, and posterior mesial temporal. Only the posterolateral temporal quadrant can contribute to classification of a positive tau PET scan. Uptake in the anterior and medial temporal lobe does not meet visual interpretation criteria for a positive tau PET scan. Abnormal uptake in the parietal lobe/precuneus or in the occipital lobes may also qualify a scan as positive for widely distributed tau pathology. Abnormal frontal uptake may or may not be identified in positive scans. Negative scans may have ^{18}F-flortaucipir uptake in the medial or anterolateral temporal lobes, frontal lobes, or deep gray nuclei and white matter (*32,34*).

As with amyloid PET radiotracers, volume loss can be a pitfall, rendering distinction of neocortical binding from white matter uptake difficult. Careful correlation with anatomic images can be useful in the setting of parenchymal volume loss. Small noncontiguous foci of uptake should be interpreted with caution, particularly in scans with increased noise, as these can lead to a false-positive assessment (*35*).

Off-target binding of ^{18}F-flortaucipir is a limitation (Fig. 5) and can involve structures such as the brain stem nuclei and substantia nigra, striatum, choroid plexus, leptomeninges, and blood vessels (*36*). Possible mechanisms have been suggested for off-target binding, such as radiotracer affinity for monoamine oxidase A and B, pigmented compounds such as neuromelanin, and mineralized structures (*32,36*). ^{18}F-flortaucipir binding has also been reported within meningiomas (Supplemental Fig. 2) (*37*). Binding to the leptomeningeal structures could be mistaken for cortical uptake, a pitfall that may be avoided with careful attention to coregistered anatomic images. Off-target binding may potentially be ameliorated with next-generation tau radiotracers (*36*).

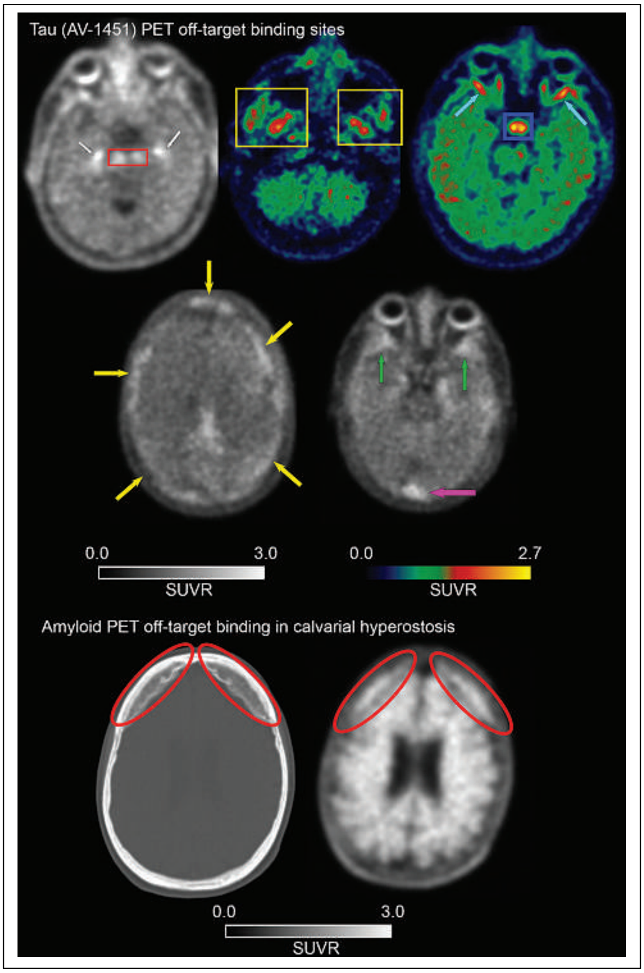

FIGURE 5. Off-target binding on tau and amyloid PET. (Top 2 rows) ^{18}F-flortaucipir PET shows off-target uptake in substantia nigra (red rectangle), choroid plexus (white arrows), muscles of mastication (yellow rectangles), extraocular muscles (cyan arrows), and multiple osseous structure including calvarium (yellow arrows), occiput (pink arrow), and sphenoid bones (green arrows). (Bottom row) Off-target osseous uptake can also be seen on amyloid PET (^{18}F-florbetapir PET/CT) showing avid region of hyperostosis frontalis interna (ellipses), which in some cases could mimic cortical uptake without anatomic correlation. SUVR = SUV ratio.

^{18}F-flortaucipir uptake correlates strongly with the 3R + 4R isoform of tau associated with AD but is not strongly associated with preferential 3R or 4R isoforms of tau, a limitation of the radiotracer's ability to assess other non-AD tauopathies in cases of Pick disease (3R predominant), corticobasal degeneration (4R predominant), or progressive supranuclear palsy (4R predominant). Weak binding to TDP-43 (transactive response DNA binding protein of 43 kDa) may confound diagnosis in cases of frontotemporal lobar degeneration TDP. Although tau PET is an important biomarker

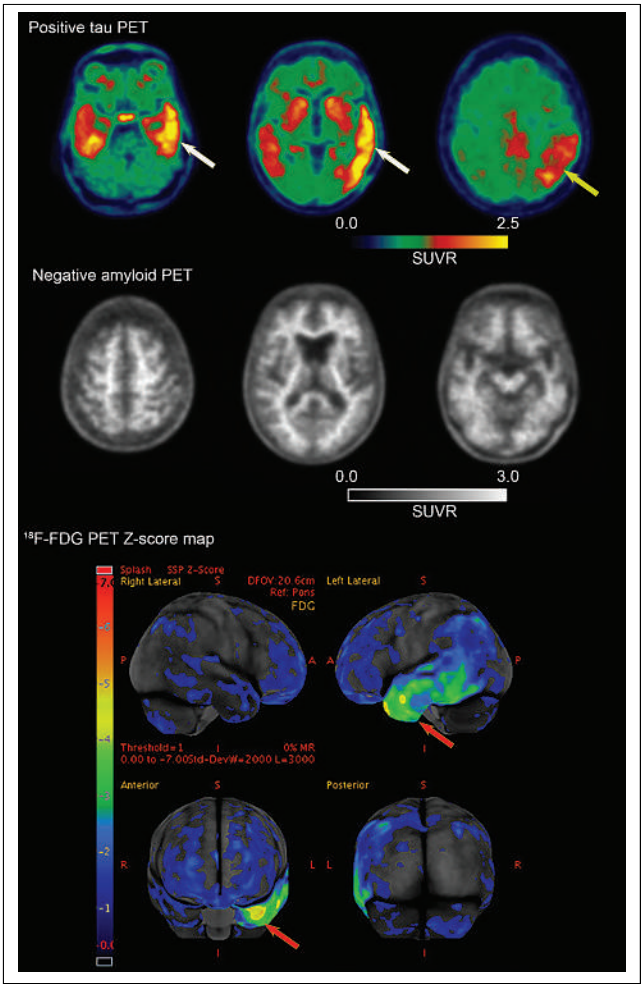

FIGURE 6. Positive tau PET in semantic dementia. (Top row) Multiple PET examinations from patient with semantic dementia, commonly with underlying TDP-43 proteinopathy. ^{18}F-flortaucipir PET was positive, more prominently in left than right temporal lobes (white arrows) and left parietal lobe (yellow arrow). (Second row) ^{11}C-PiB PET was negative, with preserved gray–white contrast indicating lack of moderate or frequent amyloid-β neuritic plaques. (Third and fourth rows) ^{18}F-FDG PET *z* score maps demonstrated regions of hypometabolism correlating with tau PET, worst in left anterior temporal lobe (arrows). Pattern of hypometabolism is characteristic of semantic dementia. Although tau PET was positive, which can be seen with AD, alternative neurodegenerative entities can also result in abnormal tau PET. In this case, negative amyloid PET and pattern of ^{18}F-FDG hypometabolism suggest semantic dementia. SUVR = SUV ratio.

for AD, positive uptake on tau PET can be seen in alternative neurodegenerative conditions such as semantic dementia (Fig. 6) and prion protein defects (Supplemental Fig. 3) (*27,28*).

A significant limitation of ^{18}F-flortaucipir PET in evaluation of AD is poor detection of early tau deposition. According to the FDA package insert instruction for ^{18}F-flortaucipir PET, the regions of early tau deposition corresponding to early Braak stages are to be excluded from visual interpretation (Fig. 4). In general, pathologic tau neurofibrillary tangle accumulation occurs earliest in the mesial temporal structures such as the entorhinal cortex, corresponding with early Braak stage distribution (*38*). Specificity for diagnosing AD on the basis of medial temporal involvement alone may be limited, as this can occur in cognitively unimpaired patients. Tau uptake in the entorhinal cortex, hippocampal formations, parahippocampal gyrus, and middle temporal lobe gyrus strongly correlates with poor memory performance, even in cognitively unimpaired individuals (*39*). One factor limiting accurate assessment of early tau on PET is the detection of low levels of uptake above background noise. Technical developments and innovative image processing techniques may help to improve early tau detection, such as the use of the overlap index in sequential scans (*40*). Future updates in Alzheimer diagnostic criteria may incorporate distinct categories of positive tau PET, distinguishing categories of isolated medial temporal uptake and moderate or high neocortical uptake (*11*). At present, these distinctions are not made in the clinical visual interpretation of tau PET (*32*).

Tau PET in cognitively unimpaired individuals has demonstrated uptake in regions that would correspond to early Braak stage involvement but also in extratemporal locations corresponding to more advanced Braak stages (*38*). The variable distribution of tau pathology in both cognitively unimpaired and cognitively impaired individuals underscores the need for placing a positive tau PET scan within a greater clinical context to support a diagnosis of AD.

DOPAMINERGIC PET

Dopaminergic PET is indicated for the evaluation of parkinsonian syndromes in adults (Table 5) (*41*). Parkinsonian syndromes result from loss of the dopaminergic neurons projecting from the substantia nigra pars compacta to the striatum and presents as a movement disorder characterized by bradykinesia, rigidity, tremor, or postural instability. Typical parkinsonian syndrome (idiopathic Parkinson disease) is the most common parkinsonian syndrome (*13,42*). Other distinct neurodegenerative entities that present as parkinsonian syndromes include dementia with Lewy bodies, progressive supranuclear palsy, multisystem atrophy, and corticobasal degeneration and are collectively termed atypical parkinsonian syndromes (*43*). Typical parkinsonian syndrome is a clinical diagnosis relying of the presence of bradykinesia and either rigidity or rest tremor, as well as other supportive criteria and absence of findings suggesting an alternative diagnosis. Response to dopaminergic therapy is an important supportive criterion for typical parkinsonian syndrome, and poor response is suggestive of an atypical parkinsonian syndrome (*44*).

^{18}F-DOPA is a molecular precursor of the dopamine neurotransmitter, and physiologic uptake is expected in viable presynaptic dopaminergic neurons (*45*). One hour before intravenous radiotracer injection, 150 mg of oral carbidopa should be administered to inhibit peripheral decarboxylation of ^{18}F-FODA and augment brain radiotracer availability. Multiple drug classes used in treated

TABLE 5
^{18}F-DOPA Properties

Administered activity (MBq)	Uptake time (min)	PET scan duration	Positive scan criteria
185	80	20	Loss of caudate or putamen uptake above background

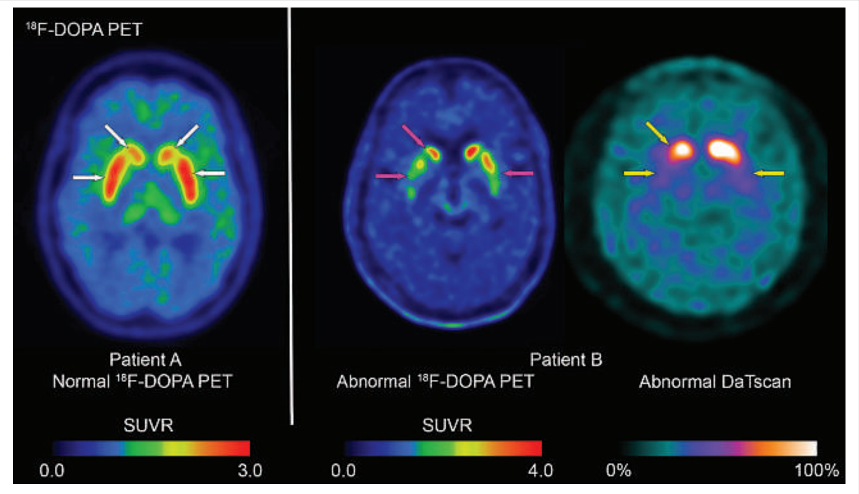

FIGURE 7. Dopaminergic PET. (Left) Normal ^{18}F-DOPA PET examination with expected uptake in caudate and putamen bilaterally (arrows). (Center) Abnormal ^{18}F-DOPA PET examination in 43-y-old woman with onset of Parkinson disease at early age. Abnormal examination shows diminished uptake in bilateral putamina, asymmetrically worse on patient's right, and subtle decreased uptake in patient's right caudate (arrows). (Right) In same patient, ^{123}I-ioflupane SPECT (DaTscan; GE Healthcare) was also abnormal, with decreased basal ganglia uptake (arrows) causing loss of expected comma-shaped region of uptake, asymmetrically worse on patient's right. SUVR = SUV ratio.

parkinsonian syndromes should be discontinued 12 h before radiotracer injection, including dopamine agonists, reuptake inhibitors, releasing agents, catechol-*O*-methyltransferase inhibitors, and monoamine oxidase inhibitors. After ^{18}F-DOPA injection and uptake, a 3-dimensional PET acquisition is recommended. Axial images should be reconstructed along the anterior–posterior commissure line. Images are to be interpreted on the basis of visual inspection, without collateral clinical information used to influence the classification as normal or abnormal (*41*).

A normal (negative) scan should demonstrate radiotracer-avid basal ganglia structures including the caudate head and putamen (Fig. 7), together forming a crescent shape. A positive (abnormal) scan may have asymmetric or symmetric reduction of uptake in the putamen, resulting in either diminished intensity of uptake or a truncated region of uptake in the putamen. Uptake may also be reduced in the caudate nuclei in a positive scan.

A positive scan may indicate a typical or atypical parkinsonian syndrome by detecting loss of striatal dopaminergic neurons in Parkinson disease, progressive supranuclear palsy, corticobasal degeneration, and multiple-system atrophy. Dopaminergic PET may also be useful in diagnosing dementia with Lewy bodies (*46*). These different entities cannot be distinguished on the basis of dopaminergic PET. Conditions resulting in a negative scan may include essential tremor or other causes of parkinsonian syndromes including pharmacologic, psychogenic, or vascular etiologies (*15*). In vascular parkinsonism, correlation with anatomic imaging may help avoid an interpretation pitfall. A basal ganglia infarct may explain the patient's symptoms and could result in an abnormal truncated appearance on dopaminergic PET.

^{18}F-DOPA PET has been reported to have a diagnostic performance similar to that of ^{123}I-ioflupane SPECT/CT; however, some discrepancies have been reported, suggesting that more cases are positive with ^{123}I-ioflupane SPECT (*47–49*). In the setting of dopaminergic neuron loss, upregulation of dopamine synthesis in the residual neurons could preserve uptake of ^{18}F-DOPA relative to ^{123}I-ioflupane. Advantages of ^{18}F-DOPA PET include improved spatial resolution and a shorter uptake time of 1.5 h, compared with 3–6 h for ^{123}I ioflupane SPECT (*41,50*). At present, ^{123}I-ioflupane SPECT is more widely available and reimbursed.

Multiple investigational agents can image the dopaminergic and monoaminergic systems, including postsynaptic dopamine receptor ligands and presynaptic targets such as the dopamine active transporter. ^{18}F-DOPA and ^{123}I-ioflupane are the radiopharmaceuticals used clinically in the United States, with ^{123}I-ioflupane being more frequently used (*51,52*).

In addition to parkinsonian syndromes, dopaminergic PET has been investigated for use in evaluation of schizophrenia, psychosis, and glioma but does not have current FDA regulatory approval for these indications (*53,54*).

CONCLUSION

Multiradiopharmaceutical assessment with amyloid, tau, and ^{18}F-FDG PET provides a relatively comprehensive characterization of the different components of Alzheimer pathophysiology. Amyloid and tau PET contribute a greater level of detail and diagnostic certainty in characterizing AD pathophysiology, which may be critical, particularly when evaluating patients for antiamyloid therapies. Furthermore, amyloid PET confirms the therapeutic target for these therapies.

The multiple PET radiopharmaceuticals discussed in this review can yield a robust characterization of neuropathologic processes, but inherent limitations to the multiple-biomarker approach remain. Challenges remain in detecting early abnormal amyloid and tau on PET. At present, no clinically available radiopharmaceuticals are available for evaluation of some important proteinopathies, including TDP-43 and certain isoforms of tau. Furthermore, reliance on multiple-radiopharmaceutical PET examinations come with increased societal health care costs, increased direct costs to patients, and practical challenges of performing multiple imaging studies. For these reasons, the ability of ^{18}F-FDG PET to distinguish a variety of neurodegenerative patterns and functional information with a single examination is one advantage over the amyloid, tau, and dopaminergic PET examinations discussed in this review.

Familiarity with the visual interpretation methods and protocols for amyloid and tau PET is essential for accurate categorization of a positive or negative scan. For amyloid PET, careful correlation with anatomic imaging may help avoid pitfalls in interpretation such as the common scenario of an abnormal amyloid PET scan with advanced brain parenchymal volume loss, which can mimic normal white matter uptake. For tau PET, knowledge of which regions may have off-target radiotracer binding and which brain parenchymal regions should be excluded from visual interpretation is important for accurate interpretation.

Dopaminergic PET characterizes parkinsonian syndromes but may be abnormal in a variety of parkinsonian syndrome etiologies. Awareness that multiple medications may interfere with uptake is important for avoid a misleading result.

The variety of brain PET radiopharmaceuticals increasingly seen in clinical practice is an indicator of the complexity of dementia. Advances in the in vivo characterization of dementia with PET will likely continue to augment our understanding of the underlying pathophysiology and facilitate evaluation of innovative therapies.

REFERENCES

1. *The Global Dementia Observatory Reference Guide.* World Health Organization; 2018.
2. Hall B, Mak E, Cervenka S, Aigbirhio FI, Rowe JB, O'Brien JT. In vivo tau PET imaging in dementia: pathophysiology, radiotracer quantification, and a systematic review of clinical findings. *Ageing Res Rev.* 2017;36:50–63.
3. Minoshima S, Cross D, Thientunyakit T, Foster NL, Drzezga A. ^{18}F-FDG PET imaging in neurodegenerative dementing disorders: insights into subtype classification, emerging disease categories, and mixed dementia with copathologies. *J Nucl Med.* 2022;63(supp 1):2S–12S.
4. Burkett BJ, Babcock JC, Lowe VJ, Graff-Radford J, Subramaniam RM, Johnson DR. PET imaging of dementia: update 2022. *Clin Nucl Med.* 2022;47:763–773.
5. Mena AM, Strafella AP. Imaging pathological tau in atypical parkinsonisms: a review. *Clin Park Relat Disord.* 2022;7:100155.
6. Jack CR, Bennett DA, Blennow K, et al. NIA-AA research framework: toward a biological definition of Alzheimer's disease. *Alzheimers Dement.* 2018;14:535–562.
7. Kantarci K. 2021 marks a new era for Alzheimer's therapeutics. *Lancet Neurol.* 2022;21:3–4.
8. Jack CR Jr, Bennett DA, Blennow K, et al. A/T/N: an unbiased descriptive classification scheme for Alzheimer disease biomarkers. *Neurology.* 2016;87:539–547.
9. Mukku SSR, Sivakumar PT, Nagaraj C, Mangalore S, Harbishettar V, Varghese M. Clinical utility of ^{18}F-FDG-PET/MRI brain in dementia: preliminary experience from a geriatric clinic in South India. *Asian J Psychiatr.* 2019;44:99–105.
10. Pagani M, Nobili F, Morbelli S, et al. Early identification of MCI converting to AD: a FDG PET study. *Eur J Nucl Med Mol Imaging.* 2017;44:2042–2052.
11. Revised Criteria for Diagnosis and Staging of Alzheimer's Disease: Alzheimer's Association Workgroup. Alzheimer's Association website. https://aaic.alz.org/diagnostic-criteria.asp#drafts. Accessed April 8, 2024.
12. Oldan JD, Jewells VL, Pieper B, Wong TZ. Complete evaluation of dementia: PET and MRI Correlation and diagnosis for the neuroradiologist. *AJNR.* 2021;42:998–1007.
13. Broski SM, Hunt CH, Johnson GB, Morreale RF, Lowe VJ, Peller PJ. Structural and functional imaging in parkinsonian syndromes. *Radiographics.* 2014;34:1273–1292.
14. Mhyre TR, Boyd JT, Hamill RW, Maguire-Zeiss KA. Parkinson's disease. *Subcell Biochem.* 2012;65:389–455.
15. Ibrahim N, Kusmirek J, Struck AF, et al. The sensitivity and specificity of F-DOPA PET in a movement disorder clinic. *Am J Nucl Med Mol Imaging.* 2016;6:102–109.
16. Johnson KA, Minoshima S, Bohnen NI, et al. Appropriate use criteria for amyloid PET: a report of the Amyloid Imaging Task Force, the Society of Nuclear Medicine and Molecular Imaging, and the Alzheimer's Association. *J Nucl Med.* 2013;54:476–490.
17. Minoshima S, Drzezga AE, Barthel H, et al. SNMMI procedure standard/EANM practice guideline for amyloid PET imaging of the brain 1.0. *J Nucl Med.* 2016;57:1316–1322.
18. Ramanan VK, Day GS. Anti-amyloid therapies for Alzheimer disease: finally, good news for patients. *Mol Neurodegener.* 2023;18:42.
19. Budd Haeberlein S, Aisen PS, Barkhof F, et al. Two randomized phase 3 studies of aducanumab in early Alzheimer's disease. *J Prev Alzheimers Dis.* 2022;9:197–210.
20. McDade E, Cummings JL, Dhadda S, et al. Lecanemab in patients with early Alzheimer's disease: detailed results on biomarker, cognitive, and clinical effects from the randomized and open-label extension of the phase 2 proof-of-concept study. *Alzheimers Res Ther.* 2022;14:191.
21. Swanson CJ, Zhang Y, Dhadda S, et al. A randomized, double-blind, phase 2b proof-of-concept clinical trial in early Alzheimer's disease with lecanemab, an anti-Aβ protofibril antibody. *Alzheimers Res Ther.* 2021;13:80.
22. Klunk WE, Engler H, Nordberg A, et al. Imaging brain amyloid in Alzheimer's disease with Pittsburgh compound-B. *Ann Neurol.* 2004;55:306–319.
23. Vizamyl^{TM} flutemetamol F 18 injection. U.S. Food and Drug Administration website. https://www.accessdata.fda.gov/drugsatfda_docs/label/2017/203137s008lbl.pdf. Revised February 2017. Accessed April 8, 2024.
24. Amyvid (florbetapir F 18 injection) for intravenous use. U.S. Food and Drug Administration website. https://www.accessdata.fda.gov/drugsatfda_docs/label/2012/202008s000lbl.pdf. Revised April 2012. Accessed April 8, 2024.
25. NEURACEQ (florbetaben F 18 injection), for intravenous use. U.S. Food and Drug Administration website. https://www.accessdata.fda.gov/drugsatfda_docs/label/2014/204677s000lbl.pdf. Revised March 2014. Accessed April 8, 2024.
26. Johnson DR, Hunt CH, Nathan MA, et al. Pittsburgh compound B (PiB) PET imaging of meningioma and other intracranial tumors. *J Neurooncol.* 2018;136:373–378.
27. Lowe VJ, Lundt ES, Albertson SM, et al. Neuroimaging correlates with neuropathologic schemes in neurodegenerative disease. *Alzheimers Dement.* 2019;15:927–939.
28. Lowe VJ, Lundt ES, Albertson SM, et al. Tau-positron emission tomography correlates with neuropathology findings. *Alzheimers Dement.* 2020;16:561–571.
29. Nedelska Z, Schwarz CG, Lesnick TG, et al. Association of longitudinal β-amyloid accumulation determined by positron emission tomography with clinical and cognitive decline in adults with probable Lewy body dementia. *JAMA Netw Open.* 2019;2:e1916439.
30. Whitwell JL, Tosakulwong N, Weigand SD, et al. Longitudinal amyloid-β PET in atypical Alzheimer's disease and frontotemporal lobar degeneration. *J Alzheimers Dis.* 2020;74:377–389.
31. Fleisher AS, Pontecorvo MJ, Devous MD Sr, et al. Positron emission tomography imaging with [^{18}F]flortaucipir and postmortem assessment of Alzheimer disease neuropathologic changes. *JAMA Neurol.* 2020;77:829–839.
32. TAUVID^{TM} (flortaucipir F 18 injection), for intravenous use. U.S. Food and Drug Administration website. https://www.accessdata.fda.gov/drugsatfda_docs/label/2020/212123s000lbl.pdf. Revised May 2020. Accessed April 8, 2024.
33. Tian M, Civelek AC, Carrio I, et al. International consensus on the use of tau PET imaging agent ^{18}F-flortaucipir in Alzheimer's disease. *Eur J Nucl Med Mol Imaging.* 2022;49:895–904.
34. Groot C, Villeneuve S, Smith R, Hansson O, Ossenkoppele R. Tau PET imaging in neurodegenerative disorders. *J Nucl Med.* 2022;63(suppl 1):20S–26S.
35. Chen CD, Ponisio MR, Lang JA, et al. Comparing tau PET visual interpretation with tau PET quantification, cerebrospinal fluid biomarkers, and longitudinal clinical assessment. *J Alzheimers Dis.* 2023;93:765–777.
36. Lowe VJ, Curran G, Fang P, et al. An autoradiographic evaluation of AV-1451 tau PET in dementia. *Acta Neuropathol Commun.* 2016;4:58.
37. Bruinsma TJ, Johnson DR, Fang P, et al. Uptake of AV-1451 in meningiomas. *Ann Nucl Med.* 2017;31:736–743.
38. Lowe VJ, Wiste HJ, Senjem ML, et al. Widespread brain tau and its association with ageing, Braak stage and Alzheimer's dementia. *Brain.* 2018;141:271–287.
39. Lowe VJ, Bruinsma TJ, Wiste HJ, et al. Cross-sectional associations of tau-PET signal with cognition in cognitively unimpaired adults. *Neurology.* 2019;93:e29–e39.
40. Lee J, Burkett BJ, Min HK, et al. Deep learning-based brain age prediction in normal aging and dementia. *Nat Aging.* 2022;2:412–424.
41. FLUORODOPA F 18 injection, for intravenous use. U.S. Food and Drug Administration website. https://www.accessdata.fda.gov/drugsatfda_docs/label/2019/200655s000lbl.pdf. Revised October 2019. Accessed April 8, 2024.
42. Postuma RB, Berg D, Stern M, et al. MDS clinical diagnostic criteria for Parkinson's disease. *Mov Disord.* 2015;30:1591–1601.
43. Levin J, Kurz A, Arzberger T, Giese A, Höglinger GU. The differential diagnosis and treatment of atypical parkinsonism. *Dtsch Arztebl Int.* 2016;113:61–69.
44. Goetz CG, Tilley BC, Shaftman SR, et al. Movement Disorder Society-sponsored revision of the Unified Parkinson's Disease Rating Scale (MDS-UPDRS): scale presentation and clinimetric testing results. *Mov Disord.* 2008;23:2129–2170.
45. Pretze M, Wängler C, Wängler B. 6-[^{18}F]fluoro-L-DOPA: a well-established neurotracer with expanding application spectrum and strongly improved radiosyntheses. *BioMed Res Int.* 2014;2014:674063.
46. Hu XS, Okamura N, Arai H, et al. ^{18}F-fluorodopa PET study of striatal dopamine uptake in the diagnosis of dementia with Lewy bodies. *Neurology.* 2000;55:1575–1577.
47. Eshuis SA, Maguire RP, Leenders KL, Jonkman S, Jager PL. Comparison of FP-CIT SPECT with F-DOPA PET in patients with de novo and advanced Parkinson's disease. *Eur J Nucl Med Mol Imaging.* 2006;33:200–209.
48. Ishikawa T, Dhawan V, Kazumata K, et al. Comparative nigrostriatal dopaminergic imaging with iodine-123-beta CIT-FP/SPECT and fluorine-18-FDOPA/PET. *J Nucl Med.* 1996;37:1760–1765.
49. Wallert E, Letort E, van der Zant F, et al. Comparison of [^{18}F]-FDOPA PET and [^{123}I]-FP-CIT SPECT acquired in clinical practice for assessing nigrostriatal degeneration in patients with a clinically uncertain parkinsonian syndrome. *EJNMMI Res.* 2022;12:68.
50. Banks KP, Peacock JG, Clemenshaw MN, Kuo PH. Optimizing the diagnosis of parkinsonian syndromes with ^{123}I-ioflupane brain SPECT. *AJR.* 2019;213:243–253.
51. Kanthan M, Cumming P, Hooker JM, Vasdev N. Classics in neuroimaging: imaging the dopaminergic pathway with PET. *ACS Chem Neurosci.* 2017;8:1817–1819.
52. Post MR, Sulzer D. The chemical tools for imaging dopamine release. *Cell Chem Biol.* 2021;28:748–764.
53. Veronese M, Santangelo B, Jauhar S, et al. A potential biomarker for treatment stratification in psychosis: evaluation of an [^{18}F] FDOPA PET imaging approach. *Neuropsychopharmacology.* 2021;46:1122–1132.
54. Pafundi DH, Laack NN, Youland RS, et al. Biopsy validation of ^{18}F-DOPA PET and biodistribution in gliomas for neurosurgical planning and radiotherapy target delineation: results of a prospective pilot study. *Neuro Oncol.* 2013;15:1058–1067.

MRI and ^{18}F-FET PET for Multimodal Treatment Monitoring in Patients with Brain Metastases: A Cost-Effectiveness Analysis

Jurij Rosen[1], Jan-Michael Werner[2], Garry S. Ceccon[2], Elena K. Rosen[2], Michael M. Wollring[2,3], Isabelle Stetter[2], Philipp Lohmann[3], Felix M. Mottaghy[4–6], Gereon R. Fink[2,3], Karl-Josef Langen[3,4,6], and Norbert Galldiks[2,3,6]

[1]Department of Psychiatry, Faculty of Medicine and University Hospital Cologne, University of Cologne, Cologne, Germany; [2]Department of Neurology, Faculty of Medicine and University Hospital Cologne, University of Cologne, Cologne, Germany; [3]Institute of Neuroscience and Medicine, Research Center Juelich, Juelich, Germany; [4]Department of Nuclear Medicine, RWTH University Hospital Aachen, Aachen, Germany; [5]Department of Radiology and Nuclear Medicine, Maastricht University Medical Center, Maastricht, The Netherlands; and [6]Center for Integrated Oncology, Aachen Bonn Cologne Duesseldorf, Germany

PET using the radiolabeled amino acid *O*-(2-[^{18}F]fluoroethyl)-L-tyrosine (^{18}F-FET) has been shown to be of value for treatment monitoring in patients with brain metastases after multimodal therapy, especially in clinical situations with equivocal MRI findings. As medical procedures must be justified socioeconomically, we determined the effectiveness and cost-effectiveness of ^{18}F-FET PET for treatment monitoring of multimodal therapy, including checkpoint inhibitors, targeted therapies, radiotherapy, and combinations thereof in patients with brain metastases secondary to melanoma or non–small cell lung cancer. **Methods:** We analyzed already-published clinical data and calculated the associated costs from the German statutory health insurance system perspective. Two clinical scenarios were considered: decision tree model 1 determined the effectiveness of ^{18}F-FET PET alone for identifying treatment-related changes, that is, the probability of correctly identifying patients with treatment-related changes confirmed by neuropathology or clinicoradiographically using the Response Assessment in Neuro-Oncology criteria for immunotherapy. The resulting cost-effectiveness ratio showed the cost for each correctly identified patient with treatment-related changes in whom MRI findings remained inconclusive. Decision tree model 2 calculated the effectiveness of both ^{18}F-FET PET and MRI, that is, the probability of correctly identifying nonresponders to treatment. The incremental cost-effectiveness ratio was calculated to determine cost-effectiveness, that is, the cost for each additionally identified nonresponder by ^{18}F-FET PET who would have remained undetected by MRI. One-way deterministic and probabilistic sensitivity analyses tested the robustness of the results. **Results:** ^{18}F-FET PET identified 94% of patients with treatment-related changes, resulting in €1,664.23 (€1.00 = $1.08 at time of writing) for each correctly identified patient. Nonresponders were correctly identified in 60% by MRI and in 80% by ^{18}F-FET PET, resulting in €3,292.67 and €3,915.83 for each correctly identified nonresponder by MRI and ^{18}F-FET PET, respectively. The cost to correctly identify 1 additional nonresponder by ^{18}F-FET PET, who would have remained unidentified by MRI, was €5,785.30. **Conclusion:** Given the considerable annual cost of multimodal therapy, the integration of ^{18}F-FET PET can potentially improve patient care while reducing costs.

Key Words: amino acid PET; economic evaluation; immunotherapy; treatment monitoring; treatment-related changes

J Nucl Med 2024; 65:838–844
DOI: 10.2967/jnumed.123.266687

In patients with late-stage cancer, brain metastases develop in up to 40% of cases, worsening the patient's clinical status and prognosis, frequently necessitating a treatment change. In these patients, oligometastasis resection, stereotactic radiosurgery, whole-brain radiotherapy, and conventional cytotoxic chemotherapy are common treatment options (*1*). In recent years, the advent of checkpoint inhibitor immunotherapy and targeted therapies has amplified treatment options by enhancing local tumor control, thereby improving the patient's prognosis. Monitoring the effects of these therapies on brain metastases by contrast-enhanced anatomic MRI has proved challenging regarding the differentiation of treatment-related changes from brain metastasis relapse (*2*). Notably, MRI signal changes may reflect treatment-related changes, especially in combination with radiotherapy, or metastasis relapse.

Considering the limited specificity of anatomic MRI for monitoring treatment effects in patients with brain metastases, PET has increasingly been used to metabolically assess cerebral lesions. Although PET using ^{18}F-FDG is the tracer of choice for numerous diagnostic approaches in patients with cancer, the Response Assessment in Neuro-Oncology Working Group has recommended the use of PET with radiolabeled amino acids such as *O*-(2-[^{18}F]fluoroethyl)-L-tyrosine (^{18}F-FET), as it shows an excellent lesion-to-background ratio due to the relatively low uptake in the normal brain parenchyma (*3*).

Moreover, a recent study by our group (*4*) has suggested that assessing the metabolic activity in patients with brain metastases using ^{18}F-FET PET is both helpful and superior to conventional MRI for monitoring the treatment effects. In particular, we investigated the value of ^{18}F-FET PET in patients with brain metastases secondary to malignant melanoma or non–small cell lung cancer for treatment monitoring of multimodal therapy, including immune checkpoint inhibitors, targeted therapies, radiotherapy, or combinations thereof. We concluded that static ^{18}F-FET PET parameters are valuable for differentiating treatment-related changes from brain metastasis relapse and identifying responders with a longer stable clinical course after treatment. Notably, anatomic MRI could not provide this essential clinical information alone.

Received Sep. 23, 2023; revision accepted Mar. 13, 2024.

For correspondence or reprints, contact Norbert Galldiks (norbert.galldiks@uk-koeln.de).

Nevertheless, integrating ^{18}F-FET PET in the care of patients with brain metastases is associated with additional costs that must be weighed against relevant clinical benefits for affected patients. In recent years, only 1 study has addressed the cost-effectiveness of ^{18}F-FET PET for the differentiation of treatment-related changes from brain metastasis relapse after radiotherapy (*5*). In contrast to that study, the patients included in our analysis were additionally treated with concurrently or subsequently applied checkpoint inhibitors, targeted therapies, or combinations thereof. These agents, particularly when used in combination with radiotherapy, may render MRI findings highly variable, resulting in difficulties in terms of interpretation (*6*). Other studies focused on the cost-effectiveness of ^{18}F-FET PET in glioma patients for surgical target selection or response assessment after different treatment options (*7–10*). Recently, another study analyzed the cost-effectiveness of the somatostatin receptor PET ligand ^{68}Ga-DOTATATE for postresection radiotherapy planning in meningioma patients (*11*). Overall, these studies consistently suggested that PET is cost-effective regarding the analyzed clinical scenario.

Considering the diagnostic improvements and additional costs of ^{18}F-FET PET compared with anatomic MRI, our group's already-published study (*4*) was evaluated regarding the effectiveness and cost-effectiveness of ^{18}F-FET PET in identifying treatment-related changes and nonresponders after multimodal therapy, including immune checkpoint inhibitors, targeted therapies, radiotherapy, or combinations thereof. This analysis was performed from the perspective of the statutory health insurance system in Germany. To our knowledge, this is the first study investigating the effectiveness and cost-effectiveness of ^{18}F-FET PET imaging for managing this patient group.

MATERIALS AND METHODS

Input Data

Our group's study on the value of ^{18}F-FET PET for treatment monitoring of multimodal therapy in patients with brain metastases secondary to malignant melanoma or non–small cell lung cancer was published in 2021 (*4*). In that retrospective study, 40 adults (mean age, 59 ± 13 y) with 107 contrast-enhancing lesions on cerebral MRI were included. Of those 40 patients, 2 patients had to be excluded from further analysis (one patient was lost to follow-up, and the other patient died and the death was not cancer-related), resulting in 38 patients. The institutional review board approved this study, and all subjects gave written informed consent for study participation and evaluation of their data for scientific purposes. The patients were predominantly heavily pretreated with different combinations of immune checkpoint inhibitors, targeted therapies (e.g., BRAF inhibitors), and radiotherapy, and all underwent both MRI and ^{18}F-FET PET during subsequent follow-up for treatment monitoring. A single ^{18}F-FET PET scan was additionally performed on a subgroup of patients ($n = 27$) to differentiate treatment-related changes from brain metastasis relapse when anatomic MRI resulted in equivocal findings. In this group, the static ^{18}F-FET PET parameter mean tumor-to-brain ratio (threshold, 1.95) was found to differentiate best between treatment-related changes and brain metastasis relapse (accuracy, 85%). Clinical verification of the ^{18}F-FET PET imaging diagnosis was based on a stable clinical course during subsequent follow-up and either a neuropathologic diagnosis or a clinicoradiologic diagnosis using the Response Assessment in Neuro-Oncology criteria for immunotherapy (*12*). In the remaining patients ($n = 11$), ^{18}F-FET PET and MRI were performed both at baseline and at follow-up to assess response to treatment. Metabolic response was defined as a relative reduction in the mean tumor-to-brain ratio of 10% or more for ^{18}F-FET PET, a threshold that we found separates best responders from nonresponders using receiver-operating-characteristic curve analyses (*4*). A stable clinical course for at least 6 mo served as the reference for validating the respective imaging diagnosis. We concluded that ^{18}F-FET PET imaging added valuable information for the differentiation of treatment-related changes from brain metastasis relapse when prior MRI remained inconclusive and treatment response evaluation was beyond the information provided by MRI alone.

Decision Tree Models for Assessment of Effectiveness

Similar to earlier studies (*7–10,13*), 2 decision tree models were developed for both analyzed subgroups to assess effectiveness (Fig. 1). Each model integrates the temporal sequence of the applied therapies and neuroimaging and assigns the patients according to their respective imaging findings and, subsequently, their definite diagnosis.

Model 1. After multimodal therapy and subsequent equivocal MRI findings, ^{18}F-FET PET was additionally performed to differentiate between treatment-related changes and a relapse of brain metastases. Chance node 1 (N1) divided patients into groups depending on individual ^{18}F-FET PET findings, and subsequent chance nodes N2 and N3 assigned both groups to the patient's outcomes. We defined the probability of correct identification of treatment-related changes as the primary outcome of model 1.

Model 2. After baseline ^{18}F-FET PET and MRI, and subsequent multimodal therapy, ^{18}F-FET PET and MRI were performed at follow-up to assess response to treatment. Chance nodes divided patients into responders or nonresponders according to ^{18}F-FET PET metabolic findings (N1) or MRI changes according to the Response Assessment in Neuro-Oncology criteria for immunotherapy (N2). The subsequent chance nodes N3–N6 assigned each of the 4 groups of ^{18}F-FET PET and MRI responders (and nonresponders) to the patients' outcomes. In contrast to model 1, model 2 was designed to compare the effectiveness of ^{18}F-FET PET and MRI. We defined the probability of correct identification of a nonresponder to multimodal therapy as the primary outcome of model 2.

Cost Calculation

The costs were calculated from the perspective of the German statutory health insurance system. As the German statutory health insurance companies usually do not cover ^{18}F-FET PET costs in the care of patients with brain metastases, the costs for both ^{18}F-FET PET and conventional MRI were based on the medical fee schedule for care outside the statutory health insurance scheme (http://www.e-bis.de/goae/defaultFrame.htm) to provide an equal and consistent determination of the cost.

As described previously (*10*), the costs taken into consideration for ^{18}F-FET PET were as follows: patient consultation, €10.72 (€1.00 = $1.08 at time of writing) (procedure index no. 1); report on diagnostic findings, €17.43 (procedure index no. 75); intravenous injection, €9.38 (procedure index no. 253); scintigraphy of the brain, €125.91 (procedure index no. 5430); and ^{18}F-FET PET with quantitative analysis, €786.89 (procedure index no. 5489). Tracer production costs were €616.00. For MRI, the costs were as follows: patient consultation, €10.72 (procedure index no. 1); physical examination, €10.72 (procedure index no. 5); report on diagnostic findings, €17.43 (procedure index no. 75); high-pressure intravenous injection, €40.23 (procedure index no. 346); surcharge for perfusion imaging, €75.19 (procedure index no. 3051); MRI with 3-dimensional and apparent-diffusion-coefficient reconstruction requiring substantial technical effort, €641.16 (procedure index no. 5700); additional MRI series with 3-dimensional and apparent-diffusion-coefficient reconstruction requiring substantial technical effort, €145.72 (procedure index no. 5731); and surcharge for computer analysis, €46.63 (procedure index no. 5733).

Thus, the neuroimaging cost was estimated at €1,566.33 for 1 ^{18}F-FET PET scan and €987.80 for 1 MRI scan. In decision tree model 1, because

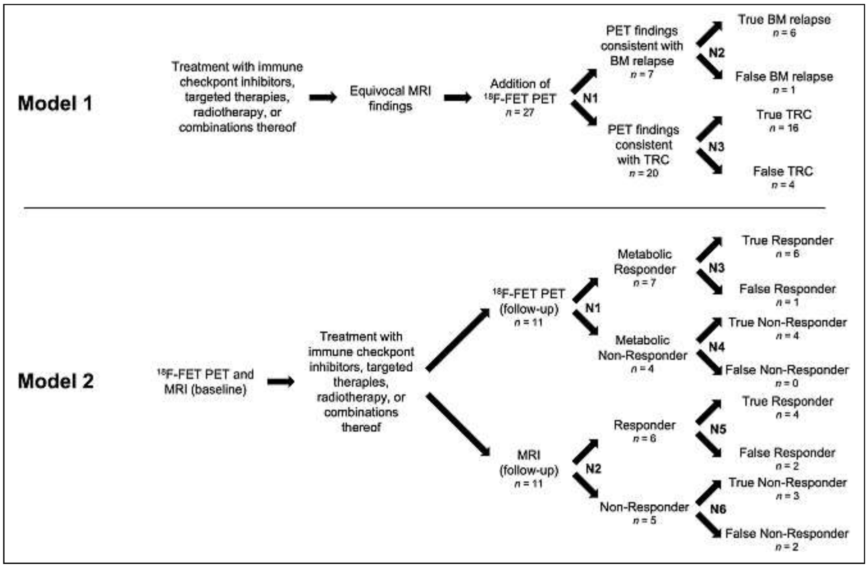

FIGURE 1. Model 1 (upper panel): Decision tree for assessing effectiveness of additional ^{18}F-FET PET for differentiating treatment-related changes (TRC) from brain metastasis (BM) relapse after multimodal therapy. Twenty-seven patients underwent ^{18}F-FET PET. N1 divides patients into those diagnosed with brain metastasis relapse or treatment-related changes according to ^{18}F-FET PET criteria (i.e., mean tumor-to-brain ratio of more or less than 1.95, respectively). N2 and N3 assign both groups to patients' outcomes based on both clinical course during subsequent follow-up and either neuropathologic diagnosis or Response Assessment in Neuro-Oncology criteria for immunotherapy. Model 2 (lower panel): Decision tree model for assessing effectiveness of ^{18}F-FET PET and MRI to identify nonresponder to multimodal therapy based on stable clinical course for <6 mo. Eleven patients underwent serial ^{18}F-FET PET and MRI. N1 and N2 represent chance nodes to be responder or nonresponder according to ^{18}F-FET PET and MRI criteria (i.e., relative reduction or increase in mean tumor-to-background ratio of 10% for ^{18}F-FET PET, respectively; Response Assessment in Neuro-Oncology criteria for immunotherapy for MRI). N3–N6 divide each of 4 groups of ^{18}F-FET PET and MRI responders (and nonresponders) into true and false responders (and nonresponders), respectively.

the differentiation of treatment-related changes from brain metastasis relapse comprised a single ^{18}F-FET PET scan, the cost for each patient was €1,566.33. In decision tree model 2, the assessment of response comprised, on average, 2 ^{18}F-FET PET and 2 MRI scans, resulting in total costs for each patient of €3,132.66 for ^{18}F-FET PET and €1,975.60 for MRI.

Cost-Effectiveness

In decision tree model 1, the effectiveness of correctly identifying treatment-related changes after multimodal therapy was calculated for ^{18}F-FET PET alone. Thus, the cost for 1 ^{18}F-FET PET scan divided by its effectiveness resulted in the cost-effectiveness ratio (CER):

$$\mathrm{CER} = \frac{\mathrm{cost}\ (^{18}\mathrm{F\text{-}FET\ PET})}{\mathrm{effectiveness}\ (^{18}\mathrm{F\text{-}FET\ PET})}.$$

In decision tree model 2, the effectiveness of correctly detecting a nonresponder to multimodal therapy was compared between ^{18}F-FET PET and MRI (i.e., incremental effectiveness [IE]). Thus, the difference in cost between 2 serial ^{18}F-FET PET and 2 MRI scans divided by the IE resulted in the incremental cost-effectiveness ratio (ICER):

$$\mathrm{ICER} = \frac{\mathrm{cost}\ (^{18}\mathrm{F\text{-}FET\ PET}) - \mathrm{cost}\ (\mathrm{MRI})}{\mathrm{effectiveness}\ (^{18}\mathrm{F\text{-}FET\ PET}) - \mathrm{effectiveness}\ (\mathrm{MRI})}.$$

Sensitivity Analyses

Deterministic and probabilistic sensitivity analyses were performed to test the robustness of the calculated effectiveness. In particular, 1-way deterministic sensitivity analysis evaluated the impact of each independent variable (model 1, N1–N3; model 2, N1–N6) on the resulting effectiveness and, thus, the CER and ICER. Because of a lack of previous studies evaluating the cost-effectiveness of ^{18}F-FET PET in patients with brain metastases after multimodal therapy, available CIs already used in a comparable study, which evaluated the cost-effectiveness of ^{18}F-FET PET for the differentiation of brain metastasis relapse from radiation-induced changes after radiotherapy, were applied to each variable (Table 1) (*5*). In model 2, because the calculated value for N4 was 100% (as shown in the corresponding decision tree), changing that chance node value within the deterministic sensitivity analysis resulted in theoretic values of more than 100%. Thus, the resulting IE and ICER based on these values are likewise considered theoretic.

For probabilistic sensitivity analysis, a Monte Carlo simulation was performed using 10,000 sets of positive random values for the independent variables (model 1, N1–N3; model 2, N1–N6). The distribution of these random values was defined by the mean of the decision trees and SD of ^{18}F-FET PET already used in the mentioned study (Table 2) (*5*). For each set of random values, we determined the effectiveness of ^{18}F-FET PET alone (model 1) or the effectiveness of both MRI and ^{18}F-FET PET and their respective difference (i.e., IE) (model 2). The CER and ICER were based on the effectiveness values. All results for the 97.5th percentile and maximum value of effectiveness of ^{18}F-FET PET exceeded 100%, and should be considered theoretic. Meanwhile, when these values served as the basis for calculation of the CI (i.e., the interval between the 2.5th and 97.5th percentiles of distributions derived from the Monte Carlo simulations) of both effectiveness and cost-effectiveness, they were set to a ceiling value of 100%. Moreover, imaging costs were modeled by a γ-distribution with the mean cost for 1 ^{18}F-FET PET scan (model 1) or the difference in cost between 2 serial ^{18}F-FET PET and MRI scans (model 2) and an SD of 50% of the corresponding mean. The probabilistic sensitivity analysis results for effectiveness values are displayed by mean, median, SD, 95% CI, and minimum and maximum values and by the 2.5th, 10th, 90th, and 97.5th percentiles. All calculations, figures, and simulations were performed using the statistical computing language and environment R (https://www.r-project.org/; https://readxl.tidyverse.org/) (*14*). The graphical abstract was created with BioRender.com.

RESULTS

Effectiveness

Decision tree model 1 revealed that ^{18}F-FET PET correctly identified treatment-related changes after multimodal therapy in 94% of patients when MRI findings were equivocal. Thus, 2 patients had to be examined to identify 1 patient with treatment-related changes. Decision tree model 2 revealed that serial ^{18}F-FET PET increased the number of correctly identified nonresponders to multimodal therapy compared with MRI. The proportion of nonresponders additionally identified by ^{18}F-FET PET was 20% higher than by MRI

TABLE 1

Chance Node Intervals and Corresponding Effectiveness and CER in 1-Way Deterministic Sensitivity Analysis for Decision Tree Models 1 and 2

Chance node	Parameter	Decision tree model 1 (identification of treatment-related changes)		Decision tree model 2 (identification of nonresponder)	
		Lower interval	Upper interval	Lower interval	Upper interval
N1	Value (%)	20.4	31.4	58.1	69.1
	Effectiveness (%)	95.6	92.4	23.4	15.8
	CER (€)	1,638.13	1,694.51	4,935.10	7,343.11
N2	Value (%)	76.2	95.2	49.0	60.0
	Effectiveness (%)	90.6	97.9	14.8	25.5
	CER (€)	1,729.33	1,599.13	7,795.63	4,537.22
N3	Value (%)	71.5	88.5	76.2	95.2
	Effectiveness (%)	93.5	94.7	10.6	32.3
	CER (€)	1,675.86	1,654.82	10,906.40	3,585.31
N4	Value (%)			91.5	108.5*
	Effectiveness (%)	NA	NA	18.5	21.3*
	CER (€)			6,240.62	5,439.00*
N5	Value (%)			64.7	68.7
	Effectiveness (%)	NA	NA	21.4	18.5
	CER (€)			5,405.24	6,246.08
N6	Value (%)			58.0	62.0
	Effectiveness (%)	NA	NA	20.8	19.2
	CER (€)			5,558.43	6,021.43

*Theoretic result, because value for N4 is >100%.

NA = not applicable.

Effectiveness and CER were based on indicated chance node values. Decision tree model 1 comprises only N1–N3. Values for effectiveness and CER of decision tree model 2 correspond to incremental values (difference in ^{18}F-FET PET and MRI).

(^{18}F-FET PET metabolic nonresponders, 80%; MRI nonresponders according to the Response Assessment in Neuro-Oncology criteria for immunotherapy, 60%). Thus, 5 patients had to be examined to identify 1 additional nonresponder by ^{18}F-FET PET.

Cost Calculation

For decision tree model 1, the CER resulted in a cost of €1,664.23 for each patient with treatment-related changes identified by ^{18}F-FET PET alone. For decision tree model 2, the cost to

TABLE 2

Input Variables Used in Monte Carlo Analysis

Chance node	Decision tree model 1 (identification of treatment-related changes)		Decision tree model 2 (identification of nonresponder)	
	Calculated value (%)	SD (%)	Calculated value (%)	SD (%)
N1	25.9	5	63.6	5
N2	85.7	8	54.5	5
N3	80.0	8	85.7	8
N4	NA	NA	100.0	8
N5	NA	NA	66.7	8
N6	NA	NA	60.0	8

NA = not applicable.

Calculated values for chance nodes were taken from decision tree models, and SDs were set similar to earlier study (*5*). Decision tree model 1 comprises only N1–N3.

correctly identify 1 nonresponder was €3,292.67 and €3,915.83 for MRI and ^{18}F-FET PET, respectively. The ICER, that is, the cost to correctly identify 1 additional nonresponder by ^{18}F-FET PET who would have remained unidentified by MRI, was €5,785.30.

Sensitivity Analyses

For decision tree model 1, the resulting CER for the chance node intervals of the deterministic sensitivity analysis is presented in Table 1. The upper panel in Figure 2 shows the corresponding tornado diagram. The range of CERs was €1,599.13–€1,729.33. The results of the probabilistic sensitivity analysis showed both a narrow distribution around the mean and a close relation to the calculated effectiveness and CERs of the decision tree (mean effectiveness, 94%; 95% CI, 86%–100%; mean CER, €1,664.61; 95% CI, €1,566.33–€1,814.31) (Table 3; upper panel in Fig. 3). This close relation confirmed the robustness and reliability of the calculated values of the decision tree.

For decision tree model 2, the resulting ICER for the chance node intervals of the deterministic sensitivity analysis is presented in Table 1. The lower panel in Figure 2 shows the corresponding tornado diagram. The range of ICERs was €3,585.31–€10,906.40. The results of the probabilistic sensitivity analysis showed both a narrow distribution around the mean and a close relation to the calculated IE and ICERs of the decision tree (mean IE, 21%; 95% CI, 17%–24%; mean ICER, €5,619.37; 95% CI, €4,894.90–€6,638.61) (Table 3; lower panel in Fig. 3). This close relation confirmed the robustness and reliability of the calculated values of the decision tree.

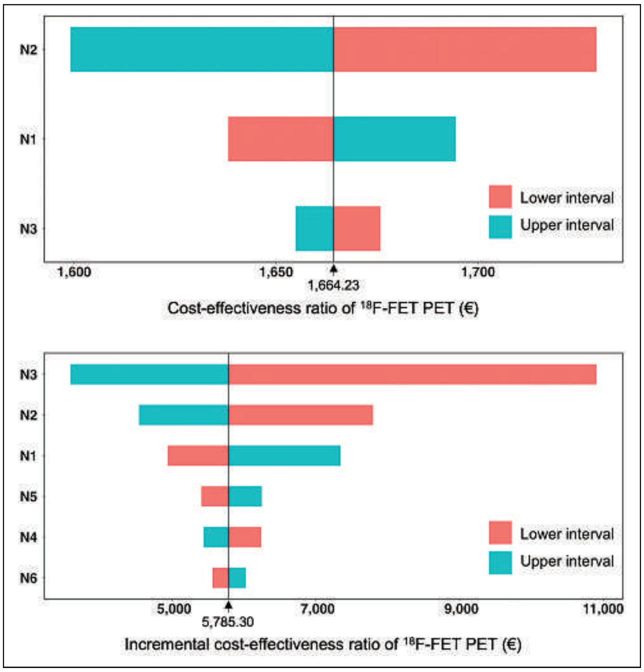

FIGURE 2. Tornado diagrams of cost-effectiveness ratio of additional ^{18}F-FET PET scans for identification of treatment-related changes (upper panel) and ICER of ^{18}F-FET PET for identification of nonresponder (lower panel) after multimodal therapy. Cost-effectiveness ratios and ICERs were calculated by applying upper and lower interval values, as shown in Table 1, onto N1–N3 and N1–N6, respectively.

DISCUSSION

The main finding of the present study is that ^{18}F-FET PET is both clinically effective and cost-effective in identifying treatment-related changes and nonresponders to multimodal therapy among patients with brain metastases secondary to malignant melanoma or non–small cell lung cancer.

Regarding decision tree model 1, our results are based on identifying treatment-related changes as a surrogate since this identification considerably influences further treatment planning in affected patients. This particularly applies to scenarios in which equivocal clinical and MRI findings after multimodal therapy might challenge the continuation of a benefitting treatment, possibly based on the false assumption of a brain metastasis relapse. In these cases, a premature change to a more aggressive treatment regimen, with the risk of severe side effects, reduced survival, and decreased health-related quality of life, can be avoided. Regarding decision tree model 2, our results are based on nonresponsiveness to treatment as a surrogate since this nonresponsiveness likewise heavily influences further treatment planning. This applies to clinical scenarios in which a noneffective and expensive treatment regimen can be discontinued, avoiding further treatment cost.

Given the considerable annual cost of immune checkpoint inhibitors or targeted therapies, ranging from approximately €35,000 to €100,000 in Germany (according to the Federal Joint Committee, https://www.g-ba.de), the expense for ^{18}F-FET PET for treatment monitoring seems to be cost-effective. This particularly applies when considering the total costs for patient care and a potential cost reduction if ineffective treatment is discontinued for nonresponsiveness. Thus, a neuroimaging approach combining conventional MRI and ^{18}F-FET PET can potentially improve the respective strengths of each imaging modality at acceptable cost.

To date, only a limited number of studies on the effectiveness and cost-effectiveness of ^{18}F-FET PET are available, although there is considerable evidence confirming its usefulness in the care of patients with brain malignancies. To our knowledge, this is the first study evaluating the cost-effectiveness of ^{18}F-FET PET for monitoring multimodal therapy in patients with brain metastases. A similar study (*5*) investigated the effectiveness and cost-effectiveness of ^{18}F-FET PET for the differentiation of brain metastasis recurrence from radiation injury after radiotherapy in a similar clinical scenario to that shown in decision tree model 1 but without comedication using immune checkpoint inhibitors or targeted therapies. The authors concluded that ^{18}F-FET PET appears to be cost-effective for that purpose. Compared with our results, the respective ICER was higher (€4.014, based on an "adjusted cost scenario" that was most similar to the present cost calculation) because of lower effectiveness of ^{18}F-FET PET (42%). Nevertheless, in that study, the model assumed initial MRI findings suggestive of brain metastasis relapse for all patients, potentially prompting further invasive diagnostic procedures (e.g., stereotactic biopsy). In contrast, the present model assumed initially equivocal MRI findings. In the present study, this was reflected by the calculation of effectiveness for ^{18}F-FET PET alone, hence limiting the meaningfulness of comparing the CERs of the mentioned study with the present results.

Other studies evaluated the cost-effectiveness of ^{18}F-FET PET in the care of glioma patients for surgical target selection or response assessment after different treatment regimens (*7–10*). In brief, the respective calculated ICERs were roughly comparable to the present results, and the authors concluded that ^{18}F-FET PET

TABLE 3
Statistics Resulting from Monte Carlo Analysis (10,000 Samples) for Effectiveness

	Decision tree model 1 (identification of treatment-related changes)		Decision tree model 2 (identification of nonresponder)			
Value or percentile	^{18}F-FET PET (%)	Cost for ^{18}F-FET PET (€)	MRI (%)	^{18}F-FET PET (%)	IE (%)	Difference in cost ^{18}F-FET PET − MRI (€)
Mean	94.1	1,551.39	60.1	80.7	20.6	1,146.03
SD	3.6	777.79	8.2	10.3		574.56
Minimum	76.7	89.00	28.5	45.3	16.9	65.74
2.5th	86.3	440.92	44.2	61.6	17.4	325.71
10th	89.5	685.46	49.5	68.3	18.8	506.36
Median	94.4	1,420.00	60.0	80.2	20.2	1,048.97
90th	98.4	2,585.29	70.5	93.5	23.0	1,909.78
97.5th	100.5*	3,441.53	76.4	102.7*	26.3*	2,542.28
Maximum	109.2*	6,515.79	98.5	150.6*	52.1*	4,813.26

*Theoretic result, because calculated value for effectiveness of ^{18}F-FET PET is >100%.

Columns for decision tree model 1 indicate, first, probability of correctly detecting treatment-related changes after treatment with immune checkpoint inhibition, targeted therapy, radiotherapy, or combinations thereof by ^{18}F-FET PET alone and, second, γ-distributed cost for 1 ^{18}F-FET PET scan. Columns for decision tree model 2 indicate probability of correctly detecting nonresponder to immune checkpoint inhibition, targeted therapy, radiotherapy, or combinations thereof by MRI or ^{18}F-FET PET, respectively. Column IE indicates their difference and thus IE in using ^{18}F-FET PET. Rightmost column indicates γ-distributed difference in cost between 2 serial ^{18}F-FET PET and MRI scans.

might likewise be cost-effective concerning the analyzed clinical scenario. However, the meaningfulness of a direct comparison of ICERs is limited, given the relevant differences in patients' diagnoses and treatment conditions.

One limitation of the present study is that both decision tree models are based on merely 1 study relying on longitudinal within-group comparisons in a subgroup of predominantly heavily pretreated patients with brain metastases. For example, the relatively low number of included patients analyzed in model 2 may result in a greater degree of uncertainty in terms of ICER. Thus, the present results warrant confirmation by a comparable study with more patients. Another limitation is that the cost was calculated within the context of a specific, that is, German, health care system. As a consequence, the present results for the CERs and ICERs cannot directly be transferred to other countries because of national differences in health care systems and cost structures. On the other hand, the present results for the incremental effectiveness (i.e., the probability of correctly identifying patients with treatment-related changes) appear to be transferable to other countries because these depend predominantly on the information obtained from the respective neuroimaging modality. Thus, incremental effectiveness may help physicians choose the most appropriate neuroimaging approach during follow-up and considerably facilitate further cost evaluations from the perspective of non-German health economics. In addition, earlier studies evaluating the effectiveness and cost-effectiveness of ^{18}F-FET PET for other applications in patients with brain tumors have used an equivalent approach (*5,7–10*), also from the perspective of the Belgian health care system (*13*).

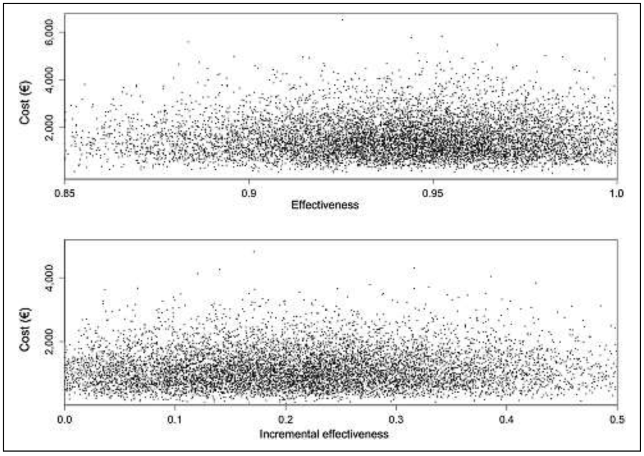

FIGURE 3. Distribution of results from Monte Carlo analysis (dots) about effectiveness of additional ^{18}F-FET PET for identification of treatment-related changes (upper panel) and IE of ^{18}F-FET PET for identification of nonresponder (lower panel) after multimodal therapy. Note different scaling of axes. Margin values for effectiveness (upper panel, values < 0.85 and > 1.0, 5.0% of values; lower panel, values < 0 and > 0.5, 7.4% of values) are not shown.

CONCLUSION

This study suggests that ^{18}F-FET PET is clinically effective and cost-effective for monitoring multimodal therapy in patients with brain metastases secondary to malignant melanoma or non–small cell lung cancer and improves patient care at acceptable costs.

DISCLOSURE

Norbert Galldiks received honoraria for lectures from Blue Earth Diagnostics and for advisory board participation from Telix Pharmaceuticals. Karl-Josef Langen and Felix M. Mottaghy received honoraria for consultancy service from Telix Pharmaceuticals. Philipp Lohmann received speaker honoraria from Blue Earth Diagnostics. No other potential conflict of interest relevant to this article was reported.

KEYPOINTS

QUESTION: Is ^{18}F-FET PET cost-effective for multimodal treatment monitoring in patients with brain metastases secondary to malignant melanoma or non–small cell lung cancer?

PERTINENT FINDINGS: On the basis of published data, ^{18}F-FET PET is cost-effective in identifying both treatment-related changes and nonresponders after multimodal therapy, including immune-checkpoint inhibitors, targeted therapy, radiotherapy, and combinations thereof.

IMPLICATIONS FOR PATIENT CARE: Regarding the considerable annual costs of treatments with immune checkpoint inhibitors or targeted therapies, the integration of ^{18}F-FET PET may improve patient care and reduce costs.

REFERENCES

1. Soffietti R, Abacioglu U, Baumert B, et al. Diagnosis and treatment of brain metastases from solid tumors: guidelines from the European Association of Neuro-Oncology (EANO). *Neuro Oncol.* 2017;19:162–174.
2. Galldiks N, Kocher M, Ceccon G, et al. Imaging challenges of immunotherapy and targeted therapy in patients with brain metastases: response, progression, and pseudoprogression. *Neuro Oncol.* 2020;22:17–30.
3. Galldiks N, Langen KJ, Albert NL, et al. PET imaging in patients with brain metastasis: report of the RANO/PET group. *Neuro Oncol.* 2019;21:585–595.
4. Galldiks N, Abdulla DS, Scheffler M, et al. Treatment monitoring of immunotherapy and targeted therapy using ^{18}F-FET PET in patients with melanoma and lung cancer brain metastases: initial experiences. *J Nucl Med.* 2021;62:464–470.
5. Heinzel A, Muller D, Yekta-Michael SS, et al. *O*-(2-^{18}F-fluoroethyl)-L-tyrosine PET for evaluation of brain metastasis recurrence after radiotherapy: an effectiveness and cost-effectiveness analysis. *Neuro Oncol.* 2017;19:1271–1278.
6. Okada H, Weller M, Huang R, et al. Immunotherapy response assessment in neuro-oncology: a report of the RANO working group. *Lancet Oncol.* 2015;16: e534–e542.
7. Heinzel A, Muller D, Langen KJ, et al. The use of *O*-(2-^{18}F-fluoroethyl)-L-tyrosine PET for treatment management of bevacizumab and irinotecan in patients with recurrent high-grade glioma: a cost-effectiveness analysis. *J Nucl Med.* 2013;54: 1217–1222.
8. Heinzel A, Stock S, Langen KJ, Muller D. Cost-effectiveness analysis of FET PET-guided target selection for the diagnosis of gliomas. *Eur J Nucl Med Mol Imaging.* 2012;39:1089–1096.
9. Heinzel A, Stock S, Langen KJ, Muller D. Cost-effectiveness analysis of amino acid PET-guided surgery for supratentorial high-grade gliomas. *J Nucl Med.* 2012; 53:552–558.
10. Rosen J, Ceccon G, Bauer EK, et al. Cost effectiveness of ^{18}F-FET PET for early treatment response assessment in glioma patients after adjuvant temozolomide chemotherapy. *J Nucl Med.* 2022;63:1677–1682.
11. Rodriguez J, Martinez G, Mahase S, et al. Cost-effectiveness analysis of ^{68}Ga-DOTATATE PET/MRI in radiotherapy planning in patients with intermediate-risk meningioma. *AJNR.* 2023;44:783–791.
12. Lin NU, Lee EQ, Aoyama H, et al. Response assessment criteria for brain metastases: proposal from the RANO group. *Lancet Oncol.* 2015;16:e270–e278.
13. Baguet T, Verhoeven J, De Vos F, Goethals I. Cost-effectiveness of [^{18}F] fluoroethyl-L-tyrosine for temozolomide therapy assessment in patients with glioblastoma. *Front Oncol.* 2019;9:814.
14. Wickham H, Averick M, Bryan J, et al. Welcome to the tidyverse. *J Open Source Softw.* 2019;4:1686.

Detecting Metastatic Patterns of Oligometastatic Breast Cancer: A Comparative Analysis of ^{18}F-FDG PET/CT and Conventional CT Imaging

Rebecca Moser[1], Sophie Pfeiffer[1], Lisena Cala[2], Evelyn Klein[3], Marion Kiechle[3], Sophie T. Behzadi[1], Eva Fallenberg[3], Stephanie E. Combs[1,4,5], Wolfgang Weber[2], and Kai J. Borm[1]

[1]Department of Radiation Oncology, Klinikum Rechts der Isar, TUM School of Medicine and Health, Technical University Munich, Munich, Germany; [2]Department of Nuclear Medicine, Klinikum Rechts der Isar, TUM School of Medicine and Health, Technical University Munich, Munich, Germany; [3]Department of Obstetrics and Gynecology, Klinikum Rechts der Isar, TUM School of Medicine and Health, Technical University Munich, Munich; [4]Department of Radiation Sciences, Germany Institute of Innovative Radiotherapy, Helmholtz Zentrum München, Oberschleißheim, Germany; and [5]German Consortium for Translational Cancer Research, Munich, Germany

Metastasis-directed therapy has the potential to improve progression-free and overall survival in oligometastatic disease (OMD). For breast cancer, however, randomized trials have failed so far to confirm this finding. Because the concept of metastasis-directed therapy in OMD is highly dependent on the accuracy of the imaging modality, we aimed to assess the impact of ^{18}F-FDG PET/CT on the definition of OMD in breast cancer patients. **Methods:** Eighty patients with a total of 150 ^{18}F-FDG PET/CT images (between October 2006 and January 2022) were enrolled in this retrospective study at the Technical University of Munich. The inclusion criteria were OMD, defined as 1–5 distant metastases, at the time of ^{18}F-FDG PET/CT. For the current study, we systemically compared the metastatic pattern on ^{18}F-FDG PET/CT with conventional CT. **Results:** At the time of ^{18}F-FDG PET/CT, 21.3% of patients ($n = 32$) had a first-time diagnosis of metastatic disease, 40.7% ($n = 61$) had a previous history of OMD, and 38% ($n = 57$) had a previous history of polymetastatic disease. In 45.3% of cases, the imaging modality (^{18}F-FDG PET/CT vs. conventional CT) had an impact on the assessment of whether OMD was present. An identical metastatic pattern was observed in only 32% of cases. ^{18}F-FDG PET/CT detected additional metastases in 33.3% of cases, mostly in the nonregional lymph node system. **Conclusion:** The use of ^{18}F-FDG PET/CT had a substantial impact on the definition of OMD and detection of metastatic pattern in breast cancer. Our results emphasize the importance of establishing a standardized definition for imaging modalities in future trials and clinical practices related to metastasis-directed therapy in breast cancer patients.

Key Words: breast cancer; ^{18}F-FDG PET/CT; oligometastatic breast cancer; OMD

J Nucl Med 2024; 65:845–850
DOI: 10.2967/jnumed.123.266925

Oligometastatic disease (OMD) can be considered an intermediate stage between a locally limited tumor and disseminated metastatic disease, as postulated by Hellman and Weichselbaum in 1995. They hypothesized that local treatment of all identified metastases in OMD may prevent progression of the disease (*1*). Most recently, several randomized trials have supported this hypothesis with promising clinical results (*2–4*).

The SABR-COMET trial showed a benefit in overall survival after ablative treatment of up to 5 metastases (*5*). The most common primary tumor types in the study were breast ($n = 18$), lung ($n = 18$), colorectal ($n = 18$), and prostate ($n = 16$). For some of these tumor entities, such as lung and prostate cancer, specific randomized trials have been published, and they confirmed an oncologic benefit of metastasis-directed radiotherapy (MDRT) (*2,6–8*). Additionally, there is growing evidence that MDRT may improve outcomes and delay the need for a change in systemic therapy in oligorecurrent and oligopersistent OMD patients (*9*).

In breast cancer, up to 20% of patients with metastatic disease present with OMD (*10*). Nevertheless, the evidence regarding the benefit of MDRT in these patients is sparse (*11*). Data from the randomized controlled trial of standard-of-care systemic therapy with or without stereotactic body radiotherapy or surgical resection for newly oligometastatic breast cancer (NRG-BR002) suggest that local ablative therapy in addition to systemic therapy does not improve progression-free or overall survival in de novo breast cancer with OMD (1–4 metastases) (*12*). The CURB trial, on the other hand, investigates the benefit of MDRT in oligoprogressive breast and lung cancer patients. In a preplanned interim analysis, the authors showed a progression-free survival benefit. However, the benefit was driven only by the non–small cell lung cancer patients, and no benefit was observed for breast cancer patients (*9*). Even though the results of other randomized trials are pending, the recent data raise questions regarding the role of MDRT in OMD in breast cancer. The value of MDRT in breast cancer is of particular interest because of the large patient collective with OMD and favorable characteristics (luminal A/B, solitary metastasis, bone-only metastasis, long metastasis-free interval), which are associated with a chance of long-term survival (*11*).

So far, the definition of OMD depends solely on the number of imaging-detected metastases, and no clinical or molecular biomarkers exist to aid the detection of OMD (*13–17*). The European Society for Medical Oncology guidelines of 2021 define OMD as a maximum of 5 metastatic lesions, all susceptible to ablative local treatment (*18*). Thus, given the large differences in sensitivity, the

---

Received Oct. 23, 2023; revision accepted Mar. 5, 2024.

For correspondence or reprints, contact Kai J. Borm (kai.borm@mri.tum.de).

imaging modality has an important impact on the OMD definition (*14*). Previous studies demonstrated that ^{18}F-FDG PET/CT had a significantly higher sensitivity in detecting breast cancer metastases than did conventional imaging (*19*). Furthermore, ^{18}F-FDG PET/CT allows differentiation of active from inactive metastases. Nevertheless, to our knowledge, the impact of ^{18}F-FDG PET/CT on the definition of breast cancer with OMD has not been investigated. This is of importance, since unlike tumor entities such as lung cancer and prostate cancer, ^{18}F-FDG PET/CT is not considered a standard procedure for staging in high-risk breast cancer patients (*20*).

MATERIALS AND METHODS

Patient Collective

The retrospective analysis was approved by the local institutional review board (2022-432-S-NP), and the requirement to obtain informed consent was waived. All patients in the current study underwent ^{18}F-FDG PET/CT for breast cancer between October 2006 and January 2022 at the department of nuclear medicine at the Technical University of Munich.

The study included patients with oligometastatic breast cancer, defined as 1–5 distant metastases. Patients with brain metastases or a history of a second malignancy were excluded from the study. In total, the study enrolled 175 patients with 345 ^{18}F-FDG PET/CT scans obtained at different times during the course of their disease. After exclusion of scans that showed no change in metastatic pattern from the previous scan, 80 patients with 150 ^{18}F-FDG PET/CT scans remained for analysis.

The consensus recommendation of the European Society for Radiotherapy and Oncology and the European Organization for Research and Treatment of Cancer (*21*) was used to characterize OMD as follows: de novo OMD: first time diagnosis of metastatic disease, repeat OMD: previous history of OMD, and induced OMD: previous history of polymetastatic disease.

Image Acquisition

^{18}F-FDG PET/CT scans were acquired using a Siemens Biograph 64 (2006–2011; $n = 6$) or a Siemens mCT128 (2012–2022; $n = 144$). The amount of activity injected was adjusted per body weight as recommended by the European Association of Nuclear Medicine guidelines (*22*). Patients with hyperglycemia were excluded from the study. The CT images of the ^{18}F-FDG PET/CT scans were of diagnostic quality. Oral contrast medium was administered to all patients. Patients also received intravenous contrast medium unless there were contraindications, such as significantly impaired renal function or previous allergic reactions. For the diagnostic CT scan, imaging was started in the portal venous phase with the arms raised above the head unless the patient was unable to do so for the duration of the ^{18}F-FDG PET/CT scan. The tube current was modulated according to an exposure control scout scan. Axial CT images of 3- or 5-mm thickness were reconstructed and displayed together with the corresponding ^{18}F-FDG PET/CT images on a Siemens Syngo. In addition, a breath-hold CT scan was acquired for improved detection of small pulmonary nodules.

Assessment of Metastatic Pattern

Each ^{18}F-FDG PET/CT image underwent evaluation by an experienced specialist in nuclear medicine and radiology. For each case, the interdisciplinary team analyzed first conventional CT images alone (conventional CT) and subsequently ^{18}F-FDG PET/CT images. The images, clinical information, and corresponding clinical reports (of only the corresponding imaging modality) were available for the assessment of metastases. For each metastasis, we recorded the localization and assessed the congruence between conventional CT and ^{18}F-FDG PET/CT (Fig. 1). Data were analyzed using SPSS version 26.0.

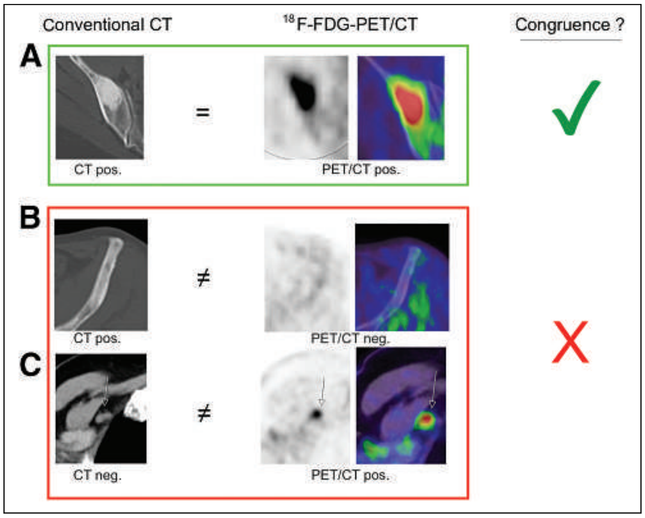

FIGURE 1. Comparison of conventional CT and ^{18}F-FDG PET/CT. (A) Congruence between CT and ^{18}F-FDG PET/CT: suspected metastasis on CT with confirmation on ^{18}F-FDG PET/CT. (B and C) No congruence between imaging modalities: suspected metastasis on CT rated as nonspecific lesion on ^{18}F-FDG PET/CT (B) and nonspecific finding on CT images (occult metastases) with suggestive presentation on ^{18}F-FDG PET/CT (C).

RESULTS

Patient Collective

The patients' characteristics can be found in Table 1. Thirty-two (21.3%) cases were classified as de novo OMD (group 1 according to the consensus recommendation of the European Society for Radiotherapy and Oncology and the European Organization for Research and Treatment of Cancer), 61 cases as repeat

TABLE 1
Patient Characteristics

Category	Characteristic	*n*	%
Histology	Invasive ductal	47	58.7
	Invasive lobular	7	8.8
	Mixed	3	3.8
	Medullary	1	1.3
	Unknown	22	27.5
Molecular subtype	HR+/HER2−	52	65.0
	HR+/HER2+	10	12.5
	HR−/HER2+	6	7.5
	TNBC	9	11.25
	Unknown	3	3.8
Grading	1	4	5
	2	28	35
	3	31	38.75
	Unknown	17	21.3

HR = hormone receptor; + = positive; HER2 = human epidermal growth factor receptor 2; − = negative; TNBC = triple-negative breast cancer.

Mean age was 49.0 y.

TABLE 2
Classification of OMD According to Consensus Recommendation of European Society for Radiotherapy and Oncology and European Organization for Research and Treatment of Cancer

Group	Description	*n*	%
1			
a	Synchronous OMD	8	5.3
b	Metachronous oligorecurrence	2	1.3
c	Metachronous oligoprogression	22	14.7
Total		32	21.3
2			
a	Repeat oligorecurrence	1	0.7
b	Repeat oligopersistence	9	6
c	Repeat oligoprogression	51	34
Total		61	40.6
3			
a	Induced oligorecurrence	0	(0)
b	Induced oligopersistence	14	9.3
c	Induced oligoprogression	43	28.7
Total		57	38

OMD (group 2), and 57 cases as induced OMD (group 3). A detailed description is provided in Table 2. Thirty-two patients (21.3%) had no systemic therapy for metastatic disease before the staging, and in 118 cases (78.7%), patients had systemic therapy for metastatic disease before ^{18}F-FDG PET/CT.

Differences Between ^{18}F-FDG PET/CT and Conventional CT

In only 54.7% ($n = 82$) of cases was OMD diagnosed on both imaging modalities. In the remaining cases, either polymetastatic disease or no distant metastases were detected on 1 of the 2 imaging modalities (Table 3).

The proportion of patients with an identical metastatic pattern on conventional CT and ^{18}F-FDG PET/CT was low, at 32% ($n = 48$) (Fig. 2). In most cases, the number of metastases ($n = 54$; 36%), the location of metastases ($n = 2$; 1.3%), or both ($n = 46$; 30.7%) differed between^{18}F-FDG PET/CT and conventional CT.

In patients with de novo OMD, we observed the best congruence between ^{18}F-FDG PET/CT and conventional CT, whereas in patients with induced OMD, only 12.3% of cases had an identical metastatic pattern on both imaging entities. The differences were attributed mostly to suggestive findings on conventional CT that were rated as unspecific lesions or inactive metastases on ^{18}F-FDG PET/CT (Fig. 3).

TABLE 3
Number of Cases with OMD on ^{18}F-FDG PET/CT Only, on Conventional CT Only, or on Both Imaging Modalities

OMD type	PET/CT	CT	Both modalities
De novo ($n = 32$)	4 (12.5%)	6 (18.8%)	22 (68.8%)
Repeat ($n = 61$)	12 (19.7%)	4 (6.6%)	45 (73.8%)
Induced ($n = 57$)	38 (66.7%)	4 (7.0%)	15 (26.3%)
Total ($n = 150$)	54 (36%)	14 (9.3%)	82 (54.7%)

In 50 cases (33.3%), ^{18}F-FDG PET/CT revealed metastases that were not detected with conventional CT. In 31 (20.7%) cases, less than 50% of ^{18}F-FDG PET/CT–positive lesions were detected on conventional CT (Fig. 3).

Most metastases in our study were in the skeletal system (49.5%), followed by the nonregional lymph nodes (27.1%). The largest deviation between conventional CT and ^{18}F-FDG PET/CT was in the skeletal system. Here, the differences were attributed mostly to pathologic findings on conventional CT that were rated as unspecific lesions or inactive metastases on ^{18}F-FDG PET/CT.

In the nonregional lymph system, on the other hand, 24.3% of metastases were detected only on ^{18}F-FDG PET/CT, being occult on conventional CT. The results are summarized in Table 4.

DISCUSSION

Both the definition and the optimal treatment of OMD are subjects of current research. Currently, the definition of OMD is based on the imaging-detected number of metastases. A 2020 consensus report by the European Society for Radiotherapy and Oncology and American Society for Radiation Oncology defined OMD as a disease with 1–5 metastatic lesions that must be safely treatable regardless of the status of the primaries (*23*). In this report, the authors emphasized the importance of diagnostic imaging: 92% of participants agreed that there are minimum imaging requirements to define an oligometastatic state and that "diagnostic imaging should be performed using whichever modalities are adequate to image sites of common metastases and to detect small lesions for that histology" (*23*). Eighty-two percent of participants agreed that ^{18}F-FDG PET/CT should be performed. Nevertheless, to our knowledge, in none of the large ongoing randomized trials investigating the role of MDRT in breast cancer, ^{18}F-FDG PET/CT staging is mandatory.

The large differences between ^{18}F-FDG PET/CT and conventional CT in our study were attributed to either additional metastases on ^{18}F-FDG PET/CT compared with conventional CT (scenario 1) or metastatic lesions on conventional CT without pathologic ^{18}F-FDG uptake rated as inactive metastases or an unspecific finding (scenario 2).

Both scenarios have important clinical implications. Scenario 1 applied to a third of our study collective. Differences were particularly pronounced for nonregional lymph nodes (Table 4), as can be explained by the low sensitivity (46%) of CT for lymph node metastases (*24*). This low sensitivity for lymph node metastases can be attributed to the fact that distinction is based solely on the size and shape of the lymph node. ^{18}F-FDG PET/CT, on the other hand, provides additional information about metabolic activity, resulting in a better sensitivity for detecting distant metastases. Niikura et al. compared ^{18}F-FDG PET/CT data with findings on biopsy, subsequent imaging, or clinical follow-up in 225 breast cancer patients (*25*). The sensitivity and specificity in the detection of distant metastases were 97.4% and 91.2%, respectively, for ^{18}F-FDG PET/CT and 85.9% and 67.3%, respectively, for conventional imaging (CT, ultrasonography, radiography, and skeletal scintigraphy). Further studies on ^{18}F-FDG PET/CT in breast cancer report even higher sensitivity and specificity (>98%) for the detection of distant metastases (*26*–*28*). The false-positive rate for the detection of metastatic disease is reported to be low, with values below 5% (*27*). Groheux et al. observed that ^{18}F-FDG

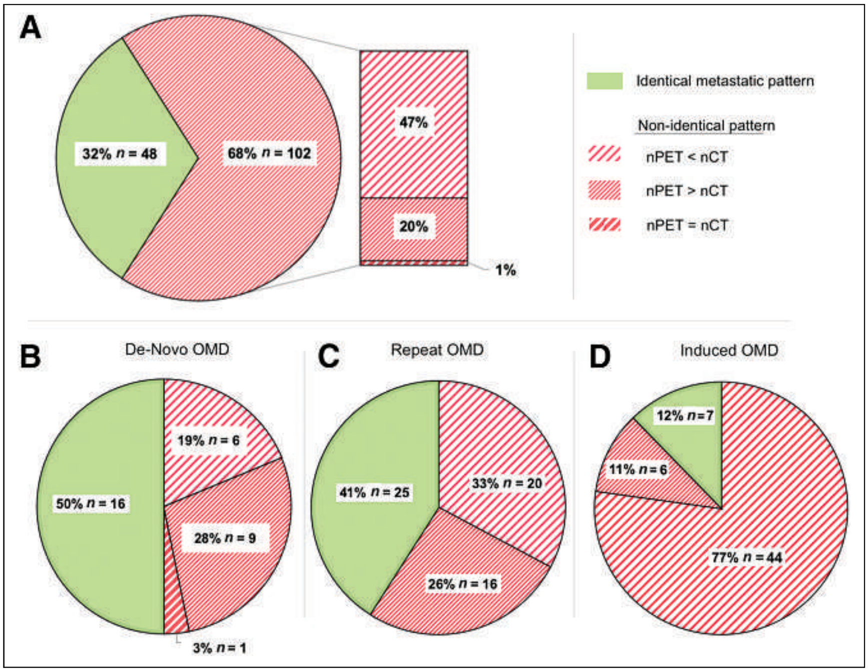

FIGURE 2. Comparison of metastatic pattern between conventional CT and ^{18}F-FDG PET/CT. (A) All groups in European Society for Radiotherapy and Oncology and European Organization for Research and Treatment of Cancer (ESTRO/EORTC) consensus recommendations. (B–D) Collective differentiated by ESTRO/EORTC OMD classification: ESTRO/EORTC group 1: de novo OMD (B); ESTRO/EORTC group 2: repeat OMD (C); and ESTRO/EORTC group 3: induced OMD (D).

PET/CT detected unsuspected metastases in more than 45% of patients with locally advanced breast cancer (*29*). Compared with this, the number of additional metastases was slightly lower in the current study.

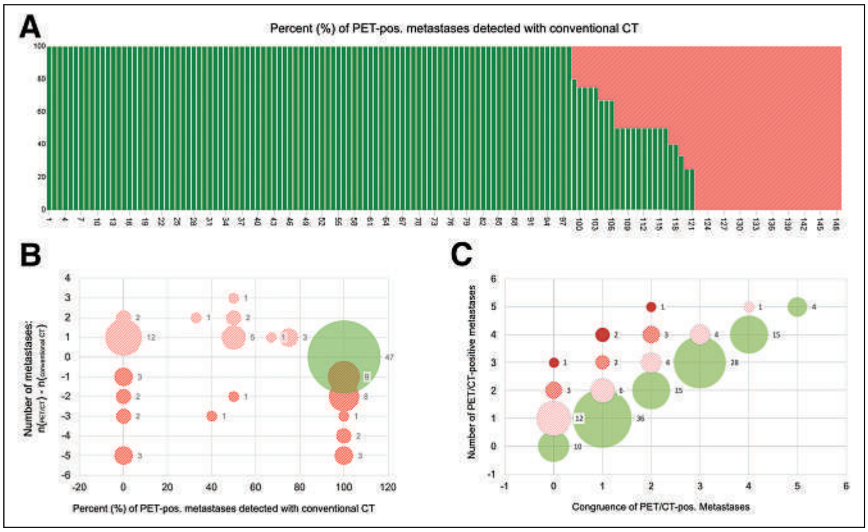

FIGURE 3. Congruence of ^{18}F-FDG PET/CT findings with conventional CT. (A) ^{18}F-FDG PET/CT–positive metastases that were detected on conventional CT (green bars). (B) Difference in detected metastases between imaging modalities (*y*) and percentage of ^{18}F-FDG PET/CT metastases that were also detected on conventional CT (*x*). (C) Number of ^{18}F-FDG PET/CT–positive metastases (*y*) compared with number of PET-positive metastases that were also detected on conventional CT (*x*). Cases with polymetastatic disease on either conventional CT or ^{18}F-FDG PET/CT are excluded from this analysis. Green circles = cases with congruent findings on conventional CT and ^{18}F-FDG PET/CT. Red circles = cases with noncongruent finding in ≥1 metastatic lesion. Diameter of circles correlates with number of cases (small numbers to right).

A high sensitivity for the detection of metastases is crucial for the concept of ablative treatment in OMD, which requires that all active lesions be treated with curative intent to erase the potential sites of origin for further metastasis or local progression (*30,31*). The persistence of a single unrecognized metastasis can jeopardize the success of ablative therapy in OMD (*32*): the ORIOLE trial randomized prostate cancer patients with OMD in stereotactic body radiotherapy versus observation alone. The treatment plan was based on conventional imaging alone, although prostate-specific membrane antigen PET/CT was available. At baseline, in 44%, prostate-specific membrane antigen PET/CT revealed additional positive lesions compared with conventional imaging. A post hoc analysis showed that the extent of undetected metastases on conventional imaging had a direct impact on the oncologic outcome (*8,33*): total consolidation of prostate-specific membrane antigen radiotracer–avid disease decreased the risk of new lesions at 6 mo (16% vs. 63%; *P* = 0.006) (*8*). In the controlled trial of standard-of-care systemic therapy with or without stereotactic body radiotherapy or surgical resection for newly oligometastatic breast cancer (NRG-BR002), new metastases outside index areas as first failure occurred in 40% of cases both in the treatment arm (receiving stereotactic ablative body irradiation and systemic therapy) and in the control arm (systemic therapy). ^{18}F-FDG PET/CT staging was not mandatory. Given the large number of patients with additional metastases on ^{18}F-FDG PET/CT in our study, it can be hypothesized that ^{18}F-FDG PET/CT–directed MDRT could lead to a better oncologic outcome. This is reinforced by the excellent outcomes of small single-arm studies that investigated ^{18}F-FDG PET/CT–directed MDRT in OMD in breast cancer, with local control of 95% and overall survival of 95% (*34,35*). Nonetheless, data directly evaluating the value of ^{18}F-FDG PET/CT in OMD in breast cancer are missing.

Scenario 2 in which ^{18}F-FDG PET/CT revealed fewer metastases than conventional CT applied to 46.7% of cases. In most of these cases, before staging, patients had systemic therapy that led to inactive metastases with normalized glucose metabolism on ^{18}F-FDG PET/CT. In de novo OMD, we found a surprisingly high number of lesions that were positive only on conventional CT, compared with earlier studies (*29,36*). This can be explained by the fact that the previous studies evaluated ^{18}F-FDG PET/CT for initial (preoperative) staging, whereas in our study, most patients in

TABLE 4
Congruence of Metastases Between Conventional CT and ^{18}F-FDG PET/CT in Different Organ Systems

Site	Congruent: PET/CT-positive/CT-positive			Noncongruent					
				PET/CT-positive/CT-negative			PET/CT-negative/CT-positive		
	n	Mean	SD	*n*	Mean	SD	*n*	Mean	SD
Bone	49	0.5	1.0	18	0.2	0.5	68	0.7	1.3
Lung	17	0.2	0.6	0	0	0	0	0	0
Liver	12	0.1	0.3	3	0.03	0.2	2	0.02	0.1
Nonregional lymph node	51	0.5	1.0	18	0.2	0.5	5	0.05	0.3
Cutaneous	1	0.01	0.1	1	0.01	0.1	0	0	0
Other	21	0.2	0.6	4	0.04	0.2	3	0.03	0.2

Cases with polymetastatic disease on either conventional CT or ^{18}F-FDG PET/CT are excluded from this analysis.

group 1 (de novo) had metachronous metastases and thus in most cases prior systemic adjuvant or neoadjuvant treatment. Overall, in our study only 12.3% of cases with induced OMD had the same metastatic pattern on conventional CT and ^{18}F-FDG PET/CT. Thirty-six percent of cases with OMD were detected on only ^{18}F-FDG PET/CT. Thus, use of only conventional CT is not suitable to reliably detect oligopersistent or oligorecurrent disease. In conventional CT, distinguishing between active metastases and inactive residual metastases is not feasible. However, bone scintigraphy in addition to conventional CT is likely to mitigate the large disparities observed in this study between ^{18}F-FDG PET/CT and conventional CT.

Given the large number of patients with repeat and induced OMD that are OMD only on ^{18}F-FDG PET/CT, ^{18}F-FDG PET/CT (or at least conventional CT and bone scintigraphy) should be used as a reference for breast cancer staging and treatment monitoring when metastasis-directed therapy in these patients is being considered. Given the improvements in systemic therapies in recent years, the role of MDRT in repeat OMD or induced OMD is gaining importance. Ablative treatment of residual or progressive oligometastases allows the eradication of potential biologically altered metastases and, in some cases, the continuation of a well-tolerated and effective systemic therapy. Our results imply that the imaging modality in this patient cohort may play a particularly important role because the differences between conventional imaging and ^{18}F-FDG PET/CT are here more pronounced than in the de novo situation.

Potential limitations of the current study include its retrospective design, potential interobserver variability, inclusion of heterogeneous groups of patients, and use of different ^{18}F-FDG PET/CT systems. Additionally, ^{18}F-FDG PET/CT was compared solely with its CT component, with no reference to histopathologic findings. Consequently, the study results are influenced by the sensitivity of imaging and the possibility of false-positive findings. It is crucial to note that the current study did not assess the accuracy of imaging modalities but rather highlighted differences in OMD definition attributable solely to the use of a different imaging modality.

Although both the sensitivity and the specificity of ^{18}F-FDG PET/CT are reported to be high for detecting distant metastases in breast cancer patients (*24–28,37*), some molecular subtypes, such as lobular cancer, may benefit from ^{18}F-flouroestradiol PET/CT for superior detection of estrogen receptor–positive distant metastases (*38*). Therefore, the use of more specific PET/CT tracers could potentially yield even larger differences than observed in the current study, which investigated exclusively ^{18}F-FDG PET/CT. Despite its limitations, this study, to our knowledge, was the first to demonstrate the impact of ^{18}F-FDG PET/CT on defining OMD in breast cancer. It underscores the need for a standardized definition of imaging modality when OMD is being characterized in breast cancer patients.

CONCLUSION

In breast cancer patients with OMD, ^{18}F-FDG PET/CT leads in a third of cases to the detection of additional metastases. Furthermore, conventional CT alone is not suitable for reliably detecting patients with repeat or induced OMD. Thus, the use of ^{18}F-FDG PET/CT has a substantial impact on the definition of OMD and detection of metastatic patterns in breast cancer patients. A standardized definition of the imaging modality is recommended for future trials of, and clinical practice regarding, metastasis-directed therapy in breast cancer patients.

DISCLOSURE

No potential conflict of interest relevant to this article was reported.

KEY POINTS

QUESTION: What is the impact of ^{18}F-FDG PET/CT on detection and diagnosis of OMD in breast cancer?

PERTINENT FINDINGS: In almost half the cases, the imaging modality (^{18}F-FDG PET/CT vs. conventional CT) had an impact on the assessment of whether OMD was present. An identical metastatic pattern was observed in only 32% of cases. ^{18}F-FDG PET/CT detected additional metastases in 33.3% of cases.

IMPLICATIONS FOR PATIENT CARE: The imaging modality has a large impact on the definition of OMD in breast cancer, and conventional CT staging may not be the optimal for future trials regarding OMD in breast cancer.

REFERENCES

1. Hellman S, Weichselbaum RR. Oligometastases. *J Clin Oncol.* 1995;13:8–10.
2. Gomez DR, Tang C, Zhang J, et al. Local consolidative therapy vs. maintenance therapy or observation for patients with oligometastatic non-small-cell lung cancer: long-term results of a multi-institutional, phase II, randomized study. *J Clin Oncol.* 2019;37:1558–1565.
3. Iyengar P, Wardak Z, Gerber DE, et al. Consolidative radiotherapy for limited metastatic non-small-cell lung cancer: a phase 2 randomized clinical trial. *JAMA Oncol.* 2018;4:e173501.
4. Ruers T, Van Coevorden F, Punt CJ, et al. Local treatment of unresectable colorectal liver metastases: results of a randomized phase II trial. *J Natl Cancer Inst.* 2017;109:djx015.
5. Palma DA, Olson R, Harrow S, et al. Stereotactic ablative radiotherapy for the comprehensive treatment of oligometastatic cancers: long-term results of the SABR-COMET phase II randomized trial. *J Clin Oncol.* 2020;38:2830–2838.
6. Ost P, Reynders D, Decaestecker K, et al. Surveillance or metastasis-directed therapy for oligometastatic prostate cancer recurrence: a prospective, randomized, multicenter phase II trial. *J Clin Oncol.* 2018;36:446–453.
7. Wang X, Bai YF, Zeng M. First-line tyrosine kinase inhibitor with or without aggressive upfront local radiation therapy in patients with EGFRm oligometastatic non-small-cell lung cancer: interim results of a randomized phase III, open-label clinical trial (SINDAS) (NCT02893332) [abstract]. *Int J Radiat Oncol Biol Phys.* 2020;108(suppl):e81.
8. Phillips R, Shi WY, Deek M, et al. Outcomes of observation vs stereotactic ablative radiation for oligometastatic prostate cancer: the ORIOLE phase 2 randomized clinical trial. *JAMA Oncol.* 2020;6:650–659.
9. Tsai CJ, Yang JT, Guttmann DM, et al. Final analysis of consolidative use of radiotherapy to block (CURB) oligoprogression trial: a randomized study of stereotactic body radiotherapy for oligoprogressive metastatic lung and breast cancers [abstract]. *Int J Radiat Oncol Biol Phys.* 2022;114:1061.
10. Miglietta F, Visani L, Marini S, et al. Oligometastatic breast cancer: dissecting the clinical and biological uniqueness of this emerging entity. Can we pursue curability? *Cancer Treat Rev.* 2022;110:102462.
11. Piroth MD, Krug D, Feyer P, et al. Oligometastasis in breast cancer: current status and treatment options from a radiation oncology perspective. *Strahlenther Onkol.* 2022;198:601–611.
12. Chmura SJ, Winter KA, Woodward WA, et al. A phase IIR/III trial of standard of care systemic therapy with or without stereotactic body radiotherapy (SBRT) and/or surgical resection (SR) for newly oligometastatic breast cancer (NCT02364557) [abstract]. *J Clin Oncol.* 2022;40(suppl):1007.
13. Dingemans AC, Hendriks LEL, Berghmans T, et al. Definition of synchronous oligometastatic non-small cell lung cancer: a consensus report. *J Thorac Oncol.* 2019; 14:2109–2119.
14. deSouza NM, Tempany CM. A risk-based approach to identifying oligometastatic disease on imaging. *Int J Cancer.* 2019;144:422–430.
15. Pitroda SP, Weichselbaum RR. Integrated molecular and clinical staging defines the spectrum of metastatic cancer. *Nat Rev Clin Oncol.* 2019;16:581–588.
16. Lussier YA, Xing HR, Salama JK, et al. MicroRNA expression characterizes oligometastasis(es). *PLoS One.* 2011;6:e28650.
17. Dhondt B, De Bleser E, Claeys T, et al. Discovery and validation of a serum microRNA signature to characterize oligo- and polymetastatic prostate cancer: not ready for prime time. *World J Urol.* 2019;37:2557–2564.
18. Gennari A, Andre F, Barrios CH, et al. ESMO clinical practice guideline for the diagnosis, staging and treatment of patients with metastatic breast cancer. *Ann Oncol.* 2021;32:1475–1495.
19. Yararbas U, Avci NC, Yeniay L, Argon AM. The value of ^{18}F-FDG PET/CT imaging in breast cancer staging. *Bosn J Basic Med Sci.* 2018;18:72–79.
20. Breast cancer, version 3.2022, NCCN clinical practice guidelines in oncology. *J Natl Compr Canc Netw.* 2022;20:691–722.
21. Guckenberger M, Lievens Y, Bouma AB, et al. Characterisation and classification of oligometastatic disease: a European Society for Radiotherapy and Oncology and European Organisation for Research and Treatment of Cancer consensus recommendation. *Lancet Oncol.* 2020;21:e18–e28.
22. Boellaard R, Delgado-Bolton R, Oyen WJ, et al. FDG PET/CT: EANM procedure guidelines for tumour imaging: version 2.0. *Eur J Nucl Med Mol Imaging.* 2015; 42:328–354.
23. Lievens Y, Guckenberger M, Gomez D, et al. Defining oligometastatic disease from a radiation oncology perspective: An ESTRO-ASTRO consensus document. *Radiother Oncol.* 2020;148:157–166.
24. Heusner TA, Kuemmel S, Hahn S, et al. Diagnostic value of full-dose FDG PET/CT for axillary lymph node staging in breast cancer patients. *Eur J Nucl Med Mol Imaging.* 2009;36:1543–1550.
25. Niikura N, Costelloe CM, Madewell JE, et al. FDG-PET/CT compared with conventional imaging in the detection of distant metastases of primary breast cancer. *Oncologist.* 2011;16:1111–1119.
26. Groheux D, Moretti JL, Baillet G, et al. Effect of ^{18}F-FDG PET/CT imaging in patients with clinical stage II and III breast cancer. *Int J Radiat Oncol Biol Phys.* 2008;71:695–704.
27. Groheux D, Hindie E. Breast cancer: initial workup and staging with FDG PET/CT. *Clin Transl Imaging.* 2021;9:221–231.
28. Ming Y, Wu N, Qian T, et al. Progress and future trends in PET/CT and PET/MRI molecular imaging approaches for breast cancer. *Front Oncol.* 2020;10:1301.
29. Groheux D, Hindie E, Delord M, et al. Prognostic impact of ^{18}FDG-PET-CT findings in clinical stage III and IIB breast cancer. *J Natl Cancer Inst.* 2012;104: 1879–1887.
30. Samim M, Molenaar IQ, Seesing MFJ, et al. The diagnostic performance of ^{18}F-FDG PET/CT, CT and MRI in the treatment evaluation of ablation therapy for colorectal liver metastases: a systematic review and meta-analysis. *Surg Oncol.* 2017;26:37–45.
31. Hansen JA, Naghavi-Behzad M, Gerke O, et al. Diagnosis of bone metastases in breast cancer: lesion-based sensitivity of dual-time-point FDG-PET/CT compared to low-dose CT and bone scintigraphy. *PLoS One.* 2021;16:e0260066.
32. Beckham TH, Yang TJ, Gomez D, Tsai CJ. Metastasis-directed therapy for oligometastasis and beyond. *Br J Cancer.* 2021;124:136–141.
33. Alberto M, Yim A, Papa N, et al. Role of PSMA PET-guided metastases-directed therapy in oligometastatic recurrent prostate cancer. *Front Oncol.* 2022;12:929444.
34. Trovo M, Furlan C, Polesel J, et al. Radical radiation therapy for oligometastatic breast cancer: results of a prospective phase II trial. *Radiother Oncol.* 2018;126: 177–180.
35. David S, Tan J, Savas P, et al. Stereotactic ablative body radiotherapy (SABR) for bone only oligometastatic breast cancer: a prospective clinical trial. *Breast.* 2020; 49:55–62.
36. Ko H, Baghdadi Y, Love C, Sparano JA. Clinical utility of ^{18}F-FDG PET/CT in staging localized breast cancer before initiating preoperative systemic therapy. *J Natl Compr Canc Netw.* 2020;18:1240–1246.
37. Sasada S, Masumoto N, Kimura Y, et al. Identification of axillary lymph node metastasis in patients with breast cancer using dual-phase FDG PET/CT. *AJR.* 2019;213:1129–1135.
38. Ulaner GA, Jhaveri K, Chandarlapaty S, et al. Head-to-head evaluation of ^{18}F-FES and ^{18}F-FDG PET/CT in metastatic invasive lobular breast cancer. *J Nucl Med.* 2021;62:326–331.

Early Metabolic Response by PET Predicts Sensitivity to Next-Line Targeted Therapy in *EGFR*-Mutated Lung Cancer with Unknown Mechanism of Acquired Resistance

Martin Schuler[1–3], Jörg Hense[1–3], Kaid Darwiche[2–4], Sebastian Michels[3,5,6], Hubertus Hautzel,[2,3,7], Carsten Kobe[3,6,8], Smiths Lueong[2,3,9], Martin Metzenmacher[1–3], Thomas Herold[2,3,10], Gregor Zaun[1–3], Katharina Laue[1,2], Alexander Drzezga[3,6,8], Dirk Theegarten[2,3,10], Felix Nensa[2,3,11], Jürgen Wolf[3,5,6], Ken Herrmann[2,3,7], and Marcel Wiesweg[1–3]

[1]Department of Medical Oncology, West German Cancer Center, University Hospital Essen, Essen, Germany; [2]Medical Faculty, University Duisburg–Essen, Essen, Germany; [3]National Center for Tumor Diseases West, Essen, Germany; [4]Department of Pulmonary Medicine, West German Cancer Center, University Medicine Essen–Ruhrlandklinik, Essen, Germany; [5]Department of Medicine I, Center for Integrated Oncology, University Hospital Cologne, Cologne, Germany; [6]Medical Faculty, University of Cologne, Cologne, Germany; [7]Department of Nuclear Medicine, West German Cancer Center, University Hospital Essen, Essen, Germany; [8]Department of Nuclear Medicine, Center for Integrated Oncology, University Hospital Cologne, Cologne, Germany; [9]Bridge Institute for Experimental Tumor Therapy, West German Cancer Center, University Hospital Essen, Essen, Germany; [10]Institute of Pathology, West German Cancer Center, University Hospital Essen, Essen, Germany; and [11]Institute of Diagnostic and Interventional Radiology and Neuroradiology, University Hospital Essen, Essen, Germany

---

Targeted therapy with epidermal growth factor receptor (EGFR) tyrosine kinase inhibitors (TKIs) has established the precision oncology paradigm in lung cancer. Most patients with *EGFR*-mutated lung cancer respond but eventually acquire resistance. **Methods:** Patients exhibiting the *EGFR* p.T790M resistance biomarker benefit from sequenced targeted therapy with osimertinib. We hypothesized that metabolic response as detected by ^{18}F-FDG PET after short-course osimertinib identifies additional patients susceptible to sequenced therapy. **Results:** Fourteen patients with *EGFR*-mutated lung cancer and resistance to first- or second-generation EGFR TKI testing negatively for *EGFR* p.T790M were enrolled in a phase II study. Five patients (36%) achieved a metabolic ^{18}F-FDG PET response and continued osimertinib. In those, the median duration of treatment was not reached (95% CI, 24 mo to not estimable), median progression-free survival was 18.7 mo (95% CI, 14.6 mo to not estimable), and median overall survival was 41.5 mo. **Conclusion:** Connecting theranostic osimertinib treatment with early metabolic response assessment by PET enables early identification of patients with unknown mechanisms of TKI resistance who derive dramatic clinical benefit from sequenced osimertinib. This defines a novel paradigm for personalization of targeted therapies in patients with lung cancer dependent on a tractable driver oncogene.

Key Words: targeted therapy; resistance; EGFR TKI; metabolic response; FDG PET/CT

J Nucl Med 2024; 65:851–855
DOI: 10.2967/jnumed.123.266979

The term *personalized cancer therapy* describes the administration of targeted cancer medicines on the basis of predictive biomarkers. Among solid tumors, non–small cell lung cancer (NSCLC) features the most diverse spectrum of globally approved precision medicines. Although the first line of personalized NSCLC therapies has a high likelihood of response, acquired resistance eventually limits their long-term benefit in most patients. Activating somatic epidermal growth factor receptor (EGFR) mutations define a lung cancer entity with high susceptibility to EGFR tyrosine kinase inhibitor (TKI) treatment. They are detected in 10%–15% of lung adenocarcinomas (>40% in East Asian populations), with predominance in nonsmokers and women. Analyses of tissue biopsy samples and circulating tumor DNA taken at progression have identified resistance mechanisms to NSCLC precision medicines (*1–3*). These may inform sequenced targeted therapies using non–cross-resistant agents (*4*) or drug combinations (*5*). Osimertinib treatment in *EGFR* p.T790M-associated acquired resistance is a prime example of sequenced personalized therapy (*6*). *EGFR* p.T790M is detected in approximately 60% of *EGFR*-mutant NSCLC progressing under first- (gefitinib, erlotinib) or second-generation (afatinib, dacomitinib) EGFR TKI (*7*). In those patients, sequenced osimertinib is superior to platinum-based chemotherapy (*8*). Sequenced osimertinib is not available to patients with undetectable *EGFR* p.T790M. We hypothesized that this population still includes patients who may benefit from osimertinib and are thus deprived of an effective therapy because of limitations of current biomarker assay technologies.

PET using the tracer ^{18}F-FDG is an established staging modality in NSCLC and detects metabolically active tumor lesions. The term *metabolic response* describes a reduction in tumor metabolic activity by treatment as detected by sequential ^{18}F-FDG PET scanning (*9*). In NSCLC, metabolic responses have been reported with cytotoxic chemotherapy (*10*), radiation therapy (*11*), and targeted therapies (*12*).

Against this background, we assessed whether a metabolic response by ^{18}F-FDG PET after short-course osimertinib treatment identifies patients with *EGFR* p.T790M-negative resistance to EGFR TKI who still benefit from next-line osimertinib.

Received Nov. 6, 2023; revision accepted Feb. 26, 2024.

For correspondence or reprints, contact Martin Schuler (martin.schuler@uk-essen.de).

TABLE 1
Patient Characteristics ($n = 14$)

Characteristic	*n*	%
Sex		
Female	7	50
Male	7	50
Age at initial diagnosis*		
<60	5	35.7
60–75	7	50
≥75	2	14.3
ECOG performance status		
0	7	50
1	7	50
Histology: adenocarcinoma	14	100
Initial stage		
I–III (with later recurrence)	3	21.4
IV	11	78.6
Prior first- or second-generation TKI		
Afatinib	11	78.6
Afatinib, then gefitinib	1	7.1
Erlotinib	2	14.3
Prior treatment lines		
1	8	57.1
2	4	28.6
3 or 4	2	14.3
TP53 comutation		
Wild type	9	64.3
Mutation	5	35.7

*Median, 69.5 y; range, 50–82 y.

MATERIALS AND METHODS

The open-label, single-armed phase II study THEROS (NCT03810066) explored the feasibility of combining a short course of osimertinib treatment with sequential ^{18}F-FDG PET scanning. The study enrolled patients with metastatic *EGFR*-mutant NSCLC experiencing radiologically confirmed acquired resistance to first- or second-generation EGFR TKI. All patients tested negatively for *EGFR* p.T790M by centrally performed analysis of circulating free DNA. Absence of the *EGFR* p.T790M mutation was also confirmed in a tissue rebiopsy whenever medically safe and feasible. At least 1 tumor lesion with visually clearly increased ^{18}F-FDG uptake above the background level by baseline PET/CT scanning was required. The target lesion was defined as the lesion with the highest ^{18}F-FDG uptake, with no restrictions regarding tissue or organ type (i.e., local recurrence, lymph node and organ metastases). Following PERCIST 1.0, the metabolic volume of a target lesion for calculating the SUV_{peak} corrected for lean body mass was 1 mL. Patients received a single course (28 d) of osimertinib (80 mg daily). The early metabolic response was evaluated per PERCIST (*9*) by a second ^{18}F-FDG PET/CT scan, which per protocol was scheduled between days 15 and 28. Patients with a metabolic response continued taking osimertinib until progression or withdrawal of consent. Patients without a metabolic response were offered standard-of-care therapy (Supplemental Fig. 1A). The primary study endpoint was the rate of metabolic responses to osimertinib, which was assessed using a modified Simon 2-stage design. Methods are further detailed in the supplemental materials (*13*–*19*).

RESULTS

From May 2019 to June 2021, 23 patients were screened, and 14 patients (50% female; median age, 69.6 y [range, 50.6–81.8 y]) were enrolled at 2 sites (Supplemental Fig. 1B; Table 1). Screening failures were due to detection of *EGFR* p.T790M in the central liquid biopsy ($n = 4$), other exclusion criteria ($n = 2$), patient refusal, and rapid clinical deterioration (1 patient each). Of note, a suitable ^{18}F-FDG–avid lesion could be detected in all screening ^{18}F-FDG PET/CT scans. We report clinical follow-up as of January 2023, with a median follow-up time of 27 mo (range of censored overall survival events, 16.6–34.2 mo). Twelve of 14 patients were evaluable for metabolic response. Two patients progressed clinically before the planned ^{18}F-FDG PET/CT

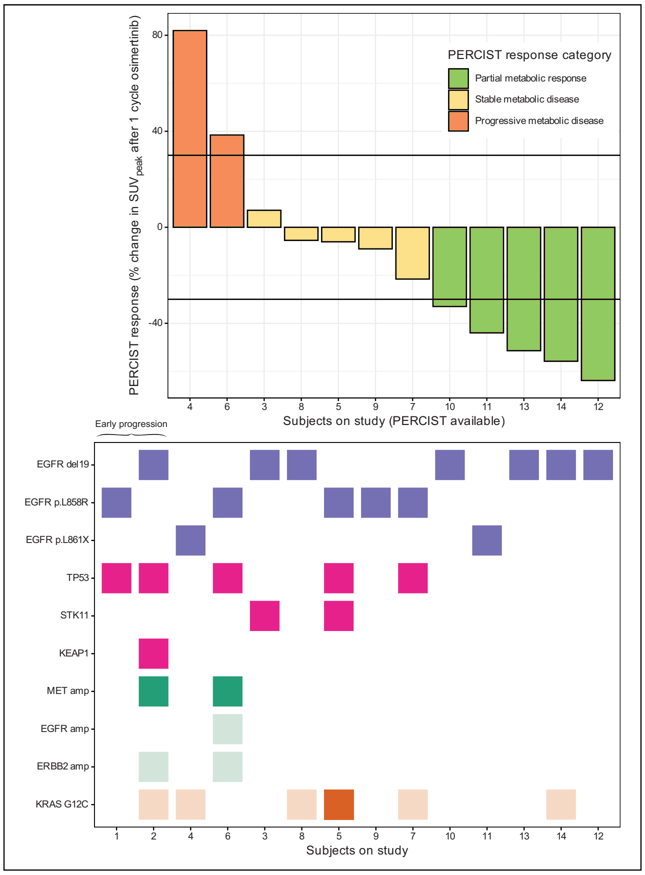

FIGURE 1. Response according to PERCIST and molecular profile. (Top) Relative change in SUV_{peak} corrected for lean body mass (SUL_{peak}) on days 15–28 of osimertinib treatment ($n = 12$). Two patients (patients 1 and 2) were not evaluable because of clinical progression before protocol-defined metabolic response assessment. Patient responses were categorized according to PERCIST as metabolic response (green), metabolically stable disease (yellow), and metabolically progressive disease (orange). (Bottom) Somatic gene mutations detected in tumor and liquid biopsies from each patient, including 2 patients (patients 1 and 2) with rapid disease progression not preceding second ^{18}F-FDG PET (left). Color-coded boxes indicate genomic alterations detected in tissue-derived DNA and circulating free DNA of respective patient (blue = *EGFR* mutations; magenta = *TP53, KEAP1, STK11* mutations; green = *MET, EGFR, ERBB2* copy number gain; brown = *KRAS* p.G12C mutation). Lighter colors indicate alterations detected at low variant allele frequencies.

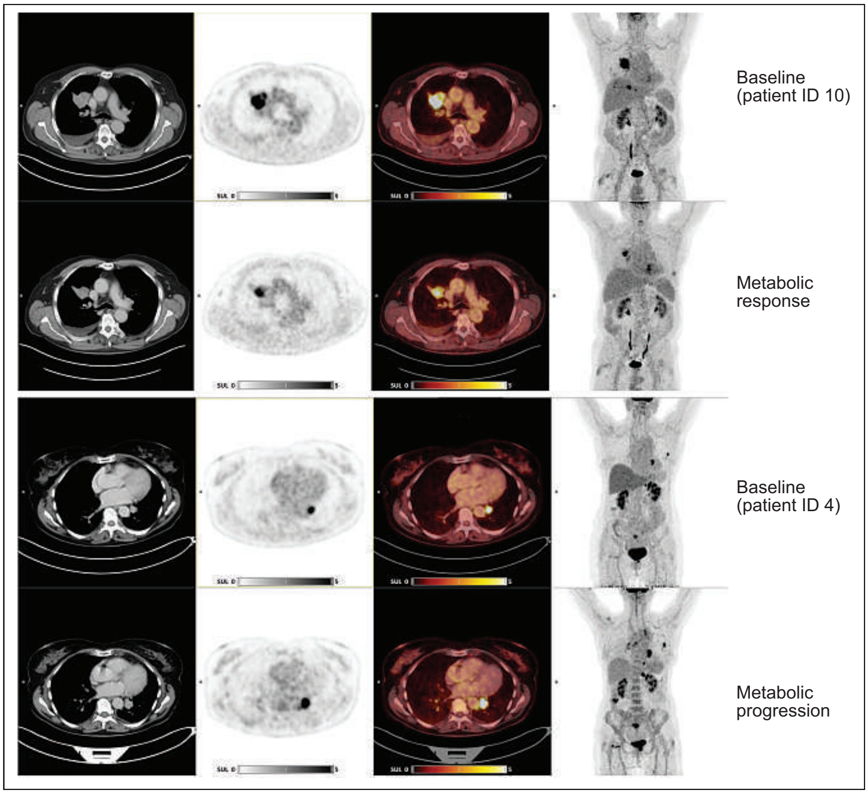

FIGURE 2. Representative ^{18}F-FDG PET/CT images from 2 patients illustrating partial response (top) and progressive disease (bottom) per PERCIST. At baseline, patient 10 had $\mathrm{SUV_{peak}}$ corrected for lean body mass of 18.8, which was reduced to 7.2 (−33%) by 1 cycle of osimertinib, whereas patient 4 increased from 9.2 at baseline to 15.6 at second imaging time point (+82%). ID = identification number.

evaluation and were taken off the study. PET/CT was performed after a median of 21.5 d (interquartile range, 2.75 d; range, 13–31 d). Five patients of the intention-to-treat population (36%) achieved metabolic responses and continued study therapy (Figs. 1 and 2). At 12 mo, all 5 metabolic responders (100%) were still on treatment (Fig. 3). Median progression-free survival in these patients continuing study therapy was 18.7 mo (4 progression-free survival events; 95% CI, 14.6 mo to not estimable; Kaplan–Meier plot in Supplemental Fig. 2A). The protocol allowed continuation of osimertinib beyond progression in patients who maintained clinical benefit. All 4 metabolically responding patients who eventually experienced a progression-free survival event per RECIST continued osimertinib (Fig. 3). With 3 patients still on treatment, the median time to treatment failure in metabolic responders has not been reached.

Postprogression biopsies in 2 patients revealed potential mechanisms of osimertinib resistance, thus confirming the selective pressure of PET response–informed treatment: the *EGFR* p.C797S resistance mutation (*20*) was identified in an adrenal metastasis from 1 patient progressing on osimertinib. Subsequently, this patient responded to gefitinib reexposure. Phenotypic transformation from adenocarcinoma to large cell neuroendocrine lung cancer was confirmed in another patient progressing on osimertinib, who was subsequently managed with chemoimmunotherapy.

Early assessment of metabolic response was highly predictive of survival outcomes (Fig. 4; Supplemental Fig. 2): metabolic responders clearly had superior overall survival (only 1 death at 41.5 mo, $P = 0.011$ compared with patients with stable or progressive disease per PERCIST). Metabolically stable disease per PERCIST selected a subgroup with an intermediate prognosis. Three patients in this group—all experiencing a minor reduction in metabolic activity on ^{18}F-FDG PET/CT—continued osimertinib outside the study (median progression-free survival, 7.2 mo). Patients with metabolically progressive disease had poor outcomes (Fig. 4).

The presence of the *EGFR* p.T790M resistance mutation in circulating free DNA was excluded in all patients by centrally performed next-generation sequencing (*21*). In addition, biobanked blood samples from study patients were retrospectively analyzed using highly sensitive Avenio circulating free DNA technology (Roche). This revealed a complex genomic environment including potential resistance mechanisms such as copy number gains of *MET, EGFR*, and *ERBB2*, and *KRAS* and *CDKN2A* mutations. No metabolically responding patient exhibited mutations in *TP53* and *STK11* or in *MET* and *ERBB2* copy number gain (Fig. 1; Supplemental Fig. 3). In a single metabolically responding patient, the *EGFR* p.T790M mutation was retrospectively detected at a very low variant allele frequency (variant allele frequency, 0.78%) as compared with the original activating *EGFR* exon 19 indel (variant allele frequency, 1.6%). Of note, oncogenic *KRAS* p.G12C mutations were detected at low variant allele frequencies (0.23%–1.5%) in 7 patients. Only one of these patients (variant allele frequency, 0.23%) achieved a PERCIST response to osimertinib. Interestingly, patients not achieving a metabolic response to osimertinib had comutations of *TP53, STK11*, and *KEAP1*, and copy number gains of *MET, ERBB2*, and *EGFR*. Also, *KRAS* mutations were detected at low variant allele frequencies.

DISCUSSION

The study THEROS provides proof of concept for the utility of early metabolic response evaluation by ^{18}F-FDG PET/CT as a predictor of clinical benefit from sequenced EGFR TKI therapy in patients with *EGFR*-mutated NSCLC. Currently, targeted therapy of NSCLC is offered on the basis of predictive genomic biomarkers. Although the predictive specificity of this approach is strong for first-line therapy, a targeted approach to next-line therapy is less developed. Using the well-defined clinical setting of acquired resistance to first- or second-generation EGFR TKI, we identified a considerable risk of withholding effective targeted therapy to biomarker-negative patients. Early metabolic response by ^{18}F-FDG PET/CT was highly predictive of a patient population benefitting from sequenced osimertinib despite not demonstrating the appropriate predictive genomic biomarker, *EGFR* p.T790M.

To our knowledge, this was the first prospective study to explore a theranostic approach toward personalizing next-line therapy in patients with *EGFR*-mutant NSCLC acquiring resistance to

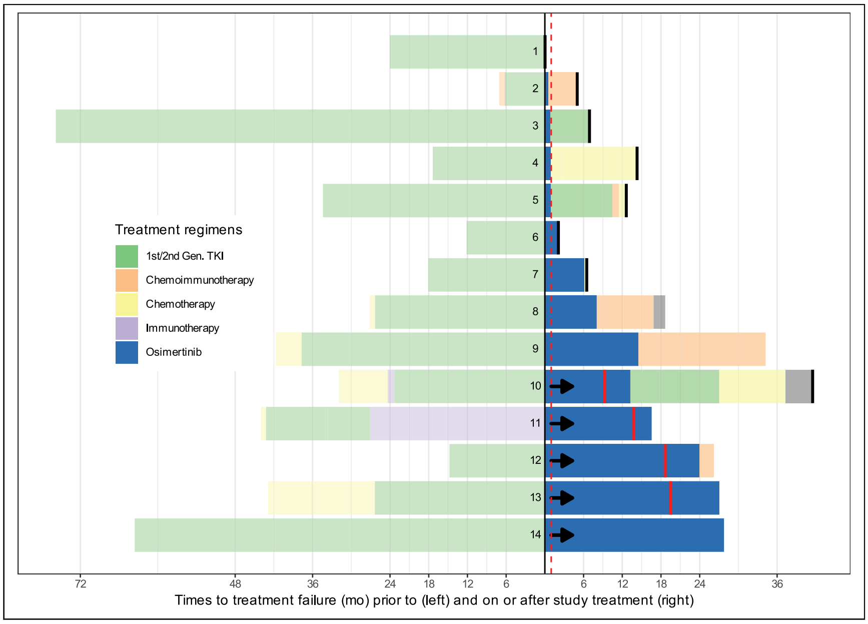

FIGURE 3. Individual treatment trajectories of study patients. Duration of each treatment line before study enrollment (left of vertical black line indicating day 0 of study entry), study treatment, and post-progression treatment (right of vertical black line) is represented on *x*-axis. Individual treatment lines are color-coded (green = first- and second-generation EGFR-TKI; blue = osimertinib [study treatment and treatment beyond progression]; yellow = chemotherapy; orange = chemoimmunotherapy; purple = immunotherapy). Dashed red vertical lines indicate timing of protocol-defined metabolic response assessment per ^{18}F-FDG PET/CT. Within each patient trajectory, arrows indicate ongoing osimertinib treatment at data cutoff (study treatment or treatment beyond progression). Red vertical bars indicate individual time points of progressive disease per RECIST. Vertical black bars indicate patient death.

EGFR TKI treatment of unknown mechanism. We showed that patients achieving an early metabolic response under theranostic short-term osimertinib treatment may derive a dramatic long-term clinical benefit. A key limitation of this proof-of-concept study is its modest cohort size. The introduction of early PET response assessment in prospective clinical studies of next-line TKI therapies is required to establish this novel theranostic approach in clinical practice.

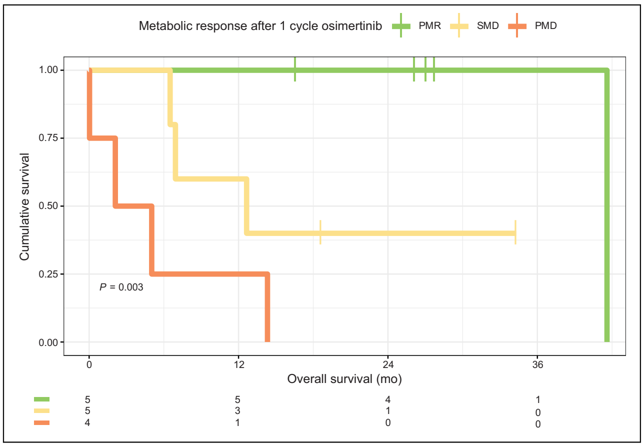

FIGURE 4. Early metabolic response by ^{18}F-FDG PET/CT indicates clinical benefit from osimertinib in patients with unknown resistance mechanisms to EGFR TKI. Shown is overall survival from initiation of study treatment according to PERCIST metabolic response category. PMD = progressive metabolic disease; PMR = partial metabolic response; SMD = stable metabolic disease.

In post hoc analyses, we have characterized the genomic landscape of our study patients with EGFR TKI resistance of unknown mechanism. Interestingly, patients not achieving a metabolic response to osimertinib had comutations of *TP53, STK11,* and *KEAP1* and copy number gains of *MET*, *ERBB2,* and *EGFR*. Also, *KRAS* mutations were detected at low variant allele frequencies. Because the functional significance of these findings is unknown, they are purely hypothesis-generating.

CONCLUSION

Early metabolic response per ^{18}F-FDG PET after short-course osimertinib is a promising dynamic biomarker for personalization of next-line therapy in *EGFR*-mutated NSCLC with acquired resistance to EGFR TKI. Next to *EGFR*-mutated NSCLC, this predictive paradigm could be translated to further settings of NSCLC with dominant driver oncogenes, in which multiple, non–cross-resistant targeted agents are available.

DISCLOSURE

This study received grant support (ESR-16-12451) and study medication from AstraZeneca. The West German Cancer Center and the Center for Integrated Oncology are supported by Oncology Center of Excellence grants from German Cancer Aid (Deutsche Krebshilfe). The West German Cancer Center received federal and state funding as a partner site of the German Cancer Consortium. None of the funding sources were involved in the collection, analysis, and interpretation of data; in the writing of the report; or in the decision to submit the article for publication. Martin Schuler reported fees for consulting from Amgen, AstraZeneca, Blueprint Medicines, Boehringer Ingelheim, Bristol Myers Squibb, GlaxoSmithKline, Janssen, Merck Serono, Novartis, Roche, Sanofi, and Takeda; honoraria for continuing medical education presentations from Amgen, Boehringer Ingelheim, Bristol Myers Squibb, Janssen, MSD, Novartis, Roche, and Sanofi; and research funding to University Hospital Essen from AstraZeneca and Bristol Myers Squibb. Sebastian Michels reported fees for consulting and honoraria for continuing medical education presentations from Janssen and Lilly and research funding to the University of Cologne from Bristol Myers Squibb, Janssen, Novartis, and Pfizer. Martin Metzenmacher reported fees for consulting from Amgen, Astra Zeneca, Bristol Myers Squibb, GlaxoSmithKline, Janssen, MSD, Novartis, Roche, and Takeda. Jürgen Wolf reported fees for consulting and honoraria for continuing medical education presentations from Amgen, AstraZeneca, Bayer, Blueprint, Bristol Myers Squibb, Boehringer Ingelheim, Chugai, Daiichi Sankyo, Janssen, Lilly, Loxo, Merck, Mirati, MSD, Novartis, Nuvalent, Pfizer, Roche, Seattle Genetics, Takeda, and Turning Point and research funding to the University of Cologne from Bristol Myers Squibb, Janssen, Novartis, and Pfizer. Alexander Drzezga reported fees for consulting and speaker honoraria from Siemens Healthineers, Sanofi, GE Healthcare, Biogen, Novo Nordisk, Invicro, Novartis/AAA, and Bayer Vital; research support from Siemens Healthineers, Life Molecular Imaging, GE Healthcare, AVID Radiopharmaceuticals, Sofie, Eisai, and Novartis/AAA; stock from Siemens Healthineers and Lantheus Holding; and a patent for ^{18}F-JK-PSMA7 (patent no. EP3765097A1). Ken Herrmann reported fees for consulting and continuing medical education presentations from Bayer, Sofie Biosciences, SIRTEX, Adacap Curium, Endocyte, IPSEN, Siemens Healthineers, GE Healthcare, Amgen, Fusion, Immedica, Onkowissen.de, Novartis, Molecular Partners, ymabs, Aktis Oncology, Theragnostics, Pharma15, Debiopharm, AstraZeneca, and Janssen; nonfinancial support from ABX; and grants and personal fees from BTG. No other potential conflict of interest relevant to this article was reported.

ACKNOWLEDGMENTS

We thank the patients and their families who participated in the THEROS trial and all staff involved in patient care, study conduct, and translational studies at University Hospital Essen, University Hospital Cologne, and the CRO, ClinAssess, Leverkusen. The West German Biobank Essen is acknowledged for supporting the exploratory biomarker analyses.

KEY POINTS

QUESTION: Can early metabolic response evaluation by ^{18}F-FDG PET/CT serve as a predictor of clinical benefit from sequenced TKI therapy in patients with EGFR-mutated NSCLC?

PERTINENT FINDINGS: ^{18}F-FDG PET after short-course osimertinib treatment identified patients with unknown mechanisms of TKI resistance deriving dramatic clinical benefit from sequenced osimertinib.

IMPLICATIONS FOR PATIENT CARE: The study provides proof of concept that early metabolic response assessment by ^{18}F-FDG PET can be used as a novel paradigm for personalization of multiple lines of targeted therapies in patients with driver oncogene-dependent NSCLC.

REFERENCES

1. Sequist LV, Waltman BA, Dias-Santagata D, et al. Genotypic and histological evolution of lung cancers acquiring resistance to EGFR inhibitors. *Sci Transl Med.* 2011;3:75ra26.
2. Chabon JJ, Simmons AD, Lovejoy AF, et al. Circulating tumour DNA profiling reveals heterogeneity of EGFR inhibitor resistance mechanisms in lung cancer patients. *Nat Commun.* 2016;7:11815.
3. Zhao Y, Murciano-Goroff YR, Xue JY, et al. Diverse alterations associated with resistance to KRAS(G12C) inhibition. *Nature.* 2021;599:679–683.
4. Dagogo-Jack I, Brannon AR, Ferris LA, et al. Tracking the evolution of resistance to ALK tyrosine kinase inhibitors through longitudinal analysis of circulating tumor DNA. *JCO Precis Oncol.* 2018:2018:PO.17.00160.
5. Wu Y-L, Cheng Y, Zhou J, et al. Tepotinib plus gefitinib in patients with EGFR-mutant non-small-cell lung cancer with MET overexpression or MET amplification and acquired resistance to previous EGFR inhibitor (INSIGHT study): an open-label, phase 1b/2, multicentre, randomised trial. *Lancet Respir Med.* 2020;8:1132–1143.
6. Jänne PA, Yang JC-H, Kim D-W, et al. AZD9291 in EGFR inhibitor–resistant non–small-cell lung cancer. *N Engl J Med.* 2015;372:1689–1699.
7. Yu HA, Arcila ME, Rekhtman N, et al. Analysis of tumor specimens at the time of acquired resistance to EGFR-TKI therapy in 155 patients with EGFR-mutant lung cancers. *Clin Cancer Res.* 2013;19:2240–2247.
8. Mok TS, Wu Y-L, Ahn M-J, et al. Osimertinib or platinum–pemetrexed in EGFR T790M–positive lung cancer. *N Engl J Med.* 2017;376:629–640.
9. Wahl RL, Jacene H, Kasamon Y, Lodge MA. From RECIST to PERCIST: evolving considerations for PET response criteria in solid tumors. *J Nucl Med.* 2009;50(suppl 1): 122S–150S.
10. Decoster L, Schallier D, Everaert H, et al. Complete metabolic tumour response, assessed by 18-fluorodeoxyglucose positron emission tomography (^{18}FDG-PET), after induction chemotherapy predicts a favourable outcome in patients with locally advanced non-small cell lung cancer (NSCLC). *Lung Cancer.* 2008;62:55–61.
11. Pöttgen C, Gauler T, Bellendorf A, et al. Standardized uptake decrease on [^{18}F]-fluorodeoxyglucose positron emission tomography after neoadjuvant chemotherapy is a prognostic classifier for long-term outcome after multimodality treatment: secondary analysis of a randomized trial for resectable stage IIIA/B non–small-cell lung cancer. *J Clin Oncol.* 2016;34:2526–2533.
12. Zander T, Scheffler M, Nogova L, et al. Early prediction of nonprogression in advanced non–small-cell lung cancer treated with erlotinib by using [^{18}F]fluorodeoxyglucose and [^{18}F]fluorothymidine positron emission tomography. *J Clin Oncol.* 2011;29:1701–1708.
13. Boellaard R, Delgado-Bolton R, Oyen WJG, et al. FDG PET/CT: EANM procedure guidelines for tumour imaging: version 2.0. *Eur J Nucl Med Mol Imaging.* 2015;42:328–354.
14. Ivanova A, Deal AM. Two-stage design for phase II oncology trials with relaxed futility stopping. *Stat Interface.* 2016;9:93–98.
15. Oxnard GR, Thress KS, Alden RS, et al. Association between plasma genotyping and outcomes of treatment with osimertinib (AZD9291) in advanced non–small-cell lung cancer. *J Clin Oncol.* 2016;34:3375–3382.
16. Wickham H. *ggplot2: Elegant Graphics for Data Analysis.* Springer-Verlag; 2016.
17. Wickham H, Averick M, Bryan J, et al. Welcome to the tidyverse. *J Open Source Softw.* 2019;4:1686.
18. Therneau TM. A package for survival analysis in S. Mayo Clinic website. https://www.mayo.edu/research/documents/tr53pdf/DOC-10027379. Published February 1999. Accessed March 18, 2024.
19. Drawing survival curves using ggplot2. R Packages website. https://rpkgs.datanovia.com/survminer/reference/ggsurvplot.html. Accessed March 18, 2024.
20. Thress KS, Paweletz CP, Felip E, et al. Acquired EGFR C797S mutation mediates resistance to AZD9291 in non–small cell lung cancer harboring EGFR T790M. *Nat Med.* 2015;21:560–562.
21. Büttner R, Wolf J, Kron A. Nationales Netzwerk Genomische Medizin. The national Network Genomic Medicine (nNGM): Model for innovative diagnostics and therapy of lung cancer within a public healthcare system [in German]. *Pathologe.* 2019;40:276–280.

^{68}Ga-NC-BCH Whole-Body PET Imaging Rapidly Targets Claudin18.2 in Lesions in Gastrointestinal Cancer Patients

Changsong Qi*[1], Rui Guo*[2], Yan Chen*[2], Chenzhen Li*[3], Chang Liu[1], Miao Zhang[1], Cheng Zhang[1], Xiaotian Zhang[1], Xingguo Hou[2], Bo Chen[4], Bing Jia[3], Zhi Yang[2], Lin Shen[1], and Hua Zhu[2]

[1]Department of Early Drug Development, State Key Laboratory of Holistic Integrative Management of Gastrointestinal Cancers, Beijing Key Laboratory of Carcinogenesis and Translational Research, Peking University Cancer Hospital and Institute, Beijing, China; [2]Department of Nuclear Medicine, NMPA Key Laboratory for Research and Evaluation of Radiopharmaceuticals (National Medical Products Administration), State Key Laboratory of Holistic Integrative Management of Gastrointestinal Cancers, Beijing Key Laboratory of Carcinogenesis and Translational Research, Peking University Cancer Hospital and Institute, Beijing, China; [3]Medical Isotopes Research Center, Department of Radiation Medicine, School of Basic Medical Sciences, Peking University, Beijing, China; and [4]Chengdu AlpVHHs Co. Ltd., Chengdou, China

^{68}Ga-labeled nanobody (^{68}Ga-NC-BCH) is a single-domain antibody–based PET imaging agent. We conducted a first-in-humans study of ^{68}Ga-NC-BCH for PET to determine its in vivo biodistribution, metabolism, radiation dosimetry, safety, and potential for quantifying claudin-18 isoform 2 (CLDN18.2) expression in gastrointestinal cancer patients. **Methods:** Initially, we synthesized the probe ^{68}Ga-NC-BCH and performed preclinical evaluations on human gastric adenocarcinoma cell lines and xenograft mouse models. Next, we performed a translational study with a pilot cohort of patients with advanced gastrointestinal cancer on a total-body PET/CT scanner. Radiopharmaceutical biodistribution, radiation dosimetry, and the relationship between tumor uptake and CLDN18.2 expression were evaluated. **Results:** ^{68}Ga-NC-BCH was stably prepared and demonstrated good radiochemical properties. According to preclinical evaluation, ^{68}Ga-NC-BCH exhibited rapid blood clearance, high affinity for CLDN18.2, and high specific uptake in CLDN18.2-positive cells and xenograft mouse models. ^{68}Ga-NC-BCH displayed high uptake in the stomach and kidney and slight uptake in the pancreas. Compared with ^{18}F-FDG, ^{68}Ga-NC-BCH showed significant differences in uptake in lesions with different levels of CLDN18.2 expression. **Conclusion:** A clear correlation was detected between PET SUV and CLDN18.2 expression, suggesting that ^{68}Ga-NC-BCH PET could be used as a companion diagnostic tool for optimizing treatments that target CLDN18.2 in tumors.

Key Words: ^{68}Ga-NC-BCH; PET; CLDN18.2; gastrointestinal cancers

J Nucl Med 2024; 65:856–863
DOI: 10.2967/jnumed.123.267110

Gastrointestinal cancer is a global disease that seriously endangers human public health. In 2018, gastrointestinal cancers accounted for approximately 4.8 million new cases of cancer and 3.4 million deaths worldwide, or more than a quarter of the total cancer incidence and more than one third of the total cancer-related mortality, respectively (*1*). Because of the insidiousness of early symptoms, most gastrointestinal cancers are diagnosed at an advanced stage, often leading to a poor prognosis and increased mortality.

Claudin-18 isoform 2 (CLDN18.2) is a subtype of CLDN18, a member of the tight junction protein family (*2*). CLDN18.2 is involved in the formation of intercellular adhesion structures, cell polarity control, paracellular transport, tissue permeability regulation, and signal transduction (*3*). Generally, its expression is strictly limited to the normal gastric mucosa; however, CLDN18.2 can also be abnormally activated during the appearance, metastasis, and invasion of gastrointestinal malignancies such as stomach, colon, pancreatic, esophageal, ovarian, and lung tumors (*4–6*). The randomized phase IIb study showed that zolbetuximab in combination with epirubicin plus oxaliplatin plus capecitabine improved overall survival and progression-free survival in patients with higher CLDN18.2 expression (>70%) relative to those with lower CLDN18.2 expression (40%–69%) (*7*). Therefore, the detection of CLDN18.2 expression levels is essential for identifying patients who can achieve greater clinical benefit.

To date, there is no standard test for CLDN18.2, and most detection methods involve immunohistochemistry (*8*). Immunohistochemistry is an invasive process that covers only a small amount of tissue and does not reflect the heterogeneity of CLDN18.2 expression within the tumor. Previously, we reported the first—to our knowledge—clinical results of the ^{124}I-labeled CLDN18.2 humanized monoclonal antibody ^{124}I-18B10(10L), which showed that CLDN18.2 can be detected in tumor lesions (*9*). However, the large molecular weight of the monoclonal antibodies results in a long imaging cycle that cannot be completed in a day. Single-domain antibodies are the smallest antibody units with complete functions, stability, and binding antigens; a molecular weight of approximately 15 kDa; and a short circulating half-life in the body with rapid blood clearance, allowing for the matching of radionuclides with short half-lives for same-day PET imaging (*10, 11*).

In this study, we constructed the single-domain antibody molecular probe, ^{68}Ga-labeled nanobody (^{68}Ga-NC-BCH). With the advantages of whole-body PET, we initiated an open-label, single-center, single-arm, first-in-humans phase 0 trial to study the safety, systemic

---

Received Nov. 23, 2023; revision accepted Mar. 4, 2024.

For correspondence or reprints, contact Hua Zhu (zhuhuabch@pku.edu.cn) or Lin Shen (shenlin@bjmu.edu.cn).

*Contributed equally to this work.

distribution and dosimetry, and CLDN18.2-targeting ability of ^{68}Ga-NC-BCH in patients with gastrointestinal tumors. We focused on assessing whole-body physiologic CLDN18.2 expression and tumor uptake and exploring its main relationship with patient prognosis before and after anti-CLDN18.2 therapy using ^{68}Ga-NC-BCH.

MATERIALS AND METHODS

Cell and Animal Models

The human gastric adenocarcinoma cell AGS was obtained at Peking University Cancer Hospital and Institute. The AGS$^{\text{CLDN18.2}}$ cell line was generated by transfection with the full-length CLDN18.2. All animal experiments were performed in accordance with the guidelines of the Peking University Institutional Animal Care and Use Committee (approval number EAEC 2022-01).

Small-Animal PET/CT Protocol

Normal Kunming mice and AGS$^{\text{CLDN18.2}}$/AGS model nude mice were injected with 7.4 MBq of ^{68}Ga-NC-BCH via the tail vein ($n = 3$). Then, 10-min static PET scans were acquired at each time point. Imaging was performed with a small-animal PET/CT scanner (Super Nova PET/CT; PINGSENG).

Patient Enrollment

The study was approved by the Medical Ethics Committee of the Peking University Cancer Hospital and registered at ClinicalTrials.gov (NCT02760225). All patients signed informed consent forms. All procedures performed in studies involving human participants complied with the ethical standards of institutional or national research councils and the 1964 Declaration of Helsinki and its subsequent amendments or similar ethical standards.

^{68}Ga-NC-BCH PET/CT Scanning

All imaging was performed on a whole-body PET/CT uEXPLORER scanner (United Imaging). No specific preparation was required for patients. An intravenously administered dose of ^{68}Ga-NC-BCH (101.99 ± 44.65 MBq; range, 56.61–177.97 MBq) was used. Five patients underwent dynamic PET/CT imaging. A low-dose CT scan (120 kV, 50 mA, 5-mm slices) was first performed, and then the dynamic PET acquisition was started upon injection of the tracer.

RESULTS

Synthesis and Characterization of ^{68}Ga-NC-BCH

The molecular weight of the obtained primary single-domain antibody, CLDN18.2-targeting nanobody (ACN376), was defined as 16,075 atomic mass units. The molecular weight of ACN376-GGGGC was determined to be 15,380 atomic mass units (Supplemental Figs. 1A, 1B, and 1D; supplemental materials are available at http://jnm.snmjournals.org). Maleimidomonoamide-NOTA was site-specifically conjugated to ACN376-GGGGC via the maleimide-thiol reaction (Supplemental Fig. 2A). NOTA-ACN376 was obtained with an average NOTA–to–single-domain antibody ratio of approximately 1:1 (Supplemental Fig. 1C). ^{68}Ga-NC-BCH was produced with a radiochemical yield of more than 95% and a radiochemical purity of more than 98%. The in vitro stability of ^{68}Ga-NC-BCH in 0.01 M phosphate-buffered saline and 5% human serum albumin was demonstrated by a radiochemical purity of more than 98% over 6 h (Supplemental Fig. 3). The quality control results are shown in Supplemental Table 1.

Saturation Binding Affinity and Cellular Uptake

The binding potency of ^{68}Ga-NC-BCH to the CLDN18.2 protein was detected with a dissociation constant of 27.85 nmol/L (Supplemental Fig. 2B). Flow cytometry experiments revealed that 80.2% of the cells in the AGS$^{\text{CLDN18.2}}$ group were positively stained with anti-CLDN18.2 antibody (1D5; 1D5 refers to the CLDN18.2 monoclonal antibody used for flow cytometry analysis). Western blotting results confirmed that the expression of CLDN18.2 in AGS$^{\text{CLDN18.2}}$ cells significantly differed from that in AGS cells, and the relative expression of CLDN18.2 in the AGS$^{\text{CLDN18.2}}$ and AGS cell lines was 0.94 ± 0.16 and 0.28 ± 0.06, respectively ($P = 0.0027$; Supplemental Figs. 4A–4C). The results of the cellular experiment showed that uptake of ^{68}Ga-NC-BCH in AGS$^{\text{CLDN18.2}}$ cells increased in a time-dependent manner (2.79% ± 0.39% at 10 min, 3.43% ± 0.24% at 30 min, 3.89% ± 0.25% at 60 min, and 4.04% ± 0.18% at 120 min), whereas no significant changes were observed in the AGS group (0.96% ± 0.10% at 10 min, 0.68% ± 0.11% at 30 min, 0.63% ± 0.26% at 60 min, and 0.83% ± 0.07% at 120 min). Moreover, an excess of unlabeled ACN376 and TST001 significantly blocked the uptake of ^{68}Ga-NC-BCH (3.89% ± 0.25% vs. 0.77% ± 0.12% vs. 0.93% ± 0.09% at 60 min and 4.04% ± 0.18% vs. 0.69% ± 0.11% vs. 1.07% ± 0.25% at 120 min,

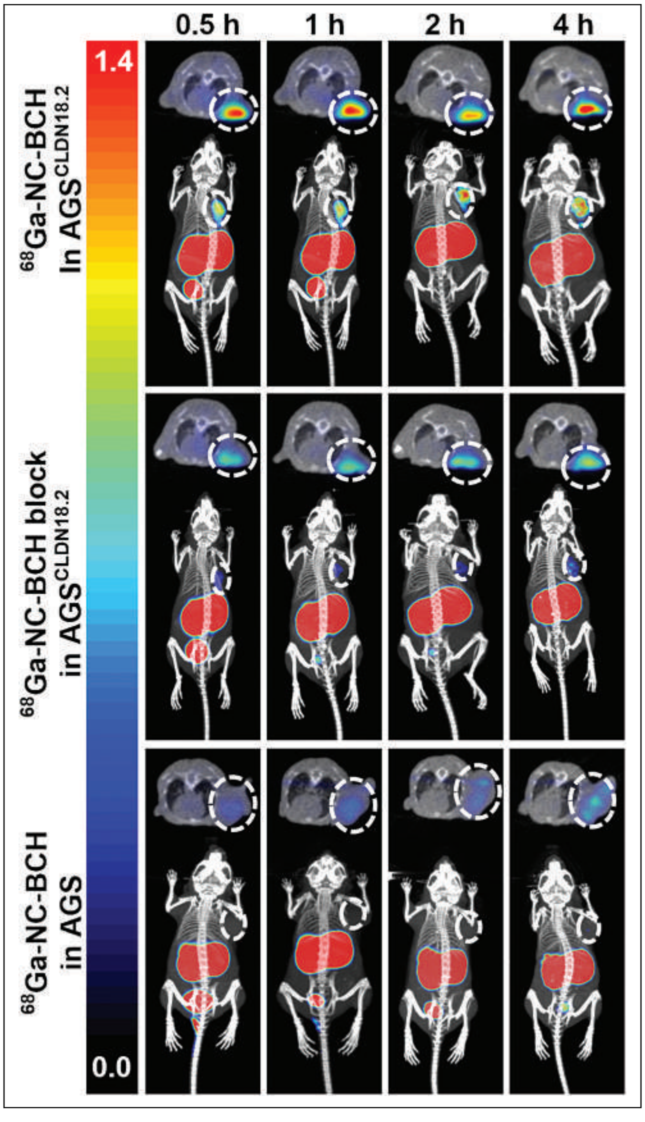

FIGURE 1. ^{68}Ga-NC-BCH PET images of mice bearing AGS$^{\text{CLDN18.2}}$ and AGS tumors. Block = incubation with 1 mg of TST001 in mice bearing AGS$^{\text{CLDN18.2}}$ xenografted 24 h in advance.

TABLE 1
Patient Characteristics

Patient no.	Age (y)	Sex	Weight (kg)	Clinical stage	CLDN18.2-targeted therapy before PET
1	60	M	61	cT4aN+M1	No
2	30	F	54	cT3N3M1	No
3	68	F	58	cT4bN2M1	No
4	40	M	69	cT4N2M1	No
5	51	F	52	T3N2M0	No
6	37	M	59	pT2N1Mx	Yes
7	41	M	60	cT4bNxM1	Yes
8	31	F	41	pT4aN3a	No
9	28	F	47	T4aN3aM1	Yes
10	31	F	43	pT3N1M1	Yes
11	37	F	55	cT4aN2M0	Yes

respectively) (Supplemental Fig. 2C). Uptake of ^{68}Ga-NC-BCH by AGS$^{CLDN18.2}$ cells at 120 min was 4.93-fold greater than that by AGS cells and 5.86-fold greater than that by the blocking group.

Small-Animal PET/CT Imaging and Immunohistochemistry Study

High uptake in the stomach was observed via static ex vivo imaging and a PET/CT image of Kunming mice spanning 1 h (Supplemental Fig. 5).

Small-animal PET/CT images of AGS$^{CLDN18.2}$ tumor–bearing mice, AGS$^{CLDN18.2}$ tumor–bearing mice pretreated with the antibody TST001 (1 mg) for 24 h, and AGS tumor–bearing mice were obtained at 30, 60, 120, and 240 min after injection of ^{68}Ga-NC-BCH (Fig. 1). The kidney SUV$_{mean}$ at 1 h after injection was 14.56 ± 0.29 in the AGS$^{CLDN18.2}$ group, 11.87 ± 0.16 in the AGS$^{CLDN18.2}$ blocking group, and 8.80 ± 0.32 in the AGS group. The SUV$_{mean}$ of the stomach at 1 h after injection was 2.43 ± 0.09 in the AGS$^{CLDN18.2}$ group, 1.65 ± 0.03 in the AGS$^{CLDN18.2}$ blocking group, and 1.67 ± 0.01 in the AGS group. The SUV$_{mean}$ in the AGS$^{CLDN18.2}$, AGS$^{CLDN18.2}$ blocking, and AGS groups at 1 h after injection was 1.14 ± 0.01, 0.54 ± 0.01, and 0.42 ± 0.03, respectively. The tumor-to-muscle ratios at each time point after injection of ^{68}Ga-NC-BCH were significantly greater than those of the other control groups, and at 2 h after injection, the tumor-to-muscle ratio reached its maximum of 34.86 ± 4.68 (Supplemental Fig. 6A). The results of immunohistochemistry revealed high and homogeneous CLDN18.2 expression in AGS$^{CLDN18.2}$ tumors, whereas AGS xenograft tumors were negative for CLDN18.2. The gastric mucosa of AGS$^{CLDN18.2}$ and AGS tumor–bearing mice showed substantially positive expression of CLDN18.2 (Supplemental Fig. 6C).

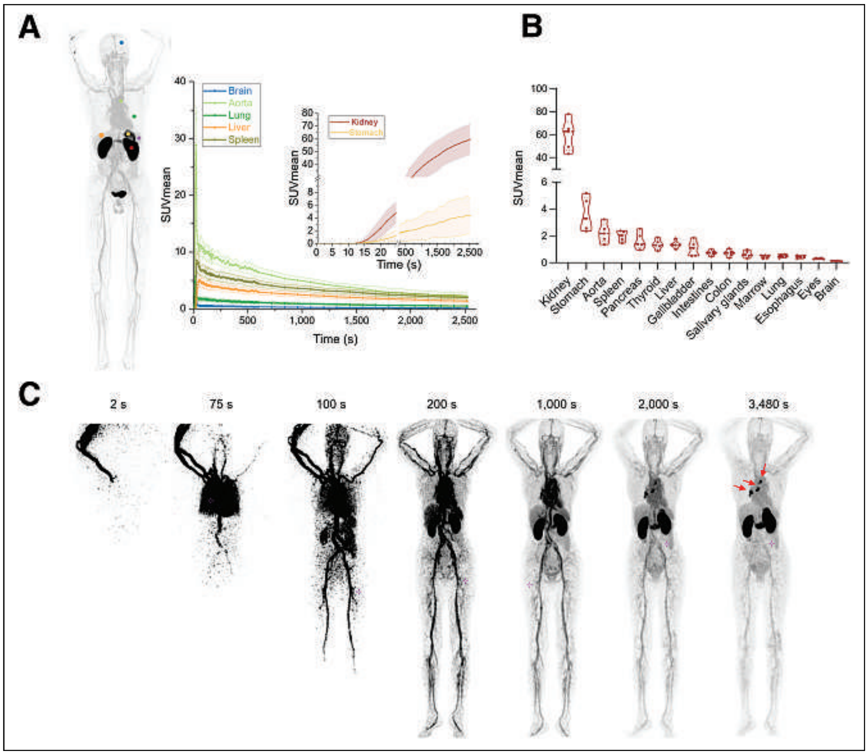

FIGURE 2. (A) Dynamic changes in SUV$_{mean}$ of selected organs at 0–42 min (n = 5). (B) Rank ordering of ^{68}Ga-NC-BCH uptake in different organs indicated by SUV$_{mean}$ at 42 min (n = 5). (C) Pilot translational study on dynamic total-body PET/CT imaging of ^{68}Ga-NC-BCH illustrating time distribution of radiotracers within tumors to optimize imaging window.

Biodistribution, Pharmacokinetics, and Safety Study

The biodistribution of ^{68}Ga-NC-BCH in AGS$^{CLDN18.2}$ and AGS tumor–bearing mice and the pharmacokinetics study in Kunming mice are presented in Supplemental Figure 6. At 2 h after injection, the stomachs of the mice in all 3 groups exhibited relatively high uptake (6.04 ± 0.66 percentage injected dose [%ID]/g in the AGS$^{CLDN18.2}$ group, 6.36 ± 1.43 %ID/g in the AGS group, and 4.96 ± 0.04 %ID/g in the blocking group). The uptake value of the kidney was higher than that of the stomach (194.86 ± 5.56 %ID/g in the AGS$^{CLDN18.2}$ group, 128.79 ± 0.64 %ID/g

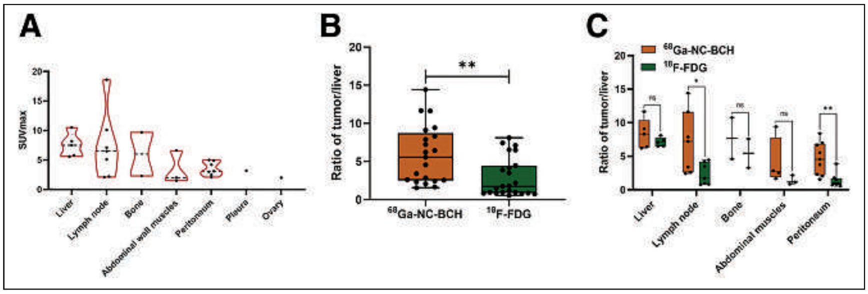

FIGURE 3. (A) Tumor uptake of ^{68}Ga-NC-BCH in different metastatic lesions. (B) Comparison of tumor-to-liver ratio between ^{68}Ga-NC-BCH and ^{18}F-FDG. (C) Comparison of tumor-to-nontumor ratio between ^{68}Ga-NC-BCH and ^{18}F-FDG in different metastatic lesions. *$P < 0.05$. **$P < 0.01$. ns = not statistically significant.

in the AGS group, and 129.70 ± 8.55 %ID/g in the blocking group). Tumor uptake in the AGS$^{\text{CLDN18.2}}$ tumor–bearing mice was greater (6.61 ± 0.41 %ID/g) than that in the AGS group (0.39 ± 0.13 %ID/g) and the blocking group (1.69 ± 0.84 %ID/g). The pharmacokinetics study showed that ^{68}Ga-NC-BCH was cleared quickly from the blood, with a half-life of 22.77 min. After the injection of excess ^{68}Ga-NC-BCH (18.5 MBq, 925 MBq/kg), no obvious toxicity was observed in terms of body weight (Supplemental Fig. 7), blood biochemical parameters (Supplemental Table 2; Supplemental Fig. 8), or hematoxylin and eosin staining of main organ tissue slides (Supplemental Fig. 9).

^{68}Ga-NC-BCH Dosimetry and Biodistribution

Between July 2022 and November 2022, 11 patients were enrolled: 10 with advanced gastric cancer and 1 with advanced colon cancer. Among all patients, the expression of CLDN18.2 was 40% or above. Patient characteristics are shown in Table 1. No tracer-related adverse events were observed in any patients after injection of ^{68}Ga-NC-BCH.

All 11 patients underwent ^{68}Ga-NC-BCH PET/CT. The injection dose of ^{68}Ga-NC-BCH was 101.99 ± 44.65 MBq (range, 56.61–177.97 MBq). The highest organ dose values for ^{68}Ga-NC-BCH were estimated to be for the kidneys, gallbladder, stomach, spleen, and liver. The effective dose of ^{68}Ga-NC-BCH was estimated to be 0.042 ± 0.02 mSv/MBq (Supplemental Table 3), which was lower than the radiation dose used for conventional ^{18}F-FDG PET/CT (7.0–14.0 mSv) (*12*). Whole-body PET reduces the total radiation dose and facilitates translational research on this new type of radiopharmaceutical.

Five patients were subjected to dynamic scanning via total-body full-motion PET/CT scans. A 42-min whole-body static PET/CT scan was selected to determine the SUV$_{\text{mean}}$ in the major organs of these 5 participants. The dynamic curve showed that the ^{68}Ga-NC-BCH activity in the selected organs increased rapidly and gradually decreased to a steady state over time except in the stomach and kidneys (Fig. 2A). A static total-body PET/CT scan at 60 min was selected to determine the SUV$_{\text{mean}}$ of the main organs in all 5 participants (Fig. 2B). Except for the stomach wall, the SUV$_{\text{mean}}$ for ^{68}Ga-NC-BCH in normal tissues (including the spleen, pancreas, liver, brain, and ovaries) was extremely low, as is consistent with previous reports of immunohistochemistry staining of healthy human tissues (*6*). Since single-domain antibodies are excreted from the body through the kidneys, the probe exhibited strong renal retention in humans. The SUV$_{\text{mean}}$ of the positive lesions gradually increased over time from 0 to 58 min (Fig. 2C). The temporal radioactivity curve of the mediastinal metastatic lymph nodes and stomach wall showed a gradual upward trend, and radiotracer accumulation gradually increased over time (Supplemental Fig. 10B).

Surprisingly, all patients with preserved gastric walls had significantly greater uptake of imaging agents in the gastric mucosa (Supplemental Fig. 10A). To our knowledge, this was the first study in which whole-body PET has shown stomach accumulation of a radioactive tracer targeting CLDN18.2 in humans.

Tumor ^{68}Ga-NC-BCH Uptake and Correlation

In total, 215 CLDN18.2-positive lesions were detected in 9 (9/11, 81.8%) patients by ^{68}Ga-NC-BCH PET/CT, including 4 patients who had not received CLDN18.2-targeted therapy before imaging and 5 patients who had. The mean SUV$_{\text{max}}$ of positive lesions detected by ^{68}Ga-NC-BCH PET/CT did not significantly differ among different locations (Fig. 3A). Positive lesions were detected in all patients who had received CLDN18.2-targeted therapy before imaging; these lesions were distributed in the lymph nodes, peritoneum, abdominal muscle, and subcutaneous tissue. The other 4 patients, who had not received CLDN18.2-targeted therapy, had positive lesions distributed among the lymph nodes, peritoneum, liver, bone, and ovaries. The mean SUV$_{\text{max}}$ of positive lesions in patients without prior CLDN18.2-targeted therapy was significantly greater than that in treated patients (Fig. 4B).

The CLDN18.2 expression intensity was ++ or +++ in all patients enrolled in the study. ^{68}Ga-NC-BCH–positive lesions

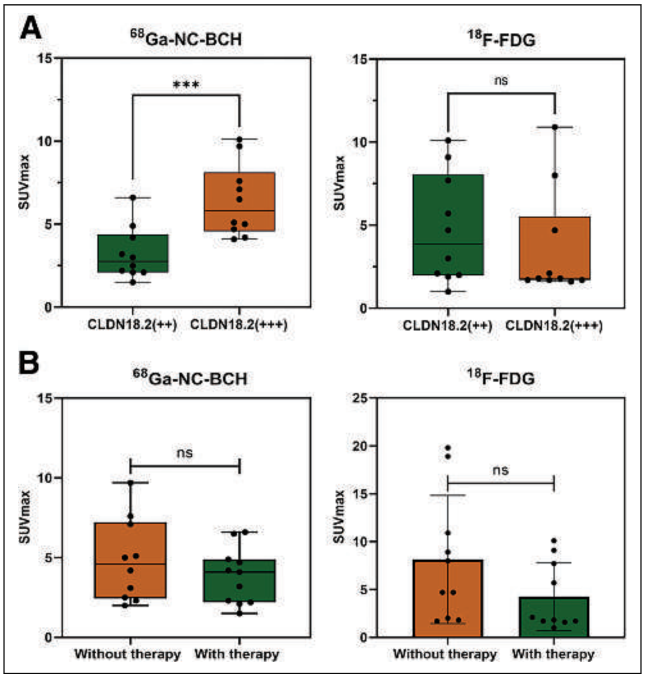

FIGURE 4. (A) Box plot of ^{68}Ga-NC-BCH SUV$_{\text{max}}$ and ^{18}F-FDG SUV$_{\text{max}}$ for all lesions in 11 patients with CLDN18.2 +++ and CLDN18.2 ++ by immunohistochemistry staining. (B) Box plot of ^{68}Ga-NC-BCH for all lesions in 11 patients with CLDN18.2-targeted therapy and without CLDN18.2-targeted therapy. Data are mean ± SD.***$P < 0.001$. ns = not statistically significant.

TABLE 2
Comparison of SUV_{max} of ^{68}Ga-NC-BCH with ^{18}F-FDG in Metastases

Patient no.	Tumor type	CLDN18.2 expression	Time between prior anti-CLDN18.2 therapy and experiment (mo)	Prior therapy lines	Gastrectomy	Metastatic lesion	^{68}Ga-NC-BCH	^{18}F-FDG
1	Gastric cancer	90%, 3+	–	3	Yes	Peritoneum	5	4.7
						Bone	9.7	19.8
						Liver	7.6	18.9
						Lymph node	7.1	10.9
2	Gastric cancer	80%, 3+	–	3	No	Lymph node	Negative	8.9
3	Gastric cancer	40%, 2+	–	3	No	Peritoneum	2.5	2
						Lymph node	18.6	4.7
4	Colorectal cancer	40%, 3+	–	3	No	Peritoneum	3.1	2.1
						Lymph node	5.1	1.7
5	Gastric cancer	90%, 3+	–	3	No	—	Negative	Negative
6	Gastric cancer	50%, 2+	10.5	3	Yes	Anastomosis	4.2	7.7
						Lymph node	2.2	9.1
						Peritoneum	2.1	10.1
						Subcutaneous tissue	1.5	5.7
7	Gastric cancer	90%, 3+	3	3	No	Lymph node	6.5	Negative
						Abdominal wall	2.3	1.7
						Peritoneum	4.1	1.7
8	Gastric cancer	90%, 3+	–	3	No	Peritoneum	4.2	Negative
						Bone	2.3	8
						Ovary	2.0	1.8
9	Gastric cancer	40%, 2+	5.5	3	Yes	Peritoneum	4.9	1
						Subcutaneous tissue	6.6	2.1
						Pleura	3.2	Negative
10	Gastric cancer	90%, 3+	15	2	Yes	Peritoneum	4.7	1.8
						Lymph node	10.1	1.6
						Muscle	2.0	Negative
11	Gastric cancer	60%, 2+	6.5	3	No	Peritoneum	3	3
						Lymph node	2.1	1.9

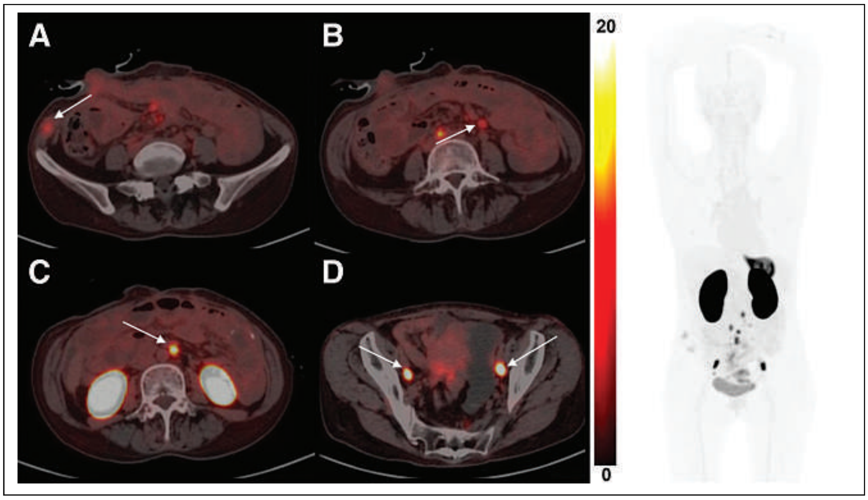

FIGURE 5. (A) Muscle metastases in right lower abdominal wall with mild elevated uptake. (B–D) Multiple lymph node metastasis showing CLDN18.2 expression degree from low (B) to high (D) (left) and imaging of ^{68}Ga-NC-BCH of patient (right).

were detected in 9 patients, including 4 patients with ++ CLDN18.2 expression and 5 patients with +++ expression. The positive lesions were distributed in the liver, lymph nodes, bone, peritoneum, pleura, abdominal muscle, and ovaries (Table 2). ^{68}Ga-NC-BCH uptake was highest in liver metastases, followed by lymph nodes and bone. There were statistically significant differences in SUV$_{max}$ between patients with ++ and +++ CLDN18.2 expression in positive lesions (Fig. 4A). Moreover, there was no significant difference in the SUV$_{max}$ of the lesions that were positive on ^{18}F-FDG PET/CT regardless of the expression intensity of CLDN18.2 or whether the patients had received CLDN18.2-targeted treatment. Moreover, CLDN18.2 expression differed among metastatic lesions from the same patient (Fig. 5).

^{68}Ga-NC-BCH PET/CT and ^{18}F-FDG PET/CT

In total, 225 lesions were positive on ^{68}Ga-NC-BCH PET/CT, distributed in the liver, lymph nodes, bone, peritoneum, pleura, abdominal muscle, and ovaries. In total, 209 lesions were positive on ^{18}F-FDG PET/CT, distributed in the liver, lymph nodes, bone, peritoneum, abdominal muscle, and ovaries. There was a significant difference in the tumor-to-nontumor (T/NT) ratio between all positive lesions detected by the 2 methods. According to a subgroup analysis of the T/NT ratio comparing metastatic lesions at different sites, the T/NT ratio of the lymph nodes and peritoneal metastases detected by ^{68}Ga-NC-BCH PET/CT was significantly greater than that detected by ^{18}F-FDG PET/CT (Figs. 3B and 3C). ^{68}Ga-NC-BCH PET/CT was also able to detect small peritoneal and pleural metastases well. Patient 9, a woman with advanced gastric cancer, had a CLDN18.2 expression level of 40%, 2+. The left pleural metastatic nodule and thickened peritoneum did not show obvious uptake on ^{18}F-FDG PET/CT, whereas ^{68}Ga-NC-BCH PET/CT showed high uptake (SUV$_{max}$, 3.1 and 5.7). ^{68}Ga-NC-BCH PET/CT was also effective at detecting the expression of CLDN18.2 in colon cancer metastases. Patient 4, a man with colon cancer, had a CLDN18.2 expression level of 40%, 3+. On ^{18}F-FDG PET/CT, abdominal metastatic lymph nodes showed mild uptake, whereas the same lymph nodes on ^{68}Ga-NC-BCH PET/CT showed high uptake (SUV$_{max}$, 1.4 vs. 5.6) (Figs. 6A and 6B). Typical cases are shown in Supplemental Figure 11.

The log-rank method was used to test the difference in survival time distribution between the 2 groups. There was no significant difference in survival time distribution between patients with different CLDN18.2 expression levels ($P = 0.2988$) and no significant difference in clinical stage between the 2 groups ($P = 0.2599$). Moreover, there was no significant difference in survival time between the 2 groups ($P = 0.1865$, SUV$_{max}$ ≥ 2.5 vs. SUV$_{max}$ < 2.5; Fig. 7).

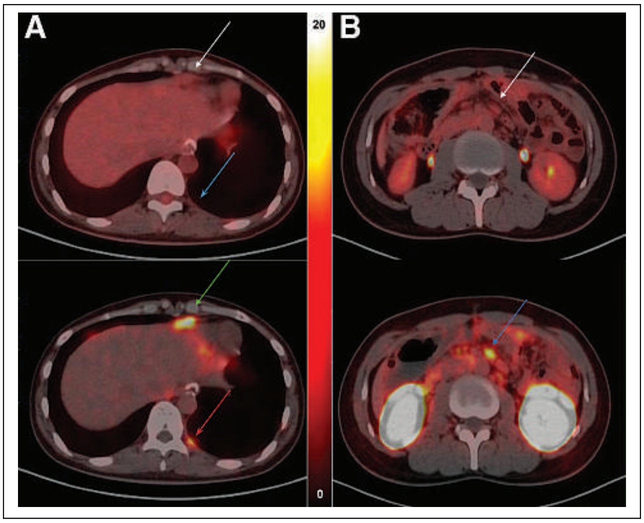

FIGURE 6. (A) Patient 9 was woman with advanced gastric cancer whose CLDN18.2 expression level was 40%, 2+. Left pleural metastatic nodule (blue arrow) and thickened peritoneum (white arrow) did not show obvious uptake on ^{18}F-FDG PET/CT, whereas ^{68}Ga-NC-BCH PET/CT showed high uptake (SUV$_{max}$, 3.1 [red arrow] and 5.7 [green arrow]). (B) Patient 4 was man with colon cancer whose CLDN18.2 expression level was 40%, 3+. On ^{18}F-FDG PET/CT, abdominal metastatic lymph node (white arrow) showed mild uptake, whereas same lymph nodes on ^{68}Ga-NC-BCH PET/CT (blue arrow) showed high uptake (SUV$_{max}$, 1.4 vs. 5.6).

DISCUSSION

Several forms of CLDN18.2-targeting therapeutic agents, including monoclonal antibodies, antibody–drug conjugates, and chimeric antigen receptor T (CAR-T) cell therapies, are currently undergoing clinical trials worldwide (*13, 14*). Our group previously published interim results of a phase I clinical trial of CLDN18.2-specific CAR-T cells, which showed that the overall response rate and disease control rate of CAR-T cells reached 48.6% and 73.0%, respectively (*14*). Although CLDN18.2-targeting therapy has achieved good results in clinical studies, we have also noted that the expression level of CLDN18.2 affects therapeutic efficacy to a certain extent.

In this study, we selected a single-domain antibody as a precursor of the radiotracer and labeled it with the short-half-life nuclide ^{68}Ga based on its small molecular weight and short cycle time in vivo.

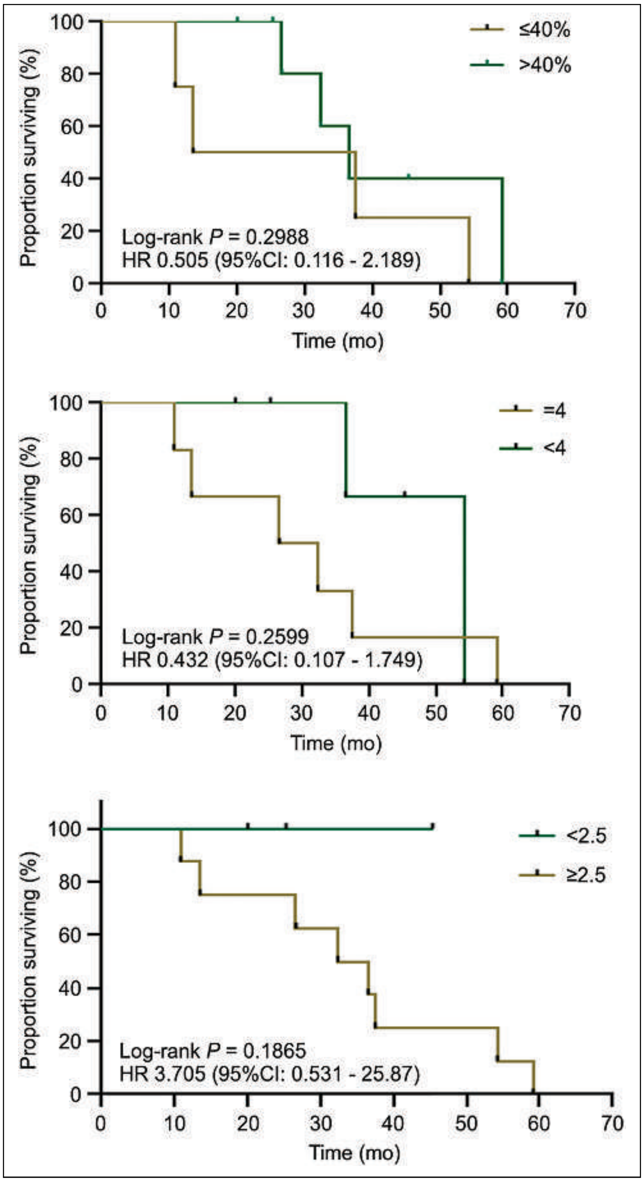

FIGURE 7. Graphs of survival time. (Top) Green depicts group above—and dark yellow, group below—mean CLDN18.2 expression of 40%. (Middle) Green depicts clinical stage of 4, and dark yellow depicts clinical stage < 4. (Bottom) Green depicts group below—and dark yellow, group above—mean SUV$_{max}$ of 2.5. HR = hazard ratio.

Compared with those of traditional antibodies, the rapid tissue penetration and renal clearance rate of single-domain antibodies enable high image contrast to be obtained within 1 h after probe injection, allowing patients to complete the whole imaging workflow within 1 d, greatly increasing compliance and reducing radiation exposure. A preclinical study indicated that ^{68}Ga-NC-BCH has good affinity for CLDN18.2 and can specifically bind to CLDN18.2-positive cells. ^{68}Ga-NC-BCH was taken up strongly by the gastric mucosa in a mouse model, indicating that the smaller molecular architecture allows it to reach the insidious and dense CLDN18.2 epitope on the gastric mucosa. However, since CLDN18.2 is typically buried in the gastric mucosa, neither of the previous monoclonal antibody-based probes—^{89}Zr-DFO-TST001 and ^{124}I-18B10(10L)—was available in normal tissue (*9, 15, 16*). In addition to gastric organ and positive tumors, probes have a high nonspecific radioactive accumulation in the kidneys, as previously reported (*17*). The prominent renal uptake is due to excretion of single-domain antibodies through the kidney–urinary system. In addition, nonspecific tubular reuptake after glomerular blood flow is another important factor contributing to elevated renal uptake. Indeed, ^{68}Ga-NC-BCH exhibited a longer renal retention time (207.66 ± 19.99 %ID/g, 2 h after injection) than did other single-domain antibody tracers described in previous studies (*17–19*). The increase in nonspecific radioactive accumulation in the kidneys can lead to high radiation doses in patients and may seriously impede the diagnosis of small perirenal lesions.

Then, we described the results of the first, to our knowledge, ^{68}Ga-NC-BCH PET/CT study on patients. According to dosimetry studies, the effective radiation dose of ^{68}Ga-NC-BCH was much lower than that of ^{124}I-18B10(10L). All results showed that ^{68}Ga-NC-BCH PET/CT is a safe, noninvasive imaging method for detecting CLDN18.2 in patients receiving CLDN18.2-targeted therapy.

All 11 patients in the study underwent both ^{68}Ga-NC-BCH PET/CT and ^{18}F-FDG PET/CT within 1 wk. There was a significant difference in the T/NT ratio between all lesions positive on the 2 methods. Surprisingly, in the subgroup analysis, the T/NT ratio of the lymph nodes and peritoneal metastases detected by ^{68}Ga-NC-BCH PET/CT was significantly greater than that detected by ^{18}F-FDG PET/CT. Lymph nodes and the peritoneum are the most common metastatic sites of advanced gastric cancer. The T/NT ratio of lesions detected by ^{68}Ga-NC-BCH PET/CT was significantly greater, and this high ratio is more conducive to lesion detection. ^{68}Ga-NC-BCH PET/CT reflects the expression level of CLDN18.2 in tumor lesions because the tracer is a CLDN18.2-targeting single-domain antibody.

The study included patients who did or did not receive CLDN18.2-targeted therapy before ^{68}Ga-NC-BCH PET/CT. Uptake in lesions receiving CLDN18.2-targeted therapy was higher than that in lesions not receiving CLDN18.2-targeted therapy ($P = 0.2695$). This could be because after the first CLDN18.2-targeted therapy, the lesions progressed approximately 1 y later; these advanced lesions still highly expressed CLDN18.2, which also provided a basis for the second CAR-T treatment. More significantly, results showed that metastatic lesions with a higher CLDN18.2 expression level had a higher SUV$_{max}$. This provides some basis for noninvasive detection of CLDN18.2 expression levels in the future.

There were several limitations to the study. First, the small sample size of patients may impede the comprehensive performance of the radiotracer. Also, the small sample challenges us to accurately assess ^{68}Ga-NC-BCH uptake in primary gastric tumors because of interference with physiologic uptake in the gastric mucosa and therapeutic response.

CONCLUSION

We developed a CLDN18.2-specific single-domain antibody nuclide probe that enables same-day PET imaging, and we demonstrated this ability using whole-body PET. Uptake of ^{68}Ga-NC-BCH correlated significantly with the expression level of CLDN18.2. ^{68}Ga-NC-BCH PET/CT has great potential in the selection of CLDN18.2-targeted therapy strategies and the monitoring of treatment responses by systematically quantifying the systemic expression of CLDN18.2.

DISCLOSURE

This research was funded by the National Key R&D Program of China (2022YFA0912400), the National Natural Science

Foundation of China (82272627, 82171973, and 82171980), Capital's Funds for Health Improvement and Research (2022-2Z-2154 and 2022-2Z-2155), and Science Foundation of Peking University Cancer Hospital (2022-14). Intellectual properties protection has been filed by Chengdu AlpVHHs Co. Ltd. No other potential conflict of interest relevant to this article was reported.

KEY POINTS

QUESTION: How can CLDN18.2 expression be detected rapidly and accurately in gastrointestinal cancer patients?

PERTINENT FINDINGS: We demonstrated the feasibility of ^{68}Ga-NC-BCH for quantifying CLDN18.2 levels in preclinical models and in patients, in whom a high affinity for CLDN18.2 was detected.

IMPLICATIONS FOR PATIENT CARE: ^{68}Ga-NC-BCH can be used to image CLDN18.2-positive tumors and identify patients with high CLDN18.2 expression as potential candidates for targeted therapy through noninvasive PET imaging.

REFERENCES

1. Arnold M, Abnet CC, Neale RE, et al. Global burden of 5 major types of gastrointestinal cancer. *Gastroenterology.* 2020;159:335–349.e15.
2. Tsukita S, Furuse M, Itoh M. Multifunctional strands in tight junctions. *Nat Rev Mol Cell Biol.* 2001;2:285–293.
3. Kubota Y, Kawazoe A, Mishima S, et al. Comprehensive clinical and molecular characterization of claudin 18.2 expression in advanced gastric or gastroesophageal junction cancer. *ESMO Open.* 2023;8:100762.
4. Günzel D, Yu AS. Claudins and the modulation of tight junction permeability. *Physiol Rev.* 2013;93:525–569.
5. Tabariès S, Siegel PM. The role of claudins in cancer metastasis. *Oncogene.* 2017; 36:1176–1190.
6. Sahin U, Koslowski M, Dhaene K, et al. Claudin-18 splice variant 2 is a pan-cancer target suitable for therapeutic antibody development. *Clin Cancer Res.* 2008;14:7624–7634.
7. Sahin U, Türeci Ö, Manikhas G, et al. FAST: a randomised phase II study of zolbetuximab (IMAB362) plus EOX versus EOX alone for first-line treatment of advanced CLDN18.2-positive gastric and gastro-oesophageal adenocarcinoma. *Ann Oncol.* 2021;32:609–619.
8. Dai J, Zheng H, Jin J, Cheng Y, Xu H. Claudin18.2 expression and clinicopathological features in cytology effusion specimens from gastric adenocarcinoma: a comparative study with tissue specimens. *Cancer Cytopathol.* 2023;131:365–372.
9. Wang S, Qi C, Ding J, et al. First-in-human CLDN18.2 functional diagnostic PET imaging of digestive system neoplasms enables whole-body target mapping and lesion detection. *Eur J Nucl Med Mol Imaging.* 2023;50:2802–2817.
10. Bao G, Tang M, Zhao J, Zhu X. Nanobody: a promising toolkit for molecular imaging and disease therapy. *EJNMMI Res.* 2021;11:6.
11. Chakravarty R, Goel S, Cai W. Nanobody: the "magic bullet" for molecular imaging? *Theranostics.* 2014;4:386–398.
12. Delbeke D, Coleman RE, Guiberteau MJ, et al. Procedure guideline for tumor imaging with ^{18}F-FDG PET/CT 1.0. *J Nucl Med.* 2006;47:885–895.
13. Lordick F, Chao J, Buxò E, et al. Phase I study evaluating safety and tolerability of AMG 910, a half-life extended bispecific T cell engager targeting claudin-18.2 (CLDN18.2) in gastric and gastroesophageal junction (G/GEJ) adenocarcinoma [abstract]. *Ann Oncol.* 2020;31(suppl 4):S928–S929.
14. Qi C, Gong J, Li J, et al. Claudin18.2-specific CAR T cells in gastrointestinal cancers: phase 1 trial interim results. *Nat Med.* 2022;28:1189–1198.
15. Chen Y, Hou X, Li D, et al. Development of a CLDN18.2-targeting immuno-PET probe for non-invasive imaging in gastrointestinal tumors. *J Pharm Anal.* 2023;13: 367–375.
16. Zhang J, Dong R, Shen L. Evaluation and reflection on claudin 18.2 targeting therapy in advanced gastric cancer. *Chin J Cancer Res.* 2020;32:263–270.
17. Wang Z, Zhao C, Ding J, et al. Screening, construction, and preliminary evaluation of CLDN18.2-specific peptides for noninvasive molecular imaging. *ACS Pharmacol Transl Sci.* 2023;6:1829–1840.
18. Li L, Liu T, Shi L, et al. HER2-targeted dual radiotracer approach with clinical potential for noninvasive imaging of trastuzumab-resistance caused by epitope masking. *Theranostics.* 2022;12:5551–5563.
19. Qin X, Guo X, Liu T, et al. High in-vivo stability in preclinical and first-in-human experiments with [^{18}F]AlF-RESCA-MIRC213: a ^{18}F-labeled nanobody as PET radiotracer for diagnosis of HER2-positive cancers. *Eur J Nucl Med Mol Imaging.* 2023;50:302–313.

Detecting High-Dose Methotrexate–Induced Brain Changes in Pediatric and Young Adult Cancer Survivors Using [^{18}F]FDG PET/MRI: A Pilot Study

Lucia Baratto[1], Shashi B. Singh[1], Sharon E. Williams[2], Sheri L. Spunt[3], Jarrett Rosenberg[4], Lisa Adams[1], Vidyani Suryadevara[1], Michael Iv[5], and Heike Daldrup-Link[1,3]

[1]Division of Pediatric Radiology, Department of Radiology, Stanford University School of Medicine, Stanford, California; [2]Child and Adolescent Psychiatry Clinic, Department of Psychiatry and Behavioral Sciences–Child and Adolescent Psychiatry and Child Development, Stanford University, Stanford, California; [3]Department of Pediatrics–Hematology/Oncology, Lucile Packard Children's Hospital, Stanford University, Stanford, California; [4]Department of Radiology, Stanford University School of Medicine, Stanford University, Stanford, California; and [5]Neuroimaging Division, Radiology Department, Stanford Health Care, Stanford University, Stanford, California

Significant improvements in treatments for children with cancer have resulted in a growing population of childhood cancer survivors who may face long-term adverse outcomes. Here, we aimed to diagnose high-dose methotrexate–induced brain injury on [^{18}F]FDG PET/MRI and correlate the results with cognitive impairment identified by neurocognitive testing in pediatric cancer survivors. **Methods:** In this prospective, single-center pilot study, 10 children and young adults with sarcoma ($n = 5$), lymphoma ($n = 4$), or leukemia ($n = 1$) underwent dedicated brain [^{18}F]FDG PET/MRI and a 2-h expert neuropsychologic evaluation on the same day, including the Wechsler Abbreviated Scale of Intelligence, second edition, for intellectual functioning; Delis–Kaplan Executive Function System (DKEFS) for executive functioning; and Wide Range Assessment of Memory and Learning, second edition (WRAML), for verbal and visual memory. Using PMOD software, we measured the SUV$_{\text{mean}}$, cortical thickness, mean cerebral blood flow (CBF$_{\text{mean}}$), and mean apparent diffusion coefficient of 3 different cortical regions (prefrontal cortex, cingulate gyrus, and hippocampus) that are routinely involved during the above-specified neurocognitive testing. Standardized scores of different measures were converted to z scores. Pairs of multivariable regression models (one for z scores < 0 and one for z scores > 0) were fitted for each brain region, imaging measure, and test score. Heteroscedasticity regression models were used to account for heterogeneity in variances between brain regions and to adjust for clustering within patients. **Results:** The regression analysis showed a significant correlation between the SUV$_{\text{mean}}$ of the prefrontal cortex and cingulum and DKEFS–sequential tracking (DKEFS-TM4) z scores ($P = 0.003$ and $P = 0.012$, respectively). The SUV$_{\text{mean}}$ of the hippocampus did not correlate with DKEFS-TM4 z scores ($P = 0.111$). The SUV$_{\text{mean}}$ for any evaluated brain regions did not correlate significantly with WRAML–visual memory (WRAML-VIS) z scores. CBF$_{\text{mean}}$ showed a positive correlation with SUV$_{\text{mean}}$ ($r = 0.56$, $P = 0.01$). The CBF$_{\text{mean}}$ of the cingulum, hippocampus, and prefrontal cortex correlated significantly with DKEFS-TM4 (all $P < 0.001$). In addition, the hippocampal CBF$_{\text{mean}}$ correlated significantly with negative WRAML-VIS z scores ($P = 0.003$). **Conclusion:** High-dose methotrexate–induced brain injury can manifest as a reduction in glucose metabolism and blood flow in specific brain areas, which can be detected with [^{18}F]FDG PET/MRI. The SUV$_{\text{mean}}$ and CBF$_{\text{mean}}$ of the prefrontal cortex and cingulum can serve as quantitative measures for detecting executive functioning problems. Hippocampal CBF$_{\text{mean}}$ could also be useful for monitoring memory problems.

Key Words: cancer survivors; methotrexate; neurocognitive test; neurotoxicity; PET

J Nucl Med 2024; 65:864–871
DOI: 10.2967/jnumed.123.266760

The 5-y overall survival rate of children with cancer has increased in recent decades, and it is currently over 80% for all cancers, with variations depending on the type of cancer. Children with osteosarcoma, non-Hodgkin lymphoma, and acute lymphoblastic leukemia have an overall survival rate of 75%, 80%, and 90%, respectively (*1–3*). These substantial improvements in survival have led to a growing population of pediatric cancer survivors who are at risk for health problems that appear to increase with age. The Childhood Cancer Survivor Study, which included more than 14,000 childhood cancer survivors, reported a cumulative incidence of 53.6% for disabling, life-threatening, or fatal health conditions in survivors, compared with 19.8% in a sibling control group (*4*). Among others, long-term neurocognitive problems have been described in adult survivors of childhood cancer (*5–9*). Survivors who received antimetabolite chemotherapy, cranial irradiation, or neurosurgery for their tumors are at higher risk of developing neurocognitive late effects (*5,10–12*), which may significantly impair intelligence, learning, attention, memory, and executive function and have long-term effects on educational and vocational attainment (*13,14*).

Methotrexate is an antimetabolite agent used routinely to treat various childhood cancers, including acute lymphoblastic leukemia, non-Hodgkin lymphoma, and osteosarcoma (*15–17*). Recent studies have shown that methotrexate treatment leads to inflammation of the brain by activation of microglia, which in turn impairs the differentiation of oligodendrocyte precursor cells and the myelination of neurons (*18,19*). In mouse models of methotrexate-induced brain injury, microglial depletion with colony-stimulating

---

Received Oct. 2, 2023; revision accepted Feb. 26, 2024.

For correspondence or reprints, contact Heike Daldrup-Link (heiked@stanford.edu).

factor 1 receptor inhibitors rescued neurocognitive deficits (*19*). Executive dysfunction has been described in long-term survivors treated with high-dose methotrexate (HDMTX) (*20,21*). Longitudinal neuropsychologic assessments of 187 adult survivors of childhood-diagnosed non-Hodgkin lymphoma and treated with HDMTX showed worse memory, executive function, processing speed, and academic performance than did either the normal population or community controls (*22*). The impact of methotrexate therapy on the brain is influenced by several factors, including dose and method of administration, concurrent treatments, and the patient's age, sex, and coexisting medical conditions (*23*). Currently, there is no objective imaging biomarker for methotrexate-induced brain injury. A noninvasive imaging test that could visualize and quantify methotrexate-induced neurotoxicity could be used to identify childhood cancer survivors at risk for long-term neurocognitive problems. Early intervention, such as pharmacologic treatment (with antiinflammatory medications (*19*), deescalation of methotrexate dose, changes in chemotherapeutic regimen, and cognitive rehabilitation), could be offered along with monitoring of treatment efficacy (*24*).

Both [^{18}F]FDG PET and MRI have been demonstrated to be useful imaging tools for the detection of cognitive impairment and white matter injury in pediatric patients treated with methotrexate (*21,23,25,26*). However, to our knowledge, none of these previous studies correlated [^{18}F]FDG PET/MRI findings with neurocognitive tests, the current clinical reference standard. To close this gap, the purpose of our study was to identify imaging changes of HDMTX-induced neurotoxicity on [^{18}F]FDG PET/MRI and correlate results with neurocognitive testing. We hypothesized that imaging metrics of brain morphology and physiology on integrated [^{18}F]FDG PET/MRI scans would correlate well with neurocognitive assessments as our reference standard.

MATERIALS AND METHODS

Study Population

The Institutional Review Board approved this study, and all subjects gave written informed consent. We prospectively enrolled pediatric cancer survivors who were diagnosed with lymphoma, leukemia, or sarcoma and were treated with HDMTX. The inclusion criteria were as follows: cancer patient undergoing HDMTX therapy (≥1,000 mg/m^2), age between 6 and 30 y, and written informed consent. The exclusion criteria included contraindications to MRI, active disease at the time of the study, inability to complete the study examinations, and pregnancy. All patients were evaluated by a child psychologist using a brief neurocognitive battery on the same day as the [^{18}F]FDG PET/MRI brain scan. The child psychologist did not know the results of the imaging tests, and the imaging team did not know the results of the neurocognitive assessment. Between January 2021 and August 2022, 22 eligible patients were referred as candidates for study participation by collaborating oncologists. Among the 22 eligible patients, 12 were screened out. Six of these patients did not respond to our study invitation (n = 3) or declined to participate (n = 3), and the other six were excluded because they had progressive disease at the time of the study (n = 4), could not undergo their research scan because of technical issues with the PET/MRI scanner on the day of the study (n = 1), or did not complete neurocognitive testing (n = 1). Our final study population consisted of 10 children and young adults with sarcoma (n = 5), lymphoma (n = 4), or leukemia (n = 1). There were 7 male and 3 female patients with an age range of 9–23 y (mean ± SD, 17.4 ± 4.7 y). Ten subjects received intravenous methotrexate (86,455.80 ± 103,596.04 mg); 5 subjects also received intrathecal methotrexate (98.70 ± 120.15 mg). All participants had completed HDMTX therapy at the time of the brain [^{18}F]FDG PET/MRI. The time between the start of HDMTX therapy and the brain [^{18}F]FDG PET/MRI was 3.92 ± 1.61 y, with a range of 1–6 y. The time between the end of therapy and PET was 3.5 ± 1.5 mo. The participant flowchart is shown in Figure 1.

Brain [^{18}F]FDG PET/MRI Protocol

Subjects were scanned using a 3-T PET/MRI scanner (Signa; GE Healthcare), allowing for simultaneous acquisition of PET and MR images. The subjects fasted for at least 4 h before the [^{18}F]FDG PET study. Serum glucose levels were measured at the time of [^{18}F]FDG injection, and all subjects demonstrated a glucose level below 120 mg/dL. [^{18}F]FDG PET/MRI was performed 30–45 min after intravenous administration of a 3.7 MBq/kg dose of [^{18}F]FDG as recommended by the guidelines of the Society of Nuclear Medicine and Molecular Imaging and the European Association of Nuclear Medicine (*27*). [^{18}F]FDG was injected in a dedicated room for each subject with the light turned off, and all subjects were required to remain resting with their eyes closed before the PET/MRI scan. No sedation was administered. All subjects underwent MRI of the brain with an 8-channel brain coil. No contrast agent was injected. Axial 3-dimensional (3D) T1 spoiled gradient-recalled images (SPGR) were acquired for PET attenuation correction, with the generation of in-phase, out-of-phase, fat, and water images using the Dixon method. Our MRI protocol included 3D T1 inversion recovery fast SPGR, whole-brain echo-planar diffusion-weighted imaging with 2 diffusion weightings (b = 0 and 1,000 s/mm^2), and an arterial spin labeling perfusion sequence. 3D T2 fluid-attenuated inversion recovery and 3D multiple-echo gradient echo images were also acquired. The apparent diffusion coefficient map was automatically generated from diffusion-weighted imaging by the scanner. Arterial spin labeling imaging was performed with a 3D background-suppressed fast spin-echo technique without vascular suppression using a pseudocontinuous labeling time of 1.5 s, followed by a 2-s postlabeling delay. Postprocessed arterial spin labeling imaging was performed by an automated reconstruction script that sent cerebral blood flow (CBF) images to a PACS. Details of the brain [^{18}F]FDG PET/MRI parameters are shown in Table 1.

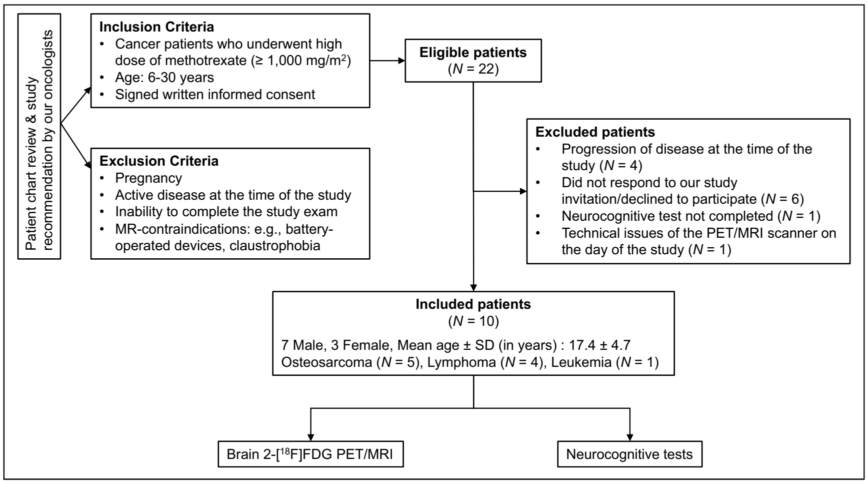

FIGURE 1. Flowchart showing selection of study participants.

TABLE 1
Brain [^{18}F]FDG PET/MRI Parameters

Modality	Parameter	Specification
[^{18}F]FDG PET	Image protocol	30-min static acquisition
	Image plane	Axial
	Slice thickness (mm)	2.78
	Field of view (cm)	60
	Matrix size (mm)	192 × 192
	Reconstruction algorithm	Time of flight (28 subsets, 8 iterations)
	Glucose uptake (mg/dL)	85.9 ± 10.16 (mean ± SD)
	Dose (MBq/kg)	176.49 ± 42.55 (mean ± SD)
	Uptake time (min)	43.50 ± 6.67 (mean ± SD)
MRI*	3D inversion recovery fast SPGR	
	Image plane	Axial
	Slice thickness (mm)	1
	Field of view (cm)	27
	Matrix size (mm)	256 × 256
	Echo time (ms)	3.1
	Repetition time (ms)	7,664
	Flip angle	11°
	Number of excitations	1.00
	2D diffusion-weighted imaging†	
	Image plane	Axial
	Slice thickness (mm)	5
	Field of view (cm)	24
	Matrix size (mm)	128 × 128
	Echo time (ms)	76.5
	Repetition time (ms)	5,000
	Flip angle	90°
	Number of excitations	3.00
	3D arterial spin labeling†	
	Image plane	Axial
	Slice thickness (mm)	4
	Field of view (cm)	24
	Matrix size (mm)	512 × 8
	Echo time (ms)	10.7
	Repetition time (ms)	4,854
	Flip angle	111°
	Number of excitations	3.00

3D T2 fluid-attenuated inversion recovery and 3D multiple-echo gradient-echo (QSM/R2) sequences were also acquired.

†Diffusion-weighted images were acquired with 2 diffusion weightings (b = 0 and 1,000 s/mm^2). Apparent diffusion coefficient maps were automatically generated by software. Postprocessed arterial spin labeling imaging was performed by automated reconstruction script that sent CBF images directly to PACS.

Neurocognitive Battery

Each subject completed a brief neuropsychologic evaluation with a child psychologist. All measures used had sound psychometric properties and were established and well normed. The battery included the Wechsler Abbreviated Scale of Intelligence, second edition (WASI) (Pearson Assessments), a measure of overall intellectual functioning; screening memory subtests of the Wide Range Assessment of Memory and Learning, second edition (WRAML) (*28*), a measure of verbal and visual memory functioning; and subtests of the Delis–Kaplan Executive Function System (DKEFS) (*29*), a measure of executive functioning. The measures were administered in the same order and according to standardized instructions. The tests were selected for their ability to provide information on subjects' overall intellectual functioning, executive functioning (e.g., working memory, inhibition, set

TABLE 2
Neurocognitive Tests

Function	Measure	Average range	Anatomic region	Broadman area
Executive function	DKEFS	10 ± 3	Prefrontal cortex	Middle frontal gyrus and gyrus rectus (9 and 10/11)
			Cingulum	Anterior cingulate gyrus (24, 32, 33); posterior cingulate gyrus (23, 26, 29, 30, and 31)
Intellectual quotient	WASI	100 ± 10	Prefrontal cortex	9 and 10/11
Verbal and nonverbal memory	WRAML	100 ± 10	Hippocampus	27, 28, 34, 35, 36, and 48

Each neurocognitive test comprised 2 or more battery sets: Delis Kaplan Executive Function System (DKEFS)-sequential tracking (TM4), DKEFS–design/nonverbal tasks, DKEFS–inhibition, Wechsler Abbreviated Scale of Intelligence (WASI)–full-scale intellectual quotient, WASI–verbal comprehension index, WASI–perceptual reasoning index, Wide Range Assessment of Memory and Learning (WRAML)–screening memory, WRMAL–verbal memory, and WRMAL-VIS.

shifting, interference control, and planning), and immediate verbal and visual memory skills. Details are shown in Table 2.

Image Analysis

Both PET and MR images were analyzed using PMOD software (version 4.2; PMOD Technologies LLC). One nuclear medicine physician with 7 y of experience performed all the PET analyses. For the PET analysis, each image was normalized to the template space and analyzed with a set of atlas regions. After spatial normalization, all images were visually inspected to ensure accurate registration. We used an automated tool (PNEURO) to segment and generate 3D volumes of interest and measure SUVs. SUV_{mean} was calculated according to body weight. The cortical and gray matter regions analyzed were the prefrontal cortex, cingulate gyrus, and hippocampus. These 3 brain regions were chosen because they are activated or involved during the battery of neurocognitive tests administered in this study, as described in Table 2. The DKEFS test evaluates executive function; the anatomic regions responsible for this function are the prefrontal cortex and the cingulum. The WASI test evaluates the intellectual quotient; the anatomic region responsible for this function is mainly the prefrontal cortex. Similarly, the WRAML test evaluates verbal and nonverbal memory; the anatomic region responsible for this function is mainly the hippocampus. A board-certified neuroradiologist with more than 10 y of image analysis experience and a nuclear medicine physician performed the quantitative MRI data analyses. The same set of atlas regions was used on T1 3D SPGR MR images to calculate the cortical volume of the gray matter in the prefrontal cortex, cingulum, and hippocampus. We used the automatic tool FUSION from PMOD software (PMOD Technologies LLC, version 4.2) to spatially match apparent diffusion coefficient and CBF images to T1 3D SPGR images. We then applied the same set of atlas regions to apparent diffusion coefficient and CBF images and measured the mean apparent diffusion coefficient and mean CBF (CBF_{mean}) for each region. 3D axial susceptibility-weighted angiography MRI sequences were also analyzed to check for any microhemorrhage in the brain parenchyma.

Statistical Analysis

Stanford scores for neurocognitive data were used for analysis (*28–30*). The mean and SD of Stanford scores ($\bar{x} = 100$, SD = 10) were converted to *z* scores to determine deviation from the mean, with positive *z* scores representing above-average or higher functioning and negative *z* scores representing below-average or lower functioning. The relationship between the *z* scores and other measures is unlikely to be simply linear since we would expect correlations only in cases with a deficit. To simplify the analyses, we assumed that only *z* scores less than zero represented possible deficits and, thus, potential correlations, whereas *z* scores greater than zero represented typical nondeficit variation, which would not be correlated. Thus, pairs of multivariable regression models (one for *z* scores < 0 and one for *z* scores > 0)

TABLE 3
Model Estimates of Marginal Effects of Negative *z* Score on Imaging Measures

		Hippocampus		Cingulum		Prefrontal cortex	
Neurocognitive test	PET/MRI measure	Slope	*P*	Slope	*P*	Slope	*P*
WRAML-VIS (*n* = 16)	SUV_{mean}	0.46	0.285	1.02	0.143	1.01	0.173
	CBFmean	−6.04	0.003	−5.97	0.071	−5.93	0.052
DKEFS-TM4 (*n* = 10)	SUV_{mean}	2.70	0.111	4.82	0.012	5.41	0.003
	CBFmean	8.68	<0.001	19.6	<0.001	10.9	<0.001

n = number of measurements.

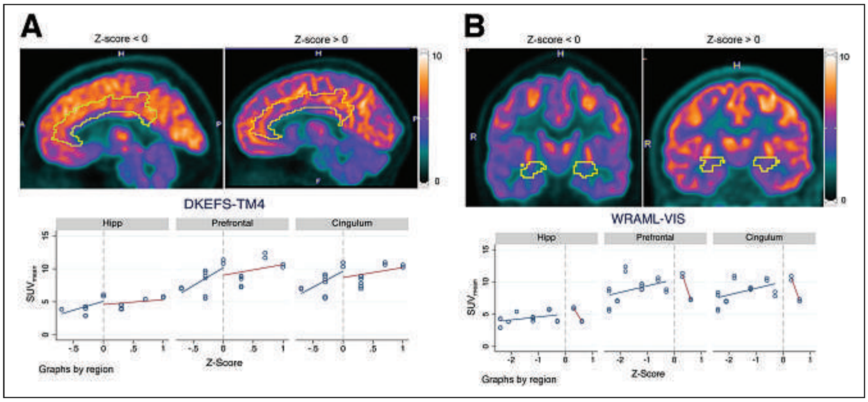

FIGURE 2. Comparison of [^{18}F]FDG uptake in cingulum and hippocampus (Hipp) for patients with low (*z* score $<$ 0) vs. high (*z* score $>$ 0) performance on DKEFS-TM4 (A) and WRAML-VIS (B), respectively. (A) Regression analysis showed significant correlation between SUV_{mean} and DKEFS-TM4 for prefrontal cortex and cingulum ($P = 0.003$ and $P = 0.012$, respectively) but not for hippocampus ($P = 0.111$). (B) There was no significant correlation between SUV_{mean} and WRAML-VIS for prefrontal cortex, cingulum, or hippocampus.

were fitted for each region for each imaging measure and test score (the single case with a *z* score of zero was included in both models rather than being excluded). Heteroscedastic regression models were used to account for heterogeneity in variances among brain regions. As each region had measurements made on both the left and the right sides (the values were similar), adjustment was made for clustering within the patient. As this was an exploratory study with a small sample, no adjustment was made for multiple comparisons. The results of WASI–verbal comprehension index, WRAML–visual memory (WRAML-VIS), WRAML–sentence memory, and DKEFS–sequential tracking (DKEFS-TM4) Stanford score conversions to *z* scores yielded *z* scores of ±1 or greater and were used for subsequent correlation analysis with SUV_{mean} and CBF_{mean}; therefore, only these tests were considered for the correlation analysis. Because WRAML-VIS and WRAML–sentence memory were highly correlated (0.88) and thus redundant, we used only WRMAL-VIS for the statistical analysis.

RESULTS

Neurocognitive Tests

We used the *z* score to detect evidence of deficits in neurocognitive functions in our patients. Nine of 10 patients showed a negative *z* score for at least 1 test (mean, 3; range, 1–7). Only 1 patient showed a positive *z* score for all neurocognitive tests.

WASI–verbal comprehension index, WRAML-VIS, and DKEFS-TM4 showed 3 or more negative *z* scores among the patients. Eight subjects for WRAML-VIS, 6 for WASI–verbal comprehension index, and 4 for DKEFS-TM4 demonstrated *z* scores of −1 or lower (Supplemental Table 1; supplemental materials are available at http://jnm.snmjournals.org).

WRAML-VIS correlated significantly with CBF_{mean}. DKEFS-TM4 correlated significantly with both SUV_{mean} and CBF_{mean}. WASI–verbal comprehension index did not correlate with any of the PET/MRI measures (Table 3).

Brain [^{18}F]FDG PET

Significant differences in average SUV_{mean} among all 3 brain regions were detected ($P < 0.001$). SUV_{mean} measurements of the hippocampus (4.46 ± 0.94) were significantly lower than measurements of the cingulum (8.58 ± 1.67, $P < 0.001$) and the prefrontal cortex (8.94 ± 1.90; $P < 0.001$), but the latter 2 were not significantly different from each other ($P = 0.35$). Mean SUV_{mean} data between the left and right sides of each region were not significantly different (Supplemental Table 2).

Figure 2 compares [^{18}F]FDG uptake in the cingulum and the hippocampus for patients with low (*z* score $<$ 0) versus high (*z* score $>$ 0) performance on DKEFS-TM4 (Fig. 2A) and WRAML-VIS (Fig. 2B), respectively. The regression analysis showed a significant correlation between SUV_{mean} and DKEFS-TM4 *z* score for the prefrontal cortex and cingulum ($P = 0.003$ and $P = 0.012$, respectively) but not for the hippocampus ($P = 0.111$). We did not find a significant correlation between SUV_{mean} and WRAML-VIS for any evaluated brain regions. Marginal estimates from the model are shown in Table 3. SUV_{mean} did not correlate with the cumulative dose of methotrexate ($P = 0.537$).

Brain MRI

No anatomic or structural abnormalities were found in the affected brain areas on 3D T1 SPGR or 3D T2 fluid-attenuated inversion recovery imaging. One of 10 patients demonstrated microhemorrhages in the left frontal opercular cortex.

We found significant differences in the average CBF_{mean} among all 3 brain regions, that is, prefrontal cortex, cingulum, and hippocampus ($P < 0.001$). CBF_{mean} for the hippocampus (48.54 ± 5.99) was significantly lower than for the cingulum (64.54 ± 9.04,

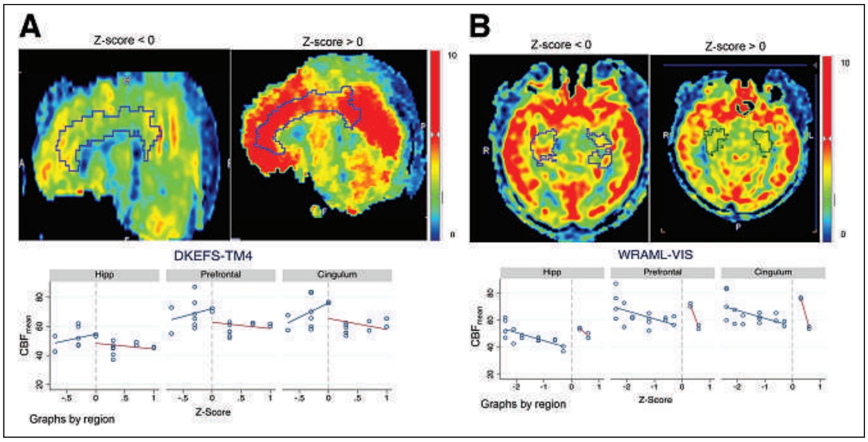

FIGURE 3. Comparison of CBF_{mean} in cingulum and hippocampus (Hipp) for patients with low (*z* score $<$ 0) vs. high (*z* score $>$ 0) performance on DKEFS-TM4 (Fig. 3A) and WRAML-VIS (Fig. 3B), respectively. (A) Regression analysis showed significant correlation between CBF_{mean} and DKEFS-TM4 for cingulum, hippocampus, and prefrontal cortex (all $P < 0.001$). (B) CBF_{mean} for hippocampus and WRAML-VIS was inversely correlated ($P = 0.003$). However, there was no correlation between CBF_{mean} and WRAML-VIS for cingulum ($P = 0.071$) and prefrontal cortex ($P = 0.052$).

$P < 0.001$) and prefrontal cortex (63.77 ± 8.60, $P < 0.001$), but the latter 2 were not significantly different from each other ($P = 0.34$). CBF_{mean} did not significantly differ between the left and right sides of each region (Supplemental Table 2).

Figure 3 compares CBF_{mean} in the cingulum and the hippocampus for patients with low (z score < 0) versus high (z score > 0) performance on DKEFS-TM4 (Fig. 3A) and WRAML-VIS (Fig. 3B), respectively. The regression analysis showed a significant correlation between CBF_{mean} and DKEFS-TM4 for the cingulum, hippocampus, and prefrontal cortex (all $P < 0.001$). In addition, CBF_{mean} for the hippocampus and WRAML-VIS were inversely correlated ($P = 0.003$). No correlation was found between CBF_{mean} and WRAML-VIS for the cingulum ($P = 0.071$) or prefrontal cortex ($P = 0.052$). Marginal estimates from the model are shown in Table 3. Overall, CBF_{mean} showed a positive correlation with SUV_{mean} ($r = 0.56$, $P = 0.01$). CBF_{mean} was negatively correlated with the cumulative dose of methotrexate ($r = -0.30$, $P = 0.002$). No significant correlations were found between apparent diffusion coefficient or cortical volume and any of the metrics we analyzed.

DISCUSSION

Our data suggest that [^{18}F]FDG PET/MRI can potentially detect imaging changes indicating HDMTX-induced neurotoxicity. Our observations suggest that the SUV_{mean} and CBF_{mean} of the prefrontal cortex and cingulum may serve as quantitative measures for detecting executive functioning issues. The CBF_{mean} of the hippocampus could also be useful for monitoring memory issues. To our knowledge, this is the first prospective correlation of [^{18}F]FDG PET findings with a matched set of neurocognitive tests in pediatric cancer survivors.

Krull et al. reported a significant association between increased brain functional MRI activity in the frontal and anterior cingulate cortices and poorer executive function scores in a cohort of 218 long-term childhood cancer survivors after therapy with methotrexate (*21*). These findings align with ours. In fact, we also found a significant correlation between the CBF_{mean} of the cingulum and prefrontal cortex and lower scores on the executive functioning test. Overall, these data suggest that MRI can detect long-term HDMTX-induced neurotoxicity and help identify a subgroup of subjects who are more susceptible to future cognitive deficits.

In our pilot study, 8 of 10 subjects had a memory test with a z score of less than 0. The hippocampus is the brain region related to memory functions. Both SUV_{mean} and CBF_{mean} were significantly lower in the hippocampus than in the cingulum or prefrontal cortex. Although the relationship between the SUV_{mean} of the hippocampus and WRAML-VIS was positive, it did not reach significance, potentially because of the small sample size. Tauty et al. retrospectively evaluated [^{18}F]FDG PET/CT images of 20 children with Hodgkin lymphoma at baseline and 2 mo after starting methotrexate chemotherapy (*26*). The authors noted hypometabolic areas in the insular cortex, lateral frontal lobe, and posterior cingulate cortex. Decreased [^{18}F]FDG uptake after chemotherapy has been shown by several studies, with the limbic regions, prefrontal cortex, and cingulum being the most affected ones (*31,32*). It is important to note that these impairments in the acute phase after chemotherapy may be reversible. Findings on posttreatment scans, such as in our study, are more likely to be chronic and may be more useful for detecting clinically significant toxicity, although additional investigation is needed. The findings of both acute and chronic abnormalities could support the use of imaging biomarkers to predict who is at risk for developing long-term neurocognitive problems; such patients could receive antiinflammatory preventive therapies and closer monitoring for earlier implementation of rehabilitative services.

Given the recent discovery that the brain toxicity induced by methotrexate can be reversed by administering antiinflammatory drugs (*19*), our study holds significant importance. During the past decade, several registries of pediatric cancer survivors have been established both in the United States and in Europe with the purpose of recognizing and treating long-term disabilities after chemotherapy (*7,33–35*). Most of these longitudinal studies used siblings as controls and measured neurocognitive impairments with self-assessed questionnaires. A cohort study including 840 survivors and 247 siblings showed that survivors encountered significantly more impairment in concentration (12% vs. 6%), working speed (20% vs. 8%), and memory (33% vs. 15%) than controls. Patients who had received cranial irradiation were most severely affected (*7*). Although there is a large amount of survey-based data, there is a lack of data on imaging findings, which are arguably more objective. Pediatric cancer survivors are more likely to complete a survey than undergo brain imaging during their follow-up visits. However, our preliminary data suggest that dedicated brain [^{18}F]FDG PET/MRI performed after HDMTX therapy could help select a subgroup of patients who have developed HDMTX-induced neurotoxicity. With timely and appropriate interventions (e.g., antiinflammatory medication (*19*) or neurocognitive rehabilitation (*24*)), there is a possibility to prevent long-term neurocognitive complications. As research uncovers the mechanisms of neurotoxicity for other chemotherapy drugs, imaging may become increasingly important to screen for effects that may be reversible with treatment or remediable with other interventions.

In our pilot study, we found an association between higher CBF_{mean} values and lower scores on WRAML-VIS. Studies on mouse models show that methotrexate first leads to microglia activation, which may transiently increase CBF, followed by neuronal myelination impairment, which would be expected to cause decreased CBF values (*19*). Thus, in patients, we would expect initially increased CBF values, followed by a CBF decline. Further evaluations are needed to better evaluate the time course of changes in CBF values and their correlation with measures of visual memory.

The cumulative dose of methotrexate inversely correlated with CBF_{mean} but not with $SUV_{mean.}$ This can be explained by the many factors that affect the drug's neurotoxic effects, including the inherent vulnerabilities and the presence of preexisting neurologic conditions, among others (*23*). It is well known that methotrexate-induced brain toxicity has a multifactorial etiology; some pediatric patients may experience no or minor neurologic issues, whereas others may experience severe and long-term neurocognitive deficits (*36*). A noninvasive imaging test that could visualize and quantify HDMTX-induced neurotoxicity could be used to identify childhood cancer survivors at high risk for long-term neurocognitive problems who may benefit from targeted interventions. It would be interesting to examine the usefulness of other PET radiotracers, such as [^{11}C]PK11195, in this context. [^{11}C]PK11195 is expressed by reactive glial cells and macrophages and has been used as a PET tracer to visualize brain inflammation in vivo (*37*).

Our study had several limitations. First, this was a pilot study with small patient numbers and heterogeneity in disease conditions (osteosarcoma, lymphoma, and leukemia), clinical features, and methotrexate exposures (systemic and intrathecal). Larger cohorts of patients treated with and without HDMTX may be helpful in clarifying the effects of this drug. Nevertheless, to our knowledge, this was the first prospective clinical trial that has correlated [^{18}F]FDG PET/MRI metrics with neurocognitive tests in a cohort of pediatric cancer survivors. We encountered difficulties in the recruitment process. The main one was that this study was funded in 2021, immediately after the coronavirus disease 2019 pandemic. Several subjects were not comfortable coming to the hospital strictly for research purposes. We believe that performing brain imaging during regularly scheduled clinical follow-up visits would address this obstacle in future studies. Five of our patients received intrathecal methotrexate, which can be a confounding factor for correlations of intravenous methotrexate doses with neurocognitive injuries. Although it is well known that patients who were treated with HDMTX developed neurocognitive problems (*20–22*), it has been also described that the administered methotrexate dose did not correlate with the degree or location of specific brain injuries (*21*). Our data close this gap, demonstrating that the degree and location of specific brain injuries on [^{18}F]FDG PET/MRI correlated with neurocognitive impairments. Our [^{18}F]FDG PET/MR assessment can be applied to patients who received intravenous methotrexate, intrathecal methotrexate, or both. Another limitation of the study is related to the radiation exposure from the radiotracer and the potential need for sedation in younger children. However, these exposures may be worthwhile if they identify remediable abnormalities or suggest interventions that could prevent long-term complications. Moreover, our study lacked a control group. This is a well-known limitation of imaging studies in pediatric patients. Many authors, including our group, have used baseline imaging as personal subject-based controls, but this is not always useful in pediatric patients because their brain develops with increasing age. Furthermore, some patients who underwent HDMTX treatment, such as leukemia patients, did not undergo routine PET scans before starting chemotherapy. Besides, we could not rule out whether some of the findings in this study were due to neuroplasticity in the young-aged participants. Although [^{18}F]FDG PET/MR images can provide valuable insights into changes in brain structure and function indicative of neuroplasticity, interpreting these changes accurately often requires a multidisciplinary approach.

CONCLUSION

Our study suggests that [^{18}F]FDG PET/MRI may be useful for diagnosing the imaging effects of HDMTX therapy on the brains of pediatric cancer survivors. This could facilitate earlier interventions using antiinflammatory treatments. Furthermore, it may enable more effective monitoring of treatment outcomes, particularly for a subset of patients more prone to developing HDMTX-associated neurocognitive impairment. However, further assessments in larger, more homogeneous cohorts are needed.

DISCLOSURE

This research was funded by an NIH grant from the National Cancer Institute (R21 HD101129). No other potential conflict of interest relevant to this article was reported.

KEY POINTS

QUESTION: Can [^{18}F]FDG PET/MRI detect brain injury after HDMTX therapy in pediatric cancer survivors?

PERTINENT FINDINGS: A significant correlation was found between the *z* score for the DKEFS test and SUV_{mean} and CBF_{mean} values in the cingulum and prefrontal cortex.

IMPLICATIONS FOR PATIENT CARE: Using [^{18}F]FDG PET/MRI for assessing the cerebral impact of methotrexate therapy in pediatric cancer survivors holds the potential to expedite interventions with antiinflammatory remedies and enable effective monitoring of treatment outcomes. This is particularly crucial for patients with a heightened vulnerability to HDMTX-associated neurocognitive impairment.

REFERENCES

1. Cairo MS, Beishuizen A. Childhood, adolescent and young adult non-Hodgkin lymphoma: current perspectives. *Br J Haematol.* 2019;185:1021–1042.
2. Inaba H, Mullighan CG. Pediatric acute lymphoblastic leukemia. *Haematologica.* 2020;105:2524–2539.
3. Wu Y, Xu L, Yang P, et al. Survival prediction in high-grade osteosarcoma using radiomics of diagnostic computed tomography. *EBioMedicine.* 2018;34:27–34.
4. Armstrong GT, Kawashima T, Leisenring W, et al. Aging and risk of severe, disabling, life-threatening, and fatal events in the childhood cancer survivor study. *J Clin Oncol.* 2014;32:1218–1227.
5. Hudson MM, Ness KK, Gurney JG, et al. Clinical ascertainment of health outcomes among adults treated for childhood cancer. *JAMA.* 2013;309:2371–2381.
6. Clanton NR, Klosky JL, Li C, et al. Fatigue, vitality, sleep, and neurocognitive functioning in adult survivors of childhood cancer: a report from the Childhood Cancer Survivor Study. *Cancer.* 2011;117:2559–2568.
7. Wengenroth L, Rueegg CS, Michel G, et al. Concentration, working speed and memory: cognitive problems in young childhood cancer survivors and their siblings. *Pediatr Blood Cancer.* 2015;62:875–882.
8. Cheung YT, Brinkman TM, Li C, et al. Chronic health conditions and neurocognitive function in aging survivors of childhood cancer: a report from the Childhood Cancer Survivor Study. *J Natl Cancer Inst.* 2018;110:411–419.
9. Prasad PK, Hardy KK, Zhang N, et al. Psychosocial and neurocognitive outcomes in adult survivors of adolescent and early young adult cancer: a report from the Childhood Cancer Survivor Study. *J Clin Oncol.* 2015;33:2545–2552.
10. Ellenberg L, Liu Q, Gioia G, et al. Neurocognitive status in long-term survivors of childhood CNS malignancies: a report from the Childhood Cancer Survivor Study. *Neuropsychology.* 2009;23:705–717.
11. Jacola LM, Krull KR, Pui C-H, et al. Longitudinal assessment of neurocognitive outcomes in survivors of childhood acute lymphoblastic leukemia treated on a contemporary chemotherapy protocol. *J Clin Oncol.* 2016;34:1239–1247.
12. Kadan-Lottick NS, Zheng DJ, Wang M, et al. Patient-reported neurocognitive function in adult survivors of childhood and adolescent osteosarcoma and Ewing sarcoma. *J Cancer Surviv.* 2023;17:1238–1250.
13. Kirchhoff AC, Krull KR, Ness KK, et al. Physical, mental, and neurocognitive status and employment outcomes in the childhood cancer survivor study cohort. *Cancer Epidemiol Biomarkers Prev.* 2011;20:1838–1849.
14. Mitby PA, Robison LL, Whitton JA, et al. Utilization of special education services and educational attainment among long-term survivors of childhood cancer: a report from the Childhood Cancer Survivor Study. *Cancer.* 2003;97:1115–1126.
15. Campbell M, Kiss C, Zimmermann M, et al. Childhood acute lymphoblastic leukemia: results of the randomized acute lymphoblastic leukemia intercontinental-Berlin-Frankfurt-Münster 2009 trial. *J Clin Oncol.* 2023;41:3499–3511.
16. Hayashi RJ, Winter SS, Dunsmore KP, et al. Successful outcomes of newly diagnosed T lymphoblastic lymphoma: results from Children's Oncology Group AALL0434. *J Clin Oncol.* 2020;38:3062–3070.
17. Marina NM, Smeland S, Bielack SS, et al. Comparison of MAPIE versus MAP in patients with a poor response to preoperative chemotherapy for newly diagnosed high-grade osteosarcoma (EURAMOS-1): an open-label, international, randomised controlled trial. *Lancet Oncol.* 2016;17:1396–1408.
18. Geraghty AC, Gibson EM, Ghanem RA, et al. Loss of adaptive myelination contributes to methotrexate chemotherapy-related cognitive impairment. *Neuron.* 2019; 103:250–265.e8.

19. Gibson EM, Nagaraja S, Ocampo A, et al. Methotrexate chemotherapy induces persistent Tri-glial dysregulation that underlies chemotherapy-related cognitive impairment. *Cell.* 2019;176:43–55.e13.
20. Krull KR, Brinkman TM, Li C, et al. Neurocognitive outcomes decades after treatment for childhood acute lymphoblastic leukemia: a report from the St. Jude lifetime cohort study. *J Clin Oncol.* 2013;31:4407–4415.
21. Krull KR, Cheung YT, Liu W, et al. Chemotherapy pharmacodynamics and neuroimaging and neurocognitive outcomes in long-term survivors of childhood acute lymphoblastic leukemia. *J Clin Oncol.* 2016;34:2644–2653.
22. Ehrhardt MJ, Mulrooney DA, Li C, et al. Neurocognitive, psychosocial, and quality-of-life outcomes in adult survivors of childhood non-Hodgkin lymphoma. *Cancer.* 2018;124:417–425.
23. Bhojwani D, Sabin ND, Pei D, et al. Methotrexate-induced neurotoxicity and leukoencephalopathy in childhood acute lymphoblastic leukemia. *J Clin Oncol.* 2014; 32:949–959.
24. Phillips NS, Duke ES, Schofield H-LT, Ullrich NJ. Neurotoxic effects of childhood cancer therapy and its potential neurocognitive impact. *J Clin Oncol.* 2021;39: 1752–1765.
25. Shrot S, Abebe-Campino G, Toren A, Ben-Haim S, Hoffmann C, Davidson T. Fluorodeoxyglucose detected changes in brain metabolism after chemotherapy in pediatric non-Hodgkin lymphoma. *Pediatr Neurol.* 2019;92:37–42.
26. Tauty A, Noblet V, Paillard C, Fornecker L-M, Namer IJ, Bund C. Evaluation of the effects of chemotherapy on brain glucose metabolism in children with Hodgkin's lymphoma. *Ann Nucl Med.* 2019;33:564–569.
27. Vali R, Alessio A, Balza R, et al. SNMMI procedure standard/EANM practice guideline on pediatric 18F-FDG PET/CT for oncology 1.0. *J Nucl Med.* 2021;62: 99–110.
28. Ritchie D, Nierenberg B. Wide range assessment of memory and learning. In: *Encyclopedia of Child Behavior and Development.* Springer; 2011:1567–1569.
29. Fine EM, Delis DC. Delis–Kaplan executive functioning system. In: *Encyclopedia of Clinical Neuropsychology.* Springer; 2011:796–801.
30. Wechsler D. *Wechsler Abbreviated Scale of Intelligence*, 2nd ed. https://www.pearsonassessments.com/store/usassessments/en/store/professional-assessments/cognition-%26-neuro/wechsler-abbreviated-scale-of-intelligence-%7c-second-edition/p/100000593.html?tab=overview. Published 2011. Accessed March 27, 2024.
31. Baudino B, D'agata F, Caroppo P, et al. The chemotherapy long-term effect on cognitive functions and brain metabolism in lymphoma patients. *Q J Nucl Med Mol Imaging.* 2012;56:559–568.
32. Chiaravalloti A, Pagani M, Cantonetti M, et al. Brain metabolic changes in Hodgkin disease patients following diagnosis and during the disease course: an 18F-FDG PET/CT study. *Oncol Lett.* 2015;9:685–690.
33. Suh E, Stratton KL, Leisenring WM, et al. Late mortality and chronic health conditions in long-term survivors of early-adolescent and young adult cancers: a retrospective cohort analysis from the Childhood Cancer Survivor Study. *Lancet Oncol.* 2020;21:421–435.
34. Howell CR, Bjornard KL, Ness KK, et al. Cohort profile: the St. Jude Lifetime Cohort Study (SJLIFE) for paediatric cancer survivors. *Int J Epidemiol.* 2021;50: 39–49.
35. Bhakta N, Liu Q, Ness KK, et al. The cumulative burden of surviving childhood cancer: an initial report from the St Jude Lifetime Cohort Study (SJLIFE). *Lancet.* 2017;390:2569–2582.
36. Halsey C, Buck G, Richards S, Vargha-Khadem F, Hill F, Gibson B. The impact of therapy for childhood acute lymphoblastic leukaemia on intelligence quotients; results of the risk-stratified randomized central nervous system treatment trial MRC UKALL XI. *J Hematol Oncol.* 2011;4:42.
37. Rojas S, Martín A, Arranz MJ, et al. Imaging brain inflammation with [11C]PK11195 by PET and induction of the peripheral-type benzodiazepine receptor after transient focal ischemia in rats. *J Cereb Blood Flow Metab.* 2007;27:1975–1986.

Diagnostic Potential of Supplemental Static and Dynamic ^{68}Ga-FAPI-46 PET for Primary ^{18}F-FDG–Negative Pulmonary Lesions

Manuel Röhrich[1–3], Johanna Daum[1,3], Ewgenija Gutjahr[4], Anna-Maria Spektor[1,3], Frederik M. Glatting[1,5,6], Yasemin Aylin Sahin[2], Hans Georg Buchholz[2], Jorge Hoppner[1,3], Cathrin Schroeter[1,3], Eleni Mavriopoulou[1,3], Kai Schlamp[3,7], Matthias Grott[3,8], Florian Eichhorn[3,8], Claus Peter Heußel[3,7], Hans Ulrich Kauczor[3,9,10], Michael Kreuter[11,12], Frederik Giesel[1,3,13–15], Mathias Schreckenberger[2], Hauke Winter[3,7] and Uwe Haberkorn[1,3,9,16]

[1]Department of Nuclear Medicine, University Hospital Heidelberg, Heidelberg, Germany; [2]Department of Nuclear Medicine, University Hospital Mainz, Mainz, Germany; [3]German Center of Lung Research, Heidelberg, Germany; [4]Institute of Pathology, University Hospital Heidelberg, Heidelberg, Germany; [5]Clinical Cooperation Unit Molecular and Radiation Oncology, German Cancer Research Center, Heidelberg, Germany; [6]Department of Radiation Oncology, University Hospital Heidelberg, Heidelberg, Germany; [7]Department of Radiology, Thoraxklinik, University Hospital Heidelberg, Heidelberg, Germany; [8]Department of Thoracic Surgery, Thoraxklinik, University Hospital Heidelberg, Heidelberg, Germany; [9]Department of Diagnostic and Interventional Radiology, University Hospital Heidelberg, Heidelberg, Germany; [10]Center for Interstitial and Rare Lung Diseases, Pneumology, and Respiratory Critical Care Medicine, Thoraxklinik, University of Heidelberg, Heidelberg, Germany; [11]Department of Pneumology, Mainz Center for Pulmonary Medicine, Mainz University, Mainz, Germany; [12]Medical Center and Department of Pulmonary, Critical Care, and Sleep Medicine, Marienhaus Clinic Mainz, Mainz, Germany; [13]Department of Nuclear Medicine, Medical Faculty, University Hospital Düsseldorf, Heinrich Heine University, Düsseldorf, Germany; [14]Institute for Radiation Sciences, Osaka University, Osaka, Japan; [15]German Cancer Consortium, Heidelberg, Germany; and [16]Clinical Cooperation Unit Nuclear Medicine, German Cancer Research Center, Heidelberg, Germany

PET using ^{68}Ga-labeled fibroblast activation protein (FAP) inhibitors (FAPIs) holds high potential for diagnostic imaging of various malignancies, including lung cancer (LC). However, ^{18}F-FDG PET is still the clinical gold standard for LC imaging. Several subtypes of LC, especially lepidic LC, are frequently ^{18}F-FDG PET–negative, which markedly hampers the assessment of single pulmonary lesions suggestive of LC. Here, we evaluated the diagnostic potential of static and dynamic ^{68}Ga-FAPI-46 PET in the ^{18}F-FDG–negative pulmonary lesions of 19 patients who underwent surgery or biopsy for histologic diagnosis after PET imaging. For target validation, FAP expression in lepidic LC was confirmed by FAP immunohistochemistry. **Methods:** Hematoxylin and eosin staining and FAP immunohistochemistry of 24 tissue sections of lepidic LC from the local tissue bank were performed and analyzed visually. Clinically, 19 patients underwent static and dynamic ^{68}Ga-FAPI-46 PET in addition to ^{18}F-FDG PET based on individual clinical indications. Static PET data of both examinations were analyzed by determining SUV_{max}, SUV_{mean}, and tumor-to-background ratio (TBR) against the blood pool, as well as relative parameters (^{68}Ga-FAPI-46 in relation to ^{18}F-FDG), of histologically confirmed LC and benign lesions. Time–activity curves and dynamic parameters (time to peak, slope, k_1, k_2, k_3, and k_4) were extracted from dynamic ^{68}Ga-FAPI-46 PET data. The sensitivity and specificity of all parameters were analyzed by calculating receiver-operating-characteristic curves. **Results:** FAP immunohistochemistry confirmed the presence of strongly FAP-positive cancer-associated fibroblasts in lepidic LC. LC showed markedly elevated ^{68}Ga-FAPI-46 uptake, higher TBRs, and higher ^{68}Ga-FAPI-46–to–^{18}F-FDG ratios for all parameters than did benign pulmonary lesions. Dynamic imaging analysis revealed differential time–activity curves for LC and benign pulmonary lesions: initially increasing time–activity curves with a decent slope were typical of LC, and steadily decreasing time–activity curve indicated benign pulmonary lesions, as was reflected by a significantly increased time to peak and significantly smaller absolute values of the slope for LC. Relative ^{68}Ga-FAPI-46–to–^{18}F-FDG ratios regarding SUV_{max} and TBR showed the highest sensitivity and specificity for the discrimination of LC from benign pulmonary lesions. **Conclusion:** ^{68}Ga-FAPI-46 PET is a powerful new tool for the assessment of single ^{18}F-FDG–negative pulmonary lesions and may optimize patient stratification in this clinical setting.

Key Words: fibroblast activation protein; FAPI; PET; lung cancer; pulmonary lesions

J Nucl Med 2024; 65:872–879
DOI: 10.2967/jnumed.123.267103

Lung cancer (LC) is the most frequently occurring type of cancer and is associated with a high rate of cancer-related death worldwide (*1*). Accurate and timely diagnosis of LC is crucial for treatment stratification of patients. CT is the most frequently used imaging method for primary staging of LC. CT imaging can be supplemented by ^{18}F-FDG PET to improve tumor staging or to further characterize suggestive pulmonary lesions. Although tumor staging is clearly improved by ^{18}F-FDG PET compared with CT, the additional diagnostic value of ^{18}F-FDG for characterization of suggestive pulmonary lesions is limited (*2*). Different subtypes of LC have been shown to exhibit largely variable ^{18}F-FDG avidity, such as lepidic LC, which are frequently ^{18}F-FDG–negative, or other acinar- or papillary-dominant adenocarcinomas, which are

---

Received Nov. 24, 2023; revision accepted Feb. 20, 2024.

For correspondence or reprints, contact Manuel Röhrich (manuel.roehrich@med.uni-heidelberg.de).

^{18}F-FDG–negative or show low ^{18}F-FDG avidity in a substantial percentage of cases (*3*,*4*).

PET with ^{68}Ga- or ^{18}F-labeled fibroblast activation protein (FAP) inhibitors (FAPIs) has recently been introduced as a novel imaging technique for various cancers and nonmalignant diseases with tissue remodeling (*5–9*). Although the clinically well-established ^{18}F-FDG PET is based on increased glucose metabolism of neoplastic cells, FAPI PET allows visualization of the stromal tumor compartment in terms of FAP-positive fibroblasts (*9*). Because of the vast stromal portion and minor neoplastic-cell portion in many epithelial tumor entities, including LC, FAPIs have a high tumor accumulation in these types of cancer (*10–13*). Several studies have compared the diagnostic performance of FAPI PET and ^{18}F-FDG PET with respect to the imaging properties of both PET examinations and with respect to potential additional FAPI-positive findings that may lead to differential staging (*14*,*15*). In consideration of LC, previous studies have focused on patients with advanced LC and evaluated staging on the basis of FAPI PET compared with ^{18}F-FDG or CT imaging (*13*,*16–18*). To our knowledge, no evaluation of FAPI PET yet exists focusing on the characterization of single suggestive pulmonary lesions in the primary situation. Here, we applied static and dynamic ^{68}Ga-FAPI-46 PET imaging in 19 treatment-naïve patients with ^{18}F-FDG PET–negative suggestive pulmonary lesions. All patients underwent biopsy or surgical histologic confirmation of their lesions after imaging. For target validation, FAP expression patterns in 24 separate cases of lepidic LC were evaluated by FAP immunohistochemistry. The purpose of this analysis was to demonstrate the potential diagnostic benefit of supplemental ^{68}Ga-FAPI-46 PET for primary assessment of patients with single suggestive pulmonary lesions.

MATERIALS AND METHODS

Patients

Between February 2022 and April 2023, 19 patients with suggestive pulmonary lesions were examined by CT, ^{18}F-FDG PET, and ^{68}Ga-FAPI-46 PET at the University Hospital Heidelberg. All patients underwent CT and ^{18}F-FDG PET as clinical routine scans and were individually referred for additional ^{68}Ga-FAPI-46 PET by their treating physicians because of inconclusive findings on CT and ^{18}F-FDG PET (^{18}F-FDG negativity despite suggestive CT morphology or patient-related risk factors according to the Fleischner Society guidelines (*19*)). Written informed consent was obtained from all patients on an individual-patient basis following the regulations of the German Pharmaceuticals Act §13(2b). After imaging, all patients underwent resection or biopsy of their pulmonary lesions followed by histopathologic diagnosis. Retrospective analysis of imaging, clinical, and pathologic data was approved by the local institutional review board (study number S-115/2020).

Diagnostic CT, ^{18}F-FDG PET/CT, and ^{68}Ga-FAPI-46 PET

All 19 patients underwent diagnostic contrast-enhanced CT imaging of the chest before PET imaging. ^{18}F-FDG PET/CT was performed according to standard care as previously described (*14*). ^{68}Ga-FAPI-46 was synthesized and labeled according to established protocols (*9*). Static and dynamic ^{68}Ga-FAPI-46 PET/CT was performed using a Biograph mCT Flow scanner (Siemens) as previously described (*20*). In short, after injection of 187–329 MBq of ^{68}Ga-labeled FAPI-46, low-dose CT without contrast medium was performed, followed by dynamic PET (28 frames over 60 min) to characterize tracer uptake over time, followed by whole-body PET/CT 60 min after tracer injection in 16 of 19 patients. In 3 patients, only whole-body PET/CT 60 min after tracer injection was performed. Reconstructions were performed with corrections for scatter, decay, and attenuation. The average time (±SD) between ^{18}F-FDG PET/CT and ^{68}Ga-FAPI-46 PET/CT was 6.2 ± 6.4 d.

Image Analysis

For static ^{18}F-FDG PET/CT and ^{68}Ga-FAPI-46 PET/PET/CT data, all pulmonary lesions were contoured manually on the basis of their CT appearance. For all lesions, SUV_{max}, SUV_{mean}, and tumor-to-background ratio (TBR) against blood pool, as well as relative parameters (^{68}Ga-FAPI-46 in relation to^{18}F-FDG), were calculated. All cases selected for this analysis were classified as ^{18}F-FDG–negative according to lesional ^{18}F-FDG uptake equal to or below the blood pool level (in terms of a maximum and mean TBR of less than 1.3) as previously published (*21*). Differences between histologically confirmed LC and benign lesions were analyzed. For dynamic ^{68}Ga-FAPI-46 PET data, time–activity curves and quantitative dynamic parameters (time to peak [time between start of the dynamic image acquisition and the frame with the highest activity] and slope [relative gradient between the time–activity curve peak and the lowest activity of the following time–activity curve section in analogy to

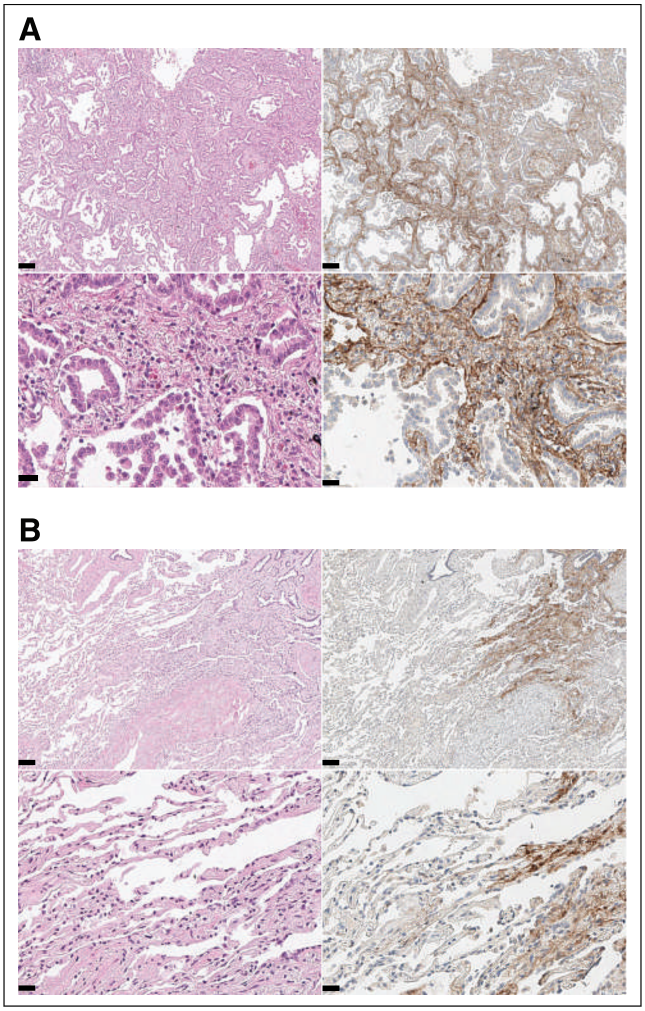

FIGURE 1. FAP expression in lepidic LC. (A and B) Representative hematoxylin and eosin staining (left) and immunohistochemical staining against FAP (right) of central part of lepidic LC biopsy, which shows strong stromal FAP positivity (A), and tumor front of lepidic LC, showing transition from FAP-positive LC tumor rim into FAP-negative physiologic lung tissue (B) (magnification: upper rows, ×10; lower rows, ×40) (scale bars: upper rows, 100 μm; lower rows, 20 μm).

TABLE 1
Clinical Parameters and Diagnoses of 19 Patients with ^{18}F-FDG–Negative Pulmonary Lesions

Patient no.	Age (y)	Sex	Dynamic PET imaging	Localization	Largest diameter (mm)	Histologic confirmation	Diagnosis	Growth pattern	TNM stage
1	64	M	No	Right upper lobe	20	Wedge resection	Tuberculosis	Not applicable	Not applicable
2	73	M	Yes	Left hilus	14	Bronchoscopy with biopsy	Calcified lymph node	Not applicable	Not applicable
3	68	F	Yes	Right lower lobe	29	Lobectomy	Adenocarcinoma	Lepidic	T1cN0M0
4	58	M	Yes	Right upper lobe	10	Wedge resection	Granuloma	Not applicable	Not applicable
5	75	M	Yes	Left lower lobe	16	Lobectomy	Adenocarcinoma	Acinar/lepidic	T1bN0M0
6	70	F	Yes	Left lower lobe	23	Lobectomy	Adenocarcinoma	Acinar	T1cN0M0
7	62	M	Yes	Right lower lobe	79	Lobectomy	Sarcoidosis	Not applicable	Not applicable
8	50	M	Yes	Left upper lobe	13	CT-guided biopsy	Adenocarcinoma	Acinar	T1bN0M0
9	57	F	Yes	Right lower lobe	17	Lobectomy	Adenocarcinoma	Acinar	T1cN0M0
10	63	M	Yes	Right upper lobe	15	CT-guided biopsy	Adenocarcinoma	Acinar	T1bN1M0
11	41	M	No	Left lower lobe	17	Wedge resection	Hamartoma	Not applicable	Not applicable
12	45	M	Yes	Right lower lobe	16	Enucleation	Hamartoma	Not applicable	Not applicable
13	70	M	Yes	Right upper lobe	16	Lobectomy	Adenocarcinoma	Acinar	T2aN0M0
14	72	M	Yes	Left upper lobe	23	Lobectomy	Adenocarcinoma	Acinar	T1bN0M0
15	65	M	Yes	Right upper lobe	29	Lobectomy	Adenocarcinoma	Lepidic	T1cN0M0
16	50	M	No	Right lower lobe	18	CT-guided biopsy	Typical carcinoid	Not applicable	T1bN0M0
17	51	F	Yes	Right upper lobe	29	CT-guided biopsy	Adenocarcinoma	Lepidic/acinar	T2aN0M0
18	64	F	Yes	Left upper lobe	28	Segment resection	Adenocarcinoma	Lepidic	T1aN0M0
19	77	M	Yes	Left lower lobe	15	CT-guided biopsy	Lung tissue	Not applicable	Not applicable

previously published dynamic PET data analyses (*22*)]) were extracted, and differences between histologically confirmed LC and benign lesions were analyzed. All image analysis was performed using PMOD software (version 4.1; PMOD Technologies).

Immunohistochemistry

To validate FAP expression in lepidic LC, 24 tissue sections of histologically proven lepidic LC from the local tissue bank were stained for hematoxylin and eosin and FAP. These 24 cases were not examined by ^{68}Ga-FAPI-46 PET/CT. For FAP immunohistochemistry, semithin tissue sections of 4-μm thickness were prepared from corresponding paraffin blocks being generated from resection tissue after its fixation in 4% buffered formalin for 24 h at room temperature. Tissue sections were treated with cell conditioning 2 (Roche) buffer (pH 8.0) for antigen retrieval. Immunohistochemical staining was performed using the antibody anti–FAP-α (1:100; Abcam [catalog no. ab207178]). Automated immunostaining was done using the automated Ventana BenchMark Ultra with the OptiView DAB Kit (Roche), Dako Autostainer-Link 48, and the EnVision Flex Kit (Agilent). Stained tissue sections were mounted with Consul-Mount (Thermo Fisher Scientific) and scanned by Aperio AT2 (Leica; magnification 1:400) for analysis. All samples were provided by the Tissue Bank of the National Center for Tumor Diseases, in accordance with the regulations of the tissue bank and the approval of the ethics committee of Heidelberg University.

Statistical Analysis

We performed descriptive analyses for patients and their characteristics. For determination of static and dynamic PET parameters, median and range were used. For determination of significance, a 2-sided *t* test was used, and *P* values of less than 0.05 were defined as statistically significant. Receiver-operating-characteristic curves and corresponding estimates of area under the curve, including 95% CIs, were computed for static and dynamic PET parameters. GraphPad Prism, version 10, was used for all statistical analyses.

RESULTS

Target Confirmation of FAP in Lepidic LC

To evaluate FAP expression in lepidic LC, we performed FAP immunohistochemistry of 24 biopsy samples of lepidic LC. In all samples, we found variably intensive FAP-positive areas. FAP positivity was particularly pronounced in stroma-rich tumor areas (Fig. 1A) but was also clearly detectable in the tumor rim within single alveolar septa, which showed a desmoplastic reaction to the tumor (Fig. 1B). In contrast, adjacent lung tissue was fully FAP-negative (Fig. 1B).

Patient Characteristics and Histologic Results

The cohort consisted of 19 patients (5 female, 14 male) aged from 41 to 77 y (average, 61.8 ± 10.5 y). The average size of the CT-graphically suggestive lesions was 22.47 ± 14.9 mm. After ^{18}F-FDG and ^{68}Ga-FAPI-46 PET imaging, tissue from all patients was obtained by either biopsy or surgery and subjected to definitive pathologic diagnosis. Seven patients had benign diagnoses

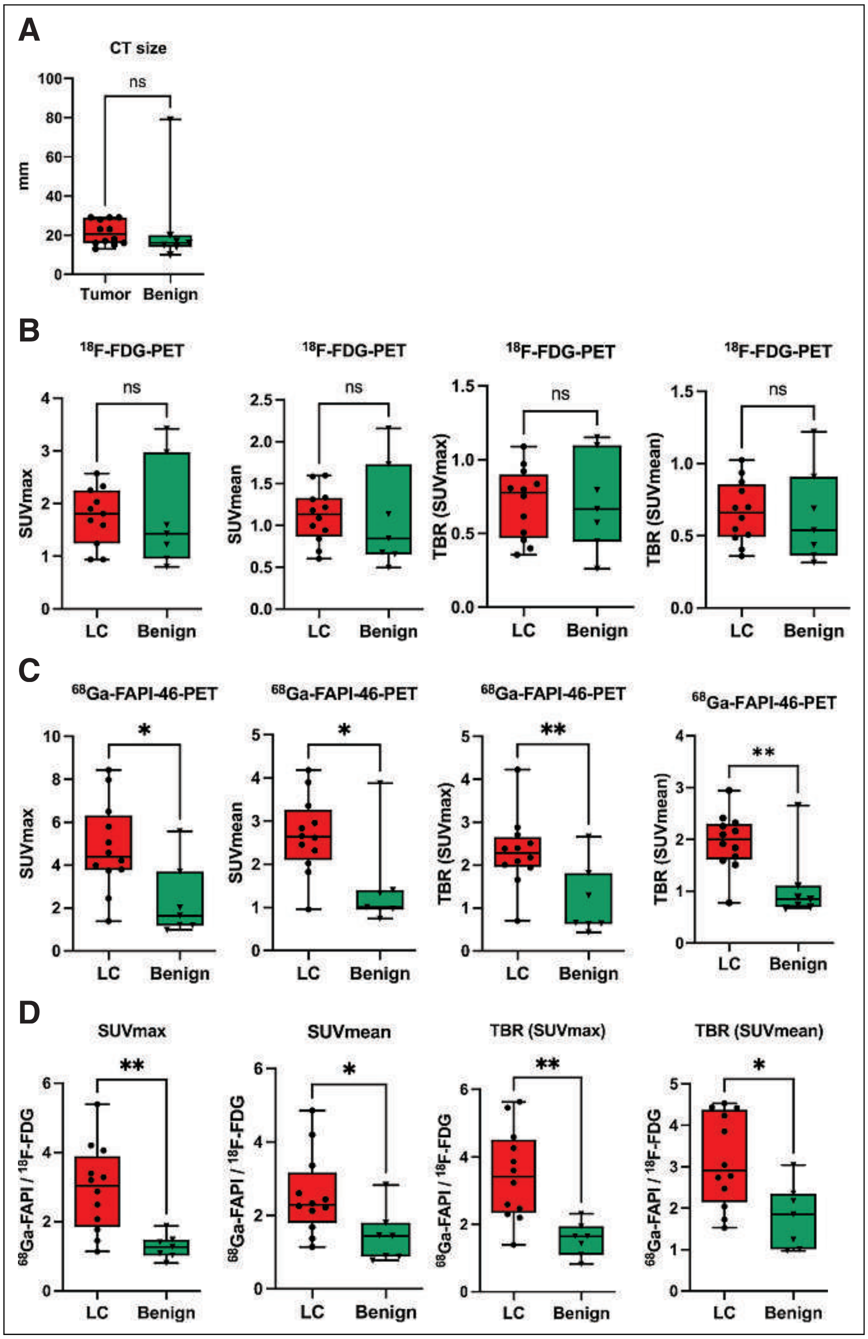

FIGURE 2. Quantitative analysis of ^{18}F-FDG and ^{68}Ga-FAPI-46 uptake in LC and benign pulmonary lesions of 19 patients. (A–C) Box plots of SUV_{max}, SUV_{mean}, and their corresponding TBRs against mediastinal blood pool for LC and benign pulmonary lesions calculated for ^{18}F-FDG (A) and ^{68}Ga-FAPI-46 (B) and fold changes of all parameters calculated for ratio of ^{68}Ga-FAPI-46 to ^{18}F-FDG (C). Boxes represent interquartile range, whiskers represent interquartile range of 1.5, and horizontal line within box indicates median. Data outliers are shown separately within graph. *$P < 0.05$. **$P < 0.01$. ns = not significant.

(2 hamartomas, 1 tuberculosis, 1 sarcoidosis, 1 granuloma, 1 calcified lymph node, and 1 lung tissue without evidence of pathology), and 12 patients were diagnosed with LC (11 adenocarcinomas [4 of them with a predominantly lepidic growth pattern] and 1 typical carcinoid). Detailed patientwise information on the clinical status and applied imaging methods is given in Table 1.

CT Size and ^{18}F-FDG and ^{68}Ga-FAPI-46 Uptake of LC and Benign Lesions

LC and benign lesions showed no significant differences in their average CT size or ^{18}F-FDG uptake in terms of SUV_{max}, SUV_{mean}, or corresponding TBR (Figs. 2A and 2B). In contrast, the average ^{68}Ga-FAPI-46 uptake of LC lesions was significantly higher than that of benign lesions (Fig. 2C). Similarly, ratios between ^{68}Ga-FAPI-46 uptake and ^{18}F-FDG uptake were also significantly higher in LC than in benign lesions (Fig. 2D). With respect to benign subentities, moderately higher ^{18}F-FDG and ^{68}Ga-FAPI-46 uptake was seen in sarcoidosis, tuberculosis, and the calcified lymph node than in the other benign lesions (Supplemental Fig. 1; supplemental materials are available at http://jnm.snmjournals.org). Supplemental Table 1 provides a lesionwise overview of all static PET parameters (SUV_{max}, SUV_{mean}, and corresponding TBR for ^{18}F-FDG and ^{68}Ga-FAPI-46 PET) for all LC and benign lesions analyzed. Figures 3 and 4 show ^{18}F-FDG PET and ^{68}Ga-FAPI-46 images of an example patient with a lepidic LC that had ^{18}F-FDG uptake below the blood pool level and strong ^{68}Ga-FAPI-46 positivity (Fig. 3) and an example patient with a hamartoma that showed only faint uptake of both tracers (Fig. 4).

Dynamic ^{68}Ga-FAPI-46 PET Imaging Characteristics of LC and Benign Lesions

Dynamic ^{68}Ga-FAPI-46 PET imaging was performed on 11 patients with LC and 5 patients with benign lesions. LC and benign

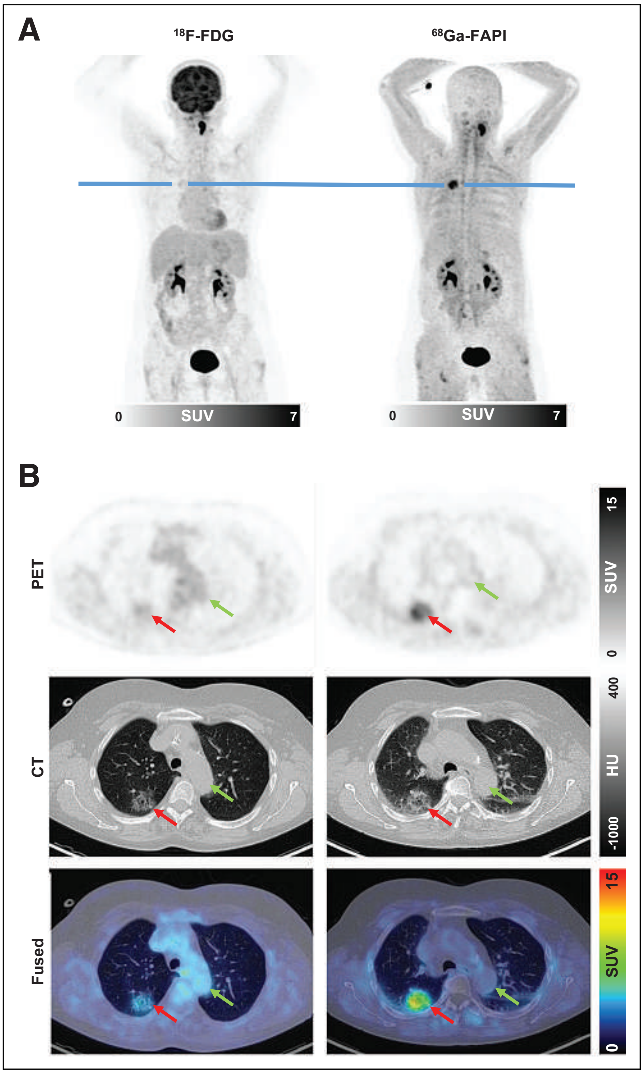

FIGURE 3. Example ^{18}F-FDG and ^{68}Ga-FAPI-46 images of 51-y-old woman with adenocarcinoma with lepidic growth pattern in right upper lobe. (A) Maximum-intensity-projection PET images. (B) Axial images of suggestive lesion (red arrows) with low CT density in right lower lobe. Green arrows show blood pool in aortic arch. Lesion had ^{18}F-FDG uptake below blood pool niveau but was strongly ^{68}Ga-FAPI-46–positive. CT-guided biopsy led to pathologic diagnosis of adenocarcinoma, and patient was treated by stereotactic body radiation therapy because of functional inoperability. HU = Hounsfield units.

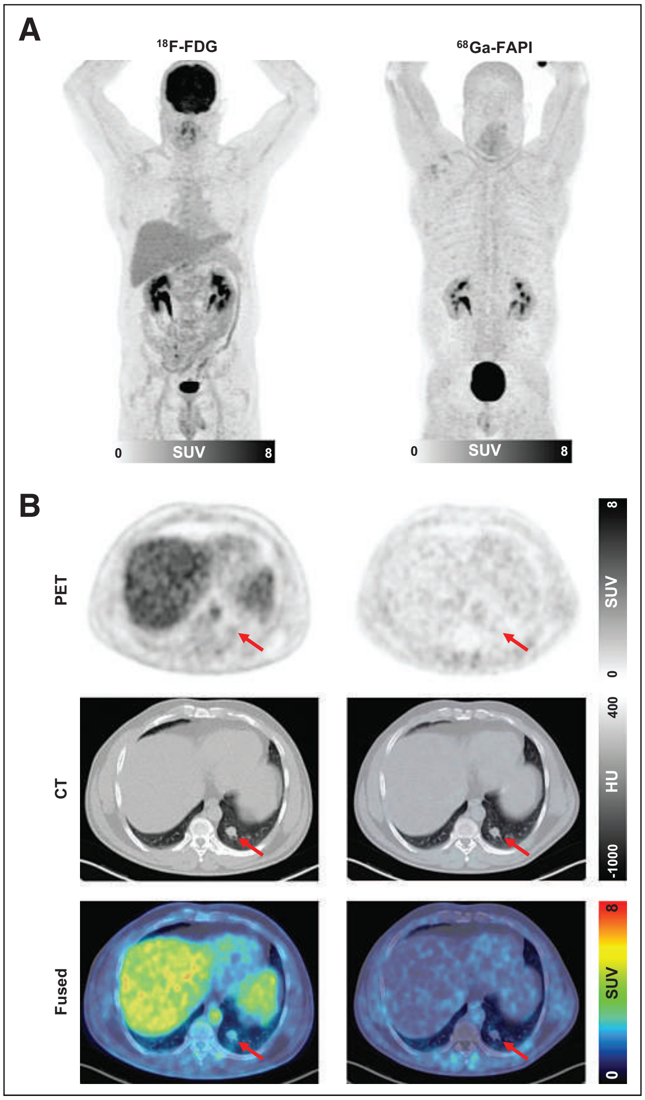

FIGURE 4. Example ^{18}F-FDG and ^{68}Ga-FAPI-46 images of 41-y-old man with hamartoma in left lower lobe. (A) Maximum-intensity-projection PET images. (B) Axial images of suggestive lesion (arrows) in left lower lobe. After wedge resection, hamartoma was diagnosed by pathology. HU = Hounsfield units.

lesions showed marked differences regarding their time–activity curve characteristics. As shown by the averaged time–activity curves in Figure 5A, LC was characterized by a delayed peak at 500–1,000 s after injection followed by a slow, continuous washout phase. In contrast, benign lesions typically showed an early peak within the first 2 min after injection followed by a rapid washout phase resulting in a reduction in activity to approximately 50% at 60 min after injection. Quantitative analysis of time to peak and slope showed a significantly prolonged time to peak and significantly smaller absolute values of slopes for LC than for benign lesions (Fig. 5B). Figure 5C shows 2 cases of LC and sarcoidosis, both of which had intermediate ^{68}Ga-FAPI-46 uptake on static imaging but time–activity curves typical of LC and benign lesions, respectively.

Sensitivity and Specificity of Static and Dynamic ^{68}Ga-FAPI-46 PET Imaging Parameters

Receiver-operating-characteristic curves calculated for all static parameters and for the dynamic parameters time to peak and slope showed high sensitivity and specificity for discriminating LC from benign lesions. The highest areas under the curve were calculated for ^{68}Ga-FAPI-46/^{18}F-FDG SUV$_{max}$ TBR (0.9167), ^{68}Ga-FAPI-46/^{18}F-FDG SUV$_{mean}$ (0.9167), SUV$_{mean}$ TBR (0.8831), and SUV$_{max}$ TBR (0.8571) (Fig. 6). The calculated sensitivity and specificity of ^{68}Ga-FAPI-46/^{18}F-FDG SUV$_{max}$ TBR were 85.71 (95% CI, 48.69–99.27) and 83.33 (95% CI, 55.20–97.04), respectively, for a cutoff of 1.62. The other static and the dynamic ^{68}Ga-FAPI-46 PET parameters showed slightly lower areas under the curve, and the ^{18}F-FDG PET parameters and CT size showed significantly lower areas under the curve (Supplemental Fig. 2).

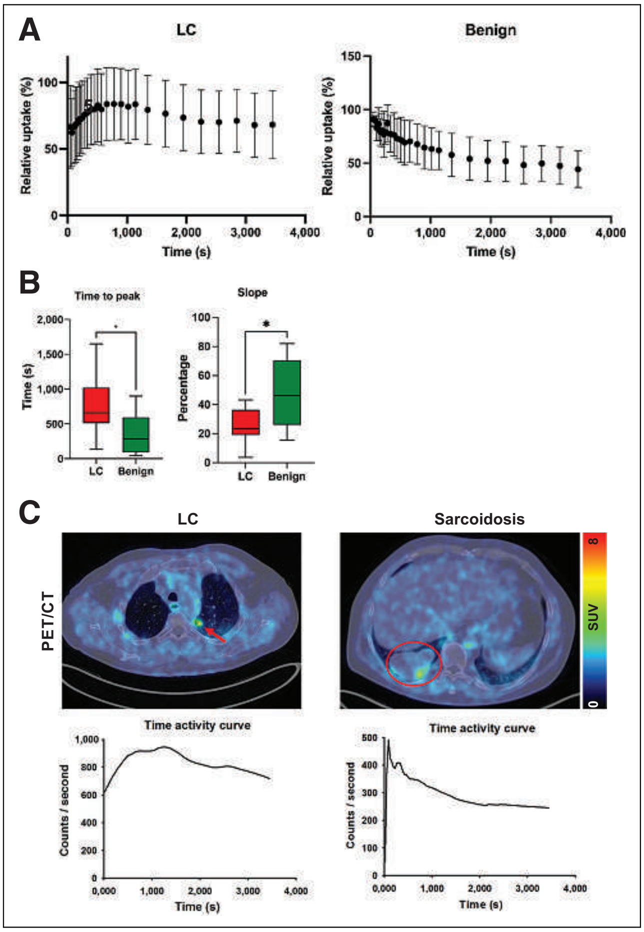

FIGURE 5. Dynamic ^{68}Ga-FAPI-46 PET imaging properties of LC and benign pulmonary lesions. (A) Averaged time–activity curves (relative to peak) of LC and benign pulmonary lesions. (B) Box plot of time to peak and slope of LC and benign pulmonary lesions. Boxes represent interquartile range, whiskers represent interquartile range of 1.5, and horizontal line within box indicates median. (C) Representative cases: 63-y-old man with adenocarcinoma (arrow) of left upper lobe and 62-y-old man with focally ^{68}Ga-FAPI-46–avid sarcoid mass (encircled) in right lower lobe. Images are from static PET, and time–activity curves are from dynamic PET. Although both lesions show intermediate ^{68}Ga-FAPI-46 uptake, time–activity curves clearly differ, with delayed peak of LC and markedly pronounced slope of sarcoidosis. *$P < 0.05$.

DISCUSSION

This retrospective analysis evaluated the ^{68}Ga-FAPI-46 uptake of primary, ^{18}F-FDG–negative LC and benign pulmonary lesions, as well as their kinetic behavior in dynamic ^{68}Ga-FAPI-46 PET imaging. To characterize lepidic LC as a particularly promising ^{18}F-FDG–negative target for ^{68}Ga-FAPI-46 PET, we performed additional FAP immunohistochemistry of 24 tissue sections of lepidic LC and found strong FAP positivity in all specimens. This advance target characterization was of crucial interest for our analysis, as the presence of cancer-associated fibroblasts in lepidic LC has already been described histologically but the FAP expression of this entity had not, to our knowledge, been evaluated before (*23*). The strong FAP expression of lepidic LC is noteworthy because FAP-positive cancer-associated fibroblasts are crucially involved in tumor desmoplasia (*24*,*25*)—a process that is canonically considered a feature of more invasive LC subtypes, but not lepidic LC, as recently proposed by the International Association for the Study of Lung Cancer pathology committee (*26*). However, the results of our immunohistochemical and PET studies seem to indicate that a stromal reaction resulting in FAP positivity of the tumors is present even in early-stage, relatively noninvasive cancers such as lepidic LC.

In our analysis, all cases of LC showed markedly elevated ^{68}Ga-FAPI-46 uptake, increased TBRs, and increased ^{68}Ga-FAPI-46/^{18}F-FDG ratios for all parameters compared with benign pulmonary lesions. One prospective study and large retrospective analyses have demonstrated that ^{68}Ga-FAPI-46 PET in addition to gold standard imaging methods holds high potential for the staging and clinical management of LC (*13*–*15*,*27*). However, these studies were focused on advanced-stage cancers and did not address the value of ^{68}Ga-FAPI-46 PET for the assessment of unclear single pulmonary lesions. In their recent prospective study on 34 patients with advanced, metastatic LC, Wang et al. showed that ^{68}Ga-FAPI PET in addition to ^{18}F-FDG PET/CT detects additional suspected metastases in lymph nodes, brain, bone, and pleura. However, the metabolic tumor volume and SUV$_{max}$ in primary and recurrent primaries were mostly identical for both tracers (*13*). Similarly, Giesel et al. found no significant difference in ^{68}Ga-FAPI and ^{18}F-FDG uptake by primary tumors in 71 patients with various cancers, including 9 patients with LC (*14*). The missing difference in ^{18}F-FDG and ^{68}Ga-FAPI PET signal behavior for LC primaries in these studies might be explained by the inclusion of patients with primary and recurrent stage IV disease only, which is biologically more aggressive and more ^{18}F-FDG–avid than the nonmetastatic ^{18}F-FDG–negative primaries in our analysis. Chen et al. analyzed ^{68}Ga-FAPI– and ^{18}F-FDG–based staging of 54 cancer patients, including 8 with LC, and reported higher SUVs for LC primaries for ^{68}Ga-FAPI than for ^{18}F-FDG. Furthermore, they

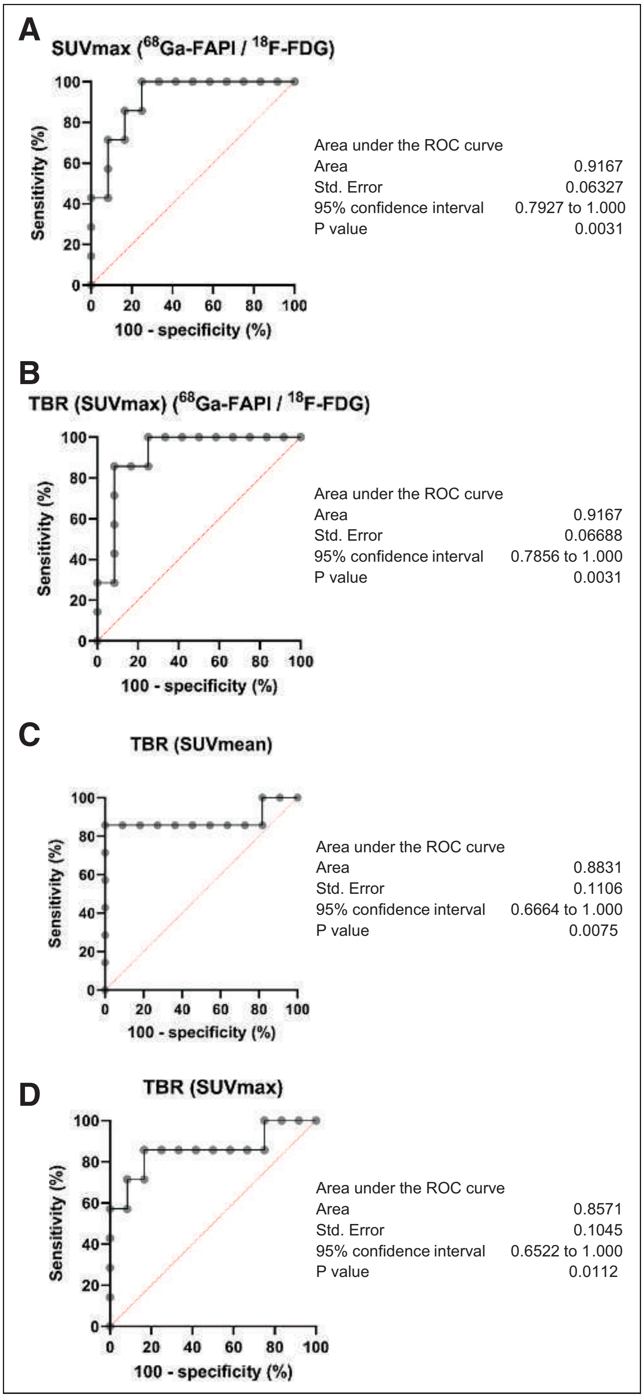

FIGURE 6. Receiver-operating-characteristic (ROC) curves of 4 quantitative PET parameters with highest discriminatory power: ^{68}Ga-FAPI-46/^{18}F-FDG SUV$_{max}$ (A), ^{68}Ga-FAPI-46/^{18}F-FDG TBR SUV$_{max}$ (B), SUV$_{mean}$ TBR (C), and SUV$_{max}$ TBR (D).

included 2 LC cases in which the primary tumor was detectable with ^{68}Ga-FAPI PET but not ^{18}F-FDG PET (*15*). However, because only 2 stage I LC cases were included, there is reduced comparability between their results and ours.

Dynamic imaging analysis revealed differential time–activity curves for LC and benign pulmonary lesions: initially increasing time–activity curves with a decent slope were typical of LC, and steadily decreasing time–activity curve indicated benign pulmonary lesions, as reflected by a significantly increased time to peak and absolute value of the slope for LC. These results are in line with our previously published data on dynamic ^{68}Ga-FAPI-46 PET in LC and fibrosing interstitial lung diseases, intraductal papillary mucinous neoplasms of the pancreas, and pancreatic ductal adenocarcinomas. In that work, we observed similar time–activity curve patterns related to whether tumors were benign or malignant (*20*,*28*). On the basis of our summed experiences, we would generally recommend dynamic ^{68}Ga-FAPI PET acquisition in primary patients with unclear and potentially malignant lesions, such as screening-detected pulmonary lesions.

Relative (^{68}Ga-FAPI-46/^{18}F-FDG) SUV$_{max}$ and TBR showed the highest sensitivity and specificity for the discrimination of LC from benign pulmonary lesions, and the other static and dynamic PET parameters had only slightly lower sensitivity and specificity. CT size, which is in general the most important imaging feature for the risk stratification of pulmonary lesions (*29*,*30*), showed significantly lower sensitivity and specificity for the discrimination of LC from benign lesions, as can be explained by the relatively low number of patients included. The sensitivity and specificity of the ^{68}Ga-FAPI-46 PET–derived parameters calculated for our dataset were similar to those reported for ^{18}F-FDG (*31*,*32*). However, as our dataset included only highly selected ^{18}F-FDG–negative cases, a comparison between the discriminatory power of ^{68}Ga-FAPI-46 PET and ^{18}F-FDG PET for single pulmonary lesions cannot be made.

Our results suggest that supplemental ^{68}Ga-FAPI-46 PET may improve the noninvasive assessment of primary pulmonary lesions compared with ^{18}F-FDG PET and CT alone. Noninvasive assessment of pulmonary lesions is of great clinical relevance because there are several contraindications, such as coagulopathies, reduced cardiopulmonary function, or reduced lung function, that can disfavor surgery or biopsy interventions, especially in elderly patients (*33*). In particular, for lepidic LC, ^{68}Ga-FAPI-46 PET holds great potential to facilitate and accelerate clinical decision making toward biopsy or operative resection, as ^{18}F-FDG PET frequently leads to inconclusive results, and CT-morphologic progression of these slowly growing tumors can be detected only over a relatively long time (*34*). On the other hand, supplemental ^{68}Ga-FAPI-46 PET could be helpful to avoid overtreatment in terms of unnecessary resections, as double-negative (^{18}F-FDG and ^{68}Ga-FAPI-46) lesions appear to have a high probability of being benign. Dynamic imaging can support the assessment of pulmonary lesions in cases without clearly suggestive high or low ^{68}Ga-FAPI-46 uptake. However, the results of our recent analysis should be considered preliminary and hypothesis-generating, and 2 major limitations must be mentioned. First, the number of patients analyzed was relatively small—with the subgroups thus being even smaller, especially with regard to benign subentities. Second, because the patients were highly selected according to ^{18}F-FDG negativity of suggestive pulmonary lesions, our dataset does not allow comparison of the diagnostic accuracy of ^{18}F-FDG and ^{68}Ga-FAPI-46 PET for primary pulmonary lesions in general. Larger, confirmative studies are necessary to gain more evidence on the clinical value of ^{68}Ga-FAPI-46 PET for assessment of primary pulmonary lesions.

CONCLUSION

The intense ^{68}Ga-FAPI-46 uptake of primary, ^{18}F-FDG–negative LC compared with benign pulmonary lesions, as well as their differential kinetic behavior on dynamic ^{68}Ga-FAPI-46 PET imaging, suggests that supplemental ^{68}Ga-FAPI-46 PET may optimize patient stratification in this clinical scenario. The promising results of this analysis should be confirmed by larger studies.

DISCLOSURE

This work was funded by the Federal Ministry of Education and Research (grant 13N 13341). Uwe Haberkorn has filed a patent application for quinoline-based FAP-targeting agents for imaging and therapy in nuclear medicine and has shares of a consultancy group for iTheranostics. No other potential conflict of interest relevant to this article was reported.

KEY POINTS

QUESTION: Can supplemental ^{68}Ga-FAPI-46 PET help to assess ^{18}F-FDG–negative single pulmonary lesions?

PERTINENT FINDINGS: LC showed markedly elevated ^{68}Ga-FAPI-46 uptake, increased TBRs, and increased ^{68}Ga-FAPI-46/^{18}F-FDG ratios for all parameters compared with benign pulmonary lesions. Dynamic imaging analysis revealed differential time–activity curves for LC and benign pulmonary lesions. Relative (^{68}Ga-FAPI-46/^{18}F-FDG) SUV_{max} and TBR showed the highest sensitivity and specificity for discrimination of LC from benign pulmonary lesions.

IMPLICATIONS FOR PATIENT CARE: Supplemental ^{68}Ga-FAPI-46 PET appears extremely promising in the clinical scenario of ^{18}F-FDG–negative single pulmonary lesions, especially when biopsy or resection is hampered by reduced health status of patients and noninvasive methods are crucial for assessment of malignancy.

REFERENCES

1. Bade BC, Dela Cruz CS. Lung cancer 2020: epidemiology, etiology, and prevention. *Clin Chest Med.* 2020;41:1–24.
2. Ruilong Z, Daohai X, Li G, Xiaohong W, Chunjie W, Lei T. Diagnostic value of ^{18}F-FDG-PET/CT for the evaluation of solitary pulmonary nodules: a systematic review and meta-analysis. *Nucl Med Commun.* 2017;38:67–75.
3. Lococo F, Guerrera F, Rena O, et al. Accuracy of ^{18}F-FDG in detecting stage I lung adenocarcinomas according to IASLC/ATS/ERS classification. *Heart Lung Circ.* 2022;31:726–732.
4. Nakamura H, Saji H, Shinmyo T, et al. Close association of IASLC/ATS/ERS lung adenocarcinoma subtypes with glucose-uptake in positron emission tomography. *Lung Cancer.* 2015;87:28–33.
5. Kratochwil C, Flechsig P, Lindner T, et al. ^{68}Ga-FAPI PET/CT: tracer uptake in 28 different kinds of cancer. *J Nucl Med.* 2019;60:801–805.
6. Mori Y, Dendl K, Cardinale J, Kratochwil C, Giesel FL, Haberkorn U. FAPI PET: fibroblast activation protein inhibitor use in oncologic and nononcologic disease. *Radiology.* 2023;306:e220749.
7. Lindner T, Loktev A, Altmann A, et al. Development of quinoline-based theranostic ligands for the targeting of fibroblast activation protein. *J Nucl Med.* 2018;59:1415–1422.
8. Loktev A, Lindner T, Burger EM, et al. Development of fibroblast activation protein-targeted radiotracers with improved tumor retention. *J Nucl Med.* 2019;60:1421–1429.
9. Loktev A, Lindner T, Mier W, et al. A tumor-imaging method targeting cancer-associated fibroblasts. *J Nucl Med.* 2018;59:1423–1429.
10. Röhrich M, Syed M, Liew DP, et al. ^{68}Ga-FAPI-PET/CT improves diagnostic staging and radiotherapy planning of adenoid cystic carcinomas: imaging analysis and histological validation. *Radiother Oncol.* 2021;160:192–201.
11. Röhrich M, Naumann P, Giesel FL, et al. Impact of ^{68}Ga-FAPI PET/CT imaging on the therapeutic management of primary and recurrent pancreatic ductal adenocarcinomas. *J Nucl Med.* 2021;62:779–786.
12. Giesel FL, Adeberg S, Syed M, et al. FAPI-74 PET/CT using either ^{18}F-AlF or Cold-Kit ^{68}Ga labeling: biodistribution, radiation dosimetry, and tumor delineation in lung cancer patients. *J Nucl Med.* 2021;62:201–207.
13. Wang L, Tang G, Hu K, et al. Comparison of ^{68}Ga-FAPI and ^{18}F-FDG PET/CT in the evaluation of advanced lung cancer. *Radiology.* 2022;303:191–199.
14. Giesel FL, Kratochwil C, Schlittenhardt J, et al. Head-to-head intra-individual comparison of biodistribution and tumor uptake of ^{68}Ga-FAPI and ^{18}F-FDG PET/CT in cancer patients. *Eur J Nucl Med Mol Imaging.* 2021;48:4377–4385.
15. Chen H, Pang Y, Wu J, et al. Comparison of [^{68}Ga]Ga-DOTA-FAPI-04 and [^{18}F] FDG PET/CT for the diagnosis of primary and metastatic lesions in patients with various types of cancer. *Eur J Nucl Med Mol Imaging.* 2020;47:1820–1832.
16. Koerber SA, Rohrich M, Walkenbach L, et al. Impact of ^{68}Ga-FAPI PET/CT on staging and oncologic management in a cohort of 226 patients with various cancers. *J Nucl Med.* 2023;64:1712–1720.
17. Zhou X, Wang S, Xu X, et al. Higher accuracy of [^{68}Ga]Ga-DOTA-FAPI-04 PET/CT comparing with 2-[^{18}F]FDG PET/CT in clinical staging of NSCLC. *Eur J Nucl Med Mol Imaging.* 2022;49:2983–2993.
18. Wei Y, Ma L, Li P, et al. FAPI compared with FDG PET/CT for diagnosis of primary and metastatic lung cancer. *Radiology.* 2023;308:e222785.
19. Bueno J, Landeras L, Chung JH. Updated Fleischner Society guidelines for managing incidental pulmonary nodules: common questions and challenging scenarios. *Radiographics.* 2018;38:1337–1350.
20. Röhrich M, Leitz D, Glatting FM, et al. Fibroblast activation protein-specific PET/CT imaging in fibrotic interstitial lung diseases and lung cancer: a translational exploratory study. *J Nucl Med.* 2022;63:127–133.
21. Cheran SK, Nielsen ND, Patz EF Jr. False-negative findings for primary lung tumors on FDG positron emission tomography: staging and prognostic implications. *AJR.* 2004;182:1129–1132.
22. Maurer GD, Brucker DP, Stoffels G, et al. ^{18}F-FET PET imaging in differentiating glioma progression from treatment-related changes: a single-center experience. *J Nucl Med.* 2020;61:505–511.
23. Yotsukura M, Asamura H, Suzuki S, et al. Prognostic impact of cancer-associated active fibroblasts and invasive architectural patterns on early-stage lung adenocarcinoma. *Lung Cancer.* 2020;145:158–166.
24. Zeltz C, Primac I, Erusappan P, Alam J, Noel A, Gullberg D. Cancer-associated fibroblasts in desmoplastic tumors: emerging role of integrins. *Semin Cancer Biol.* 2020;62:166–181.
25. Lo A, Wang LS, Scholler J, et al. Tumor-promoting desmoplasia is disrupted by depleting FAP-expressing stromal cells. *Cancer Res.* 2015;75:2800–2810.
26. Thunnissen E, Beasley MB, Borczuk A, et al. Defining morphologic features of invasion in pulmonary nonmucinous adenocarcinoma with lepidic growth: a proposal by the International Association for the Study of Lung Cancer pathology committee. *J Thorac Oncol.* 2023;18:447–462.
27. Koerber SA, Rohrich M, Walkenbach L, et al. Impact of ^{68}Ga-FAPI PET/CT on staging and oncologic management in a cohort of 226 patients with various cancers. *J Nucl Med.* 2023;64:1712–1720.
28. Lang M, Spektor AM, Hielscher T, et al. Static and dynamic ^{68}Ga-FAPI PET/CT for the detection of malignant transformation of intraductal papillary mucinous neoplasia of the pancreas. *J Nucl Med.* 2023;64:244–251.
29. Chen B, Li Q, Hao Q, et al. Malignancy risk stratification for solitary pulmonary nodule: a clinical practice guideline. *J Evid Based Med.* 2022;15:142–151.
30. Mazzone PJ, Lam L. Evaluating the patient with a pulmonary nodule: a review. *JAMA.* 2022;327:264–273.
31. Groheux D, Quere G, Blanc E, et al. FDG PET-CT for solitary pulmonary nodule and lung cancer: literature review. *Diagn Interv Imaging.* 2016;97:1003–1017.
32. Cronin P, Dwamena BA, Kelly AM, Carlos RC. Solitary pulmonary nodules: meta-analytic comparison of cross-sectional imaging modalities for diagnosis of malignancy. *Radiology.* 2008;246:772–782.
33. Young M, Sankari A. Percutaneous lung lesion biopsy. StatPearls website. https://www.statpearls.com/point-of-care/30515. Updated February 14, 2024. Accessed March 20, 2024.
34. Hong JH, Park S, Kim H, et al. Volume and mass doubling time of lung adenocarcinoma according to WHO histologic classification. *Korean J Radiol.* 2021;22:464–475.

^{68}Ga-Fibroblast Activation Protein Inhibitor PET/CT Improves Detection of Intermediate and Low-Grade Sarcomas and Identifies Candidates for Radiopharmaceutical Therapy

Helena Lanzafame[1,2], Ilektra A. Mavroeidi[2,3], Kim M. Pabst[1,2], Mélanie Desaulniers[1,2,4], Marc Ingenwerth[3,5], Nader Hirmas[1,2], Lukas Kessler[1,2,6], Michael Nader[1,2], Timo Bartel[1,2], Stephan Leyser[1,2], Francesco Barbato[1,2], Martin Schuler[2,7], Sebastian Bauer[2,3,7], Jens T. Siveke[2,7,8], Ken Herrmann[1,2,6], Rainer Hamacher*[2,3], and Wolfgang P. Fendler*[1,2]

[1]Department of Nuclear Medicine, West German Cancer Center, University Hospital Essen, Essen, Germany; [2]Cancer Consortium partner site Essen/Düsseldorf, DKFZ and University Hospital Essen, Essen, Germany; [3]Department of Medical Oncology, West German Cancer Center, University Hospital Essen, Essen, Germany; [4]Department of Nuclear Medicine and Radiobiology, Université de Sherbrooke, Sherbrooke, Québec, Canada; [5]Institute of Pathology, University Hospital Essen, Essen, Germany; [6]Institute of Diagnostic and Interventional Radiology and Neuroradiology, University Hospital Essen, Essen, Germany; [7]National Center for Tumor Diseases West, Campus Essen, Essen, Germany; and [8]Bridge Institute of Experimental Tumor Therapy and Division of Solid Tumor Translational Oncology, West German Cancer Center, University Hospital Essen, Essen, Germany

Fibroblast activation protein-α (FAP) is often highly expressed by sarcoma cells and by sarcoma-associated fibroblasts in the tumor microenvironment. This makes it a promising target for imaging and therapy. The level of FAP expression and the diagnostic value of ^{68}Ga-FAP inhibitor (FAPI) PET for sarcoma subtypes are unknown. We assessed the diagnostic performance and accuracy of ^{68}Ga-FAPI PET in various bone and soft-tissue sarcomas. Potential eligibility for FAP-targeted radiopharmaceutical therapy (FAP-RPT) was evaluated. **Methods:** This prospective observational trial enrolled 200 patients with bone and soft-tissue sarcoma who underwent ^{68}Ga-FAPI PET/CT and ^{18}F-FDG PET/CT (186/200, or 93%) for staging or restaging. The number of lesions detected and the uptake (SUV_{max}) of the primary tumor, lymph nodes, and visceral and bone metastases were analyzed. The Wilcoxon test was used for semiquantitative assessment. The association of ^{68}Ga-FAPI uptake intensity, histopathologic grade, and FAP expression in sarcoma biopsy samples was analyzed using Spearman *r* correlation. The impact of ^{68}Ga-FAPI PET on clinical management was investigated using questionnaires before and after PET/CT. Eligibility for FAP-RPT was defined by an SUV_{max} greater than 10 for all tumor regions. **Results:** ^{68}Ga-FAPI uptake was heterogeneous among sarcoma subtypes. The 3 sarcoma entities with the highest uptake (mean SUV_{max} ± SD) were solitary fibrous tumor (24.7 ± 11.9), undifferentiated pleomorphic sarcoma (18.8 ± 13.1), and leiomyosarcoma (15.2 ± 10.2). Uptake of ^{68}Ga-FAPI versus ^{18}F-FDG was significantly higher in low-grade sarcomas (10.4 ± 8.5 vs. 7.0 ± 4.5, $P = 0.01$) and in potentially malignant intermediate or unpredictable sarcomas without a World Health Organization grade (not applicable [NA]; 22.3 ± 12.5 vs. 8.5 ± 10.0, $P = 0.0004$), including solitary fibrous tumor. The accuracy, as well as the detection rates, of ^{68}Ga-FAPI was higher than that of ^{18}F-FDG in low-grade sarcomas (accuracy, 92.2 vs. 80.0) and NA sarcomas (accuracy, 96.9 vs. 81.9). ^{68}Ga-FAPI uptake and the histopathologic FAP expression score ($n = 89$) were moderately correlated (Spearman $r = 0.43$, $P < 0.0002$). Of 138 patients, 62 (45%) with metastatic sarcoma were eligible for FAP-RPT. **Conclusion:** In patients with low-grade and NA sarcomas, ^{68}Ga-FAPI PET demonstrates uptake, detection rates, and accuracy superior to those of ^{18}F-FDG PET. ^{68}Ga-FAPI PET criteria identified eligibility for FAP-RPT in about half of sarcoma patients.

Key Words: ^{68}Ga-FAPI PET; sarcoma; fibroblast activation protein; theranostic; cancer imaging

J Nucl Med 2024; 65:880–887
DOI: 10.2967/jnumed.123.267248

Sarcomas are rare and heterogeneous tumors that develop from the connective tissue of bone and soft tissue. There are more than 150 subtypes, including low-grade or intermediate or unpredictable tumors without a World Health Organization grade (not applicable [NA]). The outcome for patients with metastatic disease remains poor, with a median overall survival period of approximately 12–18 mo (*1–3*). Fibroblast activation protein-α (FAP) is a type II membrane glycoprotein belonging to the dipeptyl-peptidase family and is present in cancer-associated stromal fibroblasts (*4*,*5*). Cancer-associated stromal fibroblasts constitute an essential component of the tumor microenvironment (*6–8*). With the recent development of radiolabeled FAP inhibitors (FAPIs), these stromal markers have opened up opportunities for molecular imaging and FAP-targeted radiopharmaceutical therapy (FAP-RPT) (*9*). FAPI compounds have been used for the detection of malignant lesions with high stromal content on high-contrast PET/CT images. In recent years, numerous clinical studies have demonstrated high FAPI uptake in various solid tumors, including sarcomas (*10–12*). In addition, for several sarcoma subentities, such as myofibroblastic sarcoma, osteosarcoma, and undifferentiated pleomorphic sarcoma (UPS), histogenesis-specific FAP expression has been reported (*13*). In a previous subgroup analysis, our group proved the high intensity of intratumoral ^{68}Ga-FAPI uptake in sarcoma patients (*14*). Furthermore, we demonstrated a higher detection rate and reproducibility, as well as a more advanced stage of disease, with ^{68}Ga-FAPI PET

Received Dec. 15, 2023; revision accepted Mar. 15, 2024.

For correspondence or reprints, contact Helena Lanzafame (helena.lanzafame@uk-essen.de).

*Contributed equally to this work.

than with ^{18}F-FDG PET (*14*). Accurate staging is of great importance in planning appropriate therapy. In the advanced stage, FAP-RPT has demonstrated signs of efficacy (*15–17*) and is the subject of a prospective phase II safety and tolerability trial in patients with metastatic solid tumors (*18*). FAP-RPT has the potential to improve outcomes for many patients for whom approved therapeutic options are scarce or unfulfilling, including patients with advanced sarcomas. However, sarcoma is a basket term for a broad spectrum of distinct molecular subtypes that show heterogeneous uptake intensity, hence the importance of identifying subentities potentially more suitable for FAP-RPT. To address this issue, we assessed the diagnostic performance and accuracy of ^{68}Ga-FAPI PET versus ^{18}F-FDG PET in a large cohort of sarcoma patients. In addition, we investigated the association between ^{68}Ga-FAPI PET uptake intensity and histopathologic expression of FAP and explored the eligibility of certain sarcoma subentities for FAP-RPT.

MATERIALS AND METHODS

Patient Population

The patient flowchart is illustrated in Figure 1. This is a subgroup analysis of an ongoing ^{68}Ga-FAPI PET observational trial at University Hospital Essen (NCT04571086). Between October 2019 and 2022, ^{68}Ga-FAPI PET was used for the staging or follow-up of sarcomas. In total, 200 bone sarcoma (BS) and soft-tissue sarcoma (STS) patients who underwent ^{68}Ga-FAPI PET were included (31.8% of the cohort). Before enrollment, patients gave written informed consent to undergo ^{68}Ga-FAPI PET for a clinical indication.

Image Acquisition and Evaluation

The synthesis and administration of ^{68}Ga-FAPI-04 ($n = 14$) and ^{68}Ga-FAPI-46 ($n = 186$) have been described previously (*9*,*19*). Patients did not require specific preparation before ^{68}Ga-FAPI PET. Clinical PET/CT was performed craniocaudally on 200 patients: 3 (1.5%) with Biograph mMR, 6 (3%) with Biograph mCT, and 191 (95.5%) with Biograph mCT Vision (Siemens Healthineers). The mean activity ± SD injected intravenously was 120 ± 38.3 MBq for ^{68}Ga-FAPI and 248.6 ± 89.2 MBq for ^{18}F-FDG. The mean acquisition time after injection ± SD was 23.5 ± 19.0 min for ^{68}Ga-FAPI PET and 69.5 ± 15.5 min for ^{18}F-^{18}F FDG PET. A diagnostic CT scan was obtained using a standard protocol (80–100 mA, 120 kV) before PET imaging (*20*). For each imaging modality, the number of lesions per region and per patient was recorded. Focal tracer uptake higher than the surrounding background and not associated with physiologic uptake was considered suggestive of malignancy. SUV$_{max}$ was determined for lesions with the highest tracer uptake per region, using Syngo.via software (Siemens Healthineers). All devices had been cross-calibrated to European Association of Nuclear Medicine Research Ltd. accreditation standards. SUV$_{mean}$ was measured in 3 regions normalized according to tumor-to-background ratio (TBR): mediastinal blood pool (center of ascending aorta), liver (unaffected areas of the right lobe), and surrounding normal tissue, including bone or normal soft tissue. The images were read by 2 nuclear medicine physicians or radiologists during a joint reading session. Divergent findings were discussed and resolved by consensus between the readers.

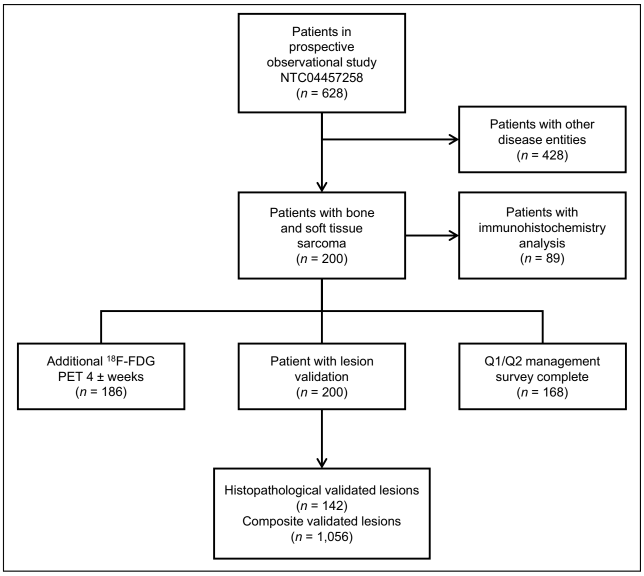

FIGURE 1. Enrollment flowchart. Q = questionnaire.

Lesion Validation

Patients underwent histopathologic analysis of biopsy samples and surgical excision. Lesions that were histopathologically validated within 3 mo of a ^{68}Ga-FAPI PET scan were included in the accuracy analysis. When histopathology was unavailable, validation was performed by correlative or follow-up imaging, that is, CT, MRI, or PET.

Immunohistochemistry

Biopsy and surgical specimens were stained with standard hematoxylin and eosin, as well as FAP immunohistochemistry, and evaluated as previously described (*14*,*21*). FAP expression is categorized semiquantitatively in the histologic section of the tumor as the percentage of FAP-positive cells. Semiquantitative analysis of FAP expression in stroma and tumor cells is assessed using the following scoring system: 0 is the absence or a low degree of FAP-positive cells (<1%), 1+ is FAP-positive in 1%–10% of cells, 2+ is FAP-positive in 11%–50% of cells, and 3+ is FAP-positive in more than 50% of cells. Pathologists were not informed of PET findings.

Management Questionnaires

To assess changes in planned treatment management after ^{68}Ga-FAPI PET, referring physicians completed a questionnaire before PET, which was necessary to assess the patient's existing treatment plan without the contribution of ^{68}Ga-FAPI PET, and a second questionnaire after PET and after reviewing ^{68}Ga-FAPI PET images, which was used to check for implemented change in management.

Statistical Analysis

Descriptive statistics and individual patient data are reported. For continuous data, the mean ± SD SUV$_{max}$ and TBR were compared and tested for statistical differences using Wilcoxon and Mann–Whitney *U* tests. The sensitivity, specificity, and accuracy of ^{68}Ga-FAPI PET on a per-region basis for the detection of tumor location, confirmed by histopathology or a composite reference standard, were calculated, along with the corresponding 2-sided 95% CIs. A difference of more than 10% was considered relevant. CIs were determined using the Wilson score method. The association of ^{68}Ga-FAPI uptake intensity, grade, and histopathologic FAP expression was analyzed using Spearman *r* correlation. All statistical analyses were performed using SPSS software (version 20.0; SPSS Inc.) and GraphPad Prism (version 9.1.1; GraphPad Software).

RESULTS

Patient Characteristics

The clinical characteristics of the study population are summarized in Table 1 and Supplemental Table 1 (supplemental materials are available at http://jnm.snmjournals.org). Between October 2020 and 2022, 200 patients were included, 91 (45%) women and 109 (55%) men. Of the 200 patients, 65 (33%) had BS and 135

TABLE 1
Patient Characteristics (n = 200)

Characteristic	Data
Age (y)	55 (39–65)
Sex	
Female	91 (45)
Male	109 (55)
Indication	
Staging	49 (25)
Restaging	151 (75)
BS	65 (33)
Osteosarcoma	17 (9)
Chondrosarcoma	17 (9)
Other BS	15 (7)
Ewing sarcoma	8 (4)
Spindle cell sarcoma	5 (3)
UPS	3 (1)
STS	135 (67)
Other STS	41 (21)
SFT	22 (12)
UPS	15 (7)
Dedifferentiated liposarcoma	15 (7)
Myxoid liposarcoma	14 (6)
Leiomyosarcoma	14 (6)
Synovial sarcoma	7 (4)
Spindle cell sarcoma	7 (4)
Grading	
NA	27 (14)
Low	32 (16)
High	141 (70)

Continuous data are median and interquartile range; qualitative data are number and percentage.

(67%) had STS; 141 (70%) cases were high grade, 32 (16%) cases were low grade, and 27 (14%) cases had no World Health Organization grade (NA). Patients underwent clinical ^{68}Ga-FAPI PET imaging for either staging (49/200 [25%]) or follow-up (151/200 [75%]). Fourteen (7%) patients were imaged with ^{68}Ga-FAPI-04, and 186 (93%) were imaged with ^{68}Ga-FAPI-46. All patients imaged with ^{68}Ga-FAPI-46 underwent ^{18}F-FDG PET imaging within 4 wk. No PET-related adverse events were reported.

FAP Expression in Sarcoma Subtypes

Tumor SUV$_{max}$ and the tumor-to-liver ratio for ^{68}Ga-FAPI versus ^{18}F-FDG in different sarcoma subentities (n = 12) are summarized in Figure 2. We observed heterogeneous tumor uptake of ^{68}Ga-FAPI in our cohort, ranging from an SUV$_{max}$ of 3.1 in myxoid liposarcoma to an SUV$_{max}$ of 47.1 in solitary fibrous tumor (SFT). In terms of mean SUV$_{max}$ ± SD, the 3 sarcoma entities with the highest FAP expression were SFT (24.7 ± 11.9), UPS (18.8 ± 13.1), and leiomyosarcoma (15.2 ± 10.0). By descriptive comparison, the mean SUV$_{max}$ was higher for ^{68}Ga-FAPI than for ^{18}F-FDG in most sarcoma subentities, with the exception of synovial sarcoma, spindle cell sarcoma, and other BS. According to the Wilcoxon test, SUV$_{max}$ and the tumor-to-liver ratio of ^{68}Ga-FAPI PET were significantly higher than those of ^{18}F-FDG PET for SFT (mean SUV$_{max}$ ± SD, 24.7 ± 11.9 vs. 6.8 ± 8.7, P = 0.0005; mean tumor-to-liver ratio ± SD, 22.0 ± 11.9 vs. 4.1 ± 8.9, P = 0.0005) and myxoid liposarcoma (mean SUV$_{max}$ ± SD, 5.6 ± 2.2 vs. 3.5 ± 2.1, P = 0.03; mean tumor-to-liver ratio ± SD, 1.7 ± 1.9 vs. 0.8 ± 1.7, P = 0.04). Additional information on SUVs and TBR is shown in Supplemental Figures 1 and 2 and in Supplemental Table 2.

Based on our previous results (*15*), intense FAP expression, defined by an SUV$_{max}$ of at least 10 in each tumor region, was deemed sufficient for FAP-RPT, as shown in Figure 2A. These PET criteria were met in 62 of 138 (45%) patients with metastatic disease: 16 of 20 with SFT, 3 of 9 with UPS, 7 of 11 with leiomyosarcoma, 5 of 10 with osteosarcoma, 3 of 8 with undifferentiated liposarcoma, 13 of 27 with other STS, 4 of 8 with spindle cell sarcoma, 5 of 13 with chondrosarcoma, 3 of 11 with other BS, 2 of 8 with Ewing sarcoma, and 1 of 4 with synovial sarcoma. FAP expression was highly intense (SUV$_{max}$ of 20 or higher in all regions, as shown in Fig. 2A) in 25 of 138 (18%) patients: 10 of 20 with SFT, 3 of 9 with UPS, 1 of 11 with leiomyosarcoma, 1 of 10 with osteosarcoma, 1 of 8 with undifferentiated liposarcoma, 5 of 27 with other STS, 2 of 8 with spindle cell sarcoma, 1 of 13 with chondrosarcoma, and 1 of 11 with other BS. A complete list of subentities included in the other BS and other STS groups is given in Supplemental Table 3.

^{68}Ga-FAPI versus ^{18}F-FDG uptake was assessed separately for high-grade, NA, and low-grade sarcomas (Fig. 3). Uptake of ^{68}Ga-FAPI versus ^{18}F-FDG was significantly higher in low-grade sarcomas (10.36 ± 8.5 vs. 7.0 ± 4.5, P = 0.01) and NA sarcomas (22.3 ± 12.5 vs. 8.5 ± 10, P = 0.0004), particularly SFT. An example patient is shown in Figure 4.

Detection Efficacy

Detection efficiency is given in Table 2 for primary tumors, lymph nodes, and distant metastases (lung, muscle, viscera [organ], liver, and bone). The detection efficacy of ^{68}Ga-FAPI PET was superior to that of ^{18}F-FDG PET for distant metastases in NA (100% vs. 67%) and low-grade (95% vs. 81%) sarcomas.

Overall, ^{68}Ga-FAPI PET versus ^{18}F-FDG PET detected 1,181 (95%) versus 1,023 (85%) lesions. ^{68}Ga-FAPI PET outperformed ^{18}F-FDG PET in detecting primary tumors (144 [100%] vs. 124 [86%]) and distant metastases (945 [97%] vs. 797 [83%]).

Accuracy

The accuracy of per-region analysis is summarized in Table 3. In total, 142 lesions were histologically validated (110 [77%] primary tumors, 7 [5%] lymph nodes, 22 [15%] visceral metastases, and 3 [2%] bone metastases). In addition, 1,056 lesions were validated by correlative or follow-up imaging (34 [3%] primary tumors, 97 [9%] lymph nodes, 659 [63%] visceral metastases, and 266 [25%] bone metastases). In patients with high-grade sarcomas, sensitivity (96% vs. 94%), specificity (86% vs. 68%), and accuracy (95% vs. 92%) were higher for ^{68}Ga-FAPI than for ^{18}F-FDG. The same was true for patients with NA sarcomas (sensitivity, 96% vs. 83%; specificity, 80% vs. 67%; and accuracy, 95% vs. 82%) and patients with low-grade sarcomas (sensitivity, 93% vs. 85%; specificity, 89% vs. 44%; and accuracy, 92% vs. 80%). Relevant improvement, defined as a difference of 10% or more, was observed with ^{68}Ga-FAPI PET in the specificity of detection of high-grade sarcomas and for all 3 accuracy measures for NA and low-grade sarcomas.

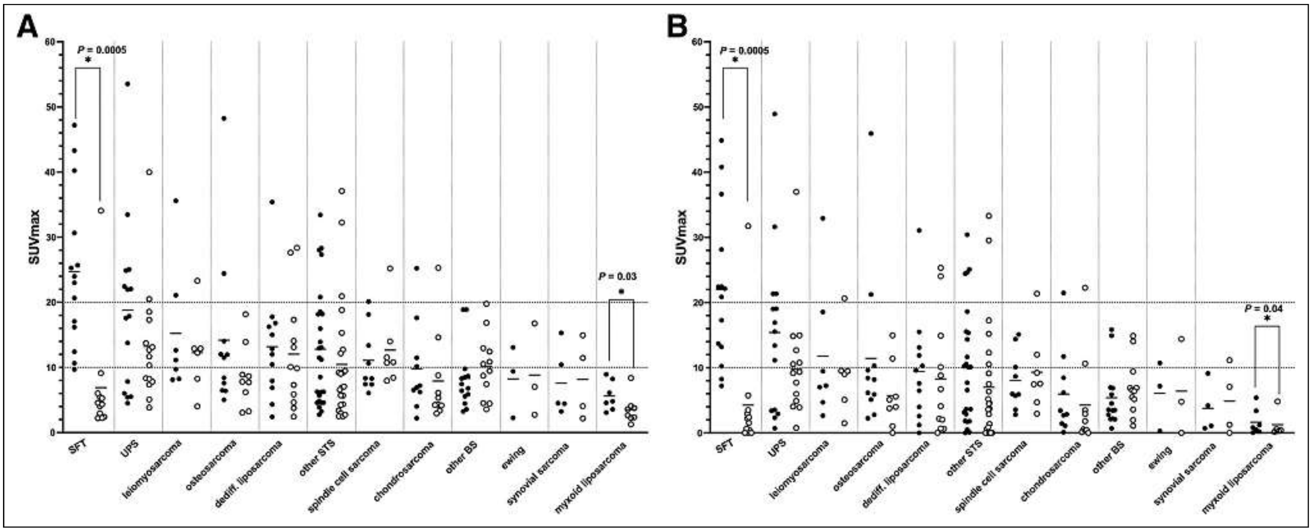

FIGURE 2. Comparison of ^{68}Ga-FAPI and ^{18}F-FDG PET SUV$_{max}$ (A) and tumor-to-liver ratio (B) for sarcoma subentities. Individual data and mean (bars) are shown. Horizontal dotted lines in A indicate patients with SUV$_{max}$ greater than 10 and 20. Black dot = ^{68}Ga-FAPI; white dot = ^{18}F-FDG.

Change in Therapeutic Management

Changes in therapeutic management are presented in Supplemental Table 4. For 168 of 200 (84%) patients, questionnaires completed and returned before and after imaging were available. The management implemented was assessed by reviewing the clinical files. Therapeutic changes based on ^{68}Ga-FAPI PET results were documented in 33 of 168 (20%) patients: 20 (61%) patients changed from active surveillance to chemotherapy, 6 (18%) patients changed from isolated limb perfusion to surgery, 3 (9%) patients changed from a biopsy to surgery, 1 (3%) patient changed from a biopsy to chemotherapy, 1 (3%) patient changed from surgery to chemotherapy, 1 (3%) patient underwent resection plan adjustment, and 1 (3%) patient changed from therapy to active surveillance. Moreover, of the 62 patients with metastatic disease and an SUV$_{max}$ greater than 10, 17 (27%) patients were deemed eligible and underwent at least 1 cycle of FAP-RPT. A patient flowchart is presented in Supplement Figure 3.

PET Versus Immunohistochemistry Target Expression

The association between ^{68}Ga-FAPI PET uptake intensity and FAP immunohistochemistry score is shown in Figure 5 and Supplemental Table 5. Of 89 samples, 30 (34%) samples demonstrated no FAP expression on immunohistochemistry (score 0), and 59 samples had scores 1–3. A moderate positive correlation (Spearman $r = 0.43$, $P = 0.0002$) was found between SUV$_{max}$ and histopathologic FAP expression. Higher uptake values (mean SUV$_{max}$ ± SD) were observed on lesions with FAP score 3 (22.7 ± 14.2) than on those with FAP score 0 (11.4 ± 7.0).

DISCUSSION

In recent years, FAP has been identified as a promising theranostic target for various cancers, including sarcomas (*14*,*15*,*22*,*23*). We analyzed ^{68}Ga-FAPI PET images of 200 patients with 13 subentities of sarcoma. Our study revealed the heterogeneous tumor uptake intensity of FAP, with a mean SUV$_{max}$ ± SD ranging from 5.6 ± 2.2 in myxoid liposarcoma to 24.7 ± 11.9 in SFT. In addition, we report

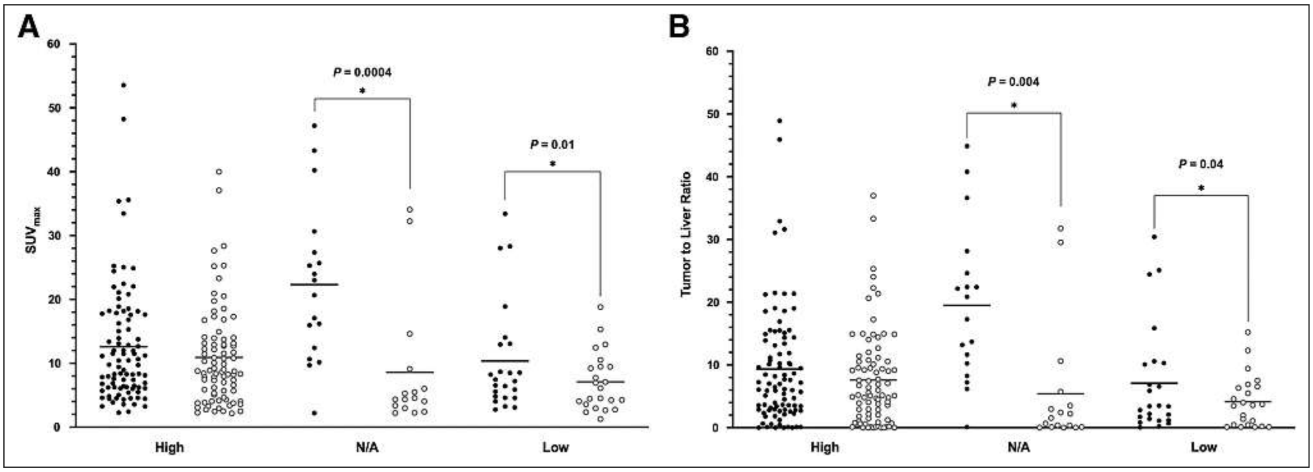

FIGURE 3. Comparison of ^{68}Ga-FAPI and ^{18}F-FDG PET SUV$_{max}$ (A) and tumor-to-liver ratio (B) separated into high-grade, NA, and low-grade groups. Individual data and mean (bars) are shown. Black dot = ^{68}Ga-FAPI; white dot = ^{18}F-FDG.

that diagnostic performance of ^{68}Ga-FAPI PET is superior to that of ^{18}F-FDG PET in patients with low-grade and NA sarcomas.

Numerous previous studies have demonstrated the usefulness of ^{18}F-FDG PET imaging for high-grade sarcomas (*24–26*). However, sarcomas are highly heterogeneous in terms of aggressiveness and tumor origin. Consequently, imaging these tumors with ^{18}F-FDG PET, as currently indicated for follow-up (*4*,*27*), is often challenging and does not appear to be a viable universal imaging method. In an analysis of 21 tumor entities, Hirmas et al. (*28*) reported that ^{68}Ga-FAPI versus ^{18}F-FDG had higher absolute uptake and TBR, as well as better tumor detection, in sarcomas and pancreatic cancers. Concordant with this observation, we demonstrated that the mean absolute uptake and TBR of ^{68}Ga-FAPI were higher than those of ^{18}F-FDG in all sarcoma subentities except synovial sarcoma, spindle cell sarcoma, and other BS. In a recent prospective study of 45 STS patients, low-grade STS had significantly higher FAP uptake, whereas high-grade STS had significantly higher ^{18}F-FDG uptake (*29*). We also found significantly higher ^{68}Ga-FAPI versus ^{18}F-FDG uptake in low-grade and NA sarcomas. Here, SFT demonstrated high FAP expression, almost twice the average level for all sarcomas. In addition, higher tumor uptake of ^{68}Ga-FAPI translated into a higher per-region detection rate and higher accuracy of ^{68}Ga-FAPI than of ^{18}F-FDG in NA and low-grade sarcomas. ^{68}Ga-FAPI PET led to a change in therapeutic management in around 20% of patients. In around a third of these patients, ^{68}Ga-FAPI PET led from active surveillance to systemic treatment. A small subgroup switched from locoregional to systemic therapy, and a single patient switched from systemic therapy to active surveillance. Most of our cohort were patients with advanced metastatic disease who had already undergone extensive imaging, so ^{68}Ga-FAPI PET only moderately affected clinical decision-making. Nevertheless, we believe that the impact on clinical management will increase if ^{68}Ga-FAPI-PET is performed at earlier stages of the disease. The better tumor detection and specificity of FAPI versus current imaging standards, especially for NA and low-grade sarcomas, could be pivotal to implement staging (i.e., M0 vs. M1) and hence affect therapy planning adjustment (i.e., curative vs. palliative). Moreover, it could implement the assessment of disease extent before local therapies (i.e., target tumor volume before external beam radiotherapy).

Immunohistochemistry analysis was performed on 89 patients. A high level of FAP expression in tumor stroma has been reported previously (*6*,*10*,*30*,*31*). In our study, immunohistochemistry confirmed the presence of the FAP target in tumor lesions and showed a moderate positive correlation, with a higher FAP score associated with higher ^{68}Ga-FAPI PET uptake.

Because of their origin in soft tissue, most sarcomas intrinsically express FAP on the surface of tumor cells and surrounding fibroblasts (*8*,*13*,*32*), which may make this tumor entity particularly suitable for ^{68}Ga-FAPI PET and FAP-RPT (*14*,*28*,*33*,*34*). Metastatic sarcoma has a poor prognosis, with an overall 5-y survival rate of 15% (*35*). Treatment options for this metastatic disease are scarce

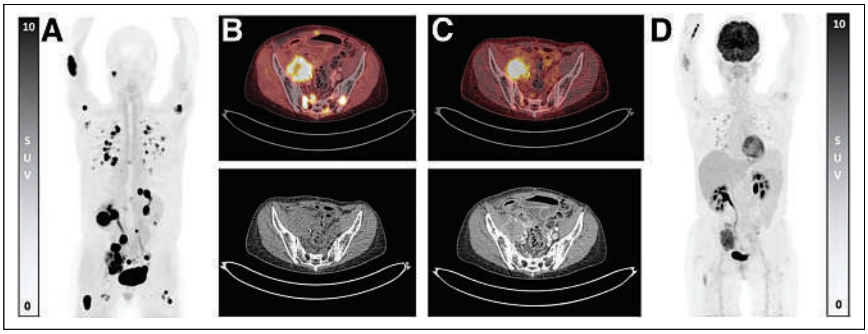

FIGURE 4. 62-y-old patient with metastatic SFT. Higher ^{68}Ga-FAPI uptake (A and B) than ^{18}F-FDG uptake (C and D) is shown in images of primary tumor in right pelvis (SUV_{max} of 25.1 in B vs. 9.0 in C) and multiple pelvic bone metastases (right sacrum, SUV_{max} of 23.0 in B vs. 2.2 in C). Shown are maximum-intensity projection PET images (A and D), axial PET images (B and C, top), and axial CT images (B and C, bottom).

TABLE 2
Detection Efficacy on Per-Region Basis in High-Grade (n = 141), NA (n = 27), and Low-Grade (n = 32) Groups

Lesion	Overall	^{68}Ga-FAPI-46	^{18}F-FDG
High grade			
Primary tumor	100 (100)	100 (100)	84 (84)
Lymph nodes	73 (100)	63 (70)	73 (100)
Distant metastases	563 (100)	563 (100)	524 (93)
Lung	252 (100)	252 (100)	243 (96)
Muscle	52 (100)	52 (100)	49 (94)
Viscera	87 (100)	87 (100)	83 (95)
Liver	32 (100)	32 (100)	28 (88)
Bone	140 (100)	140 (100)	121 (86)
NA			
Primary tumor	17 (100)	17 (100)	15 (88)
Lymph nodes	16 (100)	16 (100)	14 (88)
Distant metastases	286 (100)	286 (100)	191 (67)
Lung	118 (100)	118 (100)	87 (74)
Muscle	25 (100)	25 (100)	14 (56)
Viscera	26 (100)	26 (100)	11 (42)
Liver	12 (100)	12 (100)	8 (67)
Bone	105 (100)	105 (100)	71 (68)
Low grade			
Primary tumor	27 (100)	27 (100)	25 (93)
Lymph nodes	15 (100)	13 (87)	15 (100)
Distant metastases	101 (100)	96 (95)	82 (81)
Lung	31 (100)	31 (100)	22 (71)
Muscle	11 (100)	9 (82)	11 (100)
Viscera	23 (100)	23 (100)	20 (87)
Liver	12 (100)	12 (100)	5 (42)
Bone	24 (100)	21 (88)	24 (100)

Data are number and percentage.

TABLE 3
Accuracy of Detection of Sarcoma on Per-Region Basis in High-Grade (*n* = 141), NA (*n* = 27), and Low-Grade (*n* = 32) Groups

Imaging	Sensitivity	Specificity	Accuracy
High grade			
^{68}Ga-FAPI-46	96.4 (93.5–98.3)	85.7 (67.3–95.9)	95.5 (92.5–97.5)
^{18}F-FDG	94.2 (90.8–96.8)	67.9 (47.6–84.2)	91.8 (88.0–94.7)
NA			
^{68}Ga-FAPI-46	95.9 (88.5–99.1)	80.0 (28.4–99.5)	94.9 (87.4–98.6)
^{18}F-FDG	83.3 (72.1–91.4)	66.7 (22.3–95.7)	81.9 (71.1–90.0)
Low grade			
^{68}Ga-FAPI-46	92.6 (83.6–97.6)	88.9 (51.7–99.7)	92.2 (83.8–97.1)
^{18}F-FDG	85.2 (73.8–93.0)	44.4 (13.7–78.8)	80.0 (68.73–88.6)

Data are percentage and 95% CI.

and unfulfilling. FAP-positive cells play a vital role in remodeling the tumor microenvironment. Therefore, FAP is increasingly considered a potential pantumoral target for the design of tumor-targeting drugs, which explains why several in vitro and vivo studies are ongoing.

The development of immunomodulatory therapies based on oncolytic viruses is playing an increasingly important role in the treatment of solid tumors, involving both direct cell lysis and immunogenic cell death. In this context, oncolytic viruses armed with an FAP-targeting bispecific T-cell engager have been designed to target infiltrating lymphocytes toward cancer-associated stromal fibroblasts, thereby enhancing viral propagation and T-cell–mediated cytotoxicity against tumor stroma to improve therapeutic activity (*36*). FAP-targeting bispecific T-cell engager activators, which costimulate T cells and improve tumor cell destruction in FAP-expressing tumors, are the subject of several phase I studies in patients with advanced solid tumors, with preliminary results demonstrating tolerability and safety (*37*,*38*), as well as signs of response (*39*).

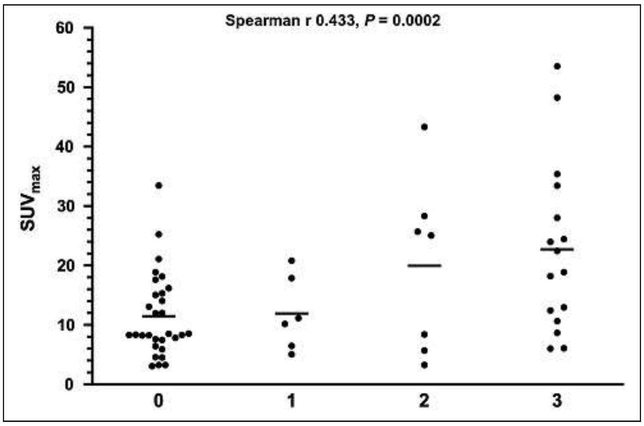

FIGURE 5. Association between ^{68}Ga-FAPI PET uptake intensity (SUV$_{max}$) and FAP immunohistochemistry score (*n* = 89). Individual data and mean (bars) are shown. Immunohistochemistry scoring: 0 = no expression (<1%), 1 = 1%–10%, 2 = 11%–49%, + = ≥50% FAP-positive cells. Comparison of SUV$_{max}$ with established immunohistochemistry scoring system showed moderate linear relationship (Spearman *r* = 0.43, *P* = 0.0002).

Moreover, when conjugated with doxorubicin, FAP has been used to generate chemotherapeutic prodrugs, activated only in the tumor microenvironment, to selectively release anticancer agents and improve the targeting effect of these cytotoxic agents, thus reducing their systemic side effects (*40*). FAP represents a promising target for other potential treatments, such as immunotherapy (*41*,*42*); FAP-targeted chimeric antigen receptor–T-cell therapy, which is being investigated in 2 phase I clinical trials in patients with malignant pleural mesothelioma (*43*); nectin-4–positive advanced solid malignancies (*44*); and RPT.

RPT is capable of delivering radiation to FAP- and stroma-rich tumor lesions while limiting damage to surrounding tissue. This new therapeutic approach has been widely applied to metastatic neuroendocrine tumors and prostate cancers, improving quality of life and overall survival (*45*,*46*). Several FAP ligands are being investigated in preclinical and clinical settings as theranostic agents. In a head-to-head comparison, ^{177}Lu-labeled FAP ligands were evaluated in vitro in cell lines with low and high human FAP expression and in mice bearing low and high FAP-expressing models. The ^{177}Lu-FAPI-46 dimer presented higher uptake and longer tumor retention than those of the monomer, whereas the tumor–to–critical organ values were in favor of cyclic peptide FAP-2286 (*47*). In a first-in-human dosimetry study, ^{177}Lu-FAP-2286 showed longer tumor retention than a small FAPI tracer, such as FAPI-02/04, and the doses absorbed by the whole body, bone marrow, and kidney were comparable to those of other radiopharmaceuticals previously reported to be effective, namely, ^{177}Lu-DOTATATE and ^{177}Lu-PSMA-617 (*48*). The results of the studies available so far ultimately indicate that dimerization of FAPI small molecules and the cyclic peptide are 2 promising strategies for enhancing the tumor radiation dose.

Various radionuclides are taken into consideration for labeling. If on one side, the β-particle energy of ^{90}Y is higher than that of ^{177}Lu, then on the other side, the longer range of ^{90}Y-β could increase the risk of bone marrow and renal toxicity. Because of the high and precise energy delivery to the tumor per unit of radioactivity, α-emitters, such as ^{225}Ac, could also be potential candidates, as reported in a proof-of-concept study (*49*). FAP-RPT with

^{90}Y-FAPI and ^{177}Lu-FAPI has been documented in several case reports and case series for the treatment of various tumor entities (*17*,*50–52*). Our group has previously reported favorable safety and evidence of the efficacy of FAP-RPT in a mixed cohort of patients mainly with metastatic sarcomas (*15*). Furthermore, FAP-RPT is undergoing a prospective phase II safety and tolerability trial in patients with advanced solid tumors (*18*), with preliminary results showing no significant toxicity and some signs of early efficacy (*53*). In accordance with therapeutic criteria (*45*,*54*), intense FAP expression, defined by an SUV$_{max}$ of at least 10 for all tumor lesions, indicated eligibility for FAP-RPT. Based on these criteria, more than half of our patients could be eligible for FAP-RPT. Several subentities of sarcoma, including SFT, UPS, and leiomyosarcoma, demonstrated ^{68}Ga-FAPI uptake that ranged up to highly intense (SUV$_{max}$ > 20), indicating favorable target expression for FAP-RPT. Because of the heterogeneous expression of the target, ^{68}Ga-FAPI PET could become a tool for determining eligibility for FAP-RPT and identifying subentities of sarcoma likely to benefit from this therapeutic approach.

Several limitations were identified. We found a moderate correlation between ^{68}Ga-FAPI uptake by PET and target expression by immunohistochemistry. Thus, SUV$_{max}$ may not be representative of the entire tumor lesion, which may underestimate the intralesional heterogeneity of FAP expression. Moreover, some patients did not undergo ^{18}F-FDG PET, potentially leading to a selection bias.

In this analysis, we focus on the diagnostic accuracy of ^{68}Ga-FAPI PET. This study does not include mandatory follow-up. The absence of follow-up data may have led to bias. FAP-RPT eligibility was in line with previously published criteria (*15*). However, these criteria have not yet been validated on the basis of oncologic outcomes.

CONCLUSION

^{68}Ga-FAPI PET demonstrates tumor uptake, detection rate, and accuracy superior to that of ^{18}F-FDG PET in patients with low-grade and NA sarcomas. Tumor uptake for ^{68}Ga-FAPI PET correlated moderately with FAP expression for immunohistochemistry. ^{68}Ga-FAPI PET criteria identified eligibility for FAP-RPT in about half of sarcoma patients, especially those with SFT, UPS, and leiomyosarcoma.

DISCLOSURE

No potential conflict of interest relevant to this article was reported.

KEY POINTS

QUESTION: Does the diagnostic performance of ^{68}Ga-FAPI PET in BS and STS vary according to grade of disease and subentities, and if so, which subentities are more likely to be good candidates for FAP-RPT?

PERTINENT FINDINGS: We observed diagnostic performance and accuracy of ^{68}Ga-FAPI superior to that of ^{18}F-FDG in intermediate and low-grade sarcomas. The subentities that consistently show intense FAPI uptake (SUV$_{max}$ > 20), namely, SFT, UPS, and leiomyosarcomas, are more likely to benefit from this therapeutic approach.

IMPLICATIONS FOR PATIENT CARE: ^{68}Ga-FAPI PET is a diagnostic tool for low-grade and NA sarcomas and allows the determination of eligibility for FAP-RPT.

REFERENCES

1. Casali PG, Blay JY, Abecassis N, et al. Gastrointestinal stromal tumours: ESMO–EURACAN–GENTURIS clinical practice guidelines for diagnosis, treatment and follow-up. *Ann Oncol.* 2022;33:20–33.
2. Gronchi A, Miah AB, Dei Tos AP, et al. Soft tissue and visceral sarcomas: ESMO-EURACAN-GENTURIS clinical practice guidelines for diagnosis, treatment and follow-up. *Ann Oncol.* 2021;32:1348–1365.
3. Strauss SJ, Frezza AM, Abecassis N, et al. Bone sarcomas: ESMO–EURACAN–GENTURIS–ERN PaedCan clinical practice guideline for diagnosis, treatment and follow-up. *Ann Oncol.* 2021;32:1520–1536.
4. Classification of Tumours Editorial Board, World Health Organization. *WHO Classification of Tumours.* Vol 3. 5th ed. International Agency for Research on Cancer; 2020.
5. Liu F, Qi L, Liu B, et al. Fibroblast activation protein overexpression and clinical implications in solid tumors: a meta-analysis. *PLoS One.* 2015;10:e0116683.
6. Garin-Chesa P, Old LJ, Rettig WJ. Cell surface glycoprotein of reactive stromal fibroblasts as a potential antibody target in human epithelial cancers. *Proc Natl Acad Sci USA.* 1990;87:7235–7239.
7. Kelly T, Huang Y, Simms AE, Mazur A. Fibroblast activation protein-α: a key modulator of the microenvironment in multiple pathologies. In: Jeon KW, ed. *International Review of Cell and Molecular Biology.* Vol 297. Academic Press; 2012:83–116.
8. Rettig WJ, Garin-Chesa P, Beresford HR, Oettgen HF, Melamed MR, Old LJ. Cell-surface glycoproteins of human sarcomas: differential expression in normal and malignant tissues and cultured cells. *Proc Natl Acad Sci USA.* 1988;85: 3110–3114.
9. Lindner T, Loktev A, Altmann A, et al. Development of quinoline-based theranostic ligands for the targeting of fibroblast activation protein. *J Nucl Med.* 2018;59: 1415–1422.
10. Altmann A, Haberkorn U, Siveke J. The latest developments in imaging of fibroblast activation protein. *J Nucl Med.* 2021;62:160–167.
11. Ballal S, Yadav MP, Moon ES, et al. Biodistribution, pharmacokinetics, dosimetry of [^{68}Ga]Ga-DOTA.SA.FAPi, and the head-to-head comparison with [^{18}F]F-FDG PET/CT in patients with various cancers. *Eur J Nucl Med Mol Imaging.* 2021;48: 1915–1931.
12. Giesel FL, Kratochwil C, Lindner T, et al. ^{68}Ga-FAPI PET/CT: biodistribution and preliminary dosimetry estimate of 2 DOTA-containing FAP-targeting agents in patients with various cancers. *J Nucl Med.* 2019;60:386–392.
13. Dohi O, Ohtani H, Hatori M, et al. Histogenesis-specific expression of fibroblast activation protein and dipeptidylpeptidase-IV in human bone and soft tissue tumours. *Histopathology.* 2009;55:432–440.
14. Kessler L, Ferdinandus J, Hirmas N, et al. ^{68}Ga-FAPI as a diagnostic tool in sarcoma: data from the ^{68}Ga-FAPI PET prospective observational trial. *J Nucl Med.* 2022;63:89–95.
15. Fendler WP, Pabst KM, Kessler L, et al. Safety and efficacy of ^{90}Y-FAPI-46 radioligand therapy in patients with advanced sarcoma and other cancer entities. *Clin Cancer Res.* 2022;28:4346–4353.
16. Ferdinandus J, Fragoso Costa P, Kessler L, et al. Initial clinical experience with ^{90}Y-FAPI-46 radioligand therapy for advanced-stage solid tumors: a case series of 9 patients. *J Nucl Med.* 2022;63:727–734.
17. Baum RP, Schuchardt C, Singh A, et al. Feasibility, biodistribution, and preliminary dosimetry in peptide-targeted radionuclide therapy of diverse adenocarcinomas using ^{177}Lu-FAP-2286: first-in-humans results. *J Nucl Med.* 2022; 63:415–423.
18. A study of ^{177}Lu-FAP-2286 in advanced solid tumors (LuMIERE). ClinicalTrials.gov website. https://clinicaltrials.gov/study/NCT04939610. Updated February 6, 2024. Accessed April 9, 2024.
19. Nader M, Valla DF, Vriamont C, et al. [^{68}Ga]/[^{90}Y]FAPI-46: automated production and analytical validation of a theranostic pair. *Nucl Med Biol.* 2022;110–111: 37–44.
20. Boellaard R, Delgado-Bolton R, Oyen WJG, et al. FDG PET/CT: EANM procedure guidelines for tumour imaging—version 2.0. *Eur J Nucl Med Mol Imaging.* 2015;42:328–354.
21. Henry LR, Lee H-O, Lee JS, et al. Clinical implications of fibroblast activation protein in patients with colon cancer. *Clin Cancer Res.* 2007;13:1736–1741.
22. Giesel FL, Kratochwil C, Schlittenhardt J, et al. Head-to-head intra-individual comparison of biodistribution and tumor uptake of ^{68}Ga-FAPI and ^{18}F-FDG PET/CT in cancer patients. *Eur J Nucl Med Mol Imaging.* 2021;48:4377–4385.
23. Hamacher R, Lanzafame H, Mavroeidi IA, et al. Fibroblast activation protein inhibitor theranostics: the case for use in sarcoma . *PET Clin.* 2023;18:361–367.
24. Charest M, Hickeson M, Lisbona R, Novales-Diaz J-A, Derbekyan V, Turcotte RE. FDG PET/CT imaging in primary osseous and soft tissue sarcomas: a retrospective review of 212 cases. *Eur J Nucl Med Mol Imaging.* 2009;36:1944–1951.

25. Lim HJ, Johnny Ong C-A, Tan JW-S, Ching Teo MC. Utility of positron emission tomography/computed tomography (PET/CT) imaging in the evaluation of sarcomas: a systematic review. *Crit Rev Oncol Hematol.* 2019;143:1–13.
26. Macpherson RE, Pratap S, Tyrrell H, et al. Retrospective audit of 957 consecutive ^{18}F-FDG PET-CT scans compared to CT and MRI in 493 patients with different histological subtypes of bone and soft tissue sarcoma. *Clin Sarcoma Res.* 2018;8:9.
27. Strauss SJ, Frezza AM, Abecassis N, et al. Bone sarcomas: ESMO-EURACAN-GENTURIS-ERN PaedCan clinical practice guideline for diagnosis, treatment and follow-up. *Ann Oncol.* 2021;32:1520–1536.
28. Hirmas N, Hamacher R, Sraieb M, et al. Fibroblast-activation protein PET and histopathology in a single-center database of 324 patients and 21 tumor entities. *J Nucl Med.* 2023;64:711–716.
29. Gu B, Liu X, Wang S, et al. Head-to-head evaluation of [^{18}F]FDG and [^{68}Ga]Ga-DOTA-FAPI-04 PET/CT in recurrent soft tissue sarcoma. *Eur J Nucl Med Mol Imaging.* 2022;49:2889–2901.
30. Liu F, Qi L, Liu B, et al. Fibroblast activation protein overexpression and clinical implications in solid tumors: a meta-analysis. *PLoS One.* 2015;10:e0116683.
31. Sgouros G, Bodei L, McDevitt MR, Nedrow JR. Radiopharmaceutical therapy in cancer: clinical advances and challenges. *Nat Rev Drug Discov.* 2020;19:589–608.
32. Dolznig H, Schweifer N, Puri C, et al. Characterization of cancer stroma markers: in silico analysis of an mRNA expression database for fibroblast activation protein and endosialin. *Cancer Immun.* 2005;5:10.
33. Kratochwil C, Flechsig P, Lindner T, et al. ^{68}Ga-FAPI PET/CT: tracer uptake in 28 different kinds of cancer. *J Nucl Med.* 2019;60:801–805.
34. Koerber SA, Finck R, Dendl K, et al. Novel FAP ligands enable improved imaging contrast in sarcoma patients due to FAPI-PET/CT. *Eur J Nucl Med Mol Imaging.* 2021;48:3918–3924.
35. Survival rates for soft tissue sarcoma. American Cancer Society website. https://www.cancer.org/cancer/types/soft-tissue-sarcoma/detection-diagnosis-staging/survival-rates.html. Updated February 2, 2021. Accessed April 9, 2024.
36. de Sostoa J, Fajardo CA, Moreno R, Ramos MD, Farrera-Sal M, Alemany R. Targeting the tumor stroma with an oncolytic adenovirus secreting a fibroblast activation protein-targeted bispecific T-cell engager. *J Immunother Cancer.* 2019;7:19.
37. Simon G, Subbiah V, Rosen L, et al. First-in-human phase 1a study of NG-641, a tumour-selective vector expressing a FAP-TAc bispecific antibody and immune enhancer module, in patients with metastatic/advanced epithelial tumours (STAR) [abstract]. *J Immunother Cancer.* 2022;10:762.
38. Gomez-Roca CA, Steeghs N, Gort EH, et al. Phase I study of MP0317, a FAP-dependent DARPin, for tumor-localized CD40 activation in patients with advanced solid tumors [abstract]. *J Clin Oncol.* 2023;41:2584.
39. Melero I, Tanos T, Bustamante M, et al. A first-in-human study of the fibroblast activation protein–targeted, 4-1BB agonist RO7122290 in patients with advanced solid tumors. *Sci Transl Med.* 2023;15:eabp9229.
40. McLaughlin F, Poplawski SE, Sanford DG, et al. AVA6000, a novel precision medicine, targeted to the tumor microenvironment via fibroblast activation protein (FAP) mediated cleavage [abstract]. *Cancer Res.* 2022;82:1815.
41. Lee IK, Noguera-Ortega E, Xiao Z, et al. Monitoring therapeutic response to anti-FAP CAR T cells using [^{18}F]AlF-FAPI-74. *Clin Cancer Res.* 2022;28:5330–5342.
42. Bughda R, Dimou P, D'Souza RR, Klampatsa A. Fibroblast activation protein (FAP)-targeted CAR-T cells: launching an attack on tumor stroma. *ImmunoTargets Ther.* 2021;10:313–323.
43. Hiltbrunner S, Britschgi C, Schuberth P, et al. Local delivery of CAR T cells targeting fibroblast activation protein is safe in patients with pleural mesothelioma: first report of FAPME, a phase I clinical trial. *Ann Oncol.* 2021;32:120–121.
44. Interventional therapy sequential with the fourth-generation CAR-T targeting nectin4/FAP for malignant solid tumors. ClinicalTrials.gov website. https://clinicaltrials.gov/study/NCT03932565. Updated November 18, 2020. Accessed April 9, 2024.
45. Strosberg JR, Caplin ME, Kunz PL, et al. ^{177}Lu-DOTATATE plus long-acting octreotide versus high-dose long-acting octreotide in patients with midgut neuroendocrine tumours (NETTER-1): final overall survival and long-term safety results from an open-label, randomised, controlled, phase 3 trial. *Lancet Oncol.* 2021;22:1752–1763.
46. Sartor O, Hope TA, Calais J, Fendler WP. Oliver Sartor talks with Thomas A. Hope, Jeremie Calais, and Wolfgang P. Fendler about FDA approval of PSMA. *J Nucl Med.* 2021;62:146–148.
47. Millul J, Koepke L, Haridas GR, Sparrer KMJ, Mansi R, Fani M. Head-to-head comparison of different classes of FAP radioligands designed to increase tumor residence time: monomer, dimer, albumin binders, and small molecules vs peptides. *Eur J Nucl Med Mol Imaging.* 2023;50:3050–3061.
48. Baum RP, Schuchardt C, Singh A, et al. Feasibility, biodistribution, and preliminary dosimetry in peptide-targeted radionuclide therapy of diverse adenocarcinomas using ^{177}Lu-FAP-2286: first-in-humans results. *J Nucl Med.* 2022;63:415–423.
49. Watabe T, Liu Y, Kaneda-Nakashima K, et al. Theranostics targeting fibroblast activation protein in the tumor stroma: ^{64}Cu- and ^{225}Ac-labeled FAPI-04 in pancreatic cancer xenograft mouse models. *J Nucl Med.* 2020;61:563.
50. Assadi M, Rekabpour SJ, Jafari E, et al. Feasibility and therapeutic potential of ^{177}Lu-fibroblast activation protein inhibitor-46 for patients with relapsed or refractory cancers: a preliminary study. *Clin Nucl Med.* 2021;46:e523–e530.
51. Ballal S, Yadav MP, Kramer V, et al. A theranostic approach of [^{68}Ga]Ga-DOTA.SA.FAPi PET/CT-guided [^{177}Lu]Lu-DOTA.SA.FAPi radionuclide therapy in an end-stage breast cancer patient: new frontier in targeted radionuclide therapy. *Eur J Nucl Med Mol Imaging.* 2021;48:942–944.
52. Kaghazchi F, Aghdam RA, Haghighi S, Vali R, Adinehpour Z. ^{177}Lu-FAPI therapy in a patient with end-stage metastatic pancreatic adenocarcinoma. *Clin Nucl Med.* 2022;47:e243–e245.
53. McConathy J, Dhawan M, Goenka A, et al. ^{177}Lu-FAP-2286 in patients with advanced or metastatic solid tumors: initial data from a phase 1/2 study investigating safety, pharmacokinetics, dosimetry, and preliminary antitumor activity (LuMIERE) [abstract]. *J Nucl Med.* 2022;63:2271.
54. Sartor O, de Bono J, Chi KN, et al. Lutetium-177–PSMA-617 for metastatic castration-resistant prostate cancer. *N Engl J Med.* 2021;385:1091–1103.

A Systematic Review on the Diagnostic Value of Fibroblast Activation Protein Inhibitor PET/CT in Genitourinary Cancers

Marinus J. Hagens[1], Pim J. van Leeuwen[1], Maurits Wondergem[2], Thierry N. Boellaard[3], Francesco Sanguedolce[4], Daniela E. Oprea-Lager[5], Axel Bex[1], André N. Vis[6], Henk G. van der Poel[1], and Laura S. Mertens[1]; in collaboration with the EAU Section of Urological Imaging

[1]Department of Urology, Netherlands Cancer Institute–Antoni van Leeuwenhoek Hospital, Amsterdam, The Netherlands; [2]Department of Nuclear Medicine, Noordwest Ziekenhuisgroep, Alkmaar, The Netherlands; [3]Department of Radiology, Netherlands Cancer Institute–Antoni van Leeuwenhoek Hospital, Amsterdam, The Netherlands; [4]Department of Urology, Fundació Puigvert, Autonomous University of Barcelona, Barcelona, Spain; [5]Department of Radiology and Nuclear Medicine, Amsterdam University Medical Centers, Location VUmc, Amsterdam, The Netherlands; and [6]Department of Urology, Amsterdam University Medical Centers, Location VUmc, Amsterdam, The Netherlands

In contemporary oncologic diagnostics, molecular imaging modalities are pivotal for precise local and metastatic staging. Recent studies identified fibroblast activation protein as a promising target for molecular imaging across various malignancies. Therefore, we aimed to systematically evaluate the current literature on the utility of fibroblast activation protein inhibitor (FAPI) PET/CT for staging patients with genitourinary malignancies. **Methods:** A systematic Embase and Medline search was conducted, according to the Preferred Reporting Items for Systematic Reviews and Meta-Analyses (PRISMA) process, on August 1, 2023. Relevant publications reporting on the diagnostic value of FAPI PET/CT in genitourinary malignancies were identified and included. Studies were critically reviewed using a modified version of a tool for quality appraisal of case reports. Study results were summarized using a narrative approach. **Results:** We included 22 retrospective studies with a cumulative total of 69 patients, focusing on prostate cancer, urothelial carcinoma of the bladder and of the upper urinary tract, renal cell carcinoma, and testicular cancer. FAPI PET/CT was able to visualize both local and metastatic disease, including challenging cases such as prostate-specific membrane antigen (PSMA)–negative prostate cancer. Compared with radiolabeled ^{18}F-FDG and PSMA PET/CT, FAPI PET/CT showed heterogeneous performance. In selected cases, FAPI PET/CT demonstrated superior tumor visualization (i.e., better tumor-to-background ratios and visualization of small tumors or metastatic deposits visible in no other way) over ^{18}F-FDG PET/CT in detecting local or metastatic disease, whereas comparisons with PSMA PET/CT showed both superior and inferior performances. Challenges in FAPI PET/CT arise from physiologic urinary excretion of most FAPI radiotracers, hindering primary-lesion visualization in the bladder and upper urinary tract, despite generally providing high tumor-to-background ratios. **Conclusion:** The current findings suggest that FAPI PET/CT may hold promise as a future tool to aid clinicians in detecting genitourinary malignancies. Given the substantial heterogeneity among the included studies and the limited number of patients, caution in interpreting these findings is warranted. Subsequent prospective and comparative investigations are anticipated to delve more deeply into this innovative imaging modality and elucidate its role in clinical practice.

Key Words: prostate cancer; urothelial carcinoma; renal cell carcinoma; testicular cancer; metastatic screening; FAPI PET/CT

J Nucl Med 2024; 65:888–896
DOI: 10.2967/jnumed.123.267260

Accurate staging of genitourinary malignancies is crucial for optimizing treatment planning and patient outcomes (*1–6*). Recent advances in molecular imaging modalities, such as radiolabeled ^{18}F-FDG and prostate-specific membrane antigen (PSMA) PET/CT, have significantly advanced the staging of genitourinary malignancies, compared with conventional imaging methods (*7–9*). These molecular imaging modalities excel at detecting metastatic disease even in anatomically nonanomalous structures. However, challenges persist. For instance, current molecular imaging modalities often struggle to detect all metastatic lesions, demonstrating the relatively low sensitivity of ^{18}F-FDG and PSMA PET/CT, false positives due to physiologic uptake in tissues not within the region of interest or (postoperative) inflammation, and the occasional absence of PSMA avidity. Thus, exploring alternative imaging modalities is essential to enhance staging accuracy and guide therapeutic decisions (*10–12*).

Malignancies, including genitourinary cancers, comprise diverse cell types and not just autonomic neoplastic cells (Fig. 1) (*13*). Activated fibroblasts or myofibroblasts, also known as cancer-associated fibroblasts, are abundant in the tumor microenvironment and possess various significant functions, such as promotion of tumor growth, cell invasion and metastasis, angiogenesis, and regulation of immune response (*14*). Distinguishing themselves from normal fibroblasts, most cancer-associated fibroblasts exhibit remarkable overexpression of the fibroblast activation protein (FAP), making them an appealing target for noninvasive molecular imaging techniques (*15,16*). Recently, a quinoline-based FAP inhibitor (FAPI) was identified, which binds selectively to this epitope, and after being labeled with positron-emitting isotopes, the tumor microenvironment could be visualized in vivo using PET/CT imaging (*17*).

Received Dec. 18, 2023; revision accepted Mar. 4, 2024.

For correspondence or reprints, contact Marinus J. Hagens (m.hagens@nki.nl).

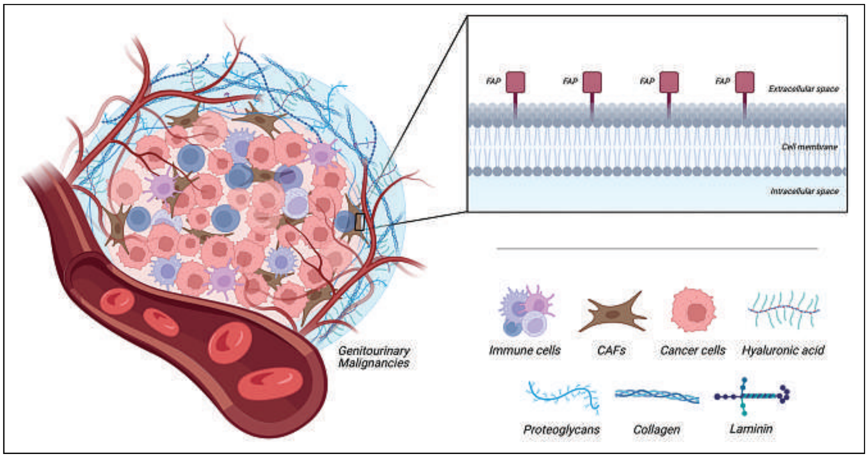

FIGURE 1. Graphic illustration of tumor microenvironment with cancer-associated fibroblasts (CAFs) and their overexpression of FAP. (Created with BioRender.com.)

Several publications have shown that FAPI PET/CT yields strong positive signals in various malignancies, suggesting its potential as a highly cancer-specific imaging modality that may overcome the limitations of ^{18}F-FDG and PSMA PET/CT (*18–20*). In this review, we systematically assess the current literature regarding the diagnostic value of FAPI PET/CT for genitourinary malignancies.

MATERIALS AND METHODS

This systematic review was registered in the International Prospective Register of Systematic Reviews database on July 9, 2023 (CRD42023443837). The subsequent methodology followed the Preferred Reporting Items for Systematic Reviews and Meta-Analyses (PRISMA) statement (*21*).

Search Strategy

A systematic Embase and Medline search was conducted on August 1, 2023. The initial search included some of the following key terms: “Fibroblast Activation Protein Inhibitor” OR “FAPI” AND (“Bladder Cancer” OR “Prostate Cancer” OR “Penile Cancer” OR “Renal Cancer” OR “Urachal Cancer” OR “Testicular Cancer” OR “Urethral Cancer” OR “Upper Tract Urinary Cancer”). The complete free-text search terms are attached as supplemental material (supplemental materials are available at http://jnm.snmjournals.org). For searches, publication dates were limited to the preceding 10 y, because the first FAPI tracer was introduced in the preceding decade. No other limits were applied.

Inclusion and Exclusion Criteria

Studies were included for review if they explored the diagnostic value of FAPI PET/CT in patients with genitourinary malignancies (i.e., urothelial carcinoma of the bladder and upper urinary tract, prostate cancer [PCa], penile cancer, renal cell carcinoma [RCC], mucinous urachal adenocarcinoma, and testicular cancer). Hence, in accordance with the PRISMA statement, we used a strategy considering population, intervention, comparison, and outcome elements to select studies that report on the diagnostic value of FAPI PET/CT in patients with genitourinary malignancies, comparing it with established molecular imaging modalities. Publications were excluded if they were not written in English, related to nonclinical results, or were published as letters to the editor, editorials, study protocols, or commentaries or were in the gray literature. Finally, if multiple studies reported results from overlapping cohorts, only the most recent publication was retrieved.

Systematic Review Process

The abstract and full-text screening and the subsequent data extraction were performed by 2 reviewers independently. Discrepancies between reviewers were resolved by consensus. Relevant publication reference lists were screened manually to identify further studies. The PRISMA flowchart describing the systematic review process, with the numbers of papers identified and included or excluded at each stage, is presented in Figure 2.

Data Extraction

Information on study characteristics was extracted from all included studies by 2 of the authors, who subsequently cross-checked these to ensure their accuracy. A standardized data extraction form was created a priori to collect article information (first author name, year of publication, study design, and number of participants), population characteristics of interest (tumor type, histologic subtype, and disease stage), and imaging details (radiotracer and comparative imaging modality) and findings. Additionally, comparative information with other imaging modalities or histopathologic specimens was likewise collected, ensuring a comprehensive evaluation of the diagnostic performance of FAPI PET/CT in relation to alternative imaging techniques and pathologic findings.

Quality Appraisal

Assuming that identified reports would involve primarily nonrandomized studies, such as cohort studies and case reports, identified studies were critically reviewed using a modified version of a tool for quality appraisal of case reports (*22*). The assessment determined 4 items: whether the patient was described adequately (i.e., main complaint, history, clinical and laboratory evaluations, treatments), whether an accurate diagnosis was provided (i.e., valid and reliable outcome measures were used), whether convincing evidence in support of the diagnosis

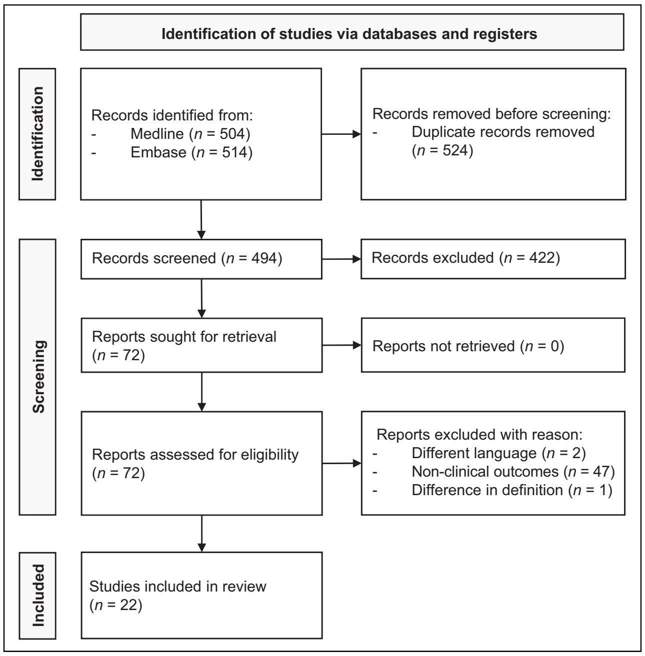

FIGURE 2. PRISMA flow diagram showing outcome of searches and selection of full studies included in review.

was presented (i.e., according to the criteria for diagnosis of antiphospholipid syndrome or catastrophic antiphospholipid syndrome, or describing the evidence for diagnosis), and whether alternate explanations were considered and refuted (differential diagnosis was illustrated and scientifically excluded, or underlying possible mechanisms that could explain the finding were addressed). Possible item ratings were yes, partially, or no.

Statistical Analysis

Studies were assessed using a narrative synthesis of included studies and descriptive statistics to summarize the data on extracted baseline characteristics. The diagnostic value of FAPI PET/CT was described with regard to its ability to detect metastatic disease, and it was compared with current molecular imaging modalities if possible. A metaanalysis was not performed, because of the expected heterogeneity of the included studies.

RESULTS

The first reviewer identified 65 potentially eligible studies, and the second reviewer identified 75 potential studies, resulting in an 87% agreement rate. Ultimately, 22 studies were eligible for inclusion, all of which were retrospective and with a high or unclear risk of bias (*19,23–43*). Supplemental Table 1 summarizes the quality appraisal. All 22 studies focused on assessing the diagnostic value of FAPI PET/CT in various genitourinary malignancies, including PCa (n = 12), urothelial carcinoma of the bladder and upper urinary tract (n = 4), RCC (n = 6), and testicular cancer (n = 1). The systematic review encompassed a cumulative total of 69 patients. Table 1 presents article information, population characteristics, and molecular imaging details stratified by tumor type.

FAPI PET/CT in PCa

Of the 69 patients assessed, 33 (48%) underwent FAPI PET/CT for staging PCa. Most FAPI PET/CT scans were performed on a known-metastatic population with a history of prior treatment (*19,29,34,37,40–42*). FAPI PET/CT was able to visualize metastatic PCa lesions (nodal, skeletal, or visceral) because of the generally high tracer uptake and minimal background activity of FAPI radiotracers, resulting in high tumor-to-background ratios (TBRs). Similarly, in newly diagnosed PCa patients, the primary tumor exhibited excellent visualization, with high radiotracer uptake (*23,26,28,31,32*).

In comparison to ^{18}F-FDG and PSMA PET/CT, FAPI PET/CT demonstrated a variable diagnostic performance, including instances of both higher and lower diagnostic yields, such as numbers of metastases (*23,26,29,34,40–42*). Improved diagnostic outcomes (i.e., higher diagnostic yield) were particularly observed in cases with more advanced stages of PCa (*37,40–42*). Interestingly, several cases demonstrated the ability of FAPI PET/CT to visualize local and metastatic disease in patients with PSMA-negative tumors (*26,37,40,42*).

Given the focus on an established metastatic population, histopathologic confirmation was infrequently pursued. In studies with histopathologic evidence, this confirmation was limited to the primary tumor (*23,26,29*). Hence, a direct comparison of FAPI PET/CT with conventional molecular imaging using histopathology as a reference standard was generally not possible in the included cases.

FAPI PET/CT in Urothelial Carcinoma of the Bladder and Upper Urinary Tract

FAPI PET/CT was performed on 29 patients to stage urothelial carcinoma of the bladder (n = 22) and upper urinary tract (n = 7). FAPI PET/CT focused primarily on newly diagnosed patients, constituting 20 of 29 cases (*25,30,33,43*). The notably high TBRs in FAPI PET/CT generally facilitated excellent visualization of metastatic lesions (*25,30,33,43*). However, because of the elevated background signal resulting from renal and urinary excretion of most FAPI radiotracers, primary tumors in the bladder and upper urinary tract were often not visible (*25,30,33*). Similarly, lymph nodes near the urinary tract posed a similar challenge due to overlapping urinary activity (*30*).

Compared with ^{18}F-FDG PET/CT, FAPI PET/CT has shown enhanced diagnostic value in included cases. FAPI PET/CT yielded an increased number of identified lesions compared with ^{18}F-FDG PET/CT and correctly reclassified suggestive (reactive) lesions as nonsuggestive (*25,30,43*). Histopathologic confirmation, however, remained limited in these studies, with the report by Unterrainer et al. being the only one with histopathologic confirmation (*30*). Their findings showed that FAPI PET/CT could accurately identify lymph node metastases; only 1 histopathologically confirmed lymph node was missed.

FAPI PET/CT in RCC

Of the evaluated patients, 6 underwent FAPI PET/CT for RCC (*19,24,27,35,38,39*). Noteworthy is the fact that these RCC cases encompassed different subtypes, including sarcomatoid, chromophobe, papillary, and clear cell. Both newly diagnosed and known-metastatic patient populations were studied, with 4 of 6 cases falling within the latter category. Despite the report by Kratochwil et al. (*19*) of low tumoral tracer uptake in RCC, other investigators reported excellent visualization of both primary and metastatic lesions. Notably, FAPI PET/CT detected a solitary choroid plexus metastasis because of lack of physiologic cerebral uptake with FAPI radiotracers (*39*).

In comparison to ^{18}F-FDG PET/CT, FAPI PET/CT detected an equal or greater number of metastatic lesions and provided enhanced delineation of these lesions due to the higher TBRs of FAPI radiotracers. Additionally, if the primary tumor was not visualized on ^{18}F-FDG PET/CT, FAPI PET/CT successfully revealed the primary lesion (*27*). Dong et al., Pang et al., and Yang et al. provided histopathologic confirmation for both metastatic and primary lesions, with FAPI-positive lesions consistently confirmed to harbor metastatic disease (*24,27,39*).

FAPI PET/CT in Testicular Cancer

The diagnostic value of FAPI PET/CT in testicular cancer has been studied only once, involving a patient diagnosed with a metastatic mixed germ cell tumor (*36*). In contrast to previously mentioned genitourinary malignancies, this study demonstrated only mild tumoral tracer uptake. Nevertheless, the uptake was increased with FAPI PET/CT compared with ^{18}F-FDG PET/CT. Regrettably, histopathologic confirmation of the metastatic lesions was not provided.

DISCUSSION

Molecular imaging techniques have demonstrated added diagnostic value for various genitourinary malignancies, such as PSMA PET/CT for PCa and ^{18}F-FDG PET/CT for urothelial carcinoma of the bladder and upper urinary tract (*7,44,45*). Nevertheless, the pursuit of more sensitive and specific imaging modalities continues, as an ideal imaging modality for metastatic screening must combine near-perfect specificity with maximized sensitivity (*1–6*). This systematic review summarizes the existing evidence regarding the diagnostic value of FAPI PET/CT across genitourinary malignancies. Despite an adequate number of identified studies, limitations in the patient cohorts staged with this novel imaging modality within our

TABLE 1
Included Studies Using FAPI PET/CT in Various Genitourinary Malignancies

Malignancy	Study design	Patients (*n*)	Type of histology	Molecular imaging findings: Disease stage	Setting	Radiotracer	Disease evaluation
PCa							
Kratochwil et al. (*19*)	CS	16	Neuroendocrine carcinoma and adenocarcinoma	NA	NA	^{68}Ga-FAPI-04	No comparative MI modality was performed; FAPI PET/CT was valuable in several highly prevalent cancers, with excellent tumor visualization in primary and metastatic lesions
Cai et al. (*23*)	CR	1	Mixed large-cell neuroendocrine carcinoma-acinar adenocarcinoma	Metastatic	Staging	^{68}Ga-FAPI-46	With more metastatic lesions detected, FAPI PET/CT was superior to PSMA PET/CT; ^{18}F-FDG PET/CT was superior to both FAPI and PSMA PET/CT, as additional metastatic liver lesions were visualized
Pang et al. (*26*)	CR	1	Adenocarcinoma	Metastatic	Staging	^{68}Ga-FAPI-04	With equal metastatic lesions detected, FAPI PET/CT was comparable to PSMA and ^{18}F-FDG PET/CT
Tatar et al. (*28*)	CR	1	Signet ringlike cell carcinoma	Metastatic	Staging	^{68}Ga-FAPI-04	No comparative MI modality was performed; FAPI PET/CT was valuable, with excellent tumor visualization in primary and metastatic lesions
Tatar et al. (*29*)	CR	1	Adenocarcinoma	Localized	Restaging	^{68}Ga-FAPI-04	With no metastatic lesions detected, FAPI PET/CT was comparable to PSMA and ^{18}F-FDG PET/CT; primary lesion was more clearly visualized on ^{18}F-FDG PET/CT
Xu et al. (*31*)	CR	1	Adenocarcinoma	Unknown*	Staging	^{68}Ga-FAPI-04	With equal (metastatic) lesions detected, FAPI PET/CT was comparable to ^{18}F-FDG PET/CT
Yang et al. (*32*)	CR	1	Solitary fibrous tumor	Localized	Staging	^{68}Ga-FAPI-04	With no metastatic lesions detected, FAPI PET/CT was comparable to ^{18}F-FDG PET/CT; primary lesion was more clearly visualized on ^{18}F-FDG PET/CT
Aryana et al. (*34*)	CR	1	Adenocarcinoma	Metastatic	Restaging	^{68}Ga-FAPI-46	With fewer metastatic lesions detected, FAPI PET/CT was inferior to PSMA PET/CT; metastatic lesions were more clearly visualized

(*continued*)

TABLE 1
Included Studies Using FAPI PET/CT in Various Genitourinary Malignancies (cont.)

				Molecular imaging findings			
Malignancy	Study design	Patients (*n*)	Type of histology	Disease stage	Setting	Radiotracer	Disease evaluation
Kesch et al. (*37*)	CR	1	Adenocarcinoma	Metastatic	Restaging	^{68}Ga-FAPI-04	No comparative MI modality was performed; FAPI PET/CT was valuable, with excellent tumor visualization in metastatic lesions
Kessel et al. (*40*)	CS	6	Neuroendocrine carcinoma and adenocarcinoma	Metastatic	Restaging	^{68}Ga-FAPI-46	With both more and less metastatic lesions detected, FAPI PET/CT was neither superior nor inferior to ^{18}F-FDG PET/CT
Isik et al. (*41*)	CR	2	Adenocarcinoma	Metastatic	Restaging	^{68}Ga-FAPI-46	With more metastatic lesions detected, FAPI PET/CT was superior to ^{18}F-FDG PET/CT; PSMA PET/CT detected more metastatic lesions in one patient yet less in other patient
Khreish et al. (*42*)	CR	1	Adenocarcinoma	Metastatic	Restaging	^{68}Ga-FAPI-04	With more metastatic lesions detected, FAPI PET/CT was superior to ^{18}F-FDG and PSMA PET/CT
Urothelial carcinoma of bladder/upper urinary tract							
Novruzov et al. (*25*)	CS	8	Urothelial carcinoma	Metastatic	Staging and restaging	^{68}Ga-FAPI-04 and -46	With more metastatic lesions detected, FAPI PET/CT was superior to ^{18}F-FDG PET/CT
Unterrainer et al. (*30*)	CS	15	Urothelial carcinoma	Metastatic	Staging and restaging	^{68}Ga-FAPI-46	No comparative MI modality was performed. However, FAPI PET/CT was valuable, with excellent tumor visualization in primary and metastatic lesions
Dendl et al. (*33*)	CS	4	Urothelial carcinoma	Localized and metastatic	Staging and restaging	^{68}Ga-FAPI-04, -46, and -74	No comparative MI modality was performed; FAPI PET/CT was valuable, with excellent tumor visualization in primary and metastatic lesions
Viergever et al. (*43*)	CS	2	Urothelial carcinoma	Metastatic	Staging	^{68}Ga-FAPI-04	With more metastatic lesions detected, FAPI PET/CT was superior to ^{18}F-FDG PET/CT
RCC							
Kratochwil et al. (*19*)	CS	1	RCC	NA	NA	^{68}Ga-FAPI-04	No comparative MI modality was performed; FAPI PET/CT was valuable in several highly prevalent cancers, with excellent tumor visualization in primary and metastatic lesions

(*continued*)

TABLE 1

Included Studies Using FAPI PET/CT in Various Genitourinary Malignancies (cont.)

				Molecular imaging findings			
Malignancy	Study design	Patients (*n*)	Type of histology	Disease stage	Setting	Radiotracer	Disease evaluation
Dong et al. (*24*)	CR	1	Sarcomatoid RCC	Metastatic	Staging	^{68}Ga-FAPI-04	No comparative MI modality was performed; FAPI PET/CT was valuable, with excellent tumor visualization in primary and metastatic lesions
Pang et al. (*27*)	CR	1	Chromophobe RCC	Metastatic	Staging	^{68}Ga-FAPI-04	With more metastatic lesions detected, FAPI PET/CT was superior to ^{18}F-FDG PET/CT; in contrast to ^{18}F-FDG PET/CT, primary lesion was visualized on FAPI PET/CT
Civan et al. (*35*)	CR	1	Papillary RCC	Metastatic	Restaging	^{68}Ga-FAPI-04	With equal metastatic lesions detected, FAPI PET/CT was comparable to ^{18}F-FDG PET/CT
Xie et al. (*38*)	CR	1	Chromophobe RCC	Metastatic	Restaging	^{68}Ga-FAPI-04	With more metastatic lesions detected, FAPI PET/CT was superior to ^{18}F-FDG PSMA PET/CT
Yang et al. (*39*)	CR	1	Clear cell RCC	Metastatic	Restaging	^{68}Ga-FAPI-04	No comparative MI modality was performed; FAPI PET/CT was valuable, with excellent tumor visualization in primary and metastatic lesions
Testicular cancer: Kaplan et al. (*36*)	CR	1	Mixed germ cell tumor	Metastatic	Restaging	^{68}Ga-FAPI-04	With equal metastatic lesions detected, FAPI PET/CT was superior to ^{18}F-FDG PET/CT; metastatic lesions were more clearly visualized on FAPI PET/CT

---

*Abnormal uptake was observed in intracranial lesion, though metastatic disease was undetermined.

CS = case series; NA = data not available; CR = case report; MI = molecular imaging.

Extracted data of included studies on methodology, patient population, and molecular imaging findings.

review, along with the overall low quality of studies, preclude definitive conclusions regarding its value in staging both local and metastatic disease. Nevertheless, this comprehensive review offers valuable insights for future research.

It is evident that research on FAPI PET/CT imaging is extremely limited and lacks high-level data. However, in contrast to genitourinary malignancies, for which such data are lacking, research on the diagnostic value of FAPI PET/CT has significantly advanced in other types of malignancies (*46–52*). Particularly, FAPI PET/CT has displayed significant potential in gastrointestinal malignancies such as colorectal, gastric, pancreatic, and liver cancers, as well as in lung cancer. Its superior performance compared with ^{18}F-FDG PET/CT in identifying primary tumors, local recurrences, lymph node involvement, and diverse metastatic lesions highlights its value in clinical management within these oncologic domains. In contrast, its management impact in genitourinary malignancies is yet to be determined. As research continues, it is worth noting that ongoing trials, as registered on ClinicalTrials.gov, are also extending their investigations to encompass a broader spectrum of malignancies, such as oral, breast, ovarian, prostate, and bladder cancers. These ongoing investigations are poised to provide a more comprehensive understanding of the diagnostic capabilities of FAPI PET/CT, bridging the gap in research within the genitourinary domain and enhancing the broader landscape of its applications in oncology as a whole.

Similar to its application in these other malignancies, FAPI PET/CT has demonstrated potential advantages and disadvantages in genitourinary malignancies (*19,33,53–55*). One reported advantage of FAPI PET/CT in genitourinary malignancies is its ability to achieve a high TBR, facilitating excellent tumor visualization, precise delineation, and accurate localization of metastatic disease. Particularly advantageous is the minimal accumulation of FAPI radiotracers in the abdomen and intestinal tract, improving detection of metastatic disease in these regions (i.e., peritoneal metastases) (*33,43,54–58*). FAPI radiotracers, however, come in various forms (*58*). Although their biodistribution is generally comparable, variations can be observed in physiologic uptake and tumor-to-blood ratios, among others. Head-to-head comparisons between different FAPI radiotracers are currently still lacking, highlighting the need for further research in this area. Challenges generally associated with all FAPI radiotracers relate to urinary excretion, a characteristic shared with ^{18}F-FDG and certain PSMA radiotracers. This excretion hampers the visualization of primary tumors in the bladder and upper urinary tract (*30,56,57,59*). Nevertheless, a promising aspect of FAPI radiotracers is their rapid and high tumoral tracer uptake, often detectable within 10 min after tracer administration (*33*). This rapid and intense FAPI uptake suggests a potential solution: enabling early PET image acquisition even before urinary excretion has occurred, addressing the challenge posed by urinary activity (*33*).

Comparing FAPI PET/CT with PSMA and ^{18}F-FDG PET/CT in genitourinary malignancies provides significant insights. Unlike ^{18}F-FDG, both PSMA and FAPI specifically target overexpressed molecules in malignancies. FAPI PET/CT's distinctive feature of avoiding metabolic activity assessment potentially enhances visualization in challenging cases, such as cerebral metastases of RCC, and may enable differentiation of reactive from metastatic lymph nodes (*25,30,39,60*), unlike ^{18}F-FDG PET/CT. However, FAPI PET/CT exhibited varying diagnostic value compared with PSMA PET/CT across the included reports, indicating potential dependence on the varying FAP expression in PCa (*37,61*). FAP expression significantly increases with disease progression, reaching its lowest detection in benign and treatment-naïve patients (*37*). This indicates a potentially greater diagnostic value of FAPI PET/CT in more advanced disease stages. Moreover, FAPI PET/CT demonstrated radiotracer uptake in both local and metastatic lesions of PSMA-negative PCa patients, suggesting its potential as an alternative diagnostic tool in this specific subset (*26,37,40,42*). However, we also found that FAPI PET/CT is not devoid of false-positive findings. Although FAP overexpression is common in malignancies, it can also be present during extracellular matrix remodeling, wound healing, and other benign conditions, such as arthritis, fibrosis, and ischemic heart tissue after a myocardial infarction (*15,31*), as well as atherosclerosis, autoimmune disease, and metabolic diseases. Given FAP's role in tissue remodeling and expression on activated fibroblasts of scarring tissue, FAP expression is related to diseases of uncontrolled scarring (fibrosis). FAP has been reported elevated in fibrotic conditions involving the liver, lung, and colon (e.g., cirrhosis, idiopathic pulmonary fibrosis, keloid formation, Crohn disease). Hence, false negatives and false positives remain possible with FAPI PET/CT; however, their rates cannot be reliably assessed in this review because of the limited number of patients and lack of histopathologic confirmation.

FAPI PET/CT has shown promising initial results in genitourinary malignancies; however, a comprehensive assessment of the full spectrum of these malignancies was not achieved. This systematic review did not encompass research on specific rare cancers, including mucinous urachal adenocarcinoma, urethral carcinoma, and penile squamous cell carcinoma. Studies on the application of FAPI PET/CT within these rare genitourinary malignancies were either not identified or ineligible for inclusion. Noteworthy findings concerning the application of FAPI PET/CT in penile squamous cell carcinoma, however, have been reported in a conference abstract by Eismann et al. (*62*), who reported the successful identification of all histopathologically confirmed lymph node metastases by FAPI PET/CT. Interestingly, in half of their patients, focal uptake of FAPI was observed in primary lesions, whereas in the remaining half, visualization of primary lesions was hindered by increased urinary activity—a pattern consistent with previous observations (*30,56,57*). Refined imaging protocols (i.e., omission of furosemide and micturition before the scan) might improve the visualization of primary lesions, although these results are still awaited (*62*).

Signifying substantial promise in diagnostics, targeting of FAP offers not only diagnostic potential but also the prospect of theranostic applications. The high TBR and long retention allow for potential therapeutic use by labeling FAPI with α- or β-emitting isotopes, yielding a potent therapeutic agent (*63*). Currently, early-stage clinical exploration focuses primarily on assessing the feasibility, biodistribution, and dosimetry of FAPI radioligand therapy in various malignancies, demonstrating good tolerability and acceptable side effects (*64*). Although data on FAPI radioligand therapy in genitourinary malignancies are limited, there is growing recognition of its potential benefits. This is particularly notable for specific patients exhibiting inadequate responses to current management options or for individuals for whom existing therapeutic alternatives are unsuitable because of factors such as insignificant PSMA expression (*28,30,33–35,40–42*).

Because of the novelty of this imaging modality, our review is constrained by the retrospective nature of all included studies, predominantly consisting of case reports, case series, and retrospective cohort studies. Consequently, inherent limitations such as selection bias and publication bias are present. The studies we incorporated displayed a significant or unclear risk of bias and lacked a standardized approach to reporting outcomes. Moreover, because of the lack of histopathologic confirmation or follow-up imaging, FAPI PET/CT findings have yet to be validated. Furthermore, the overall number of patients investigated was small, and significant heterogeneity was observed across disease types, clinical settings, and FAPI PET/CT (i.e., radiotracer use and acquisition techniques), making it impossible to draw any conclusion or make any statement on the sensitivity of FAPI PET/CT. These findings underscore the limitations of the current body of research and emphasize the imperative for meticulous and comprehensive exploration and documentation of this imaging modality in the context of genitourinary malignancies.

CONCLUSION

This systematic review synthesizes the existing evidence regarding the diagnostic value of FAPI PET/CT in various genitourinary malignancies, emphasizing the limited availability and low quality of data. Current preliminary research hints at the potential of FAPI PET/CT to effectively visualize both local and metastatic disease in selected patients with various genitourinary malignancies. However, given the scarcity of comprehensive data, the use of FAPI PET/CT seems most appropriate for experimental settings until its potential in clinical practice is established.

DISCLOSURE

No potential conflict of interest relevant to this article was reported.

KEY POINTS

QUESTION: What is the current evidence regarding the diagnostic value of FAPI PET/CT for genitourinary malignancies?

PERTINENT FINDINGS: This systematic review, emphasizing the limited availability and low quality of data, hints at the potential of FAPI PET/CT to effectively visualize both local and metastatic disease in patients with various genitourinary malignancies. Notably, FAPI PET/CT shows potential in distinguishing between reactive and metastatic lymph nodes and in visualizing local and metastatic disease in patients with PSMA-negative tumors.

IMPLICATIONS FOR PATIENT CARE: Metastatic screening using FAPI PET/CT could potentially aid in more accurate staging of genitourinary malignancies and thereby optimize treatment planning and patient outcomes.

REFERENCES

1. Mottet N, van den Bergh RCN, Briers E, et al. EAU-EANM-ESTRO-ESUR-SIOG guidelines on prostate cancer: 2020 update. Part 1: screening, diagnosis, and local treatment with curative intent. *Eur Urol.* 2021;79:243–262.
2. Witjes JA, Bruins HM, Cathomas R, et al. European Association of Urology Guidelines on muscle-invasive and metastatic bladder cancer: summary of the 2020 guidelines. *Eur Urol.* 2021;79:82–104.
3. Brouwer OR, Albersen M, Parnham A, et al. European Association of Urology-American Society of Clinical Oncology collaborative guideline on penile cancer: 2023 update. *Eur Urol.* 2023;83:548–560.
4. Ljungberg B, Albiges L, Abu-Ghanem Y, et al. European Association of Urology guidelines on renal cell carcinoma: the 2022 update. *Eur Urol.* 2022;82:399–410.
5. Patrikidou A, Cazzaniga W, Berney D, et al. European Association of Urology guidelines on testicular cancer: 2023 update. *Eur Urol.* 2023;84:289–301.
6. Rouprêt M, Seisen T, Birtle AJ, et al. European Association of Urology guidelines on upper urinary tract urothelial carcinoma: 2023 update. *Eur Urol.* 2023;84:49–64.
7. Hofman MS, Lawrentschuk N, Francis RJ, et al. Prostate-specific membrane antigen PET-CT in patients with high-risk prostate cancer before curative-intent surgery or radiotherapy (proPSMA): a prospective, randomised, multicentre study. *Lancet.* 2020;395:1208–1216.
8. Richters A, van Ginkel N, Meijer RP, et al. Staging fluorodeoxyglucose positron emission tomography/computed tomography for muscle-invasive bladder cancer: a nationwide population-based study. *BJU Int.* 2023;132:420–427.
9. Ottenhof SR, Djajadiningrat RS, Versleijen MWJ, et al. F-18 fluorodeoxyglucose positron emission tomography with computed tomography has high diagnostic value for pelvic and distant staging in patients with high-risk penile carcinoma. *Eur Urol Focus.* 2022;8:98–104.
10. Einerhand SMH, Zuur LG, Wondergem MJ, et al. The implementation of FDG PET/CT for staging bladder cancer: changes in the detection and characteristics of occult nodal metastases at upfront radical cystectomy? *J Clin Med.* 2023;12:3367.
11. Leijte JA, Graafland NM, Valdés Olmos RA, et al. Prospective evaluation of hybrid ^{18}F-fluorodeoxyglucose positron emission tomography/computed tomography in staging clinically node-negative patients with penile carcinoma. *BJU Int.* 2009;104:640–644.
12. Jansen BHE, Bodar YJL, Zwezerijnen GJC, et al. Pelvic lymph-node staging with ^{18}F-DCFPyL PET/CT prior to extended pelvic lymph-node dissection in primary prostate cancer: the SALT trial. *Eur J Nucl Med Mol Imaging.* 2021;48:509–520.
13. Valkenburg KC, de Groot AE, Pienta KJ. Targeting the tumour stroma to improve cancer therapy. *Nat Rev Clin Oncol.* 2018;15:366–381.
14. Mueller MM, Fusenig NE. Friends or foes: bipolar effects of the tumour stroma in cancer. *Nat Rev Cancer.* 2004;4:839–849.
15. Dendl K, Koerber SA, Kratochwil C, et al. FAP and FAPI-PET/CT in malignant and non-malignant diseases: a perfect symbiosis? *Cancers (Basel).* 2021;13:4946.
16. Costa A, Kieffer Y, Scholer-Dahirel A, et al. Fibroblast heterogeneity and immunosuppressive environment in human breast cancer. *Cancer Cell.* 2018;33:463–479.e10.
17. Jansen K, Heirbaut L, Cheng JD, et al. Selective inhibitors of fibroblast activation protein (FAP) with a (4-quinolinoyl)-glycyl-2-cyanopyrrolidine scaffold. *ACS Med Chem Lett.* 2013;4:491–496.
18. Lindner T, Loktev A, Giesel F, et al. Targeting of activated fibroblasts for imaging and therapy. *EJNMMI Radiopharm Chem.* 2019;4:16.
19. Kratochwil C, Flechsig P, Lindner T, et al. ^{68}Ga-FAPI PET/CT: tracer uptake in 28 different kinds of cancer. *J Nucl Med.* 2019;60:801–805.
20. Giesel FL, Kratochwil C, Lindner T, et al. ^{68}Ga-FAPI PET/CT: biodistribution and preliminary dosimetry estimate of 2 DOTA-containing FAP-targeting agents in patients with various cancers. *J Nucl Med.* 2019;60:386–392.
21. Moher D, Liberati A, Tetzlaff J, et al. Preferred reporting items for systematic reviews and meta-analyses: the PRISMA statement. *PLoS Med.* 2009;6:e1000097.
22. Abdel-Wahab N, Lopez-Olivo MA, Pinto-Patarroyo GP, Suarez-Almazor ME. Systematic review of case reports of antiphospholipid syndrome following infection. *Lupus.* 2016;25:1520–1531.
23. Cai J, Xu W, Meng T, et al. Visualization of intermetastatic heterogeneity in mixed neuroendocrine carcinoma-acinar adenocarcinoma of the prostate by ^{68}Ga-PSMA, ^{68}Ga-FAPI, and ^{18}F-FDG PET/CT. *Clin Nucl Med.* 2023;48:743–745.
24. Dong A, Yang B, Bai Y, et al. ^{68}Ga-FAPI-04 PET/CT in a small sarcomatoid renal cell carcinoma with widespread metastases. *Clin Nucl Med.* 2023;48:457–459.
25. Novruzov E, Dendl K, Ndlovu H, et al. Head-to-head intra-individual comparison of [^{68}Ga]-FAPI and [^{18}F]-FDG PET/CT in patients with bladder cancer. *Mol Imaging Biol.* 2022;24:651–658.
26. Pang Y, Meng T, Xu W, et al. ^{68}Ga-FAPI PET/CT detected non-PSMA/FDG-avid primary tumor in de novo metastatic prostate cancer. *Clin Nucl Med.* 2022;47:1108–1111.
27. Pang Y, Wei J, Shang Q, et al. ^{68}Ga-fibroblast activation protein inhibitor, a promising radiopharmaceutical in PET/CT to detect the primary and metastatic lesions of chromophobe renal cell carcinoma. *Clin Nucl Med.* 2021;46:177–179.
28. Tatar G, Baykal Koca S, Sevindir İ, Ergül N, Çermik TF. ^{68}Ga-FAPI-04 PET/CT in primary signet ring-like cell carcinoma of prostate with bone metastases. *Clin Nucl Med.* 2023;48:e188–e189.
29. Tatar G, Ergül N, Baloğlu MC, et al. ^{68}Ga-PSMA and ^{68}Ga-FAPI-04 PET/CT findings with ^{18}F-FDG PET/CT in a patient with recurrent prostate cancer. *Clin Nucl Med.* 2023;48:e135–e137.
30. Unterrainer LM, Lindner S, Eismann L, et al. Feasibility of [^{68}Ga]Ga-FAPI-46 PET/CT for detection of nodal and hematogenous spread in high-grade urothelial carcinoma. *Eur J Nucl Med Mol Imaging.* 2022;49:3571–3580.
31. Xu T, Zhao Y, Ding H, et al. [^{68}Ga]Ga-DOTA-FAPI-04 PET/CT imaging in a case of prostate cancer with shoulder arthritis. *Eur J Nucl Med Mol Imaging.* 2021;48:1254–1255.
32. Yang T, Zhu R, Guo Z, et al. Solitary fibrous tumor of the prostate shown on FAPI PET/CT. *Clin Nucl Med.* 2023;48:530–531.

33. Dendl K, Finck R, Giesel FL, et al. FAP imaging in rare cancer entities: first clinical experience in a broad spectrum of malignancies. *Eur J Nucl Med Mol Imaging.* 2022;49:721–731.
34. Aryana K, Manafi-Farid R, Amini H, et al. ^{68}Ga-FAPI-46 PET/CT in a metastatic castration-resistant prostate cancer patient with low PSMA expression. *Clin Nucl Med.* 2022;47:972–973.
35. Civan C, Isik EG, Karadogan S, et al. ^{68}Ga-FAPI-04 PET/CT and ^{18}F-FDG PET/CT in metastatic papillary renal cell cancer. *Clin Nucl Med.* 2023;48:e223–e224.
36. Kaplan İ, Can C, Güzel Y, et al. ^{68}GA-FAPI-04 PET/CT versus ^{18}F-FDG PET/CT in imaging of malignant mixed germ cell testicular tumor. *Clin Nucl Med.* 2023;48: e195–e197.
37. Kesch C, Yirga L, Dendl K, et al. High fibroblast-activation-protein expression in castration-resistant prostate cancer supports the use of FAPI-molecular theranostics. *Eur J Nucl Med Mol Imaging.* 2021;49:385–389.
38. Xie F, Fu L, Zhou W. Superiority of ^{68}Ga-FAPI-04 in delineation of soft tissue and liver metastases in chromophobe renal cell carcinoma for restaging. *Clin Nucl Med.* 2022;47:e758–e759.
39. Yang J, Dong A, Zuo C. ^{68}Ga-FAPI-04 PET/CT in solitary choroid plexus metastasis from renal cell carcinoma. *Clin Nucl Med.* 2022;47:885–887.
40. Kessel K, Seifert R, Weckesser M, et al. Prostate-specific membrane antigen and fibroblast activation protein distribution in prostate cancer: preliminary data on immunohistochemistry and PET imaging. *Ann Nucl Med.* 2022;36:293–301.
41. Isik EG, Has-Simsek D, Sanli O, et al. Fibroblast activation protein-targeted PET imaging of metastatic castration-resistant prostate cancer compared with ^{68}Ga-PSMA and ^{18}F-FDG PET/CT. *Clin Nucl Med.* 2022;47:e54–e55.
42. Khreish F, Rosar F, Kratochwil C, et al. Positive FAPI-PET/CT in a metastatic castration-resistant prostate cancer patient with PSMA-negative/FDG-positive disease. *Eur J Nucl Med Mol Imaging.* 2020;47:2040–2041.
43. Viergever BJ, Strating E, Lam M, et al. Fibroblast activation protein identifies progressive bladder cancer and allows peritoneal metastasis detection by ^{68}Ga-FAPI PET/CT imaging. Europe PMC website. https://europepmc.org/article/ppr/ppr686003. Published July 3, 2023. Accessed March 27, 2024.
44. Voskuilen CS, van Gennep EJ, Einerhand SMH, et al. Staging ^{18}F-fluorodeoxyglucose positron emission tomography/computed tomography changes treatment recommendation in invasive bladder cancer. *Eur Urol Oncol.* 2022;5:366–369.
45. Voskuilen CS, Schweitzer D, Jensen JB, et al. Diagnostic value of ^{18}F-fluorodeoxyglucose positron emission tomography with computed tomography for lymph node staging in patients with upper tract urothelial carcinoma. *Eur Urol Oncol.* 2020;3:73–79.
46. Yang L, Xu S, Cheng L, et al. [^{18}F] AlF-NOTA-FAPI-04 PET/CT as a promising tool for imaging fibroblast activation protein in gastrointestinal system cancers: a prospective investigation of comparative analysis with ^{18}F-FDG. *Eur J Nucl Med Mol Imaging.* 2023;50:4051–4063.
47. Wu M, Wang Y, Yang Q, et al. Comparison of baseline ^{68}Ga-FAPI and ^{18}F-FDG PET/CT for prediction of response and clinical outcome in patients with unresectable hepatocellular carcinoma treated with PD-1 inhibitor and lenvatinib. *J Nucl Med.* 2023;64:1532–1539.
48. Rasinski P, Af Burén S, Holstensson M, et al. Tumor characterization by [^{68}Ga]FAPI-46 PET/CT can improve treatment selection for pancreatic cancer patients: an interim analysis of a prospective clinical trial. *J Nucl Med.* 2023;64: 1232–1237.
49. Wei Y, Ma L, Li P, et al. FAPI compared with FDG PET/CT for diagnosis of primary and metastatic lung cancer. *Radiology.* 2023;308:e222785.
50. Xu W, Cai J, Peng T, et al. Fibroblast activation protein-targeted PET/CT with ^{18}F-fibroblast activation protein inhibitor-74 for evaluation of gastrointestinal cancer: comparison with ^{18}F-FDG PET/CT. *J Nucl Med.* 2024;65:40–51.
51. Wu C, Zhang X, Zeng Y, et al. [^{18}F]FAPI-42 PET/CT versus [^{18}F]FDG PET/CT for imaging of recurrent or metastatic gastrointestinal stromal tumors. *Eur J Nucl Med Mol Imaging.* 2022;50:194–204.
52. Qin C, Song Y, Gai Y, et al. Gallium-68-labeled fibroblast activation protein inhibitor PET in gastrointestinal cancer: insights into diagnosis and management. *Eur J Nucl Med Mol Imaging.* 2022;49:4228–4240.
53. Giesel FL, Kratochwil C, Schlittenhardt J, et al. Head-to-head intra-individual comparison of biodistribution and tumor uptake of ^{68}Ga-FAPI and ^{18}F-FDG PET/CT in cancer patients. *Eur J Nucl Med Mol Imaging.* 2021;48:4377–4385.
54. Chen H, Pang Y, Wu J, et al. Comparison of [^{68}Ga]Ga-DOTA-FAPI-04 and [^{18}F]FDG PET/CT for the diagnosis of primary and metastatic lesions in patients with various types of cancer. *Eur J Nucl Med Mol Imaging.* 2020;47: 1820–1832.
55. Chen H, Zhao L, Ruan D, et al. Usefulness of [^{68}Ga]Ga-DOTA-FAPI-04 PET/CT in patients presenting with inconclusive [^{18}F]FDG PET/CT findings. *Eur J Nucl Med Mol Imaging.* 2021;48:73–86.
56. Giesel FL, Adeberg S, Syed M, et al. FAPI-74 PET/CT using either ^{18}F-AlF or cold-kit ^{68}Ga labeling: biodistribution, radiation dosimetry, and tumor delineation in lung cancer patients. *J Nucl Med.* 2021;62:201–207.
57. Kou Y, Jiang X, Yao Y, et al. Physiological tracer distribution and benign lesion incidental uptake of Al^{18}F-NOTA-FAPI-04 on PET/CT imaging. *Nucl Med Commun.* 2022;43:847–854.
58. Sharma P, Singh SS, Gayana S. Fibroblast activation protein inhibitor PET/CT: a promising molecular imaging tool. *Clin Nucl Med.* 2021;46:e141–e150.
59. Mertens LS, Bruin NM, Vegt E, et al. Catheter-assisted ^{18}F-FDG-PET/CT imaging of primary bladder cancer: a prospective study. *Nucl Med Commun.* 2012;33: 1195–1201.
60. Shang Q, Zhao L, Pang Y, et al. ^{68}Ga-FAPI PET/CT distinguishes the reactive lymph nodes from tumor metastatic lymph nodes in a patient with nasopharyngeal carcinoma. *Clin Nucl Med.* 2022;47:367–368.
61. Hintz HM, Gallant JP, Vander Griend DJ, et al. Imaging fibroblast activation protein alpha improves diagnosis of metastatic prostate cancer with positron emission tomography. *Clin Cancer Res.* 2020;26:4882–4891.
62. Eismann L, Toms J, Holzgreve A, et al. [^{68}Ga]Ga-FAPI-46 PET/CT prior to surgery in squamous penile cancer: preliminary clinical results [abstract]. *J Urol.* 2023;209(suppl 4):e685–e686.
63. Calais J, Mona CE. Will FAPI PET/CT replace FDG PET/CT in the next decade? Point: an important diagnostic, phenotypic, and biomarker role. *AJR.* 2021;216: 305–306.
64. Baum RP, Schuchardt C, Singh A, et al. Feasibility, biodistribution, and preliminary dosimetry in peptide-targeted radionuclide therapy of diverse adenocarcinomas using ^{177}Lu-FAP-2286: first-in-humans results. *J Nucl Med.* 2022;63:415–423.

Prospective Comparison of ^{68}Ga-NeoB and ^{68}Ga-PSMA-R2 PET/MRI in Patients with Biochemically Recurrent Prostate Cancer

Heying Duan[1], Hong Song[1], Guido A. Davidzon[1], Farshad Moradi[1], Tie Liang[1], Andreas Loening[2], Shreyas Vasanawala[2], and Andrei Iagaru[1]

[1]*Division of Nuclear Medicine and Molecular Imaging, Department of Radiology, Stanford University, Stanford, California; and* [2]*Division of Body MRI, Department of Radiology, Stanford University, Stanford, California*

Prostate-specific membrane antigen (PSMA) and gastrin-releasing peptide receptors are both overexpressed in prostate cancer (PC) but may provide complementary information.^{68}Ga-PSMA-R2 and ^{68}Ga-NeoB (DOTA-*p*-aminomethylaniline-diglycolic acid-DPhe-Gln-Trp-Ala-Val-Gly-His-NH-CH[CH_2-$CH(CH_3)_2$]$_2$) are novel PET radiopharmaceuticals that were developed for theranostic use. In this phase II imaging study, we assessed the feasibility, safety, and diagnostic performance of ^{68}Ga-NeoB and ^{68}Ga-PSMA-R2 PET/MRI for detection of biochemically recurrent PC. **Methods:** We prospectively enrolled 27 men with suspected biochemically recurrent PC after initial treatment but noncontributory conventional imaging results (negative or equivocal findings on MRI, CT, and/or bone scan). Participants underwent ^{68}Ga-NeoB and ^{68}Ga-PSMA-R2 PET/MRI within 2 wk in noncontrolled order. The SUV_{max} of putative PC lesions was measured and compared with a composite reference standard (histopathology, follow-up imaging, prostate-specific antigen change). The SUV_{max} and SUV_{mean} of background organs were measured. Vital signs were recorded before injection of the radiopharmaceuticals and after the scans. Adverse events were recorded up to 72 h after each scan. **Results:** The prostate-specific antigen level at enrollment was 3.5 ± 3.9 ng/mL (range, 0.3–13.5 ng/mL). ^{68}Ga-NeoB PET/MRI detected 31 lesions in 18 patients (66.7%), whereas ^{68}Ga-PSMA-R2 identified 20 lesions in 15 participants (55.6%). ^{68}Ga-NeoB PET/MRI showed higher sensitivity (85.7% vs. 71.4%), accuracy (88.9% vs. 77.8%), and negative predictive value (66.7% vs. 50.0%) than ^{68}Ga-PSMA-R2, whereas specificity and positive predictive value were equally high (100.0% for both). In 6 patients, ^{68}Ga-NeoB PET/MRI identified 14 lesions that were false-negative on ^{68}Ga-PSMA-R2 PET/MRI. The mean lesion SUV_{max} was 6.6 ± 3.2 (range, 2.9–13.2) for ^{68}Ga-NeoB and 4.4 ± 1.5 (range, 2.6–8.8) for ^{68}Ga-PSMA-R2 ($P = 0.019$). Overall lower uptake was noted in tumors and background organs for ^{68}Ga-PSMA-R2. There were no significant changes in vital signs before and after the scans. No adverse events were reported in the 72-h period after scans. **Conclusion:** ^{68}Ga-NeoB and ^{68}Ga-PSMA-R2 are safe for diagnostic imaging. ^{68}Ga-NeoB PET/MRI showed better diagnostic performance than ^{68}Ga-PSMA-R2. ^{68}Ga-PSMA-R2 showed overall lower uptake, equally in background organs and tumors, and might therefore not be an ideal theranostic compound. Further evaluation in larger cohorts is needed to confirm our preliminary data.

Key Words: prostate cancer; GRPR; PSMA; ^{68}Ga-NeoB; ^{68}Ga-PSMA-R2

J Nucl Med 2024; 65:897–903
DOI: 10.2967/jnumed.123.267017

Prostate cancer (PC) remains the most diagnosed cancer in men and the second leading cause of cancer-related death among men in the United States (*1,2*). Initial treatment with curative intent for localized disease includes radical prostatectomy and radiation therapy. Nonetheless, in up to 53% of patients, biochemically recurrent (BCR) disease will develop within 10 y after definitive treatment (*3,4*). Early identification and localization of recurrent disease is critical to guide treatment and improve patient outcomes. U.S. and European guidelines (*4,5*) recommend conventional imaging consisting of CT, MRI, and bone scintigraphy at the time of biochemical recurrence; however, these modalities all bear certain limitations, particularly at low prostate-specific antigen (PSA) levels and in low-volume disease (*6,7*). Therefore, the most recent National Comprehensive Cancer Network guideline includes prostate-specific membrane antigen (PSMA) PET.

Molecular imaging using radiopharmaceuticals that target tumor-specific cell receptors has revolutionized oncologic imaging. PSMA is overexpressed in 90% of PC cells (*8*). ^{68}Ga-PSMA-R2 is a novel, urea-based ligand of PSMA that was developed for theranostic use (*9*). Preliminary results of the phase I/II PROfind trial (NCT03490032) showed a favorable biodistribution with rapid blood clearance (*10*). Gastrin-releasing peptide receptors (GRPRs) are also overexpressed in PC (*11*) and BCR PC (*12–14*). ^{68}Ga-NeoB (DOTA-*p*-aminomethylaniline-diglycolic acid-DPhe-Gln-Trp-Ala-Val-Gly-His-NH-CH[CH_2-$CH(CH_3)_2$]$_2$), formerly known as ^{68}Ga-NeoBOMB1, is a DOTA-coupled GRPR antagonist and was also developed for theranostic use. In preclinical and clinical studies, ^{68}Ga-NeoB showed an appropriate pharmacokinetic profile with high receptor affinity, high in vivo stability, and a high tumor-to-background ratio as well as a favorable safety profile (*15,16*). PSMA- and GRPR-targeting radiotracers have been reported as complementary to each other (*14,17,18*), however, more studies are needed to understand their respective expression patterns.

In this prospective phase II study we aimed to assess the feasibility, safety, and diagnostic performance of ^{68}Ga-NeoB and ^{68}Ga-PSMA-R2 PET/MRI in patients with BCR PC and prior negative or equivocal findings on conventional imaging.

MATERIALS AND METHODS

Participants

Informed oral and written consent was obtained from each participant before enrollment. The participants who were enrolled had noncontributory conventional imaging findings (negative or equivocal

---

Received Nov. 5, 2023; revision accepted Mar. 15, 2024.

For correspondence or reprints, contact Andrei Iagaru (aiagaru@stanford.edu).

findings on CT, MRI, and/or bone scan; Supplemental Table 1; supplemental materials are available at http://jnm.snmjournals.org) but clinically suspected BCR disease of histopathologically proven PC or PSA persistence after initial treatment (radical prostatectomy or radiation therapy). BCR disease was defined as a PSA level of at least 0.2 ng/mL with a second confirmatory PSA measurement of at least 0.2 ng/mL after radical prostatectomy (*19*), or a PSA level of at least 2 ng/mL above the nadir after radiation therapy (*20*). Further inclusion criteria were an age of at least 18 y and a Karnofsky performance status of at least 50. Exclusion criteria were an inability to lie supine for the duration of the scan or metallic implants. Participants were scheduled to undergo either ^{68}Ga-NeoB followed by ^{68}Ga-PSMA-R2 PET/MRI within 2 wk or vice versa. This prospective phase II study was approved by the local institutional review board and registered on ClinicalTrials.gov (NCT03698370). Patients' vital signs (heart rate, blood pressure, respiratory rate, pulse oximetry) were collected before injection of the radiopharmaceuticals and after completion of the imaging study. Adverse events were recorded for up to 72 h after each scan and were categorized according to the Common Terminology Criteria for Adverse Events, version 5, as part of the safety analysis.

PET/MRI Protocol

Imaging was performed using a 3-tesla time-of-flight–enabled PET/MRI scanner (Signa; GE Healthcare), as previously described (*17,21*). Simultaneous PET/MRI was acquired from vertex to mid thighs with an acquisition time of 4 min per bed position. Additional dedicated 20-min pelvic images were acquired.

Image Analysis

PET/MRI data were anonymized and then reviewed and analyzed by 2 nuclear medicine physicians independently and in random order. The readers were not aware of any clinical information other than that patients were scanned for BCR PC. Any focal uptake of ^{68}Ga-NeoB or ^{68}Ga-PSMA-R2 in putative sites of disease with an SUV_{max} above the background level and not associated with a physiologic accumulation was recorded as suggestive of PC. A region of interest was drawn over suspected lesions to measure SUV_{max}. SUV_{max} and SUV_{mean} were measured in a volume of interest of 1 cm^3 for the blood pool (aortic arch), liver (segment VIII), and background organs bone (femur head) and gluteal muscle, as well as the pancreas (body) for ^{68}Ga-NeoB and parotid gland for ^{68}Ga-PSMA-R2 PET. Tumor-to-background ratios were calculated to quantify uptake in tumors relative to background organs. MRI was used for anatomic and lesion correlation.

Lesion Validation

A composite reference standard was used for lesion validation: histopathology whenever available, subsequent imaging within 2 mo, and posttreatment PSA within 2 mo. A continuous decrease or rise in PSA identified at 2 time points with a minimum interval of 4 wk was considered a treatment response or progressive disease.

^{68}Ga-NeoB or ^{68}Ga-PSMA-R2 PET/MRI was considered true-positive when at least one of the following criteria was met: histopathologic confirmation; progression in number of uptake sites or uptake intensity on follow-up molecular imaging with respective increase in PSA; confirmation on follow-up conventional imaging (CT or MRI); or disappearance or reduction of disease on molecular or conventional imaging after focal or systemic treatment, with a respective decrease in PSA.

^{68}Ga-NeoB or ^{68}Ga-PSMA-R2 PET/MRI was considered true-negative when there was no evidence of disease on follow-up conventional or molecular imaging or when PSA was stable or decreased.

Participants without any composite reference standard correlation were excluded from the analyses.

Statistical Analysis

Statistical analyses were performed using Stata 17.0 (StataCorp LP). Patients' clinical and imaging characteristics are reported as descriptive statistics, given as mean ± SD, range, and percentage. Sensitivity, specificity, accuracy, positive predictive value, and negative predictive value are given in percentage with 95% CI. A post hoc analysis was performed to stratify the detection rates of ^{68}Ga-NeoB and ^{68}Ga-PSMA-R2 PET/MRI by PSA value ($<$0.5 ng/mL; 0.5 to $<$1.0 ng/mL; 1.0 to $<$2.0 ng/mL; 2.0 to $<$5.0 ng/mL; $\geq$5.0 ng/mL) and PSA doubling time ($<$3 mo; 3 to $<$6 mo; 6 to $<$9 mo; 9 to $<$12 mo; $\geq$12 mo). A 2-sample proportion test was used to compare the SUV_{max} of positive and negative lesions and to compare the SUV_{max} and SUV_{mean} of background organs. A *P* value of less than 0.05 was considered significant.

RESULTS

Patient Characteristics

Twenty-seven men, 67.8 ± 8.8 y old (range, 49.0–82.0 y), were prospectively enrolled. The PSA level at the time of the scan was 3.5 ± 3.9 ng/mL (range, 0.3–13.5 ng/mL). The PSA doubling time was 6.4 ± 5.2 mo (range, 1.2–22.4 mo); 3 participants showed PSA persistence after radical prostatectomy. The image acquisition started at 49.7 ± 7.2 min (range, 43–77 min) after administration

TABLE 1
Patients' Characteristics

Characteristic	Data
Patients	27 (100%)
Age (y)	67.8 ± 8.8 (49.0–82.0)
Initial treatment	Radical prostatectomy: 25/27 (93%); radiation therapy: 2/27 (7%)
Initial Gleason score	7: 18/27 (66.7%); 8: 1/27 (3.7%); 9: 8/27 (29.6%)
PSA (ng/mL)	3.5 ± 3.9 (0.3–13.5)
PSA doubling time (mo)	6.4 ± 5.2 (1.2–22.4)*
^{68}Ga-NeoB	
Injected activity (MBq)	198.1 ± 25.5 (145.1–245.6)
Uptake time (min)	49.7 ± 7.2 (43–77)
Duration of PET/MRI (min)	58.5 ± 4.5 (42–66)
Delay to pelvic PET/MRI (min)	35.9 ± 5.4 (21–46)
^{68}Ga-PSMA-R2	
Injected activity (MBq)	186.1 ± 29.2 (108.4–228.6)
Uptake time (min)	47.0 ± 2.8 (44–55)
Duration of PET/MRI (min)	58.1 ± 3.2 (52–65)
Delay to pelvic PET/MRI (min)	37.4 ± 4.5 (29–54)
Time between scans (d)	11.0 ± 15.2 (1–72)

*Three patients showed PSA persistence after radical prostatectomy.

Qualitative data are number and percentage; continuous data are mean ± SD, followed by range in parentheses.

TABLE 2
SUV of Lesions and Organs for ^{68}Ga-NeoB and ^{68}Ga-PSMA-R2 PET/MRI and Their Significance

Location	^{68}Ga-NeoB	^{68}Ga-PSMA-R2	*P*
SUV$_{max}$			
Lesion	6.6 ± 3.2 (2.9–13.2)	4.4 ± 1.5 (2.6–8.8)	0.019*
Tumor-to-background ratio	11.4 ± 5.1 (4.9–23.2)	7.4 ± 3.1 (3.4–15.1)	0.013*
Blood pool	2.7 ± 0.5 (1.7–3.9)	3.0 ± 0.5 (2.0–4.1)	0.011*
Liver	5.5 ± 1.0 (3.3–8.0)	2.4 ± 0.7 (1.4–5.2)	0.000*
Bone	0.4 ± 0.2 (0.1–1.2)	0.3 ± 0.1 (0.1–0.7)	0.075
Gluteal muscle	0.6 ± 0.1 (0.4–0.9)	0.6 ± 0.1 (0.5–0.8)	0.149
Pancreas	44.1 ± 14.9 (21.2–88.0)	—	
Parotid gland	—	3.3 ± 0.8 (2.0–5.2)	
SUV$_{mean}$			
Blood pool	2.1 ± 0.4 (1.2–3.0)	2.4 ± 0.5 (1.6–3.7)	0.026*
Liver	4.6 ± 0.9 (2.7–6.4)	1.6 ± 0.4 (1.0–2.6)	0.000*
Bone	0.2 ± 0.1 (0.1–0.5)	0.2 ± 0.1 (0.1–0.6)	0.106
Gluteal muscle	0.4 ± 0.1 (0.1–0.5)	0.4 ± 0.1 (0.3–0.6)	0.263
Pancreas	30.4 ± 13.2 (10.5–78.9)	—	
Parotid gland	—	2.8 ± 0.8 (1.6–5.3)	

*Statistically significant.
Data are mean ± SD, followed by range in parentheses.

of 198.1 ± 25.5 MBq (range, 145.1–245.6 MBq) of ^{68}Ga-NeoB and at 47.0 ± 2.8 min (range, 44–55 min) after administration of 186.1 ± 29.2 MBq (range, 108.4–228.6 MBq) of ^{68}Ga-PSMA-R2. Pelvic images were acquired after a delay of 35.9 ± 5.4 min (range, 21–46 min) for ^{68}Ga-NeoB and 37.4 ± 4.5 min (range, 29–54 min) for ^{68}Ga-PSMA-R2. The PET/MRI scans were performed 11.0 ± 15.2 d (range, 1–72 d) apart. Because the study was conducted during the coronavirus disease 2019 pandemic, the 2-wk interval between scans could not always be maintained. In 4 participants, scans were performed 21, 35, 40, and 72 d apart. The participants' characteristics are summarized in Table 1.

Patients were followed for 24.8 ± 3.9 mo (range, 17.2–31.7 mo) after the PET/MRI scans. Subsequent patient management included radiation therapy in 6 (22%) of the 27 participants; radiation therapy in combination with androgen deprivation therapy in 7 (26%), and androgen deprivation therapy in 8 (30%). Six participants (22%) were under active surveillance.

Safety

There were no significant changes in heart rate, blood pressure, respiratory rate, or pulse oximetry before and after injection of either radiopharmaceutical, nor were there any grade 1 or worse adverse events reported in the 24- to 72-h period after image studies for either radiopharmaceutical.

Lesion Analyses

Lesion validation was follow-up imaging for 18 (63%) of the 27 patients, PSA change in 7 (26%), and histology in 3 (11%).

TABLE 3
Diagnostic Performance of ^{68}Ga-NeoB and ^{68}Ga-PSMA-R2 PET/MRI in Detection of Recurrent PC on Per-Patient Basis

Index	^{68}Ga-NeoB	^{68}Ga-PSMA-R2
True positive (*n*)	18	15
True negative (*n*)	6	6
False positive (*n*)	0	0
False negative (*n*)	3	6
Sensitivity (%)	85.7 (63.7–97.0)	71.4 (47.8–88.7)
Specificity (%)	100.0 (54.1–100.0)	100.0 (54.1–100.0)
Accuracy (%)	88.9 (70.8–97.6)	77.8 (57.7–91.4)
Positive predictive value (%)	100.0 (81.5–100.0)	100.0 (78.2–100.0)
Negative predictive value (%)	66.7 (29.9–92.5)	50.0 (21.1–78.9)

Data in parentheses are 95% CI.

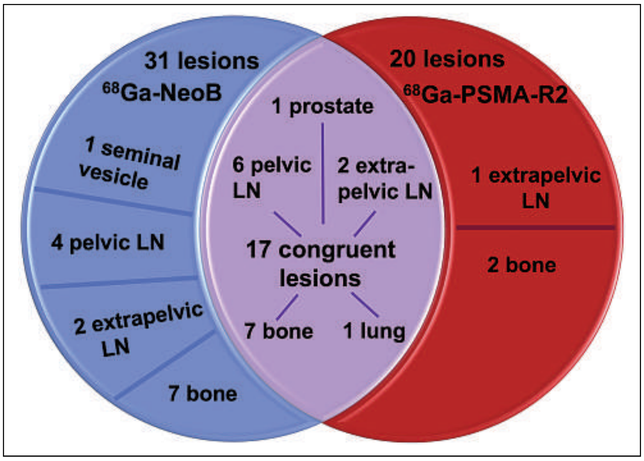

FIGURE 1. Venn diagram of lesion detected on ^{68}Ga-NeoB and ^{68}Ga-PSMA-R2 PET/MRI, by site. All identified lesions were true-positive.

^{68}Ga-NeoB PET/MRI

^{68}Ga-NeoB PET/MRI identified 31 lesions in 18 (66.7%) of the 27 patients: 1 (3.2%) of these 31 lesions was local recurrence in the prostate, 1 (3.2%) was in the seminal vesicle, 10 (32.3%) were in pelvic lymph nodes, 4 (13%) were in extrapelvic lymph nodes, 14 (45.2%) were in bone, and 1 (3.2%) was a lung metastasis. On a per-lesion level, all were confirmed true-positive using the reference standard (Supplemental Table 2). The mean lesion SUV$_{\text{max}}$ was 6.6 ± 3.2 (range, 2.9–13.2), with a mean tumor-to-background ratio of 11.4 ± 5.1 (range, 4.9–23.2). All SUVs are summarized in Table 2 and Supplemental Table 3. The PSA levels of patients with positive ^{68}Ga-NeoB findings were significantly higher than those of patients with negative ^{68}Ga-NeoB findings (3.9 ± 4.1 ng/mL [range, 0.3–13.5 ng/mL] vs. 1.2 ± 1.9 ng/mL [range, 0.3–6.5 ng/mL], $P = 0.034$). ^{68}Ga-NeoB PET/MRI was negative in 9 (33.3%) of 27 participants, with 3 (33.3%) of these 9 being false-negative (Table 3).

^{68}Ga-PSMA-R2 PET/MRI

^{68}Ga-PSMA-R2 PET/MRI showed 20 lesions in 15 (55.6%) of 27 patients: 1 (5%) of these 20 lesions was local recurrence in the prostate, 6 (30%) were pelvic nodal, 2 (10%) were extrapelvic nodal, 10 (50%) were bone, and 1 (5%) was a lung metastasis. All ^{68}Ga-PSMA-R2 PET–positive patients were confirmed true-positive using the reference standard (Supplemental Table 2). Mean lesion SUV$_{\text{max}}$ was 4.4 ± 1.5 (range, 2.6–8.8), with a mean tumor-to-background ratio of 7.4 ± 3.1 (range, 3.4–15.1). All SUVs are summarized in Table 2 and Supplemental Table 3. The PSA levels for patients with positive ^{68}Ga-PSMA-R2 findings were not different from those of patients with negative ^{68}Ga-PSMA-R2 findings (3.9 ± 4.1 ng/mL [range, 0.3–13.5 ng/mL] vs. 1.9 ± 2.8 ng/mL [range, 0.3–9.3 ng/mL], $P = 0.156$). ^{68}Ga-PSMA-R2 PET/MRI was negative in 12 (44.4%) patients but false-negative in 6 (50%) of these 12 (Table 3).

^{68}Ga-NeoB PET/MRI Versus ^{68}Ga-PSMA-R2 PET/MRI

The detection rate for ^{68}Ga-NeoB PET/MRI was not significantly higher than that of ^{68}Ga-PSMA-R2 on either a per-patient basis (66.7% vs. 55.6%, $P = 0.083$) or a per-lesion basis (31 vs. 20 lesions, $P = 0.141$). There were 17 true-positive lesions that were detected by both ^{68}Ga-NeoB and ^{68}Ga-PSMA-R2 PET/MRI (Fig. 1). There were also 17 lesions that were incongruent between the 2 radiopharmaceuticals: 14 (82%) of 17 were positive on ^{68}Ga-NeoB and negative on ^{68}Ga-PSMA-R2 PET/MRI (Fig. 2), correlating to 1 seminal vesicle lesion, 4 pelvic and 2 extrapelvic nodal lesions, and 7 bone metastases, which were true-positive according to the standard reference; 3 (18%) of 17 lesions were positive on ^{68}Ga-PSMA-R2 but negative on ^{68}Ga-NeoB PET/MRI, correlating to 1 extrapelvic lymph node and 2 bone metastases (Fig. 3). These lesions were also true-positive according to the reference standard but did not change overall detection rates on a per-patient level. Three participants were negative on both scans, as verified by the reference standard, and were subsequently under active surveillance.

^{68}Ga-NeoB PET/MRI had a higher sensitivity (85.7% vs. 71.4%), accuracy (88.9% vs. 77.8%), and negative predictive value (66.7% vs. 50.0%) than did ^{68}Ga-PSMA-R2, whereas specificity and positive predictive value were equally high (100.0% for both) (Table 3). In 6 patients, ^{68}Ga-NeoB detected 14 lesions that were false-negative on ^{68}Ga-PSMA-R2 PET/MRI (Figs. 4 and 5).

The lesional SUV$_{\text{max}}$ and tumor-to-background ratio of ^{68}Ga-NeoB were significantly higher than those of ^{68}Ga-PSMA-R2 ($P = 0.019$ and 0.013, respectively). All background tissues, gluteal muscle and bone, showed similar tracer uptake, whereas blood pool activity and liver uptake were significantly lower for ^{68}Ga-PSMA-R2.

PSA

Differences in PSA values between positive ^{68}Ga-NeoB and ^{68}Ga-PSMA-R2 PET/MRI findings, as well as between negative

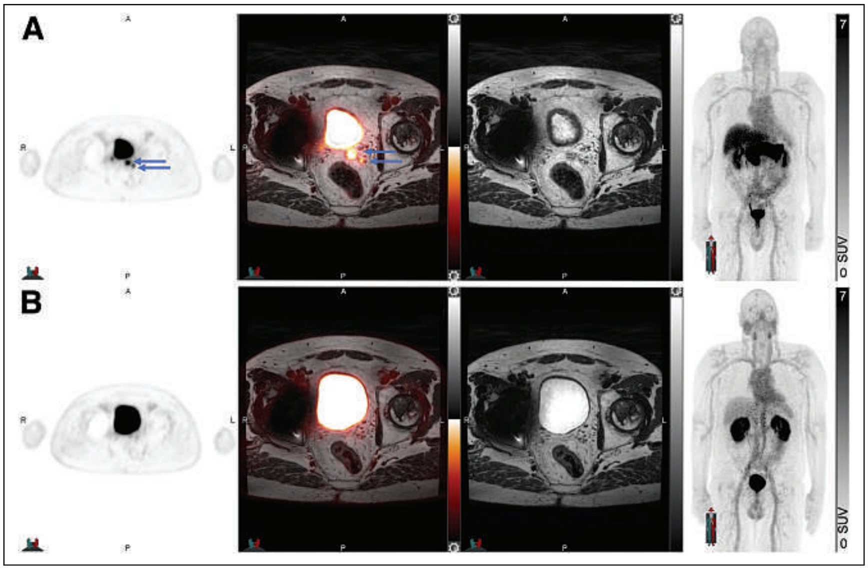

FIGURE 2. 71-y-old man with BCR PC after radical prostatectomy (from left to right: axial PET, axial PET/MRI, axial MRI, and maximum-intensity projection). PSA at time of PET/MRI was 3.63 ng/mL. ^{68}Ga-NeoB PET/MRI (top row) shows intense uptake in left seminal vesicle and pelvic lymph node (arrows), whereas ^{68}Ga-PSMA-R2 PET/MRI (bottom row) was negative. Lesions were confirmed on follow-up ^{18}F-DCFPyL PET/CT and by PSA decrease as treatment response after initiation of androgen deprivation therapy. ^{68}Ga-NeoB and ^{68}Ga-PSMA-R2 PET/MRI were performed within 2 d.

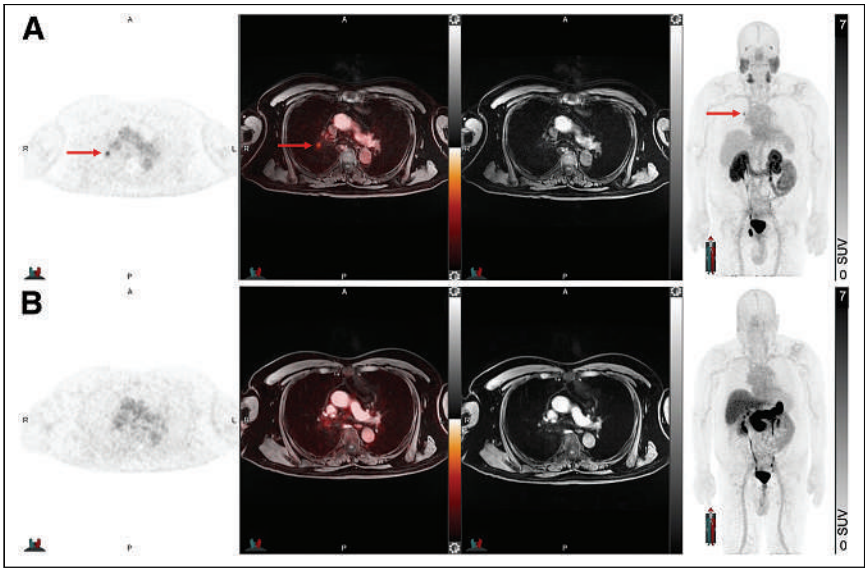

FIGURE 3. 76-y-old man with BCR PC after radical prostatectomy (from left to right: axial PET, axial PET/MRI, axial MRI, and maximum-intensity projection). PSA at time of PET/MRI was 8.26 ng/mL. ^{68}Ga-PSMA-R2 PET/MRI (top row) shows uptake in right hilar lymph node (arrows), whereas ^{68}Ga-NeoB (bottom row) was negative. Additional lung metastasis (not shown) was seen with both radiopharmaceuticals. Patient was treated with androgen deprivation therapy, with consecutive PSA decrease. PET/MRI scans were performed within 14 d.

^{68}Ga-NeoB and ^{68}Ga-PSMA-R2 PET/MRI findings, were not significant ($P = 0.156$ and $P = 0.550$, respectively).

The detection rates of ^{68}Ga-NeoB PET/MRI per PSA range ($<$0.5 ng/mL, 0.5 to $<$1.0 ng/mL, 1.0 to $<$2.0 ng/mL, 2.0 to $<$5.0 ng/mL, and $\geq$5.0 ng/mL) were higher than those of ^{68}Ga-PSMA-R2 (33.3%, 50.0%, 66.7%, 100.0%, and 85.7% vs. 16.7%, 50.0%, 66.7%, 80.0%, and 71.4%, respectively) (Fig. 6) as well as per PSA doubling time ($<$3 mo, 3 to $<$6 mo, 6 to $<$9 mo, 9 to $<$12 mo, and $\geq$12 mo: 100.0%, 66.7%, 50.0%, 33.3%, and 33.3% vs. 85.7%, 50.0%, 50.0%, 0.0%, and 33.3%, respectively) (Supplemental Table 4).

DISCUSSION

Here, we assessed the feasibility, safety, and diagnostic performance of ^{68}Ga-NeoB and ^{68}Ga-PSMA-R2 at the time of BCR PC when findings on conventional imaging were negative or equivocal. This specific cohort is clinically challenging to manage because treatment can be given only blindly as radiation therapy to the pelvis or systemic androgen deprivation therapy. Both ^{68}Ga-NeoB and ^{68}Ga-PSMA-R2 were feasible and safe for diagnostic imaging. ^{68}Ga-NeoB PET/MRI showed higher detection rates on a per-patient and per-lesion basis than did ^{68}Ga-PSMA-R2, along with a higher sensitivity, accuracy, and negative predictive value. Specificity and positive predictive value were equally high.

Both radiopharmaceuticals, ^{68}Ga-PSMA-R2 and ^{68}Ga-NeoB, were developed in an effort to advance compounds that are suitable for theranostics. Preliminary results for ^{68}Ga-PSMA-R2 showed a low absorbed radiation dose in the salivary glands, indicating its potential for therapeutic use (*10*). Our results corroborate low uptake of ^{68}Ga-PSMA-R2 in the parotid gland. However, lower tumor uptake was also noted as expressed by the low tumor-to-background ratio. In comparison to ^{68}Ga-PSMA-11 and ^{18}F-DCFPyL, lower uptake in the salivary glands, liver, and tumor lesions was seen with ^{68}Ga-PSMA-R2 (*22*). This suggests that ^{68}Ga-PSMA-R2 might not be an ideal theranostic compound. The overall diminished uptake may have contributed to lower detection rates and sensitivity. The sensitivity of 71% for ^{68}Ga-PSMA-R2 lies on the lower end of the published pooled sensitivity of 70%–95.5% for ^{68}Ga-PSMA-11 and ^{18}F-DCFPyL but is comparable to the detection rate of 61% from the PROfind trial for ^{68}Ga-PSMA-R2 PET/CT in 18 patients with BCR PC. Specificity compares with the published pooled specificity of 70%–100% (*23*–*27*). However, in the selected cohort of BCR PC patients with prior negative or equivocal conventional imaging results, a lower detection rate of 57.6% was reported for ^{18}F-DCFPyL (*23*).

^{68}Ga-NeoB has an improved, higher affinity for the GRPR, on which it acts as an antagonist. The highest physiologic uptake was

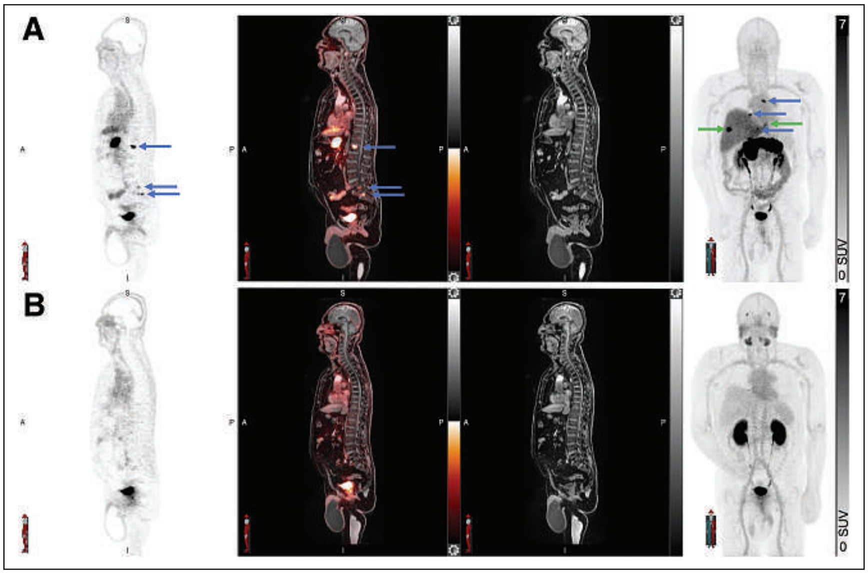

FIGURE 4. 67-y-old man with BCR PC after radiation therapy (from left to right: sagittal PET, sagittal PET/MRI, sagittal MRI, and maximum-intensity projection). PSA at time of PET/MRI was 9.3 ng/mL. ^{68}Ga-NeoB PET/MRI (top row) shows multiple foci in skeleton: T10, T12, L1, sacrum, and right eighth rib, as well as additional left paratracheal lymph node metastasis (blue arrows). High uptake is seen in gallbladder (physiologic as means of hepatobiliary excretion) and in distal esophagus (green arrows). ^{68}Ga-PSMA-R2 PET/MRI (bottom row) was negative. Lesions were confirmed on subsequent ^{18}F-DCFPyL PET/CT and by PSA decrease after combined treatment of radiation therapy and androgen deprivation therapy. PET/MRI scans were performed within 7 d.

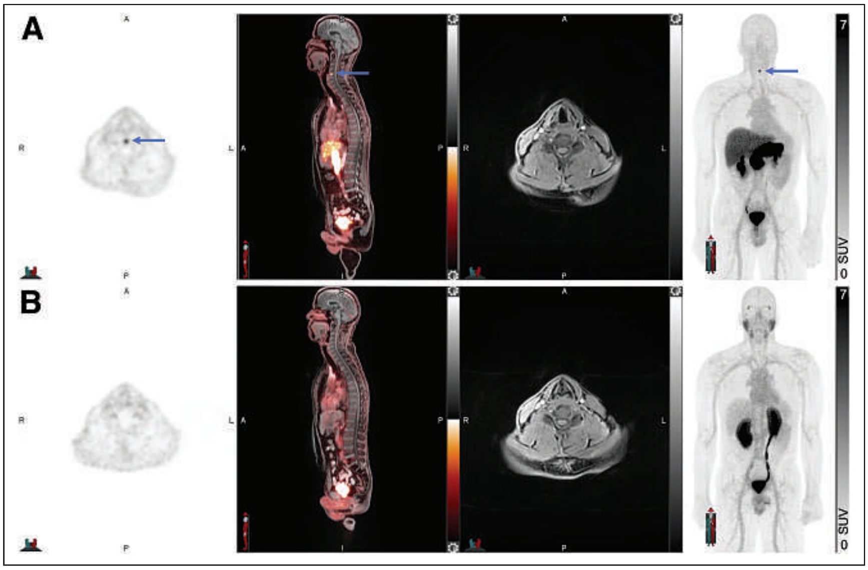

FIGURE 5. 55-y-old man with BCR PC after radical prostatectomy (from left to right: axial PET, sagittal PET/MRI, axial MRI, and maximum-intensity projection). PSA at time of PET/MRI was 0.3 ng/mL. ^{68}Ga-NeoB PET/MRI (top row) shows intense uptake in sixth cervical vertebra (arrows), whereas ^{68}Ga-PSMA-R2 (bottom row) was negative despite 40 d between scans (no treatment initiated). Lesion was confirmed on subsequent ^{18}F-DCFPyL PET/CT and by PSA decrease after androgen deprivation therapy.

seen in the pancreas, followed by the liver, as is consistent with data from a phase I/IIa study evaluating ^{68}Ga-NeoBOMB1 in gastrointestinal stromal tumors (*28*). Compared with ^{68}Ga-RM2, the currently most investigated GRPR antagonist, tumor uptake of ^{68}Ga-NeoB was comparable, whereas physiologic uptake was lower in the pancreas and higher in the liver (*29*). The sensitivity of 86% for ^{68}Ga-NeoB is higher than what has been reported for ^{68}Ga-RM2 PET/MRI at the time of biochemical recurrence, with detection rates ranging from 70% to 75% in larger cohorts (*14,17,30*) and 63% for ^{68}Ga-RM2 PET/CT in a small cohort of 16 patients with BCR PC and noncontributory ^{18}F-fluoroethylcholine PET/CT results (*12*). Taken together, these findings indicate that ^{68}Ga-NeoB seems to be a suitable theranostic compound.

The detection rate of ^{68}Ga-NeoB, stratified by the respective PSA ranges, was higher at low PSA levels. The detection rates increased with increasing PSA for both GRPR- and PSMA-targeting radiopharmaceuticals. In line with the overall lower detection rate of ^{68}Ga-PSMA-R2, the rates of localizing disease by PSA range and PSA doubling time was also lower than seen in previously published data for ^{18}F-DCFPyL (*31*) and ^{68}Ga-PSMA-11 (*14*). Despite comparable sensitivity, ^{68}Ga-NeoB showed slightly lower detection rates by PSA range than did previous findings for ^{68}Ga-RM2 PET/MRI (*14*).

There are some limitations to this study: first, there were 4 participants for whom the scans could not be performed within the 2-wk frame because of restrictions caused by the coronavirus disease 2019 pandemic. However, despite the long interval between scans, no progression was seen. The imaging studies that were performed 21 and 35 d apart showed identical results, whereas the scans with a 72-d interval were both negative; the results of the PET/MRI scan that was performed 40 d after an initial positive scan were found to be false-negative. A second limitation was the lack of histopathology as a gold standard for all participants. The setback of using a composite reference is that it may lead to higher specificity calculations because there may not be a significant number of false-negative results. Nonetheless, obtaining histopathology for all potential metastatic lesions is technically unfeasible and impractical and is not ethical; treating physicians often rely on posttreatment PSA changes. A third limitation was the small patient cohort, although not uncommon for a phase II trial.

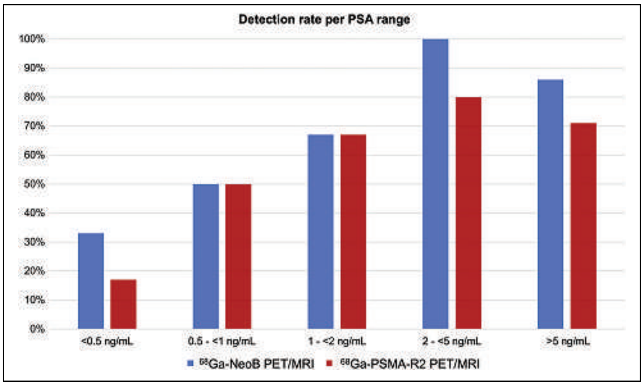

FIGURE 6. Detection rates of ^{68}Ga-NeoB and ^{68}Ga-PSMA-R2 PET/MRI per PSA range. ^{68}Ga-NeoB performed better overall, particularly at low PSA level.

CONCLUSION

^{68}Ga-NeoB and ^{68}Ga-PSMA-R2 are safe radiopharmaceuticals. In the setting of BCR PC with prior noncontributory conventional imaging results, ^{68}Ga-NeoB performed better than ^{68}Ga-PSMA-R2 PET/MRI in localizing recurrent disease, particularly at low PSA levels. The overall lower uptake of ^{68}Ga-PSMA-R2 in tumors and background organs might limit its use as a theranostic compound. These results need to be confirmed in larger studies.

KEY POINTS

QUESTION: What is the diagnostic performance of the GRPR-targeting ^{68}Ga-NeoB and the PSMA-targeting ^{68}Ga-PSMA-R2 for localization of recurrent PC?

PERTINENT FINDINGS: In this prospective phase II study, ^{68}Ga-NeoB PET/MRI demonstrated higher sensitivity (86% vs. 71%), accuracy (89% vs. 78%), and negative predictive value (67% vs. 50%) than ^{68}Ga-PSMA-R2 PET/MRI. Specificity and positive predictive value were equally high for both radiopharmaceuticals (100%). ^{68}Ga-NeoB PET/MRI detected 14 lesions in 6 patients whose imaging results were false-negative with ^{68}Ga-PSMA-R2.

IMPLICATIONS FOR PATIENT CARE: Both ^{68}Ga-NeoB and ^{68}Ga-PSMA-R2 are safe radiopharmaceuticals that have shown high and accurate diagnostic performance in evaluating biochemical recurrence of PC. Interrogating 2 targets, PSMA and GRPR, at a stage when the disease is characterized by high tumor heterogeneity may ultimately allow for personalized medicine.

DISCLOSURE

The study was supported by Novartis. Andrei Iagaru reports institutional research support and consulting fees from Novartis. No other potential conflict of interest relevant to this article was reported.

REFERENCES

1. Siegel RL, Miller KD, Wagle NS, Jemal A. Cancer statistics, 2023. *CA Cancer J Clin.* 2023;73:17–48.
2. Sung H, Ferlay J, Siegel RL, et al. Global Cancer Statistics 2020: GLOBOCAN Estimates of Incidence and Mortality Worldwide for 36 Cancers in 185 Countries. *CA Cancer J Clin.* 2021;71:209–249.
3. Isbarn H, Wanner M, Salomon G, et al. Long-term data on the survival of patients with prostate cancer treated with radical prostatectomy in the prostate-specific antigen era. *BJU Int.* 2010;106:37–43.
4. Cornford P, van den Bergh RCN, Briers E, et al. EAU-EANM-ESTRO-ESUR-SIOG Guidelines on Prostate Cancer. Part II-2020 Update: Treatment of Relapsing and Metastatic Prostate Cancer. *Eur Urol.* 2021;79:263–282.
5. Lowrance W, Dreicer R, Jarrard DF, et al. Updates to Advanced Prostate Cancer: AUA/SUO Guideline (2023). *J Urol.* 2023;209:1082–1090.
6. Hövels AM, Heesakkers RA, Adang EM, et al. The diagnostic accuracy of CT and MRI in the staging of pelvic lymph nodes in patients with prostate cancer: a meta-analysis. *Clin Radiol.* 2008;63:387–395.
7. Jilg CA, Schultze-Seemann W, Drendel V, et al. Detection of lymph node metastasis in patients with nodal prostate cancer relapse using (18)F/(11)C-choline positron emission tomography/computerized tomography. *J Urol.* 2014;192:103–110.
8. Morigi JJ, Stricker PD, van Leeuwen PJ, et al. Prospective Comparison of ^{18}F-Fluoromethylcholine Versus ^{68}Ga-PSMA PET/CT in Prostate Cancer Patients Who Have Rising PSA After Curative Treatment and Are Being Considered for Targeted Therapy. *J Nucl Med.* 2015;56:1185–1190.
9. Muzio V, Ravasi L, Sacchetti L, et al. Biodistribution of PSMA-R2 in mice bearing prostate cancer [abstract]. *Eur J Nucl Med Mol Imaging.* 2019;46(suppl):S1–S952.
10. Lindenberg ML, Hope T, Lin F, et al. Safety and tolerability of ^{68}Ga-PSMA-R2 as an imaging agent in patients with biochemical recurrence or metastatic prostate cancer [abstract]. *J Nucl Med.* 2021;62(suppl 1):1319.
11. Reubi JC, Wenger S, Schmuckli-Maurer J, Schaer J-C, Gugger M. Bombesin receptor subtypes in human cancers: detection with the universal radioligand ^{125}I-[d-TYR6, β-ALA11, PHE13, NLE14] bombesin(6–14). *Clin Cancer Res.* 2002;8:1139–1146.
12. Wieser G, Popp I, Christian Rischke H, et al. Diagnosis of recurrent prostate cancer with PET/CT imaging using the gastrin-releasing peptide receptor antagonist ^{68}Ga-RM2: preliminary results in patients with negative or inconclusive [^{18}F]fluoroethylcholine-PET/CT. *Eur J Nucl Med Mol Imaging.* 2017;44:1463–1472.
13. Minamimoto R, Sonni I, Hancock S, et al. Prospective evaluation of ^{68}Ga-RM2 PET/MRI in patients with biochemical recurrence of prostate cancer and negative conventional imaging. *J Nucl Med.* 2018;59:803–808.
14. Baratto L, Song H, Duan H, et al. PSMA- and GRPR-targeted PET: results from 50 patients with biochemically recurrent prostate cancer. *J Nucl Med.* 2021;62:1545–1549.
15. Dalm SU, Bakker IL, de Blois E, et al. ^{68}Ga/^{177}Lu-NeoBOMB1, a novel radiolabeled GRPR antagonist for theranostic use in oncology. *J Nucl Med.* 2017;58:293–299.
16. Nock BA, Kaloudi A, Lymperis E, et al. Theranostic perspectives in prostate cancer with the gastrin-releasing peptide receptor antagonist NeoBOMB1: preclinical and first clinical results. *J Nucl Med.* 2017;58:75–80.
17. Minamimoto R, Sonni I, Hancock S, et al. Prospective evaluation of ^{68}Ga-RM2 PET/MRI in patients with biochemical recurrence of prostate cancer and negative findings on conventional imaging. *J Nucl Med.* 2018;59:803–808.
18. Touijer KA, Michaud L, Alvarez HAV, et al. Prospective study of the radiolabeled GRPR antagonist BAY86-7548 for positron emission tomography/computed tomography imaging of newly diagnosed prostate cancer. *Eur Urol Oncol.* 2019;2:166–173.
19. Cookson MS, Aus G, Burnett AL, et al. Variation in the definition of biochemical recurrence in patients treated for localized prostate cancer: the American Urological Association Prostate Guidelines for Localized Prostate Cancer Update Panel report and recommendations for a standard in the reporting of surgical outcomes. *J Urol.* 2007;177:540–545.
20. Roach M III, Hanks G, Thames H Jr, et al. Defining biochemical failure following radiotherapy with or without hormonal therapy in men with clinically localized prostate cancer: recommendations of the RTOG-ASTRO Phoenix Consensus Conference. *Int J Radiat Oncol Biol Phys.* 2006;65:965–974.
21. Minamimoto R, Hancock S, Schneider B, et al. Pilot comparison of ^{68}Ga-RM2 PET and ^{68}Ga-PSMA-11 PET in patients with biochemically recurrent prostate cancer. *J Nucl Med.* 2016;57:557–562.
22. Dietlein M, Kobe C, Kuhnert G, et al. Comparison of [^{18}F]DCFPyL and [^{68}Ga]Ga-PSMA-HBED-CC for PSMA-PET imaging in patients with relapsed prostate cancer. *Mol Imaging Biol.* 2015;17:575–584.
23. Pienta KJ, Gorin MA, Rowe SP, et al. A phase 2/3 prospective multicenter study of the diagnostic accuracy of prostate specific membrane antigen PET/CT with ^{18}F-DCFPyL in prostate cancer patients (OSPREY). *J Urol.* 2021;206:52–61.
24. Perera M, Papa N, Roberts M, et al. Gallium-68 prostate-specific membrane antigen positron emission tomography in advanced prostate cancer: updated diagnostic utility, sensitivity, specificity, and distribution of prostate-specific membrane antigen-avid lesions—a systematic review and meta-analysis. *Eur Urol.* 2020;77:403–417.
25. Fourquet A, Lahmi L, Rusu T, et al. Restaging the biochemical recurrence of prostate cancer with [^{68}Ga]Ga-PSMA-11 PET/CT: diagnostic performance and impact on patient disease management. *Cancers (Basel).* 2021;13:1594.
26. Afshar-Oromieh A, Avtzi E, Giesel FL, et al. The diagnostic value of PET/CT imaging with the ^{68}Ga-labelled PSMA ligand HBED-CC in the diagnosis of recurrent prostate cancer. *Eur J Nucl Med Mol Imaging.* 2015;42:197–209.
27. Martinez J, Subramanian K, Margolis D, et al. ^{68}Ga-PSMA-HBED-CC PET/MRI is superior to multiparametric magnetic resonance imaging in men with biochemical recurrent prostate cancer: a prospective single-institutional study. *Transl Oncol.* 2022;15:101242.
28. Gruber L, Jimenez-Franco LD, Decristoforo C, et al. MITIGATE-NeoBOMB1, a phase I/IIa study to evaluate safety, pharmacokinetics, and preliminary imaging of ^{68}Ga-NeoBOMB1, a gastrin-releasing peptide receptor antagonist, in GIST patients. *J Nucl Med.* 2020;61:1749–1755.
29. Baratto L, Duan H, Laudicella R, et al. Physiological ^{68}Ga-RM2 uptake in patients with biochemically recurrent prostate cancer: an atlas of semi-quantitative measurements. *Eur J Nucl Med Mol Imaging.* 2020;47:115–122.
30. Ghezzo S, Mapelli P, Samanes Gajate AM, et al. Diagnostic accuracy of fully hybrid [^{68}Ga]Ga-PSMA-11 PET/MRI and [^{68}Ga]Ga-RM2 PET/MRI in patients with biochemically recurrent prostate cancer: a prospective single-center phase II clinical trial. *Eur J Nucl Med Mol Imaging.* 2024;51:907–918.
31. Song H, Harrison C, Duan H, et al. Prospective evaluation of ^{18}F-DCFPyL PET/CT in biochemically recurrent prostate cancer in an academic center: a focus on disease localization and changes in management. *J Nucl Med.* 2020;61:546–551.

Development of a Visually Calculated SUV_{mean} (HIT Score) on Screening PSMA PET/CT to Predict Treatment Response to ^{177}Lu-PSMA Therapy: Comparison with Quantitative SUV_{mean} and Patient Outcomes

Mina Swiha[1,2], Nathan Papa[3], Zahra Sabahi[1], Narjess Ayati[1,3,4], Nikeith John[1,4], Sarennya Pathmanandavel[1], Megan Crumbaker[1,3–5], Sherrington Li[1], Shikha Agrawal[1], Maria Ayers[1], Adam Hickey[1], Shikha Sharma[1], Andrew Nguyen[1,4], and Louise Emmett[1,3,4]

[1]Department of Theranostics and Nuclear Medicine, St. Vincent's Hospital, Sydney, New South Wales, Australia; [2]Nuclear Medicine Division, Department of Medical Imaging, University of Western Ontario, London, Ontario, Canada; [3]Garvan Institute of Medical Research, Sydney, New South Wales, Australia; [4]St. Vincent's Clinical School, University of New South Wales, Sydney, New South Wales, Australia; and [5]Kinghorn Cancer Centre, St. Vincent's Hospital, Sydney, New South Wales, Australia

^{177}Lu-PSMA therapy is an effective treatment in patients with metastatic castration-resistant prostate cancer. SUV_{mean} is a valuable screening biomarker to assess the suitability for ^{177}Lu-PSMA therapy but requires quantitative software. This study aims to develop a simple, clinically applicable prostate-specific membrane antigen PET/CT score that encompasses the elements of SUV_{mean} without requiring additional quantification. **Methods:** Datasets from ethics-approved trials of patients with metastatic castration-resistant prostate cancer after androgen receptor signaling inhibition and taxane chemotherapy (or unfit for taxane), who were treated with ^{177}Lu-PSMA-617 and ^{177}Lu-PSMA I&T with a pretreatment screening with ^{68}Ga-PSMA-11 PET/CT, and clinical outcome data, including a prostate-specific antigen (PSA) 50% response rate (PSA50), PSA progression-free survival (PSA-PFS), and overall survival (OS), were included. The screening ^{68}Ga-PSMA-11 PET/CT of all participants was analyzed both semiquantitatively and visually. Semiquantitative analysis was used to derive the SUV_{mean}. Visual analysis of the ^{68}Ga-PSMA-11 PET/CT images involved a binary visual heterogeneity assessment (homogeneous or heterogeneous), allocating a tumor SUV_{max} range (<15, 15–29, 30–49, 50–79, or ≥ 80). A 4-category score incorporating both heterogeneity and intensity of tumors (HIT) was then developed as a combination of heterogeneity and intensity (SUV_{max} range). The SUV_{max} was less than 15 for score 1, 15–79 with heterogeneous intensity for score 2, 15–79 with homogeneous intensity for score 3, and 80 or greater for score 4. This score was evaluated according to clinical outcomes (PSA50, PSA-PFS, and OS) and compared with SUV_{mean}. **Results:** Data from 139 participants were analyzed. In total, 75 (54%) patients achieved a PSA50 with a median PSA-PFS of 5.5 mo (95% CI, 4.1–6.0 mo) and an OS of 13.5 mo (95% CI, 11.1–17.9 mo). SUV_{mean} was associated with PSA50 and survival outcomes when analyzed as a continuous variable or as quartiles. The PSA50 for HIT scores 1–4 was 0%, 39%, 65%, and 76%, respectively. The HIT score was strongly related to PSA-PFS and OS (log-rank test, $P < 0.001$ and $P = 0.002$). The median PSA-PFS for HIT scores 1–4 was 1.0, 4.1, 6.0, and 8.5, respectively, and the median OS was 7.6, 12.0, 18.5, and 16.9 mo, respectively. Cohen κ between readers for the HIT score was 0.71. **Conclusion:** A prostate-specific membrane antigen PET/CT score incorporating HIT derived from tools on a standard PET workstation is comparable with quantitative SUV_{mean} as a prognostic tool following ^{177}Lu-PSMA therapy.

Key Words: SUV_{mean}; prostate cancer; ^{177}Lu-PSMA; PSMA PET/CT

J Nucl Med 2024; 65:904–908
DOI: 10.2967/jnumed.123.267014

Treatment with ^{177}Lu-PSMA-617 improves the overall survival (OS) in men with metastatic castration-resistant prostate cancer (mCRPC) after androgen signaling inhibition and taxane chemotherapy (*1*). ^{177}Lu-PSMA is well tolerated and shows improved quality of life compared with second-line chemotherapy (*2*). Despite this, approximately one third of patients will have upfront treatment resistance or a limited duration of response to ^{177}Lu-PSMA radiopharmaceutical therapy (*3*). Developing imaging biomarkers to better predict response is important to further improve patient outcomes. The TheraP and VISION trials found that semiquantitatively derived SUV_{mean} from prostate-specific membrane antigen (PSMA) PET/CT imaging is predictive of treatment response with ^{177}Lu-PSMA-617 (*4*–*6*). However, deriving SUV_{mean} requires dedicated software programs not currently clinically available. The aim of this study is to develop a reproducible assessment method using standard PET workflow tools that correlates with SUV_{mean} and is predictive of patient outcomes with ^{177}Lu-PSMA.

MATERIALS AND METHODS

Study Population

This study is a retrospective analysis of screening ^{68}Ga-PSMA-11 PET/CT parameters and patient outcomes including prostate-specific membrane (PSA) 50% response rate (PSA50), PSA progression-free survival (PSA-PFS), and OS from 3 previously published clinical trials in men with progressive mCRPC who were undergoing ^{177}Lu-PSMA therapy after at least 1 line of androgen receptor signaling inhibition and 1 line of taxane chemotherapy or who were determined ineligible for taxane chemotherapy (*7*–*9*). The institutional review board of

---

Received Nov. 5, 2023; revision accepted Mar. 15, 2024.

For correspondence or reprints, contact Louise Emmett (louise.emmett@svha.org.au).

St. Vincent's Hospital approved this retrospective study (Human Research Ethics Committee approval number 2022/ETH00924), and the requirement to obtain informed consent was waived.

PSMA PET/CT Acquisition and Visual Analysis

^{68}Ga-PSMA-11 PET/CT imaging was undertaken per institutional or clinical trial protocols before treatment with ^{177}Lu-PSMA. Images were analyzed both visually and semiquantitatively. Visual assessment included evaluation of heterogeneity and tumor intensity relative to parotid and liver avidity on rotating 3-dimensional maximum-intensity-projection images adjusted to the SUV window range (0–15). First, visual analysis was performed by 3 experienced nuclear medicine specialists who were masked to the clinical outcomes. Heterogeneity was a binary score. If at least 80% of all lesions not impacted by partial-volume effects (larger lesions) had similar intensities, this was classified as homogeneous. If more than 20% of larger lesions had variable intensity (inter- or intralesional), this was classified as heterogeneous (Fig. 1). Second, the readers measured the SUV$_{max}$ of the most intense lesions and allocated an SUV$_{max}$ range ($<$15, 15–29, 30–49, 50–79, or $\geq$80). Third, the readers evaluated if the most intense lesions were above the parotid intensity or between the liver and parotid intensities. No patients in whom the highest lesional intensity was below the liver intensity were enrolled. All readers participated in a 30-min training session that involved an explanation of the heterogeneity binary assessment and a consensus read of 20 ^{68}Ga-PSMA-11 PET/CT scans outside the study dataset. The heterogeneity category given by most readers was used for analysis.

PSMA PET/CT Quantitative Analysis

Semiautomated segmentation of baseline ^{68}Ga-PSMA-11 PET/CT was performed using MIM software (LesionID; MIM Software Inc.) and a standardized semiautomated workflow to delineate regions of interest with a minimum SUV$_{max}$ cutoff of 3 and a lesion size of at least 0.5 mm. All lesions identified quantitatively were reviewed by experienced nuclear medicine physicians. Output parameters included SUV$_{mean}$, SUV$_{max}$, and total tumor volume.

Interreader Reliability

After development of the heterogeneity-and-intensity-of-tumors (HIT) score, a full reread of the same dataset was performed by an additional 2 experienced nuclear medicine specialists using HIT scores 1–4 with comparison of Cohen κ between these readers.

Clinical Outcomes

All patients were treated with ^{177}Lu-PSMA until they were no longer clinically benefiting. Clinical outcomes included PSA50, PSA-PFS, and OS. PSA50 was defined as a PSA decline of 50% or more compared with baseline at any time during the treatment. PSA-PFS was defined as the time from treatment initiation to PSA progression or death from any cause. PSA progression was defined as at least a 25% increase in PSA of at least 2.0 ng/mL above nadir per the criteria of the Prostate Cancer Clinical Trials Working Group 3 (*10*). OS was defined as the time from treatment initiation to death from any cause.

Statistical Analysis

The analysis followed 3 main phases. First, SUV$_{mean}$ was confirmed as a predictor of outcomes in the sample by entering it continuously as a restricted cubic spline function with knots at the tertiles into a logistic (for PSA50) or Cox regression (for PSA-PFS and OS) and plotting the results. In the Cox regression, the (near) median value of 8 was set as the reference, and analysis time began on the date of cycle 1. Kaplan–Meier plots were also generated with SUV$_{mean}$ entered as quartiles and log-rank tests used to identify differences in the survival curves. Second, the relation between SUV$_{mean}$ and a combination of SUV$_{max}$ range and visual heterogeneity was examined. Nested linear regression models and the likelihood ratio test were used to assess whether heterogeneity, above the SUV$_{max}$ range alone, added significantly to the model fit predicting SUV$_{mean}$. A scatterplot with locally weighted regression curves of log-transformed SUV$_{mean}$ versus SUV$_{max}$ range, by heterogeneity, was generated to visually guide the creation of the 4-category HIT score. HIT score 1 was derived separately from the scatterplot on the basis of data demonstrating no PSA response in patients with an SUV$_{max}$ less than 15 (*8*). HIT scores 2–4 were derived on the basis of the scatterplot. Score 4 required an SUV$_{max}$ of at least 80 and was derived from the scatterplot as a point above which heterogeneous or homogeneous curves joined with no significant differences between the 2 groups—and with higher treatment responses. Finally, the relation between the 4-category HIT score and outcomes was assessed similarly to quartiles of SUV$_{mean}$. The predictive power of the Cox survival models including the HIT score, the quartiles of SUV$_{mean}$, or the quartiles of SUV$_{max}$ range was quantified with the Somers D statistic. Exploratory analysis assessed the survival outcomes according to tumor intensity relative to parotid intensity with Kaplan–Meier plots and log-rank tests, and interrater agreement of the HIT score was calculated on the basis of image readings by 2 readers once the HIT score had been created. Analysis was performed with Stata/MP version 17.0 (StataCorp LLC), and tests were 2-sided with significance set at less than 0.05.

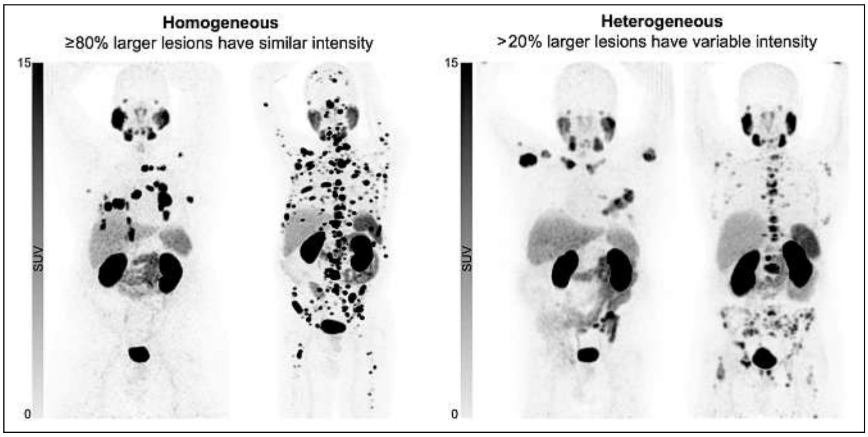

FIGURE 1. Maximum-intensity projection of PSMA PET/CT showing 2 patients with homogeneous PSMA uptake in lesions (left) and 2 patients with heterogeneous PSMA uptake in lesions (right).

RESULTS

Patient Characteristics

In total, 139 patients who had received ^{177}Lu-PSMA-617 or ^{177}Lu-PSMA I&T in two phase 2 clinical trials and a published clinical therapy program between 2016 and 2022 were included in this analysis (Table 1). All patients received a median of 4 doses of 7.5 GBq of ^{177}Lu-PSMA. The overall PSA50 was 54%, the number of PSA-PFS events was 120 with a median PSA-PFS of 5.5 mo (95% CI, 4.1–6.0 mo), and the number of deaths was 82, with a median OS of 13.5 mo (95% CI, 11.1–17.9 mo).

TABLE 1
Patient Characteristics

Characteristic	Value
n	139
Age (y)	69 (64–74)
Time since diagnosis (y)	6 (3–9)
ECOG status	
0–1	122 (88)
2	17 (12)
Baseline PSA (ng/mL)	94 (34–325)
LDH (NR, 120–250 U/L)	245 (216–317)
ALP (NR, 30–110 U/L)	112 (74–203)
Hemoglobin (NR, 130–180 g/L)	118 (106–129)
Previous systemic treatments	
Androgen receptor signaling inhibitors	139 (100)
Docetaxel	125 (90)
Cabazitaxel	88 (63)
Disease volume from PSMA PET/CT	
<20 metastases	49 (35)
≥20 metastases	90 (65)
Sites of disease on PSMA PET/CT	
Bone	133 (96)
Nodal*	72 (52)
Visceral	31 (22)

*Pelvic or distant.

ECOG = Eastern Cooperative Oncology Group; LDH = lactate dehydrogenase; NR = normal range; ALP = alkaline phosphatase.

Quantitative data are number and percentage. Continuous data are median and interquartile range.

SUV_{mean}

The median semiquantitatively derived SUV_{mean} was 8.0 (interquartile range, 6.6–9.9). Increasing SUV_{mean} as a continuous variable demonstrated a strong relationship with a higher probability of PSA50 and lower hazard ratio of PSA-PFS and OS, evidenced by a near-monotonic function with these outcomes (Supplemental Fig. 1; supplemental materials are available at http://jnm.snmjournals.org). When assessed as quartiles, SUV_{mean} significantly predicted PSA-PFS ($P < 0.001$) with borderline significance for OS ($P = 0.051$) (Fig. 2).

HIT Score

The 4-category HIT score was derived from an evaluation of heterogeneity and allocation of an SUV_{max} range. Inclusion of heterogeneity significantly improved the prediction of SUV_{mean} above that of the SUV_{max} range (likelihood ratio test, $P = 0.0041$); hence, both factors were required. On evaluation of the scatterplot and locally weighted regression curves (Fig. 3), in association with results from previous studies, the following categories were devised: score 1 was all patients with an SUV_{max} of less than 15; score 2 included patients defined as having heterogeneous disease visually with an SUV_{max} between 15 and 79; score 3 included patients with visually homogeneous disease and an SUV_{max} between 15 and 79; score 4 included all patients with an SUV_{max} of at least 80 independent of whether the tumor was homogeneous or heterogeneous (Fig. 4). The distribution of the HIT score among the sample was as follows: score 1, $n = 5$ (3.6%); score 2, $n = 54$ (39%); score 3, $n = 63$ (45%); and score 4, $n = 17$ (12%).

HIT-Score Agreement

Following HIT-score development, images were read by 2 readers and a score was assigned. The interrater agreement (Cohen κ) of the HIT score was 0.71 (95% CI, 0.60–0.82), and the percentage agreement was 82%.

HIT Score and Outcomes

The PSA50 for a HIT score of 1–4 was 0% (0/5), 39% (21/54), 65% (41/63), and 76% (13/17), respectively. The HIT score statistically significantly predicted both PFS and OS (log-rank test, $P < 0.001$ and $P = 0.002$, respectively) (Fig. 5). The differences in survival curves between scores 2 and 3 (same SUV_{max} range but heterogeneous vs. homogeneous) were also significant for PFS ($P < 0.001$) and OS ($P = 0.040$). The median PFS (95% CI) for HIT scores 1–4 was 1.0 mo (0.6 mo to not estimable), 4.1 mo (2.9–5.5 mo), 6.0 mo (5.1–9.4 mo), and 8.5 mo (3.3–14.5 mo), respectively. The corresponding median OS (95% CI) was 7.6 mo (5.5 mo to not estimable), 12.0 mo (8.9–17.9 mo), 18.5 mo (12.0–21.6 mo), and 16.9 mo (7.1 mo to not reached). Cox models with a HIT score had predictive power comparable to that of SUV_{mean} quartiles for PSA-PFS (Somers D of 0.25 vs. 0.27) and OS (Somers D of 0.15 vs. 0.16) and exceeded those for SUV_{max} range quartiles (0.17 for PFS and 0.12 for OS).

Physiologic Activity and Heterogeneity

Most patients had lesion intensity that was greater than parotid intensity, $n = 126$ (91%), with the remainder having an intensity between those of the liver and parotid. No statistically significant difference in survival curves for PSA-PFS or OS between those with intensity above or below that of the parotid was observed (Supplemental Fig. 2).

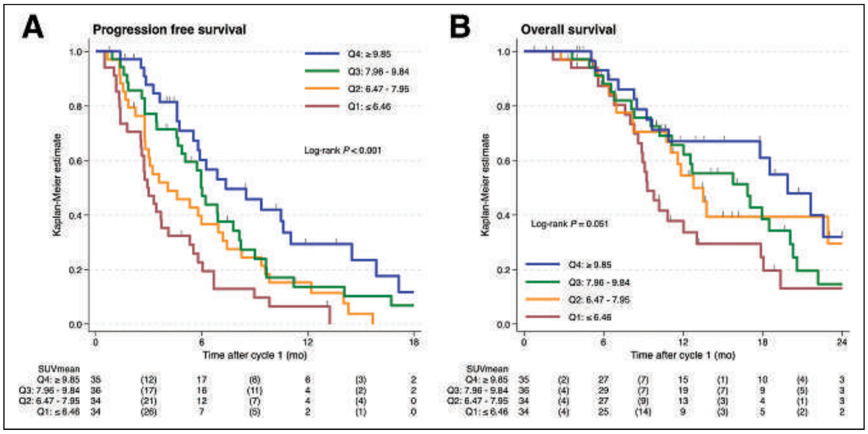

FIGURE 2. Kaplan–Meier curve (log-rank tests) of PSA-PFS (A) and OS (B) for semiquantitative SUV_{mean} quartiles (Q1–Q4).

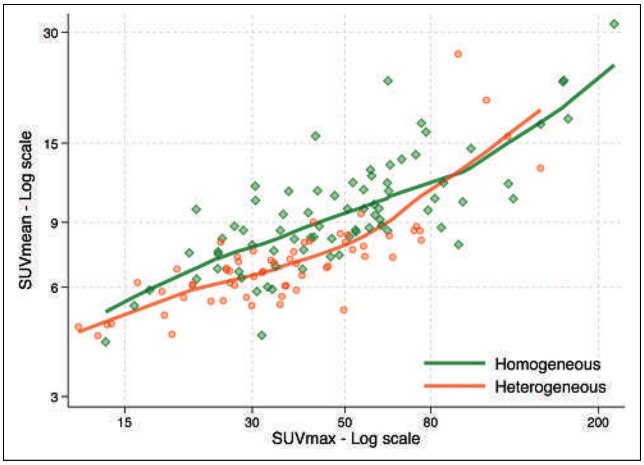

FIGURE 3. Scatterplot of weighted regression curves of log SUV_{mean} vs. SUV_{max} range, by visual heterogeneity score (homogeneous vs. heterogeneous).

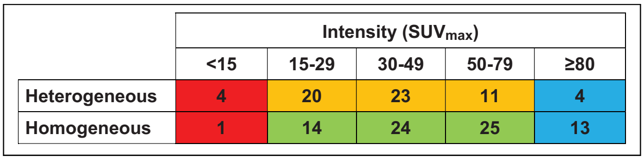

	Intensity (SUV_{max})				
	<15	15-29	30-49	50-79	≥80
Heterogeneous	4	20	23	11	4
Homogeneous	1	14	24	25	13

FIGURE 4. Color-coded table of HIT scores 1–4 incorporating SUV_{max} range (most intense lesion) and binary visual heterogeneity with patient numbers in each group. Red = HIT score 1; yellow = HIT score 2; green = HIT score 3; blue = HIT score 4.

DISCUSSION

Developing screening imaging biomarkers that can predict response to ^{177}Lu-PSMA is important to improve patient outcomes and to better personalize treatment options. Quantitative whole-body SUV_{mean} has shown value in predicting treatment response in men treated with ^{177}Lu-PSMA in both TheraP and VISION trials; however, the clinical application of this tool is limited by the onerous requirements for image quantitation (*4*,*5*). This study has found that the HIT score, derived using tools available on clinical PET workstations, shows promising predictive capability for both PFS and OS in men being treated with ^{177}Lu-PSMA therapy.

SUV_{mean} is a semiquantitatively derived calculation of the mean voxel intensity of total-body tumor deposits. It gives a good measure of both the intensity of PSMA expression in tumor deposits and the variability of PSMA expression intra- and intertumorally. A patient with heterogeneous PSMA expression may have a low SUV_{mean} despite some deposits demonstrating high PSMA expression. Metastatic prostate cancer is inherently heterogeneous, with PSMA expression shown to be variable both within and between tumoral deposits (*11*). This heterogeneity could significantly impact the response to ^{177}Lu-PSMA (*12*). The HIT score using the most intense lesion SUV_{max} ranges with a binary visual tumor heterogeneity scoring on ^{68}Ga-PSMA PET/CT screening successfully predicts both PSA-PFS and OS in response to ^{177}Lu-PSMA therapy in men with mCRPC, with comparable predictability to quantitative SUV_{mean} quartiles.

Several previous studies have shown that PSMA SUV_{max} is not predictive of treatment response to ^{177}Lu-PSMA (*4*,*13*–*15*). However, these studies used PSMA SUV_{max} as a continuous or binary variable ($SUV_{max} < 20$ and ≥ 20). In this study, 5 ranges of PSMA SUV_{max} (<15, 15–29, 30–49, 50–79, and ≥80) were used. This was to allow better separation of intensity levels between patients and to reduce the impact of inherent limitations of SUV_{max} reproducibility. SUV_{max} is dependent on several variables that limit its reproducibility such as variation in body habitus, size of the maximal voxel between different scanners, and the statistical quality of the images (*16*). The HIT score, through combining a binary visual heterogeneity evaluation and SUV_{max} range, optimizes the clinical value of SUV_{max}, while minimizing the limitations of reproducibility.

The PSMA PET/CT tumor–to–salivary gland ratio proposed a visual method for assessment of tumor intensity using parotid intensity. A cohort of 237 patients was classified as high (>80% lesions above parotid), intermediate, and low (>80% lesions below parotid) (*13*). That study found that a high tumor-to–salivary gland ratio had higher PSA50 (63% vs. 17%) and longer PSA-PFS and OS than did the low tumor-to–salivary gland ratio (6.7 vs. 1.9 mo and 14.3 vs. 12.9 mo, respectively) (*13*). The current study shows no significant difference in patient outcome using PSMA intensity of the most active lesion above or below the parotid intensity but did not compare parotid with tumor intensity at all sites. Using whole-body lesions in tumor–to–salivary gland ratios provided an indirect measure of tumor heterogeneity and thus allowed stratification. HIT score integrating SUV_{max} ranges and binary heterogeneity score significantly correlates with PSA50 and both PSA-PFS and OS with higher separation between the highest and lowest scores in PSA50, PSA-PFS, and OS (76% vs. 0%, 8.5 vs. 1.0 mo, and 16.9 vs. 7.6 mo, respectively).

The current study has several limitations. Analysis of the screening ^{68}Ga-PSMA-11 PET/CT was undertaken retrospectively using data from single-institution trials. Results will need to be reproduced and validated in more diverse clinical datasets before clinical implementation, including full assessment of the reproducibility of the HIT score between multiple readers. Screening criteria for trial enrollment required minimal levels of PSMA intensity on ^{68}Ga-PSMA-11 PET/CT images; hence, the number of patients

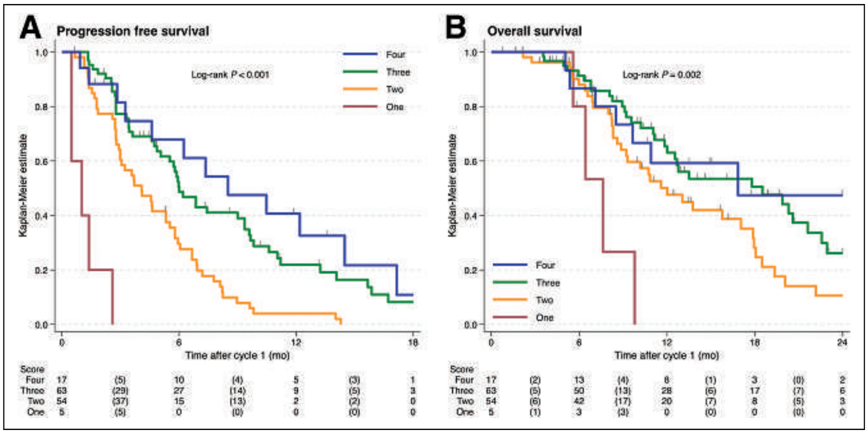

FIGURE 5. Kaplan–Meier curve (log-rank tests) of PSA-PFS (A) and OS (B) for HIT scores 1–4.

with an SUV_{max} less than 15 (HIT score 1) is low. ^{68}Ga-PSMA-11 was the only PET radiopharmaceutical used for screening patients in this study. The use of a heterogeneity score should be applicable across PSMA PET/CT ligands, and the use of the SUV_{max} range rather than using absolute SUV_{max} may mitigate differences between PSMA ligands, but this needs separate evaluation for confirmation.

CONCLUSION

A PSMA PET/CT score incorporating the HIT score derived from tools on a standard PET workstation is comparable to SUV_{mean} as a prognostic tool for PFS and OS following ^{177}Lu-PSMA therapy without the need for total-body quantitation. Further studies are warranted to validate the clinical utility of the HIT score.

DISCLOSURE

No potential conflict of interest relevant to this article was reported.

ACKNOWLEDGMENTS

We thank the patients and the clinical staff at the Department of Theranostics and Nuclear Medicine at St. Vincent's Hospital, Sydney, for their support.

KEY POINTS

QUESTION: Can a visually based score using standard PET workstation tools predict patient outcomes with ^{177}Lu-PSMA therapy on PSMA PET/CT screening and correlate with semiquantitative SUV_{mean}?

PERTINENT FINDINGS: The HIT score using standard PET workstation tools to measure tumor PSMA intensity and heterogeneity predicted PSA50, PSA-PFS, and OS and was comparable to quantitative SUV_{mean}.

IMPLICATIONS FOR PATIENT CARE: The HIT score is a simple clinically applicable PSMA PET/CT score that shows promising capability to predict patient outcomes with ^{177}Lu-PSMA therapy without requiring further quantification.

REFERENCES

1. Sartor O, de Bono J, Chi KN, et al. Lutetium-177-PSMA-617 for metastatic castration-resistant prostate cancer. *N Engl J Med.* 2021;385:1091–1103.
2. Hofman MS, Emmett L, Sandhu S, et al. [^{177}Lu]Lu-PSMA-617 versus cabazitaxel in patients with metastatic castration-resistant prostate cancer (TheraP): a randomised, open-label, phase 2 trial. *Lancet.* 2021;397:797–804.
3. Emmett L, John N, Pathmanandavel S, et al. Patient outcomes following a response biomarker-guided approach to treatment using ^{177}Lu-PSMA-I&T in men with metastatic castrate-resistant prostate cancer (Re-SPECT). *Ther Adv Med Oncol.* 2023;15:17588359231156392.
4. Buteau JP, Martin AJ, Emmett L, et al. PSMA and FDG-PET as predictive and prognostic biomarkers in patients given [^{177}Lu]Lu-PSMA-617 versus cabazitaxel for metastatic castration-resistant prostate cancer (TheraP): a biomarker analysis from a randomised, open-label, phase 2 trial. *Lancet Oncol.* 2022;23:1389–1397.
5. Kuo PH, Hesterman J, Rahbar K, et al. [^{68}Ga]Ga-PSMA-11 PET baseline imaging as a prognostic tool for clinical outcomes to [^{177}Lu]Lu-PSMA-617 in patients with mCRPC: a VISION substudy. *J Clin Oncol.* 2022;40(suppl 16):5002.
6. Kuo PH, Morris M, Kendi AT, et al. Association of baseline quantitative [^{68}Ga]Ga-PSMA-11 PET imaging parameters with clinical outcomes in patients with mCRPC receiving [^{177}Lu]Lu-PSMA-617: a VISION sub-study [abstract]. *Eur J Nucl Med Mol Imaging.* 2023;50(suppl):S1–S898.
7. Crumbaker M, Pathmanandavel S, Yam AO, et al. Phase I/II trial of the combination of ^{177}lutetium prostate specific membrane antigen 617 and idronoxil (NOX66) in men with end-stage metastatic castration-resistant prostate cancer (LuPIN). *Eur Urol Oncol.* 2021;4:963–970.
8. Emmett L, Crumbaker M, Ho B, et al. Results of a prospective phase 2 pilot trial of ^{177}Lu-PSMA-617 therapy for metastatic castration-resistant prostate cancer including imaging predictors of treatment response and patterns of progression. *Clin Genitourin Cancer.* 2019;17:15–22.
9. John N, Pathmanandavel S, Crumbaker M, et al. ^{177}Lu-PSMA SPECT quantitation at 6 weeks (dose 2) predicts short progression-free survival for patients undergoing ^{177}Lu-PSMA-I&T therapy. *J Nucl Med.* 2023;64:410–415.
10. Scher HI, Morris MJ, Stadler WM, et al. Trial design and objectives for castration-resistant prostate cancer: updated recommendations from the Prostate Cancer Clinical Trials Working Group 3. *J Clin Oncol.* 2016;34:1402–1418.
11. Paschalis A, Sheehan B, Riisnaes R, et al. Prostate-specific membrane antigen heterogeneity and DNA repair defects in prostate cancer. *Eur Urol.* 2019;76:469–478.
12. Swiha M, Ayati N, Oprea-Lager DE, Ceci F, Emmett L. How to report PSMA PET. *Semin Nucl Med.* 2024;54:14–29.
13. Hotta M, Gafita A, Murthy V, et al. PSMA PET tumor-to-salivary gland ratio to predict response to [^{177}Lu]PSMA radioligand therapy: an international multicenter retrospective study. *J Nucl Med.* 2023;64:1024–1029.
14. Pathmanandavel S, Crumbaker M, Yam AO, et al. ^{177}Lu-PSMA-617 and idronoxil in men with end-stage metastatic castration-resistant prostate cancer (LuPIN): patient outcomes and predictors of treatment response in a phase I/II trial. *J Nucl Med.* 2022;63:560–566.
15. Seifert R, Seitzer K, Herrmann K, et al. Analysis of PSMA expression and outcome in patients with advanced prostate cancer receiving ^{177}Lu-PSMA-617 radioligand therapy. *Theranostics.* 2020;10:7812–7820.
16. Wahl RL, Jacene H, Kasamon Y, Lodge MA. From RECIST to PERCIST: evolving considerations for PET response criteria in solid tumors. *J Nucl Med.* 2009;50(suppl 1):122S–150S.

Safety and Efficacy of Extended Therapy with [^{177}Lu]Lu-PSMA: A German Multicenter Study

Robert Seifert*[1–5], Tugce Telli*[1–3], Constantin Lapa[2,6], Mélanie Desaulniers[1–3], Turkay Hekimsoy[2,7,8], Wolfgang A. Weber[2,7,8], Christian Pfob[2,6], Boris Hadaschik[2,3,9], Martin Bögemann[3,10], Michael Schäfers[3,5], Ken Herrmann[1–3], Kambiz Rahbar[†3,5], Matthias Eiber[†2,7,8], and Wolfgang P. Fendler[†1–3]

[1]Department of Nuclear Medicine, University Hospital Essen, Essen, Germany; [2]German Cancer Consortium, University Hospital Essen, Essen, Germany; [3]West German Cancer, University Hospital Essen, Essen, Germany; [4]Department of Nuclear Medicine, University Hospital Bern, Bern, Switzerland; [5]Department of Nuclear Medicine, University Hospital Münster, Münster, Germany; [6]Department of Nuclear Medicine, Faculty of Medicine, University of Augsburg, Augsburg, Germany; [7]Department of Nuclear Medicine, Klinikum Rechts der Isar, Technical University Munich, Munich, Germany; [8]Bavarian Cancer Research Center, Erlangen, Germany; [9]Department of Urology, University Hospital Essen, Essen, Germany; and [10]Department of Urology, University Hospital Münster, Münster, Germany

Prospective results have demonstrated favorable safety and efficacy of [^{177}Lu]Lu-PSMA radiopharmaceutical therapy for up to 6 cycles in men with metastatic castration-resistant prostate cancer. However, no systematic data are available outlining the feasibility of extended therapy beyond 6 cycles. We aim to evaluate the safety and efficacy of extended [^{177}Lu]Lu-PSMA radiopharmaceutical therapy in patients who have received more than 6 cycles. **Methods:** In total, 111 patients were included in this multicenter retrospective analysis. Based on individual decisions, patients underwent uninterrupted continuation of therapy (continuous treatment) or reexposure after a therapy break (rechallenge treatment) between 2014 and 2023. Overall survival, 50% prostate-specific antigen (PSA) decline (measured 8–12 wk after treatment initiation or rechallenge), PSMA PET response, and grades per Common Terminology Criteria for Adverse Events were assessed. χ^2 tests, multivariable Cox regression analysis, and log-rank tests were applied for statistical analyses. **Results:** Patients received extended treatment with [^{177}Lu]Lu-PSMA, either as a continuous treatment (43/111, 38.7%) or as a rechallenge (68/111, 61.3%) treatment, with median cumulative doses of 57.4 or 60.8 GBq, respectively. Overall survival from the initiation of [^{177}Lu]Lu-PSMA was 31.3, 23.2, and 40.2 mo for the entire cohort, the continuous treatment group, and the rechallenge treatment group, respectively. The initial 50% PSA decline was significantly higher in the retreated group than in the continuous group (57/63 [90.4%] vs. 26/42 [61.9%]; $P = 0.006$). A 50% PSA decline was observed in 23 of 62 patients (37.1%) after the first rechallenge. The rate of grades 3–4 toxicity was comparable between continuous and rechallenge treatments (anemia, 7/43 [16.3%] vs. 13/68 [19.1%)], $P = 0.6$; leukocytopenia, 1/43 [2.3%] vs. 2/67 [3.0%], $P = 0.3$; thrombocytopenia, 3/43 [7.0%] vs. 3/68 [4.4%], $P = 0.3$; renal, 2/43 [4.7%] vs. 5/68 [7.4%], $P = 0.2$). **Conclusion:** Extended therapy with [^{177}Lu]Lu-PSMA is safe and has not been associated with increased grades 3–4 toxicity. Patient candidates for extended treatment experienced a favorable median survival of 31.3 mo from the first administration. Response under [^{177}Lu]Lu-PSMA rechallenge demonstrated preserved efficacy of [^{177}Lu]Lu-PSMA after a treatment break.

Key Words: prostate cancer; PSMA therapy; mCRPC

J Nucl Med 2024; 65:909–916
DOI: 10.2967/jnumed.123.267321

Prostate-specific membrane antigen (PSMA)–targeted radiopharmaceutical therapy (RPT) is an approved option for patients with metastatic castration-resistant prostate cancer (mCRPC). The VISION trial demonstrated that [^{177}Lu]Lu-PSMA significantly prolonged overall survival (OS) compared with the control arm (*1*). The VISION trial allowed up to 6 cycles of 7.4 GBq of [^{177}Lu]Lu-PSMA-617. This was partly based on a German multicenter retrospective study that reported early clinical experience (*2*).

In the VISION trial, approximately one third of patients in the [^{177}Lu]Lu-PSMA arm did not experience biochemical response, which was defined as a greater than 50% decrease in prostate-specific antigen (PSA) levels (*1*). In addition, patients who responded to treatment demonstrated highly variable depth or duration of response. It may be beneficial to extend the use of [^{177}Lu]Lu-PSMA beyond 6 cycles, and this approach is currently being applied in clinical practice. However, systematic data on safety and the antitumor effect of [^{177}Lu]Lu-PSMA RPT beyond 6 cycles are scarce (*1*,*3*,*4*).

Treatment extension beyond 6 cycles may be conducted as an uninterrupted continuation of treatment (continuous treatment) or reexposure after a therapy break (rechallenge treatment). Rechallenge treatment is usually conducted following biochemical and imaging responses after initial cycles and disease progression after treatment cessation. Rechallenge treatment in these good responders could potentially delay the risk of [^{177}Lu]Lu-PSMA–related side effects. However, it is unclear whether the initial treatment effect is preserved after a therapy break. Thus, the aim of this retrospective analysis was to evaluate the safety and efficacy of extended [^{177}Lu]Lu-PSMA therapy (i.e., beyond 6 cycles) and to investigate potential differences in safety and efficacy of continuous and rechallenge treatments.

MATERIALS AND METHODS

Patient Cohort and [^{177}Lu]Lu-PSMA RPT

The data from patients who underwent more than 6 cycles of [^{177}Lu]Lu-PSMA therapy between December 2014 and March 2023

Received Dec. 22, 2023; revision accepted Mar. 25, 2024.

For correspondence or reprints, contact Wolfgang P. Fendler (wolfgang.fendler@uk-essen.de).

*Contributed equally to this work.

†Contributed equally to this work.

were retrospectively extracted from the databases of the University Hospitals in Augsburg, Essen, Münster, and Munich (Technical University). All patients signed an informed consent form and were treated under the conditions of the Declaration of Helsinki article 37 (unproven interventions in clinical practice). The multicenter retrospective analysis was approved by the ethics committee in Essen (19-8570-BO and 2021-576-f-S), and the retrospective analysis was approved by local ethics committees (Augsburg, 2020-40 and 23-0847; Münster, 2016-585-f-S; and Munich, 115/18S). [^{177}Lu]Lu-PSMA was prepared according to good manufacturing practices and the German Medicinal Products Act (AMG §13 2b) at all respective centers. Either [^{177}Lu]Lu-PSMA-617 or [^{177}Lu]Lu-PSMA I&T was administered as summarized in Table 1.

European Association of Nuclear Medicine guidelines were followed for patient selection for [^{177}Lu]Lu-PSMA therapy, radionuclide preparation, therapy administration, radiation protection, and follow-up monitoring (*5*,*6*). The treatment decision was made by an interdisciplinary tumor committee. Patients had to have received androgen deprivation therapy, androgen receptor signaling inhibitors, and at least 1 line of chemotherapy in the absence of contraindications. The degree of PSMA expression was determined by PSMA PET before the initiation of treatment. PSMA PET–based eligibility was based on VISION trial criteria, that is, higher lesion uptake than in the liver and the absence of PSMA-negative lesions. Patients with macroscopic residual disease, that is, stable disease or with a partial response, underwent continued treatment beyond 6 cycles (continuous treatment). Patients showing excellent biochemical and imaging responses by judgment of the treating physician were offered a therapy break after 4–6 cycles and were reexposed to [^{177}Lu]Lu-PSMA RPT (rechallenge treatment). Eligibility and choice of treatment protocol were decided by an interdisciplinary tumor committee. A therapy break was defined as a period of at least 4 mo without [^{177}Lu]Lu-PSMA administration, which was chosen as twice the maximum treatment interval of 8 wk and thus prevented patient logistic-induced breaks from qualifying as rechallenge regimens.

TABLE 1
Patient Characteristics (n = 111)

Parameter	Continuous treatment	Rechallenge treatment
Number of patients	43 (38.7)	68 (62.3)
Age at [^{177}Lu]Lu-PSMA therapy (y)	73.0 (67.7–79)	72.0 (65.3–77.0)
Time from diagnosis to [^{177}Lu]Lu-PSMA therapy (mo)	84.4 (40.9–119.6)	102.7 (67.8–146.5)
Local therapy to the prostate		
Prostatectomy	11 (25.6)	23 (33.8)
Radiotherapy	3 (7.0)	8 (11.8)
Both	8 (18.6)	17 (25.0)
None	21 (48.8)	19 (27.9)
Not available	0 (0.0)	1 (1.5)
Number of prior treatment lines for mCRPC	3 (2–4)	3 (3–4)
Systemic therapy after ADT		
Docetaxel	32 (74.4)	54 (79.4)
Cabazitaxel	11 (25.6)	23 (33.8)
Abiraterone	35 (81.4)	63 (92.6)
Enzalutamide	38 (88.4)	62 (91.2)
^{223}Ra	3 (7.0)	8 (11.8)
Other	4 (9.3)	5 (7.4)
ECOG performance status before initial [^{177}Lu]Lu-PSMA RPT		
0	20 (46.5)	35 (51.5)
1	19 (44.2)	27 (39.7)
2	1 (2.3)	5 (7.4)
3	2 (4.7)	0 (0.0)
Not available	1 (2.3)	1 (1.4)
Initial PSMA PET response after 2 cycles of [^{177}Lu]Lu-PSMA RPT (RECIP)		
PR	10/38 (26.3)	33/59 (55.9)
SD	26/38 (68.4)	25/59 (42.4)
PD	2/38 (5.3)	1/59 (1.7)
CR	0/38 (0.0)	0/59 (0.0)

ADT = androgen deprivation therapy; ECOG = Eastern Cooperative Oncology Group; PR = partial response; SD = stable disease; PD = progressive disease; CR = complete response.

Qualitative data are number and percentage. Continuous data are median and interquartile range.

Therapy Response

Biochemical response to therapy was defined as a PSA decline of at least 50% 8–12 wk after treatment initiation (initial change in PSA). For patients who underwent rechallenge treatment, the biochemical response at rechallenge was calculated using the first cycle of the rechallenge as a baseline (rechallenge change in PSA). Interim PSMA PET (after 2 cycles of initial [^{177}Lu]Lu-PSMA therapy) was interpreted using visual assessment following Response Evaluation Criteria in PSMA PET/CT (*7*). Figure 1 shows the assessment of the response to treatment.

Adverse Events

Serum parameters, such as hemoglobin, leukocyte, and thrombocyte counts, and kidney and liver function values were recorded during each treatment cycle and, where possible, during 3 mo of follow-up. Adverse events were assessed according to Common Terminology Criteria for Adverse Events version 5.0 for each category.

OS

OS was calculated from the initial [^{177}Lu]Lu-PSMA treatment until loss of follow-up or death.

Statistical Analysis

The R language (The R Project for Statistical Computing) was used for statistical analyses and graphical representation (Kaplan–Meier curve, box, and swimmer plots). Normal distribution was assessed by the Kolmogorov–Smirnov test. Descriptive data were given as mean and SD for normally distributed parameters, as median and interquartile range for skewed parameters, or as number and percentage. Cox regression analysis and log-rank tests were used for censored data, and the χ^2 exact test was used for categoric data. A *P* value of less than 0.05 was considered statistically significant. CIs represent the 95% range.

RESULTS

Patient Characteristics and [^{177}Lu]Lu-PSMA Therapy Regimes

In total, 111 patients were included. Of those patients, 43 (38.7%) received continuous treatment whereas 68 (71.3%) underwent rechallenge treatment (Fig. 2). Median cumulative activity per patient in the continuous and rechallenge treatments was 57.4 GBq (range, 51.6–59.5 GBq) versus 60.8 GBq (range, 54.9–73.1 GBq), respectively, and the median interval between therapy cycles in each sequence of continuous and rechallenge treatments was 1.4 mo (range, 1.4–1.8 mo) versus 1.5 mo (range, 1.4–1.9 mo), respectively. The median interval between the end of the initial [^{177}Lu]Lu-PSMA RPT and initiation of rechallenge treatment was 7.2 mo (range, 5.4–11.5 mo). Of the patients who received continuous therapy, 24 of 43 (55.8%) received therapy once or twice within an interval of 10–16 wk; otherwise, therapy occurred within an interval of 8–10 wk. For the continuous and rechallenge groups, respectively, the median number of treatment cycles was 8 versus 9, and the median dose per cycle was 7.2 versus 6.8 GBq. In the rechallenge group, 80.1% of patients received 1 rechallenge treatment, whereas the remainder received 2–4 additional rechallenge treatments: 10 of 68 (14.7%) received 2 additional treatments, 2 of 68 (2.9%) received 3 additional treatments, and 1 of 68 (1.5%) received 4 additional treatments. Patient characteristics and [^{177}Lu]Lu-PSMA treatment regimes are presented in Tables 1 and 2.

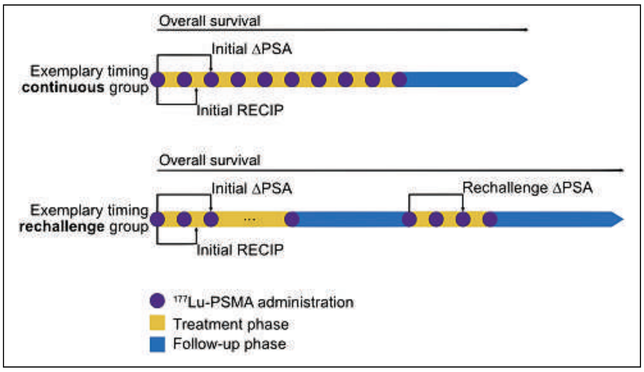

FIGURE 1. Patients received extended administration of [^{177}Lu]Lu-PSMA (>6 cycles), either continuously (continuous treatment) or as reexposure after therapy pause (rechallenge treatment). PSA response was measured at 8–12 wk after treatment initiation and start of rechallenge. Imaging response by Response Evaluation Criteria in PSMA PET/CT (RECIP) was assessed after 2 cycles. ΔPSA = change in PSA.

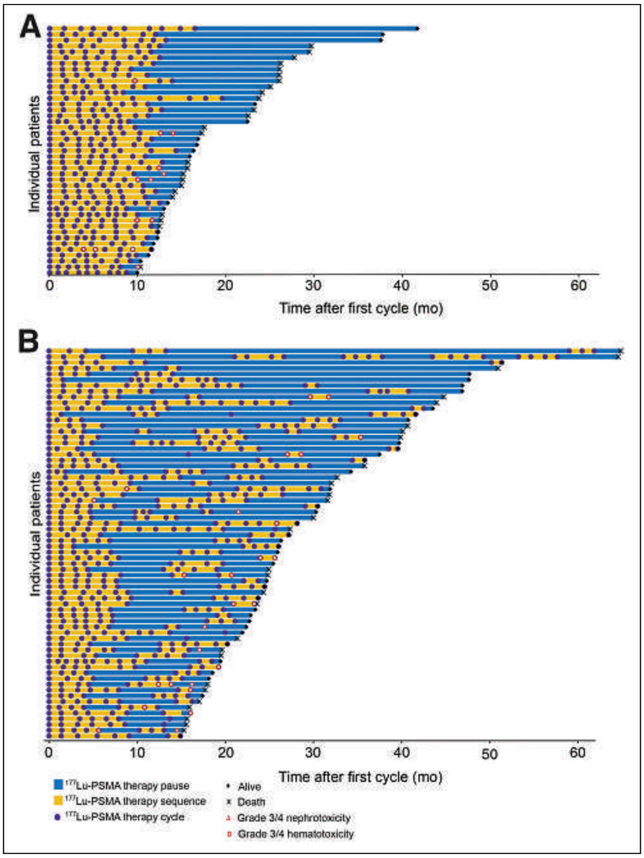

FIGURE 2. Swimmer plots depicting individual treatment sequence, outcome, and toxicity. Data are presented separately for continuous (A) and rechallenge treatment (B).

Safety

Higher-grade adverse events according to Common Terminology Criteria for Adverse Events version 5.0 are presented in Table 3 and are illustrated in Figure 3. Rates of grades 3–4 hematotoxicities were not significantly different between the continuous and rechallenge groups for anemia (16.3% vs. 19.1%; $P = 0.6$), leukocytopenia (2.3% vs. 3.0%; $P = 0.3$), and thrombocytopenia (7.0% vs. 4.4%; $P = 0.3$).

Hematologic parameters in the last treatment cycle were significantly lower than those in the first cycle for both the continuous and rechallenge groups (Table 4). In the overall cohort (20 total events), the frequency of grades 3 and 4 anemia was higher in the

TABLE 2
[^{177}Lu]Lu-PSMA RPT Regimen

Parameter	Continuous treatment	Rechallenge treatment
PSMA ligand	43 (38.7)	68 (62.3)
PSMA-617	3 (7.0)	21 (30.8)
PSMA I&T	40 (93.0)	46 (67.6)
PSMA-617 and PSMA I&T	0 (0.0)	1 (1.5)
Number of [^{177}Lu]Lu-PSMA cycles		
7	10 (23.3)	8 (11.8)
8	25 (58.1)	22 (32.4)
9	4 (9.3)	9 (13.2)
10	4 (9.3)	13 (19.1)
11	0 (0.0)	2 (2.9)
12	0 (0.0)	10 (14.7)
≥13	0 (0.0)	4 (5.9)
Cumulative activity (GBq)		
40–50	6 (14.0)	6 (8.8)
>50–60	29 (67.4)	28 (41.2)
>60–70	5 (11.6)	11 (16.2)
>70–80	3 (7.0)	11 (16.2)
>80	0 (0.0)	12 (17.6)
Time between therapy cycles (mo)	1.4 (1.38–1.83)	1.5 (1.4–1.9)[*]
Duration of therapy break before rechallenge sequences (mo)	–	7.2 (5.4–11.5)

---

[*] Time interval between cycles of therapy was calculated for rechallenge group without considering period of therapy break.
Qualitative data are number and percentage. Continuous data are median and interquartile range.

extended treatment sequence (cycle 7 and beyond) than in the initial treatment sequence (cycles 1–6) (12/20 [60%] vs. 8/20 [40%]). Grade 4 thrombocytopenia occurred in 1 patient during the rechallenge therapy cycles.

Few occurrences of grades 3–4 renal toxicity (7/111 [6.3%]) were observed in the overall cohort, with most occurring in the extended treatment sequence (cycle 7 and beyond) (4/7 [57.1%]). The rate of renal toxicity was not significantly different between

TABLE 3
Incidence of Grades 3–4 Adverse Events Stratified by Continuous vs. Rechallenge Treatment

	Continuous treatment ($n = 43$)		Rechallenge treatment ($n = 68$)		After rechallenge ($n = 68$)	
Event	Grade 3	Grade 4	Grade 3	Grade 4	Grade 3	Grade 4
Hematologic						
Leukocytopenia	1 (2.3)	0 (0.0)	2[*] (3.0)	0 (0.0)	0 (0.0)	0 (0.0)
Neutropenia	1[†] (2.6)	0 (0.0)	0[‡] (0.0)	0 (0.0)	0 (0.0)	0 (0.0)
Anemia	7 (16.3)	0 (0.0)	13 (19.1)	0 (0.0)	10 (14.7)	0 (0.0)
Thrombocytopenia	3 (7.0)	0 (0.0)	2 (2.9)	1 (1.5)	2 (2.9)	1 (1.5)
Renal						
Decrease in GFR	2 (4.7)	0 (0.0)	5 (7.4)	0 (0.0)	5 (7.4)	0 (0.0)
Adverse event leading to discontinuation	5 (11.6)		10 (14.7)		10 (14.7)	
Adverse event leading to dose reduction	7 (16.2)		10 (14.7)		10 (14.7)	

---

[*] $n = 67$ patients.
[†] $n = 39$ patients.
[‡] $n = 66$ patients.
Data are number and percentage.

the continuous and rechallenge groups (2/43 [4.7%] vs. 5/68 [7.4%]; $P = 0.2$). Median glomerular filtration rates (GFRs) were significantly lower in the last treatment cycle than in the first in both continuous and rechallenge groups (Table 4).

Any grade of xerostomia was detected in 58 of 111 patients in the overall cohort (52%, $n = 29$ for the continuous group and $n = 29$ for the rechallenge group) with most occurring in the initial 6 cycles rather than in the extended treatment sequence (40/58 [69%] vs. 18/58 [31%]). Any grade of dry eyes was detected in 13 of 111 patients in the overall cohort (12%, $n = 5$ for the continuous group and $n = 8$ for the rechallenge group), with most occurring in the first 6 cycles rather than in the extended treatment sequence (11/13 [85%] vs. 2/13 [15%]).

Administered activity was reduced to a range of 3 and 6 GBq in 17 patients (5.3%) because of a decrease in GFR (35.3%) and hematotoxicity (64.7%), respectively.

[^{177}Lu]Lu-PSMA RPT was discontinued in 15 patients (15/111 [13.5%]) because of decreased GFR (7/15 [46.7%]) or hematotoxicity (8/15 [53.3%]) (Table 3). In the continuous group, therapy was discontinued in 3 patients because of a decrease in GFR and in 2 patients because of thrombocytopenia. In the rechallenge group, therapy was discontinued in 4 patients because of a decrease in GFR, in 3 patients because of thrombocytopenia, in 1 patient because of bicytopenia, in 1 patient because of pancytopenia, and in 1 patient because of anemia.

Interestingly, patients who had not previously received docetaxel or cabazitaxel had a tendency toward higher rates of adverse events, resulting in dose reduction, than did those who received one or both treatments (7/24 [29.2%] vs. 6/54 [11.1%] vs. 4/33 [12.1%]; $P = 0.1$).

Biochemical Response

The rate of the initial 50% PSA decline was significantly higher in the rechallenge group than in the continuous group (57/63 [90.4%] vs. 26/42 [61.9%]; $P = 0.006$; Table 5). In the continuous group, the rate of 50% PSA decline after the first 6 cycles was 36 of 42 (85.7%), whereas the rate of 50% PSA decline between the sixth cycle and the last cycle was 7 of 43 (16.3%). In the rechallenge group, the rate of 50% PSA decline was 23 of 62 (37.1%) after the first rechallenge treatment and 9 of 12 (75.0%) after the second rechallenge treatment. Figure 4 shows individual PSA levels and the 50% PSA decline during the initial treatment and additional rechallenge treatments.

Imaging Response

Interim PSMA PET was available in 97 of 111 patients (87.3%) (38/43 in the continuous group and 59/68 in the rechallenge group). In the continuous versus rechallenge groups, partial response by PSMA PET/CT was observed in 10 of 38 patients (26.3%) versus 33 of 59 patients (55.9%), and stable disease was observed in 26 of 38 patients (68.4%) versus 25 of 59 patients (42.4%). The initial partial response rate was significantly lower in the continuous group than in the rechallenge group (26.3% vs. 55.9%, $P = 0.004$). Details on the PSMA PET response are shown in Table 5.

OS

Patient status was followed for a median of 33.9 mo (95% CI, 25.0–42.7 mo) after initiation of [^{177}Lu]Lu-PSMA RPT. A total of 54 patients (51.4%) died, and median OS was 31.3 mo (95% CI, 26.3–36.3 mo) for the entire cohort (Fig. 5A). Figure 5B shows that OS from the beginning of initial [^{177}Lu]Lu-PSMA therapy was significantly shorter for continuously treated patients than for rechallenge patients (23.2 mo [95% CI, 20.4–25.9 mo] vs. 40.2 mo [95% CI, 31.8–48.7 mo]; $P < 0.001$).

DISCUSSION

In this retrospective analysis, we assessed the safety and efficacy of [^{177}Lu]Lu-PSMA therapy beyond 6 cycles. After 6 cycles of standard [^{177}Lu]Lu-PSMA treatment, patients in our cohort either received continuous [^{177}Lu]Lu-PSMA treatment for residual disease or were treated again after a pause because of a good initial response. Extended treatment with [^{177}Lu]Lu-PSMA was well tolerated, with few grades 3–4 adverse events, with the most frequent being anemia after 6 cycles. Overall, extended [^{177}Lu]Lu-PSMA RPT achieved an OS of 31.3 mo from the first administration.

In our study, extended treatment with [^{177}Lu]Lu-PSMA was well tolerated. Grade 3 or 4 anemia was observed in 18% (20/111) of patients, mainly during additional cycles. Grade 3 or 4 thrombocytopenia was observed in only 5% of patients, and grade 3 neutropenia was found in only 0.1% of patients. In line with our results, Mader et al. reported grades 3–4 anemia in 15% of patients receiving extended [^{177}Lu]Lu-PSMA therapy and reversible thrombocytopenia in only 1 patient (4%) (*8*). In contrast to our cohort, mCRPC patients who received cabazitaxel as second-line chemotherapy had high rates

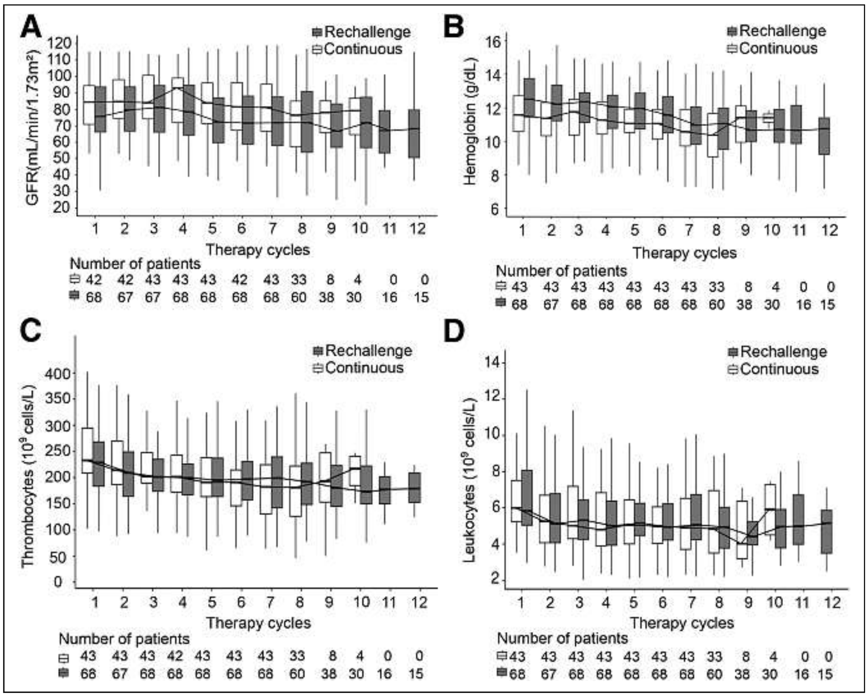

FIGURE 3. Median serum values for GFR (A), hemoglobin (B), thrombocytes (C), and leukocytes (D) per cycle from patients receiving continuous or rechallenge [^{177}Lu]Lu-PSMA. Data are only shown for first 12 cycles.

TABLE 4
Median of Laboratory Parameters During First Therapy vs. Last Therapy Cycle in Both Treatment Groups

	Continuous treatment			Rechallenge therapy		
Parameter	First cycle	Last cycle	*P*	First cycle	Last cycle	*P*
Hemoglobin (g/dL)	11.5 (10.4–12.7)	10.7 (8.9–11.5)	<0.001*	12.5 (11.3–13.7)	10.1 (8.4–11.4)	<0.001*
Leukocytes (cells/nL)	6 (5.3–7.7)	4.6 (3.4–6.9)	<0.001*	5.9 (5.1–8.2)	5.0 (3.8–6.3)	<0.001*
Thrombocytes (cells/nL)	234.0 (208.0–296.0)	180.0 (120.0–222.0)	<0.001*	231.0 (181.8–272.0)	174.0 (121.0–212.3)	<0.001*
GFR (mL/min/1.73 m^2)	85.0 (70.9–95.9)	78.2 (57.2–94.4)	0.01*	78.0 (67.0–97.5)	66.5 (50.6–87.2)	<0.001*

*Statistically significant.
Continuous data are median and interquartile range.

of grades 3–4 neutropenia (82%), and a considerable fraction had febrile neutropenia (8%) (*9*). However, the rate of grades 3–4 anemia and thrombocytopenia was similar to that found in our study (11% and 4%, respectively) (*9*). In the TheraP study, the cabazitaxel group had a higher rate of any grade 3 or 4 adverse event overall than did the [^{177}Lu]Lu-PSMA group (53% vs. 33%) (*10*). The data indicate that initial and extended [^{177}Lu]Lu-PSMA therapy may be tolerated better than cabazitaxel in mCRPC patients after docetaxel chemotherapy.

Our population demonstrated a low rate of grades 3–4 events concerning renal function assessed by the GFR (7/111, 6.3%). In line with our results, only 1 patient (4%) who received 12 cycles of [^{177}Lu]Lu-PSMA treatment experienced grade 3 nephrotoxicity in the Mader et al. study (*8*). Furthermore, Mader et al. were able to demonstrate that the critical threshold for a renal absorbed dose of 40 Gy was not significantly associated with a reduction in GFR (*8*). Our results underline favorable renal safety with a low risk of induced renal failure. However, Schäfer et al. reported 3 cases in which patients who received more than 6 cycles of [^{177}Lu]Lu-PSMA therapy showed nephropathy with severe chronic kidney disease that was likely induced by diffuse subacute renal thrombotic microangiopathy as well as acute tubular injury (*11*). In addition, most recently, Steinhelfer et al. reported that a considerable proportion (45%) of patients may experience moderate to severe decreases in estimated GFR 1 y from initiation of [^{177}Lu]Lu-PSMA, but without association with the number of treatment cycles (*12*). Follow-up after the last cycle of treatment in our study was short, precluding definitive statements on possibly delayed renal toxicity.

In the present study, the overall incidence of grades 3–4 adverse events was 32.4%, and the adverse event rate leading to dose reduction was 15.3%. In the CARD study, the rate of grades 3–4 adverse events was 56.3% in patients receiving cabazitaxel as a second-line chemotherapy (*13*). Cabazitaxel showed a higher frequency of dose reductions (cabazitaxel arm of TheraP trial, 20.8%; CARD trial, 21.4%) (*10,13*). In our study, the rate of adverse events resulting in dose reduction was relatively higher in patients who had not received docetaxel or cabazitaxel previously. Patients with comorbidities unsuitable for chemotherapy may be more likely to experience a higher rate of adverse events, leading to a dose reduction. Furthermore, we observed decreased rates of dose reduction in patients who received docetaxel or cabazitaxel (11.1%) or both (12.1%) before extended [^{177}Lu]Lu-PSMA therapy compared with the rates reported in the CARD study (21.4%) (*13*). This suggests that extended [^{177}Lu]Lu-PSMA therapy has a favorable safety profile compared with second-line cabazitaxel therapy.

OS from the initiation of [^{177}Lu]Lu-PSMA was 23.2 mo for the continuous treatment group and 40.2 mo for the rechallenge group. In both groups, the OS was considerably longer than that observed in the phase 3 VISION study (*1*). Notably, our patient cohort has a significant selection bias compared with the VISION study as only

TABLE 5
Response to [^{177}Lu]Lu-PSMA RPT Stratified for Continuous vs. Rechallenge Treatment

Parameter	Continuous treatment	Rechallenge treatment
Initial 50% PSA decline after 8–12 wk	26/42 (61.9)	57/63* (90.4)
50% PSA decline during continuous therapy		
Between first and sixth cycles	36/42 (85.7)	
Between sixth and last cycles	7/43 (16.3)	
50% PSA decline at rechallenge		
First rechallenge sequence		23/62† (37.1)
Second rechallenge sequence		9/12‡ (75.0)

*PSA response was assessed after first cycle in 2 of 63 (3.1%) patients.
†PSA response was assessed after first rechallenge cycle in 21 of 62 (33.9%) patients.
‡PSA response was assessed after first rechallenge cycle in 7 of 12 (58.3%) patients.

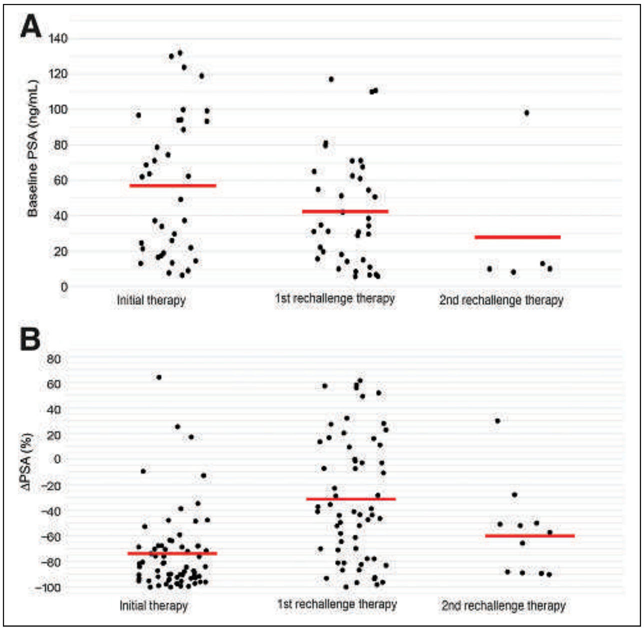

FIGURE 4. Individual initial PSA values and PSA decline for patients receiving rechallenge treatment. Baseline PSA values are given before treatment initiation and before rechallenge treatment (A). Initial and subsequent PSA decline are presented after treatment initiation and rechallenge treatments (B). ΔPSA = change in PSA.

patients who showed response after 6 cycles were eligible for extended treatment.

In our rechallenge subgroup, [^{177}Lu]Lu-PSMA therapy resulted in high biochemical response rate (first rechallenge, 37.1%; second rechallenge, 75.0%) as well as a favorable OS of 40.2 mo. These results are comparable with those of a previous study on 30 patients under [^{177}Lu]Lu-PSMA rechallenge treatment. In that study, Yordanova et al. demonstrated a biochemical response in almost 40% of patients after 2 cycles of rechallenge, and an OS of 25 mo from the first cycle (*3*). Interestingly, the biochemical response rate after the first rechallenge treatment in our [^{177}Lu]Lu-PSMA-retreated group (37.1%) was comparable to that of patients receiving cabazitaxel for the first time (36%) in the presence of progressive disease with failure of previous treatments including enzalutamide or abiraterone and docetaxel (*13*). Rechallenge therapy with docetaxel was previously studied in a phase 3 trial for mCRPC patients who progressed to mCRPC and previously received docetaxel in a metastatic hormone-sensitive prostate cancer setting (*14*). Only 14% of patients in the docetaxel rechallenge arm experienced a 50% PSA decline (*14*). Additionally, the docetaxel rechallenge did not prolong the OS of mCRPC patients who responded to the first-line docetaxel therapy when compared with OS in non–taxane-based therapy (*15*). The cabazitaxel rechallenge has also been shown to be feasible and to achieve a median OS of 51 mo from the start of the first dose of cabazitaxel, which is longer than the 40 mo reported here for the [^{177}Lu]Lu-PSMA rechallenge group (*16*).

Given the limited treatment options in mCRPC, extension or rechallenge treatment with substantial antitumor effects will be increasingly discussed for [^{177}Lu]Lu-PSMA. Therefore, the evaluation of the safety of [^{177}Lu]Lu-PSMA beyond 6 cycles is important (*17*). Currently, several ongoing clinical trials are evaluating [^{177}Lu]Lu-PSMA treatment in taxane-naïve patients, for example, PSMAfore (NCT04689828), SPLASH (NCT04647526), ECLIPSE (NCT05204927), PSMAddition (NCT04720157), and UpfrontPSMA (NCT04343885). These patients will likely experience disease progression later on and might be candidates for rechallenge with [^{177}Lu]Lu-PSMA.

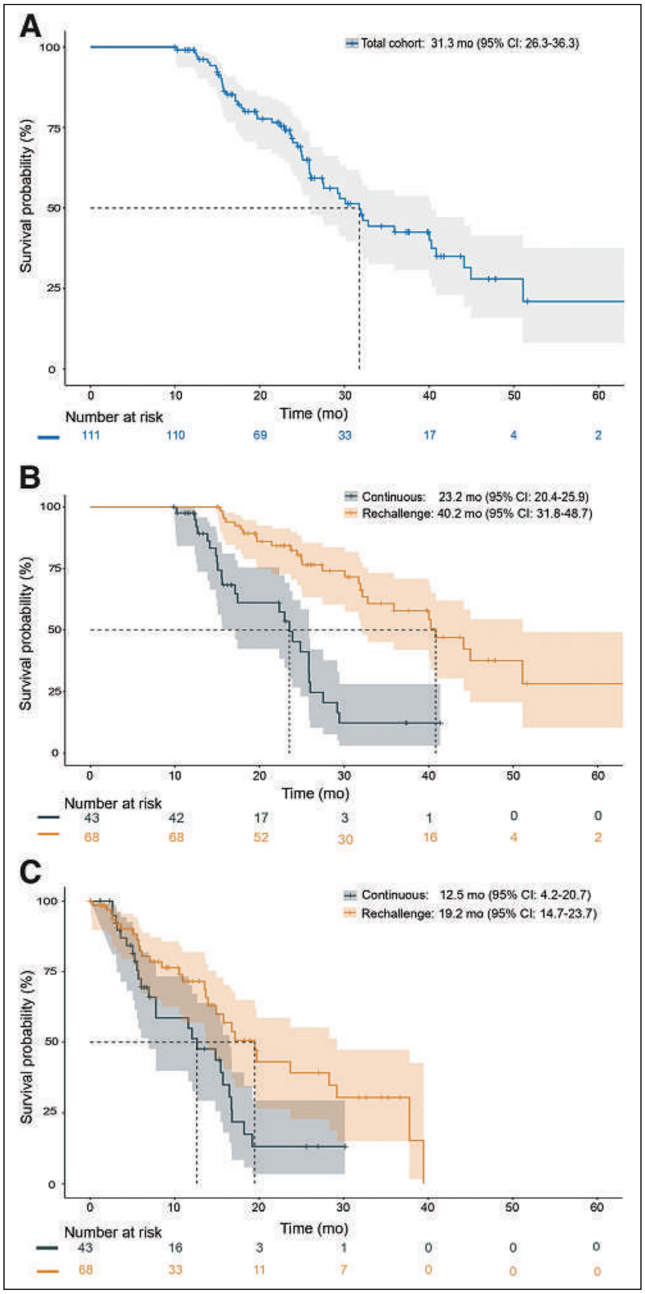

FIGURE 5. Kaplan–Meier curves for OS from first [^{177}Lu]Lu-PSMA application for entire cohort (A) and separately for continuous and rechallenge treatments (B and C).

Our retrospective analysis comes with limitations. We report here the results of extended treatment with [^{177}Lu]Lu-PSMA in selected patients with either macroscopic residual disease under stable or partial response in the continuous group or excellent initial disease reduction allowing a therapeutic pause in the retreated group. Selection criteria introduce bias toward favorable survival. The results may, therefore, not be representative of patients outside these clinical scenarios. In addition, the assessment of efficacy and safety is less accurate in a retrospective design than in a prospective one because of a lower level of control and follow-up. In particular, the follow-up period after the last treatment cycle was short, precluding definitive statements about potentially delayed renal toxicity.

CONCLUSION

Patients with mCRPC who have a favorable initial response to [^{177}Lu]Lu-PSMA therapy may benefit from extended treatment beyond 6 cycles. Extended treatment was associated with favorable safety and substantial biochemical response. The benefit of this treatment option has yet to be evaluated in prospective, randomized, and controlled trials.

DISCLOSURE

Tugce Telli declares Abx (speaker) fees outside the submitted work. Robert Seifert has received support from the Else Kröner-Fresenius-Stiftung and the Boehringer Ingelheim Fonds. Constantin Lapa reports prior consulting activities for Blue Earth Diagnostics Ltd. and Novartis outside the submitted work. Wolfgang Weber reports fees from Blue Earth Diagnostics Ltd. (consultant, research support), ITM (research support, consultant), RayzeBio (research support, consultant), Eckert-Ziegler (research support, speaker), Roche (research support, consulting), and Siemens Healthineers (research support). Boris Hadaschik is on advisory boards for Janssen, Bayer, ABX, Lightpoint, Amgen, MSD, Pfizer, and Novartis; is an invited speaker for Accord, Astellas, and Janssen R&D; received honoraria from Uromed; received research funding from AAA/Novartis, Bristol Myers Squibb, and German Research Foundation; and has leadership roles for DKG AUO and DGU. Ken Herrmann reports consultant fees from Advanced Accelerator Applications, a Novartis company, Amgen, AstraZeneca, Bain Capital, Bayer, Boston Scientific, Convergent, Curium, Debiopharm, EcoR1, Fusion, GE Healthcare, Immedica, Isotopen Technologien München, Janssen, Merck, Molecular Partners, NVision, POINT Biopharma, Pfizer, Radiopharm Theranostics, Rhine Pharma, Siemens Healthineers, SOFIE Biosciences, Telix, Theragnostics, and ymabs; received research grants from Advanced Accelerator Applications, a Novartis company, Boston Scientific, and Janssen; and has stock or other ownership interests with AdvanCell, Aktis Oncology, Convergent, NVision, Pharma 15, and SOFIE Biosciences. Kambiz Rahbar reports consulting fees from ABX, ABX-CRO, Bayer Healthcare, Pharmtrace, and AAA/Novartis and lectureship payments from AAA, Bayer Healthcare, Janssen Cilag, Sirtex, and Amgen. Matthias Eiber reports fees from Blue Earth Diagnostics Ltd. (consultant, research funding), Novartis/AAA (consultant, speaker), Telix (consultant), Bayer (consultant, research funding), RayzeBio (consultant), Point Biopharma (consultant), Eckert-Ziegler (speaker), Janssen Pharmaceuticals (consultant, speaker's bureau), Parexel (image reviews), and Bioclinica (image review) outside the submitted work and a patent application for rhPSMA. Wolfgang Fendler reports fees from SOFIE Bioscience (research funding), Janssen (consultant, speaker), Calyx (consultant, image review), Bayer (consultant, speaker, research funding), Novartis (speaker, consultant), Telix (speaker), GE Healthcare (speaker), Eczacıbaşı Monrol (speaker), Abx (speaker), and Amgen (speaker) outside the submitted work. No other potential conflict of interest relevant to this article was reported.

KEY POINTS

QUESTION: Is [^{177}Lu]Lu-PSMA therapy extension, either with continuous or rechallenge methods, safe? Does therapy extension improve survival and provide benefits?

PERTINENT FINDINGS: Extended therapy with [^{177}Lu]Lu-PSMA has been shown to be safe and has not been associated with an increased incidence of grades 3–4 toxicity. Patients treated with extended treatment experience a favorable median OS of 31.3 mo from the first administration. The response to [^{177}Lu]Lu-PSMA rechallenge demonstrates the preserved efficacy of [^{177}Lu]Lu-PSMA after a treatment break.

IMPLICATIONS FOR PATIENT CARE: Patients receiving extended [^{177}Lu]Lu-PSMA therapy experienced good responses and had long OS. Extended treatment was well tolerated.

REFERENCES

1. Sartor O, de Bono J, Chi KN, et al. Lutetium-177-PSMA-617 for metastatic castration-resistant prostate cancer. *N Engl J Med.* 2021;385:1091–1103.
2. Rahbar K, Ahmadzadehfar H, Kratochwil C, et al. German multicenter study investigating ^{177}Lu-PSMA-617 radioligand therapy in advanced prostate cancer patients. *J Nucl Med.* 2017;58:85–90.
3. Yordanova A, Linden P, Hauser S, et al. Outcome and safety of rechallenge [^{177}Lu]Lu-PSMA-617 in patients with metastatic prostate cancer. *Eur J Nucl Med Mol Imaging.* 2019;46:1073–1080.
4. Gafita A, Rauscher I, Retz M, et al. Early experience of rechallenge [^{177}Lu]-PSMA radioligand therapy after an initial good response in patients with advanced prostate cancer. *J Nucl Med.* 2019;60:644–648.
5. Kratochwil C, Fendler WP, Eiber M, et al. Joint EANM/SNMMI procedure guideline for the use of ^{177}Lu-labeled PSMA-targeted radioligand-therapy (^{177}Lu-PSMA-RLT). *Eur J Nucl Med Mol Imaging.* 2023;50:2830–2845.
6. Kratochwil C, Fendler WP, Eiber M, et al. EANM procedure guidelines for radionuclide therapy with ^{177}Lu-labelled PSMA-ligands (^{177}Lu-PSMA-RLT). *Eur J Nucl Med Mol Imaging.* 2019;46:2536–2544.
7. Gafita A, Djaileb L, Rauscher I, et al. Response Evaluation Criteria in PSMA PET/CT (RECIP 1.0) in metastatic castration-resistant prostate cancer. *Radiology.* 2023;308:e222148.
8. Mader N, Nguyen Ngoc C, Kirkgöze B, et al. Extended therapy with [^{177}Lu]Lu-PSMA-617 in responding patients with high-volume metastatic castration-resistant prostate cancer. *Eur J Nucl Med Mol Imaging.* 2023;50:1811–1821.
9. de Bono JS, Oudard S, Ozguroglu M, et al. Prednisone plus cabazitaxel or mitoxantrone for metastatic castration-resistant prostate cancer progressing after docetaxel treatment: a randomised open-label trial. *Lancet.* 2010;376:1147–1154.
10. Hofman MS, Emmett L, Sandhu S, et al. [^{177}Lu]Lu-PSMA-617 versus cabazitaxel in patients with metastatic castration-resistant prostate cancer (TheraP): a randomised, open-label, phase 2 trial. *Lancet.* 2021;397:797–804.
11. Schäfer H, Mayr S, Büttner-Herold M, et al. Extensive ^{177}Lu-PSMA radioligand therapy can lead to radiation nephropathy with a renal thrombotic microangiopathy-like picture. *Eur Urol.* 2023;83:385–390.
12. Steinhelfer L, Lunger L, Cala L, et al. Long-term nephrotoxicity of ^{177}Lu-PSMA radioligand therapy. *J Nucl Med.* 2024;65:79–84.
13. de Wit R, de Bono J, Sternberg CN, et al. Cabazitaxel versus abiraterone or enzalutamide in metastatic prostate cancer. *N Engl J Med.* 2019;381:2506–2518.
14. Lavaud P, Gravis G, Foulon S, et al. Anticancer activity and tolerance of treatments received beyond progression in men treated upfront with androgen deprivation therapy with or without docetaxel for metastatic castration-naïve prostate cancer in the GETUG-AFU 15 phase 3 trial. *Eur Urol.* 2018;73:696–703.
15. Oudard S, Kramer G, Caffo O, et al. Docetaxel rechallenge after an initial good response in patients with metastatic castration-resistant prostate cancer. *BJU Int.* 2015;115:744–752.
16. Pobel C, Auclin E, Teyssonneau D, et al. Cabazitaxel multiple rechallenges in metastatic castration-resistant prostate cancer. *Cancer Med.* 2021;10:6304–6309.
17. Mottet N, van den Bergh RCN, Briers E, et al. EAU Prostate Cancer Guidelines website. https://uroweb.org/guidelines/prostate-cancer/summary-of-changes/2023. Published 2023. Accessed April 10, 2024.

RECIP 1.0 Predicts Progression-Free Survival After [^{177}Lu]Lu-PSMA Radiopharmaceutical Therapy in Patients with Metastatic Castration-Resistant Prostate Cancer

Andrei Gafita[1,2], Loic Djaileb[2,3], Isabel Rauscher[4], Wolfgang P. Fendler[5], Boris Hadaschik[6], Steven P. Rowe[7], Ken Herrmann[5], Lilja B. Solnes[1], Jeremie Calais[2], Matthew B. Rettig[8,9], Manuel Weber[5], Andrea Farolfi[2,10], Matthias R. Benz[2,11], and Matthias Eiber[4]

[1]Division of Nuclear Medicine and Molecular Imaging, Russell H. Morgan Department of Radiology and Radiological Science, Johns Hopkins University School of Medicine, Baltimore, Maryland; [2]Ahmanson Translational Theranostics Division, Department of Molecular and Medical Pharmacology, UCLA, Los Angeles, California; [3]LRB, Nuclear Medicine Department, CHU Grenoble Alpes, INSERM, Université Grenoble Alpes, Grenoble, France; [4]Department of Nuclear Medicine, Klinikum rechts der Isar, Technical University Munich, Munich, Germany; [5]Department of Nuclear Medicine, German Cancer Consortium–University Hospital Essen, University of Duisburg–Essen, Essen, Germany; [6]Department of Urology, German Cancer Consortium–University Hospital Essen, University of Duisburg–Essen, Essen, Germany; [7]Molecular Imaging and Therapeutics, Department of Radiology, University of North Carolina School of Medicine, Chapel Hill, North Carolina; [8]Department of Urology, David Geffen School of Medicine, UCLA, Los Angeles, California; [9]VA Greater Los Angeles, Los Angeles, California; [10]Nuclear Medicine, IRCCS Azienda Ospedaliero–Universitaria di Bologna, Bologna, Italy; and [11]Department of Radiological Sciences, UCLA, Los Angeles, California

Response Evaluation Criteria in Prostate-Specific Membrane Antigen Imaging (RECIP) 1.0 is an evidence-based framework to evaluate therapeutic efficacy in metastatic prostate cancer using prostate-specific membrane antigen (PSMA) PET/CT. This study aimed to evaluate the associations of interim PSMA PET/CT by RECIP 1.0 with short-term outcome after radiopharmaceutical treatment. **Methods:** This multicenter retrospective study included patients with metastatic castration-resistant prostate cancer who underwent [^{177}Lu]Lu-PSMA radiopharmaceutical therapy at 3 academic centers and received PSMA PET/CT at baseline and at 12 wk. Pairs of PSMA PET/CT images were assessed by 5 readers for visual RECIP 1.0. The primary outcome was the association of RECIP with prostate-specific antigen progression-free survival (PSA-PFS) by Kaplan–Meier analysis. **Results:** In total, 124 of 287 screened patients met the inclusion criteria, with 0 (0%), 29 (23%), 54 (44%), and 41 (33%) of those 124 patients having complete response, partial response, stable disease, or progressive disease (PD) by visual RECIP 1.0, respectively. Patients with visual RECIP PD had a significantly shorter PSA-PFS than those with RECIP stable disease or with RECIP partial response (2.6 vs. 6.4 vs. 8.4 mo; $P < 0.001$). The median PSA-PFS among patients with RECIP PD versus those with non-RECIP PD was 2.6 versus 7.2 mo (hazard ratio, 13.0; 95% CI, 7.0–24.1; $P < 0.001$). **Conclusion:** PSMA PET/CT by RECIP 1.0 after 2 cycles of [^{177}Lu]Lu-PSMA is prognostic for PSA-PFS. PSMA PET/CT by RECIP 1.0 may be used in earlier stages of prostate cancer to evaluate drug efficacy and to predict progression-free survival.

Key Words: metastatic castration-resistant prostate cancer; PSMA PET; response evaluation; RECIP; LuPSMA; radiopharmaceutical therapy

J Nucl Med 2024; 65:917–921
DOI: 10.2967/jnumed.123.267234

Prostate-specific membrane antigen (PSMA) theranostics with [^{177}Lu]Lu-PSMA-617 improves the overall survival (OS) and progression-free survival in patients with metastatic castration-resistant prostate cancer (mCRPC) (*1*), which has led to drug approval. The U.S. Food and Drug Administration approved [^{68}Ga]Ga-PSMA-11, [^{18}F]DCFPyL, and [^{18}F]rhPSMA-7.3 PET/CT in patients with prostate cancer and suspected metastases who were candidates for initial definitive therapy or who had suspected recurrence based on elevated prostate-specific antigen (PSA) levels to determine eligibility for [^{177}Lu]Lu-PSMA-617 therapy (*2–4*).

Besides staging and restaging, cancer imaging can be used to evaluate therapeutic efficacy. Objective criteria for measuring response to cancer treatment are critical to clinical research and practice (*5*). Therapeutic clinical trials of metastatic disease often use radiographic endpoints to evaluate response to treatment (*6*).

Response Evaluation Criteria in PSMA Imaging (RECIP) version 1.0 is an evidence-based framework to evaluate therapeutic efficacy in metastatic prostate cancer using PSMA PET/CT and was developed on the basis of OS outcomes in patients treated with [^{177}Lu]Lu-PSMA (*7–9*). Further studies validated RECIP 1.0 for measuring response based on associations with OS in mCRPC patients who received androgen-receptor–signaling inhibitors (*10,11*) and in early-stage prostate cancer patients with biochemical recurrence after the initial therapy (*12*).

PSA progression-free survival (PSA-PFS) is an efficacy endpoint commonly used in metastatic prostate cancer as a surrogate for OS. Currently, evidence is lacking for the association of RECIP 1.0 with short-term outcome, that is, progression-free survival.

The current retrospective analysis aims to evaluate the associations of 12-wk PSMA PET/CT by RECIP 1.0 with progression-free survival in mCRPC patients who receive [^{177}Lu]Lu-PSMA.

Received Dec. 12, 2023; revision accepted Mar. 13, 2024.
For correspondence or reprints, contact Andrei Gafita (agafita1@jhmi.edu).

MATERIALS AND METHODS

Patients

Consecutive patients with mCRPC who were treated with [^{177}Lu]Lu-PSMA-617 or [^{177}Lu]Lu-PSMA imaging and therapy (I&T) between December 10, 2014, and July 19, 2019, at 3 academic medical centers were screened for eligibility. Eligible patients had received PSMA PET/CT at baseline and at 12 wk after 2 cycles of treatment (interim PET) using the same PSMA-targeting radiotracer for the baseline and interim PET examinations. Detailed inclusion and exclusion criteria are given in Supplemental Figure 1 (supplemental materials are available at http://jnm.snmjournals.org). Treatment protocols are detailed in the supplemental materials. All patient data were previously reported (*7–9*). These prior publications reported the development of RECIP 1.0 and evaluated its prognostic value for OS. In contrast to prior work, this study investigated the prognostic value of RECIP 1.0 for PSA-PFS after [^{177}Lu]Lu-PSMA radiopharmaceutical therapy. This retrospective analysis was approved by the ethics committee of each participating site (115/18S, 20-000954, and UKE 19-8570-BO), and the requirement for study-specific consent was waived. PSMA PET/CT image acquisition protocols were described previously (*7*) and are detailed in Supplemental Table 1.

Image Analysis

PSMA PET/CT images were interpreted independently by 5 experienced nuclear medicine physicians. Each reader was provided with guidelines for image interpretation (supplemental materials), was masked to the outcome data, and was not involved in the study design. Readers were asked to interpret the baseline and 12-wk posttreatment PSMA PET/CT scans for visual RECIP and quantitative RECIP 1.0, as described previously (*9*).

Visual RECIP was determined by combining changes in PSMA-positive total tumor volume evaluated visually by nuclear medicine physicians with the status of new lesions. Visual assessment of changes in PSMA-positive total tumor volume were approximated qualitatively by means of side-by-side comparison of baseline and follow-up maximum-intensity projection PSMA PET/CT images. In borderline cases, additional analysis of axial sections was performed.

Quantitative RECIP was determined by combining changes in PSMA-positive total tumor volume determined by a nuclear medicine physician using tumor segmentation software (qPSMA software (*13*)) with the status of new lesions. After tumor segmentation was performed, the PSMA volume was obtained by calculating the volume of all voxels that were annotated as PSMA-positive tumors. Changes in total tumor volume were determined by calculating the percentage change between baseline and follow-up PSMA PET/CT scans.

Disagreement among readers was resolved by majority rule. Definition of RECIP 1.0, including definition of occurrence of new lesions, is given in Table 1.

Statistical Analysis

Values are reported as medians with interquartile ranges for continuous variables and numbers with percentages for categoric variables. Response according to RECIP 1.0 was classified into progressive disease (PD), stable disease (SD), partial response (PR), or complete response and dichotomized for the differentiation of progression versus nonprogression (RECIP PD vs. non-PD, where non-PD included complete response, PR, and SD). The primary outcomes of our study were the associations of RECIP 1.0 with PSA-PFS. Associations between RECIP 1.0 and PSA-PFS were tested by Cox regression analyses, and the hazard ratio (HR), its 95% CI, and the corresponding *P* values were derived. PSA progression was defined per Prostate Cancer Clinical Trial Working Group 3 criteria as the time from treatment initiation to PSA progression (≥25% increase from baseline). The median survival time and its 95% CI for each group of patients and the entire cohort were calculated using Kaplan–Meier analysis. Kaplan–Meier curves were truncated when the number at risk fell below 10. Subgroup analyses were performed to evaluate associations of RECIP 1.0 with PSA-PFS for each treatment type, that is, [^{177}Lu]Lu-PSMA-617 and [^{177}Lu]Lu-PSMA I&T. A *P* value of less than 0.05 was considered indicative of a statistically significant difference. All statistical analyses were performed using SPSS Statistics, version 27 (IBM).

RESULTS

In total, 124 of 287 (43%) screened patients with mCRPC were eligible and included. Of the 124 eligible patients, 102 (82%) received treatment with [^{177}Lu]Lu-PSMA I&T and 22 (18%) received treatment with [^{177}Lu]Lu-PSMA-617. The median age was 73 y (interquartile range, 67–76 y). In total, 99 of 124 (80%) patients received taxane-based chemotherapy and 123 of 124

TABLE 1
Definitions of New Lesions and RECIP

Parameter	Definition
New lesion	Any new focal uptake of PSMA ligand
	Higher than the surrounding background
	With tumor SUV_{max} > blood-pool SUV_{max}
	Not present on baseline scan (tumor SUV_{max} < blood-pool SUV_{max})
	With tumor uptake not attributable to physiologic uptake or pitfalls
	Any new malignant lesion detected on follow-up CT images independent of PSMA-ligand uptake
RECIP 1.0	
RECIP-CR	Absence of any PSMA-ligand uptake on follow-up PET scan
RECIP-PR	≥30% decrease in PSMA-VOL without appearance of new lesion
RECIP-PD	≥20% increase in PSMA-VOL with appearance of new lesion
RECIP-SD	Does not meet the criteria for CR, PR, or PD

CR = complete response; PSMA-VOL = volume of PSMA.

(99%) received androgen-receptor–signaling inhibitors. Detailed patient characteristics are given in Table 2. The data cutoff date for the final analysis was July 1, 2022, and all patients had PSA progression at the last follow-up. The median PSA-PFS was 3.8 mo (95% CI, 3.1–4.6 mo). After the majority rule of the 5 readers for visual RECIP 1.0 was applied, 41 of 124 (33%) patients had RECIP PD and 83 of 124 (67%) had RECIP non-PD, of whom 0 (0%), 29 (23%), and 54 (44%) of the 124 patients had

TABLE 2
Patient Characteristics (*n* = 124)

Characteristic	Data
Age (y)	73 (67–76)
Time since diagnosis of prostate cancer (y)	6 (4–11)
Gleason score at diagnosis*	
<8	36 (32%)
≥8	75 (68%)
M status at diagnosis	
M0	75 (60%)
M1	49 (40%)
Primary treatment	
Prostatectomy with or without lymphadenectomy	70 (56%)
Local radiotherapy	12 (10%)
Systemic treatment	42 (34%)
PSA (ng/mL)	139 (37–427)
Lactate dehydrogenase (U/L)	286 (223–408)
Total alkaline phosphatase (U/L)	125 (81–250)
Hemoglobin (g/dL)	9.9 (11.3–12.7)
ECOG performance status	
0	31 (25%)
1	83 (67%)
2	10 (8%)
Previous mCRPC treatments	
Previous chemotherapy	99 (80%)
Docetaxel	98 (79%)
Cabazitaxel	20 (16%)
Androgen-signaling inhibitors	123 (99%)
Abiraterone	111 (90%)
Enzalutamide	78 (63%)
^{223}Ra	24 (19%)
Prior lines of mCRPC systemic treatment	
1	9 (7%)
≥2	115 (93%)
≥3	71 (57%)
≥4	33 (27%)
Sites of disease on PSMA PET/CT	
Bone	114 (92%)
Nodal	101 (81%)
Bone plus nodal	92 (74%)
Visceral	32 (26%)
Bone plus nodal plus visceral	27 (22%)

*Data missing for 13 patients.
M = metastasized; ECOG = Eastern Cooperative Oncology Group.
Continuous data are median and interquartile range. Qualitative data are number and percentage.

visual RECIP complete response, PR, and SD, respectively. After the majority rule for quantitative RECIP 1.0 was applied, 40 of 124 (32%) patients had RECIP PD and 84 of 124 (68%) had RECIP non-PD, of whom 0 (0%), 40 (32%), and 44 (36%) of the 124 patients had visual RECIP complete response, PR, and SD, respectively.

PSA-PFS

Visual RECIP. The median PSA-PFS among patients with RECIP PD versus RECIP SD versus RECIP PR was 2.6 versus 6.4 versus 8.4 mo, respectively (Fig. 1). RECIP PD was associated with a significantly shorter PSA-PFS than that with RECIP SD (HR, 11.2; 95% CI, 6.0–21.3; $P < 0.001$) and that with RECIP PR (HR, 17.1; 95% CI, 8.4–34.9; $P < 0.001$). RECIP SD was associated with shorter—albeit not statistically significant—PSA-PFS than that with RECIP PR (HR, 1.5; 95% CI, 0.9–2.5; $P = 0.10$). The median PSA-PFS among patients with RECIP PD versus RECIP non-PD was 2.6 versus 7.2 mo (HR, 13.0; 95% CI, 7.0–24.1; $P < 0.001$) (Fig. 1). In the subgroup analysis, RECIP PD was associated with shorter PSA-PFS than was RECIP non-PD in patients treated with [^{177}Lu]Lu-PSMA I&T (HR, 12.7; 95% CI 6.4–25.1; $P < 0.001$) or [^{177}Lu]Lu-PSMA-617 (HR, 10.5; 95% CI, 2.5–43.0; $P = 0.001$) (Supplemental Fig. 2).

Quantitative RECIP. The median PSA-PFS for RECIP PD versus that for RECIP SD versus that for RECIP PR was 2.7 versus 5.4 versus 8.9 mo, respectively (Fig. 1). RECIP PD was associated with significantly shorter PSA-PFS than were RECIP SD (HR, 4.7; 95% CI, 2.8–7.9; $P < 0.001$) and RECIP PR (HR, 10.7; 95% CI, 6.0–19.2; $P < 0.001$). RECIP SD was associated with significantly shorter PSA-PFS than was RECIP PR (HR, 2.9; 95% CI, 1.4–3.7; $P < 0.001$). The median PSA-PFS among patients with RECIP PD versus RECIP non-PD was 2.7 versus 6.5 mo (HR, 6.8; 95% CI, 4.1–11.2; $P < 0.001$) (Fig. 1). In the subgroup analysis, RECIP PD was associated with shorter PSA-PFS than was RECIP non-PD in patients treated with [^{177}Lu]Lu-PSMA I&T (HR, 6.3; 95% CI, 3.7–10.9; $P < 0.001$) or [^{177}Lu]Lu-PSMA-617 (HR, 10.5; 95% CI, 2.5–43.0; $P = 0.001$) (Supplemental Fig. 2).

DISCUSSION

OS is a gold standard endpoint in cancer research and is desired by regulatory authorities for drug approval in phase 3 registration

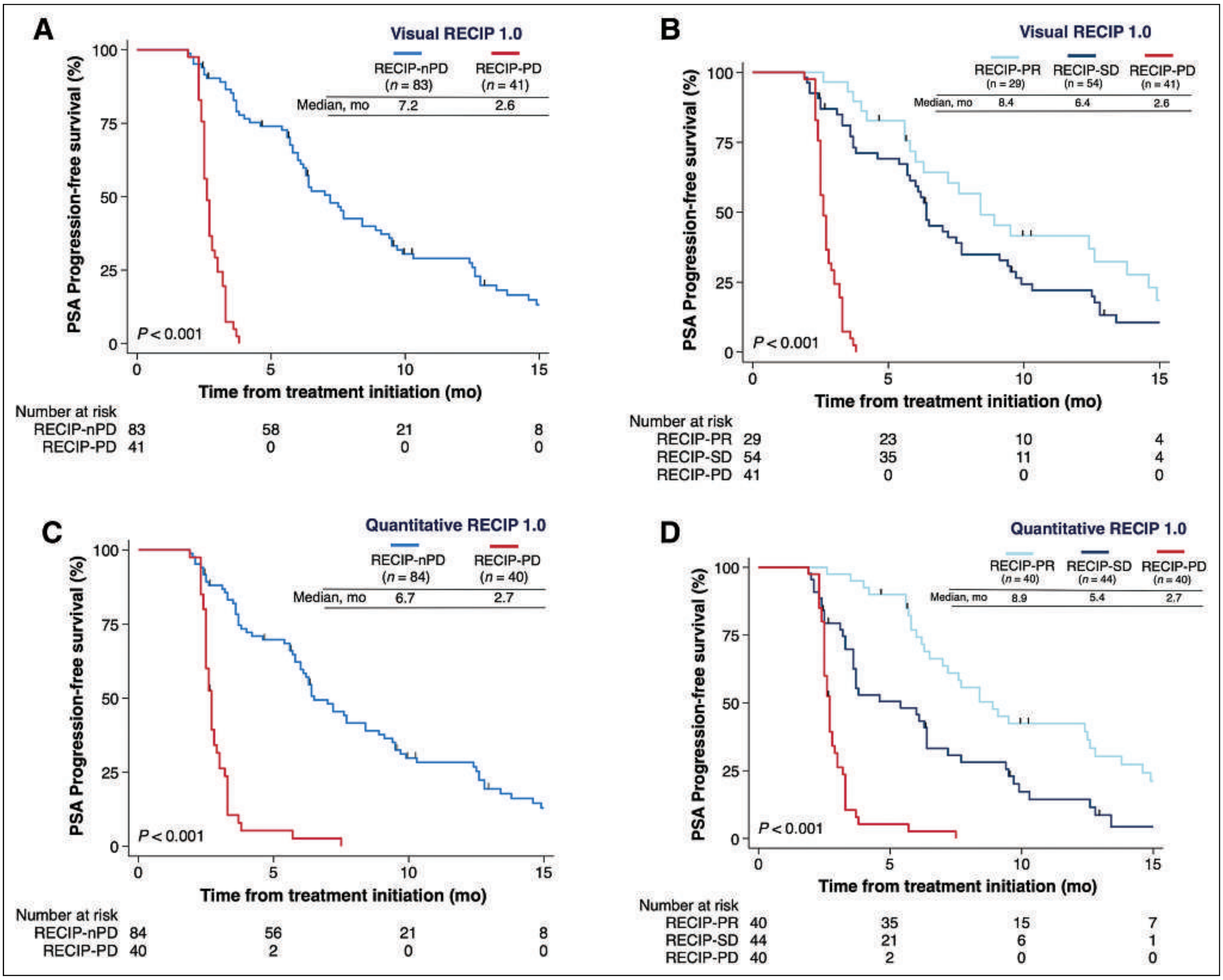

FIGURE 1. Associations between visual RECIP 1.0 (A and B) and quantitative RECIP 1.0 (C and D) responses with PSA-PFS. nPD = non-PD.

trials. Surrogate endpoints are increasingly accepted by regulatory bodies for accelerated approvals of prostate cancer therapies, particularly in earlier disease stages, for example, metastatic hormone-sensitive prostate cancer, nonmetastatic CRPC, or early-stage mCRPC, in which the average life expectancy exceeds 2 y. Up to 48% of prostate cancer therapeutic trials use progression-free survival as a surrogate endpoint for OS (*14*). PSA-PFS is often used as a primary endpoint in phase 2 clinical trials of prostate cancer to investigate principal drug efficacy. For example, the EnzaP randomized trial of enzalutamide versus enzalutamide plus [^{177}Lu]Lu-PSMA-617 in chemotherapy-naïve mCRPC patients used PSA-PFS as the primary endpoint (*15*), whereas the TheraP randomized trial of [^{177}Lu]Lu-PSMA-617 versus cabazitaxel in postchemotherapy mCRPC patients used PSA-PFS as the secondary endpoint (*16*).

The present analysis found that response evaluation by RECIP 1.0 at 12-wk PSMA PET/CT is associated with progression-free survival after [^{177}Lu]Lu-PSMA radiopharmaceutical therapy. Patients with RECIP PD had significantly shorter PSA-PFS than those patients with RECIP SD and RECIP PD. These findings suggest that PSMA PET/CT performed after 2 cycles of [^{177}Lu]Lu-PSMA may identify patients who will shortly progress by PSA. A strategy in which patients with RECIP PD at 12 wk switch to a more efficacious treatment may improve clinical outcomes.

RECIP 1.0 is a framework for response evaluation that can be determined in two ways, that is, qualitatively by visual reads of nuclear medicine physicians and radiologists (visual RECIP) or quantitatively using tumor segmentation software (quantitative RECIP). A recent study found a 95% agreement between quantitative and visual RECIP PD versus non-PD. In the present analysis, visual RECIP PR failed to show significantly superior PSA-PFS compared with that of RECIP SD (HR, 1.5; $P = 0.10$), whereas the quantitative RECIP PR showed superior PSA-PFS compared with that of RECIP SD (HR = 2.9; $P < 0.001$), highlighting the need for training in evaluating responses in total tumor volume in PSMA PET/CT before applying visual RECIP 1.0 in clinical practice.

Altogether, previous and current findings demonstrated that RECIP 1.0 is associated with PSA-PFS and OS in mCRPC. The data support the implementation of RECIP 1.0 in daily practice and clinical trials for treatment response evaluation in mCRPC patients during [^{177}Lu]Lu-PSMA radiopharmaceutical therapy. Notably, visual RECIP 1.0 should be used to determine only clinically relevant PD versus non-PD, whereas quantitative RECIP 1.0 can be used to classify PR versus SD versus PD. Further, the data encourage evaluation of associations of RECIP 1.0 with outcome data in patients who are earlier in the disease trajectory and who have a longer life expectancy.

The main limitation of this study is the use of the same patient cohort that was used to develop RECIP 1.0 (*7*). However, the current study used PSA-PFS as the study outcome, whereas the initial analysis used OS as the endpoint. Other limitations include the study's retrospective design and lack of a comparative treatment arm to test the prognostic versus predictive value of RECIP 1.0.

CONCLUSION

PSMA PET/CT by RECIP 1.0 after 2 cycles of [^{177}Lu]Lu-PSMA is prognostic for PSA-PFS. PSMA PET/CT by RECIP 1.0 may be used in earlier stages of prostate cancer to evaluate drug efficacy and to predict progression-free survival. Further studies to validate our findings in a prospective setting are warranted.

KEY POINTS

QUESTION: Is RECIP 1.0 associated with progression-free survival in patients with mCRPC who are treated with [^{177}Lu]Lu-PSMA?

PERTINENT FINDINGS: This retrospective multicenter analysis demonstrated that interim PSMA PET/CT performed after 2 cycles of [^{177}Lu]Lu-PSMA and evaluated by RECIP 1.0 is significantly associated with PSA-PFS.

IMPLICATIONS FOR PATIENT CARE: PSMA PET/CT by RECIP 1.0 may be used in earlier stages of prostate cancer to evaluate drug efficacy and predict progression-free survival.

DISCLOSURE

Andrei Gafita is supported by the Prostate Cancer Foundation (21YOUN18). Steven Rowe is a consultant for Progenics Pharmaceutical, Inc., a wholly owned subsidiary of Lantheus, Inc., and the licensee of ^{18}F-DCFPyL. Loic Djaileb is the recipient of a grant from the Fondation ARC pour la recherche sur le cancer, Nuovo Soldati Foundation, and the Phillipe Foundation Inc. (New York). Boris Hadaschik is on the advisory boards of Janssen, Bayer, ABX, Lightpoint, Amgen, MSD, Pfizer, and Novartis; is an invited speaker for Accord, Astellas, and Janssen R&D; receives research funding from AAA/Novartis, Bristol Myers Squibb, and German Research Foundation; and has leadership roles for DKG AUO and DGU. Wolfgang Fendler reports fees from SOFIE Bioscience (research funding), Janssen (consultant, speaker), Calyx (consultant, image review), Bayer (consultant, speaker, research funding), Novartis (speaker, consultant), Telix (speaker), GE Healthcare (speaker), Eczacıbaşı Monrol (speaker), Abx (speaker), and Amgen (speaker) outside the submitted work. Ken Herrmann reports receiving consultant fees from Advanced Accelerator Applications, a Novartis company, Amgen, AstraZeneca, Bain Capital, Bayer, Boston Scientific, Convergent, Curium, Debiopharm, EcoR1, Fusion, GE Healthcare, Immedica, Isotopen Technologien München, Janssen, Merck, Molecular Partners, NVision, POINT Biopharma, Pfizer, Radiopharm Theranostics, Rhine Pharma, Siemens Healthineers, SOFIE Biosciences, Telix, Theragnostics, and ymabs; receiving research grants from Advanced Accelerator Applications, a Novartis company, Boston Scientific, and Janssen; and having stock or other ownership interests with AdvanCell, Aktis Oncology, Convergent, NVision, Pharma 15, and SOFIE Biosciences. Matthias Eiber reports fees from Blue Earth Diagnostics Ltd. (consultant, research funding), Novartis/AAA (consultant, speaker), Telix (consultant), Bayer (consultant, research funding), RayzeBio (consultant), Point Biopharma (consultant), Eckert-Ziegler (speaker), Janssen Pharmaceuticals (consultant, speakers bureau), Parexel (image review), and Bioclinica (image review) outside the submitted work and has a patent application for rhPSMA. He and other inventors are entitled to royalties on sales of POSLUMA. No other potential conflict of interest relevant to this article was reported.

REFERENCES

1. Sartor O, de Bono J, Chi KN, et al. Lutetium-177-PSMA-617 for metastatic castration-resistant prostate cancer. *N Engl J Med.* 2021;385:1091–1103.
2. FDA approves second PSMA-targeted PET imaging drug for men with prostate cancer. U.S. Food and Drug Administration website. https://www.fda.gov/drugs/

news-events-human-drugs/fda-approves-second-psma-targeted-pet-imaging-drug-men-prostate-cancer. Updated May 27, 2021. Accessed April 3, 2024.

3. FDA approves first PSMA-targeted PET imaging drug for men with prostate cancer. U.S. Food and Drug Administration website. https://www.fda.gov/news-events/press-announcements/fda-approves-first-psma-targeted-pet-imaging-drug-men-prostate-cancer. Updated December 1, 2020. Accessed April 3, 2024.
4. Drug Trials Snapshot: POSLUMA. U.S. Food and Drug Administration website. https://www.fda.gov/drugs/drug-approvals-and-databases/drug-trials-snapshot-posluma. Updated January 16, 2024. Accessed April 3, 2024.
5. Eisenhauer EA, Therasse P, Bogaerts J, et al. New response evaluation criteria in solid tumours: revised RECIST guideline (version 1.1). *Eur J Cancer.* 2009;45:228–247.
6. Scher HI, Morris MJ, Stadler WM, et al. Trial design and objectives for castration-resistant prostate cancer: updated recommendations from the Prostate Cancer Clinical Trials Working Group 3. *J Clin Oncol.* 2016;34:1402–1418.
7. Gafita A, Rauscher I, Weber M, et al. Novel framework for treatment response evaluation using PSMA PET/CT in patients with metastatic castration-resistant prostate cancer (RECIP 1.0): an international multicenter study. *J Nucl Med.* 2022; 63:1651–1658. .
8. Gafita A, Rauscher I, Fendler WP, et al. Measuring response in metastatic castration-resistant prostate cancer using PSMA PET/CT: comparison of RECIST 1.1, aPCWG3, aPERCIST, PPP, and RECIP 1.0 criteria. *Eur J Nucl Med Mol Imaging.* 2022;49:4271–4281.
9. Gafita A, Djaileb L, Rauscher I, et al. Response Evaluation Criteria in PSMA PET/CT (RECIP 1.0) in metastatic castration-resistant prostate cancer. *Radiology.* 2023;308:e222148.
10. Shagera QA, Karfis I, Kristanto P, et al. PSMA PET/CT for response assessment and overall survival prediction in patients with metastatic castration-resistant prostate cancer treated with androgen receptor pathway inhibitors. *J Nucl Med.* 2023; 64:1869–1875.
11. Murthy V, Gafita A, Thin P, et al. Prognostic value of end-of-treatment PSMA PET/CT in patients treated with ^{177}Lu-PSMA radioligand therapy: a retrospective, single-center analysis. *J Nucl Med.* 2023;64:1737–1743.
12. Kendrick J, Francis RJ, Hassan GM, et al. Prognostic utility of RECIP 1.0 with manual and AI-based segmentations in biochemically recurrent prostate cancer from [^{68}Ga]Ga-PSMA-11 PET images. *Eur J Nucl Med Mol Imaging.* 2023;50: 4077–4086.
13. Gafita A, Bieth M, Krönke M, et al. qPSMA: semiautomatic software for whole-body tumor burden assessment in prostate cancer using ^{68}Ga-PSMA11 PET/CT. *J Nucl Med.* 2019;60:1277–1283.
14. Maeda H, Takeda K, Urushihara H, Kurokawa T. Searching for potential surrogate endpoints of overall survival in clinical trials for patients with prostate cancer. *Cancer Rep.* 2021;4:e1334.
15. Hofman MS, Emmett L, Sandhu S, et al. TheraP: ^{177}Lu-PSMA-617 (LuPSMA) versus cabazitaxel in metastatic castration-resistant prostate cancer (mCRPC) progressing after docetaxel: overall survival after median follow-up of 3 years (ANZUP 1603) [abstract]. *J Clin Oncol.* 2022;40(suppl 16):5000.
16. Emmett L, Subramaniam S, Joshua AM, et al. ENZA-p trial protocol: a randomized phase II trial using prostate-specific membrane antigen as a therapeutic target and prognostic indicator in men with metastatic castration-resistant prostate cancer treated with enzalutamide (ANZUP 1901). *BJU Int.* 2021;128:642–651.

Absorbed Dose–Response Relationship in Patients with Gastroenteropancreatic Neuroendocrine Tumors Treated with [^{177}Lu]Lu-DOTATATE: One Step Closer to Personalized Medicine

Kévin Hebert*[1], Lore Santoro*[1,2], Maeva Monnier[3], Florence Castan[3], Ikrame Berkane[1], Eric Assénat[4], Cyril Fersing[1–5], Pauline Gélibert[6], Jean-Pierre Pouget[2], Manuel Bardiès[1,2], Pierre-Olivier Kotzki[1,2], and Emmanuel Deshayes[1,2]

[1]Department of Nuclear Medicine, Institut du Cancer de Montpellier, Université de Montpellier, Montpellier, France; [2]Institut de Recherche en Cancérologie de Montpellier, INSERM U1194, Université de Montpellier, Montpellier, France; [3]Biometry Unit, Institut du Cancer de Montpellier, Université de Montpellier, Montpellier, France; [4]Department of Medical Oncology, CHU de Montpellier, Université de Montpellier, Montpellier, France; [5]IBMM, Université de Montpellier, CNRS, ENSCM, Montpellier, France; and [6]Centre Hospitalier Métropole Savoie, Chambéry, France

[^{177}Lu]Lu-DOTATATE has been approved for progressive and inoperable gastroenteropancreatic neuroendocrine tumors (GEP-NETs) that overexpress somatostatin receptors. The absorbed doses by limiting organs and tumors can be quantified by serial postinfusion scintigraphy measurements of the γ-emissions from ^{177}Lu. The objective of this work was to explore how postinfusion [^{177}Lu]Lu-DOTATATE dosimetry could influence clinical management by predicting treatment efficacy (tumor shrinkage and survival) and toxicity. **Methods:** Patients with GEP-NETs treated with [^{177}Lu]Lu-DOTATATE between 2016 and 2022 and who underwent dosimetry were included. Absorbed doses were calculated for healthy organs (liver, kidneys, bone marrow, and spleen) and tumors using PLANET Dose and the local energy deposition method based on serial posttreatment SPECT/CT. Up to 5 lesions per site were selected and measured on images collected at baseline and 3 mo after treatment end (measurement masked to the somatostatin receptor imaging uptake). For toxicity assessment, laboratory parameters were regularly monitored. Clinical data, including time to death or progression, were collected from the patients' health records. Correlations between absorbed doses by organs and toxicity and between absorbed doses by lesions and tumor volume variation were studied using regression models. **Results:** In total, 35 dosimetric studies were performed in patients with mostly grade 2 (77%) tumors and metastases in liver (89%), lymph nodes (77%), and bone (34%), and 146 lesions were analyzed: 1–9 lesions per patient, mostly liver metastases (65%) and lymph nodes (25%). The median total absorbed dose by tumors was 94.4 Gy. The absorbed doses by tumors significantly decreased between cycles. The absorbed dose by tumors was significantly associated with tumor volume variation ($P < 0.001$) 3 mo after treatment end, and it was a significant prognostic factor for survival. Toxicity analysis showed a correlation between the decrease of hematologic parameters such as lymphocytes or platelet concentrations and the absorbed doses by the spleen or bone marrow. The mean absorbed dose by the kidneys was not correlated with nephrotoxicity during the studied period. **Conclusion:** In patients treated with [^{177}Lu]Lu-DOTATATE for GEP-NETs, tumor and healthy organ dosimetry can predict survival and toxicities, thus influencing clinical management.

Key Words: [^{177}Lu]Lu-DOTATATE; neuroendocrine tumors; absorbed dose–response relationship

J Nucl Med 2024; 65:923–930
DOI: 10.2967/jnumed.123.267023

Well-differentiated neuroendocrine tumors (NETs) are a heterogeneous tumor type derived from the diffuse endocrine system. The primary sites are mostly the gastroenteropancreatic system and lungs. The World Health Organization proposed a prognostic classification of NETs in 3 grades based on the histologic features of proliferation (*1*). NETs usually overexpress somatostatin receptors (SSTRs), especially in grade 1 and grade 2 tumors. Since the 1990s, peptide receptor radionuclide therapy (PRRT) has been developed using radiolabeled somatostatin analogs, initially with ^{111}In (*2*) and ^{90}Y and more recently with ^{177}Lu. The NETTER-1 prospective randomized multicenter phase III trial showed an improvement in progression-free survival and health-related quality of life in patients with progressive midgut grade 1 or grade 2 NETs treated with [^{177}Lu]Lu-DOTATATE compared with patients receiving a high dose of long-acting octreotide (*3,4*). These results and a previous cohort study (*5*) led to the approval by regulatory authorities of [^{177}Lu]Lu-DOTATATE (Lutathera; AAA/Novartis) for the treatment of progressive or inoperable, well-differentiated gastroenteropancreatic NETs (GEP-NETs). This treatment has been reimbursed in Europe since 2017 and in the United States since 2018. The recommended regimen with [^{177}Lu]Lu-DOTATATE, derived from the NETTER-1 trial, consists of 4 intravenous injections of fixed activities (7.4 GBq) separated by an interval of 8 wk. This regimen is well tolerated by most patients. However, it does not take into account the full potential of [^{177}Lu]Lu compounds that can be imaged after injection to calculate the absorbed dose (AD) by organs and lesions because of coemission of γ-particles (*6*). The AD is a physical parameter that is expressed in grays and reflects the amount

---

Received Nov. 15, 2023; revision accepted Mar. 4, 2024.

For correspondence or reprints, contact Emmanuel Deshayes (emmanuel.deshayes@icm.unicancer.fr).

*Contributed equally to this work.

TABLE 1
Patient Characteristics

Parameter	Data related to dosimetric dataset
Median age at treatment start (y)	68
Sex	
Male	18 (51)
Female	17 (49)
Arterial hypertension	13 (37)
Diabetes	7 (20)
Carcinoid syndrome	9 (26)
Primary tumor site	
Small intestine	27 (77)
Pancreas	5 (14)
Rectum	3 (9)
Site of metastases at treatment start	
Lymph nodes	27 (77)
Peritoneum	7 (20)
Bone	12 (34)
Liver	31 (89)
Tumor grade	
1	6 (17)
2	27 (77)
3	1 (3)
Unknown	1 (3)
Treatment before [^{177}Lu]Lu-DOTATATE	
Chemotherapy	12 (34)
Targeted therapy	14 (40)
Radiotherapy	4 (11)
Locoregional liver therapy	15 (43)
Somatostatin analogs	35 (100)
Surgery	11 (48)
Previous PRRT with [^{177}Lu]Lu-DOTATATE	2 (6)
At least 1 treatment before [^{177}Lu]Lu-DOTATATE	35 (100)
Markers of progression	
Clinical	14 (40)
Biologic	20 (59)
Radiologic	29 (83)

Data are number and percentage, except for age.

of energy in joules released by ionizing radiation and absorbed per unit mass of tissue (in kilograms). For a given radionuclide and a given cell type, the damage to cells progressively increases with the AD. It has been shown that when [^{177}Lu]Lu-based PRRT ([^{177}Lu]Lu-PRRT) is given with a fixed regimen, the ADs by organs and tumors are heterogeneous among individuals (*7,8*). This variability is directly correlated with the drug biodistribution and its residence time in the organs of interest. In [^{177}Lu]Lu-PRRT, the relationships between ADs by healthy organs and biologic effects (i.e., toxicities) have been studied mostly using kidney dosimetry and kidney function assessment. Different methods have been proposed to calculate the ADs by kidneys after [^{177}Lu]Lu-PRRT, but none found a correlation between ADs and acute and middle–to–long-term kidney impairment (*9,10*). Concerning hematologic toxicities, some retrospective cohort studies found significant correlations between the AD of bone marrow (*11,12*) or the spleen (*13*) and the decrease of blood count parameters (i.e., platelets, white blood cells, hemoglobin). In addition, the relationship between the AD by tumors and efficacy has been little studied. A few studies found a positive correlation between the AD by the small intestine or pancreatic NETs and tumor shrinkage (*14,15*), a tumor volume decrease based on SSTR molecular imaging (*16*), and recently that the AD by NETs can predict patient survival (*17*). The aim of this study was to explore how postinfusion [^{177}Lu]Lu-DOTATATE dosimetry in

TABLE 2
Number of [^{177}Lu]Lu-DOTATATE Cycles

Cycle	Data
1	0 (0)
2	2 (6)
3	3 (8)
4	30 (86)

Data are number and percentage.

patients with GEP-NETs treated with a fixed regimen could influence the clinical management by predicting treatment efficacy (tumor shrinkage and survival) and toxicity.

MATERIALS AND METHODS

Patients and Treatments

Patients who were treated with [^{177}Lu]Lu-DOTATATE (Lutathera; AAA/Novartis) between 2016 and 2022 for progressive GEP-NETs overexpressing SSTRs and who underwent imaging for dosimetric purposes after each [^{177}Lu]Lu-DOTATATE cycle were included in this retrospective single-center study. They received an intravenous injection of a fixed activity of 7.4 GBq of [^{177}Lu]Lu-DOTATATE every 8 wk ($\leq$4 injection cycles in total). To avoid nephrotoxicity, an intravenous injection of amino acid solution (1 L, 25 g of arginine, and 25 g of lysine) was delivered to patients over 4 h, starting 30 min before [^{177}Lu]Lu-DOTATATE infusion. Clinical and biologic data were extracted from the patients' health records. The study was approved by the institutional ethics review board (ICM-ART 2023/03).

Dosimetry Workflow

The calibration steps of the SPECT/CT Discovery NM/CT 670 system (GE Healthcare) are detailed in the supplemental materials (available at http://jnm.snmjournals.org). For cycles 1 and 2, SPECT/CT images with at least 1 field of view that included the kidneys and liver were planned at 4, 24, 72, and 192 h after injection of [^{177}Lu]Lu-DOTATATE. For cycles 3 and 4, a single-time-point SPECT/CT acquisition was performed 24 h after injection, aligning with the patient's release timing. [^{177}Lu]Lu-DOTATATE scintigraphy acquisitions were performed and reconstructed according to a previously described protocol (*18*). Briefly, a medium-energy general-purpose collimator was used. For 60 projections at 45 s each, the energy window was set at 208 keV ± 20%, with a 10% scatter window centered at 177 keV. Attenuation, scatter, and recovery resolution corrections were applied. The first CT scan (4 h after injection) was acquired with 120 kV, automatic milliampere regulation, a slice thickness of 5 mm, a rotation time of 0.8 s, a pitch of 1.375, and a pixel matrix of 512 × 512. All other CT scans were acquired with parameters inducing lower irradiation (rotation time, 0.6 s; 80 mA fixed). Dosimetry was performed using the European Conformity–marked PLANET Dose software, version 3.1.1.83 (DOSIsoft SA). An automatic and rigid registration based on the first CT image, taken as a reference, was performed for all SPECT/CT images of the same cycle. The volumes of interest of healthy organs (spleen, kidneys, liver, and trabecular sections of lumbar vertebrae 2–4, representing bone marrow) were manually segmented on the reference CT image and then propagated and adjusted to the subsequent SPECT/CT images. For lesions, the volumes of interest were initially delineated on baseline, pretreatment, and contrast-enhanced CT (BL-CT) images and then drawn on scintigraphy images on the basis of an isocontour that corresponded to the volume defined on the BL-CT image. For the first 2 cycles, time-absorbed dose-rate curves were produced and fitted using a monoexponential model. ADs were calculated using the local energy deposition method with density correction. To simplify the procedure, for cycles 3 and 4, ADs were calculated with the following equation,

$$\text{AD cycle 3 or 4} = \text{AD cycle 2} \times \frac{\text{counts 24 h cycle 3 or 4}}{\text{counts 24 h cycle 2}} \times \frac{\text{V 24 h cycle 2}}{\text{V 24 h cycle 3 or 4}},$$

where AD cycle 2 is the AD calculated after cycle 2 (with 4 time points), counts 24 h is the number of counts in structures segmented on the SPECT/CT images acquired 24 h after [^{177}Lu]Lu-DOTATATE injection, and V 24 h is the volume of the related structure. A partial-volume–effect correction was performed by applying to AD a recovery coefficient based on the calibration studies (supplemental materials).

Choice of Lesions of Interest

Target lesions were selected on the BL-CT images, masked to their SSTR expression status, and manually contoured to produce a volume of interest. They were categorized by the following sites: liver, lymph nodes, mesenteric mass, pancreas, and peritoneum. A maximum of 5 lesions per organ or site was allowed per patient (including the lesions with the highest and smallest volume in each organ). Bone lesions were excluded because of the difficulty in assessing the response to treatment. Lesions smaller than 2 cm^3 were excluded to minimize the

TABLE 3
Laboratory Toxicities According to Common Terminology Criteria for Adverse Events (Version 4.03) During [^{177}Lu]Lu-DOTATATE Therapy

	Laboratory toxicity			
Blood count parameter	At least 1 grade 1	At least 1 grade 2	At least 1 grade 3	At least 1 grade 4
GFR (CKD-EPI formula) decrease	32 (91.4)	11 (31.4)	0 (0.0)	0
Hemoglobin decrease	14 (40.0)	0 (0.0)	0 (0.0)	0
Leukocyte count decrease	35 (100.0)	10 (28.6)	1 (2.9)	0
Lymphocyte count decrease	30 (85.7)	29 (82.9)	21 (60.0)	0
Platelet count decrease	14 (40.0)	4 (11.4)	1 (2.9)	0

GFR = glomerular filtration rate; CKD-EPI = Chronic Kidney Disease Epidemiology Collaboration.
Data are number and percentage.

TABLE 4

Variation in Laboratory Parameters Between First Injection and Month 3 and Then 12 Months After Last Injection

Blood count parameters	*n*	Before first injection	Month 3 after last injection	*P*	*n*	Before first injection	Month 12 after last injection	*P*
GFR (mL/min/1.73 m^2)	31	72.1 (15)	72.5 (17.3)	0.921	23	70.4 (13.9)	76 (18.1)	0.247
Hemoglobin (g/dL)	32	13.4 (1.3)	12.4 (1.4)	0.009*	24	13.2 (1.2)	12.5 (1.7)	0.095
Leukocytes ($\times 10^9$/L)	32	6.5 (2.2)	4.1 (1.2)	<0.001*	23	5.9 (1.9)	4.3 (1.2)	0.001*
Lymphocytes ($\times 10^9$/L)	32	1.5 (0.5)	0.8 (0.3)	<0.001*	24	1.5 (0.5)	0.9 (0.3)	<0.001*
Platelets ($\times 10^9$/L)	31	218 (68)	162.5 (51.1)	<0.001*	24	216.1 (68)	185.5 (69.1)	0.128

---

*$P < 0.05$.

GFR = glomerular filtration rate.

Data are means with SD in parentheses. *P* values were determined by Student *t* test.

partial-volume effect (2 cm^3 corresponds to a recovery factor of 0.5; Supplemental Fig. 1). The lesion volume was reassessed on the contrast-enhanced CT images performed 3 mo after the last [^{177}Lu]Lu-DOTATATE injection (M3-CT). Variations in the lesion volume between BL-CT and M3-CT were defined as

$$\text{DeltaV\%} = 100 \times \frac{V[\text{M3-CT}] - V[\text{BL-CT}]}{V[\text{BL-CT}]},$$

where DeltaV% is the variation of lesion volume and V[M3-CT] and V[BL-CT] are the lesion volumes of M3-CT and BL-CT, respectively.

Collected Data and Studied Parameters

Laboratory parameters were collected from the patients' health records before the first cycle and around day 15 after each cycle, including hemoglobin, white blood cell count, platelet count, creatinine concentration, and glomerular filtration rate, which was estimated using the creatinine serum levels and the Chronic Kidney Disease Epidemiology Collaboration formula. Treatment efficacy was assessed using RECIST 1.1 and by comparing BL-CT and M3-CT images. Toxicity was graded according to the Common Terminology Criteria for Adverse Events (version 4.03). Cumulative AD (CumAD) is defined as the sum of the AD calculated after each cycle for the same PRRT course and the sum used to correlate with toxicity (Supplemental Fig. 2). To define the dosimetric indices for lesions, the following variables were studied: the mean of the total AD of all lesions in each patient and the lesions with the highest (Max) and the lowest (Min) total AD among all lesions in each patient.

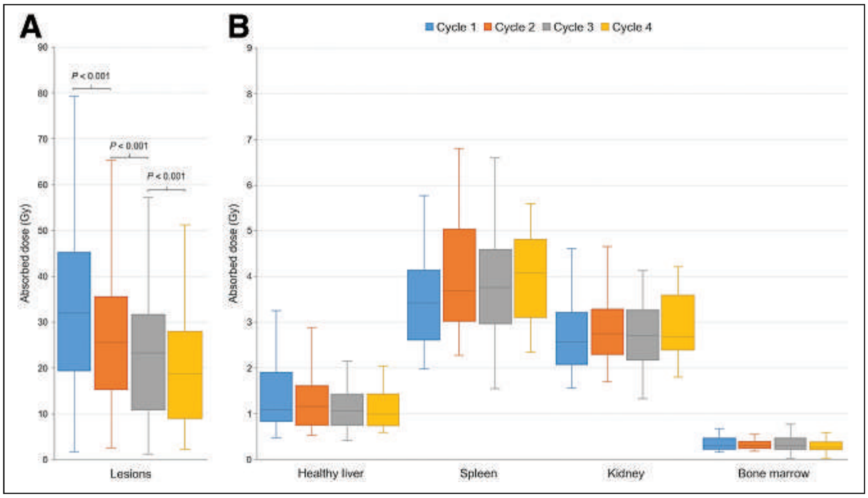

FIGURE 1. Distribution of ADs by lesions (A) and selected healthy organs (B) in 4 PPRT cycles.

Statistical Analysis

Qualitative variables were described using the number of observations and the frequency of each modality. Percentages were calculated excluding missing data. Quantitative data were described using the medians, the minimum, and the maximum or the means and the SD. Variables of interest were dichotomized using the medians. The statistical analyses are fully described in the supplemental materials. All analyses were done with SAS version 9.4 software (SAS Products & Solutions) and R version 4.0.3 software (The R Project for Statistical Computing).

RESULTS

In total, 34 patients met the inclusion criteria. Among them, 2 patients were rechallenged with [^{177}Lu]Lu-DOTATATE: 1 did not undergo the dosimetric imaging for technical reasons, leading to the final analysis of 35 dosimetric datasets. The characteristics of the studied population are presented in Table 1. Most patients (86%) received 4 injections, except for 5 patients who had kidney impairment or platelet toxicity or were receiving retreatment with [^{177}Lu]Lu-DOTATATE (2 cycles) (Table 2). In total, 146 lesions were evaluated (1–9 lesions per patient) in the liver (65%), lymph nodes (25%), mesentery (4%), pancreas (4%), and peritoneum (2%).

On the basis of RECIST 1.1 and M3-CT imaging, 5 patients presented with progressive disease (14%), 8 patients had partial response (22%), and 22 patients had stable disease (64%). Overall survival was 57 mo (95% CI, 25.3 mo to not reached) and progression-free survival was 30.72 mo (95% CI, 23.00–39.43 mo). Clinical tolerance was excellent during treatment, with only grade 3 hypertension in 5 patients (14%). One patient had grade 1 nausea, and another had grade 2 nausea with grade 1 vomiting. Intercycle tolerance was excellent (grade 1–2 asthenia in most patients), except in 3 patients who presented with

TABLE 5

Distribution of ADs by selected Healthy Organs and Lesions Throughout Cycles and at End of Treatment Course (Total AD)

Parameter	Cycle 1 (Gy)	Cycle 2 (Gy)	Cycle 3 (Gy)	Cycle 4 (Gy)	Total AD (Gy)
Healthy liver	1.08 (0.47–9.32)	1.16 (0.52–9.34)	1.06 (0.41–5.48)	0.99 (0.59–4.19)	4.05 (2.06–27.29)
Spleen	3.42 (1.98–5.77)	3.69 (2.27–6.81)	3.76 (1.55–7.04)	4.08 (2.35–5.60)	14.28 (6.87–23.87)
Kidneys	2.73 (1.97–5.46)	2.74 (1.78–4.97)	2.74 (1.41–5.32)	2.77 (1.85–5.44)	10.77 (4.99–21.12)
Bone marrow	0.29 (0.15–1.4)	0.31 (0.18–1.06	0.29 (0.15–1.18)	0.26 (0.18–0.65)	1.07 (0.63–3.74)
Lesions	31.99 (1.77–98.49)	25.64 (2.59–73.03)	23.3 (1.22–81.73)	18.74 (2.33–74.17)	94.43 (8.73–287.89)

Values are median and range in parentheses.

grade 3 asthenia. There was no grade 3–4 nephrotoxicity. Laboratory toxicities are listed in Table 3 and Table 4.

The ADs by organs and lesions are presented in Figure 1 and Table 5. The ADs by healthy organs were not significantly different among [^{177}Lu]Lu-DOTATATE cycles except for the spleen ($P < 0.05$). The median ADs by the 146 lesions were 32 Gy (cycle 1), 25.6 Gy (cycle 2), 23.3 Gy (cycle 3), and 18.7 Gy (cycle 4). The ADs by lesions decreased significantly over time from cycle 1 to cycle 4 ($P < 0.001$). The median total AD by lesions during 1 full treatment course was 94.4 Gy, with a wide distribution range (Fig. 2).

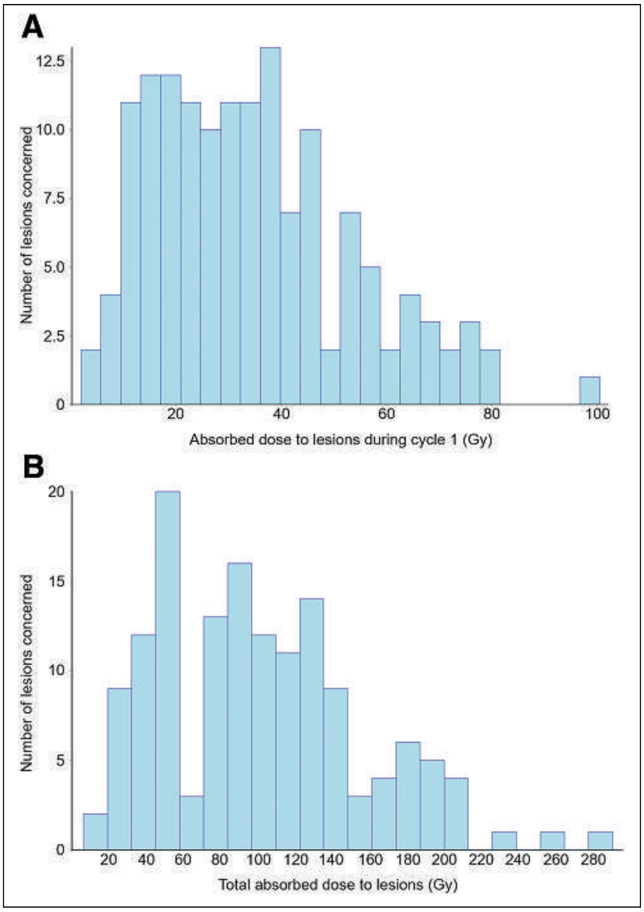

FIGURE 2. Distribution of ADs by lesions after cycle 1 (A) and after treatment end (B).

Absorbed Dose–Effect Relationship

There was a significant ($P < 0.001$) and negative correlation between the total AD by lesions and the lesion volume variations between BL-CT and M3-CT (Fig. 3). A total AD by lesions in the range of 55.8–130.7 Gy led to a decrease of 21.9% of the lesion volume. With a total AD of more than 95 Gy, all lesions were considered stable (no volume increase of >20%). The tumor control probability is presented in Figure 4.

There was no significant correlation between the glomerular filtration rates and the ADs by the kidneys during treatment (Supplemental Fig. 3). The ADs by the bone marrow (Fig. 5) and the spleen (Supplemental Fig. 4) were negatively and significantly ($P < 0.0001$) correlated with variations, compared with baseline values, of neutrophil, lymphocyte, leukocyte, and platelet counts. The AD by bone marrow better correlated with a decrease of leukocytes and platelets than did the AD by the spleen. For instance, a CumAD increase by bone marrow from 0.3 to 0.9 Gy was related to a significant decrease ($P < 0.05$) of leukocytes by 14.6% (95% CI, −20.2% to −9.0%), neutrophils by 14% (95% CI, −22.0% to −6.2%), lymphocytes by 18% (95% CI, −22.3% to −13.7), and platelets by 22% (95% CI, −30.8% to −13.3%) compared with baseline values. A change in CumAD by the spleen from 4.6 to 14.0 Gy resulted in a significant decrease in platelets by 15.7% (95% CI, −22.7% to −8.6%; $P < 0.05$) and lymphocytes by 20% (95% CI, −24.6% to −16.8%; $P < 0.05$).

The dosimetric indices for lesions in patients are presented in Table 6. Patients with a mean total AD of more than 91.36 Gy by

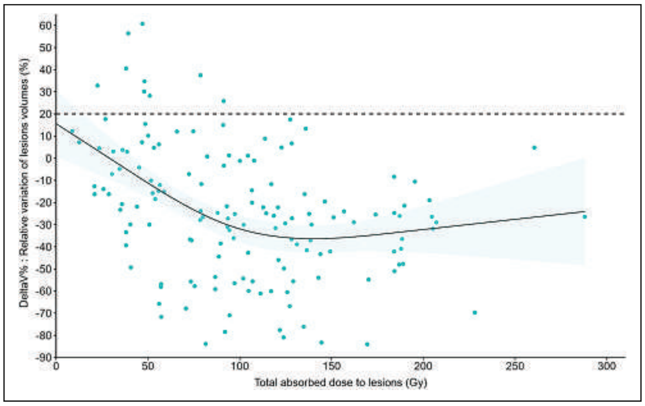

FIGURE 3. Relative tumor volume variation as function of total AD by lesions (n = 146). Solid line is prediction of model with 95% CI (blue haze region). Horizontal dotted line is 20% threshold. DeltaV% = variation of lesion volume.

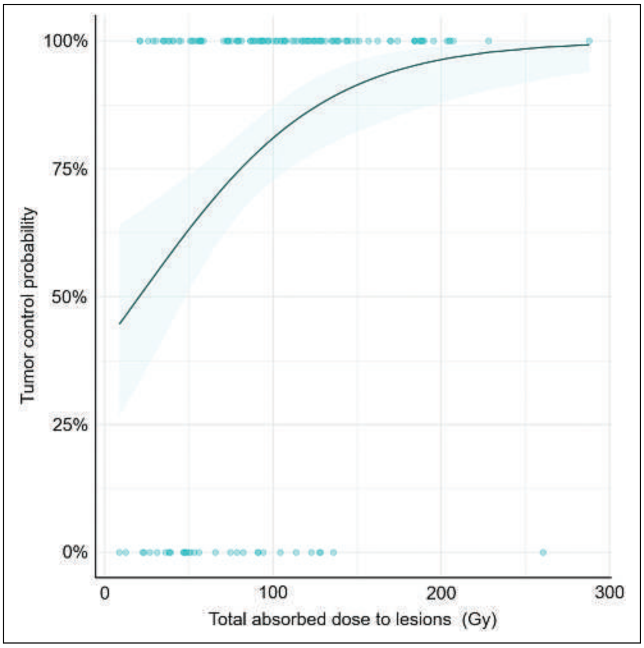

FIGURE 4. Tumor control probability. Variation of lesion volume ≤ 0% between BL-CT and M3-CT is considered as controlled tumor. Tumor control probability curve was produced using binary logistic regression model and its 95% CI.

all target lesions presented a higher probability of progression-free survival (hazard ratio [HR], 0.39; 95% CI, 0.17–0.92; $P = 0.03$) but not overall survival (HR, 0.34; 95% CI, 0.11–1.09; $P = 0.06$) (Figs. 6A and 6B). The median progression-free survival was 39.4 mo (range, 31.1 mo to not reached) in patients with a mean total AD of more than 91.36 Gy and 23.6 mo (range, 13–38.2 mo) in patients with a mean total AD of less than 91.36 Gy. Patients with a Min total AD of more than 52.52 Gy by lesions had a higher probability of progression-free survival (HR, 0.34; 95% CI, 0.14–0.81; $P = 0.01$) and overall survival (HR, 0.23; 95% CI, 0.06–0.82; $P = 0.01$) (Figs. 6C and 6D). Progression-free survival and overall survival were 41 mo (range, 31.1 mo to not reached) and not reached, respectively, in patients with a minimum total AD of more than 52.52 Gy, and progression-free survival and overall survival were 23.6 mo (range, 16.3 mo to not reached) and 26.6 mo (range, 25.2 mo to not reached), respectively, in patients with a minimum total AD of less than 52.52 Gy. The Max total AD was not associated with progression-free survival and overall survival.

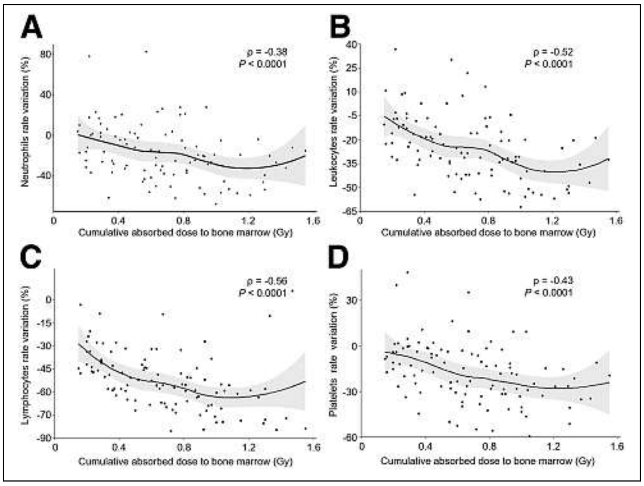

FIGURE 5. Correlation between cumulative AD by bone marrow and variations of neutrophils (A), leukocytes (B), lymphocytes (C), and platelets (D) relative to baseline. Curves are estimated using locally estimated scatterplot smoothing method, with 95% CI (gray region). Spearman correlation coefficient (ρ) is nonparametric measurement that estimates monotonic (not necessarily linear) relationship between 2 variables.

DISCUSSION

Here, we found a significant correlation between the AD by bone marrow and the decrease of hematologic parameters, which agreed with results from previous studies (*11,12*). If the baseline hematologic parameters and the stability of the AD by bone marrow over the cycles are considered, this relationship may help to better select patients and anticipate toxicities. However, one should consider that the nadir of the hematologic parameters might occur beyond day 15 after injection. The AD by the spleen was significantly higher starting from cycle 2 than it was starting from cycle 1, with a significant inverse correlation between the CumAD by the spleen and variations of hematologic parameters. Similarly, in a previous study (*13*), the CumAD by the spleen (15 vs. 14.3 Gy in our study) was inversely correlated with hemoglobin and platelet variations. In our sample, the CumAD by the kidneys never reached 23 Gy, which was considered an endpoint in recent PRRT trials (*19,20*) and was considered for external-beam radiotherapy. Moreover, patients never presented any significant glomerular filtration rate decrease during treatment and for up to 12 mo after treatment end, confirming that the kidney is not a limiting organ in PRRT with [^{177}Lu]Lu-DOTATATE when delivered as 4 cycles at 7.4 GBq and amino-acid infusion.

As shown by other works, the AD by tumors was heterogeneous (from 8.73 to 287.89 Gy) (*10*). However, the AD to target lesions was significantly correlated with variations of their volume ($P = 0.01$). The probability of tumor control also was higher above a specific threshold: all lesions were considered as responding when they received a dose of more than 95 Gy. These results, in favor of an AD–response relationship, are in agreement with 2 retrospective studies on 24 patients with pancreatic NETs (*14*) and 23 patients with small intestine NETs (*15*), in which dosimetric results were calculated using multiple-time-point SPECT imaging. We confirmed that the AD to tumors decreased significantly over cycles, probably due to a decrease in SSTR density (*15,16,21*). However, we also noticed that above a certain threshold, the AD–response relationship appeared limited, with the appearance of a plateau; adding more radiation to the lesions did not seem to improve the efficacy. This may be explained by methodologic issues or radiobiologic mechanisms of resistance to ionizing radiation that require further translational studies.

Lesion dosimetric indices had a prognostic value: patients with a mean total AD by target lesions of more than 91.36 Gy were more likely to have a longer progression-free survival (HR, 0.39; 95% CI, 0.17–0.92; $P = 0.03$). Moreover, patients with at least 1 target lesion receiving a total AD of less than 52.52 Gy had significantly lower overall survival and progression-free survival. Other prognostic factors had already been identified for patients with NETs, including tumor grade (and percentage of Ki-67–positive tumor cells), tumor heterogeneity (entropy) (*22*), tumor glucose metabolism assessed by [^{18}F]FDG PET/CT (*23*), injected activity (*24*), the size of the largest lesion (for patients receiving salvage

TABLE 6
Dosimetric Indices (Gy) in Patients (n = 35)

Mean total AD	Min total AD	Max total AD
91.36 (20.88–205.19)	52.52 (8.73–184.31)	118.59 (20.88–287.89)

Mean total AD = mean of total AD of all lesions in 1 patient; min total AD = lowest total AD value among all lesions in 1 patient; max total AD = highest total AD value among all lesions in 1 patient.

Values are median and range in parentheses.

PRRT) (*25*), tumor perfusion and SSTR density (*26*), molecular profiling (*27,28*), and inflammation-based indices (*29*). A recent retrospective cohort study with a population quite similar to ours (progressive disease, 7% vs. 14% in our study; stable disease, 70% vs. 64% in our study; partial response, 24% vs. 22% in our study) did not find that the tumor AD was predictive of patient overall survival (*16*). However, Alipour et al. used a different dose calculation methodology (imaging only at 24 h after infusion vs. SPECT/CT performed at different time points in our series for cycles 1 and 2 at least; no use of the lesion minimal AD index), with 68% of patients receiving at least 1 [^{177}Lu]Lu-DOTATATE cycle with radiosensitizing chemotherapy, and their radiologic endpoint was not based on CT imaging but on molecular imaging of the SSTR volume. This volume reflects the tumor volume and is also correlated with SSTR expression level. This may also explain why no correlation was found between the AD by lesions and the change in molecular imaging of the SSTR volume in the previous study (*16*). In a recent publication, a prospective study of 37 patients with GEP-NETs who were treated with [^{177}Lu]Lu-DOTATATE showed a significant increase of progression-free survival for patients whose target lesions received an AD of more than 35 Gy after cycle 1 (*17*). Further analysis is needed to compare results on the same basis (cycle 1), but at first sight, the presented results seem to be in the same range as ours.

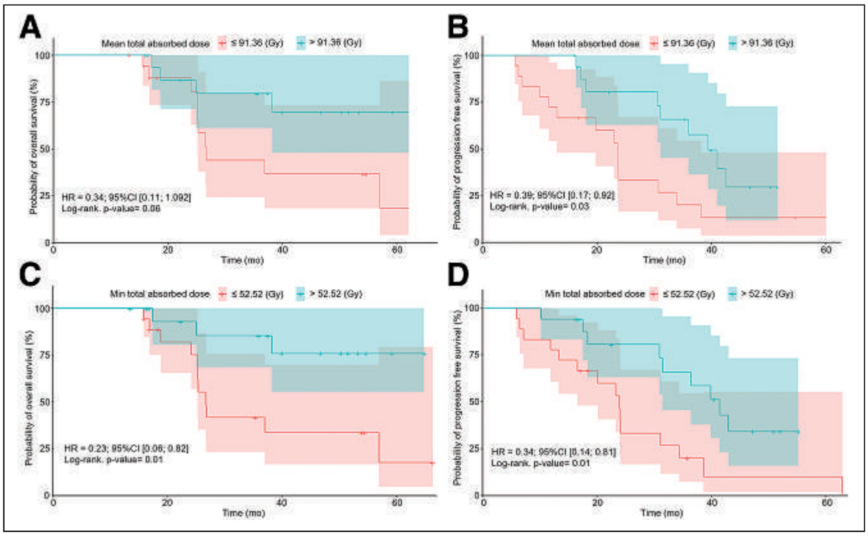

FIGURE 6. Kaplan–Meier estimates of overall survival (A) and progression-free survival (B) are shown as function of mean total AD by all lesions in each patient's course of treatment (n = 35). Kaplan–Meier estimates of overall survival (C) and progression-free survival (D) are shown as function of lowest total AD in each patient's course of treatment (n = 35). Min = minimum.

Our study has some limitations, particularly its monocentric and retrospective design. It also has some methodologic limitations: as proper delineation of the lesion on noncontrast low-dose CT of SPECT/CT is not feasible in an accurate way, a constant volume was used over cycles for lesion dosimetry. That methodology may underestimate the total AD by the lesion, especially for highly responding lesions, and could, in part, explain the aspect of the plateau in Figure 3. Whether a multiple-time-point dosimetry should be performed after several administration cycles (2 in our study) is a debated question. For obvious organizational reasons, decreasing the number of cycles with full dosimetry or decreasing the number of time points per cycle would simplify the process. We are willing to consider such simplified approaches in the future and assess how they affect the correlation between the AD and the clinical outcome. Still, our results may influence the clinical management (efficacy and toxicities) of patients treated with [^{177}Lu]Lu-DOTATATE for GEP-NETs. Indeed, as the AD by tumors decreases over cycles, the total AD after 4 cycles can be estimated, and these values can be compared with the patient dosimetric indices that are prognostic factors of survival. New PRRT algorithms may be proposed to deliver more irradiation to lesions (through higher injected activities per cycle or by adding more cycles) for patients with low lesion ADs after the first cycles. Moreover, as the ADs by the spleen and bone marrow are significantly correlated with variations of hematologic parameters, they could be considered as surrogate markers of toxicity during personalized treatment mainly driven by lesion dosimetry.

CONCLUSION

The results of this study suggest that personalized dosimetry of tumors and healthy organs during treatment with [^{177}Lu]Lu-DOTATATE may improve clinical outcomes and influence patient management. These results need to be validated in prospective clinical trials.

DISCLOSURE

Emmanuel Deshayes and Kévin Hebert received fees from AAA/Novartis. Manuel Bardiès and Lore Santoro cosupervised a student sponsored by DOSIsoft. This study was supported by SIRIC Montpellier Cancer Grant INCa-DGOS-Inserm 6045. No other potential conflict of interest relevant to this article was reported.

ACKNOWLEDGMENTS

We thank the patients and their families for their participation in the study. We also thank Hélène Sturer, Louise Combette, and Sandra Santini, nuclear medicine technologists, for their care of patients treated with PRRT.

KEY POINTS

QUESTION: Can tumor ADs predict outcome in patients with NETs who are treated with [^{177}Lu]Lu-DOTATATE?

PERTINENT FINDINGS: In a retrospective cohort of patients with NETs (mostly grade 2 small intestine NETs) treated with [^{177}Lu]Lu-DOTATATE, tumor and healthy organ dosimetry indices are predictive of survival and correlate with toxicities.

IMPLICATIONS FOR PATIENT CARE: These data are in favor of dosimetry implementation to improve patient selection for treatment with [^{177}Lu]Lu-DOTATATE.

REFERENCES

1. WHO Classification of Tumours Editorial Board. Neuroendocrine neoplasms. In: *Urinary and Male Genital Tumours.* International Agency for Research on Cancer; 2022:385–397. *WHO Classification of Tumours*; vol. 8. 5th ed.
2. Krenning EP, Kooij PP, Bakker WH, et al. Radiotherapy with a radiolabeled somatostatin analogue, [^{111}In-DTPA-D-Phe1]-octreotide: a case history. *Ann N Y Acad Sci.* 1994;733:496–506.
3. Strosberg J, El-Haddad G, Wolin E, et al. Phase 3 trial of ^{177}Lu-Dotatate for midgut neuroendocrine tumors. *N Engl J Med.* 2017;376:125–135.
4. Strosberg J, Wolin E, Chasen B, et al. Health-related quality of life in patients with progressive midgut neuroendocrine tumors treated with ^{177}Lu-Dotatate in the phase III NETTER-1 trial. *J Clin Oncol.* 2018;36:2578–2584.
5. Brabander T, van der Zwan WA, Teunissen JJM, et al. Long-term efficacy, survival, and safety of [^{177}Lu-DOTA^0,Tyr^3]octreotate in patients with gastroenteropancreatic and bronchial neuroendocrine tumors. *Clin Cancer Res.* 2017;23:4617–4624.
6. Sjögreen Gleisner K, Chouin N, Gabina PM, et al. EANM dosimetry committee recommendations for dosimetry of ^{177}Lu-labelled somatostatin-receptor- and PSMA-targeting ligands. *Eur J Nucl Med Mol Imaging.* 2022;49:1778–1809.
7. Cremonesi M, Ferrari M, Bodei L, Tosi G, Paganelli G. Dosimetry in peptide radionuclide receptor therapy: a review. *J Nucl Med.* 2006;47:1467–1475.
8. Bodei L, Kidd M, Paganelli G, et al. Long-term tolerability of PRRT in 807 patients with neuroendocrine tumours: the value and limitations of clinical factors. *Eur J Nucl Med Mol Imaging.* 2015;42:5–19.
9. Bergsma H, Konijnenberg MW, van der Zwan WA, et al. Nephrotoxicity after PRRT with ^{177}Lu-DOTA-octreotate. *Eur J Nucl Med Mol Imaging.* 2016;43:1802–1811.
10. Cremonesi M, Ferrari ME, Bodei L, et al. Correlation of dose with toxicity and tumour response to ^{90}Y- and ^{177}Lu-PRRT provides the basis for optimization through individualized treatment planning. *Eur J Nucl Med Mol Imaging.* 2018;45:2426–2441.
11. Svensson J, Ryden T, Hagmarker L, Hemmingsson J, Wangberg B, Bernhardt P. A novel planar image-based method for bone marrow dosimetry in ^{177}Lu-DOTATATE treatment correlates with haematological toxicity. *EJNMMI Phys.* 2016;3:21.
12. Bergsma H, Konijnenberg MW, Kam BL, et al. Subacute haematotoxicity after PRRT with ^{177}Lu-DOTA-octreotate: prognostic factors, incidence and course. *Eur J Nucl Med Mol Imaging.* 2016;43:453–463.
13. Svensson J, Hagmarker L, Magnander T, Wangberg B, Bernhardt P. Radiation exposure of the spleen during ^{177}Lu-DOTATATE treatment and its correlation with haematological toxicity and spleen volume. *EJNMMI Phys.* 2016;3:15.
14. Ilan E, Sandstrom M, Wassberg C, et al. Dose response of pancreatic neuroendocrine tumors treated with peptide receptor radionuclide therapy using ^{177}Lu-DOTATATE. *J Nucl Med.* 2015;56:177–182.
15. Jahn U, Ilan E, Sandstrom M, Lubberink M, Garske-Roman U, Sundin A. Peptide receptor radionuclide therapy (PRRT) with ^{177}Lu-DOTATATE: differences in tumor dosimetry, vascularity and lesion metrics in pancreatic and small intestinal neuroendocrine neoplasms. *Cancers (Basel).* 2021;13:962.
16. Alipour R, Jackson P, Bressel M, et al. The relationship between tumour dosimetry, response, and overall survival in patients with unresectable neuroendocrine neoplasms (NEN) treated with ^{177}Lu DOTATATE (LuTate). *Eur J Nucl Med Mol Imaging.* 2023;50:2997–3010.
17. Mileva M, Marin G, Levillain H, et al. Prediction of ^{177}Lu-DOTATATE PRRT outcome using multimodality imaging in patients with gastroenteropancreatic neuroendocrine tumors: results from a prospective phase II LUMEN study. *J Nucl Med.* 2024;65:236–244.
18. Santoro L, Pitalot L, Trauchessec D, et al. Clinical implementation of PLANET dose for dosimetric assessment after [^{177}Lu]Lu-DOTA-TATE: comparison with dosimetry Toolkit and OLINDA/EXM V1.0. *EJNMMI Res.* 2021;11:1.
19. Del Prete M, Buteau FA, Arsenault F, et al. Personalized ^{177}Lu-octreotate peptide receptor radionuclide therapy of neuroendocrine tumours: initial results from the P-PRRT trial. *Eur J Nucl Med Mol Imaging.* 2019;46:728–742.
20. Sundlöv A, Gleisner KS, Tennvall J, et al. Phase II trial demonstrates the efficacy and safety of individualized, dosimetry-based ^{177}Lu-DOTATATE treatment of NET patients. *Eur J Nucl Med Mol Imaging.* 2022;49:3830–3840.
21. Roth D, Gustafsson J, Warfvinge CF, et al. Dosimetric quantities in neuroendocrine tumors over treatment cycles with ^{177}Lu-DOTATATE. *J Nucl Med.* 2022;63:399–405.
22. Wetz C, Genseke P, Apostolova I, et al. The association of intra-therapeutic heterogeneity of somatostatin receptor expression with morphological treatment response in patients undergoing PRRT with [^{177}Lu]-DOTATATE. *PLoS One.* 2019;14:e0216781.
23. Chan DL, Hayes AR, Karfis I, et al. Dual [^{68}Ga]DOTATATE and [^{18}F]FDG PET/CT in patients with metastatic gastroenteropancreatic neuroendocrine neoplasms: a multicentre validation of the NETPET score. *Br J Cancer.* 2023;128:549–555.
24. Minczeles NS, de Herder WW, Feelders RA, Verburg FA, Hofland J, Brabander T. Long-term outcomes of submaximal activities of peptide receptor radionuclide therapy with ^{177}Lu-DOTATATE in neuroendocrine tumor patients. *J Nucl Med.* 2023;64:40–46.
25. Galler M, Rogasch JMM, Huang K, et al. Prognostic value of the largest lesion size for progression-free survival in patients with NET undergoing salvage PRRT with [^{177}Lu]Lu-DOTATOC. *Cancers (Basel).* 2022;14:1768.
26. Jiménez-Franco LD, Glatting G, Prasad V, Weber WA, Beer AJ, Kletting P. Effect of tumor perfusion and receptor density on tumor control probability in ^{177}Lu-DOTATATE therapy: an in silico analysis for standard and optimized treatment. *J Nucl Med.* 2021;62:92–98.
27. Bodei L, Schöder H, Baum RP, et al. Molecular profiling of neuroendocrine tumours to predict response and toxicity to peptide receptor radionuclide therapy. *Lancet Oncol.* 2020;21:e431–e443.
28. Bodei L, Kidd MS, Singh A, et al. PRRT neuroendocrine tumor response monitored using circulating transcript analysis: the NETest. *Eur J Nucl Med Mol Imaging.* 2020;47:895–906.
29. Black JRM, Atkinson SR, Singh A, Evans J, Sharma R. The inflammation-based index can predict response and improve patient selection in NETs treated with PRRT: a pilot study. *J Clin Endocrinol Metab.* 2019;104:285–292.

Safety and Efficacy of *Para*-Aminohippurate Coinfusion for Renal Protection During Peptide Receptor Radiotherapy in Patients with Neuroendocrine Tumors

Alexandros Moraitis[1,2], Walter Jentzen[1,2], Pedro Fragoso Costa[1,2], David Kersting[1,2], Stephan Himmen[1,2],
Marta Coelho[1,2], Marian Meckel[3], Cees J.A. van Echteld[4], Wolfgang P. Fendler[1,2], Ken Herrmann[1,2], and
Miriam Sraieb[1,2]

[1]Department of Nuclear Medicine, West German Cancer Center, University Hospital Essen, University of Duisburg-Essen, Essen, Germany; [2]German Cancer Consortium, Partner Site University Hospital Essen, Essen, Germany; [3]ITM Isotope Technologies Munich SE, Garching/Munich, Germany; and [4]Helacor Consultancy, Oberwil, Switzerland

Para-aminohippurate, also known as *p*-aminohippuric acid (PAH), is used clinically to measure effective renal plasma flow. Preclinically, it was shown to reduce ^{177}Lu-DOTATOC uptake in the kidneys while improving bioavailability compared with amino acid (AA) coinfusion. We report the safety and efficacy of PAH coinfusion during peptide receptor radiotherapy in patients with neuroendocrine tumors. **Methods:** Twelve patients with metastatic or unresectable gastroenteropancreatic neuroendocrine tumors received ^{177}Lu-DOTATOC in 33 treatment cycles. Either 8 g of PAH or a mixture of 25 g of arginine and 25 g of lysine were coinfused. Safety was assessed by monitoring laboratory data, including hematologic and renal data, as well as electrolytes obtained before and 24 h after treatment. For radiation dosimetry, whole-body scans were performed at 1, 24, and 48 h and a SPECT/CT scan was performed at 48 h, along with blood sampling at 5 min and 0.5, 2, 4, 24, and 48 h after administration. Absorbed dose estimations for the kidneys and bone marrow were performed according to the MIRD concept. **Results:** In 15 treatment cycles, PAH was coinfused. No changes in mean creatinine level, glomerular filtration rate, and serum electrolytes were observed before or 24 h after treatment when using PAH protection ($P \geq 0.20$), whereas serum chloride and serum phosphate increased significantly under AA (both $P < 0.01$). Kidney–absorbed dose coefficients were 0.60 ± 0.14 Gy/GBq with PAH and 0.53 ± 0.16 Gy/GBq with AA. Based on extrapolated cumulative kidney-absorbed doses for 4 cycles, 1 patient with PAH protection and 1 patient with AA protection in our patient group would exceed the 23-Gy conservative threshold. The bone marrow–absorbed dose coefficient was 0.012 ± 0.004 Gy/GBq with PAH and 0.012 ± 0.003 Gy/GBq with AA. **Conclusion:** PAH is a promising alternative to AA for renal protection during peptide receptor radiotherapy. Further research is required to systematically investigate the safety profile and radiation dosimetry at varying PAH plasma concentrations.

Key Words: dosimetry; NET; PAH; PRRT; renal protection

J Nucl Med 2024; 65:931–937
DOI: 10.2967/jnumed.123.266619

Neuroendocrine tumors (NETs) represent a heterogeneous group of neoplasms and arise in various organs, mostly the gastrointestinal tract but also the pancreas and lungs. For metastatic disease, 5-y survival is reported to be less than 50%, which poses the need for adequate treatment options (*1*). Subsequent to the results of the NETTER-I trial, peptide receptor radiotherapy (PRRT) using ^{177}Lu-DOTA ligands coupled to somatostatin analogs has evolved into a valuable strategy for patients with unresectable or metastatic NETs (*2*).

In extensively treated NET patients, hematopoietic or renal toxicity are the dose-limiting morbidities in PRRT. Although bone marrow is typically not the dose-limiting organ, grade 3 or 4 hematologic toxicity, according to the Common Terminology Criteria for Adverse Events (National Cancer Institute), has been reported in approximately 10% of patients after PRRT (*3*,*4*). Radiolabeled peptides undergo renal clearance with active retention or reabsorption by the renal proximal tubular cells. High and prolonged renal uptake may lead to radiation-induced acute chronic nephrotoxicity that can significantly affect quality of life and long-term outcomes. Consequently, in PRRT, the kidney-absorbed dose is considered one of the major dose-limiting factors (*5*,*6*).

The kidney-absorbed dose can be reduced by coinfusing agents that competitively inhibit reabsorption of radiolabeled compounds, such as positively charged amino acids (AAs), gelofusine, trypsinized albumin, or bovine serum albumin fragmented by cyanogen bromide (*5*,*7–9*). When using AA, an average reduction of absorbed dose in or uptake to the kidneys of between 23% and 47% was achieved compared with no renal protection (*8*,*10*,*11*). Although these data rely on a limited number of patients and were partially obtained with radiopharmaceuticals other than ^{177}Lu-DOTA ligands, AAs are most commonly used in PRRT (*12*).

Para-aminohippurate, also known as *p*-aminohippuric acid (PAH), is an anionic substrate and is frequently used to assess renal plasma flow and glomerular filtration rate (GFR) (*13*,*14*). Maeda et al. (*15*) reported a surprising increase in the clearance of benzylpenicillin when coadministered with PAH, suggesting a potential inhibition of renal reabsorption processes. In addition, PAH is a substrate for organic anion transmembrane transporters (OAT1, OAT2, and OAT4) that are indicated to be involved in renal clearance of somatostatin analogs (*16*,*17*). It was specifically shown that PAH comedication reduces kidney uptake of small peptide radiopharmaceuticals (*18*). Because of shorter infusion

---

Received Sep. 5, 2023; revision accepted Mar. 4, 2024.

For correspondence or reprints, contact Alexandros Moraitis (alexandros.moraitis@uk-essen.de).

times for PAH than for AA and a possible reduction of side effects reported with AA, such as nausea and hyperkalemia (*10*), administration of PAH in the clinical setting during PRRT might further improve patient throughput and tolerance to PRRT.

In this study, we investigated the safety and efficacy of PAH coinfusion during ^{177}Lu-DOTATOC treatment in patients with gastroenteropancreatic NETs in comparison to our current standard protocol of AA infusion.

MATERIALS AND METHODS

Preliminary Preclinical Biodistribution Study

A study was performed before clinical investigations in healthy male Wistar rats to assess the biodistribution profile of ^{177}Lu-DOTATOC when administered along with PAH. Before intravenous injection of a mean ± SD of 0.9 ± 0.1 MBq of ^{177}Lu-DOTATOC, rats (n = 8–10 per group) were injected intraperitoneally with 1 mL of saline solution (0.9% sodium chloride [NaCl]), AA solution containing arginine and lysine (200 mg/mL), or PAH solution (200 mg/mL). Subsequently, the rats were sacrificed 5 or 60 min after injection of ^{177}Lu-DOTATOC, and kidney activity was measured in a calibrated well counter. For each of the 3 coinfusion groups, 4–5 kidney uptake values were available at each time point after injection. The experiments were conducted by Helmholtz-Zentrum Dresden-Rossendorf on behalf of ITM Medical Isotopes Garching GmbH according to the German Animal Welfare Act and European Union directive 2010/63/EU on the protection of animals used for scientific purposes and were approved by the provincial headquarters in Dresden (protocol DD24.1-5131/450/16).

Clinical Application

Since it became available at our department (Department of Nuclear Medicine at the University Hospital in Essen, Germany), PAH has been offered alternatively to AA infusion in PRRT of patients with metastatic or unresectable gastroenteropancreatic NETs. Data of the first patients receiving PAH were analyzed retrospectively. The primary aims of the study were to assess the clinical safety of PAH and to evaluate kidney and bone marrow dosimetry of PAH coinfusion during ^{177}Lu-DOTATOC treatment. The secondary aim was to compare the findings with that of the established coinfusion of AA. All patients provided written informed consent for clinical PAH application and PRRT. The local ethics committee (University of Duisburg-Essen Medical Faculty, protocol 23-11120-BO) approved the study and waived the need for study-specific consent.

Patients and Drug Administration

Fourteen gastroenteropancreatic NET patients treated between November 2021 and November 2022 who received PAH for renal protection were initially identified. Of those, 2 patients were excluded because of disease progression after the first cycle and were not further evaluated. In addition to international joint recommendations on patient eligibility for ^{177}Lu-DOTATOC treatment (*19*), patients were offered PRRT only if they were at least 18 y of age and they had an initial GFR of at least 50 mL/min. All patients showed somatostatin receptor–positive lesions confirmed by ^{68}Ga-DOTATOC PET/CT imaging. Patient characteristics are summarized in Table 1.

Patients were administered 3 cycles of 7.4 GBq of ^{177}Lu-DOTATOC each, injected intravenously in 30–45 min via automated infusion pumps and accompanied by 500 mL of 0.9% NaCl solution. Concomitantly, either PAH or AA solution was infused for renal protection via separate tubing. A PAH amount of approximately 8 g was used, resulting in a total infusion volume of less than 100 mL (*20*). More specifically, a priming rate of 160 mg of PAH per minute for 16 min, followed by a maintenance rate of 110 mg/min for 48 min, was used to reach an estimated steady-state PAH plasma concentration of 450 mg/L (total infusion time of approximately 70 min). A detailed description of PAH pharmacokinetic assumptions used for the calculation of PAH plasma concentration is provided in supplemental materials (supplemental materials are available at http://jnm.snmjournals.org). The AA solution contained positively charged lysine and arginine (each 25 g) and was infused in 2 L of NaCl solution over 4 h (*5*).

TABLE 1
Patient Characteristics at Time of First Treatment Cycle

Patient	Sex	Age (y)	Height (cm)	Weight (kg)	Protectant at 1 cycle	Type of NET	DD (mo)	Previous therapy	Prior cum. PRRT activity (GBq)
1	M	46	181	86	PAH	Intestinal	28	S, PRRT	51.6
2	M	31	178	69	PAH	Rectal	8	CT, PRRT	22.6
3	M	50	178	88	PAH	Intestinal	162	S, CT, SIRT, PRRT	44.6
4	F	55	160	76	PAH	Intestinal	81	S, PRRT	49.5
5	M	48	181	65	PAH	Intestinal	17	S, PRRT	22.0
6	F	67	175	61	PAH	Intestinal	212	S, PRRT	66.3
7	M	52	174	69	AA	Intestinal	16	PRRT	15.1
8	M	78	192	85	AA	CUP	65	S, PRRT	15.3
9	F	77	160	49	AA	Intestinal	107	S, PRRT	22.7
10	F	84	170	67	AA	Intestinal	71	PRRT	52.3
11	M	61	177	78	AA	Intestinal	50	None	0
12	M	63	175	79	AA	Pancreatic	29	CT	0

DD = disease duration; cum. = cumulative; S = surgery; CT = chemotherapy; SIRT = selective internal radiotherapy; CUP = cancer of unknown primary.

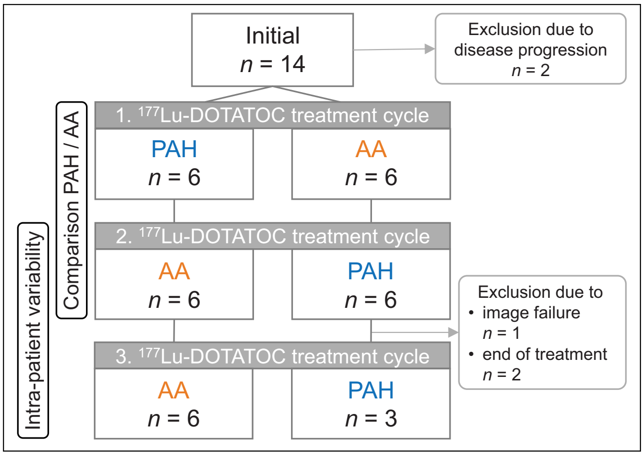

FIGURE 1. Administration flowchart.

The administration flowchart in Figure 1 illustrates the choice of renal protectant during the course of 3 treatment cycles. Of the 12 patients who were evaluated, 6 received PAH in the first cycle, followed by AA in the second cycle. The other 6 patients received the renal protectants in opposite order. The third treatment cycle was given with coinfusion of the same renal protectant as used in the second cycle to assess intrapatient variability of dosimetry calculations. For 3 patients, dosimetry data were not available for the third cycle because of imaging failure ($n = 1$) or end of treatment ($n = 2$).

Data Collection: Imaging, Blood Sampling, and Laboratory Data

The hybrid approach was used for dosimetry imaging consisting of whole-body planar imaging at 1, 24, and 48 h and 1 SPECT/CT scan 48 h after administration covering the abdomen. All scans were performed on a Symbia Intevo T2 (Siemens Healthineers) SPECT/CT system equipped with a medium-energy collimator. For anterior and posterior whole-body planar images, the peak energy window was centered at 208 keV (width, ±7.5%) and the lower and upper energy windows for scatter correction were ±5%. Images were acquired with a scan velocity of 10 cm/min in a 256 × 1,024 matrix. Each patient was scanned along with an individually prepared ^{177}Lu reference standard placed between the heels to monitor system stability. Acquisition parameters used in the SPECT/CT scans were a 208-keV energy peak (width, ±7.5%), upper and lower scatter window widths of ±5% each, 3° angular step size, 60 projections, and 20 s per projection. Standard attenuation and scatter correction were applied to reconstruct images into a 128 × 128 transverse matrix with cubical voxels of a 4.8-mm side length using an ordered-subset conjugate gradient maximization algorithm with 48 iterations, 1 subset, and no gaussian filter (xQuant; Siemens Healthineers) to provide fully quantitative images (*21*).

Venous blood samples were drawn before treatment and at 5 min, 30 min, and 2, 4, 24, and 48 h after the end of ^{177}Lu-DOTATOC infusion. Blood activity in each sample was measured in a calibrated well counter (Wizard^2 2480 3"; PerkinElmer). The activity values were corrected for detector dead time, filling level, and decay to the time of administration. Sample volumes were determined gravimetrically to obtain the blood activity concentration.

Safety was assessed by monitoring clinical laboratory parameters including hematologic data (hemoglobin, red blood cell counts, white blood cell counts, and platelet counts), renal parameters (creatinine level and estimated GFR), and electrolytes (sodium, potassium, chloride, phosphate, and calcium). These were obtained before and 24 h after treatment.

Radiation Dosimetry

Kidney and Bone Marrow Time–Activity Curves. For the kidneys, manual volume segmentation was performed for the first cycle on low-dose CT images. The volumes of interest were propagated into other cycles. The imaged SPECT/CT activity concentration of each kidney was corrected individually for the partial-volume effect by applying experimentally derived recovery coefficients (*21*). In planar imaging, background and attenuation-corrected geometric mean values from anterior and posterior counts were calculated using the conjugate view method with additional self-attenuation within the kidney, as proposed by the MIRD committee (*22*). The resulting count value from the 48-h planar images was scaled to equal the partial-volume effect–corrected activity from SPECT/CT. Subsequently, the same scaling factor was applied to the count values from the 1- and 24-h planar images to construct the time–activity curve for each kidney.

Bone marrow activity was estimated using the blood method (*23*), assuming that the activity concentration in the bone marrow was equal to that in the blood (*24*). To obtain the bone marrow activity, the blood activity concentration from each blood sample was multiplied by the respective male or female reference bone marrow mass and scaled by the ratio of individual-to-reference patient mass (*25*). To account for cross-radiation from the remainder of the body, whole-body retention curves were constructed from planar images by normalizing the geometric mean count values of the whole body to the geometric mean value from the first measurement (1 h after injection). Patients were asked not to void until the first imaging time point to preserve translation from counts to activity. Alternatively, the excreted urine was collected and scanned along with the patient.

Time-Integrated Activity Coefficients (TIACs) and Absorbed Dose Coefficients. After normalizing kidney and bone marrow time–activity curves to the administered activities, the resulting uptake curves and whole-body retention curves were used to calculate the TIACs. Point-to-point effective half-lives were derived by calculating monoexponential functions between adjacent time points for each kidney, the bone marrow, and the whole body. TIACs were obtained by integrating the point-to-point monoexponential functions (*26*). For the kidneys and bone marrow, the effective half-life between 1 and 24 h after administration was used to extrapolate to the end of infusion (t = 0). For the kidneys, an effective half-life of 50 h was assumed for integration after the last (48 h) time point (*27*,*28*), whereas for bone marrow and whole-body TIACs, the effective half-life between 24 and 48 h was used.

Dosimetry estimations were performed using the MIRD concept. The left and right kidneys were summarized into a single source organ of renal tissue, and absorbed dose coefficients were calculated individually using OLINDA/EXM 2.2 software. The bone marrow–absorbed dose was calculated as proposed by Traino et al. (*29*) to account for patient-specific S value scaling based on the individual's whole-body and bone marrow mass.

Software and Statistics

Image analysis was performed using PMOD version 4.2 software (PMOD Technologies Ltd.). Statistical analysis, performed using GraphPad Prism version 5.03 (GraphPad Software Inc.), included calculation of mean and median values and the measure of dispersion expressed as SD and interquartiles. Spearman correlation analysis and the Mann–Whitney U test were used, and significance was assumed for a P value of no more than 0.05.

RESULTS

Preliminary Preclinical Biodistribution Study

Kidney uptake in healthy male Wistar rats, expressed as the percentage of injected activity per gram of renal tissue, is shown in

Supplemental Figure 1. In evaluations of both 5 and 60 min after ^{177}Lu-DOTATOC injection, PAH significantly decreased the radioactivity in the kidneys from that occurring with NaCl solution. Elimination of ^{177}Lu-DOTATOC was also significantly faster with AA than with NaCl solution. No signs of acute and delayed toxicity were observed with the protective agents.

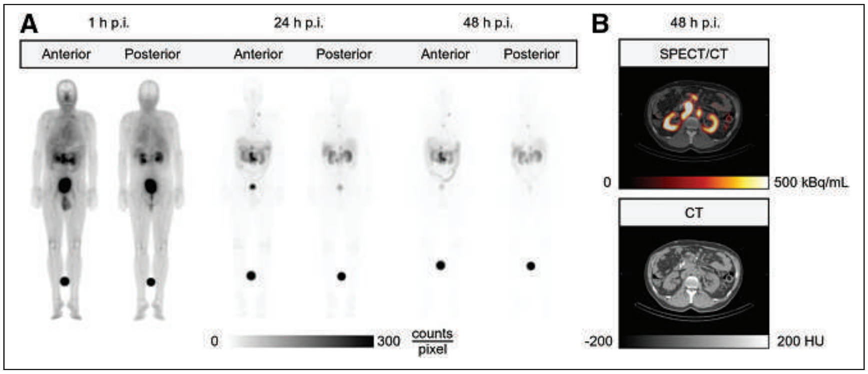

FIGURE 2. Sequential planar images (A) and 1 fused axial SPECT/CT and corresponding CT slice (B) of representative patient (patient 11, cycle 2) after PAH coinfusion during ^{177}Lu-DOTATOC treatment. HU = Hounsfield units; p.i. = postinjection.

Patients

Twelve patients, treated in 33 individual PRRT cycles, were administered a mean ± SD of 7.5 ± 0.2 GBq of ^{177}Lu-DOTATOC per cycle. In 15 cycles, PAH was coinfused for renal protection (AA was coinfused in 18 cycles). The mean time between subsequent cycles was 57 ± 12 d. The actual imaging time points after administration were 1 ± 1, 20 ± 2, and 43 ± 2 h for planar imaging and 44 ± 2 h for SPECT/CT.

Safety

No grade 3 or 4 adverse events, according to the Common Terminology Criteria for Adverse Events, were reported with either PAH or AA. No significant changes in mean serum creatinine, GFR, or serum electrolytes (sodium, potassium, chloride, phosphate, and calcium) were observed before or 24 h after treatment under PAH ($P \geq 0.20$). Under AA, serum chloride and serum phosphate increased significantly after treatment (105.8 vs. 107.8 mmol/L, $P < 0.01$, and 3.13 vs. 3.80 mg/dL, $P < 0.01$, respectively). One patient per renal protectant (patient 9 under PAH and patient 1 under AA) showed a grade 1 creatinine increase with a correlated grade 2 GFR decrease, and 1 patient (patient 6) showed grade 1 hyperkalemia under AA. Based on hematologic parameters measured before treatment of cycle 1 and then cycle 2, 2 PAH patients (patients 4 and 5) developed grade 1 anemia and 1 AA patient (patient 10) developed grade 2 anemia. One PAH patient (patient 3) showed grade 1 leukopenia and thrombocytopenia. No other adverse events were reported.

Radiation Dosimetry

Figure 2 shows planar and SPECT/CT images of a representative patient after PAH coinfusion during PRRT (patient 11, cycle 2).

TABLE 2
Kidney– and Bone Marrow–Absorbed Dose Coefficients Under Coinfusion of Either PAH or AA During ^{177}Lu-DOTATOC Treatment

	Kidney–absorbed dose coefficient (Gy/GBq)			Bone marrow–absorbed dose coefficient (Gy/GBq)		
Patient	PAH	AA	%-Δ	PAH	AA	%-Δ
1	0.43	0.34	26	0.008	0.007	14
2	0.35	0.44	−20	0.017	0.017	0
3	0.83	0.65	28	0.009	0.009	0
4	0.74	0.78	−5.1	0.009	0.010	−10
5	0.73	0.83	−12	0.010	0.012	−17
6	0.60	0.44	36	0.011	0.010	10
7	0.73	0.50	46	0.011	0.010	10
8	0.46	0.39	18	0.009	0.010	−10
9	0.52	0.67	−22	0.021	0.019	11
10	0.53	0.40	33	0.014	0.012	17
11	0.66	0.42	57	0.011	0.010	10
12	0.62	0.49	27	0.018	0.016	13
Mean	0.60	0.53		0.012	0.012	
SD	0.14	0.16		0.004	0.003	
Median	0.61	0.47		0.011	0.010	
Min	0.35	0.34		0.008	0.007	
Max	0.83	0.83		0.021	0.019	

%-Δ = intrapatient percentage difference from PAH to AA; Min = minimum; Max = maximum.

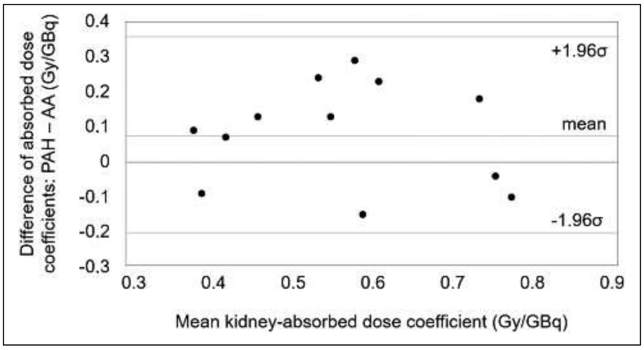

FIGURE 3. Bland–Altman plot of kidney–absorbed dose coefficients during ^{177}Lu-DOTATOC treatment with coinfusion of either PAH or AA.

Time–activity curves of the left and right kidneys are provided in Supplemental Figure 2. Kidney, bone marrow, and whole-body TIACs with coinfusion of PAH and AA are provided in Supplemental Tables 1–3.

For the kidneys, intrapatient variability, expressed as mean ± SD absolute percentage deviation of absorbed dose coefficients from cycle 3 to cycle 2 (where the same renal protectant was used), was 17.6% ± 9.9% (Supplemental Table 4). Kidney–absorbed dose coefficients of cycles 1 and 2, used to compare PAH and AA, are listed in Table 2 and illustrated by the Bland–Altman plot in Figure 3. The mean kidney–absorbed dose coefficient was higher for PAH by 0.07 Gy/GBq yet not significant ($P = 0.14$). The highest single value of 0.83 Gy/GBq was observed with both AA (patient 5) and PAH (patient 3). The largest difference in a patient using different renal protectants was observed in patient 11 (0.66 Gy/GBq with PAH vs. 0.42 Gy/GBq with AA). In Figure 4, kidney–absorbed dose coefficients are plotted against the percentage of kidney uptake at 48 h after administration (Fig. 4A) and total kidney volume (Fig. 4B). For both PAH and AA, absorbed dose to the kidneys correlated with the 48-h uptake ($\rho = 0.8$). No correlation was found between kidney–absorbed dose coefficients and total kidney volume ($\rho = -0.1$). Based on extrapolated cumulative kidney-absorbed doses for 4 cycles (assuming 7.4 GBq per cycle), 1 patient with AA and 1 patient with PAH (8% of our patient group) would exceed the 23-Gy toxicity threshold. For at least 50% of patients (6 patients for PAH and 8 patients for AA), 5 treatment cycles would have been feasible before reaching the toxicity threshold.

For bone marrow, intrapatient variability was 6.4% ± 3.9% (Supplemental Table 4). Mean ± SD bone marrow–absorbed dose coefficients were 0.012 ± 0.004 Gy/GBq with PAH and 0.012 ± 0.003 Gy/GBq with AA (Table 2). Extrapolation (4 cycles, 7.4 GBq each) of the highest single value for each PAH and AA patient would yield a cumulative bone marrow–absorbed dose of approximately 0.6 Gy (below the 2-Gy toxicity threshold for bone marrow).

DISCUSSION

This study is the first, to our knowledge, to report the safety and efficacy of PAH coinfusion in patients with gastroenteropancreatic NETs undergoing ^{177}Lu-DOTATOC PRRT. In our cohort, dosimetry revealed a comparable nephroprotective effect of PAH and AA coinfusion in terms of compliance with toxicity thresholds. In addition, PAH was well tolerated and improved patient comfort during treatment because of shorter infusion times and possible reduction of hyperkalemia.

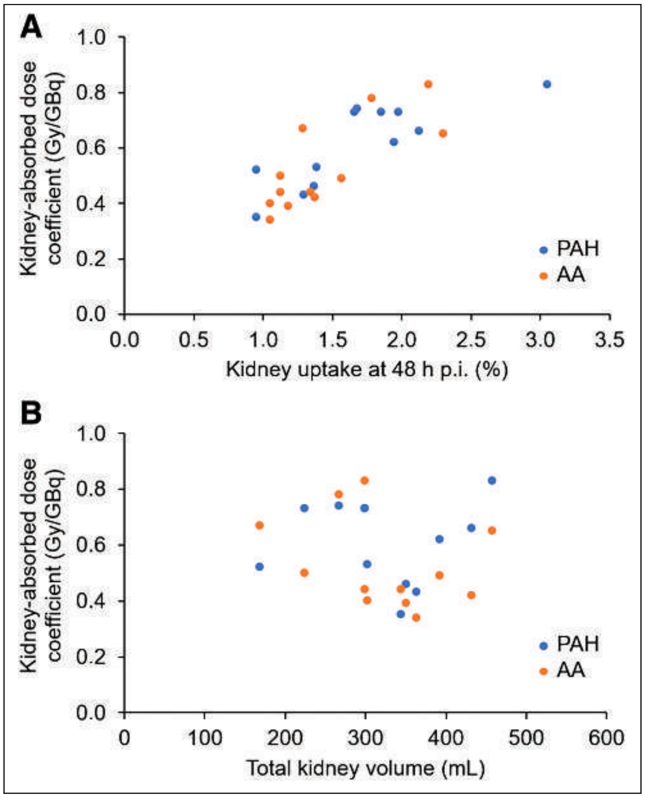

FIGURE 4. (A) Kidney–absorbed dose coefficient dependence on kidney percentage uptake 48 h after administration ($\rho = 0.80$). (B) No correlation was found between kidney–absorbed dose coefficients and total kidney volume ($\rho = -0.10$). p.i. = postinfusion.

One of the first clinical experiences with ^{90}Y-DOTATOC, performed by Otte et al. (*30*), had already identified the need to reduce renal toxicity by improving inhibition of renal uptake during PRRT. Later, Rolleman et al. (*10*) investigated the nephroprotective effect of different AA solutions and concluded that a mixture of 25 g of lysine and 25 g of arginine provides the optimal trade-off between protection and AA-induced side effects, such as vomiting and hyperkalemia. Despite its known side effects, this AA solution is considered the current standard for renal protection in PRRT (*12*,*19*). In addition, Puszkiel et al. (*31*) evaluated the impact of AA coinfusion on ^{177}Lu-DOTATATE excretion kinetics in patients with gastroenteropancreatic NETs and observed large interpatient variability. Promising alternatives to overcome these effects are under investigation (*32*,*33*). In the present study, PAH coinfusion showed no increase in mean serum potassium; however, an increase was observed with AA, revealing a potential reduction of hyperkalemia-related morbidities.

For PAH to develop a nephroprotective effect in this study, saturation of the secretory capacity in proximal tubular cells was desired. To saturate the tubular secretory capacity, Dowling et al. (*20*) used PAH plasma concentrations of more than 800 mg/L, which were well tolerated, except for a few subjects reporting a slight warming sensation at the highest priming rate (200 mg/min), which ceased within 5–10 min after administration. To avoid these side effects, 80% of this rate (160 mg/min) was used in this study. In addition, we aimed at a PAH plasma concentration of 450 mg/L, which according to Dowling et al. (*20*) corresponded to an approximate saturation of 80% of the secretory capacity.

Mean kidney-absorbed doses under PAH were 0.60 Gy/GBq compared with 0.53 Gy/GBq under AA, and the protectants showed equal nephroprotective capabilities in terms of compliance with the 23-Gy toxicity threshold for extrapolated cumulative kidney-absorbed doses (1 exceedance per renal protectant). In general, the applicability of this absorbed dose limit is questioned as being adopted from external beam radiation (*34*). Because of the lower absorbed dose rates in PRRT, the absorbed dose limit for kidney toxicity may be higher than 23 Gy. Bodei et al. (*35*) showed that a safe renal–absorbed dose limit might be a biologic effective dose of up to 40 Gy in patients without risk factors and 28 Gy in patients with certain risk factors in ^{90}Y-PRRT. Because of its nonuniform irradiation compared with ^{90}Y, application of ^{177}Lu-PRRT is expected to allow for even higher dosimetry constraints (*36*). When multiplying our extrapolated kidney-absorbed doses by 1.09—the dose–to–biologic effective dose conversion factor for PRRT suggested by Sundlöv et al. (*36*)—no patient would have exceeded the conservative 28-Gy biologic effective dose threshold, which is in line with our clinical observations.

Bone marrow–absorbed dose coefficients were equal under coinfusion of PAH and AA, with no value greater than 0.021 Gy/GBq. In extensively treated patients, hematologic toxicities might become relevant dose-limiting factors. Promising activity escalation strategies, such as the P-PRRT trial, could achieve response rates of 59% at the cost of subacute grade 3 or 4 lymphocytopenia in 52% of patients (*37*). In addition, Schäfer et al. (*38*) recently reported 3 cases of radiation nephropathy induced by renal thrombotic microangiopathy in the context of extensively treated ^{177}Lu-PSMA patients. Hence, the use of effective renal protectants should also aim at preserving kidney functions to allow faster excretion of radioactive compounds and therefore reduce systemic radiation exposure.

It was established that the renal retention of the 8-AA peptide DOTATOC primarily resulted from megalin and cubilin endocytosis, followed by transportation for protein degradation in the lysosome (*5*). However, larger proteins such as albumin (65–70 kDa) typically undergo tubular reabsorption mechanisms (*39*). The structurally similar compound ^{177}Lu-oxodotreotide (DOTATATE) was reported to exhibit excretion with a radiochemical purity close to 100% within the initial 48 h, indicating the absence of further lysosomal degradation. In addition, probenecid—an inhibitor targeting transporters similar to PAH—was shown preclinically to influence kidney retention of ^{111}In-DOTATOC (*16*). Our investigations expand on these findings, suggesting that transporters other than megalin and cubilin may also play a significant role in the renal excretion or reabsorption of DOTATOC. Several transporters located on the apical side of proximal tubular cells and the cortical collecting duct, such as OATK1, OAT-K2, OAT polypeptide 1, multidrug-resistance-associated protein 2, and sodium-dependent inorganic phosphate transporter, serve as substrates for PAH, and their role in the excretion of peptides or xenobiotics remains incompletely understood (*40*). The presented study did not delve into mechanistic details, and the explanations provided remain speculative. Further biologic studies are warranted to explore these aspects in greater depth.

The study was mainly limited by its small number of patients and patient heterogeneity with respect to their treatment history (Table 1), which could have influenced the nephroprotective effect of PAH and AA. Both protectants need to be evaluated for PRRT-naïve patients. In addition, dosimetry estimations were limited to the 48-h imaging time point. A later imaging time point would have enabled the assessment of late-phase kidney kinetics to reduce the impact of fit functions after the last imaging time point. Lastly, direct assessment of the PAH blood–plasma concentration would provide more accurate insight into individual PAH clearance to help optimize PAH dosing. These data were not available for this retrospective analysis.

CONCLUSION

Nephroprotection of PAH coinfusion during ^{177}Lu-DOTATOC PRRT was comparable to that of AA in terms of compliance with renal toxicity thresholds. It was well tolerated and may improve patient quality of life during treatment by potentially reducing hyperkalemia and nausea. In addition, implementation of PAH in treatment protocols might enhance patient tolerance to PRRT because of shorter infusion times. Further research is required to investigate the safety profile at varying PAH plasma concentrations.

DISCLOSURE

Walter Jentzen received research funding from Siemens Healthineers. Ken Herrmann reports personal fees from Bayer, SIRTEX, Adacap, Curium, Endocyte, IPSEN, Siemens Healthineers, GE Healthcare, Amgen, Novartis, Y-mAbs, Aktis Oncology, Theragnostics, Pharma15, Debiopharm, AstraZeneca, and Janssen; personal fees and other support from Sofie Biosciences; nonfinancial support from ABX; and grants and personal fees from BTG outside of the submitted work. Wolfgang Fendler reports fees from Sofie Biosciences (research funding), Janssen (consultant and speaker), Calyx (consultant and image review), Bayer (consultant, speaker, and research funding), and Novartis, Telix, GE, and Eczacıbaşı Monrol (speaker) outside of the submitted work. David Kersting reports support from the Universitätsmedizin Essen Clinician Scientist Academy and the German Research Foundation (DFG) under grant FU356/12-2, further support by the DFG, and a research grant from Pfizer outside of the submitted work. Marian Meckel, with ITM, declares patent interests related to the use of PAH as a renal protectant presented in this article. No other potential conflict of interest relevant to this article was reported.

ACKNOWLEDGMENTS

We express our gratitude to Prof. Dr. Thomas C. Dowling for his efforts to provide us with historical data, which were essential to validate our PAH pharmacokinetic model. ITM, through Marian Meckel, also acknowledges the contribution of Domokos Mathe and Ralf Bergmann for the animal handling and experiments.

KEY POINTS

QUESTION: Is PAH coinfusion for renal protection effective and safe in patients with NETs undergoing PRRT?

PERTINENT FINDINGS: PAH was well tolerated and improved patient comfort during treatment because of shorter infusion times and the potential reduction of hyperkalemia and nausea. In our cohort, dosimetry revealed a comparable nephroprotective effect between PAH and AA coinfusion in terms of compliance with toxicity thresholds.

IMPLICATIONS FOR PATIENT CARE: Implementation of PAH coinfusion in treatment protocols may enhance patient tolerance to PRRT and increase patient throughput.

REFERENCES

1. Kwekkeboom DJ, de Herder WW, Kam BL, et al. Treatment with the radiolabeled somatostatin analog [^{177}Lu-DOTA^{0},Tyr^{3}]octreotate: toxicity, efficacy, and survival. *J Clin Oncol.* 2008;26:2124–2130.
2. Strosberg J, El-Haddad G, Wolin E, et al. Phase 3 trial of ^{177}Lu-DOTATATE for midgut neuroendocrine tumors. *N Engl J Med.* 2017;376:125–135.
3. Sabet A, Ezziddin K, Pape UF, et al. Long-term hematotoxicity after peptide receptor radionuclide therapy with ^{177}Lu-octreotate. *J Nucl Med.* 2013;54:1857–1861.
4. Garkavij M, Nickel M, Sjögreen-Gleisner K, et al. ^{177}Lu-[DOTA^{0},Tyr^{3}] octreotate therapy in patients with disseminated neuroendocrine tumors: analysis of dosimetry with impact on future therapeutic strategy. *Cancer.* 2010;116:1084–1092.
5. Rolleman EJ, Melis M, Valkema R, Boerman OC, Krenning EP, de Jong M. Kidney protection during peptide receptor radionuclide therapy with somatostatin analogues. *Eur J Nucl Med Mol Imaging.* 2010;37:1018–1031.
6. Svensson J, Berg G, Wängberg B, Larsson M, Forssell-Aronsson E, Bernhardt P. Renal function affects absorbed dose to the kidneys and haematological toxicity during ^{177}Lu-DOTATATE treatment. *Eur J Nucl Med Mol Imaging.* 2015; 42:947–955.
7. Vegt E, van Eerd JE, Eek A, et al. Reducing renal uptake of radiolabeled peptides using albumin fragments. *J Nucl Med.* 2008;49:1506–1511.
8. Jamar F, Barone R, Mathieu I, et al. ^{86}Y-DOTA^{0}-D-Phe1-Tyr^{3}-octreotide (SMT487): a phase 1 clinical study—pharmacokinetics, biodistribution and renal protective effect of different regimens of amino acid co-infusion. *Eur J Nucl Med Mol Imaging.* 2003;30:510–518.
9. Vegt E, Wetzels JF, Russel FG, et al. Renal uptake of radiolabeled octreotide in human subjects is efficiently inhibited by succinylated gelatin. *J Nucl Med.* 2006; 47:432–436.
10. Rolleman EJ, Valkema R, de Jong M, Kooij PP, Krenning EP. Safe and effective inhibition of renal uptake of radiolabelled octreotide by a combination of lysine and arginine. *Eur J Nucl Med Mol Imaging.* 2003;30:9–15.
11. Bodei L, Cremonesi M, Zoboli S, et al. Receptor-mediated radionuclide therapy with ^{90}Y-DOTATOC in association with amino acid infusion: a phase I study. *Eur J Nucl Med Mol Imaging.* 2003;30:207–216.
12. Hope TA, Lisa B, Jennifer AC, et al. NANETS/SNMMI consensus statement on patient selection and appropriate use of ^{177}Lu-DOTATATE peptide receptor radionuclide therapy. *J Nucl Med.* 2020;61:222–227.
13. Chasis H, Redish J, Goldring W, Ranges HA, Smith HW. The use of sodium *p*-aminohippurate for the functional evaluation of the human kidney. *J Clin Invest.* 1945;24:583–588.
14. Smith HW, Finkelstein N, Aliminosa L, Crawford B, Graber M. The renal clearances of substituted hippuric acid derivatives and other aromatic acids in dog and man. *J Clin Invest.* 1945;24:388–404.
15. Maeda K, Tian Y, Fujita T, et al. Inhibitory effects of *p*-aminohippurate and probenecid on the renal clearance of adefovir and benzylpenicillin as probe drugs for organic anion transporter (OAT) 1 and OAT3 in humans. *Eur J Pharm Sci.* 2014; 59:94–103.
16. Stahl AR, Wagner B, Poethko T, et al. Renal accumulation of [^{111}In]DOTATOC in rats: influence of inhibitors of the organic ion transport and diuretics. *Eur J Nucl Med Mol Imaging.* 2007;34:2129–2134.
17. Sweet DH, Wolff NA, Pritchard JB. Expression cloning and characterization of ROAT1: the basolateral organic anion transporter in rat kidney. *J Biol Chem.* 1997; 272:30088–30095.
18. Meckel M, Osl T, Zhernosekov K, inventors. ITM Isotopen Technologien München AG, assignee. Para-aminohippuric acid (PAH) as a renal protective substance. Patents WO2020224780A1, PCT/EP2019/061882. November 12, 2020.
19. Bodei L, Mueller-Brand J, Baum RP, et al. The joint IAEA, EANM, and SNMMI practical guidance on peptide receptor radionuclide therapy (PRRNT) in neuroendocrine tumours. *Eur J Nucl Med Mol Imaging.* 2013;40:800–816.
20. Dowling TC, Frye RF, Fraley DS, Matzke GR. Characterization of tubular functional capacity in humans using para-aminohippurate and famotidine. *Kidney Int.* 2001;59:295–303.
21. Dickson JC, Armstrong IS, Gabina PM, et al. EANM practice guideline for quantitative SPECT-CT. *Eur J Nucl Med Mol Imaging.* 2023;50:980–995.
22. Siegel JA, Thomas SR, Stubbs JB, et al. MIRD pamphlet no. 16: techniques for quantitative radiopharmaceutical biodistribution data acquisition and analysis for use in human radiation dose estimates. *J Nucl Med.* 1999;40:37–61.
23. Sgouros G. Bone marrow dosimetry for radioimmunotherapy: theoretical considerations. *J Nucl Med.* 1993;34:689–694.
24. Forrer F, Krenning EP, Kooij PP, et al. Bone marrow dosimetry in peptide receptor radionuclide therapy with [^{177}Lu-DOTA^{0},Tyr^{3}]octreotate. *Eur J Nucl Med Mol Imaging.* 2009;36:1138–1146.
25. ICRP. Basic anatomical and physiological data for use in radiological protection reference values: ICRP publication 89. *Ann ICRP.* 2002;32:5–265.
26. Jentzen W, Freudenberg L, Eising EG, Sonnenschein W, Knust J, Bockisch A. Optimized ^{124}I PET dosimetry protocol for radioiodine therapy of differentiated thyroid cancer. *J Nucl Med.* 2008;49:1017–1023.
27. Hänscheid H, Lapa C, Buck AK, Lassmann M, Werner RA. Dose mapping after endoradiotherapy with ^{177}Lu-DOTATATE/DOTATOC by a single measurement after 4 days. *J Nucl Med.* 2018;59:75–81.
28. Hänscheid H, Lapa C, Buck AK, Lassmann M, Werner RA. Absorbed dose estimates from a single measurement one to three days after the administration of ^{177}Lu-DOTATATE/-TOC. *Nuklearmedizin.* 2017;56:219–224.
29. Traino AC, Ferrari M, Cremonesi M, Stabin MG. Influence of total-body mass on the scaling of S-factors for patient-specific, blood-based red-marrow dosimetry. *Phys Med Biol.* 2007;52:5231–5248.
30. Otte A, Herrmann R, Heppeler A, et al. Yttrium-90 DOTATOC: first clinical results. *Eur J Nucl Med.* 1999;26:1439–1447.
31. Puszkiel A, Bauriaud-Mallet M, Bourgeois R, Dierickx L, Courbon F, Chatelut E. Evaluation of the interaction of amino acid infusion on ^{177}Lu-DOTATATE pharmacokinetics in patients with gastroenteropancreatic neuroendocrine tumors. *Clin Pharmacokinet.* 2019;58:213–222.
32. Courault P, Deville A, Habouzit V, et al. Amino acid solutions for ^{177}Lu-oxodotreotide premedication: a tolerance study. *Cancers (Basel).* 2022;14:5212.
33. Lambert M, Dierickx L, Brillouet S, Courbon F, Chatelut E. Comparison of two types of amino acid solutions on ^{177}Lu-DOTATATE pharmacokinetics and pharmacodynamics in patients with metastatic gastroenteropancreatic neuroendocrine tumors. *Curr Radiopharm.* 2022;15:164–172.
34. Strigari L, Benassi M, Chiesa C, Cremonesi M, Bodei L, D'Andrea M. Dosimetry in nuclear medicine therapy: radiobiology application and results. *Q J Nucl Med Mol Imaging.* 2011;55:205–221.
35. Bodei L, Cremonesi M, Ferrari M, et al. Long-term evaluation of renal toxicity after peptide receptor radionuclide therapy with ^{90}Y-DOTATOC and ^{177}Lu-DOTATATE: the role of associated risk factors. *Eur J Nucl Med Mol Imaging.* 2008;35:1847–1856.
36. Sundlöv A, Sjögreen-Gleisner K, Svensson J, et al. Individualised ^{177}Lu-DOTATATE treatment of neuroendocrine tumours based on kidney dosimetry. *Eur J Nucl Med Mol Imaging.* 2017;44:1480–1489.
37. Del Prete M, Buteau FA, Arsenault F, et al. Personalized ^{177}Lu-octreotate peptide receptor radionuclide therapy of neuroendocrine tumours: initial results from the P-PRRT trial. *Eur J Nucl Med Mol Imaging.* 2019;46:728–742.
38. Schäfer H, Mayr S, Büttner-Herold M, et al. Extensive ^{177}Lu-PSMA radioligand therapy can lead to radiation nephropathy with a renal thrombotic microangiopathy-like picture. *Eur Urol.* 2023;83:385–390.
39. Tojo A, Kinugasa S. Mechanisms of glomerular albumin filtration and tubular reabsorption. *Int J Nephrol.* 2012;2012:481520.
40. Sekine T, Miyazaki H, Endou H. Molecular physiology of renal organic anion transporters. *Am J Physiol Renal Physiol.* 2006;290:F251–F261.

^{68}Ga-FAP-2286 PET of Solid Tumors: Biodistribution, Dosimetry, and Comparison with ^{18}F-FDG

Brad Kline[1], Surekha Yadav[1], Youngho Seo[1], Robin Cumming Ippisch[1], Jessa Castillo[1], Rahul R. Aggarwal[2], Robin Kate Kelley[2], Spencer C. Behr[1], Robert R. Flavell[1,2], Courtney Lawhn-Heath[1], Michelle Melisko[2], Hope S. Rugo[2], Victoria Wang[2], Sue S. Yom[3], Patrick Ha[4], Fei Jiang[5], and Thomas A. Hope[1]

[1]Department of Radiology and Biomedical Imaging, University of California San Francisco, San Francisco, California; [2]Helen Diller Comprehensive Cancer Center, University of California San Francisco, San Francisco, California; [3]Department of Radiation Oncology, University of California San Francisco, San Francisco, California; [4]Department of Otolaryngology–Head and Neck Surgery, University of California San Francisco, San Francisco, California; and [5]Department of Epidemiology and Biostatistics, University of California San Francisco, San Francisco, California

Fibroblast activation protein (FAP), expressed in the tumor microenvironment of a variety of cancers, has become a target of novel PET tracers. The purpose of this report is to evaluate the imaging characteristics of ^{68}Ga-FAP-2286, present the first—to our knowledge—dosimetry analysis to date, and compare the agent with ^{18}F-FDG and FAPI compounds. **Methods:** Patients were administered 219 ± 43 MBq of ^{68}Ga-FAP-2286 and scanned after 60 min. Uptake was measured in up to 5 lesions per patient and within the kidneys, spleen, liver, and mediastinum (blood pool). Absorbed doses were evaluated using MIM Encore and OLINDA/EXM version 1.1 using the International Commission on Radiological Protection publication 103 tissue weighting factor. **Results:** Forty-six patients were imaged with ^{68}Ga-FAP-2286 PET. The highest average uptake was seen in sarcoma, cholangiocarcinoma, and colon cancer. The lowest uptake was found in lung cancer and testicular cancer. The average $\mathrm{SUV_{max}}$ was significantly higher on ^{68}Ga-FAP-2286 PET than on ^{18}F-FDG PET in cholangiocarcinoma (18.2 ± 6.4 vs. 9.1 ± 5.0, $P = 0.007$), breast cancer (11.1 ± 6.8 vs. 4.1 ± 2.2, $P < 0.001$), colon cancer (13.8 ± 2.2 vs. 7.6 ± 1.7, $P = 0.001$), hepatocellular carcinoma (9.3 ± 3.5 vs. 4.7 ± 1.3, $P = 0.01$), head and neck cancer (11.3 ± 3.5 vs. 7.6 ± 5.5, $P = 0.04$), and pancreatic adenocarcinoma (7.4 ± 1.8 vs. 3.7 ± 1.0, $P = 0.01$). The total-body effective dose was estimated at 1.16E−02 mSv/MBq, with the greatest absorbed organ dose in the urinary bladder wall (9.98E−02 mGy/MBq). **Conclusion:** ^{68}Ga-FAP-2286 biodistribution, dosimetry, and tumor uptake were similar to those of previously reported FAPI compounds. Additionally, ^{68}Ga-FAP-2286 PET had consistently higher uptake than ^{18}F-FDG PET. These results are especially promising in the setting of small-volume disease and differentiating tumor from inflammatory uptake.

Key Words: dosimetry; FAP-2286; fibroblast activation protein; PET

J Nucl Med 2024; 65:938–943
DOI: 10.2967/jnumed.123.267281

Fibroblast activation protein (FAP)–targeting radioligands have emerged as promising agents in diagnostic cancer imaging and therapy. FAP is a transmembrane glycoprotein with a limited presence in healthy adult tissue but significant expression in cancer-associated fibroblasts, which are present in the stroma of most epithelial tumors and are known to be involved in disease growth and progression (*1*,*2*). The tumorigenic nature of cancer-associated fibroblasts, and the fact that they are absent from most healthy tissue, make FAP an attractive target in the development of pantumor radiopharmaceuticals.

Most of the literature on FAP-targeting PET focuses on the FAP inhibitors (FAPIs). FAPI-04, for example, has shown excellent uptake in breast cancer, esophageal cancer, lung cancer, sarcoma, and cholangiocarcinoma, as well as superior diagnostic efficacy in primary and metastatic lesions compared with ^{18}F-FDG across several tumor types (*3*,*4*). There is also considerable interest and promising results in abdominal malignancies and using FAPI tracers to identify peritoneal spread, which is poorly imaged with ^{18}F-FDG (*5*).

FAP-2286 differs from FAPI molecules using a cyclic peptide as a binding motif rather than a quinolone-based structure; however, previous evaluations have shown similar imaging characteristics to FAPI compounds (*6*). For example, Pang et al. recently presented results indicating the superiority of FAP-2286 over ^{18}F-FDG in hepatic, gastric, and pancreatic cancers (*7*). Preclinical and first-in-humans studies of ^{68}Ga-FAP-2286 and ^{177}Lu-FAP-2286 have also demonstrated prolonged tumor retention, making it a potential therapeutic target (*6*,*8*).

Here, we present our initial prospective experience with ^{68}Ga-FAP-2286, including comparison to ^{18}F-FDG PET when available, biodistribution in major organs, and radiation dosimetry analysis.

MATERIALS AND METHODS

Study Design and Patients

This single-arm, prospective study was performed at the University of California San Francisco with the approval of the local institutional review board (NCT04621435) and according to the ethical principles of the 1964 Declaration of Helsinki. Patients were eligible if they had histopathologically confirmed solid tumors. They were enrolled into cohort 1 (dosimetry cohort, which included patients with and without RECIST-measurable disease), cohort 2 (metastatic disease present on the basis of RECIST), or cohort 3 (no evidence of metastatic disease but at high risk for the presence of metastatic disease). All patients gave written informed consent. Data were collected in a central REDCap database. ^{18}F-FDG PET scans were included for comparison if

---

Received Dec. 22, 2023; revision accepted Mar. 25, 2024.

For correspondence or reprints, contact Thomas A. Hope (thomas.hope@ucsf.edu).

they were performed within 3 mo of the ^{68}Ga-FAP-2286 PET. Imaging results in patients with bladder cancer will be reported separately.

^{68}Ga-FAP-2286 Radiosynthesis

Radiosynthesis was conducted in an iQS ^{68}Ga fluidic labeling module and cassette (ITM Pharma Solutions GmbH). The precursor, FAP-2286 (Clovis Oncology, Inc.), was prepared into 41-μg/50-μL ultra-high-purity water aliquots and stored at −20°C until use. Before radiosynthesis, the precursor aliquot was mixed with 800 μL of 1 M ammonium acetate and 200 μL of 0.125 M sodium ascorbate. The reactor was preheated to 120°C, and the prepared precursor was added. ^{68}Ga was eluted from a ^{68}Ge/^{68}Ga generator (Eckert and Ziegler) with 5 mL of 0.1 M HCl into the reactor, yielding ^{68}GaCl$_3$ with radioactivity in the range of 555–1,110 MBq (15–30 mCi). The radiolabeling proceeded for 10 min, and the reaction mixture was passed through a sterilizing filter into a sterile, pyrogen-free product vial to yield ^{68}Ga-FAP-2286. The radiolabeling yield was 95%, and radiochemical purity was 97% ($n = 15$).

^{68}Ga-FAP-2286 PET Imaging

Patients were injected with 219 ± 43 MBq (allowed range, 111–296 MBq) and imaged at a mean of 61 ± 7.4 min after injection with a target uptake time of 60 min (allowed range, 50–100 min). A subset of 10 patients was also imaged at 30 and 120 min for dosimetry. Patients were imaged on either a Vision PET/CT ($n = 34$, Siemens Healthineers) or a 3.0-T Signa PET/MRI ($n = 12$, GE Healthcare). For PET/CT, continuous bed motion was used with a bed speed of 0.7 cm/s, resulting in a scan duration of 11 min and 46 s for a coverage of 495.5 cm. Noncontrast low-dose CT was used for attenuation correction, and images were reconstructed using ultraHD•PET (Siemens) time of flight with 8 iterations and 5 subsets. For PET/MRI, a whole-body PET acquisition from the mid thighs to the vertex was obtained for 3 min at each of the 6 bed positions. The following MRI sequences were obtained at each bed position: axial MR attenuation correction and axial T1-weighted images (LAVA Flex; GE Healthcare).

Image Interpretation

A board-certified nuclear medicine physician evaluated the reconstructed PET, CT, or MR images. A positive lesion on PET was defined as a focus of activity with an SUV at least 1.5 times higher than the SUV$_{\text{mean}}$ of the mediastinal blood pool and not attributable to physiologic distribution such as urinary excretion. A volume of interest was semiautomatically placed around each lesion, and the calculated SUV$_{\text{max}}$ was recorded, including lesions that were detected on standard scans but were not positive on PET. SUV$_{\text{max}}$ data were then averaged across all lesions within a given patient. To avoid clustering effects, analysis was limited to the 5 largest lesions in each individual patient. Additionally, volumes of interest were placed over the mediastinum, liver, spleen, and kidneys to measure physiologic distribution; SUV$_{\text{peak}}$ was used for quantification in the kidneys. Quantitative uptake was performed at the 60-min time point for all patients.

Radiation Dosimetry

The 10 patients in the dosimetry cohort were imaged at 30-, 60-, and 120-min time points. The data from these patients were used to estimate the internal radiation dose. MIM Encore (MIM Software) was used to segment the source organs. All activity within each organ was included. OLINDA version 2.0 was used to derive values, with curve fitting performed on the EXM module of the OLINDA version 1.1 software package (*9*). The reference adult model with International Commission on Radiological Protection publication 103 tissue weighting factor was used (*10*).

Safety

The first 35 patients enrolled in the study underwent pre- and postimaging laboratory evaluation, electrocardiography, physical examination, and vital sign assessment. Subsequent patients underwent physical examination and vital sign assessment only. All patients were monitored for adverse events up to 2 h after injection and were contacted again 1–3 d later to evaluate for delayed adverse events.

Statistical Analysis

Descriptive statistics were used to describe uptake across tumor types. The Student *t* test was used for comparison of SUVs between ^{68}Ga-FAP-2286 and ^{18}F-FDG PET. *P* values of less than 0.05 were considered statistically significant.

RESULTS

Patient Characteristics and Safety

Forty-six patients were enrolled between January 2021 and April 2023. Patient characteristics are available in Table 1. No clinically significant changes were seen in laboratory assessments or electrocardiograms in the first 35 patients who received ^{68}Ga-FAP-2286. Across all patients, there were no clinically significant changes in physical examination findings or vital signs after administration. No serious adverse events were reported.

Biodistribution

SUV$_{\text{mean}}$ was measured in the liver (2.0 ± 0.8), spleen (0.95 ± 0.31), and blood pool (1.4 ± 0.4), and SUV$_{\text{peak}}$ was measured in the kidneys (4.2 ± 1.4), at the 60-min time point in all 46 patients (Supplemental Fig. 1; supplemental materials are available at http://jnm.snmjournals.org).

Tumor Uptake and Effect of Lesion Size

Forty-three patients had ^{68}Ga-FAP-2286–positive lesions, including all patients in cohort 1 and nearly all patients in cohort 2. Sarcoma (SUV$_{\text{max}}$, 16.8 ± 7.5) and cholangiocarcinoma (SUV$_{\text{max}}$, 16.6 ± 6.5) demonstrated the highest uptake across tumor types (Fig. 1). The total number of lesions evaluated was 147, with a distribution by lesion size as follows: 5 lesions measured 0–5 mm; 23 lesions, 5–10 mm; 33 lesions, 10–15 mm; 17 lesions, 15–20 mm; and 69 lesions, more than 20 mm. Median SUV$_{\text{max}}$ generally increased with lesion size (Supplemental Fig. 2, $P = 0.037$ for the 0- to 5-mm and >20-mm groups).

Comparison to ^{18}F-FDG

Comparing ^{68}Ga-FAP-2286 PET with ^{18}F-FDG PET across all disease types, there was higher uptake on ^{68}Ga-FAP-2286 PET than on ^{18}F-FDG PET (11.5 ± 6.4 vs. 7.8 ± 5.9, $P < 0.001$; Fig. 2). The disease types with the highest relative uptake on ^{68}Ga-FAP-2286 PET compared with ^{18}F-FDG were cholangiocarcinoma ($n =$ 4, 18.2 ± 6.4 vs. 9.1 ± 5.0, $P = 0.007$), breast cancer ($n = 6$, 11.1 ± 6.8 vs. 4.1 ± 2.2, $P < 0.001$), colon cancer ($n = 1$, 13.8 ± 2.2 vs. 7.6 ± 1.7, $P = 0.001$), HCC ($n = 2$, 9.3 ± 3.5 vs. 4.7 ± 1.3, $P = 0.01$), head and neck cancer ($n = 6$, 11.3 ± 3.5 vs. 7.6 ± 5.5, $P = 0.04$), and pancreatic adenocarcinoma ($n = 1$, 7.4 ± 1.8 vs. 3.7 ± 1.0, $P = 0.01$).

Dosimetry

The dosimetry is reported in Table 2 (full table available as Supplemental Table 1). The highest absorbed dose for ^{68}Ga-FAP-2286 was in the urinary bladder wall (9.98E−02 mGy/MBq), followed by the kidneys (4.31E−02 mGy/MBq), liver (2.23E−02 mGy/MBq), and spleen (7.9E−03 mGy/MBq). The effective dose was estimated at 1.16E−02 mSv/MBq.

TABLE 1
Patient Characteristics

Characteristic	Cohort 1	Cohort 2	Cohort 3	Overall
Number of patients	10	25	11	46
Sex (*n*)				
Female	5	12	6	23
Male	5	13	5	23
Age (y)				
Range	26–83	33–80	44–78	26–83
Median	67	60	63	64
Diagnosis (*n*)				
Breast cancer	1	5	3	9
Head/neck cancer	0	0	8	8
Sarcoma	2	6	0	8
Cholangiocarcinoma	4	1	0	5
Prostate cancer	1	4	0	5
HCC	1	2	0	3
Colon cancer	0	2	0	2
Pancreatic cancer	1	1	0	2
Lung cancer	0	2	0	2
Testicular cancer	0	1	0	1
Mesothelioma	0	1	0	1
Average administered activity (MBq)	228 ± 51	218 ± 41	212 ± 38	219 ± 43
Average uptake time (min)	59 ± 3.9	62.4 ± 8.8	61.6 ± 5.3	61 ± 7.4
Average time between ^{18}F-FDG and ^{68}Ga-FAP-2286 PET (d)	40 ± 24	42 ± 27	50 ± 35	44 ± 24

Clinical Applications of Note

A total of 8 patients with head and neck cancer were enrolled, 2 of whom had no evidence of disease. $\mathrm{SUV_{max}}$ in primary lesions was 13.1 ± 5.5 and uptake in metastases was 11.5 ± 3.7, and there was higher uptake in metastases with ^{68}Ga-FAP-2286 than with ^{18}F-FDG (11.5 vs. 5.6, $P < 0.001$). One benefit of ^{68}Ga-FAP-2286 compared with ^{18}F-FDG was relatively low background uptake in mucosal, salivary, and inflammatory regions of uptake. In one case, a patient at staging had false-positive nodes on ^{18}F-FDG PET due to a recent coronavirus disease 2019 vaccination; these nodes demonstrated no uptake on the ^{68}Ga-FAP-2286 PET (Fig. 3).

In total, 9 patients with breast cancer were enrolled. Lesion $\mathrm{SUV_{max}}$ was higher on ^{68}Ga-FAP-2286 PET than on ^{18}F-FDG PET in all patients (11.1 vs. 4.1, $P < 0.001$). The largest difference in $\mathrm{SUV_{max}}$ was in 2 patients with estrogen receptor–positive/progesterone receptor–positive/human epidermal growth factor receptor 2–negative invasive ductal carcinoma, for whom the highest lesion $\mathrm{SUV_{max}}$ was 23.2 and 17.9 on ^{68}Ga-FAP-2286 PET compared with 7.5 and 7.7 on ^{18}F-FDG PET. ^{68}Ga-FAP-2286 $\mathrm{SUV_{max}}$ was higher in patients with invasive ductal carcinoma ($n = 4$) than in patients with invasive lobular carcinoma (ILC) or mixed ductolobular carcinoma ($n = 5$) ($\mathrm{SUV_{max}}$ of 14.6 for invasive ductal carcinoma vs. 4.9 for ILC/mixed; $P = 0.046$).

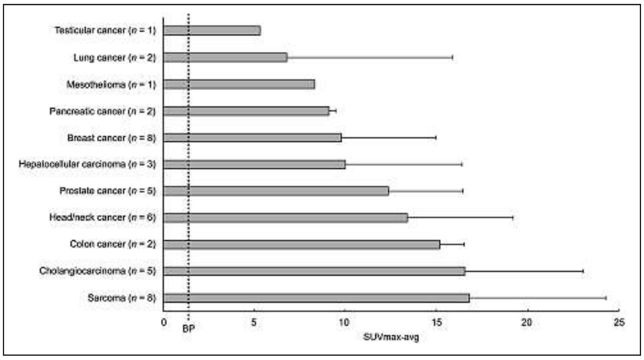

FIGURE 1. Tumor uptake by tumor type. $\mathrm{SUV_{max}}$-avg represents average $\mathrm{SUV_{max}}$ of hottest lesion per patient. Error bars represent 95% CI. Average blood pool uptake (BP) was 1.4.

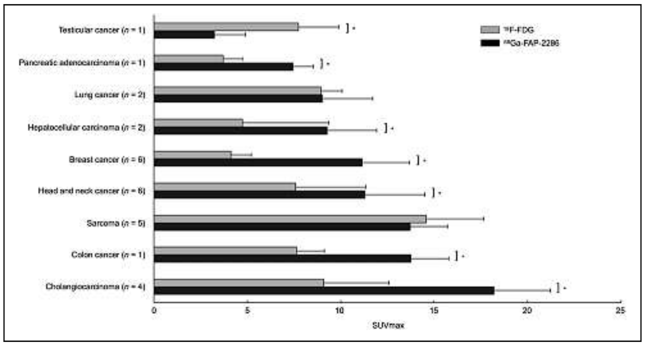

FIGURE 2. Comparison of paired $\mathrm{SUV_{max}}$ across various cancer types imaged with ^{68}Ga-FAP-2286 PET vs. ^{18}F-FDG PET. Error bars represent 95% CI. *$P < 0.05$.

TABLE 2
Selected Organ-Absorbed Dose and Effective Dose for ^{68}Ga-FAP-2286 and Other Tracers

Parameter	^{68}Ga-FAP-2286	^{68}Ga-FAPI-46 (*12*)	^{18}F-FDG (*20*)
Kidneys (mGy/MBq)	4.31E−02	1.60E−02	1.7E−02
Liver (mGy/MBq)	2.23E−02	1.01E−02	2.1E−02
Spleen (mGy/MBq)	7.93E−03	6.96E−03	1.1E−02
Urinary bladder wall (mGy/MBq)	9.98E−02	4.83E−02	1.3E−01
Effective dose (mSv/MBq)	1.16E−02	7.80E−03	1.9E−02
Typical injected activity			
MBq	229	236	370
mCi	6.18	6.38	10
Estimated effective dose per scan (mSv)	2.65	1.84	7.0

Anecdotally, the higher uptake on ^{68}Ga-FAP-2286 PET resulted in improved lesion visualization, particularly promising for ILC (Fig. 4).

In total, 5 patients with cholangiocarcinoma and 3 patients with hepatocellular carcinoma (HCC) were enrolled. The SUV$_{max}$ in cholangiocarcinoma was higher than that in HCC (13.5 vs. 8.6, $P = 0.03$), although one HCC had an SUV$_{max}$ of 15.8, overlapping with the cholangiocarcinoma patients. In patients for whom paired ^{18}F-FDG PET was available, both cholangiocarcinoma and HCC had higher uptake on ^{68}Ga-FAP-2286 PET than on ^{18}F-FDG PET (cholangiocarcinoma: 18.1 vs. 9.1, $P = 0.009$; HCC: 9.3 vs. 4.7, $P = 0.04$) (Fig. 5). There was no difference in uptake between intrahepatic cholangiocarcinoma lesions and extrahepatic disease (14.0 for intrahepatic vs. 12.7 for extrahepatic, $P = 0.7$).

DISCUSSION

Here, we report the results of patient imaging using ^{68}Ga-FAP-2286 PET. We evaluated biodistribution and dosimetry, which demonstrated that ^{68}Ga-FAP-2286 is excreted primarily via the kidneys and has a whole-body effective dose consistent with previously studied FAPI agents. Tumor uptake ranged from 5.3 to 16.8 and in general was higher on ^{68}Ga-FAP-2286 PET than on paired ^{18}F-FDG PET, although there was variation among tumor types.

The biodistribution of ^{68}Ga-FAP-2286 is similar to that of previously reported FAPI compounds, with low uptake in all organs except the kidney, consistent with predominate renal excretion. There was a slight increase in liver uptake and kidney uptake compared with the previously reported agents FAPI-04, FAPI-46, and FAPI-72 (*11*). This is similar to results reported by Pang et al., who also found that the biodistribution was similar between FAP-2286 and FAPI-46, with higher liver and kidney uptake (*7*). This was also consistent with our dosimetry analysis, which demonstrated a higher absorbed dose in the liver than was seen with ^{68}Ga-FAPI compounds (*12*,*13*), supporting greater hepatic accumulation. Overall, the average effective whole-body dose of ^{68}Ga-FAP-2286 PET was 1.16E−02 mSv/MBq, which is slightly lower than that of ^{18}F-FDG PET and similar to that of ^{68}Ga-FAPI-46 (*12*).

Uptake across tumor types was largely consistent with previous studies of FAPI compounds, including a study by Kratochwil et al. (*3*). In particular, colon and pancreatic cancer were significantly higher on ^{68}Ga-FAP-2286 PET than on ^{18}F-FDG PET, similar to what was found by Pang et al. (*7*), which may be attributable to the role of cancer-associated fibroblasts in the desmoplastic reactions surrounding pancreatic cancer cells, as well as the increased presence of fibroblasts in the tumor microenvironment of colon cancer (*14*,*15*). In our study, lesions were generally smaller than those reported previously because of cohort 3, which included patients without measurable disease and therefore biased our study toward smaller lesions. The smaller average lesion size could contribute to an underestimate of average SUV$_{max}$. This possibility is further supported by the similarity in median uptake between smaller lesions and larger ones. Lesions in the smallest grouping had a median SUV$_{max}$

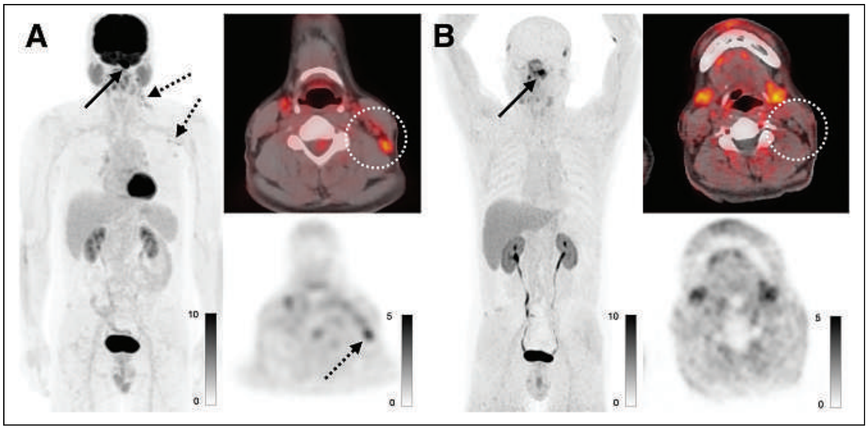

FIGURE 3. A 58-y-old man with newly diagnosed nasopharyngeal carcinoma. (A) Maximum-intensity projections, axial fused PET, and axial PET images from ^{18}F-FDG PET/CT demonstrate known nasopharyngeal mass with SUV$_{max}$ of 23.7 (solid arrow), along with small but mildly hypermetabolic left cervical and axillary lymph nodes with SUV$_{max}$ of up to 3.7 (dashed arrows, dotted circle). (B) Maximum-intensity projections, axial fused PET, and axial PET images from ^{68}Ga-FAP-2286 PET/CT demonstrate only nasopharyngeal mass with SUV$_{max}$ of 12.7 (arrow), with no uptake in the cervical lymph nodes (dotted circle). Fine-needle aspiration of left cervical node revealed reactive changes, which was attributed to recent coronavirus disease 2019 vaccine.

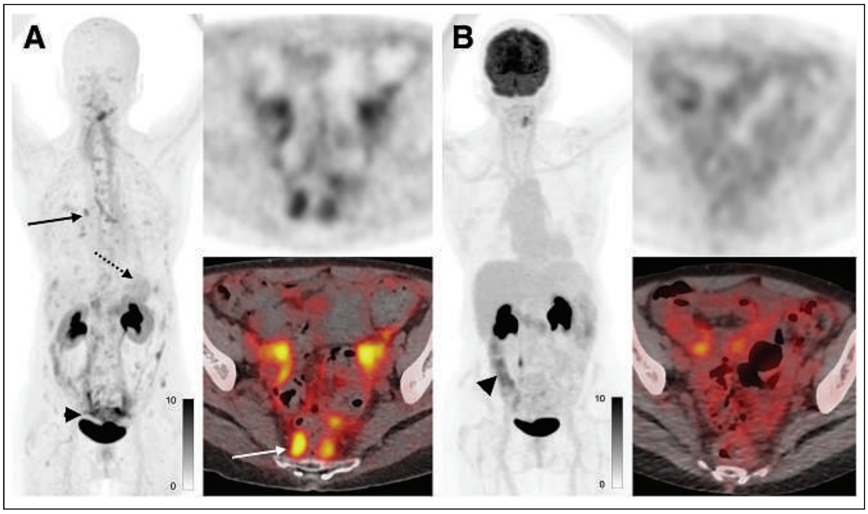

FIGURE 4. A 72-y-old woman with metastatic invasive lobular breast cancer. ^{68}Ga-FAP-2286 PET (A) revealed extensive metastatic disease not seen on ^{18}F-FDG PET (B), including small mediastinal and hilar lymph nodes (A, solid black arrow), diffuse gastric mucosal disease (A, dotted black arrow), and extensive peritoneal disease (SUV$_{max}$, 7.1; A, black arrowhead and white arrow). Uptake seen on ^{18}F-FDG PET in abdomen reflects physiologic uptake in bowel (B, black arrowhead) rather than tumor.

of 6.4, compared with 10.3 in the largest, potentially indicating good sensitivity for the detection of small sites of disease.

With head and neck cancer, uptake was greater than seen on ^{18}F-FDG PET, and maybe more importantly, there was anecdotal evidence that inflammatory nodes are not seen on ^{68}Ga-FAP-2286 PET, suggesting that ^{68}Ga-FAP-2286 may have value in nodal staging. Additionally, ^{68}Ga-FAP-2286 might better discriminate between the primary tumor and physiologic uptake in the oropharyngeal mucosa. Consistent with this possibility, previous work has shown that ^{68}Ga-FAPI-04 PET has higher sensitivity and specificity than ^{18}F-FDG PET for nodal metastases (*16*). In the setting of breast cancer, ^{68}Ga-FAP-2286 PET had higher uptake than ^{18}F-FDG PET, but this was particularly clinically relevant in ILC, for which disease frequently is not seen on ^{18}F-FDG PET (*17*). Previously, ILC that was ^{18}F-FDG–negative was shown to have uptake on ^{68}Ga-FAP-04 PET (*18*), and further work should be done in this setting. With liver tumors, there was hope that ^{68}Ga-FAP-2286 PET could help distinguish between HCC and cholangiocarcinoma. Although there was higher uptake in cholangiocarcinoma, there was overlap, which limited the ability of ^{68}Ga-FAP-2286 PET to help characterize intrahepatic lesions, as is consistent with results in prior work (*19*). One potential benefit of ^{68}Ga-FAP-2286 in cholangiocarcinoma could be the ability to distinguish between an adjacent tumor and inflammation associated with biliary ductal stents and obstruction, which is a common confounder with ^{18}F-FDG PET.

Limitations of our report include the small number of patients enrolled per cancer type, the absence of comparison to ^{18}F-FDG PET in some patients, and the possibility of disease progression within the 3-mo maximum time between ^{18}F-FDG PET and ^{68}Ga-FAP-2286 PET. Future studies with larger populations and smaller imaging windows would improve the robustness of our findings related to ^{68}Ga-FAP-2286 imaging. Additionally, ^{18}F-FDG PET was performed on different scanners, limiting the comparison between the ^{18}F-FDG and ^{68}Ga-FAP-2286 studies.

CONCLUSION

^{68}Ga-FAP-2286 biodistribution, dosimetry, and tumor uptake were similar to those of previously reported FAPI compounds. Additionally, ^{68}Ga-FAP-2286 PET had consistently higher uptake than ^{18}F-FDG PET. These results are especially promising in the setting of small-volume disease and differentiating tumor from inflammatory uptake.

DISCLOSURE

Thomas Hope has grant funding to the institution from Clovis Oncology, GE Healthcare, Lantheus, Janssen, Novartis, the Prostate Cancer Foundation, Telix Pharmaceuticals, and the National Cancer Institute (R01CA235741 and R01CA212148). He received personal fees from Bayer, Cardinal Health, BlueEarth Diagnostics, and Lantheus and received fees from and has an equity interest in RayzeBio and Curium. Robin Kelley has research funding to the institution from Agios, AstraZeneca, Bayer, BMS, Compass Therapeutics, Eli Lilly, EMD Serono, Exelixis, Genentech/Roche, Loxo Oncology, Merck, Novartis, Partner Therapeutics, QED, Relay Therapeutics, Servier, Surface Oncology, Taiho, and Tyra Biosciences. She received consulting/advisory fees from Compass, Exact Sciences, Kinnate, Regeneron, Tyra Therapeutics, and J-Pharma Inc. and to the institution from Agios, AstraZeneca, BMS, Exelixis, Ipsen, and Merck.

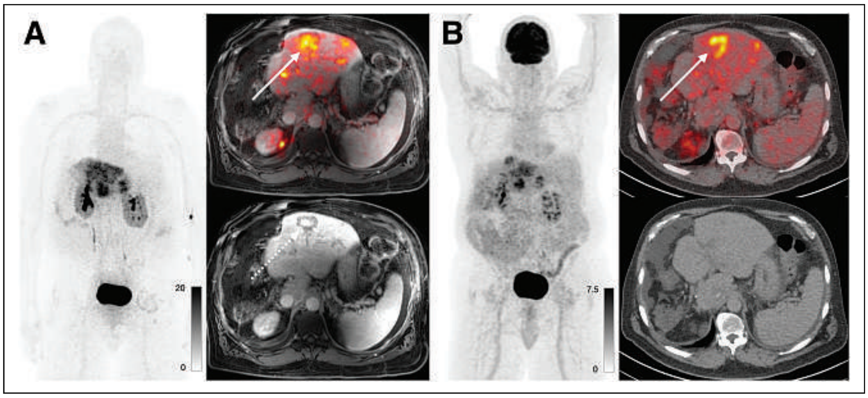

FIGURE 5. A 69-y-old man with cholangiocarcinoma imaged using PET/MRI. (A) ^{68}Ga-FAP-2286 images demonstrate uptake within hepatic metastases. Uptake is more central (solid arrow), which correlates with region of delayed enhancement on MRI (dashed arrow). (B) ^{18}F-FDG PET/CT demonstrates more peripheral uptake associated with more cellular component of tumor (arrow).

She received travel support from AstraZeneca and Merck. No other potential conflict of interest relevant to this article was reported.

KEY POINTS

QUESTION: What are the dosimetry and tumor uptake of ^{68}Ga-FAP-2286 PET?

PERTINENT FINDINGS: Our prospective study demonstrated a total-body effective dose of 1.16E−02 mSv/MBq and tumor uptake that mirrored that of other FAPI compounds. Additionally, ^{68}Ga-FAP-2286 PET had higher uptake than ^{18}F-FDG PET.

IMPLICATIONS FOR PATIENT CARE: In the setting of small-volume disease and differentiating tumor from inflammatory uptake, ^{68}Ga-FAP-2286 PET could improve staging.

REFERENCES

1. Loktev A, Lindner T, Mier W, et al. A tumor-imaging method targeting cancer-associated fibroblasts. *J Nucl Med.* 2018;59:1423–1429.
2. Garin-Chesa P, Old LJ, Rettig WJ. Cell surface glycoprotein of reactive stromal fibroblasts as a potential antibody target in human epithelial cancers. *Proc Natl Acad Sci USA.* 1990;87:7235–7239.
3. Kratochwil C, Flechsig P, Lindner T, et al. ^{68}Ga-FAPI PET/CT: tracer uptake in 28 different kinds of cancer. *J Nucl Med.* 2019;60:801–805.
4. Chen H, Pang Y, Wu J, et al. Comparison of [^{68}Ga]Ga-DOTA-FAPI-04 and [^{18}F] FDG PET/CT for the diagnosis of primary and metastatic lesions in patients with various types of cancer. *Eur J Nucl Med Mol Imaging.* 2020;47:1820–1832.
5. Zhao L, Pang Y, Luo Z, et al. Role of [^{68}Ga]Ga-DOTA-FAPI-04 PET/CT in the evaluation of peritoneal carcinomatosis and comparison with [^{18}F]-FDG PET/CT. *Eur J Nucl Med Mol Imaging.* 2021;48:1944–1955.
6. Zboralski D, Hoehne A, Bredenbeck A, et al. Preclinical evaluation of FAP-2286 for fibroblast activation protein targeted radionuclide imaging and therapy. *Eur J Nucl Med Mol Imaging.* 2022;49:3651–3667.
7. Pang Y, Zhao L, Meng T, et al. PET imaging of fibroblast activation protein in various types of cancer using ^{68}Ga-FAP-2286: comparison with ^{18}F-FDG and ^{68}Ga-FAPI-46 in a single-center, prospective study. *J Nucl Med.* 2023;64:386–394.
8. Baum RP, Schuchardt C, Singh A, et al. Feasibility, biodistribution, and preliminary dosimetry in peptide-targeted radionuclide therapy of diverse adenocarcinomas using ^{177}Lu-FAP-2286: first-in-humans results. *J Nucl Med.* 2022;63:415–423.
9. Stabin MG, Sparks RB, Crowe E. OLINDA/EXM: the second-generation personal computer software for internal dose assessment in nuclear medicine. *J Nucl Med.* 2005;46:1023–1027.
10. *ICRP Publication 103: The 2007 Recommendations of the International Commission on Radiological Protection.* International Commission on Radiological Protection; 2007.
11. Giesel FL, Kratochwil C, Schlittenhardt J, et al. Head-to-head intra-individual comparison of biodistribution and tumor uptake of ^{68}Ga-FAPI and ^{18}F-FDG PET/CT in cancer patients. *Eur J Nucl Med Mol Imaging.* 2021;48:4377–4385.
12. Meyer C, Dahlbom M, Lindner T, et al. Radiation dosimetry and biodistribution of ^{68}Ga-FAPI-46 PET imaging in cancer patients. *J Nucl Med.* 2020;61:1171–1177.
13. Giesel FL, Kratochwil C, Lindner T, et al. ^{68}Ga-FAPI PET/CT: biodistribution and preliminary dosimetry estimate of 2 DOTA-containing FAP-targeting agents in patients with various cancers. *J Nucl Med.* 2019;60:386–392.
14. Kamali Zonouzi S, Pezeshki PS, Razi S, Rezaei N. Cancer-associated fibroblasts in colorectal cancer. *Clin Transl Oncol.* 2022;24:757–769.
15. Nielsen MFB, Mortensen MB, Detlefsen S. Key players in pancreatic cancer-stroma interaction: cancer-associated fibroblasts, endothelial and inflammatory cells. *World J Gastroenterol.* 2016;22:2678–2700.
16. Jiang Y, Wen B, Li C, et al. The performance of ^{68}Ga-FAPI-04 PET/CT in head and neck squamous cell carcinoma: a prospective comparison with ^{18}F-FDG PET/CT. *Eur J Nucl Med Mol Imaging.* 2023;50:2114–2126.
17. Hogan MP, Goldman DA, Dashevsky B, et al. Comparison of ^{18}F-FDG PET/CT for systemic staging of newly diagnosed invasive lobular carcinoma versus invasive ductal carcinoma. *J Nucl Med.* 2015;56:1674–1680.
18. Eshet Y, Tau N, Apter S, et al. The role of ^{68}Ga-FAPI PET/CT in detection of metastatic lobular breast cancer. *Clin Nucl Med.* 2023;48:228–232.
19. Guo W, Pang Y, Yao L, et al. Imaging fibroblast activation protein in liver cancer: a single-center post hoc retrospective analysis to compare [^{68}Ga]Ga-FAPI-04 PET/CT versus MRI and [^{18}F]-FDG PET/CT. *Eur J Nucl Med Mol Imaging.* 2021;48:1604–1617.
20. Brix G, Lechel U, Glatting G, et al. Radiation exposure of patients undergoing whole-body dual-modality ^{18}F-FDG PET/CT examinations. *J Nucl Med.* 2005;46:608–613.

Prognostic Value of [^{99m}Tc]Tc-DPD Quantitative SPECT/CT in Patients with Suspected and Confirmed Amyloid Transthyretin–Related Cardiomyopathy and Preserved Left Ventricular Function

Federico Caobelli*[1], Nasir Gözlügöl*[1], Adam Bakula[1], Axel Rominger[1], Robin Schepers[1], Stefan Stortecky[2], Lukas Hunziker Munsch[2], Stephan Dobner[2,3], and Christoph Gräni[2]

[1]Department of Nuclear Medicine, Bern University Hospital, University of Bern, Bern, Switzerland; [2]Department of Cardiology, Bern University Hospital, University of Bern, Bern, Switzerland; and [3]Third Medical Department of Cardiology and Intensive Care Medicine, Clinic Ottakring, Vienna, Austria

Quantitative ^{99m}Tc-3,3-diphosphono-1,2-propanodicarboxylic acid ([^{99m}Tc]Tc-DPD) SPECT may be used for risk-stratifying patients with amyloid transthyretin–related cardiomyopathy (ATTR-CM). We aimed to analyze the predictive value of quantitative [^{99m}Tc]Tc-DPD SPECT/CT in suspected and confirmed ATTR-CM according to different disease stages. **Methods:** The study enrolled consecutive patients with suspected ATTR-CM who were referred to a single tertiary center and underwent quantitative [^{99m}Tc]Tc-DPD SPECT/CT allowing SUV_{max} and SUV_{peak} analysis. Patients were divided into 2 groups according to left ventricular ejection fraction (LVEF) at baseline (i.e., ≥50% and <50%). Clinical, laboratory, and echocardiographic parameters and major adverse cardiac events (i.e., all-cause death, sustained ventricular tachyarrhythmia, hospitalization for heart failure, implantation of a cardioverter defibrillator) were investigated for any correlation with quantitative uptake values. **Results:** In total, 144 patients with suspected ATTR-CM were included in the study (98 with LVEF ≥ 50% and 46 with LVEF < 50%), of whom 99 were diagnosed with ATTR-CM (68.8%; 69 with LVEF ≥ 50% and 30 with LVEF < 50%). A myocardial SUV_{max} of at least 7 was predictive of major adverse cardiac events at 21.9 ± 13.0 mo of follow-up (hazard ratio, 2.875; 95% CI, 1.23–6.71; $P = 0.015$) in patients with suspected or confirmed ATTR-CM (global $\chi^2 = 6.892$, $P = 0.02$) and an LVEF of at least 50%. SUV_{max} was not predictive in patients with an LVEF of less than 50% and suspected or confirmed ATTR-CM. **Conclusion:** In patients with suspected or confirmed ATTR-CM and preserved LVEF, representing an early disease stage, quantitative [^{99m}Tc]Tc-DPD SPECT should be considered to improve early-stage risk stratification.

Key Words: cardiac transthyretin amyloidosis; ATTR-CM; ATTR; SPECT; quantitative SPECT; DPD

J Nucl Med 2024; 65:944–951
DOI: 10.2967/jnumed.123.266926

To diagnose amyloid transthyretin–related cardiomyopathy (ATTR-CM), ^{99m}Tc-3,3-diphosphono-1,2-propanodicarboxylic acid ([^{99m}Tc]Tc-DPD) scintigraphy and SPECT/CT have become established noninvasive methods (*1–3*). Although the visual interpretation according to Perugini score (*4*) is currently the clinical diagnostic standard, this visual grading failed to show an association with adverse clinical outcomes (*5*). However, the potential of semiquantitative [^{99m}Tc]Tc-pyrophosphate SPECT/CT to predict major adverse cardiac events (MACEs) has recently been described (*6,7*). Quantitative data in these studies were based on ratios between ventricular myocardial uptake and various structures of the body rather than on SUV, and there is a need to define whether SUV-based quantitative SPECT/CT can yield a robust prognostic value in patients with suspected ATTR-CM. Recent studies suggest that SUV may be proportional to the degree of active deposition of amyloid fibrils rather than to the amyloid burden within the myocardium (*8–10*). Hence, SUV may be hypothesized to be a prognostic marker whose importance is higher if assessed in the early stages of the disease, wherein a higher rate of amyloid fibril deposition could lead to a more rapid progression of ATTR-CM, potentially associated with an adverse prognosis. The aim of the current study was to evaluate the association of quantitative [^{99m}Tc]Tc-DPD SPECT/CT at baseline with outcomes in ATTR-CM patients with preserved and reduced left ventricular ejection fraction (LVEF), representing patients at earlier and more progressive disease stages, respectively.

MATERIALS AND METHODS

Patient Selection

In this retrospective study, we included all consecutive ATTR-CM patients from the Bern Cardiac Amyloidosis Registry who had been referred to the Department of Nuclear Medicine and the Department of Cardiology at Bern University Hospital between October 2019 and December 2022. All patients underwent [^{99m}Tc]Tc-DPD SPECT/CT for suspected ATTR-CM. Clinical, laboratory, and echocardiographic data were recorded both at the time of [^{99m}Tc]Tc-DPD SPECT/CT (baseline) and during follow-up according to a prespecified schedule. Patients were divided into 2 groups: a group with preserved left ventricular function (LVEF ≥ 50% as assessed by planar transthoracic echocardiography) and a group with impaired function (LVEF < 50%). The design of the study was approved by the local ethics committee. The study was registered with ClinicalTrials.gov (NCT04776824) and conducted in accordance with the Declaration of Helsinki.

Received Oct. 24, 2023; revision accepted Apr. 3, 2024.

For correspondence or reprints, contact Federico Caobelli (federico.caobelli@insel.ch).

*Contributed equally to this work.

[^{99m}Tc]Tc-DPD Scintigraphy

The imaging protocol has been published previously (*2*). In short, 674.19 ± 10.25 MBq of [^{99m}Tc]Tc-DPD were injected intravenously. Three hours after injection, whole-body planar imaging and subsequent SPECT/CT of the thorax were performed on a hybrid SPECT/CT system (Symbia Intevo; Siemens Medical Solutions AG). Images were reconstructed to a 256 × 256 matrix with a dedicated iterative algorithm (xSPECT/CT Quant; Siemens Medical Solutions AG), and low-dose CT was performed for attenuation correction.

Two independent readers graded the images using the previously validated visual score by Perugini et al. (*4*). Myocardial uptake on SPECT/CT images (SUV_{max} and SUV_{peak}) was automatically calculated for each patient using commercial software (SyngoVia Package; Siemens Medical Solutions AG) by generating an isocontour volume of interest with a 40% threshold of peak activity around the myocardial wall.

Follow-up

The following MACEs were considered for the time-to-first-event analysis: all-cause death, hospitalization due to heart failure, sustained ventricular tachyarrhythmia (≥30 s), or the implantation of a cardioverter defibrillator. During follow-up, changes in transthyretin-stabilizing therapy and heart failure medications were also recorded.

Statistical Analysis

Clinical, image-derived, and laboratory data were compared in the whole cohort and in the subgroup of patients with confirmed ATTR-CM between patients with preserved and impaired left ventricular function by means of the Mann–Whitney *U* test for continuous variables and the Fisher exact test for nominal variables. The optimal threshold for SUV_{max} to predict a MACE was assessed by means of receiver-operating-characteristic curve analysis with calculation of the Youden index. Cox regression analysis was used to correlate various clinical and imaging-derived parameters with MACEs (i.e., body mass index [BMI], N-terminal pro–B-type natriuretic peptide [NT-proBNP], left ventricular end-diastolic diameter [LVEDD], Perugini score, SUV_{max} and SUV_{peak} as a continuous variable, and $SUV_{max} \geq 7$). If no MACEs were present in a group, the incident rate ratios were evaluated by calculating global χ^2 by means of Poisson logistic regression. All these parameters were tested in a univariate analysis; since only an SUV_{max} of 7 or higher showed significance, no multivariate analysis including nonsignificant variables was performed. The treatment with tafamidis was not entered into the Cox regression analysis. The rate of MACEs was evaluated by means of Kaplan–Meyer curves with the log-rank test. To that end, the interval between baseline SPECT and onset of the first MACE was considered. The analysis was performed with SPSS (version 28.0.1.1; IBM) for Microsoft Windows. *P* values of less than 0.05 were considered statistically significant.

RESULTS

Patient Population

In total, 144 patients underwent quantitative [^{99m}Tc]Tc-DPD SPECT/CT for suspected ATTR-CM (mean age ± SD, 81.5 ± 5.8 y; 127 men [88.2%]). Of these, 99 (68.8%) were diagnosed with ATTR-CM on the basis of clinical, laboratory, and radiologic data. The characteristics of the patient populations are summarized in Table 1 (whole cohort with suspected ATTR-CM) and Table 2 (patients diagnosed with ATTR-CM).

All patients with a Perugini score of at least 2 had a final diagnosis of ATTR-CM (65 with score 2, 27 with score 3). Among those with confirmed ATTR-CM, 7 had a Perugini score of 1. Of these, 2 patients had confirmed ATTR-CM due to evidence of increased extracellular volume (ECV) on subsequent cardiac MR (CMR); 4 patients, due to evidence of increased [^{99m}Tc]Tc-DPD uptake in the basal segments of the left ventriculum on SPECT images; and 1 patient, due to an SUV_{max} that was higher than the reference values reported in the literature (*2*).

Among patients diagnosed with ATTR-CM, 53 patients (53.5%) were started on transthyretin-stabilizing therapy (i.e., tafamidis, 61 mg administered once daily). In all patients with a Perugini score of 0, and in 2 patients with a Perugini score of 1, the diagnosis of ATTR-CM was rejected.

In the whole cohort ($n = 144$), patients with preserved LVEF had lower LVEDD and NT-proBNP levels than did subjects with impaired LVEF. Furthermore, they had a higher BMI and were on therapy more often with spironolactone and less often with sodium-glucose cotransporter 2 inhibitors and β-blockers (Table 1).

Similarly, among patients with confirmed ATTR-CM ($n = 99$), patients with preserved LVEF had a lower LVEDD than did patients with an LVEF of less than 50% but similar levels of NT-proBNP. They had a higher BMI and were under therapy more often with calcium channel antagonists and less often with sodium-glucose cotransporter 2 inhibitors and β-blockers.

Patients with an LVEF of at least 50% had a higher SUV_{max} and SUV_{peak} than did patients with an LVEF of less than 50%.

Follow-up

The median follow-up time was 21.9 ± 13.0 mo. A detailed flowchart with the main grouping is displayed in Figure 1. Of all patients, 98 presented with preserved LVEF (69 with ATTR-CM and 29 without), whereas 46 had impaired LVEF (30 with ATTR-CM and 16 without).

Considering the whole cohort, 44 MACEs occurred: 32 in patients with an LVEF of at least 50% (32.7%) and 12 in those with LVEF of less than 50% (26.1%, $P = 0.28$). Specifically, hospitalization for heart failure occurred in 17 patients with an LVEF of at least 50% (17.3%) and in 7 patients with an LVEF of less than 50% (15.2%, $P = 0.30$); sustained ventricular tachyarrhythmia occurred in 4 patients with an LVEF of at least 50% (4.1%) and in 1 patient with an LVEF of less than 50% (2.2%, $P = 0.62$); a cardioverter defibrillator was implanted in 5 patients with an LVEF of at least 50% (5.1%) and in 2 patients with an LVEF of less than 50% (4.4%, $P = 0.57$). Twenty-six patients eventually died (either as the first event or after another MACE): 16 patients with an LVEF of at least 50% (16.3%) and 10 patients with an LVEF of less than 50% (21.7%, $P = 0.29$).

In patients with ATTR-CM, 34 MACEs occurred: 25 in patients with an LVEF of at least 50% (25.3%) and 9 in those with an LVEF of less than 50% (9.1%, $P = 0.36$). Specifically, hospitalization for heart failure occurred in 16 patients with an LVEF of at least 50% (23.2%) and in 7 patients with an LVEF of less than 50% (23.3%, $P = 0.28$); sustained ventricular tachyarrhythmia occurred in 4 patients with an LVEF of at least 50% (5.8%) and in 1 patients with an LVEF of less than 50% (3.3%, $P = 0.60$); a cardioverter defibrillator was implanted in 4 patients with an LVEF of at least 50% (5.8%) and in 2 patients with an LVEF of less than 50% (6.6%, $P = 0.51$). Eighteen patients eventually died (either as the first event or after another MACE): 11 patients with an LVEF of at least 50% (15.9%) and 7 patients with an LVEF of less than 50% (23.3%, $P = 0.27$).

Summarizing, during follow-up, a total of 44 patients experienced a MACE (34 among patients with ATTR-CM [77.3%] and 10 in patients without [22.7%]).

TABLE 1
Clinical Characteristics of Whole Patient Sample

Characteristic	All patients with suspected ATTR-CM (*n* = 144)	Patients with preserved LVEF (≥50%, *n* = 98)	Patients with impaired LVEF (<50%, *n* = 46)	*P*
Clinical parameters				
BMI (kg/m^2)	26.4 ± 4.8	26.7 ± 4.4	25.1 ± 5.4	0.01*
NYHA functional class ≥ III	38 (26.4%)	24 (24.5%)	14 (30.4%)	0.29
Age (y)	81.5 ± 5.8	80.2 ± 8.2	79.7 ± 7.5	0.39
Male sex	127 (88.2%)	87 (88.8%)	40 (86.7%)	0.34
Laboratory parameters				
T-troponin (ng/L)	42 (37)	51.8 ± 39.5	60.0 ± 44.9	0.18
Median nT-proBNP (pg/mL)	2,294 (IQR, 3,368)	1,540.0 (IQR, 3,193.0)	2,925.0 (IQR, 2,452.0)	0.01*
Median creatinine-phosphokinase (IU/L)	88 (IQR, 73)	88.0 (IQR, 80.0)	104.4 (IQR, 67.0)	0.68
Echocardiographic parameters				
LVEDD (mm)	45.8 ± 7.0	44.7 ± 6.9	48.7 ± 6.3	0.01*
LVEF (%)	53.3 ± 10.8	58.8 ± 5.9	39.3 ± 7.2	<0.001*
Maximum wall thickness (mm)	15.9 ± 4.6	15.6 ± 3.1	16.5 ± 7.1	0.51
Left ventricular mass index (g/m^2)	138.13 ± 52.6	131.1 ± 41.0	156.9 ± 71.8	0.09
Scintigraphy				
Perugini score 0	43 (29.9%)	29 (29.6%)	14 (30.4%)	0.43
Perugini score 1	9 (6.3%)	6 (6.1%)	3 (6.5%)	0.60
Perugini score 2	65 (45.1%)	48 (49.0%)	17 (37.0%)	0.18
Perugini score 3	27 (18.8%)	16 (16.3%)	11 (23.9%)	0.19
SUV_{max}	9.3 ± 6.7	9.9 ± 7.0	7.9 ± 5.9	0.18
SUV_{peak}	8.7 ± 6.3	9.2 ± 6.6	7.3 ± 5.5	0.17
Therapy				
Ace inhibitors	36 (25.0%)	28 (28.6%)	8 (17.4%)	0.28
Angiotensin-II inhibitors	49 (34.0%)	36 (36.7%)	13 (28.3%)	0.51
Sacubitril/valsartan	3 (2.1%)	1 (1.0%)	2 (4.3%)	0.18
β-blockers	63 (43.8%)	36 (36.7%)	27 (58.7%)	<0.001*
Spironolactone	21 (14.6%)	11 (11.2%)	10 (2.2%)	0.03*
SGLT-2 inhibitors	19 (13.2%)	8 (8.2%)	11 (23.9%)	0.003*
Diuretics	86 (39.7%)	60 (61.2%)	26 (56.5%)	0.22
Calcium channels antagonists	32 (22.2%)	28 (28.6%)	4 (8.6%)	0.02*
Amiodaron	8 (5.6%)	5 (5.1%)	3 (6.5%)	0.38
Tafamidis	53 (36.8%)	38 (38.8%)	15 (32.6%)	0.30

*Statistically significant.

NYHA = New York Heart Association.

Qualitative data are number and percentage; continuous data are mean ± SD unless otherwise indicated. Therapies other than transthyretin stabilizer were recorded at baseline; therapy with tafamidis (if any) was started after final diagnosis was reached.

Predictive Value of SPECT

At receiver-operating-characteristic curve analysis, an SUV_{max} of 7 was the best threshold to predict a MACE in patients with preserved LVEF (sensitivity, 72%; specificity, 49%). In the whole cohort, an SUV_{max} of at least 7 was the only parameter among the abovementioned clinical and imaging-derived ones that was associated with MACEs, but the association was present only in patients with an LVEF of at least 50% (hazard ratio, 2.875; $P = 0.015$). Conversely, SUV_{max} and SUV_{peak} as a continuous variable, LVEDD, BMI, and NT-proBNP did not have an association with MACEs (Table 3). When patients with confirmed ATTR-CM were considered, an SUV_{max} of at least 7 was again associated with MACEs only in patients with an LVEF of at least 50% ($\chi^2 = 6.892$, $P = 0.009$). SUV_{max} and SUV_{peak} as a continuous variable, LVEDD, BMI, and NT-proBNP did not predict MACEs (Table 4).

At Kaplan–Meyer analysis, an SUV_{max} of at least 7 identified among patients with an LVEF of at least 50% those at a shorter MACE-free survival, both in the whole cohort ($P = 0.01$, Fig. 2A)

TABLE 2
Clinical Characteristics of Patients with Confirmed ATTR-CM

Characteristic	Patients with confirmed ATTR-CM (n = 99)	Patients with preserved LVEF (≥50%, n = 69)	Patients with impaired LVEF (<50%, n = 30)	P
Clinical parameters				
BMI (kg/m^2)	26.1 ± 4.6	26.3 ± 4.0	25.7 ± 5.8	0.04*
NYHA functional class ≥ III	27 (27.3%)	17 (24.6%)	10 (33.3%)	0.26
Age (y)	81.5 ± 5.9	81.5 ± 5.8	81.4 ± 6.3	0.74
Male sex	91 (91.9%)	64 (92.8%)	27 (90.0%)	0.29
Laboratory parameters				
T-troponin (ng/L)	57.8 ± 41.9	54.2 ± 39.7	67.0 ± 46.9	0.08
Median nT-proBNP (pg/mL)	2533.0 (IQR, 3301.0)	1564.0 (IQR, 3230.0)	2914.2 (IQR, 2364.0)	0.09
Median creatinine-phosphokinase (IU/L)	88.0 (IQR, 75.0)	88.0 (IQR, 89.0)	86.5 (IQR, 61.0)	0.43
Echocardiographic parameters				
LVEDD (mm)	45.2 ± 7.1	43.8 ± 6.8	48.9 ± 6.7	0.02*
LVEF (%)	53.4 ± 10.2	58.5 ± 6.0	40.1 ± 5.6	<0.001*
Maximum wall thickness (mm)	16.1 ± 3.1	16.2 ± 3.1	16.0 ± 3.0	0.73
Left ventricular mass index (g/m^2)	139.1 ± 41.9	133.0 ± 42.3	154.9 ± 37.2	0.05
Scintigraphy				
Perugini score 0	0 (0%)	0 (0%)	0 (0%)	—
Perugini score 1	7 (7.1%)	5 (7.2%)	2 (6.7%)	0.64
Perugini score 2	65 (65.7%)	48 (69.6%)	17 (56.7%)	0.16
Perugini score 3	27 (27.3%)	16 (23.2%)	11 (36.6%)	0.13
SUV$_{max}$	12.6 ± 5.7	13.3 ± 5.4	10.8 ± 4.8	0.04*
SUV$_{peak}$	11.8 ± 5.0	12.5 ± 5.1	10.1 ± 4.5	0.03*
Therapy				
Ace inhibitors	26 (26.3%)	21 (30.4%)	5 (16.7%)	0.16
Angiotensin-II inhibitors	34 (34.3%)	23 (33.3%)	11 (36.7%)	0.37
Sacubitril/valsartan	2 (2.2%)	1 (1.4%)	1 (3.3%)	0.50
β-blockers	43 (43.4%)	24 (34.8%)	19 (63.3%)	0.003*
Spironolactone	18 (18.2%)	11 (15.9%)	7 (23.3%)	0.22
SGLT-2 inhibitors	15 (15.2%)	7 (10.1%)	8 (26.7%)	0.03*
Diuretics	67 (67.7%)	47 (68.1%)	20 (66.7%)	0.47
Calcium channels antagonists	23 (23.2%)	20 (29.0%)	3 (10.0%)	0.04*
Amiodaron	5 (5.5%)	4 (5.8%)	1 (3.3%)	0.55
Tafamidis	53 (53.5%)	38 (55.1%)	15 (50.0%)	0.40

*Statistically significant.

NYHA = New York Heart Association.

Qualitative data are number and percentage; continuous data are mean ± SD unless otherwise indicated. Therapies other than transthyretin stabilizer were recorded at baseline; therapy with tafamidis (if any) was started after final diagnosis was reached.

and in those with confirmed ATTR-CM (P = 0.02, Fig. 3A). The same held true after subdividing the latter on the basis of transthyretin-stabilizing therapy (n = 46, P = 0.01, Supplemental Fig. 1; supplemental materials are available at http://jnm.snmjournals.org).

Conversely, also at Kaplan–Meyer analysis, an SUV$_{max}$ of at least 7 failed to predict MACE-free survival in patients with an LVEF of less than 50%, either in the whole cohort (P = 0.27, Fig. 2B) or in the those with confirmed ATTR-CM (P = 0.19, Fig. 3B).

A tertile analysis based on SUV$_{max}$ in patients with ATTR-CM (first tertile, <9.76; second tertile, ≥9.76% and <15.95; third tertile, ≥15.95) showed a clear tendency toward worse outcomes for patients with higher SUV$_{max}$ if LVEF was at least 50% (P = 0.06), whereas no differences were shown in patients with an LVEF of less than 50% (P = 0.46, Supplemental Fig. 2). After patients with a Perugini score of 1 were excluded, an SUV$_{max}$ of at least 7 was still predictive of a worse outcome in patients with an LVEF of at least 50%, both in the whole population

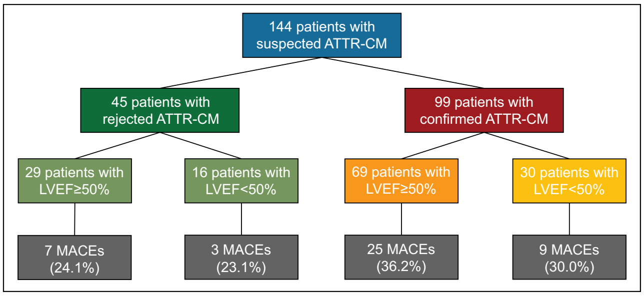

FIGURE 1. Study flowchart.

(P = 0.037) and in the subgroup of patients with confirmed ATTR-CM (P = 0.039, Supplemental Fig. 3). Again, no significance was found in patients with impaired LVEF (P = 0.401 and 0.291, respectively).

Visual analysis failed to yield prognostic value: Perugini score showed no association with the onset of MACEs in patients with and without preserved LVEF, either in the whole cohort (Table 3) or in patients with confirmed ATTR-CM (Table 4).

DISCUSSION

We demonstrated for the first time, to our knowledge, the value of quantitative [^{99m}Tc]Tc-DPD SPECT/CT in the prediction of MACEs in patients with suspected and, most importantly, confirmed ATTR-CM and preserved LVEF, representing an early disease stage. This association was not found in patients with reduced LVEF, representing later disease stages. Although previous work (*6,7*) used semiquantitative, normalized ratios, we here report a robust predictive value for myocardial SUV. This aspect provides novelty in that it supports the concept that the activity within the heart itself (and not the relative activity compared with bone or soft tissue) reflects a pathophysiologic mechanism linked to disease progression.

In this regard, the exact significance of different degrees of [^{99m}Tc]Tc-DPD uptake within the myocardium deserves a detailed discussion.

Perugini visual score failed to show prognostic value in patients with ATTR-CM (*5*). To account for the lack of prognostic value, it was hypothesized that visual interpretation does not accurately reflect the amount of amyloid burden in the myocardium. This latter would be predictive of a different outcome, but Perugini score may indicate only the presence of amyloid deposition, without information on the amyloid burden (*2*). Although quantification with SPECT/CT was expected to be more accurate in this regard, previous studies on patients at different stages of ATTR-CM showed only limited prognostic value and used normalized values only, thus raising doubts on the linear correlation between [^{99m}Tc]Tc-DPD uptake and amyloid burden (*6,7*). Conversely, studies capitalizing on CMR imaging showed that increased ECV correlates well with amyloid burden within the myocardium and allows for risk stratification (*11,12*). Hence, there is a clear discrepancy between the prognostic value of quantitative SPECT and CMR, which is probably related to the different target.

Recently published papers (*8–10*) show that myocardial [^{99m}Tc]Tc-DPD uptake decreases after therapy with tafamidis. If we assumed that the uptake is proportional to the amyloid burden, these data would be counterintuitive, as tafamidis acts essentially by preventing further deposition of amyloid fibrils rather than degrading them. Hence, it is conceivable that [^{99m}Tc]Tc-DPD uptake is proportional not to amyloid burden but rather to the degree of active deposition of amyloid fibrils within the myocardium, which can be lowered by transthyretin-targeting therapies. Of note, this concept is consistent with what is observed in other fields of cardiovascular imaging, wherein nuclear medicine techniques are preferred modalities to distinguish between the active phase and the chronic phase of the disease (*13*). The discrepancy between SPECT and CMR is further evidenced by a recent CMR study in which stabilization of ECV after treatment with tafamidis was reported, which may indicate that ECV is proportional to amyloid burden and not to its active deposition (*14*).

Taken together, these observations suggest that in an early stage of ATTR-CM, the amyloid burden may not be high but deposition of amyloid fibrils can already be rapid. In this setting, it is conceivable that assessment of the activity of such deposition by evaluating [^{99m}Tc]Tc-DPD can yield prognostic value, as it would be an indicator of the more or less rapid evolution of the disease (*15*). For that reason, we investigated for the first time, to our knowledge, specifically patients with preserved LVEF, which would indicate an earlier stage of ATTR-CM.

TABLE 3

Hazard Ratio of Relevant Clinical and Imaging-Derived Parameters for Prediction of MACEs in Whole Patient Sample (n = 144)

	All patients with suspected ATTR-CM (n = 144)			Patients with preserved LVEF (≥50%, n = 98)			Patients with impaired LVEF (<50%, n = 46)		
Parameter	HR	95% CI	P	HR	95% CI	P	HR	95% CI	P
BMI	0.980	0.927–1.037	0.489	0.982	0.917–1.051	0.594	0.962	0.855–1.083	0.521
NT-proBNP	1.0	1.0–1.0	0.127	1.0	1.0–1.0	0.168	1.0	1.0–1.0	0.168
LVEDD	0.987	0.709–2.357	0.590	0.983	0.931–1.038	0.540	0.998	0.903–1.103	0.967
Perugini score	1.183	0.896–1.561	0.236	1.306	0.934–1.825	0.118	0.916	0.541–1.552	0.745
SUV_{max} (continuous)	1.014	0.970–1.059	0.540	1.028	0.980–1.079	0.258	0.923	0.820–1.039	0.186
SUV_{peak} (continuous)	1.015	0.969–1.063	0.519	1.031	0.980–1.085	0.244	0.918	0.810–1.042	0.185
$SUV_{max} \geq 7$	1.752	0.925–3.317	0.090	2.875	1.230–6.710	0.015*	0.525	0.164–1.687	0.280

---

*Statistically significant.

TABLE 4

Hazard Ratio of Relevant Clinical and Imaging-Derived Parameters for Prediction of MACEs in Patients with Confirmed ATTR-CM (n = 99)

	All patients with suspected ATTR-CM (n = 99)			Patients with preserved LVEF (≥50%, n = 69)			Patients with impaired LVEF (<50%, n = 30)		
Parameter	HR	95% CI	P	HR	95% CI	P	HR	95% CI	P
BMI	1.006	0.940–1.076	0.867	0.999	0.916–1.090	0.984	1.004	0.896–1.126	0.939
NT-proBNP	1.0	1.0–1.0	0.059	1.0	1.0–1.0	0.240	1.0	1.0–1.0	0.612
LVEDD	0.975	0.929–1.024	0.320	0.970	0.914–1.030	0.323	0.988	0.890– 1.097	0.830
Perugini score	1.115	0.645–1.929	0.696	1.358	0.684–2.697	0.358	0.825	0.336–2.028	0.675
SUV_{max} (continuous)	0.996	0.939–1.059	0.893	1.009	0.941–1.083	0.800	0.877	0.741–1.038	0.127
SUV_{peak} (continuous)	0.997	0.934–1.064	0.928	1.012	0.939–1.070	0.760	0.868	0.725–1.040	0.125
$SUV_{max} \geq 7$	1.939	0.682–5.510	0.214	6.892*	—	0.009†	0.420	0.112–1.574	0.198

*Given lack of events in patients with $SUV_{max} < 7$ in this group, this value represents global Wald χ^2, calculated with log-Poisson regression analysis.

†Statistically significant.

HR = hazard ratio.

Consistent with previous reports, our study showed that visual Perugini scoring is not predictive of MACEs in ATTR-CM patients. Yet, SUV-based quantitative SPECT showed prognostic value, and in this regard, our study provided novelty regarding another 2 major aspects.

First, we demonstrated that patients with preserved or impaired LVEF have a similar rate of MACEs, but differences become significant if patients are further stratified according to their [^{99m}Tc]Tc-DPD uptake. This provides more evidence that the degree of active deposition of the amyloid fibrils may be the major determinant of the rate of MACEs in patients with ATTR-CM and supports the concept that quantitative [^{99m}Tc]Tc-DPD SPECT/CT allows for an in vivo assessment of this activity.

Second, the same prognostic value pertained also to patients with suspected ATTR-CM. To date, the clinical diagnosis of ATTR-CM relies on a combination of clinical, echocardiographic, and radiologic findings, and DPD scintigraphy represents a cornerstone in confirming or rejecting the diagnosis (*16*). In our population, some of the patients with suspected ATTR-CM had clinical and echocardiographic signs of the disease, but the diagnosis was eventually rejected because [^{99m}Tc]Tc-DPD SPECT had negative findings. In this regard, how to interpret a Perugini score of 1 (i.e., detectable myocardial uptake below bone activity) is contentious, and a score of 1 often does not allow for a definite diagnosis. But a proportion of our patients with confirmed ATTR-CM (n = 7) had detectable cardiac [^{99m}Tc]Tc-DPD uptake visually below bone activity. Considering the robust prognostic value in our whole cohort and in the cohort with patients diagnosed with ATTR-CM, there may be a rationale to consider patients with a Perugini score of 1 as patients with ATTR-CM in a very early stage or with a weak deposition of fibrils, which may, however, accelerate at a certain time point. This aspect has an evident

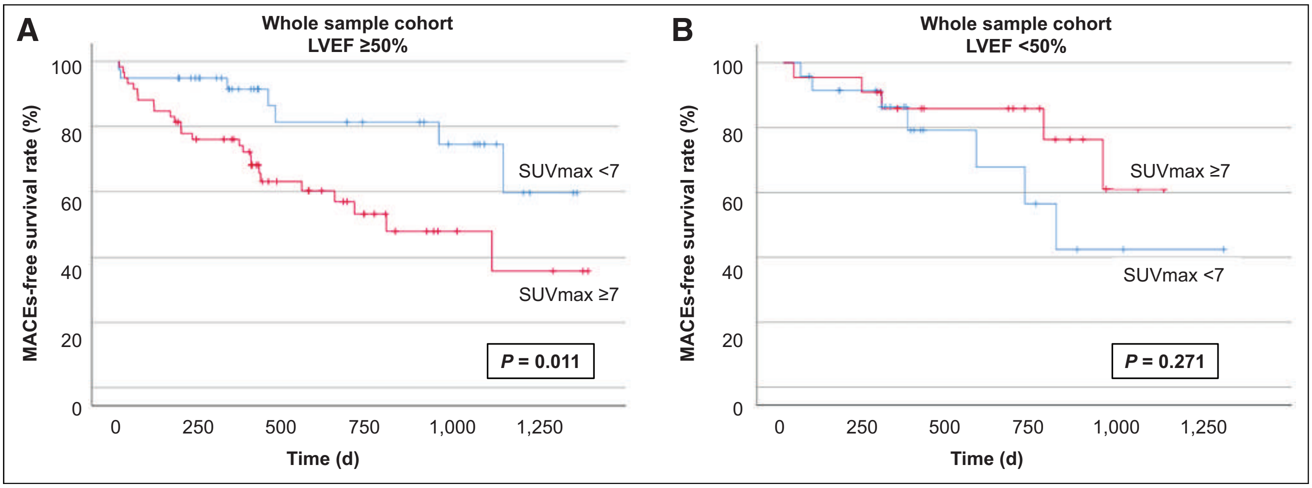

FIGURE 2. Kaplan–Meyer curves highlighting predictive role of myocardial $SUV_{max} \geq 7$ in whole cohort (n = 144). (A) In patients with preserved LVEF, $SUV_{max} \geq 7$ as separator predicted higher rate of MACEs. (B) Conversely, no predictive role was seen in patients with already-impaired LVEF.

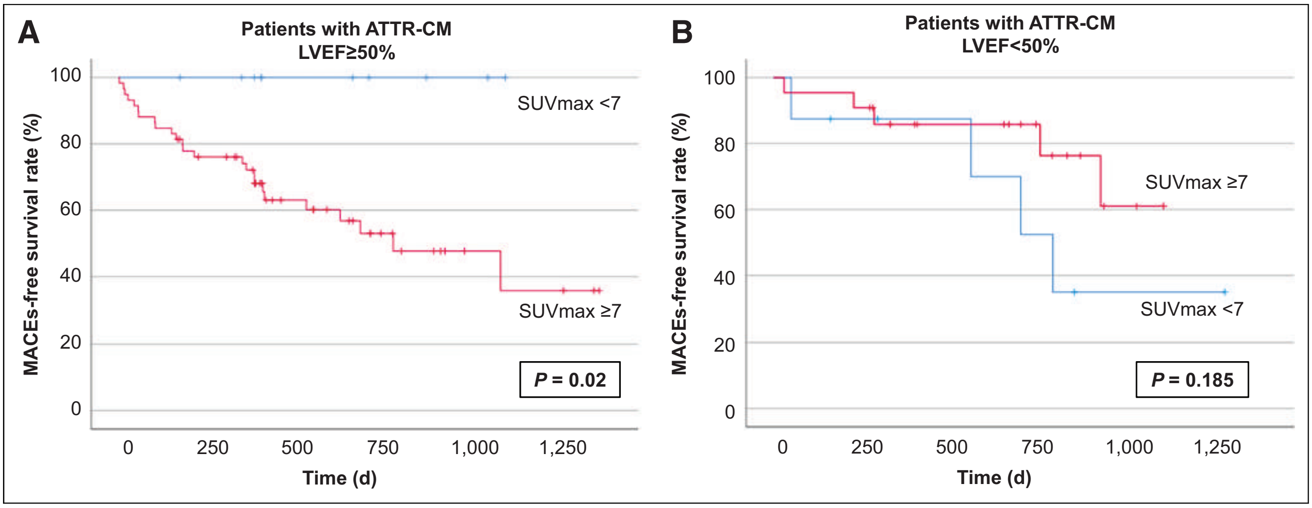

FIGURE 3. Kaplan–Meyer curves highlighting predictive role of myocardial $\text{SUV}_{\text{max}} \geq 7$ in patients with confirmed ATTR-CM ($n = 99$). Similarly to what was observed for whole cohort, $\text{SUV}_{\text{max}} \geq 7$ predicted higher rate of MACEs in patients with preserved LVEF (A) but not in patients with already-impaired LVEF (B).

impact on the management of patients with suspected ATTR-CM and may suggest the need for further SPECT imaging at shorter intervals, which will need to be defined.

This study had some limitations. Its retrospective nature prevented us from recruiting patients with standardized therapy. However, the patient cohort was large enough to allow for a subanalysis in patients not under transthyretin-stabilizing therapy. Second, this was a registry study and not a specific powered study. The fact that a clearly worse outcome was present in patients with high myocardial uptake and preserved LVEF strengthens the confidence with which [^{99m}Tc]Tc-DPD uptake can be considered an indicator of active deposition of amyloid fibrils—the more active the deposition, the more rapid the development of the disease—whereas the impact of the rate of amyloid fibril deposition is not expected to play a major role if a large amyloid burden is already present. Although further and larger studies are warranted to validate this concept, the data of our study constitute a fundamental basis for further research. Third, we used an already-validated method for quantitation relying on a proprietary hardware–software system; therefore, our results may not fit the needs of clinical centers using different quantification software, and separate validations are needed. Nevertheless, the fact that a clear predictive role was demonstrated for MACEs in patients with preserved LVEF supports the applicability of the quantitative approach in clinical practice for risk stratification. In this regard, it may be suggested that patients with an SUV_{max} of at least 7 on baseline SPECT/CT be considered for tafamidis therapy. Fourth, the choice of LVEF as a marker of a more advanced stage of ATTR-CM does not reflect the current recommendations, which suggest the use of NT-proBNP and glomerular filtration rate (eGFR) (*17*). Also, other echo-derived parameters such as global longitudinal strain have been suggested as indicative of a more advanced stage of the disease (*11*). Although this choice reflects the retrospective nature of the present study (data on NT-proBNP, eGFR, and global longitudinal strain were not all available in all patients), there still is a rationale to consider LVEF as a marker of advanced disease. A paper by Knight et al. (*11*) showed an inverse correlation between LVEF and ECV, with impaired left ventricular function in patients with higher ECV. Hence, it is conceivable that patients with impaired LVEF in our cohort were also those in a more advanced stage. Further prospective studies are warranted to support our data.

Finally, we observed that patients with impaired LVEF had a higher LVEDD, suggesting some degree of dilation, which can be seen at the end stage of the disease but is not typical. In our cohort, we could not rule out that a subset of those patients with an LVEF of less than 50% had a concomitant pathologic condition causing left ventricular dilation. The presence of a possible competing risk due an undiagnosed condition may be responsible for the lack of prognostic value of [^{99m}Tc]Tc-DPD uptake in these patients. These observations may be a starting point for further studies featuring patients with ATTR-CM and impaired LVEF.

CONCLUSION

In patients with suspected or confirmed ATTR-CM and preserved LVEF, representing an early disease stage, a myocardial SUV of at least 7 is a predictive marker for MACEs. Quantitative [^{99m}Tc]Tc-DPD SPECT should be considered for improved early-stage risk stratification of patients with ATTR-CM.

DISCLOSURE

This study (NCT04776824) was supported by Pfizer and the GAMBIT Foundation and was based on the database of the Bern Cardiac Amyloidosis Registry (B-CARE). Federico Caobelli is supported by a research grant by Siemens Healthineers and receives speaker honoraria from Bracco AG and Pfizer AG for matters not related to the present paper. Christoph Gräni receives funding from the Swiss National Science Foundation, InnoSuisse, the CAIM Foundation, and the Novartis Biomedical Research Foundation, outside the submitted work. Axel Rominger has received research support and speaker honoraria from Siemens. Stephan Dobner reports a research grant for B-CARE (NCT04776824) on behalf of the institution (Inselspital Bern) from Pfizer and travel grants and speaker fees from Alnylam and Boehringer Ingelheim and Pfizer. No other potential conflict of interest relevant to this article was reported.

KEY POINTS

QUESTION: Is quantitative [^{99m}Tc]Tc-DPD SPECT/CT suitable to identify patients at increased risk of cardiac events among those in an earlier stage of ATTR-CM?

PERTINENT FINDINGS: In a cohort study including 144 patients (99 with ATTR-CM), an [^{99m}Tc]Tc-DPD SUV_{max} of 7 or higher identified patients with preserved left ventricular function at increased risk of cardiac events. Conversely, patients with impaired function could not be risk-stratified by SPECT/CT, thus highlighting the fact that the latter are at a later stage of disease, wherein the impact of a more active deposition of amyloid fibrils is not expected to play a major role in regard to the outcome.

IMPLICATIONS FOR PATIENT CARE: Identifying patients with still-preserved left ventricular function at a higher risk of disease progression may drive the decision to choose a more aggressive therapy, such as transthyretin stabilizers.

REFERENCES

1. Gillmore JD, Maurer MS, Falk RH, et al. Nonbiopsy diagnosis of cardiac transthyretin amyloidosis. *Circulation.* 2016;133:2404–2412.
2. Caobelli F, Braun M, Haaf P, Wild D, Zellweger MJ. Quantitative ^{99m}Tc-DPD SPECT/CT in patients with suspected ATTR cardiac amyloidosis: feasibility and correlation with visual scores. *J Nucl Cardiol.* 2020;27:1456–1463.
3. Ahluwalia N, Roshankar G, Draycott L, et al. Diagnostic accuracy of bone scintigraphy imaging for transthyretin cardiac amyloidosis: systematic review and meta-analysis. *J Nucl Cardiol.* 2023;30:2464–2476.
4. Perugini E, Guidalotti PL, Salvi F, et al. Noninvasive etiologic diagnosis of cardiac amyloidosis using ^{99m}Tc-3,3-diphosphono-1,2-propanodicarboxylic scintigraphy. *J Am Coll Cardiol.* 2005;46:1076–1084.
5. Hutt DF, Fontana M, Burniston M, et al. Prognostic utility of the Perugini grading of [^{99m}Tc]Tc-DPD scintigraphy in transthyretin (ATTR) amyloidosis and its relationship with skeletal muscle and soft tissue amyloid. *Eur Heart J Cardiovasc Imaging.* 2017;18:1344–1350.
6. Ogasawara K, Shiraishi S, Tsuda N, et al. Usefulness of quantitative ^{99m}Tc-pyrophosphate SPECT/CT for predicting the prognosis of patients with wild-type transthyretin cardiac amyloidosis. *Jpn J Radiol.* 2022;40:508–517.
7. Miller RJH, Cadet S, Mah D, et al. Diagnostic and prognostic value of technetium-99m pyrophosphate uptake quantitation for transthyretin cardiac amyloidosis. *J Nucl Cardiol.* 2021;28:1835–1845.
8. Rettl R, Calabretta R, Duca F, et al. Reduction in [^{99m}Tc]Tc-DPD myocardial uptake with therapy of ATTR cardiomyopathy. *Amyloid.* 2024;31:42–51.
9. Rettl R, Wollenweber T, Duca F, et al. Monitoring tafamidis treatment with quantitative SPECT/CT in transthyretin amyloid cardiomyopathy. *Eur Heart J Cardiovasc Imaging.* 2023;24:1019–1030.
10. Papathanasiou M, Kessler L, Bengel FM, et al. Regression of myocardial [^{99m}Tc]Tc-DPD uptake after tafamidis treatment of cardiac transthyretin amyloidosis. *J Nucl Med.* 2023;64:1083–1086.
11. Knight DS, Zumbo G, Barcella W, et al. Cardiac structural and functional consequences of amyloid deposition by cardiac magnetic resonance and echocardiography and their prognostic roles. *JACC Cardiovasc Imaging.* 2019;12:823–833.
12. Haaf P, Garg P, Messroghli DR, et al. Cardiac T1 mapping and extracellular volume (ECV) in clinical practice: a comprehensive review. *J Cardiovasc Magn Reson.* 2016;18:89.
13. Wollenweber T, Roentgen P, Schäfer A, et al. Characterizing the inflammatory tissue response to acute myocardial infarction by clinical multimodality noninvasive imaging. *Circ Cardiovasc Imaging.* 2014;7:811–818.
14. Rettl R, Mann C, Duca F, et al. Tafamidis treatment delays structural and functional changes of the left ventricle in patients with transthyretin amyloid cardiomyopathy. *Eur Heart J Cardiovasc Imaging.* 2022;23:767–780.
15. Caobelli F. Recent evidence on cardiac [^{99m}Tc]Tc-DPD uptake after therapy with tafamidis may reveal the road to an ultra-early diagnosis in patients with ATTR amyloidosis [letter]. *J Nucl Med.* 2024;65:329.
16. Haaf P, Burger IA, Zellweger MJ, Garg P, Popescu CE. Cardiac amyloidosis. In: Caobelli F, ed. *Imaging of Inflammation and Infection in Cardiovascular Diseases.* Springer; 2021:37–69.
17. Gillmore JD, Damy T, Fontana M, et al. A new staging system for cardiac transthyretin amyloidosis. *Eur Heart J.* 2018;39:2799–2806.

Improved Tau PET SUVR Quantification in 4-Repeat Tau Phenotypes with [^{18}F]PI-2620

Gérard N. Bischof[1,2], Matthias Brendel[3–5], Henryk Barthel[6], Hendrik Theis[1,7], Michael Barbe[7], Peter Bartenstein[4,5], Joseph Claasen[6], Adrian Danek[8], Günter Höglinger[3,4,8], Johannes Levin[3,4,8], Ken Marek[9,10], Bernd Neumaier[11,12], Carla Palleis[3,4,8], Marianne Patt[6], Michael Rullmann[13], Dorothee Saur[6], Matthias L. Schroeter[13], John Seibyl[9,10], Mengmeng Song[5], Andrew Stephens[14], Osama Sabri[6], Alexander Drzezga[1,2,15], and Thilo van Eimeren[1,7]
for the German Imaging Initiative for Tauopathies

[1]Department of Nuclear Medicine, University Hospital Cologne, Cologne, Germany; [2]Molecular Organization of the Brain, Institute for Neuroscience and Medicine, Jülich, Germany; [3]German Center for Neurodegenerative Diseases, Munich, Germany; [4]Munich Cluster for Systems Neurology, Munich, Germany; [5]Department of Nuclear Medicine, University Hospital of Munich, LMU Munich, Munich, Germany; [6]Department of Nuclear Medicine, University Hospital of Leipzig, Leipzig, Germany; [7]Department of Neurology, Faculty of Medicine and University Hospital Cologne, University of Cologne, Cologne, Germany; [8]Department of Neurology, University Hospital of Munich, LMU Munich, Munich, Germany; [9]InviCRO, LLC, Boston, Massachusetts; [10]Molecular Neuroimaging, a division of inviCRO, New Haven, Connecticut; [11]Institute of Radiochemistry and Experimental Molecular Imaging, University of Cologne, Cologne, Germany; [12]Institute of Neuroscience and Medicine, Nuclear Chemistry, Research Center Jülich, Jülich, Germany; [13]Clinic for Cognitive Neurology, University Hospital of Leipzig, and Max Planck Institute for Human Cognitive and Brain Sciences, Leipzig, Germany; [14]Life Molecular Imaging GmbH, Berlin, Germany; and [15]German Center for Neurodegenerative Diseases, Bonn/Cologne, Germany

We used a new data-driven methodology to identify a set of reference regions that enhanced the quantification of the SUV ratio of the second-generation tau tracer 2-(2-([^{18}F]fluoro)pyridin-4-yl)-9H-pyrrolo[2,3-b:4,5-c′]dipyridine ([^{18}F]PI-2620) in a group of patients clinically diagnosed with 4-repeat tauopathy, specifically progressive supranuclear palsy or cortical basal syndrome. The study found that SUV ratios calculated using the identified reference regions (i.e., fusiform gyrus and crus-cerebellum) were significantly associated with symptom severity and disease duration. This establishes, for the first time to our knowledge, the suitability of [^{18}F]PI-2620 for tracking disease progression in this 4-repeat disease population. This is an important step toward increased clinical utility, such as patient stratification and monitoring in disease-modifying treatment trials. Additionally, the applied methodology successfully optimized reference regions for automated detection of brain imaging tracers. This approach may also hold value for other brain imaging tracers.

Key Words: molecular imaging; neurology; PET; 4R; clinical severity; tau PET

J Nucl Med 2024; 65:952–955
DOI: 10.2967/jnumed.123.265930

PET imaging with 2-(2-([^{18}F]fluoro)pyridin-4-yl)-9H-pyrrolo[2,3-b:4,5-c′]dipyridine ([^{18}F]PI-2620) has demonstrated the ability to detect tau pathology in patients diagnosed with progressive supranuclear palsy (PSP) (*1*) and corticobasal syndrome (*2*,*3*). This holds potential for refining diagnostic criteria for 4-repeat (4R) tau isoforms and addressing diagnostic challenges associated with overlapping symptoms in neurodegenerative diseases such as frontotemporal dementia and Parkinson disease (*4*). Although [^{18}F]PI-2620 meets certain criteria for an ideal biomarker, such as positivity in the symptomatic phase and specificity for pathology variants, its binding affinity and relationship with 4R tau pathology have shown some discrepancies (*4*,*5*).

Previous attempts to establish a correlation between [^{18}F]PI-2620 binding potentials and disease progression or severity have been inconclusive. A potential source of variance in SUV ratio (SUVR) sensitivity is the choice of reference region. The use of the cerebellar cortex as a reference region, common in Alzheimer disease studies, is less ideal in 4R phenotypes because of known on-target binding in the dentate nucleus (*6*,*7*). To address this issue, we used a data-driven approach akin to established count normalization procedures. This involved identifying regions in PSP patients devoid of pathology for effective count normalization (*8*). Criteria for region suitability included absence of on-target binding, plausibility (e.g., bilateral), lack of on-target binding in early disease histopathologic studies, and correlation of SUVRs with disease severity or duration. This approach aims to enhance the sensitivity of SUVR measurements by selecting reference regions that better represent areas free of pathology in PSP patients. By refining the reference region choice, we anticipate improved accuracy in assessing the relationship between [^{18}F]PI-2620 binding potentials and disease measures. This strategy contributes to the ongoing efforts to establish reliable biomarkers for neurodegenerative diseases, particularly those involving 4R tau isoforms.

MATERIALS AND METHODS

In this study, 43 patients with suspected 4R tauopathies (PSP or corticobasal syndrome) and 14 healthy controls were enrolled from 4 nuclear medicine clinics in Germany and the United States. Diagnosis

---

Received Oct. 17, 2023; revision accepted Feb. 20, 2024.

For correspondence or reprints, contact Gérard Nisal Bischof (gerard.bischof@uk-koeln.de).

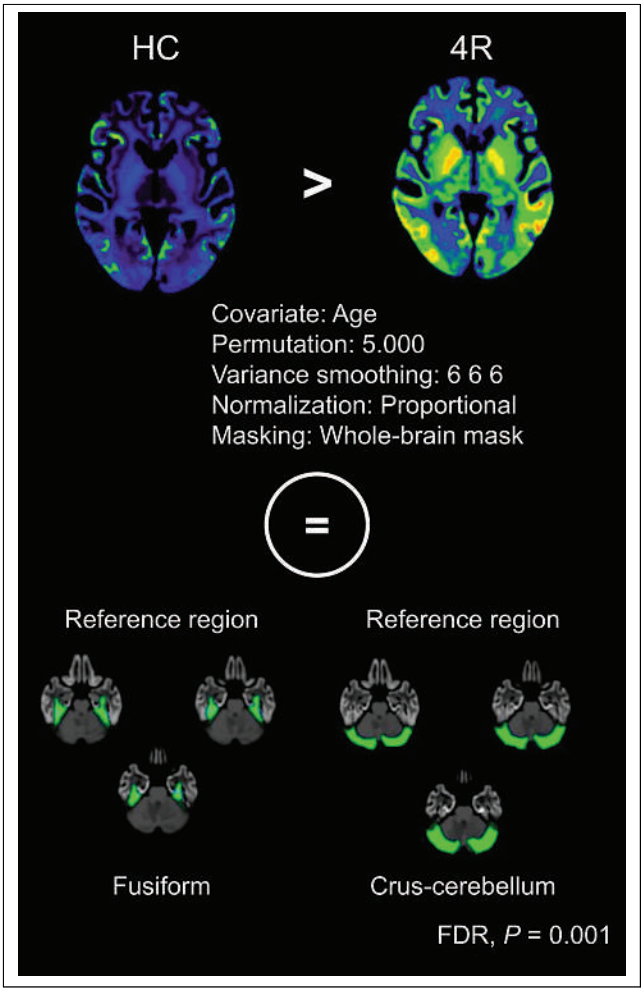

FIGURE 1. Methodologic approach of SnPM comparing healthy controls (HC) vs. patients with suspected 4R tauopathy. This statistical approach allowed us to identify reference regions void of on-target binding in patient population. Interestingly, we identified fusiform gyrus and crus-cerebellum to show nonspecific binding with using false-discovery rate of $P = 0.01$.

for PSP and corticobasal syndrome followed established criteria (*9*,*10*). All participants underwent a T1-weighted 3-dimensional MRI sequence (1 × 1 × 1 mm; 256 slices) and dynamic PET imaging (0–90 min) of [^{18}F]PI-2620 PSP severity (PSP rating scale), and disease duration data were available for most patients. Ethical approval was obtained from institutional committees, and participants provided written informed consent before the PET scans.

Participants in the healthy control cohort were amyloid-negative (based on cerebrospinal fluid or PET information) and were cognitively normal (as assessed by the Mini–Mental State Examination). Further details on the cohort have been published previously (*3*,*4*). Dynamic PET images (0–60 min) of [^{18}F]PI-2620 were realigned, the 30- to 60-min frames were averaged, and the resulting SUV images were coregistered to the individual MR images. PET images were normalized and partial-volume–corrected using the geometric transfer method (*11*). Partial-volume–corrected PET images were submitted to the statistical nonparametric mapping toolbox (SnPM (*12*)) implemented in SPM to identify regions in the patient population clearly void of pathology and therefore most effective for count normalization. SnPM was chosen because of the relatively lower degrees of freedom in the healthy control cohort and to capitalize on the individual patient data and the strong data-driven nature of our approach. Nonparametric permutation was set to 5,000 iterations, with a variance smoothing of 6 mm^3. Age served as a covariable, and a whole-brain inclusion mask was applied. The false-discovery rate was set at a P value of 0.01 (Fig. 1), and resulting clusters were regionally labeled on the basis of the automated anatomic atlas. In the patient cohort, automated anatomic atlas regions were used as reference regions, and SUVRs were extracted from target regions shown to accumulate tau pathology in 4R phenotypes (*1*,*3*). To evaluate the sensitivity of the data-driven reference regions, we performed partial correlation analyses of SUVRs in target regions, with the PSP rating scale and disease duration corrected for age ($R_{(\text{age})}$).

RESULTS

Demographic characteristics of the 43 patients and 14 healthy controls are summarized in Table 1. The statistical nonparametric mapping approach revealed differences, with elevated nonspecific binding bilaterally in the fusiform gyrus and crus-cerebellum, when comparing healthy controls versus 4R patients (Fig. 1). These regions were used as reference regions (separately and in combination), and SUVRs were computed. The partial correlation analysis (Figs. 2 and 3) using SUVRs based on the fusiform gyrus reference region revealed a significant association between disease severity and accumulating tau pathology in the globus pallidus externus ($R_{(\text{age})} = 0.34$, $P = 0.02$) and internus ($R_{(\text{age})} = 0.36$, $P = 0.02$). Disease duration was significantly associated with tau pathology in the frontal cortex ($R_{(\text{age})} = 0.39$, $P = 0.01$). For the

TABLE 1
Patient and Control Demographics

			4R phenotype	
Demographic	Control	4R	PSP	Corticobasal syndrome
n	14	43	31	12
Age (y)	64.38 (10.36)	70.6 (7.9)	70.8 (7.7)	69.6 (8.4)
Mini–Mental State Examination	29.07 (1.14)	NA	NA	NA
Montreal cognitive assessment	NA	22.3 (5.0)	22.9 (4.4)	20.4 (6.1)
PSP rating scale	NA	26.03 (10.0)	27.1 (10.5)	22.7 (7.6)
Disease duration (mo)	NA	36.48 (29.2)	37.1 (32.1)	34.5 (17.9)

NA= not applicable.
Data are mean followed by SD in parentheses.

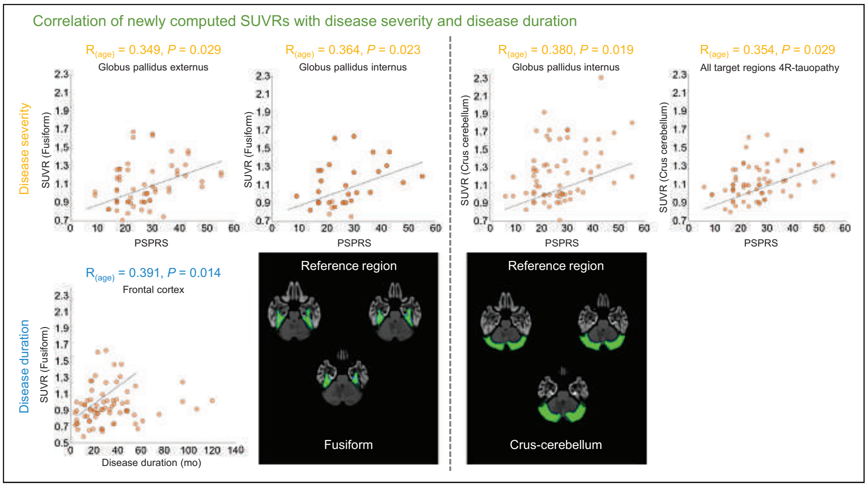

FIGURE 2. Significant partial correlations of newly computed SUVRs, using fusiform or crus-cerebellum as reference region, with disease severity (PSP rating scale [PSPRS]; upper panels) or disease duration (in months; lower panels). Automated anatomic atlas reference regions are overlayed on standard MRI template.

crus-cerebellum, SUVR estimates in the globus pallidus internus ($R_{(\mathrm{age})} = 0.38$, $P = 0.01$) and averaged across all target regions ($R_{(\mathrm{age})} = 0.35$, $P = 0.02$) showed significant associations with disease severity, whereas no significant correlations with disease duration were observed. The combination of both reference regions (Fig. 3) revealed several significant correlation coefficients with both disease severity ($R_{(\mathrm{age})}$ for all target ROIs $= 0.44$, $P = 0.01$; $R_{(\mathrm{age})}$ for frontal cortex $= 0.40$, $P = 0.01$; $R_{(\mathrm{age})}$ for globus pallidus externus $= 0.35$, $P = 0.03$; $R_{(\mathrm{age})}$ for globus pallidus internus $=$ 0.37, $P = 0.02$; $R_{(\mathrm{age})}$ for globus pallidus $= 0.36$, $P = 0.03$) and disease duration ($R_{(\mathrm{age})}$ for all target ROIs $= 0.37$, $P = 0.02$; $R_{(\mathrm{age})}$ for frontal cortex $= 0.40$, $P = 0.01$).

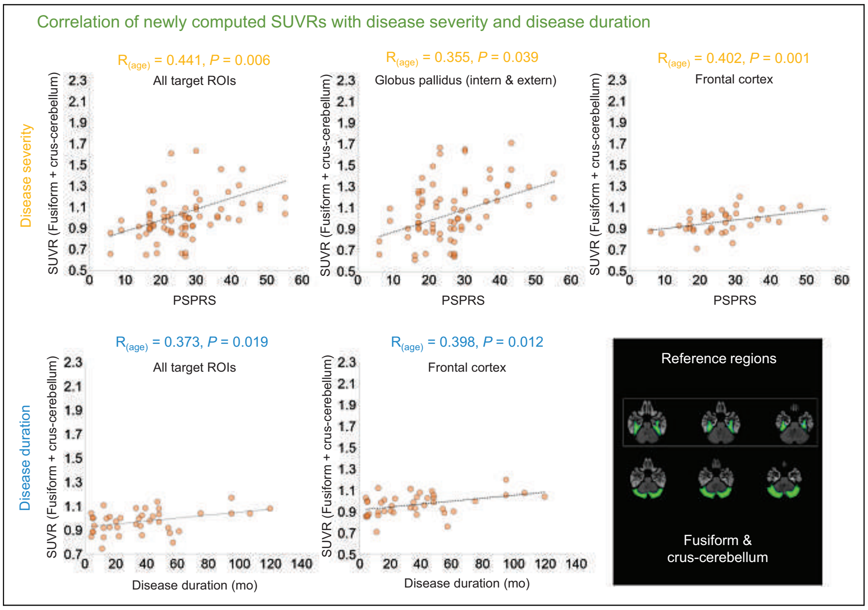

FIGURE 3. Significant partial correlations of combined reference regions (fusiform or crus-cerebellum as reference region), with disease severity (PSP rating scale [PSPRS]; upper panels) or disease duration (in months; lower panels). Automated anatomic atlas reference regions are overlayed on standard MRI template.

DISCUSSION

Here we show that using a data-driven statistical nonparametric approach to isolate regions that could serve as a potential reference region revealed several findings: regions with no on-target binding in the cohort of 4R phenotypes, plausibility due to the bilateral voxels located in both the fusiform gyrus and the crus-cerebellum, and no on-target binding based on histopathologic studies. In addition, SUVRs in target regions using either reference region showed significant relationships with clinical measures. The globus pallidus internus/externus was previously identified as the region best suited to discriminate different tauopathies using [^{18}F]PI-2620 (*1–3*), whereas our study expanded on these findings by showing sensitivity of the pallidum to disease severity measures. Additionally, the correlation with frontal tau pathology and disease duration adds plausibility to our reference regions, as cortical involvement of 4R tauopathy is known to be an indication of advanced disease stage (*6*). We therefore propose the fusiform gyrus and the crus-cerebellum as 2 potential candidates for further exploration as potential reference regions for [^{18}F]PI-2620 in a larger independent sample of 4R patients and in individuals for whom arterial blood sampling is available to further evaluate the suitability of our reference regions in 4R tauopathies.

We provide evidence that the previously established normalization count method (*8*) within the statistical nonparametric mapping context may be a sensitive automated approach to probe potential candidates for reference regions, particularly if the sample size of the target population is limited and the distribution of the tracer retention is relatively heterogeneous. Our results are important in the context of clinical trials of potential disease-modifying therapies in 4R tauopathies (*13*), as treatment effects could be quantified both on the pathophysiologic scale using [^{18}F]PI-2620 and according to disease severity. Our use of partial-volume–corrected data in our analysis may be a limitation because of the accessibility of high-resolution magnetization-prepared, rapid gradient-echo imaging in the clinical context.

CONCLUSION

Whereas recent studies have shown that the regional uptake pattern of [^{18}F]PI-2620 can assist in the differential diagnosis of primary versus secondary tauopathies, here we extend the utility of [^{18}F]PI-2620. Specifically, we show that different reference regions (i.e., fusiform gyrus, crus-cerebellum, and the combination) may improve SUVR quantification, as our newly computed SUVRs in target regions of 4R tauopathies relate to both disease severity and disease duration. We recognize that in the absence of specific criteria for appropriate reference regions, the criteria we have chosen may not be exhaustive for determining an appropriate reference region, but they may provide some initial guidance.

KEY POINTS

QUESTION: Can we improve SUVR sensitivity in 4R phenotypes using data-driven reference regions?

PERTINENT FINDINGS: We found suitable reference regions (i.e., crus-cerebellum and fusiform gyrus) in 4R phenotypes that led to SUVR estimates in target regions of 4R tauopathy that tracked with disease severity and duration.

IMPLICATIONS FOR PATIENT CARE: Our results improve the utility of ^{18}F-PI-2620 to quantify tau burden, which will improve the clinical application of ^{18}F-PI-2620 in the differential diagnosis of tauopathies.

DISCLOSURE

Gérard Bischof, Thilo van Eimeren, Hendrik Theis, and Alexander Drzezga are funded by the Deutsche Forschungsgemeinschaft (DFG), project ID 431549029-SFB 1451, and partially by DFG, DR 445/9-1. Carla Palleis was supported by DFG and under Germany's Excellence Strategy, the Munich Cluster for Systems Neurology (EXC 2145 SyNergy, ID 390857198), Lüneburg Heritage, and Friedrich-Baur-Stiftung. Matthias Brendel is partially funded by Germany's Excellence Strategy, the Munich Cluster for Systems Neurology (EXC 2145 SyNergy, ID 390857198). Hendrik Theis is funded by the Cologne Clinician Scientist Program, University of Cologne. Johannes Levin reports speaker fees from Bayer Vital, Biogen, Eisai, Teva, Zambon, and Roche; consulting fees from Axon Neuroscience, Eisai, and Biogen; and author fees from Thieme Medical Publishers and W. Kohlhammer GmbH Medical Publishers and is inventor in a patent, "Oral Phenylbutyrate for Treatment of Human 4-Repeat Tauopathies" (EP 23 156 122.6) filed by Ludwig Maxmillians University, Munich. Johannes Levin reports compensation as chief medical officer for MODAG GmbH, is beneficiary of the phantom share program of MODAG GmbH, and is inventor in a patent, "Pharmaceutical Composition and Methods of Use" (EP 22 159 408.8) filed by MODAG GmbH (all activities outside the submitted work). Andrew Stephens is a full-time employee of Life Molecular Imaging, GmbH. Thilo van Eimeren reports speaker/consultant fees from Eli Lilly, Shire, H. Lundbeck A/S, and Orion Corp. and author fees from Thieme medical publishers. No other potential conflict of interest relevant to this article was reported.

REFERENCES

1. Brendel M, Barthel H, van Eimeren T, et al. Assessment of ^{18}F-PI-2620 as a biomarker in progressive supranuclear palsy. *JAMA Neurol.* 2020;77:1408–1419.
2. Song M, Beyer L, Kaiser L, et al. Binding characteristics of [^{18}F]PI-2620 distinguish the clinically predicted tau isoform in different tauopathies by PET. *J Cereb Blood Flow Metab.* 2021;41:2957–2972.
3. Palleis C, Brendel M, Finze A, et al. Cortical [^{18}F]PI-2620 binding differentiates corticobasal syndrome subtypes. *Mov Disord.* 2021;36:2104–2115.
4. van Eimeren T, Antonini A, Berg D, et al. Neuroimaging biomarkers for clinical trials in atypical parkinsonian disorders: proposal for a Neuroimaging Biomarker Utility System. *Alzheimers Dement (Amst).* 2019;11:301–309.
5. Yap SY, Frias B, Wren MC, et al. Discriminatory ability of next-generation tau PET tracers for Alzheimer's disease. *Brain.* 2021;144:2284–2290.
6. Kovacs GG, Lukic MJ, Irwin DJ, et al. Distribution patterns of tau pathology in progressive supranuclear palsy. *Acta Neuropathol (Berl).* 2020;140:99–119.
7. Smith R, Puschmann A, Schöll M, et al. ^{18}F-AV-1451 tau PET imaging correlates strongly with tau neuropathology in MAPT mutation carriers. *Brain.* 2016;139:2372–2379.
8. Yakushev I, Hammers A, Fellgiebel A, et al. SPM-based count normalization provides excellent discrimination of mild Alzheimer's disease and amnestic mild cognitive impairment from healthy aging. *Neuroimage.* 2009;44:43–50.
9. Armstrong MJ, Litvan I, Lang AE, et al. Criteria for the diagnosis of corticobasal degeneration. *Neurology.* 2013;80:496–503.
10. Höglinger GU, Respondek G, Stamelou M, et al. Clinical diagnosis of progressive supranuclear palsy: The Movement Disorder Society criteria. *Mov Disord.* 2017;32:853–864.
11. Gonzalez-Escamilla G, Lange C, Teipel S, Buchert R, Grothe MJ; Alzheimer's Disease Neuroimaging Initiative. PETPVE12: an SPM toolbox for partial volume effects correction in brain PET—application to amyloid imaging with AV45-PET. *Neuroimage.* 2017;147:669–677.
12. Nichols TE, Holmes AP. Nonparametric permutation tests for functional neuroimaging: a primer with examples. *Hum Brain Mapp.* 2002;15:1–25.
13. Coughlin DG, Litvan I. Progressive supranuclear palsy: advances in diagnosis and management. *Parkinsonism Relat Disord.* 2020;73:105–116.

PET Quantification of [^{18}F]VAT in Human Brain and Its Test–Retest Reproducibility and Age Dependence

John L. O'Donnell[1], Anil Kumar Soda[2], Hao Jiang[2], Scott A. Norris[1,2], Baijayanta Maiti[1,2], Morvarid Karimi[†1,2], Meghan C. Campbell[1,2], Stephen M. Moerlein[2,3], Zhude Tu[2], and Joel S. Perlmutter[1,2,4]

[1]Neurology, Washington University in Saint Louis, St. Louis, Missouri; [2]Radiology, Washington University in Saint Louis, St. Louis, Missouri; [3]Biochemistry and Molecular Biophysics, Washington University in Saint Louis, St. Louis, Missouri; and [4]Neuroscience, Physical, and Occupational Therapy, Washington University in Saint Louis, St. Louis, Missouri

Molecular imaging of brain vesicular acetylcholine transporter provides a biomarker to explore cholinergic systems in humans. We aimed to characterize the distribution of, and optimize methods to quantify, the vesicular acetylcholine transporter–specific tracer (−)-(1-(8-(2-[^{18}F]fluoroethoxy)-3-hydroxy-1,2,3,4-tetrahydronaphthalen-2-yl)-piperidin-4-yl)(4-fluorophenyl)methanone ([^{18}F]VAT) in the brain using PET. **Methods:** Fifty-two healthy participants aged 21–97 y had brain PET with [^{18}F]VAT. [^{3}H]VAT autoradiography identified brain areas devoid of specific binding in cortical white matter. PET image–based white matter reference region size, model start time, and duration were optimized for calculations of Logan nondisplaceable binding potential (BP_{ND}). Ten participants had 2 scans to determine test–retest variability. Finally, we analyzed age-dependent differences in participants. **Results:** [^{18}F]VAT was widely distributed in the brain, with high striatal, thalamic, amygdala, hippocampal, cerebellar vermis, and regionally specific uptake in the cerebral cortex. [^{3}H]VAT autoradiography–specific binding and PET [^{18}F]VAT uptake were low in white matter. [^{18}F]VAT SUVs in the white matter reference region correlated with age, requiring stringent erosion parameters. Logan BP_{ND} estimates stabilized using at least 40 min of data starting 25 min after injection. Test–retest variability had excellent reproducibility and reliability in repeat BP_{ND} calculations for 10 participants (putamen, 6.8%; $r > 0.93$). We observed age-dependent decreases in the caudate and putamen (multiple comparisons corrected) and in numerous cortical regions. Finally, we provide power tables to indicate potential mean differences that can be detected between 2 groups of participants. **Conclusion:** These results validate a reference region for BP_{ND} calculations and demonstrate the viability, reproducibility, and utility of using the [^{18}F]VAT tracer in humans to quantify cholinergic pathways.

Key Words: cholinergic; brain; PET; human; acetylcholine

J Nucl Med 2024; 65:956–961
DOI: 10.2967/jnumed.123.266860

Cholinergic projections arise from 3 main centers (*1*): the basal forebrain projects throughout the neocortex; pedunculopontine-laterodorsal tegmental nuclei project heavily to the thalamus and other brain stem centers; and local cholinergic interneurons project within the striatum. These pathways play a role in neurologic disorders, including Alzheimer disease (*2*,*3*) and Parkinson disease (PD) (*4*). The degree of degeneration correlates with cognitive impairment, yet the time course and regional specificity of cholinergic dysfunction remain poorly understood.

PET radiotracers targeting the vesicular acetylcholine transporter (VAChT) permit investigation of these pathways in vivo in humans. VAChT resides predominantly in presynaptic terminals of cholinergic neurons and some cell bodies. Thus, molecular imaging of VAChT reflects primarily terminal fields. Recently, the VAChT radiotracer [^{18}F]fluoroethoxybenzovesamicol ([^{18}F]FEOBV) identified abnormalities in Alzheimer disease and possible correlations with cognitive impairment in PD (*2*,*5*–*8*). We developed a new VAChT radiotracer, (−)-(1-(8-(2-[^{18}F]fluoroethoxy)-3-hydroxy-1,2,3,4-tetrahydronaphthalen-2-yl)-piperidin-4-yl)(4-fluorophenyl)-methanone ([^{18}F]VAT), with high sensitivity and selectivity for cholinergic neurons in vitro in human brain tissue and in vivo in nonhuman primates (*9*–*12*). In the current work, we validated an image-based reference region to quantify specific binding in the brain, optimized calculation of a Logan nondisplaceable binding potential (BP_{ND}), showed the distribution of [^{18}F]VAT in normal healthy human brains, calculated regional variability of BP_{ND}, and investigated the age dependence of BP_{ND}. Finally, we calculated tables of statistical power to detect mean differences in BP_{ND} between 2 groups of participants to facilitate study planning.

MATERIALS AND METHODS

Participants and Design

The Human Research Protection Office of Washington University in St. Louis approved this study, and all participants provided written informed consent. Participants were partners of patients in the Movement Disorders Center or responded to public advertisement and were between the ages of 21 and 97 y. All had 12 or more years of education or a high-school–equivalent degree, normal findings on neurologic examination, no major neurologic or severe psychiatric illness, no history of head injury with loss of consciousness for more than 5 min or neurologic sequelae, no first-degree family history of PD, intact cognition, and no contraindication to MRI. They were taking no medications affecting the cholinergic system, and they were able to lie still for 2 h.

We performed whole-brain structural MRI and PET imaging with [^{18}F]VAT on 52 participants. Ten had 2 PET studies 1 mo apart to determine reproducibility.

Structural MRI

Each participant underwent a structural MRI scan with a Trio or Prisma 3-T scanner (Siemens) to perform a T1-weighted magnetization-prepared rapid acquisition with gradient-echo and T2-weighted fast spin-echo scans. Scans were segmented with the FreeSurfer image analysis

---

Received Oct. 16, 2023; revision accepted Mar. 13, 2024.

For correspondence or reprints, contact John L. O'Donnell (jodonn@wustl.edu).

†Deceased.

suite (version 5.3, https://surfer.nmr.mgh.harvard.edu/) (*13*). A cortical white matter reference region (WM_{REF}) was generated by merging all cortical white matter regions and applying a gaussian blur masking the image with a threshold of 0.95 to minimize tracer spillover from adjacent gray matter.

FreeSurfer identified regions including cortical gray matter, caudate, putamen, amygdala, thalamus, and hippocampus. As [^{18}F]VAT has elevated uptake in the cerebellum, we segmented the cerebellum using a spatially unbiased infratentorial template (SUIT), an atlas template of the cerebellum (*14–16*). To optimize SUIT segmentation for older participants, we used the FreeSurfer cerebellar white matter mask to remove white matter voxels, the FreeSurfer cortical ribbon to prevent inclusion of nearby gray matter, and a T2-weighted mask to reduce cerebrospinal fluid inclusion (*17*). SUIT-generated cerebellar volumes of interest (VOIs) were merged into a subset of regions to reduce multiple comparisons: anterior cerebellum (lobules I–V); posterior cerebellum (lobule VI); posterior cerebellum (crus 1 and crus 2); posterior cerebellum (lobules VIIb–IX); vestibulocerebellum (lobule X); and cerebellar nuclei. VOIs were further subdivided into left hemisphere, right hemisphere, and vermis, with the exception of the anterior vermis, which is not segmented by SUIT. Finally, FreeSurfer- and SUIT-based regions were merged into a single segmentation image for PET analyses.

PET Imaging

VAT was synthesized as previously described (*9*,*12*). PET was done with a Siemens ECAT EXACT HR+ scanner. Each participant had a 20-gauge plastic catheter inserted into an antecubital vein. An attenuation image was collected using rotating ^{68}Ga/^{68}Ge sources. [^{18}F]VAT (255–544 MBq) was injected intravenously over 20 s followed by a 10-mL saline flush. A 120-min dynamic PET scan was collected starting with tracer injection in 3-dimensional mode (septa retracted). Sixty-two scans were collected from 52 participants, with 10 having 2 scans performed 1 mo apart. For 51 scans (46 participants, 5 with repeat scans), the acquisition consisted of 71 frames with durations of 36 × 5 s, 12 × 10 s, and 23 × 300 s. Eleven scans (6 participants, 5 with repeat scans) consisted of 30 frames with durations of 3 × 60 s, 4 × 120 s, 3 × 180 s, and 20 × 300 s. Scans were reconstructed with 3-dimensional filtered backprojection with a ramp filter to yield a reconstructed resolution of about 5 mm in full width at half maximum (FWHM). For motion correction, individual frames were aligned with vector-gradient registration to a composite average of all frames (*18*). The composite PET image then was registered to the participant's T1-weighted MRI scan, and the 2 transforms were combined (individual frames to composite PET and composite PET to T1). The combined transform was applied to each frame to align the PET scans to the T1 images. Motion-corrected images and whole-brain time–activity curves were visually inspected in participant-specific PET space and T1 space to verify the accuracy of alignment.

Region-Based Analyses. Decay-corrected time–activity curves for VOIs were extracted from PET images. Regional partial-volume effects were corrected using the region-spread function approach (*19*). Briefly, the segmented image containing all FreeSurfer- and SUIT-defined VOIs was convolved with a 4.2-mm gaussian kernel to generate relative weights of the contributions from nearby regions. These weights then were applied to each time–activity curve to generate their region-spread function–corrected values. BP_{ND} values then were calculated with in-house MATLAB software (MATLAB release 2020b; The MathWorks, Inc.) using the eroded cortical white matter mask as the reference region and Logan graphical analysis (*20*).

Composite SUV images were generated by aligning each participant's dynamic PET image into that participant's T1 space. SUV parametrized images were generated by dividing all voxels by the mean intensity of the WM_{REF} from 30 to 120 min after injection. Images were single-step–aligned to the 711-2B atlas using a transformation matrix generated from an initial vector-gradient registration followed by nonlinear registration using the Functional Magnetic Resonance Imaging of the Brain Software Library's nonlinear registration tool (*21*).

Reference Region Validation. We performed reference region validation with 2 approaches: in vitro autoradiography and analysis of PET-based regions of interest.

For in vitro [^{3}H]VAT autoradiography, we tested specific uptake of [^{18}F]VAT in cortical white matter using postmortem brain tissue from 3 donors: 1 neurologically healthy female control (73 y old) and 2 PD patients (81-y-old woman and 69-y-old man). PD tissue was included to determine whether specific binding differed in advanced PD. Specific binding throughout cortical white matter was compared in deep anterior white matter, centrum semiovale, and deep occipital lobe tissue. [^{18}F]VAT uptake in caudate (high binding), vermis (intermediate binding), and occipital lobe gray matter (low binding) was compared with that in cortical white matter.

In vitro autoradiography was done with [^{3}H]VAT in frozen sections from the human brain (*22*). Twenty-micron brain sections were preincubated with Hanks balanced salt solution containing 10 mM 4-(2-hydroxyethyl)-1-piperazineethanesulfonic acid, 0.2% bovine serum albumin, and 0.1 mM ethylenediaminetetraacetic acid at pH 7.4 for 5 min at room temperature. Sections were incubated with 5 nM [^{3}H]VAT in buffer for 1 h with gentle shaking and were washed 3 times with buffer for 5 min, dipped in ice-cold H_2O for 1 min, and dried overnight. Dried slides were incubated with BioMax autoradiography film (Carestream) in a Hypercassette autoradiography cassette (Cytiva) for 20 d with ART-123 tritium standards (American Radiolabeled Chemicals). The film then was processed in film developer (Kodak). To determine nonspecific binding,

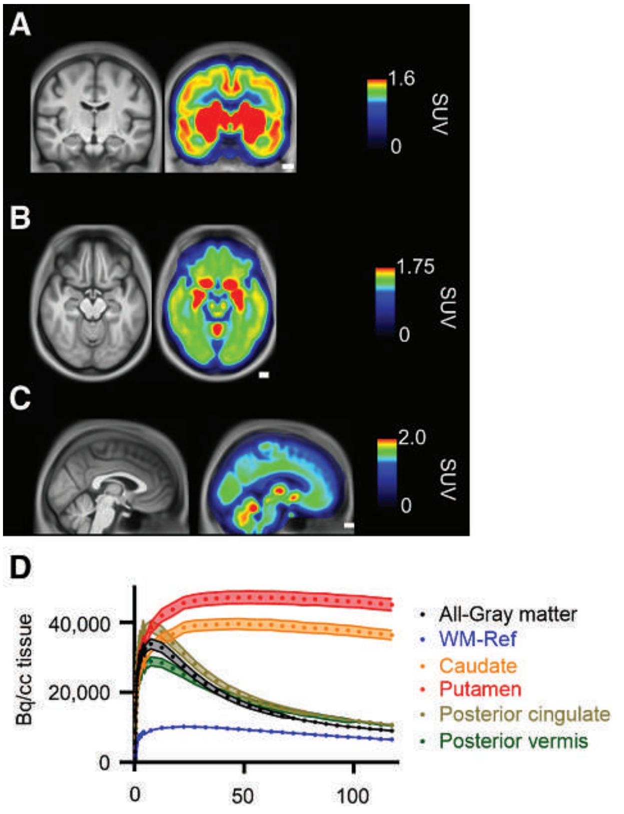

FIGURE 1. [^{18}F]VAT distribution in brain. (A–C) Sample images of composite average of SUV-parametrized images from 52 participants. Scales are varied to highlight cortical and subcortical distributions. Scale bars = 1 cm. (D) Average decay-corrected time–activity curves from select regions across 22 participants. Error bars indicate mean ± SEM.

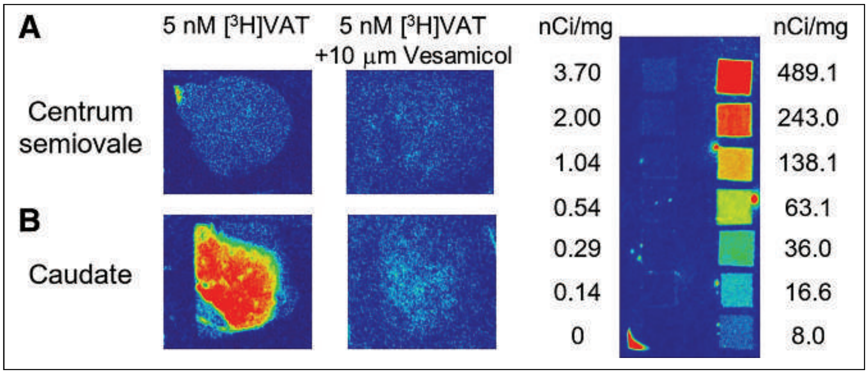

FIGURE 2. Representative control tissue [^{3}H]VAT autoradiography from cortical white matter (A) and caudate (B). Images are presented adjacent to slices with 5 nM [^{3}H]VAT + 10 μM vesamicol to demonstrate selective [^{3}H]VAT binding. 1 nCi = 37 Bq.

10 μmol of a VAChT antagonist, D-(+)-vesamicol hydrochloride (Sigma-Aldrich), were added. All images were processed and analyzed using Fiji ImageJ. In brief, regions of interest were randomly selected in the gray and white matter of brain tissues, and the intensity for each VOI was measured. Specific binding intensity was assessed by subtracting the nonspecific binding intensity from total binding. All representative images were processed using the continuous lut called Physics in Fiji ImageJ.

For analysis of PET-based regions of interest, white matter reference VOIs were optimized by minimizing intraregional variability while maintaining sufficient voxels for adequate counts. Gaussian blurs were repeated at FWHMs of 4.2, 5, 6, 7, 8, 9, and 10 mm with thresholds of 0.9, 0.95, and 0.975 for reference region comparison analyses and at a FWHM of 9 mm with a threshold of 0.95 for all other analyses. This blur strategy corresponds to final voxel erosion of 2.6 mm (FWHM, 4.2 mm; 0.90 threshold) to 6.2 mm (FWHM, 10 mm; 0.975 threshold), corresponding to 5,000 to 140,000 mean retained voxels. At 9 mm and a 0.95 gaussian blur threshold, the approximate erosion was 4.9 mm in all directions and the mean WM_{REF} was 24,000 voxels.

Statistics

Plots were generated with Prism 10 (GraphPad Software) for Windows (Microsoft). Pearson correlations between the WM_{REF} and age were done with IBM SPSS version 26.0 (IBM Corp.). Test–retest variability was calculated by taking the difference between scan 1 and scan 2 BP_{ND}, dividing by the mean regional BP_{ND} of the two, and then averaging across all participants. Analysis of age-dependent changes was done with SPSS, covarying of participant sex, and Benjamini–Hochberg multiple-comparisons correction with a false-discovery rate of 0.1. Power analyses were conducted with G*Power 3.1 (*23*,*24*). The power analyses table used an α of 0.05, with power values (1 − β) of 0.9.

RESULTS

We completed 62 [^{18}F]VAT PET scans from 52 participants (age, 60.4 ± 18.6 y [range, 21–97 y]; 17 men, 36 women). We analyzed these data to determine the brain distribution of radioactivity. SUV-parametrized [^{18}F]VAT images showed selective uptake in multiple regions (Fig. 1A). The putamen and caudate exhibited the highest uptake in the brain (SUV at 30–120 min, 5.84 ± 1.08 g/mL and 7.05 ± 1.13 g/mL, respectively) (Fig. 1A). Intermediate levels were seen in subcortical structures including the thalamus (SUV at 30–120 min, 2.35 ± 0.92 g/mL), amygdala (SUV at 30–120 min, 2.66 ± 0.48 g/mL), and hippocampus (SUV at 30–120 min, 2.27 ± 0.40 g/mL) (Figs. 1A and 1B). Although not segmented, selective uptake also was identified as localized peaks in the anterior and posterior vermis (Figs. 1B and 1C), with less uptake in the dorsal pons (Fig. 1C) and flocculus. Cortical gray matter had lower overall binding (all cortical gray matter, SUV at 30–120 min, 2.06 ± 0.42 g/mL), but some regions had higher VAT uptake, including the posterior cingulate (SUV at 30–120 min, 2.41 ± 0.48 g/mL) (Fig. 1B), pericalcarine fissure (SUV at 30–120 min, 2.40 ± 0.54 g/mL), and to a lesser extent temporal lobes (medial temporal lobe, SUV at 30–120 min, 1.95 ± 0.41 g/mL). White matter consistently had much lower uptake (SUV at 30–120 min, 1.26 ± 0.23 g/mL).

Autoradiography

Autoradiography showed higher specific binding in the caudate, vermis, and occipital lobe than in any white matter regions, with the sole exception of the occipital lobe of 1 PD participant (Fig. 2; Table 1; Supplemental Fig. 1 [supplemental materials are available at http://jnm.snmjournals.org]). Although this participant showed modestly higher, but still quite low, white matter binding than white matter regions in the other 2 participants (17.70–38.38 vs. 0.03–16.37 fmol/mg tissue), these results corroborate cortical white matter as a reference region with no binding or low binding.

Optimal Erosion Characteristics for WM_{REF}

We tested the impact of the degree of erosion used to generate WM_{ref} VOIs to minimize gray matter spillover while retaining enough voxels for reliable counting statistics. To perform this test, we used 21 levels of erosion (2.6–6.2 mm) in all directions: 7 spheres with 3 thresholds. As expected, greater erosion yielded lower time–activity curves (Fig. 3A), fewer voxels, and lower intraregional variability (Fig. 3B), but these differences in mean time–activity curve and intraregional variability largely disappeared at or above a FWHM of 7 mm. To test for systematic bias that might be missed, we then correlated the SUV_{mean} of our WM_{ref} VOI with participant ages. This demonstrated a strong correlation between the SUV of the WM_{ref} VOI and participant age

TABLE 1
Regional [^{3}H]VAT Binding (fmol/mg Tissue)

Subject	Caudate	Occipital lobe	Vermis	Anterior deep white matter	Centrum semiovale	Occipital deep white matter
Control	551.57	112.18	132.31	4.54	0.03	16.37
PD	213.70	2.19	111.05	17.70	30.07	38.38
PD	354.26	396.13	131.70	9.32	0.67	9.83

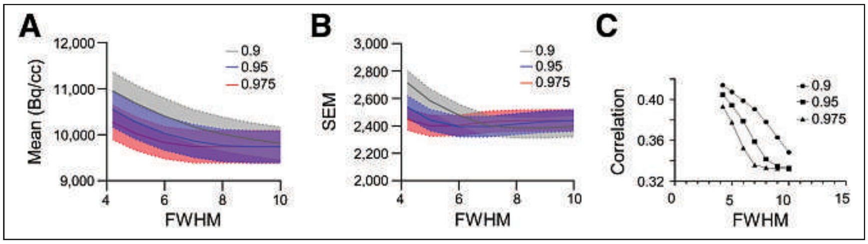

FIGURE 3. Seven erosion widths and 3 thresholds were used to generate potential WM_{REF} values. Mean region-spread function partial volume–corrected SUVs (A) and intraregional SEM (B) are shown to demonstrate region characteristics. (C) Reference region correlation with age.

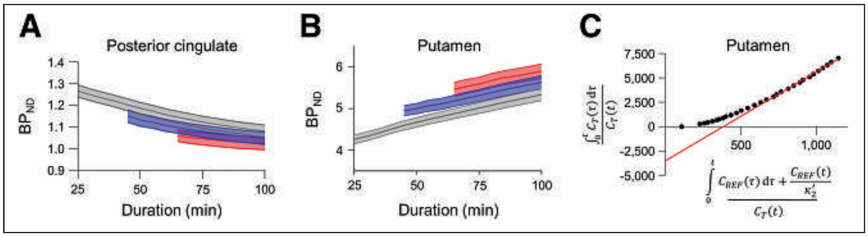

FIGURE 4. Effects of varying model start time and duration on Logan BP_{ND}. Logan binding potentials were averaged across all participants calculated for cortical gray matter (A) and putamen (B). Start times of 45 and 65 min are offset to demonstrate results ending at same time point. Error bars indicate mean ± SEM. Start times are color-coded as 25 min (gray), 45 min (blue), and 65 min (red). (C) Representative Logan plot, with regression line for 30- to 120-min model calculation shown in red. $C_T(t)$ = activity in target tissue at time t; C_{REF} = activity in reference region at time t; k_2' = population average reference region efflux constant.

that declined with increasingly stringent erosion to an approximate *R* of 0.33 for 9- and10-mm erosions with 0.95 and 0.975 thresholds (Fig. 3D). Thus, for the remainder of our analyses, we used a 9-mm erosion by a 0.95 threshold for our WM_{ref} VOI.

Effect of Model Time and Duration on Regional Binding Potentials

The effects of varying model start times and durations on BP_{ND} were calculated for high-binding subcortical regions (putamen) and cortical gray matter (posterior cingulate) (Figs. 4A–4C). The coefficient of variation across participants also was calculated for each model start and duration (Supplemental Figs. 2A–2B). These analyses demonstrated a shift in BP_{ND} requiring analyses over the same interval in every participant with a duration of at least 40 min to stabilize the coefficient of variation. Calculated BP_{ND} values converged in gray matter by 60–90 min after injection. Thus, we chose a 90-min model starting at 30 min after injection to incorporate as much data as possible. Shorter scan durations may produce similarly stable results, provided there is a minimum total scan duration of at least 65–70 min.

Test–Retest Reproducibility

We characterized the reproducibility of BP_{ND} calculations in 10 participants who had 2 [^{18}F]VAT PET scans 1 mo apart. BP_{ND} was calculated for segmented FreeSurfer and SUIT regions. High correlations occurred in high-binding areas including the putamen (percentage test–retest variability, 6.8%; $r > 0.93$; Fig. 5), with significantly more variability in regions with a BP_{ND} under 1, as expected with increased noise.

Age-Related Differences in Uptake

Widespread age-related differences were identified throughout the brain, in particular within the putamen (Fig. 6). Correlating region-spread function–corrected BP_{ND} for each region, covarying sex, and using Benjamini–Hochberg false-discovery rate multiple comparisons correction, we found significant results, including a lower BP_{ND} with increasing age in subcortical structures (caudate $r < -0.59$, putamen $r < -0.46$, and nucleus accumbens $r < -0.34$). Notably, many cortical regions exhibited opposite effects, with strong positive correlations throughout both gray matter and white matter (rostral middle frontal white matter $r > 0.68$ and inferior temporal gray matter $r > 0.60$).

Power Analyses

Power analyses were done to determine the feasibility of PET [^{18}F]VAT to detect group differences in future studies. SD varied from 15% to 35% of the mean BP_{ND} for almost all regions. In Table 2, a 1.82 difference in group-mean caudate BP_{ND} (43% of control mean, 1.7 SDs) from our control population would require 20 participants, and 200 participants would be needed to detect a difference of 0.54 (12.8% of control mean, 0.5 SDs) with 0.9 power. This shows the potential for [^{18}F]VAT in human imaging.

DISCUSSION

We demonstrated that [^{18}F]VAT is an effective PET radiotracer to study differences in the cholinergic system. The highest levels of uptake were in the striatum, thalamus, and other subcortical structures, but gray matter regions also had selective uptake. Our work provides strong validation for using eroded white matter as a reference region for calculation of BP_{ND} and demonstrates the importance of what image data should be included to obtain stable estimates. We further demonstrated correlations between [^{18}F]VAT and age in healthy participants. Finally, to facilitate planning future studies, we provide a table of power calculations to detect difference between 2 groups for given effect sizes.

Our previous work with [^{18}F]VAT in nonhuman primates showed little uptake in the cerebellar cortex, indicating no evidence of specific binding that would retain radiotracer, thereby permitting its use as a reference region (*9*). In contrast, the cerebellar vermis has a relatively high uptake in humans. Thus, we focused on validating an alternative reference region for humans. Despite known cortical cholinergic projections that pass through white matter regions, our

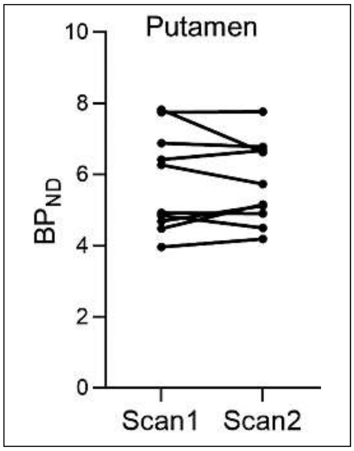

FIGURE 5. Representative Logan BP_{ND} demonstrating test–retest reproducibility of [^{18}F]VAT. Data are putamen Logan BP_{ND} for each of 10 participants scanned 1 mo apart.

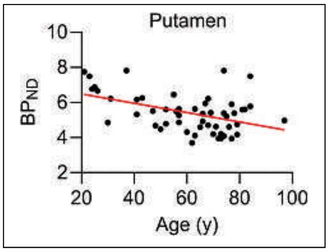

FIGURE 6. Raw Logan BP$_{ND}$ relative to age in putamen. Sample regression line is shown in red.

combined histopathologic and PET validation indicates that cortical white matter has minimal specific binding with [18F]VAT. Notably, differences between gray and white matter blood flow can bias binding potential estimates because of differences in tracer entry and egress, but this effect is quite minimal in data collected after 15–20 min after radiotracer injection. As such, our subsequent analyses use late time-points at which the impact of differences in delivery is minimized. Future studies using arterial sampling for binding potential calculations will further characterize any bias and help validate the use of the white matter as a reference region and act as a gold standard for these analyses. Nevertheless, in the present work the very low specific uptake in cortical white matter makes it an excellent reference region for [18F]VAT. Using this reference region, we found age-dependent decreases in various subcortical and cortical structures that must be considered in future [18F]VAT studies. Finally, we developed a power analysis table based on 52 healthy control participants to guide the design of future human [18F]VAT PET group-level studies.

To optimize [18F]VAT BP$_{ND}$ calculations, we first addressed potential spillover into the WM$_{REF}$ from adjacent subcortical and gray matter regions with region-spread function partial-volume correction along with testing of varying levels of erosion for the combined white matter region. Although a FWHM of 7 mm was sufficient to minimize intraregional variability, a persistent age-dependent correlation with the WM$_{REF}$ SUV required a more aggressive erosion of 9 mm (0.95 threshold). This suggests that age-dependent atrophy at lower erosion levels causes residual spillover that requires partial-volume correction and stringent erosion parameters to quantify [18F]VAT in humans with varying degrees of brain atrophy.

We then determined optimal variables for calculation of Logan-derived BP$_{ND}$ such as start time and scan duration. At least 40 min of scan data starting at least 25–30 min after injection are needed to provide stable BP$_{ND}$ estimates. Although BP$_{ND}$ estimates stabilized by 65–70 min after injection, some gray matter areas exhibited a slight upward drift in BP$_{ND}$ with increasing model duration, likely attributable to differences in clearance rates between white and gray matter. Thus, all study participants must be analyzed over the same model period.

Other groups have used the VAChT-targeting tracer [18F]FEOBV to measure cerebral cholinergic pathways in humans. Both tracers demonstrate a similar distribution in the brain, with high striatal uptake; elevated subcortical uptake in the amygdala, hippocampus, and thalamus; elevated cerebellar vermis and vestibulocerebellar uptake; and a similar topography of regional cortical uptake (*25*). Recent [18F]FEOBV studies used a roughly comparable WM$_{REF}$ (*26*). In comparison to [18F]FEOBV, both tracers perform well, with [18F]VAT appearing to demonstrate more rapid dissociation kinetics, potentially permitting shorter imaging sessions. [18F]VAT further demonstrates excellent regional uptake and variability (Table 3), demonstrating its utility for future studies.

We calculated power analyses to indicate how many participants would be needed to detect a given effect size (or difference) between the mean BP$_{ND}$ of 2 different groups. These calculations depend on the variance of the measures for each region of the brain since the level of radiotracer uptake dramatically differs across regions, thereby varying the noise in the measures. As shown in Table 2, those gray matter regions with the highest uptake permit detection of differences of as little as approximately 32% for study groups of 20 participants, and approximately 9% for large groups of 200 participants. These effect sizes compare favorably with the test–retest variability, which was 15%–35% in most regions. As such, [18F]VAT presents an opportunity for the study of small to moderate differences in the cholinergic system and may be sufficient for the detection of early abnormalities within disease states.

CONCLUSION

We demonstrated that [18F]VAT can be a reliable tracer for the study of brain cholinergic systems in humans. White matter presents a reasonable option for [18F]VAT analysis, but extra care must be taken in older populations or those with greater atrophy, as age-dependent effects on reference region uptake can persist despite correction for partial-volume effects. This approach provides stable BP$_{ND}$ estimates that permitted identification of age-dependent changes. These results indicate that [18F]VAT is a reliable tracer for the study of cholinergic pathways in the brain and can be implemented for future work investigating the role of cholinergic dysfunction in neurodegenerative conditions.

DISCLOSURE

Research funding was received from NIH (NCATS, NINDS, NIA): NS075321, NS103957, NS103988, NS107281, NS107281-03S1, NS097799, NS075527, NS097437, NS124738, NS124789, K23NS125107, F32NS105365, and P30AG066444; the Barnes-Jewish Hospital Foundation (Elliot Stein Family Fund and

TABLE 2
Power Analyses of BP$_{ND}$ Showing Necessary Group Differences ($\alpha = 0.05$, Power = 0.9)

Region	BP$_{ND}$ ± SD	*N* = 20	*N* = 50	*N* = 100	*N* = 200
Caudate	4.21 ± 1.07	1.82	1.10	0.78	0.54
Putamen	5.41 ± 1.09	1.85	1.12	0.79	0.55
Thalamus	1.10 ± 0.17	0.30	0.18	0.13	0.09
Hippocampus	0.84 ± 0.16	0.28	0.17	0.12	0.08
Amygdala	1.14 ± 0.22	0.37	0.23	0.16	0.11
Posterior cingulate	1.08 ± 0.21	0.35	0.21	0.15	0.10

TABLE 3
[^{18}F]VAT Regional Distribution

Region	[^{18}F]VAT BP_{ND} ± SD
Superior frontal cortex	0.73 ± 0.20
Medial orbitofrontal cortex	0.91 ± 0.19
Lateral orbitofrontal cortex	0.95 ± 0.18
Motor cortex	0.85 ± 0.18
Superior temporal gyrus	0.74 ± 0.16
Middle temporal gyrus	0.67 ± 0.15
Inferior temporal gyrus	0.76 ± 0.17
Superior parietal cortex	0.65 ± 0.21
Inferior parietal cortex	0.71 ± 0.18
Cuneus	0.82 ± 0.20
Entorhinal cortex	0.52 ± 0.16
Parahippocampal gyrus	0.53 ± 0.17
Postcentral gyrus	0.73 ± 0.18
Lateral occipital cortex	0.55 ± 0.18
Posterior vermis	0.94 ± 0.26

Parkinson Disease Research Fund); the American Parkinson Disease Association (APDA) Advanced Research Center at Washington University; the Greater St. Louis Chapter of the APDA; the Paula and Rodger Riney Fund; the Jo Oertli Fund; the Huntington Disease Society of America; the Murphy Fund; the Fixel Foundation; the Grant Williams Fund; CHDI; the Michael J. Fox Foundation; the Washington University Department of Radiology; the Washington University McDonnell Center; the Dystonia Medical Research Foundation; and Dysphonia International. Meghan Campbell has received an honorarium from the Parkinson Foundation. No other potential conflict of interest relevant to this article was reported.

ACKNOWLEDGMENTS

We thank our participants, our patients, and their families who make this work possible. We also thank the Charles F. and Joanne Knight Alzheimer Disease Research Center for material support.

KEY POINTS

QUESTION: How can [^{18}F]VAT analysis be optimized to study cholinergic signaling in the brain?

PERTINENT FINDINGS: The cortical white matter provides a quality reference region for kinetic analysis of [^{18}F]VAT with a minimum scan duration of 65 min. Because age-dependent atrophy can impact this reference region, careful attention to quality control methods is critical. Cholinergic signaling, as measured by [^{18}F]VAT, declines with age.

IMPLICATIONS FOR PATIENT CARE: [^{18}F]VAT can be a reliable tool in studying cholinergic dysfunction in neurologic and neuropsychiatric disease.

REFERENCES

1. Mesulam MM, Mufson EJ, Levey AI, Wainer BH. Atlas of cholinergic neurons in the forebrain and upper brainstem of the macaque based on monoclonal choline acetyltransferase immunohistochemistry and acetylcholinesterase histochemistry. *Neuroscience.* 1984;12:669–686.
2. Bohnen NI, Kanel P, Muller M. Molecular imaging of the cholinergic system in Parkinson's disease. *Int Rev Neurobiol.* 2018;141:211–250.
3. Geula C, Mesulam MM. Cortical cholinergic fibers in aging and Alzheimer's disease: a morphometric study. *Neuroscience.* 1989;33:469–481.
4. Candy JM, Perry RH, Perry EK, et al. Pathological changes in the nucleus of Meynert in Alzheimer's and Parkinson's diseases. *J Neurol Sci.* 1983;59: 277–289.
5. Albin RL, Kanel P, van Laar T, et al. No dopamine agonist modulation of brain [^{18}F]FEOBV binding in Parkinson's disease. *Mol Pharm.* 2022;19: 1176–1182.
6. Kanel P, van der Zee S, Sanchez-Catasus CA, et al. Cerebral topography of vesicular cholinergic transporter changes in neurologically intact adults: a [^{18}F]FEOBV PET study. *Aging Brain.* 2022;2:100039.
7. Aghourian M, Legault-Denis C, Soucy JP, et al. Quantification of brain cholinergic denervation in Alzheimer's disease using PET imaging with [^{18}F]-FEOBV. *Mol Psychiatry.* 2017;22:1531–1538.
8. Xia Y, Eeles E, Fripp J, et al. Reduced cortical cholinergic innervation measured using [^{18}F]-FEOBV PET imaging correlates with cognitive decline in mild cognitive impairment. *Neuroimage Clin.* 2022;34:102992.
9. Jin H, Yue X, Liu H, et al. Kinetic modeling of [^{18}F]VAT, a novel radioligand for positron emission tomography imaging vesicular acetylcholine transporter in nonhuman primate brain. *J Neurochem.* 2018;144:791–804.
10. Karimi M, Tu Z, Yue X, et al. Radiation dosimetry of [^{18}F]VAT in nonhuman primates. *EJNMMI Res.* 2015;5:73.
11. Liang Q, Joshi S, Liu H, et al. In vitro characterization of [^{3}H]VAT in cells, animal and human brain tissues for vesicular acetylcholine transporter. *Eur J Pharmacol.* 2021;911:174556.
12. Yue X, Bognar C, Zhang X, et al. Automated production of [^{18}F]VAT suitable for clinical PET study of vesicular acetylcholine transporter. *Appl Radiat Isot.* 2016; 107:40–46.
13. Fischl B. FreeSurfer. *Neuroimage.* 2012;62:774–781.
14. Diedrichsen J. A spatially unbiased atlas template of the human cerebellum. *Neuroimage.* 2006;33:127–138.
15. Diedrichsen J, Balsters JH, Flavell J, Cussans E, Ramnani N. A probabilistic MR atlas of the human cerebellum. *Neuroimage.* 2009;46:39–46.
16. Diedrichsen J, Maderwald S, Kuper M, et al. Imaging the deep cerebellar nuclei: a probabilistic atlas and normalization procedure. *Neuroimage.* 2011; 54:1786–1794.
17. Myers PS, McNeely ME, Koller JM, Earhart GM, Campbell MC. Cerebellar volume and executive function in Parkinson disease with and without freezing of gait. *J Parkinsons Dis.* 2017;7:149–157.
18. Rowland DJ, Garbow JR, Laforest R, Snyder AZ. Registration of [^{18}F]FDG microPET and small-animal MRI. *Nucl Med Biol.* 2005;32:567–572.
19. Su Y, Blazey TM, Snyder AZ, et al. Partial volume correction in quantitative amyloid imaging. *Neuroimage.* 2015;107:55–64.
20. Logan J, Fowler JS, Volkow ND, Wang GJ, Ding YS, Alexoff DL. Distribution volume ratios without blood sampling from graphical analysis of PET data. *J Cereb Blood Flow Metab.* 1996;16:834–840.
21. Jenkinson M, Beckmann CF, Behrens TE, Woolrich MW, Smith SM. FSL. *Neuroimage.* 2012;62:782–790.
22. Jiang H, Joshi S, Liu H, et al. In vitro and in vivo investigation of S1PR1 expression in the central nervous system using [^{3}H]CS1P1 and [^{11}C]CS1P1. *ACS Chem Neurosci.* 2021;12:3733–3744.
23. Faul F, Erdfelder E, Buchner A, Lang AG. Statistical power analyses using G*Power 3.1: tests for correlation and regression analyses. *Behav Res Methods.* 2009;41:1149–1160.
24. Faul F, Erdfelder E, Lang AG, Buchner AG. *Power 3: a flexible statistical power analysis program for the social, behavioral, and biomedical sciences. *Behav Res Methods.* 2007;39:175–191.
25. Albin RL, Bohnen NI, Muller M, et al. Regional vesicular acetylcholine transporter distribution in human brain: a [^{18}F]fluoroethoxybenzovesamicol positron emission tomography study. *J Comp Neurol.* 2018;526:2884–2897.
26. Bohnen NI, Kanel P, Zhou Z, et al. Cholinergic system changes of falls and freezing of gait in Parkinson's disease. *Ann Neurol.* 2019;85:538–549.

Is PET Radiomics Useful to Predict Pathologic Tumor Response and Prognosis in Locally Advanced Cervical Cancer?

Angela Collarino*[1], Vanessa Feudo*[2], Tina Pasciuto[3], Anita Florit[2], Elisabeth Pfaehler[4], Marco de Summa[5], Nicolò Bizzarri[6], Salvatore Annunziata[1], Gian Franco Zannoni[7,8], Lioe-Fee de Geus-Oei[9–11], Gabriella Ferrandina[6,12], Maria Antonietta Gambacorta[13,14], Giovanni Scambia[6,12], Ronald Boellaard[15], Evis Sala[14,16], Vittoria Rufini[1,2], and Floris HP van Velden[9]

[1]Nuclear Medicine Unit, Fondazione Policlinico Universitario A. Gemelli–IRCCS, Rome, Italy; [2]Section of Nuclear Medicine, University Department of Radiological Sciences and Hematology, Università Cattolica del Sacro Cuore, Rome, Italy; [3]Research Core Facility Data Collection G-STeP, Fondazione Policlinico Universitario A. Gemelli–IRCCS, Rome, Italy; [4]Institute of Neuroscience and Medicine, INM-4, Forschungszentrum Jülich GmbH, Jülich, Germany; [5]PET/CT Center, Fondazione Policlinico Universitario A. Gemelli-IRCCS, Rome, Italy; [6]Gynecologic Oncology Unit, Department of Woman and Child Health and Public Health, Fondazione Policlinico Universitario A. Gemelli–IRCCS, Rome, Italy; [7]Gynecopathology Unit, Department of Woman and Child Health and Public Health, Fondazione Policlinico Universitario A. Gemelli–IRCCS, Rome, Italy; [8]Section of Pathology, Department of Woman and Child Health and Public Health, Università Cattolica del Sacro Cuore, Rome, Italy; [9]Section of Nuclear Medicine, Department of Radiology, Leiden University Medical Center, Leiden, The Netherlands; [10]Biomedical Photonic Imaging Group, MIRA Institute, University of Twente, Enschede, The Netherlands; [11]Department of Radiation Science and Technology, Technical University of Delft, Delft, The Netherlands; [12]Section of Obstetrics and Gynecology, University Department of Life Sciences and Public Health, Università Cattolica del Sacro Cuore, Roma, Italy; [13]Radiation Oncology Unit, Fondazione Policlinico Universitario A. Gemelli–IRCCS, Roma, Italy; [14]Section of Radiology, University Department of Radiological Sciences and Hematology, Università Cattolica del Sacro Cuore, Rome, Italy; [15]Department of Radiology and Nuclear Medicine, Amsterdam UMC, Location VU University Medical Center, Amsterdam, The Netherlands; and [16]Advanced Radiodiagnostics Centre, Fondazione Policlinico Universitario A. Gemelli–IRCCS, Rome, Italy

This study investigated whether radiomic features extracted from pretreatment [^{18}F]FDG PET could improve the prediction of both histopathologic tumor response and survival in patients with locally advanced cervical cancer (LACC) treated with neoadjuvant chemoradiotherapy followed by surgery compared with conventional PET parameters and histopathologic features. **Methods:** The medical records of all consecutive patients with LACC referred between July 2010 and July 2016 were reviewed. [^{18}F]FDG PET/CT was performed before neoadjuvant chemoradiotherapy. Radiomic features were extracted from the primary tumor volumes delineated semiautomatically on the PET images and reduced by factor analysis. A receiver-operating-characteristic analysis was performed, and conventional and radiomic features were dichotomized with Liu's method according to pathologic response (pR) and cancer-specific death. According to the study protocol, only areas under the curve of more than 0.70 were selected for further analysis, including logistic regression analysis for response prediction and Cox regression analysis for survival prediction. **Results:** A total of 195 patients fulfilled the inclusion criteria. At pathologic evaluation after surgery, 131 patients (67.2%) had no or microscopic ($\leq$3 mm) residual tumor (pR0 or pR1, respectively); 64 patients (32.8%) had macroscopic residual tumor ($>$3 mm, pR2). With a median follow-up of 76.0 mo (95% CI, 70.7–78.7 mo), 31.3% of patients had recurrence or progression and 20.0% died of the disease. Among conventional PET parameters, SUV$_{\text{mean}}$ significantly differed between pathologic responders and nonresponders. Among radiomic features, 1 shape and 3 textural features significantly differed between pathologic responders and nonresponders. Three radiomic features significantly differed between presence and absence of recurrence or progression and between presence and absence of cancer-specific death. Areas under the curve were less than 0.70 for all parameters; thus, univariate and multivariate regression analyses were not performed. **Conclusion:** In a large series of patients with LACC treated with neoadjuvant chemoradiotherapy followed by surgery, PET radiomic features could not predict histopathologic tumor response and survival. It is crucial to further explore the biologic mechanism underlying imaging-derived parameters and plan a large, prospective, multicenter study with standardized protocols for all phases of the process of radiomic analysis to validate radiomics before its use in clinical routine.

Key Words: locally advanced cervical cancer; radiomics; [^{18}F]FDG PET/CT; response to therapy; prognosis

J Nucl Med 2024; 65:962–970
DOI: 10.2967/jnumed.123.267044

Cervical cancer is one of the most common malignancies in women worldwide (*1*). According to international guidelines (*2,3*), the preferred treatment for patients with locally advanced cervical cancer (LACC) is definitive cisplatin-based chemoradiotherapy followed by brachytherapy. However, the disease recurs in one third of LACC patients, usually within 2 y after chemoradiotherapy, and the 5-y overall survival is around 70% (*4,5*). Neoadjuvant chemoradiotherapy followed by radical surgery is an alternative strategy, aiming to remove residual tumor that is resistant to

---

Received Nov. 10, 2023; revision accepted Mar. 15, 2024.

For correspondence or reprints, contact Vittoria Rufini (vittoria.rufini@unicatt.it).

*Contributed equally to this work.

chemoradiotherapy. It has been shown that persistence of pathologic residual tumor predicts poor survival in patients treated with this approach (*6,7*).

Recently, there has been growing interest in the extraction and analysis of a variety of quantitative features from medical images, including [^{18}F]FDG PET/CT, denoted as radiomics (*8–10*). In essence, radiomics comprises the shape, intensity, and textural features of the tumor. Shape features describe geometric characteristics of tumors and provide morphologic characterization of [^{18}F]FDG uptake within a specified volume of interest (VOI). Intensity features describe the intensity signal variations in the tumor volume, without reference to their spatial distribution. Textural features are extracted from statistical matrices on the basis of local intensity spatial distribution relationships and reflect tumor [^{18}F]FDG distribution and, so, its heterogeneity (*11*). These features could better predict the histopathologic markers, therapy response, and prognosis than could conventional imaging parameters such as SUV$_{max}$, SUV$_{mean}$, SUV$_{peak}$, metabolically active tumor volume, and total lesion glycolysis (*12*). Previous studies performed on LACC patients treated with exclusive chemoradiotherapy have investigated the use of radiomics derived from pretreatment PET/CT for predicting response to therapy (*13–15*) as well as survival (*15–25*). Even though the results reported are difficult to compare because of the large variability in methodology and lack of standardization, most of the studies showed that texture features were significantly predictive of response (*13–15*) and that the combination of radiomic and clinical features was significantly predictive of recurrence and survival (*16,17,19,21–23*). The aim of our study was to investigate whether radiomic features extracted from pretreatment [^{18}F]FDG PET could predict histopathologic tumor response and survival in LACC patients treated with neoadjuvant chemoradiotherapy followed by surgery in comparison with conventional PET parameters and histopathologic features.

MATERIALS AND METHODS

Patients and Study Protocol

This retrospective study was approved by the Ethical Committee of Fondazione Policlinico Universitario A. Gemelli–IRCCS (study code 3860), and all subjects gave written informed consent. The medical records of all consecutive LACC patients who were referred to the Gynecologic Oncology Unit between July 2010 and July 2016 were reviewed. Women were included if they were at least 18 y old, underwent pretreatment [^{18}F]FDG PET/CT, and received neoadjuvant chemoradiotherapy followed by radical surgery. Additionally, a primary tumor of at least 2.6 cm in diameter on MRI (available in all patients) was necessary to allow heterogeneity quantification on PET, which requires spheric volumes to be larger than 10 cm^3 (*26*). Patients were excluded if they had distant metastatic disease, prior locoregional surgery, prior chemotherapy, locoregional radiation therapy within 5 y, or a plasma glucose level of more than 200 mg/dL before the [^{18}F]FDG PET/CT acquisition.

[^{18}F]FDG PET/CT Image Acquisition

Pretreatment [^{18}F]FDG PET/CT was performed as previously described (*27*). Briefly, images were acquired at a median of 65 min (range, 52–78 min) after intravenous administration of 2.5–4 MBq of [^{18}F]FDG per kilogram on a Gemini GXL (Philips Healthcare) or Biograph mCT (Siemens Healthineers) PET/CT scanner. A low-dose CT scan (110–120 kV, 20–40 mAs) and PET scan (2.5–3.0 min per bed position) were acquired from skull to pelvis according to the European Association of Nuclear Medicine guidelines (*28*) and reconstructed in line with the ^{18}F standard 1 provided by the European Association of Nuclear Medicine Research Ltd.

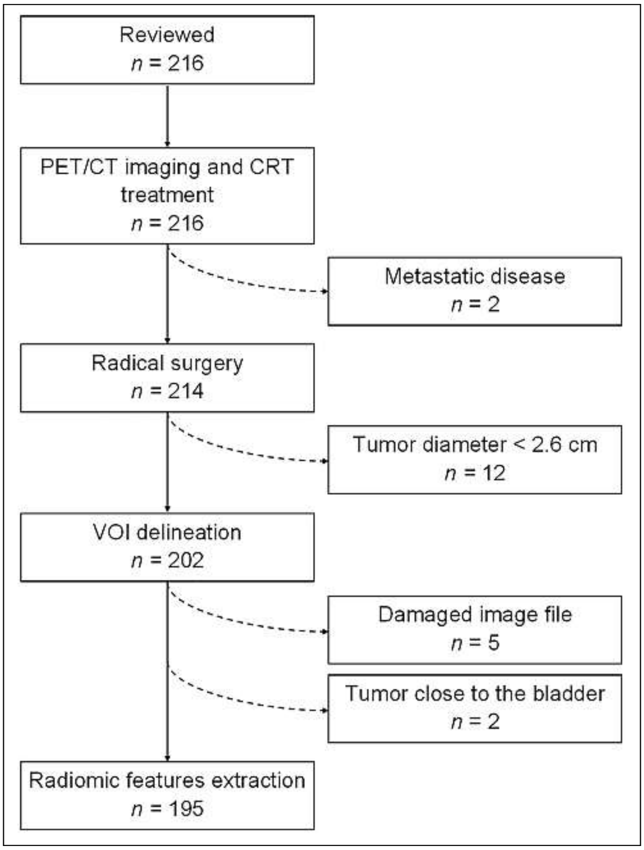

FIGURE 1. Flowchart of study population.

Image Analysis

All PET/CT images were reviewed by consensus between 2 nuclear medicine physicians (with 3 and 8 y of experience), who were masked to clinical, histopathologic, and follow-up information.

VOIs of the primary tumor were drawn semiautomatically with the ACCURATE software (*29,30*) on all PET images using a background-corrected 50% isocontour of the body-weighted SUV$_{peak}$, defined as the highest SUV$_{mean}$ of a 1-mL sphere within the VOI (*31*). Areas of high [^{18}F]FDG uptake close to the primary tumor (e.g., bladder, kidneys, ureters) were excluded manually when necessary. The conventional PET parameters SUV$_{max}$, SUV$_{mean}$, SUV$_{peak}$, metabolically active tumor volume, and total lesion glycolysis were extracted from the original VOIs. In addition, 477 radiomic features were extracted using RaCaT 1.27 software (*32*). Detailed information about the radiomic features can be found in the supplemental materials (available at http://jnm.snmjournals.org) (*11,30,32*).

Neoadjuvant Chemoradiotherapy

Neoadjuvant radiotherapy included whole-pelvis irradiation (10.8 cGy/fraction, 22 fractions) with a total dose of 39.6 Gy, and an additional dose of 10.8 Gy to the primary tumor and parametrium through the concomitant boost technique (0.9 cGy/fraction, 12 fractions every other day). Concomitant chemotherapy included cisplatin (20 mg/m^2, 2-h intravenous infusion) during the first 4 d and last 4 d of treatment, and capecitabine (1,300 mg/m^2/daily, orally administered) during the first 2 wk and last 2 wk of treatment (*33*).

TABLE 1
Clinical, Pathologic, and Treatment Characteristics and Oncologic Outcomes of Whole Study Population (n = 195)

Characteristic	Data
Age at diagnosis (y)	
Mean ± SD	51 ± 12
Median	51 (range, 20–77)
Body mass index (kg/m^2)*	24.0 (range, 15.6–44.5)
Clinical 2009 FIGO stage (*n*)	
IB2	9 (4.6%)
IIA2	16 (8.2%)
IIB	136 (69.7%)
IIIA	8 (4.1%)
IIIB	26 (13.3%)
Median maximum tumor diameter on MRI (cm)	5 (range, 2.6–11.5)
Histotype (*n*)	
Squamous cell carcinoma	169 (86.7%)
Adenocarcinoma	23 (11.8%)
Others	3 (1.5%)
Tumor grade (*n*)	
G1	7/174 (4.0%)
G2	109/174 (62.6%)
G3	58/174 (33.3%)
pR (*n*)	
Complete response	86 (44.1%)
pR1 (≤3 mm)	45 (23.1%)
pR2 (>3 mm)	64 (32.8%)
Median tumor dimension (mm)	1 (range, 0–80)
Positive pelvic or aortic lymph nodes at histology (*n*)	24 (12.3%)
Recurrence/progression (*n*)	61 (31.3%)
Site of recurrence/progression (*n*)	
Local (vaginal/cervical)	3/59 (5.1%)
Regional (pelvic/paraaortic)	16/59 (27.1%)
Distant (upper abdominal/extraabdominal)	25/59 (42.4%)
Local and regional	3/59 (5.1%)
Local and distant	2/59 (3.4%)
Regional and distant	8/59 (13.6%)
Local, regional and distant	2/59 (3.4%)
Cancer-specific death	39 (20.0%)
Median follow-up (mo)†	76.0 (95% CI, 70.7–78.7)
% probability of DFS at 6 y‡	65.5 (95% CI, 57.9–72.1)
% probability of OS at 6 y‡	77.1 (95% CI, 69.9–82.9)

*Information available for 194/195 patients.
†Calculated with inverse Kaplan–Meier technique.
‡Calculated with Kaplan–Meier method.
FIGO = International Federation of Gynecology and Obstetrics; DFS = disease-free survival; OS = overall survival.

Surgery and Histopathology

Patients underwent radical hysterectomy plus pelvic with or without aortic lymphadenectomy. Histopathologic evaluation was performed by a skilled gynecologic oncologist–pathologist. Histopathology subtype (squamous cell carcinoma, adenocarcinoma, others), tumor grade, and pelvic or paraaortic lymph nodes were assessed. Pathologic response (pR) was defined as complete (absence of any residual tumor after treatment at any site level, pR0) or partial, including microscopic (persistent

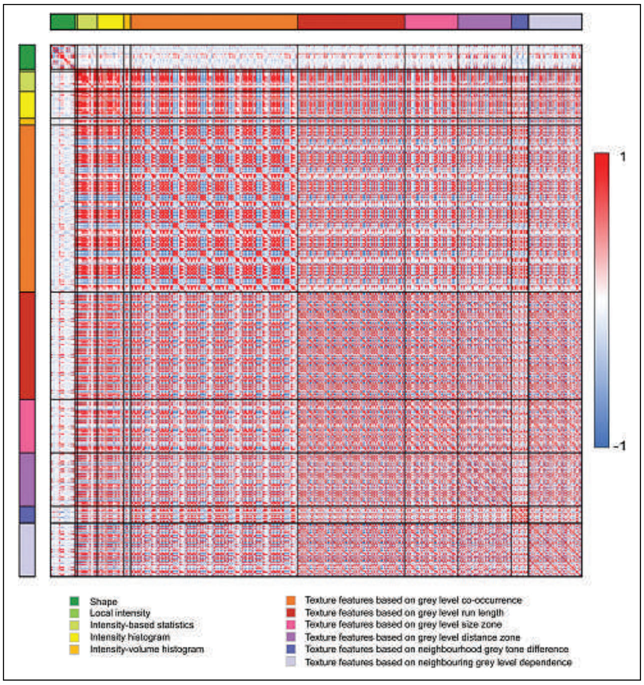

FIGURE 2. Heat map showing correlations between all radiomic features (*n* = 477). Red = high positive correlation; blue = high negative correlation; white = no correlation.

tumor foci ≤ 3 mm, pR1) and macroscopic (persistent tumor foci > 3 mm, pR2) residual tumor. pR0 and pR1 were grouped on the basis of literature results showing similar outcomes in terms of prognosis (*7,33,34*).

Follow-up

Patients underwent follow-up visits every 3 mo for 2 y, then every 6 mo from 2 to 5 y, and annually thereafter according to international guidelines (*3*). Recurrence or progression was diagnosed through biopsy or follow-up imaging. Vaginal or cervical recurrence or progression was classified as local; pelvic or paraaortic, as regional; and upper abdominal or extraabdominal, as distant (*3*).

Data Collection and Statistical Analysis

Data were extracted from the patients' medical records and collected using the REDCap tool hosted at https://redcap-irccs.policlinicogemelli.it (*35*). Study characteristics were presented as number and percentage or as median and range, as appropriate. Mean ± SD was also provided when there was a normal distribution (Shapiro–Wilk test). When necessary for readability, the original radiomic features were linearly transformed by multiplying by powers of 10. An automatic factor analysis was performed with the FMradio package for R as described by Peeters et al. (*36,37*), to identify the latent factors that better represented the extracted features. Detailed information about the dimensionality reduction and feature selection can be found in the supplemental materials (available at http://jnm.snmjournals.org) (*36–38*). The association of clinical characteristics, histopathologic parameters, and radiomic features with pathologic tumor response, disease-free survival, and overall survival was made with the Mann–Whitney *U* or Student *t* test for continuous independent variables and the Pearson χ^2 or Fisher exact test for nominal variables. Disease-free survival and overall survival were defined as the time between the date of diagnosis (biopsy) and the date of the first clinical or imaging detection of recurrence/progression and cancer-specific death, respectively. Patients who did not experience these events were censored to the date of last follow-up or death from any cause. Median follow-up was calculated according to the inverted Kaplan–Meier technique (*39*). Conventional and radiomic features were dichotomized according to receiver-operating-characteristic analysis for pR and cancer-specific death prediction. Best cutoffs were chosen with Liu's method (*40*). Areas under the curve (AUCs) and 95% CIs were provided. An AUC of greater than 0.70 was planned for further analyses (*41*), including logistic and Cox regression analysis for assessing the role of dichotomized conventional and radiomic features in pR and survival prediction, respectively (*42*). As no AUC value reached the cutoff of 0.7, the expected analysis was no longer done. The full analysis was performed both on the whole population and separately according to the PET/CT scanner used. Statistical analyses were performed using Stata Statistical Software (release 17; StataCorp LLC). Two-sided tests were used with a significance level set at a *P* value of less than 0.05, and no imputation was carried out for missing data.

RESULTS

Patients and Follow-up

The records of 216 women with LACC were reviewed. Among these, 195 fulfilled the inclusion criteria (Fig. 1). Most patients had FIGO 2009 IIB stage and histologic grade 2 disease (Table 1). Squamous cell carcinoma was the most frequent histologic subtype. After surgery, 67.2% of patients had pR, including pR0 (44.1%) and pR1 (23.1%); 32.8% had pathologic nonresponse (pR2). Most patients (87.7%) had negative findings for pelvic and aortic lymph nodes. With a median follow-up of 76.0 mo, 31.3% of patients experienced recurrence or progression, and 20.0% died of the disease. Two patients died from other causes: 1 from osteosarcoma and 1 from myocardial infarction, 81 and 31 mo after the cervical cancer diagnosis, respectively.

[^{18}F]FDG PET/CT

Most [^{18}F]FDG PET/CT images (161/195 patients, 82.6%) were acquired on the Gemini GXL. Only 32 patients (16.4%) had high-uptake areas near the primary tumor and required manual correction of the VOI after semiautomatic delineation.

Data Dimensionality Reduction and Radiomic Feature Selection. Figure 2 shows the correlations for all radiomic features. Fifty-five features were retained after performing redundancy filtering. The Kaiser–Meyer–Olkin value of the final model was 0.9, well above the minimum threshold. Factor analysis performed on the 55 features determined 11 latent factors that explained 76% of the variance. These factors corresponded best to the following 11 radiomic features: volume, center of mass shift (CMS), spheric disproportion, flatness, skewness, contrast (2-dimensional [2D] merged neighborhood gray-tone difference matrix [NGTDM] feature [$\text{contrast}_{\text{NGTDM}}$]), normalized inverse difference moment (NIDM) (2D averaged gray-level cooccurrence matrix [GLCM] feature [$\text{NIDM}_{\text{GLCM}}$]), first measure of information correlation (FMIC) (3-dimensional [3D] averaged GLCM feature [$\text{FMIC}_{\text{GLCM}}$]), normalized zone distance nonuniformity (NZDNU) (3D gray-level distance zone matrix (GLDZM) feature [$\text{NZDNU}_{\text{GLDZM}}$]), coarseness (3D NGTDM feature [$\text{coarseness}_{\text{NGTDM}}$]), and low-dependence low–gray-level emphasis (LDLGLE) (3D merged neighborhood gray-level dependence matrix [NGLDM] feature [$\text{LDLGLE}_{\text{NGLDM}}$]).

Although CMS did not show the highest loading with one of the components, it showed the least correspondence to the other components and was therefore selected instead of the best-loading feature for the specific component, that is, large-zone high–gray-level

TABLE 2
Statistically Significant Conventional and Radiomic PET Features of Whole Study Population According to pR and Survival Outcomes

Feature	pR			Recurrence or progression			Cancer-specific death		
	Responders (n = 131)	Nonresponders (n = 64)	*P*	No (n = 134)	Yes (n = 61)	*P*	No (n = 156)	Yes (n = 39)	*P*
Conventional: SUV_{mean} (g/mL)	9.05 (2.00–32.34)	8.10 (3.23–20.11)	0.039*	8.98 (2.00–32.34)	8.64 (2.50–21.85)	0.427	9.00 (2.00–32.34)	8.01 (2.50–15.48)	0.285
Radiomic									
Shape: CMS	1.97 (0.66–14.36)	2.25 (0.93–7.09)	0.035*	1.98 (0.66–14.36)	2.36 (0.81–7.09)	0.014*	2.05 (0.66–14.36)	2.35 (0.81–7.09)	0.074
Texture									
Normalized inverse difference moment (2D averaged GLCM feature) × 10^2	99.61 (94.86–99.87)	99.68 (94.39–99.88)	0.013*	99.62 (94.86–99.83)	99.67 (94.39–99.88)	0.126	99.61 (94.86–99.83)	99.68 (94.39–99.88)	0.010*
Contrast (2D merged NGTDM feature) × 10^2	10.52 (2.10–103.02)	8.54 (1.82–20.38)	0.0007*	10.07 (2.13–60.57)	8.54 (1.82–103.02)	0.023*	9.99 (2.10–103.02)	8.00 (1.82–29.79)	0.010*
Normalized zone distance nonuniformity (3D GLDZM feature) × 10^2	43.74 (22.97–100.00)	47.91 (20.70–100.00)	0.040*	44.50 (20.70–100.00)	45.33 (22.49–83.75)	0.434	44.39 (20.70–100.00)	47.00 (33.73–83.75)	0.119

---

*Statistically significant difference, calculated with 2-sided Mann–Whitney *U* test.

Data are median followed by range in parentheses.

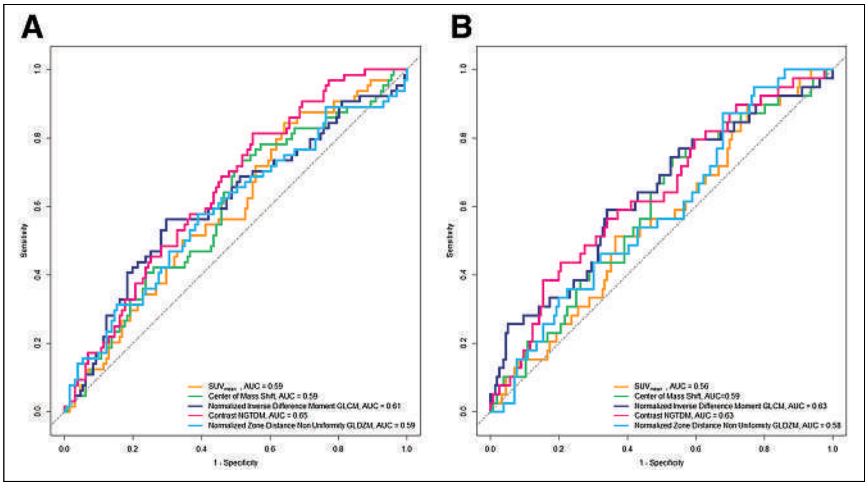

FIGURE 3. Receiver-operating-characteristics curves according to pR (A) and cancer-specific death (B).

emphasis (2D merged gray-level size zone matrix feature). A subanalysis was conducted on the Gemini GXL PET/CT cohort only (Supplemental Table 1 provides clinical data), as the sample size of the Biograph mCT cohort was too limited to perform statistical analysis separately. Ten features were selected, 5 of which had already been selected in the whole analysis (NZDNU$_{GLDZM}$, skewness, contrast$_{NGTDM}$, coarseness$_{NGTDM}$, and FMIC$_{GLCM}$) and 5 of which were different (area density axis-aligned bounding box, volume density axis-aligned bounding box, minimum intensity, large-distance low–gray-level emphasis [3D GLDZM feature], and gray-level nonuniformity [2D averaged GLDZM feature]).

Radiomic Feature Results. Among conventional features, SUV$_{mean}$ was statistically significantly higher in patients achieving pR0–pR1 than in those with pR2 ($P = 0.039$), whereas there were no statistically significant differences in SUV$_{max}$, SUV$_{peak}$, metabolically active tumor volume, and total lesion glycolysis values between the 2 groups of each comparison (Table 2; Supplemental Table 2). In the inferential analysis of the whole cohort, among radiomic features, contrast$_{NGTDM}$ was significantly higher in responders than in nonresponders, in patients without recurrence or progression than in those with recurrence or progression, and in surviving patients than in those who had died from the disease. The opposite behavior was found for CMS, NIDM$_{GLCM}$, and NZDNU$_{GLDZM}$ (Table 2; Supplemental Table 2). Supplemental Table 3 shows the results of statistical analysis of conventional and radiomic features in the Gemini GXL PET/CT cohort, with similar findings for SUV$_{mean}$ and the same radiomic features that were selected in both cohorts. The best cutoffs for conventional PET and radiomic features according to pR and cancer-specific death, and the relative AUCs of receiver-operating-characteristic analysis, are reported in Supplemental Tables 4 and 5 (*40*). All the AUCs were below 0.70; therefore, according to the study protocol, no further analysis was performed (Fig. 3).

DISCUSSION

This study explored the role of radiomic features extracted from pretreatment PET images to predict histo-pR and survival in LACC patients treated with neoadjuvant chemoradiotherapy followed by radical surgery. Among conventional PET parameters, SUV$_{mean}$ was the only discriminator between responder and nonresponder patients. Surprisingly, higher values were found in responders. Conversely, Yang et al. showed that none of the conventional PET parameters were associated with a significant difference between the 2 groups, even though in this study response assessment was imaging-based rather than histopathology-based (*14*). When applying PET-derived parameters in clinical practice, we must consider that [^{18}F]FDG uptake into tumor cells depends on many factors such as upregulation of glucose transporters and hexokinase enzymes, neoangiogenesis, and other factors, which in turn are related to tumor aggressiveness and proliferative activity (*27,43*). At the same time, many factors are responsible for intratumoral heterogeneity, such as necrosis, cellular proliferation, energy metabolism, oxygenation, and neoangiogenesis, which have been associated with tumor aggressiveness and influence biologic behavior and treatment response variability (*44,45*). Therefore, it is of clinical relevance to explore the biologic significance of functional imaging parameters and to evaluate intratumoral heterogeneity before treatment, thus allowing tailored management and improvement of outcome.

Among radiomic features, 1 shape and 3 textural features significantly differed between responders and nonresponders. The shape feature selected in our study was CMS, describing the spatial distribution of low- and high-intensity regions within the VOI; higher values are expected in nonresponders. The 3 textural features selected were NIDM$_{GLCM}$, NZDNU$_{GLDZM}$, and contrast$_{NGTDM}$. NIDM$_{GLCM}$ is a textural feature derived from GLCM matrix measuring the local homogeneity in the gray-level pattern; therefore, higher values are expected in responders. NZDNU$_{GLDZM}$ is a textural feature derived from the GLDZ matrix, measuring the distribution of groups of voxels with the same gray level and the same distance from the VOI edge. Contrast$_{NGTDM}$ is a texture feature derived from NGTD matrix describing the spatial frequency of intensity changes (*11*). Therefore, higher values are expected for these 2 latter features in nonresponders. On the basis of these explanations, the results for CMS and NZDNU$_{GLDZM}$ were no surprise, as higher values were found in nonresponders, indicating that the patterns of intratumoral [^{18}F]FDG uptake at baseline would be more heterogeneous at a regional level. Conversely, NIDM$_{GLCM}$ and contrast$_{NGTDM}$ results were not in line with expectations. In our series, 3 radiomic features significantly differed between presence and absence of recurrence or progression and between presence and absence of cancer-specific death groups. Also in this case, discrepancies were found. As expected, we observed higher CMS values in patients with a worse prognosis, whereas NIDM$_{GLCM}$ and contrast$_{NGTDM}$ values were not as expected.

We chose to dichotomize the conventional and radiomic features according to receiver-operating-characteristic analysis to retrieve cutoffs, which are a tool immediately usable by physicians for incorporating the results into clinical decision-making algorithms. Indeed, this is one of the major challenges of radiomics. The AUCs, a measure of predictive performance, were less than 0.70 for all parameters. According to the study protocol, univariate and multivariate logistic regression analyses were not performed, indicating that no conventional or radiomic features were predictive of pR and survival.

TABLE 3
Characteristics of Current and Previous Studies

Author	Study design	No. of patients	FIGO stage	Primary treatment	Imaging	Training/ validation set	Outcomes	Follow-up (mo)	Feature type	Best AUC
Yang et al. (*13*)	Retrospective	20	IB1-IVA	CCRT + BT	PET	No	RTT	—	6 texture features	NA
Yang et al. (*14*)	Retrospective	90	IB2-IVA	CCRT + BT	PET	No	RTT	—	4 texture features	RTT (energy$_{GLCM}$) = 0.659 (0.534–0.756)
Ho et al. (*15*)	Prospective	44	IB-IIIB	CCRT + BT	PET	No	RTT; OS	56 (10–83)	4 texture features	RTT (GLNU$_{GLRLM}$) = 0.76 (0.56–0.88)
Reuzé et al. (*16*)	Retrospective	118	IB1-IVB	CCRT + BT	PET	Group 1 = 79; group 2 = 39	LR	36 (median)	Mixed*	LR = 0.86 (0.75–0.97)
Altazi et al. (*17*)	Retrospective	80	IB-IVA	CCRT + BT	PET	TS = 56; VS = 24	DM; LRR	19 (mean)	Mixed*	DM = 0.92 (SE 0.07); LRR = 0.92 (SE 0.05)
Chen et al. (*18*)	Retrospective	142	IB-IIIB	CCRT + BT	PET	TS = 77; VS = 65	OS; PFS; DMFS; PRFS	40 (7–84)	7 texture features	PRFS (HGRE$_{GLRLM}$) = 0.31; PFS = 0.36
Schernberg et al. (*19*)	Retrospective	108	IB1-IVA	CCRT + BT	PET	TS = 69; VS = 39	LRC; OS	TS = 57.0 (6.8–100.6); VS = 30.8 (5.0–60.0)	Mixed*	NA
Lucia et al. (*20*)	Retrospective	102	IB1-IVA	CCRT + BT	PET; MRI	TS = 69; VS = 33	DFS; LRC	TS = 36 (6–79);VS = 17 (6–30)	1 texture feature	LRC (GLNU$_{GLRLM}$) = 0.95
Lucia et al. (*21*)	Retrospective multicenter	190	IB1-IVA	CCRT + BT	PET; MRI	TS = 112; VS = 78	DFS; LRC	TS = 24.3 (6.0–83.0); VS1 = 33 (14–50); VS2 = 26 (7–86)	Mixed*	LRC = 0.93
Mu et al. (*22*)	Retrospective multicenter	154	IIB-IVA	CCRT + BT	PET; CT	TS = 78; VS = 76	PFS; OS	TS = 28 (15–39); VS = 25 (15–36)	Mixed*	PFS = 0.72OS = 0.79
Ferreira et al. (*23*)	Retrospective multicenter	158	IB1-IVA	CCRT + BT	PET	TS 80%; VS 20%	DFS	23 (4–84)	Mixed*	DFS = 0.78 (0.67–0.88)
de Alencar et al. (*24*)	Retrospective	47	IB2-IVA	CCRT + BT	PET	No	OS	23.5 (3.7–39.0)	3 texture features	OS (LRLGE$_{GLRLM}$) = 0.74
Cho et al. (*25*)	Retrospective multicenter	68	IIB-IVA	CCRT + BT	PET	No	OS; PFS	49 (12–139)	1 texture feature	PFS (GLNU$_{GLRLM}$) = 0.85 (0.74–0.92)
Current study	Retrospective	195	IB2-IIIB	CRT + surgery	PET	No	pR; DFS; OS	76.0 (70.7–78.7)	1 shape and 3 texture features	pR = 0.65 (0.57–0.73); OS = 0.63 (0.54–0.73)

---

*Radiomic signature models with or without clinical, CT, or MRI features.

FIGO = International Federation of Gynecology and Obstetrics; CCRT = concurrent chemoradiotherapy; BT = brachytherapy; RTT = response to treatment; NA = not available; energy$_{GLCM}$ = energy derived from gray-level cooccurrence matrix; OS = overall survival; GLNU = gray-level nonuniformity; GLRLM = gray-level run-length matrix; LR = local recurrence; TS = training set; VS = validation set; DM = distant metastasis; LRR = locoregional recurrence; OS = overall survival; PFS = progression-free survival; DMFS = distant metastasis-free survival; PRFS = pelvic relapse-free survival; HGRE = high gray-level run emphasis; LRC = locoregional control; DFS = disease-free survival; LRLGE = long runs gray-level emphasis.

Several articles regarding PET radiomics in LACC patients have been published (Table 3). Just 1 study had a prospective design (*15*). Only 3 studies investigated PET radiomic features to predict response (*13–15*), whereas most assessed PET radiomic features to predict outcome (*15–25*). In most studies, texture features were significantly predictive of outcome, mainly progression-free survival and overall survival. According to Lucia et al., added value might be derived from the combination of PET and MRI radiomic features, as these 2 techniques are currently performed in standard clinical care (*20,21*). Only the study by Ferreira et al. was in line with our results, showing that no individual radiomic or clinical features were significantly associated with cancer recurrence (*23*). Importantly, the previous studies show huge variability regarding study protocol, image acquisition parameters, extraction and reduction of radiomic features, type of validation methods, and clinical outcome, affecting the reproducibility and robustness of radiomics (*8,46,47*) and emphasizing the need for further standardization of radiomic research to facilitate direct comparisons. Parallel to these considerations, we believe that our results, albeit negative, might impact current and future investigations, with the ultimate goal of exploring the biologic mechanisms underlying radiomic results (*48*).

This study had several strengths, the first being the novelty of using PET radiomic features to predict the pR in LACC patients undergoing chemoradiotherapy followed by radical surgery. A second strength was that the study included the—to our knowledge—largest cohort of LACC patients with the longest follow-up (*13–25*). Another strength was that a fixed-threshold approach was used to segment the primary tumor, which led to consistent results in the radiomic characteristics extracted from PET images (*49*). All features were extracted using software (*32*) that complies with the guidelines of the Imaging Biomarker Standardization Initiative (*11*). In radiomic studies, the problem of multiple testing or multicollinearity yields the problem of results that are falsely statistically significant (*38,49*). We addressed this problem by performing dimensionality reduction, leaving only 11 imaging features that explained most of the variance of our dataset.

This study also had some limitations. The first was its retrospective nature, like most radiomic studies (*13,14,16–25*). Second, we chose not to split our cohort into training and testing (internal validation) sets because of the limited number of events and the poor-to-moderate accuracy of the AUCs retrieved (*50*). We intend to further validate our findings in an external cohort of patients in a prospective multicenter study. Third, PET/CT images were acquired using 2 different PET/CT scanners. Nevertheless, all images were reconstructed in accordance with the European Association of Nuclear Medicine Research Ltd. standard (*28*), which has been shown to harmonize a wide range of radiomic features (*51*). Alternatively, when European Association of Nuclear Medicine Research Ltd.–compliant reconstructions are not available, radiomic features can be harmonized using ComBat (*52*).

CONCLUSION

One of the major challenges of radiomics is its incorporation into clinical decision-making algorithms for routine application. Our results in LACC patients treated by chemoradiotherapy followed by surgery indicate that this goal has not yet been reached, as [^{18}F]FDG PET radiomic features could not predict histopathologic tumor response and survival up front. In this setting, it is crucial to further explore the biologic significance of image-derived parameters and plan a large, prospective, multicenter study with standardized protocols for all phases of radiomic analysis (from image acquisition to tumor segmentation, image processing, feature extraction and reduction, and model evaluation) to assess the impact of radiomics on personalized medicine and definitively validate its use in clinical routine.

DISCLOSURE

This study was supported by an internal university grant (Università Cattolica Line D.1 2023-R4124501401) to Vittoria Rufini. No other potential conflict of interest relevant to this article was reported.

KEY POINTS

QUESTION: Does upfront PET radiomics predict treatment response and survival in LACC?

PERTINENT FINDINGS: Our retrospective study demonstrated that no radiomic features extracted from upfront PET/CT could predict pathologic tumor response or survival in 195 patients with LACC.

IMPLICATIONS FOR PATIENT CARE: Our negative results suggest that radiomic implementation in clinical routine is still a challenge and needs to be addressed by exploring the biologic significance of image-derived parameters and by performing a prospective, multicenter study with standardized protocols for all phases of radiomic analysis.

REFERENCES

1. Sung H, Ferlay J, Siegel RL, et al. Global cancer statistics 2020: GLOBOCAN estimates of incidence and mortality worldwide for 36 cancers in 185 countries. *CA Cancer J Clin.* 2021;71:209–249.
2. Cibula D, Raspollini MR, Planchamp F, et al. ESGO/ESTRO/ESP guidelines for the management of patients with cervical cancer: update 2023. *Int J Gynecol Cancer.* 2023;33:649–666.
3. Abu-Rustum NR, Yashar CM, Arend R, et al. NCCN clinical practice guidelines in oncology (NCCN guidelines): cervical cancer—version 2.2024. National Comprehensive Cancer Network website. https://www.nccn.org/professionals/physician_gls/pdf/cervical.pdf. Published February 23, 2024. Accessed March 19, 2024.
4. Grigsby PW. The prognostic value of PET and PET/CT in cervical cancer. *Cancer Imaging.* 2008;8:146–155.
5. Espenel S, Garcia MA, Trone JC, et al. From IB2 to IIIB locally advanced cervical cancers: report of a ten-year experience. *Radiat Oncol.* 2018;13:16.
6. Ferrandina G, Legge F, Fagotti A, et al. Preoperative concomitant chemoradiotherapy in locally advanced cervical cancer: safety, outcome, and prognostic measures. *Gynecol Oncol.* 2007;107(suppl 1):S127–S132.
7. Federico A, Anchora LP, Gallotta V, et al. Clinical impact of pathologic residual tumor in locally advanced cervical cancer patients managed by chemoradiotherapy followed by radical surgery: a large, multicenter, retrospective study. *Ann Surg Oncol.* 2022;29:4806–4814.
8. Lambin P, Leijenaar RTH, Deist TM, et al. Radiomics: the bridge between medical imaging and personalized medicine. *Nat Rev Clin Oncol.* 2017;14:749–762.
9. Hatt M, Le Rest CC, Tixier F, Badic B, Schick U, Visvikis D. Radiomics: data are also images. *J Nucl Med.* 2019;60(suppl 2):38S–44S.
10. Mayerhoefer ME, Materka A, Langs G, et al. Introduction to radiomics. *J Nucl Med.* 2020;61:488–495.
11. Zwanenburg A, Vallières M, Abdalah MA, et al. The image biomarker standardization initiative: standardized quantitative radiomics for high-throughput image-based phenotyping. *Radiology.* 2020;295:328–338.
12. Hatt M, Tixier F, Pierce L, Kinahan PE, Le Rest CC, Visvikis D. Characterization of PET/CT images using texture analysis: the past, the present… any future? *Eur J Nucl Med Mol Imaging.* 2017;44:151–165.
13. Yang F, Thomas MA, Dehdashti F, Grigsby PW. Temporal analysis of intratumoral metabolic heterogeneity characterized by textural features in cervical cancer. *Eur J Nucl Med Mol Imaging.* 2013;40:716–727.

14. Yang F, Young L, Grigsby P. Predictive value of standardized intratumoral metabolic heterogeneity in locally advanced cervical cancer treated with chemoradiation. *Int J Gynecol Cancer.* 2016;26:777–784.
15. Ho K-C, Fang Y-HD, Chung H-W, et al. A preliminary investigation into textural features of intratumoral metabolic heterogeneity in ^{18}F-FDG PET for overall survival prognosis in patients with bulky cervical cancer treated with definitive concurrent chemoradiotherapy. *Am J Nucl Med Mol Imaging.* 2016;6:166–175.
16. Reuzé S, Orlhac F, Chargari C, et al. Prediction of cervical cancer recurrence using textural features extracted from ^{18}F-FDG PET images acquired with different scanners. *Oncotarget.* 2017;8:43169–43179.
17. Altazi BA, Fernandez DC, Zhang GG, et al. Investigating multi-radiomic models for enhancing prediction power of cervical cancer treatment outcomes. *Phys Med.* 2018;46:180–188.
18. Chen S-W, Shen W-C, Hsieh T-C, et al. Textural features of cervical cancers on FDG-PET/CT associate with survival and local relapse in patients treated with definitive chemoradiotherapy. *Sci Rep.* 2018;8:11859.
19. Schernberg A, Reuze S, Orlhac F, et al. A score combining baseline neutrophilia and primary tumor SUVpeak measured from FDG PET is associated with outcome in locally advanced cervical cancer. *Eur J Nucl Med Mol Imaging.* 2018;45:187–195.
20. Lucia F, Visvikis D, Desseroit MC, et al. Prediction of outcome using pretreatment ^{18}F-FDG PET/CT and MRI radiomics in locally advanced cervical cancer treated with chemoradiotherapy. *Eur J Nucl Med Mol Imaging.* 2018;45:768–786.
21. Lucia F, Visvikis D, Vallières M, et al. External validation of a combined PET and MRI radiomics model for prediction of recurrence in cervical cancer patients treated with chemoradiotherapy. *Eur J Nucl Med Mol Imaging.* 2019;46:864–877.
22. Mu W, Liang Y, Hall LO, et al. ^{18}F-FDG PET/CT habitat radiomics predicts outcome of patients with cervical cancer treated with chemoradiotherapy. *Radiol Artif Intell.* 2020;2:e190218.
23. Ferreira M, Lovinfosse P, Hermesse J, et al. [^{18}F]FDG PET radiomics to predict disease-free survival in cervical cancer: a multi-scanner/center study with external validation. *Eur J Nucl Med Mol Imaging.* 2021;48:3432–3443.
24. de Alencar NRG, Machado MAD, Mourato FA, et al. Exploratory analysis of radiomic as prognostic biomarkers in ^{18}F-FDG PET/CT scan in uterine cervical cancer. *Front Med (Lausanne).* 2022;9:1046551.
25. Cho H-W, Lee ES, Lee JK, Eo JS, Kim S, Hong JH. Prognostic value of textural features obtained from F-fluorodeoxyglucose (F-18 FDG) positron emission tomography/computed tomography (PET/CT) in patients with locally advanced cervical cancer undergoing concurrent chemoradiotherapy. *Ann Nucl Med.* 2023; 37:44–51.
26. Hatt M, Majdoub M, Vallières M, et al. ^{18}F-FDG PET uptake characterization through texture analysis: investigating the complementary nature of heterogeneity and functional tumor volume in a multi-cancer site patient cohort. *J Nucl Med.* 2015;56:38–44.
27. Rufini V, Collarino A, Calcagni ML, et al. The role of ^{18}F-FDG-PET/CT in predicting the histopathological response in locally advanced cervical carcinoma treated by chemo-radiotherapy followed by radical surgery: a prospective study. *Eur J Nucl Med Mol Imaging.* 2020;47:1228–1238.
28. Boellaard R, Delgado-Bolton R, Oyen WJG, et al. FDG PET/CT: EANM procedure guidelines for tumour imaging—version 2.0. *Eur J Nucl Med Mol Imaging.* 2015;42:328–354.
29. Boellaard R. Quantitative oncology molecular analysis suite: ACCURATE [abstract]. *J Nucl Med.* 2018;59(suppl 1):1753.
30. Collarino A, Garganese G, Fragomeni SM, et al. Radiomics in vulvar cancer: first clinical experience using ^{18}F-FDG PET/CT images. *J Nucl Med.* 2018;60:199–206.
31. Frings V, Van Velden FHP, Velasquez LM, et al. Repeatability of metabolically active tumor volume measurements with FDG PET/CT in advanced gastrointestinal malignancies: a multicenter study. *Radiology.* 2014;273:539–548.
32. Pfaehler E, Zwanenburg A, de Jong JR, Boellaard R. RACAT: an open source and easy to use radiomics calculator tool. *PLoS One.* 2019;14:e0212223.
33. Ferrandina G, Margariti PA, Smaniotto D, et al. Long-term analysis of clinical outcome and complications in locally advanced cervical cancer patients administered concomitant chemoradiation followed by radical surgery. *Gynecol Oncol.* 2010; 119:404–410.
34. Zannoni GF, Vellone VG, Carbone A. Morphological effects of radiochemotherapy on cervical carcinoma: a morphological study of 50 cases of hysterectomy specimens after neoadjuvant treatment. *Int J Gynecol Pathol.* 2008;27:274–281.
35. Harris PA, Taylor R, Thielke R, Payne J, Gonzalez N, Conde JG. Research electronic data capture (REDCap): a metadata-driven methodology and workflow process for providing translational research informatics support. *J Biomed Inform.* 2009;42:377–381.
36. Peeters CFW, Übelhör C, Mes SW, et al. Stable prediction with radiomics data. arXiv website. https://doi.org/10.48550/arXiv.1903.11696. Published March 27, 2019. Accessed March 19, 2024.
37. The R project for statistical computing. R Foundation website. https://www.R-project.org/. Accessed March 19, 2024.
38. Chalkidou A, O'Doherty MJ, Marsden PK. False discovery rates in PET and CT studies with texture features: a systematic review. *PLoS One.* 2015;10:e0124165.
39. Schemper M, Smith TL. A note on quantifying follow-up in studies of failure time. *Control Clin Trials.* 1996;17:343–346.
40. Liu X. Classification accuracy and cut point selection. *Stat Med.* 2012;31:2676–2686.
41. Hosmer DW, Lemeshow S. Assessing the fit of the model. In: *Applied Logistic Regression.* John Wiley & Sons, Ltd; 2000:160–164.
42. Cox DR. Regression models and life-tables. *J R Stat Soc Series B Stat Methodol.* 1972;34:187–202.
43. Bos R, van Der Hoeven JJM, van Der Wall E, et al. Biologic correlates of ^{18}fluorodeoxyglucose uptake in human breast cancer measured by positron emission tomography. *J Clin Oncol.* 2002;20:379–387.
44. Pugachev A, Ruan S, Carlin S, et al. Dependence of FDG uptake on tumor microenvironment. *Int J Radiat Oncol Biol Phys.* 2005;62:545–553.
45. Zhao S, Kuge Y, Mochizuki T, et al. Biologic correlates of intratumoral heterogeneity in ^{18}F-FDG distribution with regional expression of glucose transporters and hexokinase-II in experimental tumor. *J Nucl Med.* 2005;46:675–682.
46. Vallières M, Zwanenburg A, Badic B, Cheze Le Rest C, Visvikis D, Hatt M. Responsible radiomics research for faster clinical translation. *J Nucl Med.* 2018;59: 189–193.
47. Sollini M, Antunovic L, Chiti A, Kirienko M. Towards clinical application of image mining: a systematic review on artificial intelligence and radiomics. *Eur J Nucl Med Mol Imaging.* 2019;46:2656–2672.
48. Buvat I, Orlhac F. The dark side of radiomics: on the paramount importance of publishing negative results. *J Nucl Med.* 2019;60:1543–1544.
49. Limkin EJ, Sun R, Dercle L, et al. Promises and challenges for the implementation of computational medical imaging (radiomics) in oncology. *Ann Oncol.* 2017;28: 1191–1206.
50. Swets JA. Indices of discrimination or diagnostic accuracy: their ROCs and implied models. *Psychol Bull.* 1986;99:100–117.
51. Pfaehler E, Van Sluis J, Merema BBJ, et al. Experimental multicenter and multivendor evaluation of the performance of PET radiomic features using 3-dimensionally printed phantom inserts. *J Nucl Med.* 2020;61:469–476.
52. Orlhac F, Eertink JJ, Cottereau AS, et al. A guide to ComBat harmonization of imaging biomarkers in multicenter studies. *J Nucl Med.* 2022;63:172–179.

Mapping ^{18}F-FDG Kinetics Together with Patient-Specific Bootstrap Assessment of Uncertainties: An Illustration with Data from a PET/CT Scanner with a Long Axial Field of View

Qi Wu[1], Fengyun Gu[1], Liam D. O'Suilleabhain[1], Hasan Sari[2], Song Xue[3], Kuangyu Shi[3], Axel Rominger[3], and Finbarr O'Sullivan[1]

[1]Department of Statistics, School of Mathematical Sciences, University College Cork, Cork, Ireland; [2]Advanced Clinical Imaging Technology, Siemens Healthcare AG, Lausanne, Switzerland; and [3]Department of Nuclear Medicine, Bern University Hospital, University of Bern, Bern, Switzerland

The purpose of this study was to examine a nonparametric approach to mapping kinetic parameters and their uncertainties with data from the emerging generation of dynamic whole-body PET/CT scanners. **Methods:** Dynamic PET ^{18}F-FDG data from a set of 24 cancer patients studied on a long-axial-field-of-view PET/CT scanner were considered. Kinetics were mapped using a nonparametric residue mapping (NPRM) technique. Uncertainties were evaluated using an image-based bootstrapping methodology. Kinetics and bootstrap-derived uncertainties are reported for voxels, maximum-intensity projections, and volumes of interest (VOIs) corresponding to several key organs and lesions. Comparisons between NPRM and standard 2-compartment (2C) modeling of VOI kinetics are carefully examined. **Results:** NPRM-generated kinetic maps were of good quality and well aligned with vascular and metabolic ^{18}F-FDG patterns, reasonable for the range of VOIs considered. On a single 3.2-GHz processor, the specification of the bootstrapping model took 140 min; individual bootstrap replicates required 80 min each. VOI time-course data were much more accurately represented, particularly in the early time course, by NPRM than by 2C modeling constructs, and improvements in fit were statistically highly significant. Although ^{18}F-FDG flux values evaluated by NPRM and 2C modeling were generally similar, significant deviations between vascular blood and distribution volume estimates were found. The bootstrap enables the assessment of quite complex summaries of mapped kinetics. This is illustrated with maximum-intensity maps of kinetics and their uncertainties. **Conclusion:** NPRM kinetics combined with image-domain bootstrapping is practical with large whole-body dynamic ^{18}F-FDG datasets. The information provided by bootstrapping could support more sophisticated uses of PET biomarkers used in clinical decision-making for the individual patient.

Key Words: dynamic PET studies; kinetic mapping; image-domain bootstrap; uncertainty assessment; compartment model

J Nucl Med 2024; 65:971–979
DOI: 10.2967/jnumed.123.266686

High-resolution dynamic whole-body PET scanning enhances the ability to map metabolic characteristics of tissue, particularly in the context of cancer. The current focus has been on dynamic PET studies with ^{18}F-FDG using the well-established Huang–Sokoloff 2-compartment (2C) modeling framework (*1–3*). Although 2C modeling has had widespread application in PET imaging, far beyond the brain setting in which it was developed, the biochemical understanding of the transporters involved in the metabolism of ^{18}F-FDG and their distribution across normal and cancerous tissues has evolved in the years since the Huang–Sokoloff construct was proposed (*4–7*). The temporal and spatial resolutions of emerging scanners have transformed the ability to objectively assess the accuracy of the 2C framework to represent ^{18}F-FDG time-course data across the diverse tissues encountered in the human body. In this context, the assessment of ^{18}F-FDG kinetics based on more flexible nonparametric analysis approaches (*8*,*9*) may be necessary. The most recent implementation of the nonparametric voxel-level analysis scheme (*9*) is particularly efficient, largely because of an extensive reliance on quadratic programming techniques, and its nonparametric aspect provides an ability to apply an image-domain bootstrapping process for evaluation of statistical uncertainties in derived kinetic maps and associated biomarkers (*10*,*11*). Uncertainties in diagnostic information recovered from PET scans could augment decision-making for individual patients that is based on complex nonlinear radiomic metrics derived from a kinetic map.

The volume of data produced by a dynamic ^{18}F-FDG PET study on a state-of-the-art scanner with a long axial field of view (FOV) is a practical computational challenge for voxel-level analysis of kinetics. The bootstrap uncertainty assessment requires that comprehensive voxel-level analyses be applied to multiple simulated datasets, each created to match the full character and extent of the original data. This significantly adds to the computational challenge involved.

The work here uses a series of dynamic ^{18}F-FDG data acquired on a long-axial-FOV scanner (*2*) to investigate the approach. Apart from the demonstration of the practical feasibility of kinetic mapping with uncertainty evaluation, the analysis allows regional comparisons between nonparametric and 2C modeling results in terms of both derived kinetics and accuracy of data representation.

Received Sep. 17, 2023; revision accepted Feb. 13, 2024.

For correspondence or reprints, contact Finbarr O'Sullivan (f.osullivan@ucc.ie).

MATERIALS AND METHODS

An extended materials and methods description is provided in the supplemental materials (supplemental materials are available at http://jnm.snmjournals.org) (*12*).

Patient Scans and Volumes of Interest (VOIs)

The data considered arise from a set of 24 patients with different types of cancer who participated in an institutionally approved ^{18}F-FDG PET/CT study at Bern University Hospital (KEK 2019-02,193). Details of the study were reported previously (*2*). In summary, PET scanning was conducted on a Biograph Vision Quadra scanner (Siemens) with a 106-cm axial FOV and a nominal in-plane resolution of 3.3 mm in full width at half maximum (*13*). Data were acquired in list mode starting 15 s before an intravenous bolus injection of ^{18}F-FDG (with activity of ∼3 MBq/kg of patient weight) to the left or right arm, followed by flushing with 50 mL of saline solution. The plasma glucose level was measured for each patient. Emission data were acquired for 65 min and binned into 62 contiguous time frames with durations of 2 × 10 s, 30 × 2 s, 4 × 10 s, 8 × 30 s, 4 × 60 s, 5 × 120 s, and 9 × 300 s. Images were reconstructed with a voxel size of 1.65 × 1.65 × 1.65 mm^3. Low-dose CT scans (voltage, 120 kV; tube current, 25 mA; CARE Dose4D and CARE kV [Siemens]) were acquired as part of the examinations. The CT images were reconstructed with a voxel size of 1.52 × 1.52 × 1.65 mm^3.

Automated segmentation algorithms based on CT and PET were used to define VOIs corresponding to several tissue structures, including gray and white matter in the brain, liver, lungs, kidneys, spleen, and bones (*2*). A further set of 49 VOIs corresponding to tumor tissue was identified by an experienced nuclear medicine physician. Finally, a VOI placed in the descending aorta was used to define the whole-blood arterial input function (AIF) used for kinetic analyses (*2*). Further scanning and study protocol details are available in the supplemental materials.

Parametric Imaging Techniques

Tissue Residue and Kinetic Parameters. When the Meier–Zierler (*14*) formalism is followed, the analysis assumes the PET-measured time course for a tissue region is represented as a convolution between the local AIF, C_p, and the regional tissue residue function. Kinetic parameters are defined in terms of this residue (Fig. 1). Large-vessel vascular blood and distribution volumes (V_b and V_d, respectively) are evaluated as areas under the tissue residue. The apparent rate of retention or flux (K_i) of the tracer, measurable by PET over the scan duration, is the height of the residue at the end of the acquisition period. Also, the mean transit time of the tracer in the tissue and extraction fraction are defined as ratios of amplitude and integral measurements. A variety of approaches might be used to approximate the residue: a nonparametric method is used here. Patlak analysis uses a constant residue (*15*). Compartmental model forms, for example, the 1-compartment Kety–Schmidt (*16*) model for water and the 2C Huang–Sokoloff (*17*) model for ^{18}F-FDG in the brain, represent residues by positive linear combination of exponentials. In the 6-parameter 2C model, there is additive adjustment for an arterial signal. By adding a sharp residue element to the 2-exponential form, a Meier–Zierler residue is also available for this model. This allows residue-defined metabolic parameters for the extended compartmental model to be evaluated via the decomposition shown in Figure 1 (*18*). Supplemental materials provide a review of how Meier–Zierler residue parameters link with rate constants in the 2C model.

Nonparametric Residue Mapping (NPRM) of Kinetics. NPRM approximates the voxel-level residue by the positive linear sum-of-basis elements that have been selected by a cross-validation–guided analysis of a comprehensive collection of time courses produced by segmentation of all the available data in the study (*10*,*18*). Individual basis elements are of the form $\mu_k(t)=\int_0^t R_k(s)C_p(s-\Delta_k)\mathrm{d}s$ for k of 1, 2,..., K. Here, R_k is the basis element residue and Δ_k is its associated delay factor. Note that cross validation is used to select the number of basis elements (K). Given the basis set, PET-measured voxel-level time-course data over the available set of J time frames, $\{z(t_j), j=1,2,\ldots,J\}$, is expressed as

$$z(t_j)=\alpha_1\mu_1(t_j-\delta)+\ldots+\alpha_K\mu_K(t_j-\delta)+\epsilon(t_j). \qquad \text{Eq. 1}$$

Here, δ and (α_1, α_2,..., α_K) are the unknown voxel-level delay and basis-amplitude parameters, respectively, and $\epsilon(t)$ represents (random) model error. A weighted least-squares criterion, with weights proportional to the product of the frame duration and the decay correction factor used to convert raw counts to decay-corrected tracer activity, is used for optimization of the unknown parameters. For any delay, the optimal set of α coefficients is found by quadratic programming. A crude grid search is used to optimize delay (*10*).

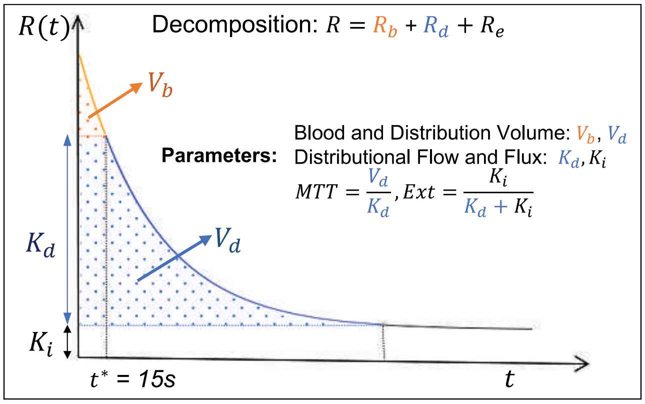

FIGURE 1. Meier–Zierler tissue residue (R) with decomposition into vascular (R_b), in-distribution (R_d), and extracted (R_e) components. Decomposition was used to define indicated metabolic parameters. MTT = mean transit time; Ext = extraction fraction.

Bootstrap Assessment of Uncertainty. Model residuals across N voxels and J time frames, $\{z_i(t_j)-\hat{z}_i(t_j), i=1,\ldots,N; j=1,2,\ldots,J\}$, are used to construct an image-domain data generation process (DGP) for bootstrapping. The DGP generates data according to

$$z_i^*(t_j)=\hat{z}_i(t_j)+\epsilon_i^*(t_j), \qquad \text{Eq. 2}$$

where $\hat{z}(t_j)=\hat{\alpha}_1\mu_1(t_j-\hat{\delta})+\ldots+\hat{\alpha}_K\mu_K(t_j-\hat{\delta})$ and the simulated error process, ϵ^*, mimic the stochastic character of analysis residuals. Analysis of bootstrapped datasets arising from the DGP leads to a set of bootstrapped kinetic parameter values at each voxel. The SD of these values estimates the voxel-level SE of the kinetic parameter. Similarly, the SEs for more complex quantities, such as the maximum-intensity projection (MIP) for a kinetic map, are created as the SD of the bootstrapped MIPs of the kinetic parameter (Fig. 2). Numeric studies (*10*,*11*) have shown that image-domain DGP bootstrapping matches the accuracy of the much more computationally intensive list-mode bootstrapping approach of Haynor and Woods (*19*).

The number of bootstrap simulations impacts the accuracy of the SEs it produces (*20*); this is discussed in the supplemental materials.

Statistical Analysis

NPRM kinetic analysis with 25 bootstrapped simulations is evaluated for each of the studies in the series. Results are examined in 4 separate ways. Technical details with formulas are in the supplemental materials.

Representation of VOI Time-Course Data. Mean VOI time-course data are compared with the corresponding mean VOIs of the fitted voxel-level time courses, $\hat{z}(t_j)$, in Equation 2. Mean VOI time-course data are also analyzed using the nonparametric model and the Huang–Sokoloff 2C model including a fractional V_b and delay of the

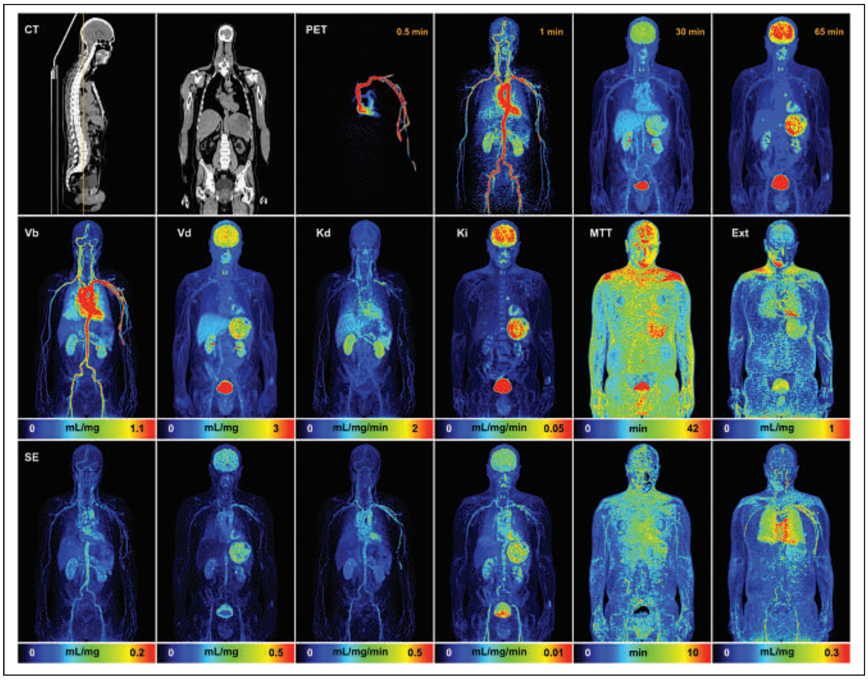

FIGURE 2. MIP maps of NPRM kinetic parameters and associated SE. SEs are based on SD of MIP results for each of 25 bootstrap replications. Top row shows CT images for selected cross sections through volume and PET MIP maps at indicated times. $K = 9$ basis elements were determined for data by NPRM methodology. MTT = mean transit time; Ext = extraction fraction.

AIF. To facilitate fitting, a wide range of delays of ±5 min is allowed in the NPRM and 2C analysis of the VOI time-course data. The Broyden–Fletcher–Goldfarb–Shanno algorithm as implemented in the optim function in R (R Foundation for Statistical Computing) is used for optimization of the 2C model; more details are shown in the supplemental materials and Supplemental Figure 1.

Results of alternative analyses for a sample case are presented graphically. Formal comparisons are focused on the weighted-residual-sums-of-squares misfit achieved with alternative analyses. The mean relative difference between alternative representations of VOI time-course data and the associated SD is evaluated for each VOI type considered.

VOI Kinetics. Means and SDs of VOI-averaged NPRM kinetics are reported for each VOI type. Kinetics based on nonparametric and 2C analyses of VOI mean time-course data are similarly summarized. Deviations between alternative VOI kinetic values are summarized, and their statistical significance is evaluated using the paired Wilcoxon test.

DGP Model. The bootstrap DGP is expressed in more detail as

$$z_i^*(t_j)=\hat{z}_i(t_j)+\hat{\sigma}_e\hat{\psi}_i\hat{\varphi}_j\epsilon_i^*(t_j), \qquad \text{Eq. 3}$$

where the random errors, $\epsilon_i^*(t)$, are in units of SD and $\hat{\sigma}_e$ is an overall scale of the model error. In Equation 3, the factors $\hat{\psi}_i$ and $\hat{\varphi}_j$ are scale-free quantities representing the relative uncertainty across voxels (i) and time frames (j). As the PET-measured activity scales with dose, the DGP error scale ($\hat{\sigma}_e$) should also scale with dose; this is examined graphically. The overall axial pattern variation is described by the scale factor $\hat{\psi}_i$. In a uniform cylindric phantom, this has a familiar U-shaped pattern related to scanner sensitivity (*10*). With a patient in the scanner, the distribution of activity and attenuation is far from uniform. Physiologic patient motions, such as breathing, may also impact axial variation. Skewness is a key feature of iteratively reconstructed PET data. A histogram of scaled residuals shows how the DGP captures this aspect. After adjustment for spatial scale factors, the 3-dimensional power spectrum of the normalized residual process provides insight into the effective resolution of the scanning. Coordinatewise autocorrelation functions associated with the spectrum give insight into the actual resolution of the scanner. Again, physiologic movements may well lead to the actual resolution's deviating from what might be predicted on the basis of static phantom measurements.

SEs of VOI Kinetics. In theory, uncertainty in parameters recovered by kinetic model fitting should be proportional to the scale of the residual model error, but it may also be a function of the relevant sensitivity matrix for the model. We examine the relation between the bootstrap assessment of mean VOI kinetic SEs and suitable explanatory factors including the weighted-residual-sums-of-squares fit of the VOI and the mean VOI kinetic values. For each kinetic parameter, linear regression analysis on a logarithmic SE scale is applied. Adjustment of this regression analysis based on the VOI type and the kinetics are explored. Regression predictions of SEs are graphically compared with the true. Correlation values are also summarized.

RESULTS

Illustration

Sample kinetic MIP maps with associated SEs obtained using the NPRM technique and bootstrapping are shown in Figure 2. A video of all coronal MIP maps is provided as Supplemental Video 1. Note that the dataset is the same as that used in a previous report (*2*). The results are of high quality and are well aligned with the vascular and metabolic ^{18}F-FDG patterns expected for key organ structures such as the brain, liver, kidneys, spleen, etc. (*2*). The uncertainties of V_b, V_d, distribution flow (K_d), and K_i are generally higher for regions with larger magnitudes for the kinetic variable. This is perhaps related to the fact that these parameters, which are linear functions of the fitted voxel-level residue, ultimately scale with the magnitude of the time-course data. Mean transit time and extraction fractions deviate somewhat from this pattern. This is likely to be related to the fact that both the mean transit time and extraction fraction are defined in terms of ratios of the V_d, K_d, and K_i variables and, as a result, do not necessarily scale with the scale of the voxel time course. The large blood vessels are seen to impact the structure of the MIP uncertainty for several parameters. The algorithms developed allow kinetic mapping, including the bootstrapping process, to be achieved in a timely fashion. On a single 3.2-GHz processor, the compute time for the NPRM kinetic analysis including the definition of the DGP is 140 min; each bootstrap replicate took 80 min.

Statistical Analysis

Representation of VOI Time-Course Data. The full time course as well as the time course over the first minute of data acquisition are shown in Figure 3. Average VOI time-course data are fit directly using the nonparametric and 2C models; averages of voxel-level fits are also provided. This gives a reference to the results reported previously (*2*). Although the 2C fitting of some VOIs is reasonable, for example, gray and white matter, there are clearly some VOIs where 2C modeling is substantially inferior (e.g., kidney, liver, bone, and bladder). The data fit achieved by the VOI averaging of the voxel-level nonparametric fit is quite good overall and especially over the first 1 min of acquisition. However, it is important to appreciate that almost half of the total number of frames occur in

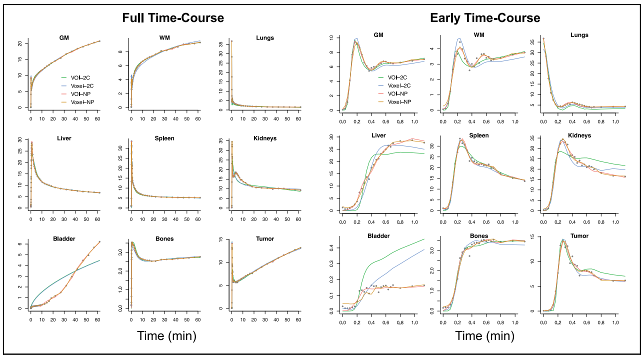

FIGURE 3. Results of alternative fitting of VOI data used in Figure 2. Data are points, and line colors correspond to methods used. Full time course is on left; first minute is on right. GM = gray matter; NP = nonparametric; WM = white matter.

the first 80 s. For this example, over the first minute, differences between the VOI average of the voxelwise 2C fits and the fit of the 2C model to the mean of the VOI time-course data are quite pronounced. In contrast, differences between the corresponding nonparametric fits are much smaller.

Quantitative summaries of the nonparametric fitting of VOI time-course data and comparisons with direct analysis of the mean VOI time-course data using nonparametric and 2C analysis are presented in Table 1. Although values from the weighted-residual-sums-of-squares fit for VOIs are similar based on the VOI average of voxel-level nonparametric fits or by direct fitting of the VOI time-course data, there is a marked increase in weighted-residual-sums-of-squares fits when the VOI time course is approximated using the best-fitting 2C model. VOI time-course fitting by the nonparametric model is consistently improved by averaging voxel-level nonparametric fits; the percent improvement is a modest 50%. VOI time-course fitting by the 2C model is substantially worse than the nonparametric fitting. The mean percent improvement here is almost 390%.

VOI Kinetics. VOI kinetics are reported in Table 2. Statistically significant deviations between the kinetics recovered by alternative methods are largely linked to early time-course parameters (Fig. 1), particularly for V_b. Deviations between voxel-averaged parameters and values recovered from nonparametric and 2C analysis of the VOI time course are much smaller for nonparametric analysis than for 2C analysis. However, it is noteworthy that, for most VOIs, K_i is quite similar in magnitude across all 3 analyses. This might be because flux is a late-time-course parameter (Fig. 1), and alternative methods fit the late time course quite similarly (Fig. 3).

DGP Model. Figure 4 and Supplemental Figure 2 show an expected linear relation between the scale of the DGP and study dose; the linear correlation of 0.68 is highly significant. The axially averaged spatial scale of the DGP increases toward the top and bottom of the patient in the FOV. As expected, the increased scale is not just a function of the nominal sensitivity but is clearly impacted by patient-specific factors including the varying uptake, attenuation, and perhaps any impacts of small patient movements. The skewed nature of random fluctuations in the DGP model, which vary on the basis of the data coefficient of variation, are fully consistent with patterns for iteratively reconstructed PET data (*10*,*21*). The full width at half maximum of the autocorrelation functions in each direction is on the order of 2–3 mm. The coordinatewise autocorrelation functions show greater spatial persistence in the *x* (perpendicular to scanning bed) and *z* (axially) directions (Supplemental Fig. 3). This could align with involuntary patient movements during scanning.

SEs of VOI Kinetics. SEs of VOI kinetics (voxel-level nonparametric) are well approximated using a log-linear model that accounts for the VOI type, the VOI mean kinetics, and the residual weighted root mean square error of the voxel-level nonparametric fit of the VOI time course (Fig. 5; Supplemental Fig. 4). The overall correlation between the bootstrap-measured SE and the SE values predicted by log-linear modeling is 0.96, which is also quite high for individual kinetic parameters.

DISCUSSION

This work demonstrates the practicality of using image-domain bootstrapping for the construction of patient-specific uncertainty assessment in kinetics variables for voxel, VOI, and more complex derived quantities such as MIPs from a whole-body dynamic ^{18}F-FDG PET study. This development creates an opportunity to

TABLE 1

VOI Time-Course Fitting Across 24 Studies

Region	Size (×10^3 voxels)*	Voxel-NP	VOI-NP	VOI-2C	Voxel-NP vs. VOI-NP	Voxel-NP vs. VOI-2C
GM	122.5 ± 23.3	0.02 ± 0.06	0.04 ± 0.14	0.09 ± 0.26	35 ± 50	161 ± 216
WM	18.8 ± 7.0	0.02 ± 0.04	0.02 ± 0.02	0.06 ± 0.20	25 ± 32	141 ± 117
Lung	434.5 ± 124.2	0.06 ± 0.27	0.08 ± 0.69	0.10 ± 0.29	70 ± 76	448 ± 690
Liver	233.0 ± 66.1	0.08 ± 0.08	0.07 ± 0.08	0.55 ± 0.30	46 ± 39	865 ± 453
Spleen	42.8 ± 48.5	0.10 ± 0.11	0.11 ± 0.16	0.13 ± 0.09	69 ± 40	64 ± 87
Kidney	40.5 ± 10.7	0.27 ± 0.26	0.35 ± 0.56	1.83 ± 1.29	83 ± 45	880 ± 576
Bladder	234.9 ± 81.6	0.04 ± 0.10	0.07 ± 0.77	3.25 ± 3.04	887 ± 783	18,266 ± 14,809
Bones	306.2 ± 82.7	0.002 ± 0.003	0.002 ± 0.003	0.007 ± 0.01	35 ± 23	327 ± 206
Tumor	2.5 ± 7.4	0.21 ± 0.25	0.23 ± 0.51	0.67 ± 3.77	28 ± 31	231 ± 250

---

*1 voxel = 1.65 × 1.65 × 1.65 mm^3.

Mean ± SD of weighted residual sums of squares (WRSS) deviations between VOI time course and VOI average of voxelwise (voxel-NP), direct NP (VOI-NP), and 2C (VOI-2C) fits are shown. Last 2 columns show mean ± SD of percent deviations between WRSS of voxel-NP and VOI-NP fits and also between voxel-NP and VOI-2C values.

GM = gray matter; WM = white matter.

TABLE 2
VOI Kinetics Recovered Using Different Methodologies

Method	Region	V_b (mL/g)	V_d (mL/g)	K_d (mL/min/g)	K_i (mL/min/100 g)	MTT (min)	Ext (%)
Voxel-NP	GM	0.05 ± 0.01	0.88 ± 0.26	0.16 ± 0.03	3.01 ± 0.81	5.80 ± 1.64	18.38 ± 5.18
	WM	0.03 ± 0.01	0.64 ± 0.27	0.10 ± 0.03	1.09 ± 0.33	6.61 ± 2.04	12.30 ± 4.12
	Lung	0.18 ± 0.04	0.09 ± 0.03	0.03 ± 0.01	0.07 ± 0.04	3.17 ± 0.77	3.17 ± 1.82
	Liver	0.09 ± 0.04	0.86 ± 0.08	0.54 ± 0.11	0.23 ± 0.08	1.77 ± 0.41	0.57 ± 0.38
	Spleen	0.21 ± 0.09	0.42 ± 0.09	0.41 ± 0.14	0.23 ± 0.16	1.39 ± 0.54	1.14 ± 2.09
	Kidney	0.25 ± 0.07	1.20 ± 0.34	0.49 ± 0.11	0.42 ± 0.25	2.62 ± 0.60	1.22 ± 0.97
	Bladder	0.00 ± 0.01	0.54 ± 0.32	0.04 ± 0.03	1.46 ± 1.13	6.73 ± 2.85	19.11 ± 11.36
	Bones	0.03 ± 0.02	0.22 ± 0.07	0.08 ± 0.02	0.27 ± 0.08	3.54 ± 0.79	4.66 ± 1.32
	Tumor	0.08 ± 0.05	0.65 ± 0.38	0.19 ± 0.08	2.33 ± 1.59	3.62 ± 1.57	12.93 ± 6.44
VOI-NP	GM	0.04 ± 0.01*	0.58 ± 0.16*	0.13 ± 0.03*	3.25 ± 0.89*	4.53 ± 1.19*	20.13 ± 5.42
	WM	0.02 ± 0.01*	0.58 ± 0.31†	0.09 ± 0.03	1.10 ± 0.38	5.99 ± 2.25†	10.96 ± 4.37
	Lung	0.17 ± 0.04†	0.08 ± 0.03‡	0.03 ± 0.02	0.08 ± 0.04†	2.43 ± 0.65*	2.66 ± 1.48
	Liver	0.05 ± 0.04*	0.83 ± 0.07‡	0.53 ± 0.13	0.28 ± 0.08*	1.64 ± 0.39*	0.57 ± 0.24
	Spleen	0.18 ± 0.09†	0.39 ± 0.11‡	0.46 ± 0.17‡	0.29 ± 0.19*	0.91 ± 0.22*	0.86 ± 1.38‡
	Kidney	0.23 ± 0.08	1.19 ± 0.37	0.51 ± 0.15	0.30 ± 0.26‡	2.46 ± 0.82	0.62 ± 0.51*
	Bladder	0.00 ± 0.01*	0.44 ± 0.29†	0.03 ± 0.03*	1.61 ± 1.21†	13.85 ± 11.15*	33.87 ± 26.48*
	Bones	0.01 ± 0.01*	0.17 ± 0.08*	0.08 ± 0.03	0.29 ± 0.07*	2.24 ± 0.50*	3.80 ± 0.90†
	Tumor	0.07 ± 0.04*	0.45 ± 0.34*	0.18 ± 0.09‡	2.48 ± 1.62*	2.62 ± 1.59*	13.27 ± 7.68
VOI-2C	GM	0.03 ± 0.01*	0.56 ± 0.23	0.09 ± 0.02*	3.12 ± 0.87†	5.91 ± 1.71‡	26.41 ± 6.41*
	WM	0.02 ± 0.01*	0.55 ± 0.16	0.05 ± 0.01*	1.13 ± 0.32	11.00 ± 3.23*	18.65 ± 4.48*
	Lung	0.15 ± 0.04*	0.09 ± 0.03‡	0.04 ± 0.01†	0.07 ± 0.04‡	1.18 ± 1.44*	1.70 ± 0.83*
	Liver	0.02 ± 0.01*	0.88 ± 0.09*	0.53 ± 0.13	0.23 ± 0.08*	1.68 ± 0.33	0.45 ± 0.21*
	Spleen	0.11 ± 0.05*	0.49 ± 0.12*	0.61 ± 0.18*	0.21 ± 0.21*	0.73 ± 0.32*	0.69 ± 1.97*
	Kidney	0.15 ± 0.05*	1.25 ± 0.36‡	0.42 ± 0.11†	0.21 ± 0.22‡	2.81 ± 1.18‡	0.52 ± 0.54
	Bladder	0.00 ± 0.00	0.05 ± 0.10*	0.01 ± 0.02*	1.63 ± 0.95	1.66 ± 5.36*	86.89 ± 29.33*
	Bones	0.00 ± 0.00*	0.20 ± 0.06†	0.08 ± 0.03	0.26 ± 0.07*	2.65 ± 0.65*	3.53 ± 0.94‡
	Tumor	0.05 ± 0.05*	0.34 ± 0.19	0.17 ± 0.10	2.38 ± 1.50‡	1.80 ± 1.26†	16.83 ± 18.38

$^*P < 0.001$.
$^\dagger P < 0.01$.
$^\ddagger P < 0.05$.

MTT = mean transit time; Ext = extraction fraction; voxel-NP = VOI-averaged voxel kinetics; GM = gray matter; WM = white matter; VOI-NP = VOI time course kinetics obtained by NP; VOI-2C = VOI time-course kinetics obtained by 2C.

Values are mean ± SD.

incorporate uncertainty about a PET-derived kinetic biomarker that might be used to guide a clinical decision for a patient. This could be particularly helpful in cases where the biomarker value is close to a boundary between alternative treatment options.

Bootstrap reliability depends both on the number of bootstrap simulations (N_B) used and on the accuracy of the representation of the data used in the DGP (*20*). Computational resources dictate the choice of N_B. The results here are based on just an N_B of 25, but for the data in Figure 2, a 4-fold increase in N_B leads to little qualitative change in derived voxel-level SE (Supplemental Fig. 5). Table 1 clearly demonstrates the benefit of using a nonparametric methodology in the DGP. Relative to the well-established 2C ^{18}F-FDG model, substantial and highly significant improvements in data representation are achieved using the nonparametric approach. These benefits are mostly associated with the ability of the nonparametric technique to capture the highly resolved early time-course pattern of data from the current generation of PET scanners. The generally more modest deviations between nonparametric and 2C fits beyond the early time period, say after 1 min, suggest that the deficiencies in the 2C model may primarily relate to the lack of sophistication in the representation of the vascular components of blood–tissue exchange (*22*). The high temporal resolution of the scans here, as well as the use of a bolus injection, contributes to the ability to scrutinize the 2C model in ways that have likely not been possible in the past. The VOIs here are large and heterogeneous—far from the assumption of homogeneous well-mixed compartments that underly the 2C model. However, it is notable that our previous work (*23*) reported significant discrepancies between 2C and nonparametric representation of dynamic ^{18}F-FDG brain data in healthy subjects using much smaller and highly homogeneous

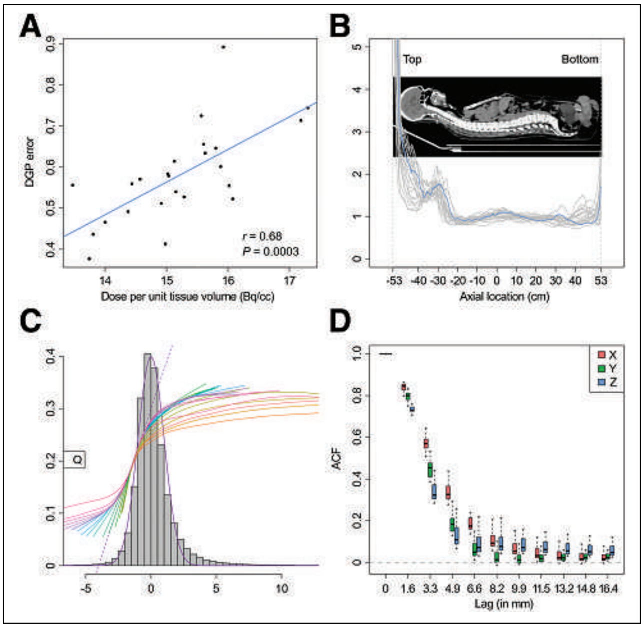

FIGURE 4. Bootstrap DGP from Equation 2: DGP scale ($\hat{\sigma}_e$) vs. injected dose per unit tissue voxel (A), axially averaged scale (B), error distribution (histogram) with comparison to standard gaussian (purple line) (C), and box plot of directional (*x*, perpendicular to scan table; *z*, axial) autocorrelation function (ACF) across all studies (D).

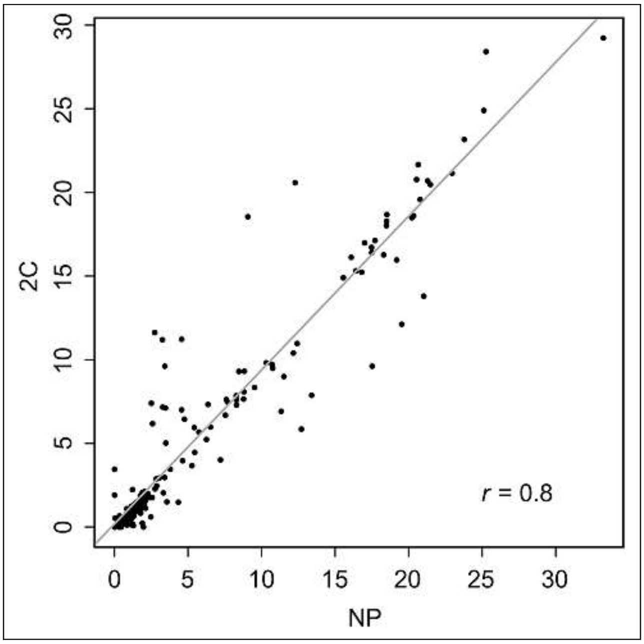

FIGURE 6. Overall relation between ^{18}F-FDG MR K_i computed using nonparametric (NP) voxel (horizontal axis) and 2C (vertical axis) analysis. Best-fit linear regression is shown as solid line.

VOIs. Similar to what is reported in Table 2 for gray and white matter, the discrepancies primarily impact the accuracy of the initial phase of the ^{18}F-FDG tissue residue—V_b especially—but have much less impact on several other variables including flux and V_d. However, statistically significant differences between voxel nonparametric and VOI 2C parameters do not imply that parameters are unrelated. For example, Figure 6 and Supplemental Figure 6 show pairwise plots and summary correlations for the ^{18}F-FDG metabolic rate (MR) flux scaled by the plasma glucose in Equation 4. The strong linear dependence in Figure 6 emphasizes the importance of differentiating statistical and practical significance. Calculated K_i based on nonparametric or 2C analysis would likely yield similarly effective diagnostic values. Indeed, it is well appreciated that even simpler assessments of ^{18}F-FDG flux by Patlak analysis and SUV are also highly effective.

The nonparametric technique here uses a linear basis, but the structure and number of elements involved are adapted to the full 4-dimensional dynamic data and guided by cross validation to prevent overfitting (*10*). The accuracy and stability of a kinetic mapping procedure are best evaluated numerically, which was reported previously (*24*)—studies based on a 2-min constant infusion injection of ^{18}F-FDG and a temporal sampling protocol in which the shortest time frames were 20 s in duration, providing mean-square-error performance characteristics of NPRM and 2C kinetic mapping of ^{18}F-FDG PET data as a function of the study dose and as a function of whether the underlying ground truth is governed by a compartmental model or not. In this study, the accuracy of the flux is largely unaffected by whether a 2C or an NPRM mapping technique is used. Across other kinetic variables, when the ground truth is noncompartmental, the NPRM approach is much better. Remarkably, when the ground truth is a 2C model, the NPRM continues to outperform the 2C approach, especially for variables such as V_b and V_d. Further study of the mean-square-error performance would clearly be useful, particularly in settings where the ground truth, study protocol, and scanning methods are similar to those encountered with the current generation of whole-body ^{18}F-FDG PET studies.

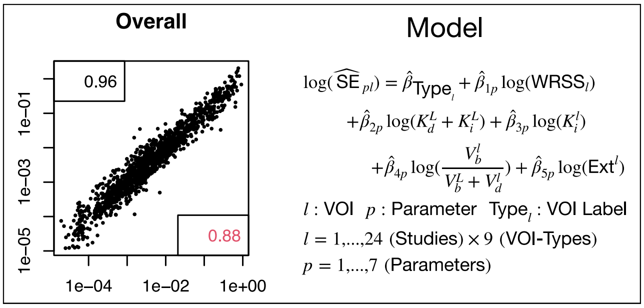

FIGURE 5. Prediction of VOI kinetic SEs (vertical axis) via log-linear model prediction ($\widehat{\text{SE}}$, horizontal axis) formula indicated. Correlation for logarithmic SE value is 0.96 and for raw scale is 0.88. WRSS = weighted residual sums of squares; Ext = extraction fraction.

VOI values of 3 variables, FDG metabolic rate (MR_{FDG}), distribution volume (DV), and vascular blood flow (BF), are compared with literature reports. Each variable is directly obtained by simple scaling of our summary kinetic values: K_i, V_d, and V_b.

$$\text{MR}_{\text{FDG}} = \mu_{\text{glc}} K_i;\ \text{DV} = V_\text{d};\ \text{BF} = \frac{V_\text{b}}{t^*/2}. \qquad \text{Eq. 4}$$

Here, μ_{glc} is the plasma glucose concentration and t^* is the value used to define the vascular component in the decomposition of the Meier–Zierler residue in Figure 1. In a cancer setting, ^{18}F-FDG MR is by far the most clinically important of these variables. Note that we do not try to use ^{18}F-FDG as a means to evaluate the glucose MR, as described in Phelps et al. (*17*). Barrio et al. (*6*) expressed considerable doubt on the ability to do this in the context of cancer applications. Consideration of the V_b variable is motivated by

TABLE 3

Comparison with Literature Values for ^{18}F-FDG MR, V_d, and V_b in Different Tissues from Equation 4

Parameter	Method	GM	WM	Lung	Liver	Spleen	Kidney	Bones
^{18}F-FDG MR (μmol/100 g/min)	Voxel-NP	18.54 ± 6.81	6.66 ± 2.44	0.42 ± 0.31	1.40 ± 0.53	1.40 ± 0.94	2.52 ± 1.51	1.63 ± 0.63
	VOI-2C*	18.98 ± 7.18	6.83 ± 2.26	0.43 ± 0.32	1.38 ± 0.47	1.08 ± 1.24	1.19 ± 1.43	1.58 ± 0.55
		20.26 ± 6.14	7.17 ± 2.09	0.47 ± 0.35	1.39 ± 0.89	1.39 ± 0.83	1.98 ± 2.20	1.72 ± 0.63
		22.22 ± 2.71	7.60 ± 1.58	0.60 ± 0.42	5.22 ± 2.67	9.40 ± 4.57	9.15 ± 6.44	1.34 ± 0.46
		17.46 [11.68–27.61]	6.03 [4.02–9.53]	0.35 [0.03–1.74]	2.02 [0.74–4.35]	2.45 [1.18–15.30]	3.81 [0.08–7.95]	3.69 [1.08–9.09]
V_d (mL/g)	Voxel-NP	0.88 ± 0.26	0.64 ± 0.27	0.09 ± 0.03	0.86 ± 0.08	0.42 ± 0.09	1.20 ± 0.34	0.22 ± 0.07
	VOI-2C†	0.56 ± 0.23	0.55 ± 0.16	0.09 ± 0.03	0.88 ± 0.09	0.49 ± 0.12	1.25 ± 0.36	0.20 ± 0.06
		0.62 ± 0.56	0.67 ± 0.22	0.26 ± 0.06	0.98 ± 0.15	0.63 ± 0.14	1.44 ± 0.55	0.23 ± 0.10
		0.81 [0.14–1.41]	0.46 [0.15–0.87]	0.15 [0.02–0.28]	0.84 [0.44–1.26]	0.58 [0.10–1.12]	0.96 [0.33–1.41]	0.31 [0.04–0.51]
V_b (mL/min/g)	Voxel-NP	0.43 ± 0.11	0.24 ± 0.08	1.41 ± 0.32	0.73 ± 0.34	1.70 ± 0.74	1.99 ± 0.58	0.22 ± 0.12
	VOI-2C	0.26 ± 0.04	0.13 ± 0.04	1.16 ± 0.34	0.14 ± 0.07	0.85 ± 0.42	1.22 ± 0.38	0.03 ± 0.02
		0.59 ± 0.11 (*32*)	0.20 ± 0.04 (*32*)	1.40 ± 0.30 (*33*)	1.11 ± 0.34 (*34*)	1.92 ± 0.76 (*35*)	1.74 ± 0.44 (*35*)	0.18 ± 0.03 (*36*)
		0.41 ± 0.11 (*37*)	0.22 ± 0.04 (*37*)	1.21 ± 0.32 (*38*)	1.78 ± 0.56 (*39*)	1.68 ± 0.12 (*40*)	1.57 ± 0.60 (*41*)	0.18 ± 0.05 (*42*)

---

*References *2*,*4*,*27*,*30*,*31*.

†References *2*,*27*.

GM = gray matter; WM = white matter; Voxel-NP = VOI-averaged voxel kinetics; VOI-2C = VOI time course kinetics obtained by 2C analysis.

Data are mean ± SD, or median followed by range in brackets.

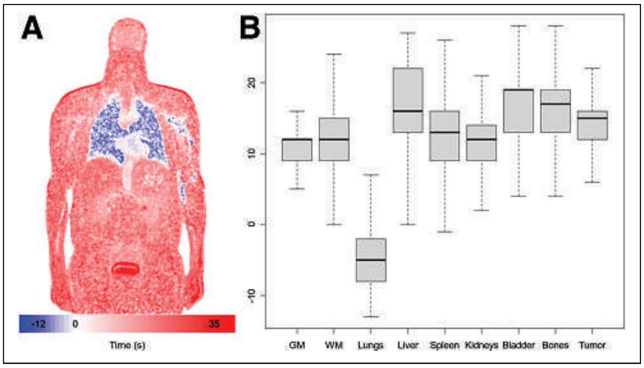

FIGURE 7. (A) Delay image corresponding to coronal CT slice in Figure 2; values are amplitude-weighted delay values, $\{\delta+\Delta_k, k=1,2,\ldots,K\}$, in Equation 1. Data are centered so that mean delay in descending aorta is 0. (B) Box plots of distribution of mapped delay values in seconds by VOI. GM = gray matter; WM = white matter.

interest in deriving potentially useful additional diagnostic information related to tissue vascularity from ^{18}F-FDG (*1*,*25*,*26*). There is no intention of questioning PET ^{15}O-H_2O as the gold standard for V_b determination. Our V_b formula is an application of the central volume theorem (*14*) based on an assumed mean transit time in the vasculature of $t^*/2$ (here, 7.5 s) for the collection of tracer atoms whose tissue transit time in the local voxel is less than 15 s.

Table 3 compares the VOI averages of 3 variables to those in the literature. For ^{18}F-FDG MR and V_d, the values are seen to be in the range reported using 2C and Patlak analyses (*27*). V_b values are compared with those in reports based on PET ^{15}O-H_2O and dynamic susceptibility contrast MR techniques. The results for the NPRM approach are remarkably similar to those in the literature, particularly given that the study group here is older and unhealthy (*28*). Further examination of the V_b variable could be merited. Viability of conducting PET ^{15}O-H_2O on this scanner was previously demonstrated (*29*). Note that some of the deviation in Table 3 may be related to scaling differences between the use of whole-blood activity as an AIF (like ours) and other analyses that used the arterial plasma activity time course as an AIF.

Although our focus has been on parameters that have traditionally been used to quantify ^{18}F-FDG PET dynamics, the nonparametric technique provides a possibility to also evaluate a summary of the arrival pattern of ^{18}F-FDG at the voxel level. A sample amplitude-weighted average of voxel-level basis element delay as shown in Equation 1 is shown in Figure 7. There is early arrival of the signal to the lung and much more delayed arrival to the bladder and more peripheral regions (*1*). More detailed consideration of the ^{18}F-FDG arrival pattern may be worthwhile.

CONCLUSION

NPRM kinetic analysis together with bootstrap assessment of uncertainty is practically feasible in the context of large-scale long-axial-FOV ^{18}F-FDG PET data. This provides an ability to incorporate patient-specific uncertainty measures of kinetic biomarkers recovered from dynamic PET to support clinical decisions.

DISCLOSURE

This research is supported by Science Foundation Ireland grant PI-11/1027 and by the National Cancer Institute USA grant R33-CA225310. Kuangyu Shi and Axel Rominger are funded by Siemens Healthineers and Novartis. Hasan Sari is an employee of Siemens Healthineers. No other potential conflict of interest relevant to this article was reported.

KEY POINTS

QUESTION: Is it feasible to map kinetics together with uncertainty in long-axial-FOV dynamic ^{18}F-FDG PET studies?

PERTINENT FINDINGS: NRPM analysis together with image-domain bootstrapping is a suitable methodology for mapping kinetics.

IMPLICATIONS FOR PATIENT CARE: The ability to derive uncertainties in complex kinetic biomarkers could enhance patient-specific decision-making for guiding treatment of cancer patients.

REFERENCES

1. Feng T, Zhao Y, Shi H, et al. Total-body quantitative parametric imaging of early kinetics of ^{18}F-FDG. *J Nucl Med.* 2021;62:738–744.
2. Sari H, Mingels C, Alberts I, et al. First results on kinetic modelling and parametric imaging of dynamic ^{18}F-FDG datasets from a long axial FOV PET scanner in oncological patients. *Eur J Nucl Med Mol Imaging.* 2022;49:1997–2009.
3. Wang G, Nardo L, Parikh M, et al. Total-body PET multiparametric imaging of cancer using a voxelwise strategy of compartmental modeling. *J Nucl Med.* 2022;63:1274–1281.
4. Spence AM, Muzi M, Graham MM, et al. Glucose metabolism in human malignant gliomas measured quantitatively with PET, 1-[C-11] glucose and FDG: analysis of the FDG lumped constant. *J Nucl Med.* 1998;39:440–448.
5. Muzi M, Spence AM, O'Sullivan F, et al. Kinetic analysis of 3′-deoxy-3′-^{18}F-fluorothymidine in patients with gliomas. *J Nucl Med.* 2006;47:1612–1621.
6. Barrio JR, Huang SC, Satyamurthy N, et al. Does 2-FDG PET accurately reflect quantitative in vivo glucose utilization? *J Nucl Med.* 2020;61:931–937.
7. Gu F, Wu Q. Quantitation of dynamic total-body PET imaging: recent developments and future perspectives. *Eur J Nucl Med Mol Imaging.* 2023;50:3538–3557.
8. Cunningham VJ, Jones T. Spectral analysis of dynamic PET studies. *J Cereb Blood Flow Metab.* 1993;13:15–23.
9. O'Sullivan F. Imaging radiotracer model parameters in PET: a mixture analysis approach. *IEEE Trans Med Imaging.* 1993;12:399–412.
10. O'Sullivan F, Gu F, Wu Q, O'Suilleabhain LD. A generalized linear modeling approach to bootstrapping multi-frame PET image data. *Med Image Anal.* 2021;72:102132.
11. Gu F, Wu Q, O'Sullivan F. Image-domain bootstrapping of PET time-course data for assessment of uncertainty in complex regional summaries of mapped kinetics. IEEE Xplore website. https://ieeexplore.ieee.org/document/9875531. Published September 9, 2022. Accessed March 22, 2024.
12. Naganawa M, Gallezot JD, Shah V, et al. Assessment of population-based input functions for Patlak imaging of whole body dynamic ^{18}F-FDG PET. *EJNMMI Phys.* 2020;7:67.
13. Prenosil GA, Sari H, Fürstner M, et al. Performance characteristics of the Biograph Vision Quadra PET/CT system with a long axial field of view using the NEMA NU 2-2018 standard. *J Nucl Med.* 2022;63:476–484.
14. Meier P, Zierler KL. On the theory of the indicator-dilution method for measurement of blood flow and volume. *J Appl Physiol.* 1954;6:731–744.
15. Patlak CS, Blasberg RG, Fenstermacher JD. Graphical evaluation of blood-to-brain transfer constants from multiple-time uptake data. *J Cereb Blood Flow Metab.* 1983;3:1–7.
16. Kety SS, Schmidt CF. The determination of cerebral blood flow in humans by the use of nitrous oxide in low concentrations. *Am J Physiol.* 1945;143:53–66.
17. Phelps ME, Huang SC, Hoffman EJ, Selin C, Sokoloff L, Kuhl DE. Tomographic measurement of local cerebral glucose metabolic rate in humans with (F-18)2-fluoro-2-deoxy-D-glucose: validation of method. *Ann Neurol.* 1979;6:371–388.
18. O'Sullivan F, Muzi M, Mankoff DA, Eary JF, Spence AM, Krohn KA. Voxel-level mapping of tracer kinetics in PET studies: a statistical approach emphasizing tissue life tables. *Ann Appl Stat.* 2014;8:1065–1094.
19. Haynor DR, Woods SD. Resampling estimates of precision in emission tomography. *IEEE Trans Med Imaging.* 1989;8:337–343.
20. Bradley E, Tibshirani RJ. *An Introduction to the Bootstrap.* CRC Press, 1994.

21. Mou T, Huang J, O'Sullivan F. The gamma characteristic of reconstructed PET images: implications for ROI analysis. *IEEE Trans Med Imaging.* 2018;37:1092–1102.
22. Li Z, Yipintsoi T, Bassingthwaighte JB. Nonlinear model for capillary-tissue oxygen transport and metabolism. *Ann Biomed Eng.* 1997;25:604–619.
23. O'Sullivan F, Mark M, Spence AM, et al. Nonparametric residue analysis of dynamic PET data with application to cerebral FDG studies in normals. *J Am Stat Assoc.* 2009;104:556–571.
24. Gu F, O'Sullivan F, Muzi M, Mankoff DA. Quantitation of multiple injection dynamic PET scans: an investigation of the benefits of pooling data from separate scans when mapping kinetics. *Phys Med Biol.* 2021.66:135010.
25. Pouzot C, Richard JC, Gros A, et al. Noninvasive quantitative assessment of pulmonary blood flow with ^{18}F-FDG PET. *J Nucl Med.* 2013;54:1653–1660.
26. Mullani NA, Herbst RS, O'Neil RG, Gould KL, Barron BJ, Abbruzzese JL. Tumor blood flow measured by PET dynamic imaging of first-pass ^{18}F-FDG uptake: a comparison with ^{15}O-labeled water-measured blood flow. *J Nucl Med.* 2008;49:517–523.
27. Dias AH, Hansen AK, Munk OL, Gormsen LC. Normal values for ^{18}F-FDG uptake in organs and tissues measured by dynamic whole body multiparametric FDG PET in 126 patients. *EJNMMI Res.* 2022;12:15.
28. Wu C, Honarmand AR, Schnell S, et al. Age-related changes of normal cerebral and cardiac blood flow in children and adults aged 7 months to 61 years. *J Am Heart Assoc.* 2016;5:e002657.
29. Knuuti J, Tuisku J, Kärpijoki H, et al. Quantitative perfusion imaging with total-body PET. *J Nucl Med.* 2023;64(suppl 2):11S–19S.
30. Liu G, Xu H, Hu P, et al. Kinetic metrics of ^{18}F-FDG in normal human organs identified by systematic dynamic total-body positron emission tomography. *Eur J Nucl Med Mol Imaging.* 2021;48:2363–2372.
31. Graham MM, Mark M, Spence AM, et al. The FDG lumped constant in normal human brain. *J Nucl Med.* 2002;43:1157–1166.
32. Huang SC, Carson RE, Hoffman EJ, et al. Quantitative measurement of local cerebral blood flow in humans by positron computed tomography and ^{15}O-water. *J Cereb Blood Flow Metab.* 1983;3:141–153.
33. Matsunaga K, Yanagawa M, Otsuka T, et al. Quantitative pulmonary blood flow measurement using ^{15}O-H_2O PET with and without tissue fraction correction: a comparison study. *EJNMMI Res.* 2017;7:102.
34. Slimani L, Kudomi N, Oikonen V, et al. Quantification of liver perfusion with [^{15}O]H_2O-PET and its relationship with glucose metabolism and substrate levels. *J Hepatol.* 2008;48:974–982.
35. Lauritsen KM, Søndergaard E, Luong TV, Møller N, Gormsen LC. Acute hyperketonemia does not affect glucose or palmitate uptake in abdominal organs or skeletal muscle. *J Clin Endocrinol Metab.* 2020;105:1785–1790.
36. Kahn D, Weiner GJ, Ben-Haim S, et al. Positron emission tomographic measurement of bone marrow blood flow to the pelvis and lumbar vertebrae in young normal adults. *Blood.* 1994;83:958–963.
37. Markus HS, Lythgoe DJ, Ostegaard L, O'Sullivan M, Williams SC. Reduced cerebral blood flow in white matter in ischaemic leukoaraiosis demonstrated using quantitative exogenous contrast based perfusion MRI. *J Neurol Neurosurg Psychiatry.* 2000;69:48–53.
38. Schuster DP, Kaplan JD, Gauvain K, Welch MJ, Markham J. Measurement of regional pulmonary blood flow with PET. *J Nucl Med.* 1995;36:371–377.
39. Materne R, Van Beers E, et al. Non-invasive quantification of liver perfusion with dynamic computed tomography and a dual-input one-compartmental model. *Clin Sci (Lond).* 2000;99:517–525.
40. Oguro A, Taniguchi H, Koyama H, et al. Quantification of human splenic blood flow: quantitative measurement of splenic blood flow with $H_2{}^{15}O$ and a dynamic state method. *Ann Nucl Med.* 1993;7:245–250.
41. Kudomi N, Koivuviita N, Liukko KE, et al. Parametric renal blood flow imaging using [^{15}O]H_2O and PET. *Eur J Nucl Med Mol Imaging.* 2009;36: 683–691.
42. Piert M, Machulla H-J, Jahn M, Stahlschmidt A, Becker GA, Zittel TT. Coupling of porcine bone blood flow and metabolism in high-turnover bone disease measured by [^{15}O]H_2O and [^{18}F]fluoride ion positron emission tomography. *Eur J Nucl Med Mol Imaging.* 2002;29:907–914.

A Deep-Learning–Based Partial-Volume Correction Method for Quantitative ^{177}Lu SPECT/CT Imaging

Julian Leube[1], Johan Gustafsson[2], Michael Lassmann[1], Maikol Salas-Ramirez[1], and Johannes Tran-Gia[1]

[1]*Department of Nuclear Medicine, University Hospital Würzburg, Würzburg, Germany; and* [2]*Medical Radiation Physics, Lund, Lund University, Lund, Sweden*

With the development of new radiopharmaceutical therapies, quantitative SPECT/CT has progressively emerged as a crucial tool for dosimetry. One major obstacle of SPECT is its poor resolution, which results in blurring of the activity distribution. Especially for small objects, this so-called partial-volume effect limits the accuracy of activity quantification. Numerous methods for partial-volume correction (PVC) have been proposed, but most methods have the disadvantage of assuming a spatially invariant resolution of the imaging system, which does not hold for SPECT. Furthermore, most methods require a segmentation based on anatomic information. **Methods:** We introduce DL-PVC, a methodology for PVC of ^{177}Lu SPECT/CT imaging using deep learning (DL). Training was based on a dataset of 10,000 random activity distributions placed in extended cardiac–torso body phantoms. Realistic SPECT acquisitions were created using the SIMIND Monte Carlo simulation program. SPECT reconstructions without and with resolution modeling were performed using the CASToR and STIR reconstruction software, respectively. The pairs of ground-truth activity distributions and simulated SPECT images were used for training various U-Nets. Quantitative analysis of the performance of these U-Nets was based on metrics such as the structural similarity index measure or normalized root-mean-square error, but also on volume activity accuracy, a new metric that describes the fraction of voxels in which the determined activity concentration deviates from the true activity concentration by less than a certain margin. On the basis of this analysis, the optimal parameters for normalization, input size, and network architecture were identified. **Results:** Our simulation-based analysis revealed that DL-PVC (0.95/7.8%/35.8% for structural similarity index measure/normalized root-mean-square error/volume activity accuracy) outperforms SPECT without PVC (0.89/10.4%/12.1%) and after iterative Yang PVC (0.94/8.6%/15.1%). Additionally, we validated DL-PVC on ^{177}Lu SPECT/CT measurements of 3-dimensionally printed phantoms of different geometries. Although DL-PVC showed activity recovery similar to that of the iterative Yang method, no segmentation was required. In addition, DL-PVC was able to correct other image artifacts such as Gibbs ringing, making it clearly superior at the voxel level. **Conclusion:** In this work, we demonstrate the added value of DL-PVC for quantitative ^{177}Lu SPECT/CT. Our analysis validates the functionality of DL-PVC and paves the way for future deployment on clinical image data.

Key Words: image processing; SPECT/CT; deep learning; Monte Carlo simulation; dosimetry; partial-volume correction

J Nucl Med 2024; 65:980–987
DOI: 10.2967/jnumed.123.266889

Quantitative SPECT/CT has become the method of choice to spatially resolve activity distributions for the dosimetry of radiopharmaceutical therapies. One of the most important radionuclides used today is ^{177}Lu (*1,2*). Mainly because of its nonperfect collimation and the resulting relatively poor spatial resolution (1–2 cm for ^{177}Lu and medium-energy collimation (*3*)), ^{177}Lu SPECT imaging reaches its limitations for small structures such as lesions or small organs (*4*). When activity quantification is based on volumes of interest, poor spatial resolution leads to spatial allocation uncertainty, which is referred to as partial-volume effect. For many imaging modalities, the acquired activity distribution can be described in good approximation by a convolution of the true activity distribution with the point-spread function of the imaging system. Since this approximation holds for PET, several techniques for partial-volume correction (PVC) of PET have been proposed (*5*). However, the fundamental problem for transferring such methodology to SPECT is that the poor spatial resolution of gamma cameras inevitably leads to information loss. Hence, purely data-driven methods, such as resolution modeling during reconstruction (resolution recovery [*RR*]) (*6*) or postreconstruction deconvolution, will never result in partial-volume effect–free activity concentration estimates. Accordingly, some form of prior information has to be supplied, as performed, for example, in the iterative Yang technique for postreconstruction PVC (*5*), an enhancement of the Yang method (*7*). Iterative Yang PVC (IY-PVC) uses prior knowledge about the spatial resolution to fold the activity back into an estimated mask of active volume. For practical implementation of PVC methods, a spatially invariant point-spread function is often assumed for the sake of simplicity, which approximately holds true for PET imaging. For SPECT, however, this may introduce substantial errors, as the spatially variant SPECT resolution cannot be well approximated by a single value (*3*). Furthermore, the exact distribution of radiopharmaceuticals in the structures under investigation is typically unknown and can be only roughly estimated from morphologic imaging such as CT. When the active regions cannot be properly defined on the basis of morphologic imaging, substantial errors may be introduced.

In recent years, convolutional neural networks have demonstrated their tremendous potential in medical image processing. In the field of SPECT imaging, convolutional neural networks have been used for automated segmentation (*8*), CT-free attenuation correction (*9*), acceleration of SPECT imaging (*10,11*), and denoising (*12*). In addition, deep learning (DL) techniques have recently been used for PVC (*13,14*). Xie et al. (*13*) trained a neural network to perform IY-PVC without the need for segmentation using uncorrected SPECT images as input and images corrected with IY-PVC as target. As mentioned above, however, the prior knowledge used to train the network can introduce systematic errors. Li et al. (*14*) proposed a DL-based

---

Received Oct. 27, 2023; revision accepted Mar. 15, 2024.

For correspondence or reprints, contact Julian Leube (leube_j@ukw.de) or Johannes Tran-Gia (tran_j@ukw.de).

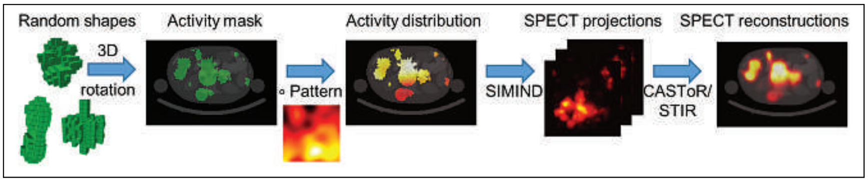

FIGURE 1. Schematic overview of dataset generation used in this study. SIMIND = Simulating Medical Imaging Nuclear Detectors. STIR = Software for Tomographic Image Reconstruction; CASToR = Customizable and Advanced Software for Tomographic Reconstruction.

enhancement of dose calculations. More specifically, they used [^{68}Ga]Ga-DOTATATE PET/CT patient data as ground truth to reduce the partial-volume effect in [^{177}Lu]Lu-DOTATATE SPECT/CT–based absorbed dose distributions. Although the method was shown to enhance the dose maps, it works only under the assumption that the distribution of radiopharmaceutical is comparable despite the different radiopharmaceuticals scanned at different measurement times after administration. In addition, differences in ligand amount, affinity, and internalization have not yet been sufficiently investigated, possibly leading to additional errors (*15*). Both studies, although demonstrating the potential of DL for PVC, suffer, like many other published implementations of DL for clinical applications, from small dataset sizes (28 and 14 patients in the work of Xie et al. (*13*) and Li et al. (*14*), respectively) and lack of ground-truth activity distributions for training.

In this work, we present DL-PVC, a methodology for PVC of ^{177}Lu SPECT/CT imaging using DL trained on a large dataset of 10,000 pairs of random patient-shaped activity distributions and associated SPECT images generated using Monte Carlo radiation transport simulations. These pairs are used as input and target for a convolutional neural network, trained to perform PVC without segmentation. For performance evaluation, we investigated the impact of different normalization (i.e., activity conservation) methods, input matrix sizes, and network architectures on the performance of DL-PVC. Subsequently, we compared our new methodology with IY-PVC as a reference method and performed a validation based on ^{177}Lu SPECT/CT measurements of 3-dimensionally printed phantoms of different geometries.

MATERIALS AND METHODS

Generation of a Dataset of Random Activity Distributions

A large database of 3-dimensional activity distributions of randomly arranged random shapes and corresponding SPECT simulations was created to train neural networks for PVC. A schematic overview of the dataset generation is given in Figure 1. First, density maps and activity masks were generated. The activity masks were then transformed into inhomogeneous activity distributions with a patientlike activity range. Next, simulations were performed in the SIMIND (SImulating Medical Imaging Nuclear Detectors) Monte Carlo simulation program (*16*), using these masks to obtain SPECT projections. Last, iterative reconstructions with RR (Software for Tomographic Image Reconstruction, STIR (*17*)) and without RR (Customizable and Advanced Software for Tomographic Reconstruction, CASToR (*18*)) were performed to obtain SPECT images. The approach is based on previously described work (*11*). A detailed description of the generation of the dataset is given in the supplemental materials (supplemental materials are available at http://jnm.snmjournals.org). In addition, the complete dataset is available at https://doi.org/10.5281/zenodo.8282567.

The most important features of the dataset are as follows:

Realistic Attenuation and Scattering Conditions. Extended cardiac–torso (XCAT) phantoms (*19*) were used to achieve realistic attenuation and scatter conditions. By varying the size scaling of individual organs or areas, 250 variations of 16 patients (6 female, 9 male; age, 18–76 y; body mass index, 18.6–38.0) resulted in a total of 4,000 different density maps. By defining 3 bed positions, we generated a total of 10,000 attenuation images (4,000 thoracic, 4,000 abdominal, and 2,000 head images; matrix, 256; voxel size, 2.4 mm).

Patientlike Binary Activity Masks. Patientlike binary activity masks (0, no activity; 1, activity) were created by placing random shapes (minimal and maximum shape sizes of 4 and 100 voxels, respectively), created using previously described methodology (*11*), inside the XCAT-based attenuation mask until a randomly selected, patient-representative target volume was reached.

Nonuniform Activity Distributions. Each activity mask was multiplied voxelwise by a spatially contiguous, nonuniform pattern (*11*) to create more complex, heterogeneous activity distributions. An example of the resulting target datasets used to train the neural network is shown in Figure 2.

Realistic Activity Distributions. To resemble ^{177}Lu SPECT patient acquisitions as closely as possible, the activity distributions were scaled on the basis of the active volumes and total activities of 717 peritherapeutic ^{177}Lu SPECT/CT acquisitions (429 [^{177}Lu]Lu-PSMA-I&T and 288 [^{177}Lu]Lu-DOTATATE SPECT/CT examinations of 202 different patients), which had been conducted at University Hospital Würzburg between January 2014 and June 2021 (waiver 20230207 04).

Monte Carlo–Based SPECT Simulations

For each of the 10,000 random activity distributions, a set of realistic SPECT projections was generated by SIMIND Monte Carlo simulations (*16*). The simulations were set up to replicate a ^{177}Lu SPECT acquisition on our Siemens Intevo Bold SPECT/CT system (9.5-mm crystal; medium-energy low-penetration collimator; 9% energy resolution; 120 projections of 30 s each; noncircular orbit; matrix, 128; pixel size, 4.79 mm; 20% main energy window at 208 keV; and 2 adjacent 10% scatter windows). As described previously (*11*), Poisson noise was added to the simulated (noise-free) projections to obtain realistic (noisy) projections for the given activities and acquisition parameters.

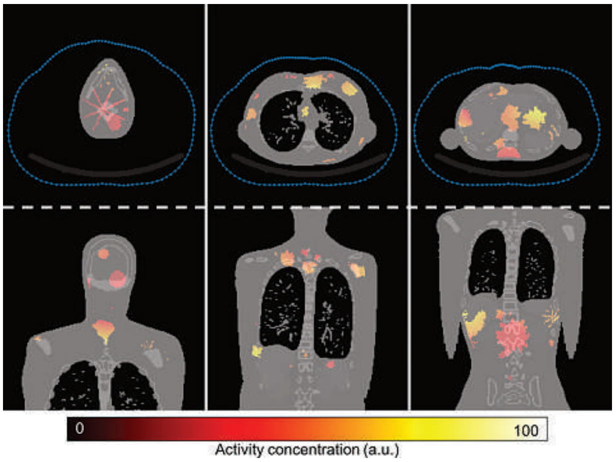

FIGURE 2. Example target dataset as used for neural network. XCAT phantom is shown in gray scale, whereas random activity distribution is shown in color map. At top are axial sections, and at bottom are coronal sections. From left to right, 3 bed positions are shown: head, thorax, and abdomen. Camera orbits are indicated as blue dotted lines.

SPECT Reconstructions

SPECT reconstructions (voxel size, 4.8 mm) were performed for all 2 × 10,000 projection sets (noise-free and noisy) using 2 different reconstructions: CASToR, an ordered-subset expectation maximization reconstruction (10 iterations, 2 subsets, attenuation correction, scatter correction) without *RR* (*18*), and STIR, an ordered-subset expectation maximization reconstruction (6 iterations, 6 subsets, attenuation correction, scatter correction) with *RR* (*17*). Accordingly, 4 different SPECT datasets were available for training and analysis of the presented approach: CASToR (*noRR*) or STIR (*RR*) performed with noise-free (*nf*) or noisy (*n*) projections (*noRR_nf*/*noRR_n* and *RR_nf*/*RR_n*, respectively).

Evaluation of Activity Conservation

An important criterion for any PVC is that the correction preserves the total activity. Before the U-Net was applied, the input SPECT images were normalized by their maximum activity concentration to an interval of [0,1]. In this study, we investigated 2 different approaches for scaling the output of the proposed PVC. The first was rescaling the output of DL-PVC with the maximum activity concentration of the input SPECT image, and the second was normalization of the sum of all voxel values of the output of DL-PVC to the total activity of the input SPECT image.

Evaluation of Input Matrix Size

In our work, we investigated 2 kernel sizes to which the PVC method was applied. In the first, DL-PVC is directly applied to the entire field of view (FOV), in which case the entire SPECT image (matrix size, 128 × 128 × 128) and the entire ground-truth activity distribution serve as input and target, respectively. In the second, DL-PVC is applied to smaller patches (cube-shaped image sections with an edge length of 32 voxels), which are subsequently reassembled (more details can be found in the supplemental materials).

Evaluation of U-Net Architecture

A 3-dimensional U-shaped convolutional neural network (U-Net) (*20*) based on the fastMRI architecture (*21*) and implemented using the PyTorch library (*22*) with Adam optimizer (*23*) was used to perform the PVC. A more detailed explanation of the architecture is given in the supplemental materials. In addition to the standard U-Net architecture, 4 other architectures were tested: R2U-Net by Alom et al. (*24*); AttU-Net by Oktay et al. (*25*); R2AttU-Net, a combination of both methods (*26*); and U-Net++, a nested U-Net proposed by Zhou et al. (*27*). The performance of these 5 network architectures was compared on the basis of the *RR_n* and *noRR_n* datasets. PVC was performed on the entire FOV, preserving the total activity.

Evaluation Criteria for PVC Performance

Several evaluation metrics were used to evaluate the quality of the different PVC methods. Their calculation was restricted to a masked region within each test dataset in which ground-truth activity was present. Besides structural similarity index measure (SSIM) (*28*) and normalized root-mean-square error (NRMSE), a volume activity accuracy (VAA) was defined. It indicates the proportion of voxels in which the relative deviation in activity concentration was less than α (fixed at 5%). More information is given in the supplemental materials. In addition, the deviation between total activity before and after PVC was calculated as percentage difference. Because not all evaluation metrics were normally distributed, paired Wilcoxon tests with a significance level of 1% were chosen for the statistical analysis.

Comparison with Iterative Yang Technique

To compare the proposed DL-PVC methodology with an already-established PVC method, IY-PVC (*5*) was applied to all SPECT reconstructions. First, a matched filter analysis (*3*) was used to determine the spatial resolution for STIR (8.75 mm; applies to *RR_n, RR_nf*) and for CASToR (21.35 mm; applies to *noRR_n, noRR_nf*). Subsequently, 10 iterations of IY-PVC were performed using the PETPVC toolbox (*29*) with spatial resolution and ground-truth activity mask as input.

Investigation of Minimum Feature Size

To determine the minimum feature size that DL-PVC can still resolve, further simulations based on the XCAT phantom dataset were performed. For this purpose, multiple SPECT simulations of random activity distributions were performed, in which a cube with an edge length of 1–10 voxels (increment, 1 voxel) was introduced centrally into the activity distribution. Recovery coefficients (RCs) were calculated to determine how well DL-PVC recovers the activity in the different-sized cubes. More detail on the simulations and the calculation of the RCs is given in the supplemental materials.

Activity Concentration–Voxel Histograms

To illustrate differences in the distribution of activity concentrations for the SPECT simulations without PVC, after IY-PVC, and after DL-PVC, activity concentration–voxel histograms (proportion of voxels containing a given relative activity concentration plotted against the respective relative activity concentration) were created. More details can be found in the supplemental materials.

Phantom Measurement

To justify application of DL-PVC in a clinical context, we validated the methodology on increasingly patient-realistic ^{177}Lu SPECT/CT phantom measurements. For this purpose, a previously published series of ^{177}Lu SPECT/CT measurements of 3 self-designed 3-dimensional phantoms (sphere, ellipsoid, and renal cortex geometry, all with the same filling volume of 100 mL) was used (*30*). In addition, a 3-dimensionally printed 2-organ phantom (International Commission on Radiological Protection publication 110 [ICRP110]–based 2-compartment kidney and spleen) was analyzed to evaluate DL-PVC on a phantom that is more representative of patient data. These data had been acquired at our institution as part of the Europe-wide MRTDosimetry comparison exercise for quantitative ^{177}Lu SPECT/CT imaging (*31*). The acquisition parameters had been the same as the parameters chosen for the Monte Carlo simulations. On the basis of these 4 measured projection datasets, SPECT reconstructions were performed with CASToR and STIR with the same parameters as for the simulated SPECT projections. For analysis, all SPECT images were interpolated to CT resolution (matrix, 512; voxel size, 0.98 mm) using trilinear interpolation. These were compared with the ground truth created by multiplying the masks used for phantom fabrication by the nominal activity concentrations (1.08 ± 0.03 MBq/mL for sphere/ellipsoid/cortex, 1.44 ± 0.04 MBq/mL for spleen/cortex, and 0.47 ± 0.01 MBq/mL for medulla of the ICRP110-based phantom), the determination of which was previously described (*30*).

RESULTS

Optimal Selection of Activity Conservation, Input Matrix Size, U-Net Architecture, and Resolution Modeling

In light of the investigations regarding activity conservation, input matrix size, U-Net architecture (*20,24–27*), and the application of *RR,* an optimal configuration and reconstruction method, DL-PVC, was determined for further analysis. It comprises the following components, the selection of which, including statistical tests based on the evaluation metrics, are described in detail in the supplemental materials: SPECT reconstruction with *RR* (*RR_nf* or *RR_n*); activity conservation based on the total activity of the uncorrected SPECT; input matrix size: direct application of PVC to the entire FOV; and R2U-Net network architecture (*24*).

TABLE 1
Mean Evaluation Metrics for Both SPECT Datasets with *RR* Without PVC, After IY-PVC, and After DL-PVC over All 500 Test Activity Distributions

SPECT reconstruction	PVC method	SSIM	NRMSE (%)	VAA (%)	AD (%)
RR_nf	None	0.899 (0.019)	9.98 (1.32)	13.57 (4.14)	0.28 (2.00)
	IY-PVC	0.945 (0.009)	8.07 (2.33)	17.05 (4.03)	4.62 (6.16)
	DL-PVC	0.971 (0.007)	5.74 (0.89)	43.30 (8.79)	0.28 (2.00)
RR_n	None	0.890 (0.022)	10.44 (1.40)	12.10 (3.18)	0.33 (2.06)
	IY-PVC	0.936 (0.013)	8.58 (1.21)	15.06 (3.27)	6.36 (4.36)
	DL-PVC	0.947 (0.015)	7.75 (1.33)	35.79 (10.06)	0.33 (2.06)

SSIM = structural similarity index measure; NRMSE = normalized root-mean-square error; VAA = voxel activity accuracy; AD = activity deviation.

Data in parentheses are SDs. Note that activity deviation is same without PVC and after DL-PVC because of activity conservation approach.

Comparison with Iterative Yang Technique as Reference Method

Table 1 and Figure 3 show a numeric and visual comparison of the evaluation metrics for SPECT without PVC, after DL-PVC, and after IY-PVC. In both cases, DL-PVC demonstrates significantly superior evaluation metrics. In addition, Figure 4 gives a visual impression of the different image qualities. Visually, activity distributions corrected with DL-PVC closely resemble the ground-truth activity distribution, which is illustrated by cross sections. A considerable increase in the number of cyan voxels in the VAA maps indicates that the activity concentration after DL-PVC better matches the true activity concentration. Furthermore, the true activity concentration is restored, especially in voxels located at the center of larger shapes. However, deviations can still be seen at the edges of larger objects or for smaller objects.

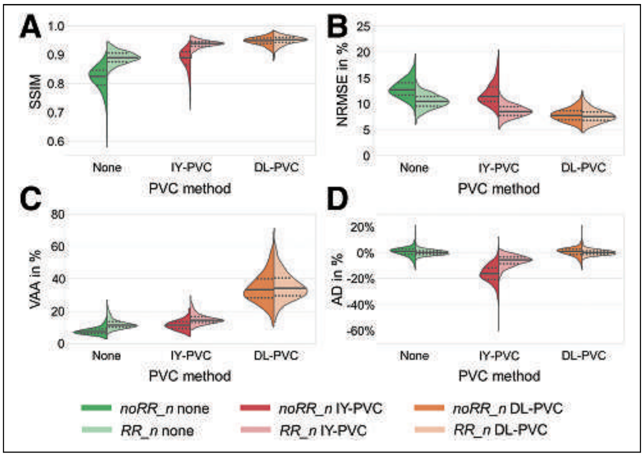

FIGURE 3. Comparison of different PVC approaches. Depicted are violin plots of evaluation metrics for SSIM (A), NRMSE (B), VAA (C), and activity deviation (D) for reconstructions without PVC, after IY-PVC, and after DL-PVC. Darker shades represent reconstructions without *RR,* and brighter shades represent reconstructions with *RR*. Inside violins, solid lines represent median, and dashed lines represent upper and lower quartiles. Note that activity deviation is same without PVC and after DL-PVC because of activity conservation in DL-PVC. For SSIM and VAA, higher values correspond to better performance, whereas for NRMSE and activity deviation, better performance is indicated by values closer to 0%. AD = activity deviation; NRMSE = normalized root-mean-square error; SSIM = structural similarity index measure; VAA = voxel activity accuracy.

Investigation of Minimum Feature Size

Figure 5 shows the results concerning the minimal feature size that DL-PVC can resolve. Without PVC (green) and after IY-PVC (red), the RCs increase continuously over all cube edge lengths investigated. In contrast, the RCs for DL-PVC are zero at edge

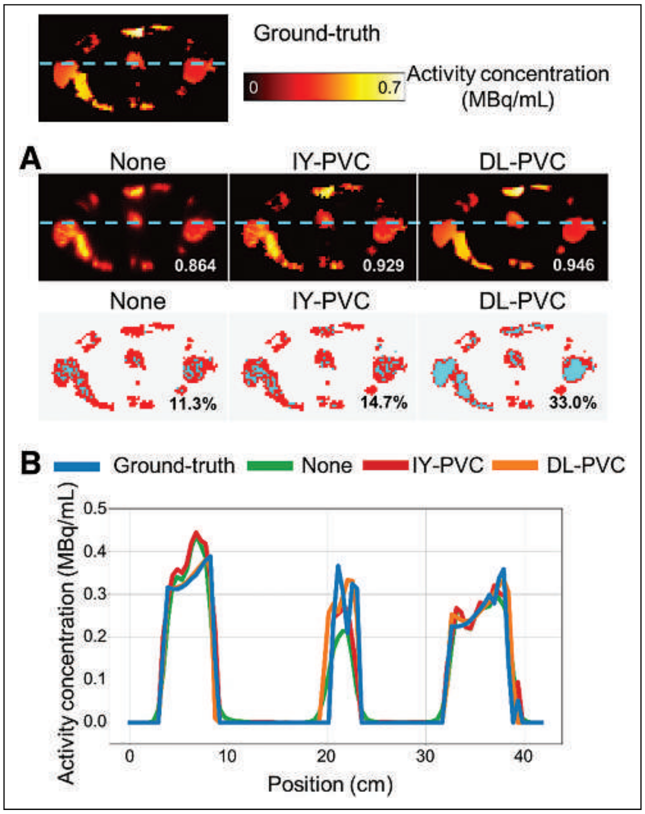

FIGURE 4. Visual performance analysis of different PVC approaches. (A) Top: axial slice of example activity distribution from test dataset reconstructed with *RR* without PVC, after IY-PVC, and after DL-PVC. White numbers correspond to SSIM values with respect to ground truth. Bottom: VAA maps of corresponding SPECT reconstructions with respect to ground truth. Red represents deviation in voxel's activity concentration by more than or equal to α=5%; cyan represents deviation smaller than α. Black numbers indicate VAA between SPECT reconstruction and ground truth. (B) Cross-sections indicated by cyan lines in SPECT reconstructions in A. SSIM = structural similarity index measure; VAA = voxel activity accuracy.

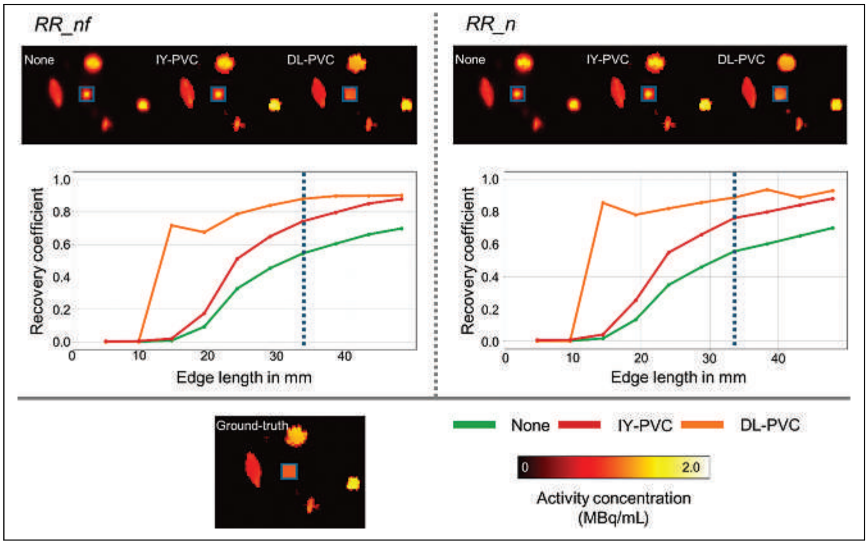

FIGURE 5. Investigation of minimum feature size. (Top) axial slices of reconstructed SPECT simulation without PVC, after IY-PVC, and after DL-PVC. (Center) RC as function of cube edge length. Dashed blue line corresponds to cube edge length in ground-truth image (bottom left).

lengths of 1 and 2 voxels (4.8 and 9.6 mm), increase rapidly from an edge length of 3 voxels (14.4 mm), and then continue to increase only slowly. Although DL-PVC does not perform adequately for structures with an edge length of less than 3 voxels (14.4 mm), it outperforms no PVC or IY-PVC for all cubes above this resolution limit.

Activity Concentration–Voxel Histograms

Figure 6 shows the activity concentration–volume histograms for the test dataset. For a perfect PVC, the histograms should closely resemble the ground-truth activity distribution. A close similarity between ground truth (blue) and DL-PVC (orange) can be observed at higher relative activity concentrations, starting at approximately 0.25. In general, substantial deviations can be seen for lower concentrations. Although, in the ground-truth activity distribution, a high proportion of voxels is associated with small concentrations between 0.05 and 0.25, the DL-PVC distribution has far fewer voxels in this concentration range. In contrast, there is a high fraction of voxels for DL-PVC in which no activity is present in comparison to the ground-truth activity distribution. This is due to the masking of the voxels displayed in the histogram based on the ground truth. The histograms of the SPECT reconstructions without PVC (green) and after IY-PVC (red) both show a distinct shift toward lower concentrations, indicating that DL-PVC outperforms IY-PVC on the voxel level.

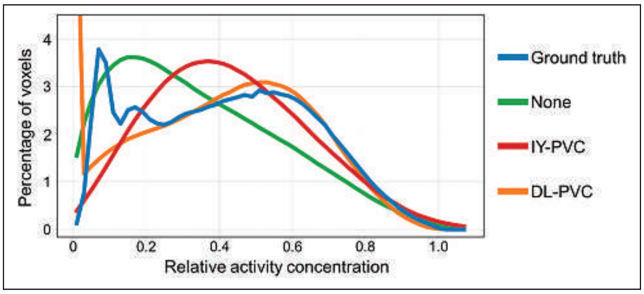

FIGURE 6. Activity concentration–volume histograms for test dataset. Depicted are ground-truth activity distribution and corresponding SPECT reconstructions (*RR_n*) without PVC, after IY-PVC, and after DL-PVC. For better visualization, *y*-axis has been truncated at 4.5%; thus, high percentage of 7.2% of voxels at relative concentration of 0 for DL-PVC is not shown in plot.

Phantom Measurement

Table 2 shows the evaluation metrics for the phantom measurements. The results for the ellipsoid phantom are given in the supplemental materials, as they are quite similar to the sphere. For all 3 phantoms, the highest SSIM and lowest NRMSE were achieved using IY-PVC. Although DL-PVC results in worse SSIM and NRMSE, there is still a clear improvement. In contrast, the highest VAA was obtained using DL-PVC for all 3 phantoms. Although the best RCs for the sphere were achieved with DL-PVC, the highest recoveries for the kidney cortex and ICRP110 kidney/spleen were achieved by IY-PVC.

Figure 7 shows the results of the phantom measurements. In the activity distributions (Fig. 7A) and the corresponding cross sections (Fig. 7B), a good visual agreement between the true activity distribution (blue) and the SPECT reconstruction after DL-PVC (orange) can be observed for sphere and ellipsoid (supplemental materials) geometry. For the reconstruction without PVC (green) and with IY-PVC (red), an overestimation of the activity at the edges and underestimation centrally can be observed for the sphere phantom. This artifact, known as Gibbs ringing, disappears after the application of DL-PVC. The VAA maps (Fig. 7A) underline this good agreement. Similar to Figure 4, the voxels at the edge of the object deviate from the true activity distribution to a greater extent. For the kidney cortex, significant deviations are observed between the DL-PVC SPECT acquisition and the true activity distribution. The image appears blurred, and the narrow structure on the right could not be restored. Hardly any cyan voxels are visible in the VAA map, indicating that the true activity distribution was poorly reproduced numerically. However, IY-PVC also does not provide satisfactory results for this phantom geometry. For the ICRP110-based kidney/spleen phantom, DL-PVC cannot correctly predict the activity difference between the 2 compartments comprising the kidney. On the other hand, the voxelwise activity quantification in the spleen is significantly better than that for IY-PVC.

The activity concentration–voxel histograms (Fig. 7C) show that for the sphere phantom and the ICRP110 kidney/spleen phantom, more voxels have the true activity concentration after DL-PVC than after IY-PVC. For the cortex phantom, the distribution of activity concentrations could at least be brought closer toward the true activity concentration.

DISCUSSION

In this work, we introduce a methodology for PVC of ^{177}Lu SPECT/CT imaging using DL. Using a dataset consisting of random activity distributions and the corresponding SPECT simulations, a neural network was trained to estimate ground-truth activity distributions from SPECT images.

From simulated data and ^{177}Lu phantom measurements, we demonstrated the superiority of the presented DL-PVC method

TABLE 2
Evaluation Metrics of Phantom Measurements for Reconstruction with *RR* (*RR_n*) Without PVC, After IY-PVC, and After DL-PVC

Phantom	PVC method	SSIM	NRMSE (%)	VAA (%)	RC
Sphere	None	0.855	18.68	19.64	0.729
	IY-PVC	0.940	11.90	24.32	0.841
	DL-PVC	0.929	14.16	65.50	0.894
ICRP110 kidney	None	0.686	21.70	1.19	0.583
	IY-PVC	0.833	14.92	1.40	0.695
	DL-PVC	0.770	19.09	3.23	0.653
ICRP110 spleen	None	0.847	18.37	12.49	0.729
	IY-PVC	0.953	10.33	19.79	0.877
	DL-PVC	0.889	16.29	28.40	0.820
Cortex	None	0.389	27.52	0.00	0.481
	IY-PVC	0.737	15.88	3.53	0.802
	DL-PVC	0.709	21.06	10.60	0.769

SSIM = structural similarity index measure; NRMSE = normalized root-mean-square error; VAA = voxel activity accuracy; RC = recovery coefficient.

over IY-PVC, an established method for PVC (5). This is despite the advantage that DL-PVC does not require any prior knowledge such as the spatial resolution of the reconstruction or a mask with the contours of the active volume. For spherelike geometries, DL-PVC achieved a recovery of the activity comparable to IY-PVC. However, Gibbs artifacts, which are typical for SPECT reconstructions with *RR,* and which were still clearly visible even after IY-PVC, could be efficiently corrected by DL-PVC. As a result, DL-PVC is clearly superior to IY-PVC in accurately restoring the true activity concentration at the voxel level, as is also reflected in the VAA. These artifacts could also be the reason why direct application of PVC to the entire FOV leads to a higher VAA than application of DL-PVC to smaller patches. For large objects, application of DL-PVC to smaller patches can no longer capture the entire object because of its $32 \times 32 \times 32$ voxel kernel. Therefore, the neural network may be less capable of correcting Gibbs artifacts for larger objects, resulting in a smaller VAA. In contrast, IY-PVC proved to be superior in the case of the kidney cortex geometry, as could be attributed to its small features, some of which fall below the minimum resolvable feature size of 3 voxels (14.37 mm) determined for DL-PVC. However, only the cube geometry was used in the resolution analysis of the different PVC methods. Therefore, these conclusions may not apply in the same way to nonuniformly shaped objects. Another important aspect when comparing DL-PVC and IY-PVC is that the activity masks for our IY-PVC analysis were based on the ground-truth activity distributions, an approach that is not feasible under real clinical conditions. This represents a clear bias in favor of IY-PVC in the context of our quantitative analysis and may explain the better performance of IY-PVC for the cortex phantom, as the complex structure was precisely specified there in the form of the segmentation mask. For a fairer comparison, activity masks could additionally be used as prior knowledge to improve DL-PVC, which could be the subject of future research.

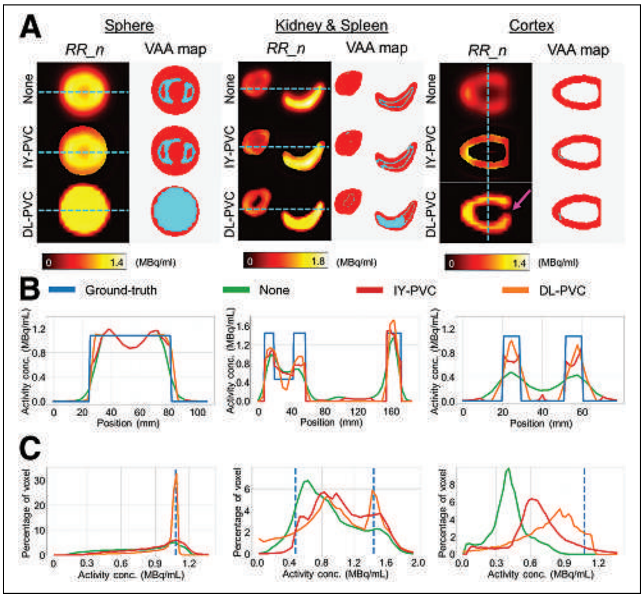

FIGURE 7. Phantom measurement. (A) SPECT reconstructions (*RR_n*) of 100-mL sphere phantom (axial slice), ICRP110-based kidney/spleen phantom (sagittal slice), and kidney cortex phantom (axial slice) without PVC, after IY-PVC, and after DL-PVC with corresponding VAA maps. Magenta arrow for cortex phantom indicates structure that could not be restored by DL-PVC. (B) Cross-sections indicated by cyan lines in SPECT reconstructions for ground-truth activity distributions and for SPECT without PVC, after IY-PVC, and after DL-PVC. (C) Corresponding activity concentration–voxel histograms; VAA = voxel activity accuracy.

There are also other potential ways to further improve the performance of DL-PVC. A notable limitation of the method in its current implementation is the relatively coarse voxel size of 4.8 mm. A subdivision of the FOV captured by the detectors into smaller pixels—and thus voxels—would leave more degrees of freedom for the neural network, especially in the transition regions between activity and background. This could in turn improve the performance of DL-PVC, especially for objects with small feature sizes such as the cortex phantom. On the other hand, a smaller voxel size will lead to a reduced signal-to-noise ratio per voxel, which could negatively impact the performance of DL-PVC. Because of the extensive computational demands of higher-resolution simulations and the limited memory capacity of the graphics processing unit used for training the neural network, we opted for the coarser resolution (4.8 mm) in this work. In future research, DL-PVC could be adapted for smaller voxel sizes such as 2.4 mm.

Although XCAT phantoms realistically describe the attenuation in a patient, there are still clear differences between the random activity distributions used for training DL-PVC and those observed in SPECT/CT measurements in patients undergoing radiopharmaceutical therapy. To close this gap and enable the method to be applied to clinical patient data, PET/CT or SPECT/CT patient images could be used to generate synthetic activity distributions. In the case of SPECT, however, the strongly pronounced partial-volume effect would have to be considered. Another limitation of the dataset used for training DL-PVC is that the variation of activity concentration within the random shapes is of relatively low frequency, thereby not demonstrating any sharp edges. These missing examples during training could explain why the performance of DL-PVC for the 2-compartment kidney of the ICRP110-based phantom is not yet optimal.

Our investigations have demonstrated that DL-PVC performs significantly better for noise-free (*RR_nf*) than for noisy (*RR_n*) datasets. Therefore, another avenue for improving DL-PVC would be to apply the method to denoised SPECT reconstructions. However, obtaining virtually noise-free projections in SPECT measurements is not realistic in a clinical setting, particularly for acquisitions a few days after administration of the radiopharmaceutical. An alternative approach would be to first denoise the SPECT data (e.g., using a second neural network) and subsequently apply DL-PVC.

At last, DL-PVC might be enhanced by further optimizing the network architecture. Although we have benchmarked various end-to-end U-Net architectures in this study, the exploration of novel convolutional neural network architectures represents a potential pathway to further improve the performance of DL-PVC.

Despite the investigation of many aspects within the scope of this work, there are still several open questions. For example, the choice of parameters for reconstructing the input data for our neural network needs further investigation. In our study, fixed numbers of iterations and subsets were used for both reconstructions (CASToR, 10 iterations and 2 subsets; STIR, 6 iterations and 6 subsets). However, the impact of these parameters on SPECT-based activity distributions is well known. Higher numbers of updates (iterations × subsets) have been shown to enhance recovery substantially, though at the expense of increased image noise (*3*). To address this issue, future studies could focus on assessing the performance of DL-PVC as a function of the number of iterations.

Another important aspect is the total activity in the FOV of the SPECT image. We determined the total activity by analyzing patients who received [^{177}Lu]Lu-PSMA-I&T or [^{177}Lu]Lu-DOTATATE radiopharmaceutical therapy at our institution. The latest acquisitions had been performed 4 d after injection of the radiopharmaceutical. When SPECT/CT is performed at even later time points (*32*), it needs to be investigated how such low activities—and thus low signal-to-noise ratios—affect the performance of DL-PVC.

Finally, an important investigation before the clinical application of DL-PVC in radiopharmaceutical therapy dosimetry is its impact on dosimetry calculations. Only by dosimetric evaluations on various organs and tumors using different PVC methods could one see what improvements DL-PVC can offer not only in terms of simplification of dosimetry calculation but also in terms of its accuracy.

CONCLUSION

In this study, a DL-PVC methodology for PVC of ^{177}Lu SPECT/CT imaging based on DL was introduced. Training of convolutional neural networks was based on a large dataset of Monte Carlo–simulated SPECT images of random activity distributions placed in different XCAT phantoms. From our investigations, we identified the optimal settings for DL-PVC in terms of activity conservation, input matrix size, and network architecture. Our analysis revealed that DL-PVC outperforms established PVC methods, such as IY-PVC, in restoring the true activity distribution without requiring resolution estimation or activity masking. Furthermore, tests on ^{177}Lu SPECT/CT measurements of 3-dimensionally printed phantoms of different geometries showed that although DL-PVC and IY-PVC achieve equivalent levels of activity recovery, DL-PVC can also correct other image artifacts such as Gibbs ringing and is therefore clearly superior at the voxel level. In summary, we have demonstrated that DL offers a wide range of improvement opportunities for PVC of quantitative ^{177}Lu SPECT/CT imaging. This is a first step toward a much-needed routine use of comparable techniques for dosimetry of radiopharmaceutical therapies.

DISCLOSURE

This study was funded by a grant from the German Research Foundation (Deutsche Forschungsgemeinschaft TR 1380/1-1) and partially by grants from the German Federal Ministry of Education and Research (13GW0357B), the Swedish Cancer Foundation (21 1754 Pj 01 H), and the Mrs. Berta Kamprad Foundation (FBKS 2019-44 and FBKS 2020-13). The funders had no role in the design of the study; in the collection, analyses, or interpretation of data; in the writing of the manuscript; or in the decision to publish the results. Michael Lassmann has received institutional grants from IPSEN Pharma, Nordic Nanovector, Novartis, and PentixaPharm. No other potential conflict of interest relevant to this article was reported.

ACKNOWLEDGMENTS

We thank Andrew Marsh for help with the generation of the random shapes and Anna-Lena Theisen for segmentation of the phantoms.

KEY POINTS

QUESTION: Is it possible to perform PVC for ^{177}Lu SPECT/CT using DL?

PERTINENT FINDINGS: From a database of 10,000 pairs of random activity distributions and realistic associated SPECT simulations, a U-shaped convolutional neural network was trained to perform PVC on ^{177}Lu SPECT images. SPECT images corrected with DL-PVC were found to resemble the underlying activity distribution much more closely than reconstructions without PVC or after application of IY-PVC.

IMPLICATIONS FOR PATIENT CARE: The potential of DL-PVC was demonstrated on ^{177}Lu SPECT/CT measurements of anthropomorphic phantoms, paving the way for clinical application. In the future, DL-based PVC could be an important tool to perform accurate patient-specific and voxel-based dosimetry for radiopharmaceutical therapies.

REFERENCES

1. Kratochwil C, Fendler WP, Eiber M, et al. Joint EANM/SNMMI procedure guideline for the use of ^{177}Lu-labeled PSMA-targeted radioligand-therapy (^{177}Lu-PSMA-RLT). *Eur J Nucl Med Mol Imaging.* 2023;50:2830–2845.
2. Sjögreen Gleisner K, Chouin N, Gabina PM, et al. EANM dosimetry committee recommendations for dosimetry of ^{177}Lu-labelled somatostatin-receptor- and PSMA-targeting ligands. *Eur J Nucl Med Mol Imaging.* 2022;49:1778–1809.
3. Tran-Gia J, Lassmann M. Characterization of noise and resolution for quantitative ^{177}Lu SPECT/CT with xSPECT Quant. *J Nucl Med.* 2019;60:50–59.
4. Hutton BF, Osiecki A. Correction of partial volume effects in myocardial SPECT. *J Nucl Cardiol.* 1998;5:402–413.
5. Erlandsson K, Buvat I, Pretorius PH, Thomas BA, Hutton BF. A review of partial volume correction techniques for emission tomography and their applications in neurology, cardiology and oncology. *Phys Med Biol.* 2012;57:R119–R159.
6. Tsui BM, Frey EC, Zhao X, Lalush DS, Johnston RE, McCartney WH. The importance and implementation of accurate 3D compensation methods for quantitative SPECT. *Phys Med Biol.* 1994;39:509–530.
7. Yang J, Huang SC, Mega M, et al. Investigation of partial volume correction methods for brain FDG PET studies. *IEEE Trans Nucl Sci.* 1996;43:3322–3327.
8. Jackson P, Hardcastle N, Dawe N, Kron T, Hofman MS, Hicks RJ. Deep learning renal segmentation for fully automated radiation dose estimation in unsealed source therapy. *Front Oncol.* 2018;8:215.
9. Chen Y, Goorden MC, Beekman FJ. Automatic attenuation map estimation from SPECT data only for brain perfusion scans using convolutional neural networks. *Phys Med Biol.* 2021;66:065006.
10. Rydén T, Van Essen M, Marin I, Svensson J, Bernhardt P. Deep-learning generation of synthetic intermediate projections improves ^{177}Lu SPECT images reconstructed with sparsely acquired projections. *J Nucl Med.* 2021;62:528–535.
11. Leube J, Gustafsson J, Lassmann M, Salas-Ramirez M, Tran-Gia J. Analysis of a deep learning-based method for generation of SPECT projections based on a large Monte Carlo simulated dataset. *EJNMMI Phys.* 2022;9:47.
12. Liu J, Yang Y, Wernick MN, Pretorius PH, King MA. Deep learning with noise-to-noise training for denoising in SPECT myocardial perfusion imaging. *Med Phys.* 2021;48:156–168.
13. Xie H, Liu Z, Shi L, et al. Segmentation-free PVC for cardiac SPECT using a densely-connected multi-dimensional dynamic network. *IEEE Trans Med Imaging.* 2023;42:1325–1336.
14. Li Z, Fessler JA, Mikell JK, Wilderman SJ, Dewaraja YK. DblurDoseNet: a deep residual learning network for voxel radionuclide dosimetry compensating for single-photon emission computerized tomography imaging resolution. *Med Phys.* 2022;49:1216–1230.
15. Begum NJ, Glatting G, Wester HJ, Eiber M, Beer AJ, Kletting P. The effect of ligand amount, affinity and internalization on PSMA-targeted imaging and therapy: a simulation study using a PBPK model. *Sci Rep.* 2019;9:20041.
16. Ljungberg M, Strand SE. A Monte-Carlo program for the simulation of scintillation camera characteristics. *Comput Methods Programs Biomed.* 1989;29:257–272.
17. Thielemans K, Tsoumpas C, Mustafovic S, et al. STIR: software for tomographic image reconstruction release 2. *Phys Med Biol.* 2012;57:867–883.
18. Merlin T, Stute S, Benoit D, et al. CASToR: a generic data organization and processing code framework for multi-modal and multi-dimensional tomographic reconstruction. *Phys Med Biol.* 2018;63:185005.
19. Segars WP, Sturgeon G, Mendonca S, Grimes J, Tsui BMW. 4D XCAT phantom for multimodality imaging research. *Med Phys.* 2010;37:4902–4915.
20. Ronneberger O, Fischer P, Brox T. U-Net: convolutional networks for biomedical image segmentation. arXiv website. https://arxiv.org/abs/1505.04597. Published May 18, 2015. Accessed March 25, 2024.
21. Zbontar J, Knoll F, Sriram A, et al. fastMRI: an open dataset and benchmarks for accelerated MRI. arXiv website. https://arxiv.org/abs/1811.08839. Published November 21, 2018. Accessed March 25, 2024.
22. Paszke A, Gross S, Massa F, et al. PyTorch: an imperative style, high-performance deep learning library. arXiv website. https://arxiv.org/abs/1912.01703. Published December 3, 2019. Accessed March 25, 2024.
23. Kingma DP, Ba J. Adam: a method for stochastic optimization. arXiv website. https://arxiv.org/abs/1412.6980. Published December 22, 2014. Accessed March 25, 2024.
24. Alom MZ, Hasan M, Yakopcic C, Taha T, Asari V. Recurrent residual convolutional neural network based on U-Net (R2U-Net) for medical image segmentation. arXiv website. https://arxiv.org/abs/1802.06955. Published February 20, 2018. Accessed March 25, 2024.
25. Oktay O, Schlemper J, Folgoc L, et al. Attention U-Net: learning where to look for the pancreas. arXiv website. https://arxiv.org/abs/1804.03999. Published April 11, 2018. Accessed March 25, 2024.
26. Wang Y, He Z, Xie P, et al. Segment medical image using U-Net combining recurrent residuals and attention. In: Su R, Liu H, eds. *Medical Imaging and Computer-Aided Diagnosis.* Springer; 2020:77–86.
27. Zhou Z, Rahman Siddiquee MM, Tajbakhsh N, Liang J. UNet++: a nested U-Net architecture for medical image segmentation. arXiv website. https://arxiv.org/abs/1807.10165. Published July 18, 2018. Accessed March 25, 2024.
28. Wang Z, Bovik AC, Sheikh HR, Simoncelli EP. Image quality assessment: from error visibility to structural similarity. *IEEE Trans Image Process.* 2004;13:600–612.
29. Thomas BA, Cuplov V, Bousse A, et al. PETPVC: a toolbox for performing partial volume correction techniques in positron emission tomography. *Phys Med Biol.* 2016;61:7975–7993.
30. Tran-Gia J, Lassmann M. Optimizing image quantification for ^{177}Lu SPECT/CT based on a 3D printed 2-compartment kidney phantom. *J Nucl Med.* 2018;59:616–624.
31. Tran-Gia J, Denis-Bacelar AM, Ferreira KM, et al. A multicentre and multinational evaluation of the accuracy of quantitative Lu-177 SPECT/CT imaging performed within the MRTDosimetry project. *EJNMMI Phys.* 2021;8:55.
32. Rinscheid A, Kletting P, Eiber M, Beer AJ, Glatting G. Influence of sampling schedules on [^{177}Lu]Lu-PSMA dosimetry. *EJNMMI Phys.* 2020;7:41.

SSTR Antagonists as Theranostic Option in Merkel Cell Carcinoma

Malte Kircher[1], Adriana Amerein[1], Mareike Augustin[2], Nic G. Reitsam[3], Johanna S. Enke[1], Marianne Patt[1], Georgine Wienand[1], Ralph A. Bundschuh[1], Christian H. Pfob[1], Constantin Lapa[1], and Alexander Dierks[1]

[1]Department of Nuclear Medicine, Faculty of Medicine, University of Augsburg, Augsburg, Germany; [2]Department of Dermatology, Faculty of Medicine, University of Augsburg, Augsburg, Germany; and [3]Department of Pathology, Faculty of Medicine, University of Augsburg, Augsburg, Germany

Merkel cell carcinoma is a rare, highly aggressive skin cancer. With multimodal treatment including chemo- and immunotherapy, the 5-y overall survival ranges from 14% to 62%, depending on the disease stage at diagnosis (*1*). New treatment options are therefore urgently needed. Given the overexpression of somatostatin receptors (SSTRs) due to its neuroendocrine features, SSTR-directed therapy could be a promising target in metastatic Merkel cell carcinoma (*2–4*).

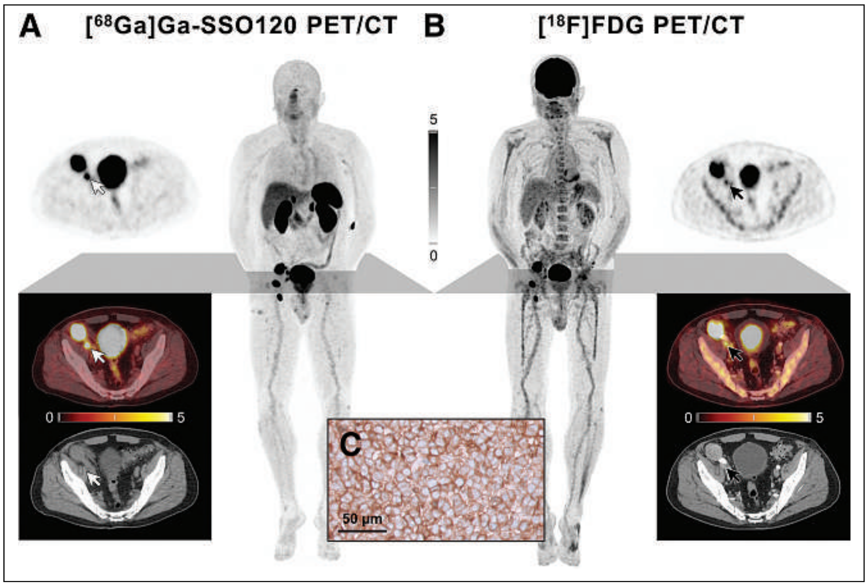

FIGURE 1. Maximum-intensity projections and axial sections of [^{68}Ga]Ga-SSO120 (A) and [^{18}F]FDG (B) PET/CT. Location of exemplary pelvic (right iliac) lymph node metastasis with SUV_{max} of 11.6 vs. 5.5 on [^{18}F]FDG PET is indicated by white and black arrows, respectively. Intensity scale bars are SUV. Immunohistochemistry showed high membranous SSTR expression on all tumor cells (score 3+; C).

To further investigate this potential, 2 clinical trials are already ongoing in which peptide receptor radionuclide therapy with SSTR agonists are being studied in combination with immunotherapy (GoTHAM trial, NCT04261855; iPRRT trial, NCT05583708).

Although various agonistic SSTR-targeting tracers have been established for years in metastatic Merkel cell carcinoma and other neuroendocrine tumor entities, tracers with antagonistic receptor interaction are recognized as a new, promising theranostic option, as they can achieve high tumor uptake and prolonged retention as compared with agonists (*5*).

We report the case of a 77-y-old man with recurrent metastatic Merkel cell carcinoma who underwent PET/CT with the ^{68}Ga-labeled SSTR antagonist SSO120 (international nonproprietary name: satoreotide trizoxetan; also known as NODAGA-JR11, OPS202, and IPN01070; injected dose, 160 MBq; scan acquisition, 60 min after injection) (*6,7*) to explore the possibility for peptide receptor radionuclide therapy (Fig. 1A). Informed consent was obtained from the patient. Compared with [^{18}F]FDG PET (Fig. 1B), a more intense tracer uptake and excellent tumor-to-background ratios were observed using [^{68}Ga]Ga-SSO120 PET, for example, in a pelvic (right iliac) lymph node metastasis with an SUV_{max} of 11.6 versus 5.5 on [^{18}F]FDG PET. The average SUV_{max} in the 6 measurable tumor lesions was 13.4 ± 5.0 with [^{68}Ga]Ga-SSO120 versus 9.5 ± 4.2 with [^{18}F]FDG PET. Given the still-localized tumor stage, the patient underwent surgery. High membranous SSTR expression on all tumor cells was confirmed by immunohistochemistry (score 3+; Fig. 1C).

In conclusion, PET/CT with SSTR antagonists could serve as a noninvasive read-out for tumor biology and allow selection of candidates for SSTR-directed peptide receptor radionuclide therapy. Further research, especially regarding advantages over agonistic vectors, is highly warranted.

Received Nov. 25, 2023; revision accepted Jan. 11, 2024.

For correspondence or reprints, contact Malte Kircher (malte.kircher@uk-augsburg.de).

DOI: 10.2967/jnumed.123.267124

DISCLOSURE

No potential conflict of interest relevant to this article was reported.

REFERENCES

1. Becker JC, Stang A, DeCaprio JA, et al. Merkel cell carcinoma. *Nat Rev Dis Primers.* 2017;3:17077.
2. Buder K, Lapa C, Kreissl MC, et al. Somatostatin receptor expression in Merkel cell carcinoma as target for molecular imaging. *BMC Cancer.* 2014;14:268.
3. Meier G, Waldherr C, Herrmann R, Maecke H, Mueller-Brand J, Pless M. Successful targeted radiotherapy with ^{90}Y-DOTATOC in a patient with Merkel cell carcinoma. *Oncology.* 2004;66:160–163.
4. Askari E, Moghadam SZ, Wild D, et al. Peptide receptor radionuclide therapy in Merkel cell carcinoma: a comprehensive review. *J Nucl Med Technol.* 2023;51:22–25.
5. Fani M, Mansi R, Nicolas GP, Wild D. Radiolabeled somatostatin analogs: a continuously evolving class of radiopharmaceuticals. *Cancers (Basel).* 2022;14:1172.
6. Zhu W, Cheng Y, Wang X, et al. Head-to-head comparison of ^{68}Ga-DOTA-JR11 and ^{68}Ga-DOTATATE PET/CT in patients with metastatic, well-differentiated neuroendocrine tumors: a prospective study. *J Nucl Med.* 2020;61:897–903.
7. Nicolas GP, Schreiter N, Kaul F, et al. Sensitivity comparison of ^{68}Ga-OPS202 and ^{68}Ga-DOTATOC PET/CT in patients with gastroenteropancreatic neuroendocrine tumors: a prospective phase II imaging study. *J Nucl Med.* 2018;59:915–921.

SSTR ANTAGONISTS IN MERKEL CELL CANCER • Kircher et al. 989

[^{18}F]Fluoroestradiol Uptake in Irradiated Lung Parenchyma and Draining Nodes

Audrey A. Rich[1], Neil K. Taunk[2], David A. Mankoff[1], Austin R. Pantel[1], and Sophia R. O'Brien[1]

[1]Division of Nuclear Medicine Imaging and Therapy, Department of Radiology, Hospital of the University of Pennsylvania, Philadelphia, Pennsylvania; and [2]Department of Radiation Oncology, Hospital of the University of Pennsylvania, Philadelphia, Pennsylvania

A 34-y-old woman with metastatic estrogen receptor (ER)–positive invasive ductal carcinoma of the left breast and biopsy-proven ER-positive sternal metastasis underwent mastectomy, chemotherapy, and radiation to the chest wall and sternum. [^{18}F]fluoroestradiol (FES) PET/CT 1 mo after radiation (Fig. 1A) demonstrated no abnormal uptake. [^{18}F]FES PET/CT 5 mo after radiation (Fig. 1B), after initiation of the ER-blocking agent tamoxifen, demonstrated new avid opacities anteriorly in the left lung (SUV_{max}, 7.7), as well as avidity in the hilar nodes (SUV_{max}, 5.6) and superior mediastinal node (SUV_{max}, 4.5), findings that were favored to represent the acute postradiation changes that can be seen 1–6 mo after completion of radiation (*1*). [^{18}F]FDG PET/CT 6.5 mo after radiation (Fig. 1C) demonstrated nearly complete resolution of the lung opacities and no abnormal lung or nodal uptake, consistent with resolving postradiation changes. Acute postradiation lung changes can progress to chronic fibrosis starting around 9 mo after radiation or can resolve, as in our patient (*1*). At 17 mo after radiation, the patient continued to have no evidence of disease.

Per appropriate use criteria, [^{18}F]FES is rarely appropriate for measuring response to therapy (*2*), and ER-blocking drugs interfere with [^{18}F]FES binding to tumor ER (*3*). This case, however, elucidates an [^{18}F]FES false-positive finding after successful ER blockade evidenced by elimination of physiologic uterine [^{18}F]FES avidity (Figs. 1A and 1B).

A retrospective study reported [^{18}F]FES-avid postradiation pulmonary changes without a clear mechanism and without [^{18}F]FES-avid regional nodes (*4*). Although the lungs have low-level ER (*5*) that may play a part in [^{18}F]FES uptake in atelectasis, increased uptake despite ER blockade suggests that [^{18}F]FES-avid postradiation lung changes are not due to ER binding and that associated [^{18}F]FES-avid regional nodes may be due to physiologic drainage of [^{18}F]FES from the lungs. This case provides some insight into the nature of false-positive changes on [^{18}F]FES PET/CT after pulmonary radiation and demonstrates the associated finding of [^{18}F]FES-positive draining nodes.

DISCLOSURE

Sophia O'Brien, Austin Pantel, and David Mankoff are consultants for GE Healthcare. No other potential conflict of interest relevant to this article was reported.

REFERENCES

1. Benveniste MF, Gomez D, Carter BW, et al. Recognizing radiation therapy-related complications in the chest. *Radiographics.* 2019;39:344–366.
2. Ulaner GA, Mankoff DA, Clark AS, et al. Summary: appropriate use criteria for estrogen receptor-targeted PET imaging with 16α-^{18}F-fluoro-17β-fluoroestradiol. *J Nucl Med.* 2023;64:351–354.
3. O'Brien SR, Edmonds CE, Lanzo SM, Weeks JK, Mankoff DA, Pantel AR. ^{18}F-fluoroestradiol: current applications and future directions. *Radiographics.* 2023;43: e220143.
4. Venema CM, de Vries EF, van der Veen SJ, et al. Enhanced pulmonary uptake on ^{18}F-FES-PET/CT scans after irradiation of the thoracic area: related to fibrosis? *EJNMMI Res.* 2019;9:82.
5. Mollerup S, Jorgensen K, Berge G, Haugen A. Expression of estrogen receptors alpha and beta in human lung tissue and cell lines. *Lung Cancer.* 2002;37:153–159.

Received Aug. 10, 2023; revision accepted Dec. 19, 2023.

For correspondence or reprints, contact Audrey Rich (audrey.rich@pennmedicine.upenn.edu) or Sophia O'Brien (sophia.obrien@pennmedicine.upenn.edu).

DOI: 10.2967/jnumed.123.266511

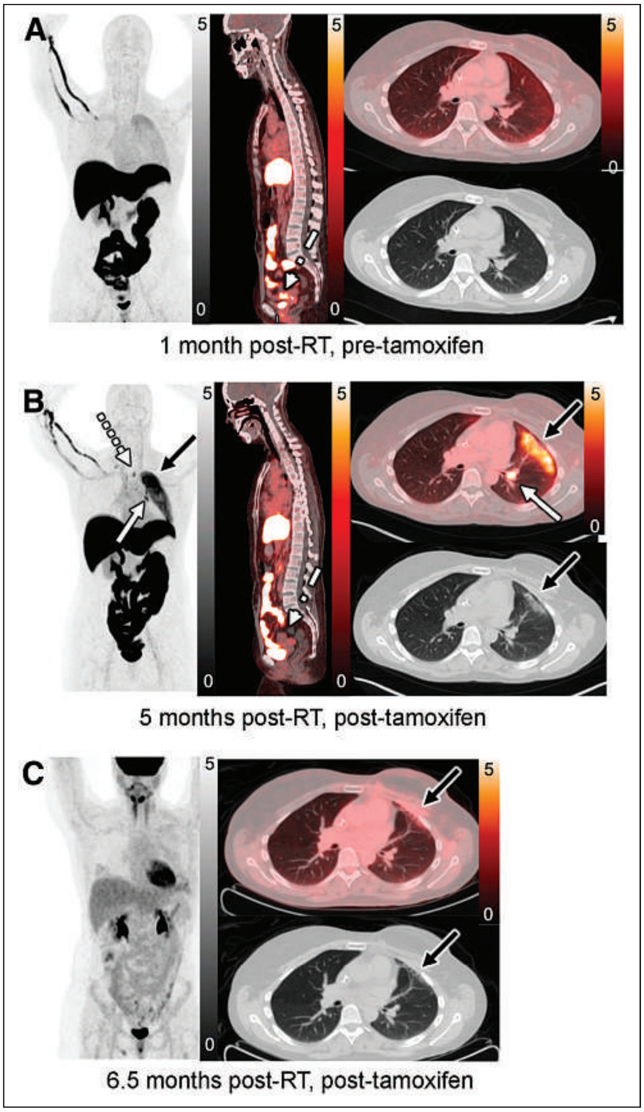

FIGURE 1. (A) [^{18}F]FES PET/CT (coronal PET maximum-intensity projection [MIP], sagittal fused PET/CT, axial fused PET/CT, and axial CT) 1 mo after radiation, showing no abnormal findings and physiologic uterine uptake (arrow). (B) [^{18}F]FES PET/CT (coronal PET MIP, sagittal fused PET/CT, axial fused PET/CT, and axial CT) 5 mo after radiation and after tamoxifen, showing new avid left lung opacities (black arrows), avid hilar nodes (solid white arrows), and avid superior mediastinal node (dashed white arrow), findings favored to represent acute postradiation changes. Because of ER blockade, no uterine uptake was seen (dotted-dashed white arrow). (C) [^{18}F]FDG PET/CT (coronal PET MIP, axial fused PET/CT, and axial CT) 6.5 mo after radiation, showing nearly resolved lung opacities (arrows) and no abnormal uptake, consistent with resolving postradiation changes. RT = radiation.

[^{18}F]FES-Avid Irradiated Lung • Rich et al. **991**

Is Permeability Surface Area Product of [^{18}F]Florbetaben Comparable to That of H_2O?

TO THE EDITOR: I have read with great interest the article by Fettahoglu et al. (*1*) on the comparison of early-phase amyloid PET tracer and [^{15}O]H_2O and found it to be highly captivating. The authors successfully demonstrated a linear relationship between early-phase [^{18}F]florbetaben and [^{15}O]H_2O with minimal bias.

Although numerous studies highlight the utility of early-phase amyloid PET, I was inclined to suggest the necessity for contrast correction (*2*) in early-phase images, as the first-pass extraction fraction of these tracers has not been estimated to be sufficiently high. For instance, the K_1 of [^{18}F]florbetaben was estimated to be 0.187 mL/mL/min in an Alzheimer disease patient, 0.216 mL/mL/min in a healthy control subject (*3*), and 0.226 mL/g/min in another estimation (*4*). Consequently, the first-pass extraction fraction (E) of [^{18}F]florbetaben would be approximately 0.5, considering a cerebral blood flow (F) of around 50 mL/100 g/min and $K_1 = FE$.

A low first-pass extraction fraction tracer would result in underestimation in regions with high cerebral blood flow, adhering to the Renkin–Crone equation, $E = 1-e^{-\frac{PS}{F}}$ (e is the Napier constant). The permeability surface area product (PS) of an extraction fraction of 0.5 at a cerebral blood flow of 50 mL/100 g/min is theoretically 35 mL/100 g/min. However, the data presented by Fettahoglu et al. (*1*) indicate that this underestimation was minimal, suggesting that the first-pass extraction fraction of amyloid tracers may be sufficiently high and comparable to that of H_2O. Consequently, there may be no need for contrast correction.

The perplexing dissociation between the PS value of water (more than 100 mL/100 g/min (*5*)) and the above-estimated PS value of [^{18}F]florbetaben (35 mL/100 g/min) may be attributed to various factors. First, estimating kinetic parameters using the least-square method might pose challenges. Second, there could be an overestimation of radioactivity in plasma. Third, the cerebral blood flow of the participants may be smaller than expected.

Mysteries persist in the kinetic analysis of nuclear medicine, and further investigations are essential to unravel and bridge these gaps.

DISCLOSURE

No potential conflict of interest relevant to this article was reported.

REFERENCES

1. Fettahoglu A, Zhao M, Khalighi M, et al. Early-frame [^{18}F]florbetaben PET/MRI for cerebral blood flow quantification in patients with cognitive impairment: comparison to an [^{15}O]water gold standard. *J Nucl Med.* 2024;65:306–312.
2. Kameyama M. Lassen's equation is a good approximation of permeability-surface model: new α values for ^{99m}Tc-HMPAO and ^{99m}Tc-ECD. *J Cereb Blood Flow Metab.* 2014;34:1157–1161.
3. Becker GA, Ichise M, Barthel H, et al. PET quantification of ^{18}F-florbetaben binding to β-amyloid deposits in human brains. *J Nucl Med.* 2013;54:723–731.
4. Heeman F, Yaqub M, Lopes Alves I, et al. Simulating the effect of cerebral blood flow changes on regional quantification of [^{18}F]flutemetamol and [^{18}F]florbetaben studies. *J Cereb Blood Flow Metab.* 2021;41:579–589.
5. Herscovitch P, Raichle ME, Kilbourn MR, Welch MJ. Positron emission tomographic measurement of cerebral blood flow and permeability-surface area product of water using [^{15}O]water and [^{11}C]butanol. *J Cereb Blood Flow Metab.* 1987;7:527–542.

Masashi Kameyama
Tokyo Metropolitan Institute for Geriatrics and Gerontology
Tokyo, Japan
E-mail: kame-tky@umin.ac.jp

DOI: 10.2967/jnumed.123.267291

Artificial Intelligence Algorithms Are Not Clairvoyant

TO THE EDITOR: Artificial intelligence (AI) systems, and computers in general, possess several advantages over humans. They have virtually perfect recall and are not subject to fatigue, mood variations, or environmental biases such as monitor contrast or room lighting conditions. However, they are not clairvoyant. Like us, they are limited by the information provided to them.

Thus, it was with a degree of concern and trepidation that I read the review article "Artificial Intelligence for PET and SPECT Image Enhancement" highlighted in the "State of the Art" section of the January 2024 issue of *The Journal of Nuclear Medicine* (*1*). The article states that "supervised deep-learning models have shown great potential in reducing radiotracer dose and scan times without sacrificing image quality and diagnostic accuracy." However, I believe this is fundamentally impossible. If photon counts are the source of information in a PET or SPECT image, then reducing scan time (and when not above peak noise-equivalent count rate, reducing dose) necessarily means less information about the patient currently being imaged.

I believe it is imperative to keep this simple fact in mind when promoting or evaluating the capabilities of any AI technique. AI models are generally trained using data or images from a separate cohort of patients. In this way, they can add information (prior information, therefore implicitly biased information) when processing a new image set. However, this should not be interpreted as additional information about the current patient. Only additional counts, or other sources of new information about the individual patient, can do that.

If I were to look at a noisy, low-resolution PET or SPECT image, the neural network in my head could imagine (based on prior experience) what it might look like if it were less noisy or had higher resolution. But this does not mean that I am better able to see the lesions that are otherwise buried in the noise. AI techniques can also "imagine," and provide for us, images that appear enhanced in their resolution and noise levels. However, this raises the question of what image enhancement is in the context of medical imaging. Prettier images do not equate to images with higher levels of useful information. Instead, an AI-enhanced image may mislead a radiologist into thinking the image data contain more information about the patient (commensurate with the perceived noise level and resolution) than is in fact present.

To its credit, the article in question also focuses on the need to switch the assessment from image quality to clinical benefit. This is important and appropriate but does not circumvent the fundamental information limitations described above. Instead, it essentially performs a kind of bait and switch. It is conceivable that an AI-based postreconstruction image enhancement technique might produce images that perform better prognostically (compared with a radiologist viewing the preprocessed images); however, that would mean that the AI algorithm was doing a better job than the radiologist when assessing the original noisy image and then enhancing the image in a way that made this assessment more obvious to the radiologist. At the extreme, the AI algorithm could simply place, for example, a big red X over the lesion. Fundamentally, though, this is lesion detection, not image enhancement. It is important to understand that this is what is going on, not actual improvement in image quality or information content. The radiologist is (effectively) no longer making the assessment. Moreover, applications to other clinical tasks (e.g., calculations of $\mathrm{SUV}_{\mathrm{max}}$, metabolic tumor volume, or total lesion glycolysis) may no longer be accurate.

When processing data to form images, we are often very careful about the type of prior information we incorporate. Generally, we understand the degree (and sometimes direction) of the bias that the prior information imposes (e.g., expectation maximization's constraint to positive solutions). However, we usually avoid biases in favor of gaining an image assay that is as independent and unbiased as possible. Thus, to the extent possible, the image assay provides completely new information.

For example, in PET image reconstruction of PET/MRI data, we generally forgo using the MRI as a prior even though these images will likely appear lower in noise and higher in resolution. This is because it is understood that biasing the PET image toward the MRI will result in a loss of PET information in precisely the regions containing the greatest amount of new information (i.e., the regions lacking mutual information between the PET and MRI).

There is some space within the context of PET and SPECT image reconstruction (or other means of generating medical images) where it might be appropriate to apply AI techniques. For PET raw or projection data, noise is distributed spatially along each projection. Thus, improving accuracy in one subregion along this projection can improve the accuracy in other regions. For this reason, using the MRI (or AI-derived prior information) during PET image reconstruction is to some extent defendable, whereas reducing scan time and then applying AI-based image enhancement after reconstruction simply is not.

In writing this letter, I do not intend to single out the aforementioned review article or its authors. They are merely reiterating an assumption that has become pervasive within the imaging community, that medical images can be improved without adding new information about the subject at hand. It is this seemingly unquestioned assumption that I am arguing against. Although it may be true in other contexts, it is not true for medical images that are used to assay a patient's condition. Given the potential risk to the quality of patient care, it has been my intent to be provocative, though hopefully not overly so. I apologize in advance to anyone who might construe this letter to be critical of their work. I have no such intent. I merely wish to kick-start a debate on this important topic.

DISCLOSURE

No potential conflict of interest relevant to this article was reported.

REFERENCE

1. Balaji V, Song TA, Malekzadeh M, Heidari P, Dutta J. Artificial intelligence for PET and SPECT image enhancement. *J Nucl Med.* 2024;65:4–12.

Bradley J. Beattie
Memorial Sloan Kettering Cancer Center
New York, NY
E-mail: beattieb@mskcc.org

DOI: 10.2967/jnumed.124.267377

REPLY: We appreciate the opportunity to respond to the commentary on our paper (*1*) by Dr. Beattie and to offer additional perspective on the topic of artificial intelligence (AI)–based PET and SPECT image enhancement.

Our article at no point suggested that AI is clairvoyant. Years of research before the introduction of AI models show that image enhancement techniques, including image denoising and partial-volume correction approaches, can lead to improved performance in terms of both image-based quantitative metrics and clinical tasks, such as lesion detectability (*2,3*). Although the advent of AI techniques has greatly expanded this arsenal, the general idea that improvements in resolution and noise could facilitate image interpretation predates the introduction of AI models to medical imaging.

Regularizers and priors tend to infuse some bias while reducing the variance. Instead of attempting to generate zero bias, which is a lofty goal, the PET image reconstruction community has traditionally relied on bias-variance studies that seek to identify as the winner a method that produces the lowest bias among a pool of competing approaches. We posit that AI-based image generation approaches for nuclear medicine could benefit from rigorous handling through bias-variance analyses (*4*).

Dr. Beattie raised concerns about learning from a population instead of a person. Fundamentally, priors rely on information that is not captured by the data. Many regularization techniques achieve this by encouraging certain local or nonlocal characteristics in an image (e.g., smoothness, edge preservation, sparsity in another domain, and cross-modality similarity). Bayesian approaches, on the other hand, assume knowledge of the prior distribution of the unknown variable or image. Deep neural networks are no different from these other non-AI methods in that they rely on inductive biases acquired from a training dataset to achieve good generalization in the validation cohort. Furthermore, many unsupervised or zero-shot image enhancement techniques use only the corrupt image for model training and do not rely on a population. Examples include the deep image prior, which leverages inductive biases intrinsic to deep convolutional architectures (*5*), and the Noise2Void approach, which uses blind-spot masking (*6*).

The relative merits and demerits of reconstruction-based approaches versus their postreconstruction counterparts raised by Dr. Beattie are also not specific to AI models. Regularizers and priors incorporated within reconstruction tend to be quantitatively more accurate than those used in denoising or deblurring frameworks applied after reconstruction. However, these methods have limited use for vast swaths of existing imaging data for which raw projection datasets may not be available. Since AI models heavily rely on data volume and variety, there is both a justifiable need for and interest in developing AI-based postreconstruction image enhancement approaches.

Hallucinations in AI-generated synthetic images are a justifiable concern of Dr. Beattie's. Notably, these are a threat to both reconstruction-based and postreconstruction AI methods alike (*7*). The only way to address these concerns is through a rigorous combination of image-based validation (where ground truth information is available and used to detect synthetically introduced spurious features) and clinical task-based validation that can affect the potential impact on clinical decision-making.

The medical imaging community has been empowered by AI tools relatively recently, and it is critical to use these methods responsibly and in ways that maximize clinical benefit. In conclusion, therefore, we would like to reiterate a key premise of the review article that image quality metric–based validation and clinical task–based validation need to go hand in hand to ensure the robustness and trustworthiness of AI approaches applied to clinical medicine.

DISCLOSURE

Joyita Dutta received NIH funding (grants R01AG072669 and R03AG070750) for AI. No other potential conflict of interest relevant to this article was reported.

REFERENCES

1. Balaji V, Song TA, Malekzadeh M, Heidari P, Dutta J. Artificial intelligence for PET and SPECT image enhancement. *J Nucl Med.* 2024;65:4–12.
2. Kim JH, Ahn IJ, Nam WH, Ra JB. An effective post-filtering framework for 3-D PET image denoising based on noise and sensitivity characteristics. *IEEE Trans Nucl Sci.* 2015;62:137–147.
3. Kato H, Shimosegawa E, Oku N, et al. MRI-based correction for partial-volume effect improves detectability of intractable epileptogenic foci on ^{123}I-iomazenil brain SPECT images. *J Nucl Med.* 2008;49:383–389.
4. Cui J, Gong K, Guo N, et al. PET image denoising using unsupervised deep learning. *Eur J Nucl Med Mol Imaging.* 2019;46:2780–2789.
5. Lempitsky V, Vedaldi A, Ulyanov D. Deep image prior. In: *IEEE/CVF Conference on Computer Vision and Pattern Recognition.* IEEE; 2018:9446–9454.
6. Song TA, Yang F, Dutta J. Noise2Void: unsupervised denoising of PET images. *Phys Med Biol.* 2021;66:214002.
7. Bhadra S, Kelkar VA, Brooks FJ, Anastasio MA. On hallucinations in tomographic image reconstruction. *IEEE Trans Med Imaging.* 2021;40:3249–3260.

Joyita Dutta*
Vibha Balaji
Tzu-An Song
University of Massachusetts Amherst
Amherst, Massachusetts
**E-mail: jdutta@umass.edu*

DOI: 10.2967/jnumed.124.267541

2024 ACNM/SNMMI **HOT TOPICS** Webinar Series

SNMMI and ACNM are excited to announce the lineup for the 2024 Hot Topics Webinar Series. **These informative webinars will take place at 12:00 pm ET on the second Tuesday of each month and are complimentary for ACNM and SNMMI members.**

- **History of Nuclear Medicine Technology**
  On Demand | *Fred Fahey*
- **AI in Nuclear Medicine: State of the Union**
  On Demand | *Katherine Zukotynski*
- **Prostate Radioligand Therapy Prior to Chemotherapy**
  On Demand | *Oliver Sartor*
- **PET/MR for Pediatrics**
  On Demand | *Helen Nadel*
- **Evolving Landscape of Prostate Cancer Imaging**
  On Demand | *François Bénard*
- **The Evolution of PRRT for NET–Y90, Lu177, Ac225**
  June-SNMMI AM | *Lisa Bodei*
- **Advancing Precision Therapeutics in Dementia–How Does Imaging Fit In?**
  July 9 | *Sandra Black*
- **Contemporary Approach to PET Myocardial Perfusion Imaging**
  August 13 | *Panithaya Chareonthaitawee*
- **ER/PR/HER2-Targeted Imaging for Breast Cancer**
  September 10 | *Farrokh Dehdashti*
- **PET for Histiocytosis/ Erdheim Chester Disease**
  October 8 | *Sonia Mahajan*
- **What is New in Infection Imaging?**
  November 12 | *Ora Israel*
- **Prostate Cancer Imaging Agents–Is There a Difference?**
  December 10 | *Wolfgang Weber*

SNMMI SOCIETY OF NUCLEAR MEDICINE & MOLECULAR IMAGING

ACNM American College of Nuclear Medicine

Register today!
www.acnmonline.org/webinars

SNMMI Qualified Systems Personnel Training Program (QSPTP)

ENHANCE YOUR EXPERTISE IN RADIOPHARMACEUTICAL SCIENCES

SNMMI

Defining the competencies in the release of manufactured radiopharmaceuticals

THROUGH DIDACTIC AND HANDS-ON LEARNING, THIS COURSE IS DESIGNED TO MEET THE FOLLOWING LEARNING OBJECTIVES:

- Provide theoretical knowledge and practical experience needed to assume responsibility for small scale manufacture, quality control, and release of radiopharmaceuticals
- Provide cross-training for chemists and nuclear pharmacists:
  - in manufacturing and quality assurance
  - in synthesis and pharmaceutical formulation of radiopharmaceuticals
- Educate learners on regulatory compliance requirements associated with radiopharmaceutical manufacturing
- Understand application of radiopharmaceuticals
- Understand the components of research applications, including IND and RDRC processes

The didactic course may be taken independently of the hands-on component. The hands-on component requires the completion of the didactic course prior to participation.

The program is designed for students with the following educational background: PharmD, B.S. or M.S. Pharmacists or B.S. or M.S. in Chemistry (or other science related degree).

For more information, visit ***snmmi.org/qsptp***

REACH EVEN GREATER HEIGHTS WITH CARDIAC PET IMAGING

RUBY™ partners with you to help establish and grow your cardiac PET program today – and well into the future. Our RUBY-FILL® (Rubidium Rb 82 Generator) and RUBY Rubidium Elution System™ are supported by our comprehensive line of offerings, including financial modeling, reimbursement consultancy, education, and marketing expertise – as well as 24-hour customer assistance to ensure your growing PET practice runs smoothly and efficiently.

Isn't it time to discover how far you can soar?

Visit booth #517 to learn more

INDICATION FOR USE:

RUBY-FILL is a closed system used to produce rubidium Rb 82 chloride injection for intravenous use. Rubidium Rb 82 chloride injection is a radioactive diagnostic agent indicated for Positron Emission Tomography (PET) imaging of the myocardium under rest or pharmacologic stress conditions to evaluate regional myocardial perfusion in adult patients with suspected or existing coronary artery disease. (1)

WARNING: HIGH LEVEL RADIATION EXPOSURE WITH USE OF INCORRECT ELUENT AND FAILURE TO FOLLOW QUALITY CONTROL TESTING PROCEDURE

Please see full prescribing information for complete boxed warning

High Level Radiation Exposure with Use of Incorrect Eluent

Using the incorrect eluent can cause high Strontium (Sr 82) and (Sr 85) breakthrough levels (5.1)

- **Use only additive-free 0.9% Sodium Chloride Injection USP to elute the generator (2.5)**
- **Immediately stop the patient infusion and discontinue the use of the affected RUBY-FILL generator if the incorrect solution is used to elute the generator (4)**
- **Evaluate the patient's radiation absorbed dose and monitor for the effects of radiation to critical organs such as bone marrow (2.9)**

Excess Radiation Exposure with Failure to Follow the Quality Control Testing Procedure

Excess radiation exposure occurs when the levels of Sr 82 or Sr 85 in the Rubidium Rb 82 Chloride injection exceed specified limits. (5.2)

- **Strictly adhere to the generator quality control testing procedure (2.6)**
- **Stop using the generator if it reaches any of its Expiration Limit. (2.7)**

The risk information provided here is not comprehensive. Please visit RUBY-FILL.com for full Prescribing Information including BOXED WARNING. You are encouraged to report negative side effects of prescription drugs to the FDA. Visit www.fda.gov/Safety/MedWatch or call 1-800-FDA-1088.

Jubilant DraxImage Inc. dba Jubilant Radiopharma™
16751 Trans-Canada Highway, Kirkland, Quebec, Canada H9H 4J4
Phone: 1.888.633.5343 / 514.630.7080
www.jubilantradiopharma.com
© 2023-US-RUBY-00002

RUBY FILL®
RUBIDIUM Rb82 GENERATOR

JUBILANT
RADIOPHARMA

6/24

The Journal of Nuclear Medicine

June 2024 ▪ Vol. 65 ▪ Pages 825–994